



Garibaldi Geothermal Energy Project - Phase 1

Final Report

Geoscience BC Report 2021-08

Grasby, S.E., Ansari, S.M., Barendregt, R.W., Borch, A., Calahorrano-DiPatre, A., Chen, Z., Craven, J.A., Dettmer, J., Gilbert, H., Hanneson, C., Harris, M., Hormozzade, F., Leiter, S., Liu, J., Muhammad, M., Quane, S.L., Russell, J.K., Salvage, R.O., Savard, G., Tschirhart, V., Unsworth, M.J., Vigouroux-Caillibot, N., Williams Jones, G., and Williamson, A., Vestrum Z.E.

The Garibaldi Volcanic Belt Geothermal Energy Project

Phase 1 Final Report

INDEX

Chapter 1 – The Garibaldi Volcanic Belt Geothermal Energy Project.....	1
Grasby, S.E., Ansari, S.M., Barendregt, R.W., Borch, A., Calahorrano-DiPatre, A., Chen, Z., Craven, J.A., Dettmer, J., Gilbert, H., Hanneson, C., Harris, M., Hormozzade, F., Leiter, S. ³ , Liu, J., Muhammad, M., Quane, S.L., Russell, J.K., Salvage, R.O., Savard, G., Tschirhart, V., Unsworth, M.J., Vigouroux-Caillibot, N., Williams Jones, G., and Williamson, A., Vestrum Z.E.	
Chapter 2 – Bedrock Mapping Results for the Mount Meager Geothermal Research Initiative.....	7
Harris, M., Russell, J.K.	
Chapter 3 – Fracture system analyses of the Mount Meager area.....	34
Chen, Z., Grasby, S.E., Liu, X.	
Chapter 4 – Gravity Survey at Mt. Meager Volcanic Complex: 2019-2020	49
Calahorrano-Di Patre, A.E., Williams-Jones, G.	
Chapter 5 – Final report on the 2019-2020 broadband magnetotelluric study at Mount Meager: Implications for structure of the hydrothermal and magmatic system	79
Unsworth, M.J., Hanneson, C.S., Williamson A.R., Vestrum, Z.E.	
Chapter 6 – Overview of the 2019 Audiomagnetotelluric Survey of the Mount Meager Geothermal Reservoir	147
Craven, J.A.; Hormozzade, F., Tschirhart, V.; Ansari, M., Bryant, R. and Montezadian, D.	
Chapter 7 – Mount Meager Passive Seismic Monitoring.....	167
Gilbert, H., Dettmer, J., Savard, G., Klaasen, S., Fichtner, A., and Su, H.	
Chapter 8 – Applications of structural geology to the exploration of geothermal systems, Mt. Meager, BC.....	177
Muhammad, M., Williams-Jones, G., Barendregt, R.W.	
Chapter 9-- Physical and chemical characteristics of hydrothermally altered volcanic deposits Cracked Mountain, Mount Meager Volcanic Complex, British Columbia.....	242
Leiter, S. and Russell, J. K.	
Chapter 10-- Distribution and Age of the Cheakamus Basalts, Garibaldi Volcanic Belt, British Columbia.....	254
Borch, A., Russell, J.K., Barendregt, R., Quane, S.L., Wilson, A.	

Chapter 1 – The Garibaldi Volcanic Belt Geothermal Energy Project

Grasby, S.E.¹, Ansari, S.M.¹, Barendregt, R.W.², Borch, A.³, Calahorrano-DiPatre, A.⁴, Chen, Z.¹, Craven, J.A.¹, Dettmer, J.⁵, Gilbert, H.⁵, Hanneson, C.⁶, Harris, M.³, Hormozzade, F.⁷, Leiter, S.³, Liu, J.¹, Muhammad, M.⁴, Quane, S.L.⁸, Russell, J.K.³, Salvage, R.O.⁵, Savard, G.⁵, Tschirhart, V.¹, Unsworth, M.J.⁶, Vigouroux-Caillibot, N.⁹, Williams Jones, G.⁴, and Williamson, A.¹⁰, Vestrum Z.E.⁶

¹Geological Survey of Canada, ²The University of Lethbridge, ³University of British Columbia, ⁴Simon Fraser University, ⁵University of Calgary, ⁶University of Alberta, ⁷Carleton University, ⁸Sea to Sky Fire & Ice Geopark, ⁹Douglas College, ¹⁰Minerva Intelligence

Introduction

Canada seeks to meet a climate target of net zero CO₂ emissions by 2050, requiring the development of renewable energy resources. Compared to other renewables, geothermal energy has numerous advantages, the most important of which is the ability to provide a stable baseload-power supply without the need for energy-storage solutions, as compared to intermittent sources such as wind or solar. However, this greater reliability of supply comes with much greater exploration risk. While it is relatively easy to determine where it is windy and sunny, defining a hot aquifer in the deep subsurface ultimately requires expensive drilling operations. Geoscience research is essential to develop new approaches to help reduce this exploration risk.

In response to the Energy Crisis of the 1970's, Canada initiated a Geothermal Energy Program that ran from 1975–1985 and provided the first insight into the thermal regime of Canada (Jessop, 2008; Grasby et al., 2011). This work included defining some of the highest temperature geothermal systems in Canada, those related to hot sedimentary basins (found in the Northwest Territories, Yukon, British Columbia [BC], Alberta and Saskatchewan), as well as volcanic belts (Yukon and BC). As part of this earlier program, geothermal-exploration wells were drilled in the Garibaldi volcanic belt of southwestern BC, near active thermal springs on the southern flank of Mount Meager. This drilling defined high-temperature geothermal resources, exceeding 250 °C (Adams and Moore, 1987; Clark et al., 1982; Jessop, 2008; Witter, 2019). However, the project was never economically viable because flow rates were too low to justify the development costs. While a technical success, in that the exploration program discovered a high temperature reservoir, development of the site was limited by the low permeability rocks at depth. Subsequent industry drilling defined higher permeability zones, but these have not been produced to date given the large hydraulic head differential for the well pads used (Witter, 2019).

With renewed interest in geothermal potential in Canada, a research project was initiated to help reduce exploration risk for geothermal energy associated with volcanic systems. The main aim of this work is to develop new techniques and tools that can be employed to predict the occurrence of hot and permeable aquifers in the sub-surface. To this end, a multidisciplinary geoscience field program, the Garibaldi Volcanic Belt Geothermal Energy Project, was initiated. The first phase reported on here was conducted at Mount Meager in the summer of 2019, with a reduced program in 2020 due to covid-19 restrictions. This report summarises the field program activities, the range of data collected as well as the raw data collected in Phase 1. Phase 2 of the project will integrate data reported here into new resource assessment models along with additional data collection in the broader Garibaldi Belt. Fully interpreted results will be presented in peer reviewed scientific journals.

Methods

Access to the Mount Meager area has been limited since a 53-million-cubic-meter landslide in 2010 (Canada's largest historic event of its kind) destroyed bridges on old logging roads. Given this, a mainly helicopter-supported field program was operated. Over 400 person-days were spent in the field, during field programs in 2019 and 2020. For 2019 a field camp was established at the Innergex bunkhouse along with fly camps. Daily set-outs by helicopter were conducted as well as work from logging roads. The field program in 2019 focused on establishing an array of seismometers (UofC), an array of magnetotelluric (MT) stations focused on the shallow geothermal system (GSC) as well as the deeper volcanic plumbing (UofA), a gravity survey (SFU), bedrock mapping (UBC), fracture and rock-property studies (GSC) (Figure 1). Covid-19 had significant impact on the 2020 field program, including cancelling a planned field camp. Alternative measures were taken to allow field parties to conduct work, while meeting all public health and safety measures. This included separate day trips for each group, staying in individual hotel rooms, and eating separately. The 2020 field program was focused on the north flank of Mount Meager within the area of the Upper Lillooet Provincial Park under a BC Parks research licence. An array of magnetotelluric (MT) stations, gravity survey (SFU), bedrock mapping (UBC), and fracture and rock-property studies were conducted, largely focused on filling data gaps from the 2019 field season. While no development is planned within the park, access to the park area allowed 3-D imaging through the Mount Meager massif to enhance resolution of geothermal systems on the south flank.

Detailed bedrock mapping was conducted to enhance understanding of the spatial distribution of volcanic rocks that form the Mount Meager Volcanic Complex, with a particular focus on rock types with preferential reservoir properties in Chapter 2. Field mapping included recording rock-property observations at 962 field stations and production of 4 new geological maps. These results support the development of hydrogeological models for bulk-rock permeability to better characterize potential fluid flow at depth, and in the future petrologic data will be integrated with MT data to support magma depth predictions.

In order to develop an understanding of the nature of fracture systems and their potential influence on bulk-rock permeability, fieldwork was conducted to measure spatial distribution and variability in fracture orientation and fracture density (over 1200 measurements) as discussed in Chapter 3. This was combined with remote-sensing image analyses and artificial intelligence to define trends, orientations and densities of lineaments through the study area. Identified lineaments were ground-truthed as part of the geological and geophysical mapping program to assess if they represent higher permeability fracture systems. Determination of the regional stress field is more complex in areas of high topographic relief, as the free surface cannot be assumed to be flat. Regional data helped to refine the tensile portion of the regional-stress field, providing insight into preferred fluid-flow directions. In phase 2 the current stress system will be integrated with geoscience information (magnitude, location and sense of motion) from historical records of earthquakes in the study area and surrounding vicinities, and will be constrained by deformation patterns and additional geoscience information from previously drilled boreholes.

Gravity measurements were taken at 122 stations around the Mount Meager Volcanic Complex with the aim of mapping its internal structure (Chapter 4). The network comprises both a dense distribution of sites near the volcanic edifice and more broadly spaced stations with increasing distance from the mountain. This distribution seeks to investigate the deep magmatic structures (depth >10 km) by comparing data from distal stations with data from the proximal dense network of stations. Smaller scale structures, such as the hydrothermal system of Mount Meager, were mapped by analyzing gravity change between stations closer to the edifice. In phase 2 inverse modeling will provide constraints for MT inverse modelling.

Collection of MT data was aimed at greatly expanding coverage beyond that collected in the 1980s (Jones and Dumas, 1993), using modern and more field-portable instruments (Chapters 5 and 6). Given the rugged topography, however, stations were largely restricted to ridges, valley bottoms, and existing road networks. The MT data collection in 2019 at the Mount Meager Volcanic Complex was performed on two spatial scales. A set of 23 MT measurements was taken by the UofA MT group to understand the deeper structure of the system, which requires longer recording time and consequently reduced the total number of measurement locations (Chapter 5). The deeper focus MT survey was designed to image pathways that carry fluids to the geothermal reservoir and the fumaroles on Job Glacier. These deep MT measurements will also define the size and content of any magma bodies beneath the volcano. In the region of the geothermal reservoir on the south side of Pylon Peak, MT measurements were made in a dense grid of 84 stations by the GSC MT group to study the details of the geothermal reservoir (Chapter 6). The goal of the survey was to use the new MT data to determine permeability variations in the subsurface and link these to flow rates observed at the surface. In the 2020 field season an additional 12 deep focused MT stations were collected along the north flank of Mount Meager. Final modeling of MT results will be based on integrating rock property measurements (Chapters 2, 3) and gravity data (Chapter 4) to produce optimized 3D inversion models. Likewise, the AMT data (Chapter 6) will be integrated with MT data to produce a single integrated 3D inversion.

Fifty-nine passive-seismic sites, each consisting of a Hawk field-station unit (INOVA Geophysical) connected to 10 Hz three-component geophones, were established for characterizing crustal structures associated with the area of high geothermal heat and how those vary within the geothermal system (Chapter 7). The observations from this array will be used to identify the distribution of low seismic-wave speeds, which can mark the distribution of fractures that serve as pathways for geothermal fluids, as well

as magma chambers. Detecting and locating the local seismicity during this brief seismic deployment provided constraints on the pattern of faults and fractures within Mount Meager that allow for fluid circulation through this geothermal system. The Hawk systems were also tested for their ability to record more distant earthquakes and whether those signals can be used to measure structures within the Garibaldi volcanic belt.

The major geologic structures controlling the geothermal fluid pathway were also documented through structural field geology mapping of faults, folds, and fractures of basement and young volcanic units (Chapter 8). As well, paleomagnetic directions of basement and young volcanic units were used to identify and verify the structural geology features and surface geology mapped. Geochronological dating for the drilled paleomag samples were also used to reconstruct the potential pre-deformed stage of structural geology features and define sequence of deformation events.

Hydrothermal alteration characteristics of the geothermal systems at Mount Meager were examined (Chapter 9) providing physical, mineralogical, and chemical characterization of hydrothermally altered volcanic rocks. These results provide insight into potential alteration along flow paths as well as estimates of temperature of alteration.

A general lack of age dating means the eruptive history of the Garibaldi Belt is poorly constrained. While age of eruption does not correlate directly with geothermal potential, more accurate age dating helps to refine the overall heat flow history of the region. Detailed study was thus conducted on the Cheakamus basalts, group of Quaternary basaltic lavas in the Garibaldi volcanic belt. Based on stratigraphic relationships, the Cheakamus basalts are some of the youngest volcanic rocks within the GVB. Work was conducted to understand the distribution, volume, eruptive duration, and age of the Cheakamus basalts (Chapter 10).

Beyond the main project activities, the field camp also supported establishment of landslide monitoring equipment in addition to examination of volcanic fumaroles in the ice caves on Job Glacier. As these are not directly part of the research activity, they are not reported on further.

Data collected

Significant new data have been collected as part of this research activity. Data are either included as tables within this report, or as online resources from GeoScience BC. Table 1 provides an indication of data available.

Report section	Data type	Source
Chapter 2	1) Bedrock map polygons 2) Rock geochemistry	1) GeoScience BC website 2) This report
Chapter 3	Fracture orientation/spacing	This report
Chapter 4	Gravity measurements	This report
Chapter 5	MT time series data	GeoScience BC website

Chapter 6	MT time series data	GeoScience BC website
Chapter 7	1) Passive seismic data 2) Distributed acoustic sensor data	GeoScience BC website
Chapter 8	Paleomagnetic data	This report
Chapter 9	1) Mineralogy 2) Rock physical properties	1) This report 2) This report

Acknowledgements

The authors gratefully acknowledge the support of T. Jenkins and M. Bruce of Lil'wat First Nation in providing guidance in the field and logistical planning and wildlife monitoring. Pilots M. Accurso, D. Vincent and R. Slinger of No Limits Helicopters provided expert service. Innergex Renewable Energy Inc. provided significant support to the field program through access to their field bunkhouse. Wayne Russell of Innergex was of great assistance throughout our field stay. Field assistance was provided by K. Biegel, R. Bryant, J. Smale, H. Su, A. Williamson and A. Wilson. Funding for this project was provided by Geoscience BC and Natural Resources Canada. The University of Alberta group was supported by funding from the Natural Sciences and Engineering Council of Canada (NSERC) through a Canada First Research Excellence Fund (CFREF) award (Future Energy Systems) and a Discovery Grant to M. Unsworth. The University of Calgary group was supported by funding from the Canada Research Co-ordinating Committee through a New Frontiers in Research Fund award and a Discovery Grant to J. Dettmer. Financial assistance was provided to R. Salvage by the Microseismic Industry Consortium. Heather King provided a helpful review and comments to improve this contribution.

References

- Adams, M.C. and Moore, J.N. (1987) Hydrothermal alteration and fluid geochemistry of the Meager Mountain geothermal system, British Columbia. 287, 720-755.
- Clark, I.D., Fritz, P., Michel, F.A. and Souther, J.G. (1982) Isotope hydrogeology and geothermometry of the Mount Meager geothermal area. 19, 1454-1473.
- Grasby, S.E., Allen, D.M., Bell, S., Chen, Z., Ferguson, G., Jessop, A., Kelman, M., Ko, M., Majorowicz, J., Moore, M., Raymond, J. and Therrien, R. (2011): Geothermal energy resource potential of Canada; Geological Survey of Canada, Open File 6914, 322 p., <<https://doi.org/10.4095/288745>>[Oc to ber2019].
- Jessop, A. (2008): Review of National Geothermal Energy Program, Phase 2 – geothermal potential of the Cordillera; Geological Survey of Canada, Open File5906, 86 p., <<https://doi.org/10.4095/225917>>[Oc to ber2019].
- Jones, A.G. and Dumas, I. (1993): Electromagnetic images of a volcanic zone; Physics of the Earth and Planetary Interiors, v. 81, no. 1–4,p. 289–314, <[https://doi.org/10.1016/0031-9201\(93\)90137-X](https://doi.org/10.1016/0031-9201(93)90137-X)>[Oc to ber2019].

Witter, J. (2019): South Meager geothermal project – new perspectives from recently unearthed data; Geoscience BC, Report2019-07, 5 p., URL<<http://www.geosciencebc.com/i/pdf/Report-2019-07-Innovate-Geothermal.pdf>>[November 2019].

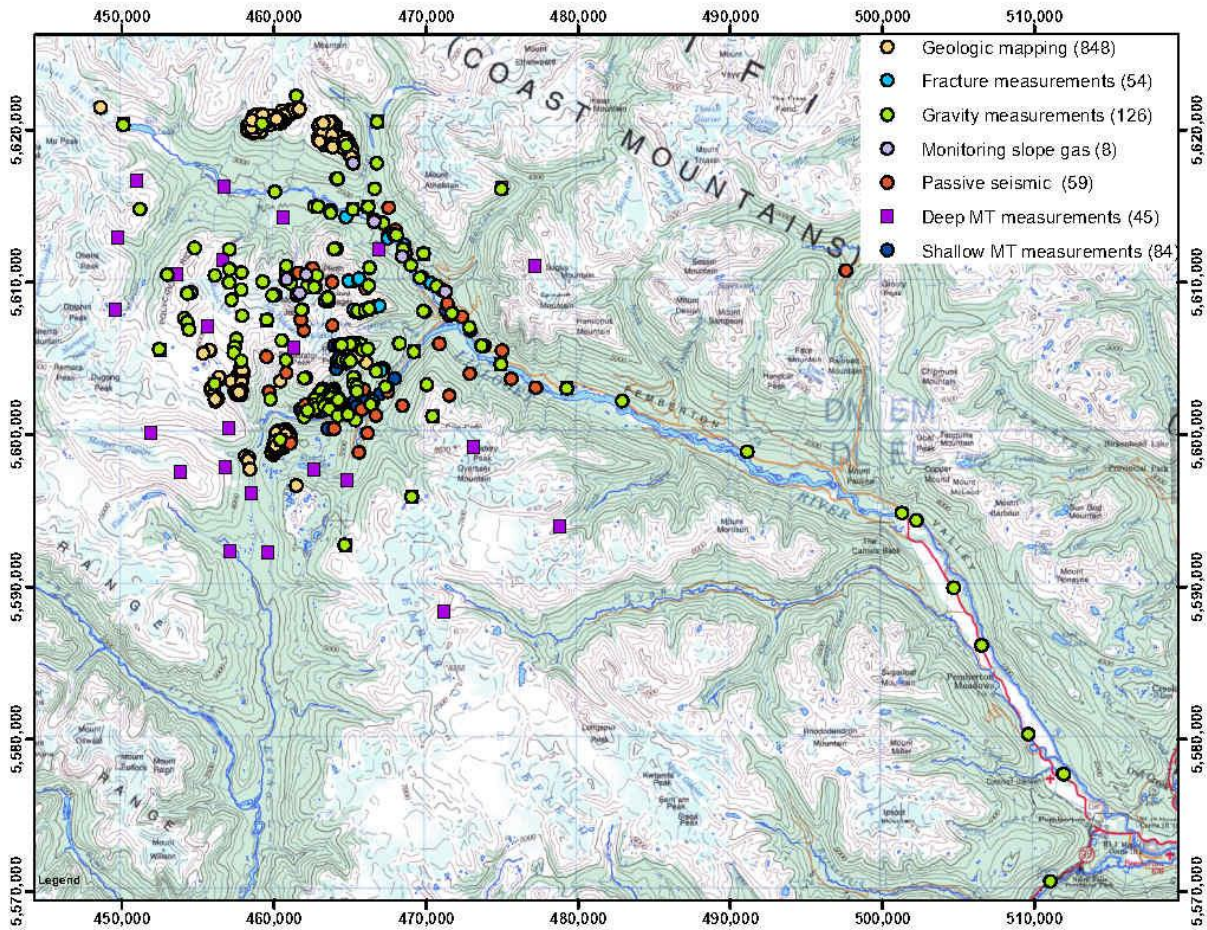


Figure 1: Map of the Mount Meager study area and field locations visited.

Chapter 2 - Bedrock Mapping Results for the Mount Meager Geothermal Research Initiative

Harris, M. and Russell, J.K.

Volcanology and Petrology Laboratory
Earth, Ocean, and Atmospheric Sciences
The University of British Columbia

Introduction

The Mount Meager Volcanic Complex (MMVC), within the Garibaldi Volcanic belt (GVB) of SW British Columbia (BC), is an active volcanic system identified for its geothermal potential (Lewis and Souther, 1978; Jessop, 1998; Grasby and Salas, 2020). As part of NRCan's continued MMVC geothermal exploration program, we conducted new geologic mapping that informs on MMVC bedrock geology (Fig. 1). Our rationale for this work was to provide new data that can constrain subsurface geological models used to assess geothermal potential. Our completed maps include: 1) a detailed, 1:7,000 scale geologic map for the Cracked Mountain volcanic edifice situated on the southwest flank of the MMVC, 2) a detailed, 1:35,000 scale geologic map for the Lillooet Ridge, situated north of MMVC, 3) a detailed, 1:70,000 scale geologic map for the West MMVC, and 4) a large-scale (1:120,000) undivided map, separating volcanic rocks from older basement rocks for the entire MMVC. Additionally, our work has bolstered the existing petrographic, geochemical, and geochronological data for MMVC which will aid future geologists in assessing magmatic origins and eruptive histories for the MMVC volcanoes. Lastly, we have used this new petrographic and geochemical data to run preliminary thermodynamic models that constrain the depths of magma storage in the MMVC.

Prior Work

Our work expands on two previous major mapping campaigns conducted by Woodsworth (1977) and Read (1977). Woodsworth mapped the entire Pemberton region including the coastal plutonic and metasedimentary uplifted basement rocks and episodic volcanic deposits. The scale of Woodsworth's map was small and, thus, volcanic units around Mount Meager were only distinguished by age between Miocene to Pleistocene. In contrast, Read's map was a finer scale and focused exclusively on the geology of the Mount Meager massif; he identified more than thirty map units comprising intrusive or extrusive igneous deposits, which were assigned to "assemblages" based on relative and absolute age relationships. Subsequent work by Green et al. (1988), and Stasiuk and Russell (1989, 1990) built upon the mapping by Woodsworth and Read and produced petrologic and geochemical classifications for the eruptive rocks of Mt Meager, with correlating age constraints ranging from 2.2 to less than 0.1 Ma (Green et al., 1988). Our work here builds upon these previous studies.

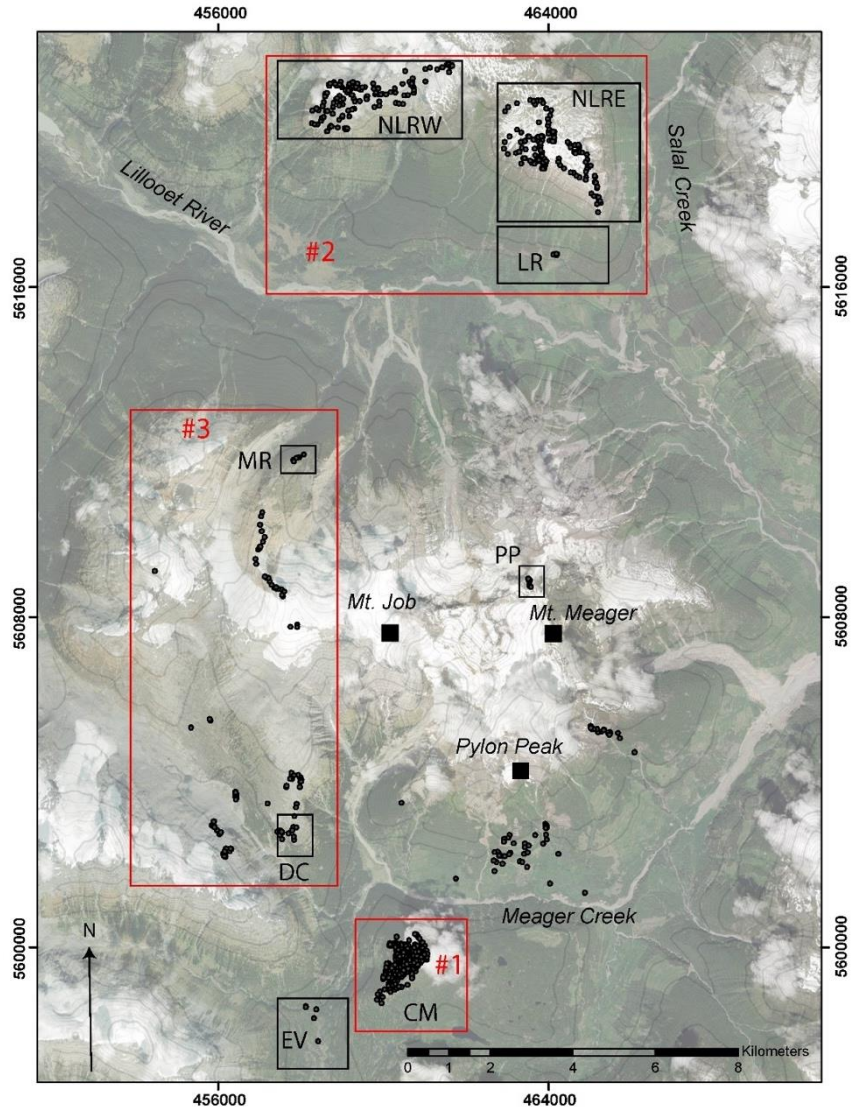


Figure 1: Visualization of data collection, mapping boundaries, and volcanic centres from MMVC mapping. There are 962 GPS tagged field sites are shown in dark grey dots. Cracked Mountain (#1), North Lillooet Ridge (#2), and W MMVC map areas are outlined in red. Also, 6 volcanic centres (CM, NLRW, NLRE, LR, MR, and EV) and two newly identified lavas (DC and PP) are outlined by black rectangles.

Methods

Our mapping work involved a combination of field traversing, outcrop locating, and sample collection. Helicopter support provided access to the more rugged terrain and allowed for mapping larger regions of the MMVC. For regions that remained inaccessible, we used high-resolution aerial imagery to interpret bedrock geology. ArcGIS software and Adobe Illustrator were used to update and digitize our geologic maps. Representative rock samples were collected and prepared and analysed for their mineralogic and textural properties. Select samples were cut and ground to 30-micron thin sections to gain higher resolution for mineral assemblage's present. X-ray fluorescence (XRF) analysis on fused discs was used to

determine major elemental weight percent (wt. %) for the volcanic rocks. The measured major element chemical compositions of select samples were used with the thermodynamic model MELTS_Excel (Gualda and Ghiorso, 2015) to constrain the origins and storage conditions of the MMVC magmas.

Data Collection

Outcrops, unit contacts, and sample locations were tagged with GPS coordinates in the field. A total of 962 GPS tagged field sites were visited (Fig. 1). Table 1 shows the distribution of geological samples within the MMVC used for thin section analysis, major element geochemistry, and radiometric age dating.

Table 1. List of MMVC samples analysed by locality including Cracked Mountain (CM), East Lillooet Ridge (NLRE), West Lillooet Ridge (NLRW), Lillooet River (LR), Mosaic Ridge (MR), and Elaho Valley (EV). Samples were prepared for petrographic thin sections (TS), whole-rock geochemical analysis (G), and geochronometry ($^{40}\text{Ar}/^{39}\text{Ar}$).

Domain	TS	G	$^{40}\text{Ar}/^{39}\text{Ar}$
CM	32	28	2
NLRE	11	9	2
NLRW	6	6	-
LR	3	4	2
MR	-	4	1
EV	3	2	3
PP*	1	2	1
DC*	1	1	1

*Denotes site-specific lava: Perkins Pillar (PP), and Devastator Creek Lava (DC)

Geologic Maps

The breadth of our geologic mapping is shown in our undivided geologic map of the MMVC (Fig. 2). Three detailed geologic map areas are outlined in Figures 1-2: #1 Cracked Mountain, #2 North Lillooet Ridge, and #3 West MMVC. A summary for each map area follows below and Appendix 1-3 contains more detailed descriptions and geologic maps for each.

Cracked Mountain, SW MMVC Map Area

Cracked Mountain (CM) (Figs. 1, 2) is a monogenetic subglacial basaltic volcano 2 km SW of Mount Meager Massif (Wilson and Russell, 2018). CM has a $^{40}\text{Ar}/^{39}\text{Ar}$ age of 190 ± 61.0 ka (Wilson, 2019 unpublished). Extensional cracks, up to 10 m wide and 20 m deep, expose the internal stratigraphic complexities of the CM volcano. Appendix 1 contains a detailed geological map and more extensive lithofacies descriptions.

North Lillooet Ridge, N MMVC Map Area

Our mapping has produced the first detailed geologic map of the North Lillooet Ridge (NLR) (Figs. 1, 2), and identified two discrete volcanic regions: East Lillooet Ridge Volcanic Assemblage (NLRE) and West Lillooet Ridge Volcanic Assemblage (NLRW) (Fig. 1). Our classification of the NLR lavas (Le Bas et al., 1986) is based on their petrographic properties and major elemental chemical compositions. See Appendix 2 for detailed Geologic Map and lithofacies descriptions.

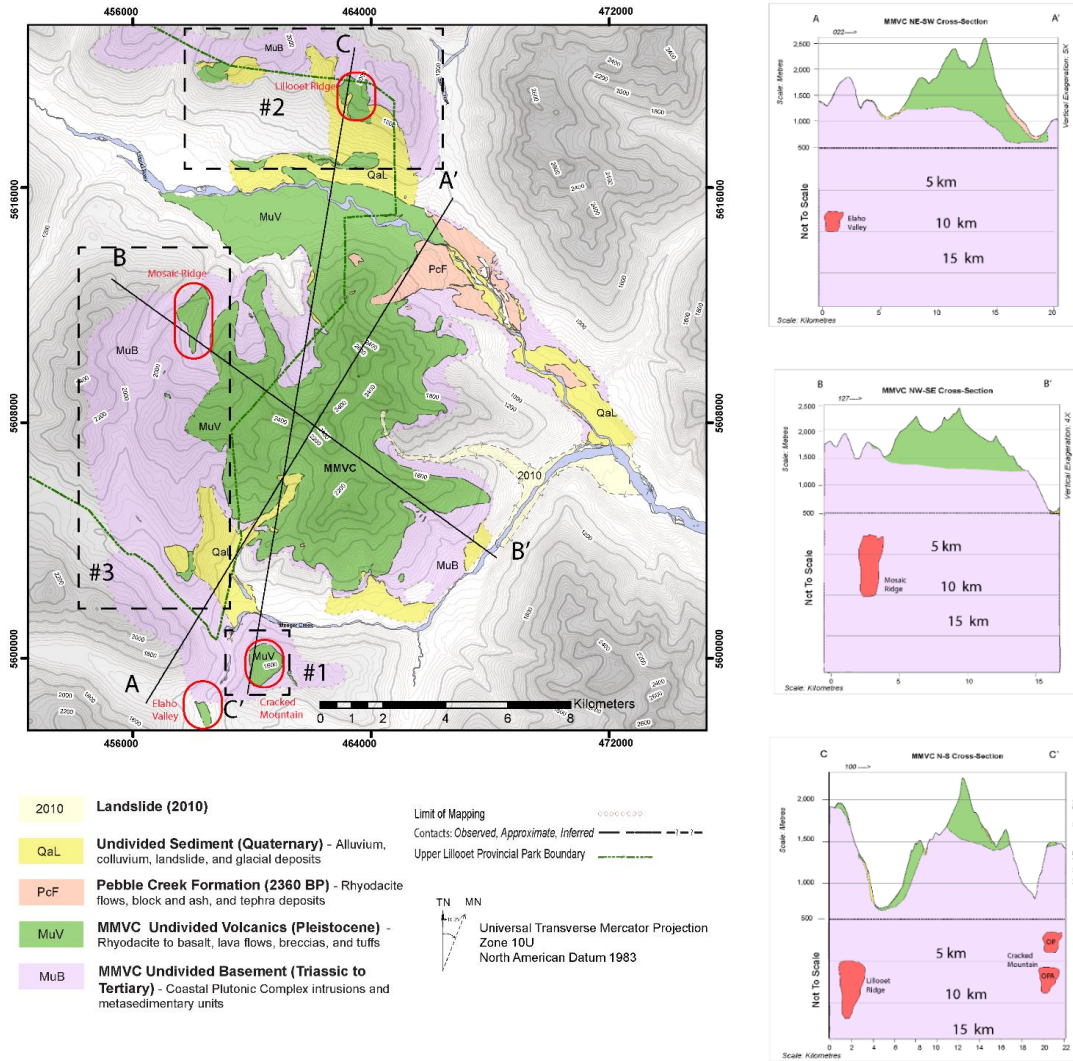


Figure 2: Undivided Geological Map of MMVC shows the large-scale dispersion of volcanics (MuV), basement (MuB), and alluvium (QaL) throughout the region. We used pre-existing large-scale maps of Read (1979) and Woodsworth (1977) as well as our field mapping to accurately depict unit locations and contacts. The youngest MMVC eruption, 2350 B.P Pebble Creek Formation (PcF) (Hickson et al., 1999; Stewart et al., 2008) and youngest landslide (2010) (Roberti et al., 2018) are differentiated. Cracked Mountain (#1), North Lillooet Ridge (#2), and West MMVC map areas are outlined in dashed-black. Cross-sections A-A', B-B', and C-C' depict basement-volcanic contacts on the Mount Meager Massif and surrounding complex. Basement rocks outcrop at elevations of: ~1,300 m SW, ~1,500 m S, ~1,300 m SE, ~1,700 m NW, ~1,900 m N, and ~600 m NE. Schematic depths of magma crustal storage are shown for volcanic centres: CM, NLRE, MR, and EV (outlined in red). These depths are based on thermodynamic modeling with Rhyolite-MELTS (Gualda and Ghiorso, 2015) and are roughly coincident with the depth of a high conductivity anomaly defined by MT (Chapter 5).

West MMVC Map Area

Our mapping expanded westward of Read's (1979) MMVC map limits, creating the first detailed geologic map spanning through the Upper Lillooet Provincial Park (ULPP) and NW MMVC, (Map area # 3, Fig. 1). Basement and volcanic rocks are mapped from Meager Creek to Mosaic Ridge, including the Devastator Creek lava (DC) in the SW, Mosaic assemblage basalts (MR) in the NW (Fig. 1). See Appendix 3 for detailed Geologic Map and map unit descriptions.

Ancillary Volcanics- Perkins Pillar and Elaho Valley

Two MMVC ancillary volcanic sites were visited and sampled: 1) Perkins Pillar Lava (PP) (Fig. 1) and 2) Elaho Valley Lava (EV) (Figs. 1, 2). Work at these sites further contributes to the understanding of MMVC volcanism through petrography, geochemistry, and geochronology. See Appendix 4 for lithofacies descriptions.

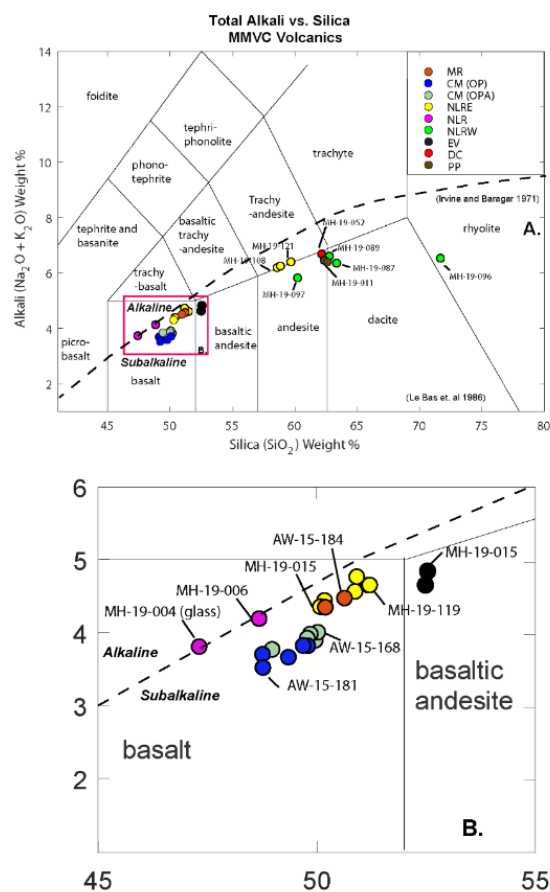


Figure 3: A) Total alkali (Na₂O + K₂O) vs Silica (SiO₂) wt. % (TAS) for MMVC volcanics. Volcanic classification fields based on Le Bas et. al 1986. A dashed black line based on Irvine and Baragar 1971 Alkaline-subalkaline discrimination. Volcanic centres and lavas of study are shown in the following colours: Mosaic Ridge (MR), Cracked Mountain (CM; OP, OPA), East Lillooet Ridge (NLRE), Lillooet River (LR), West Lillooet Ridge (NLRW), Elaho Valley (EV), Devastator Creek Lava (DC), and Perkins Pillar Lava (PP). B) Inset of TAS for MMVC Mafic centre samples: MR, CM, NLRE, LR, and EV.

Geochemical and Petrographic Diversity

The volcanic rocks comprising the MMVC are both geochemically and petrographically diverse (Figs. 3-7) with compositions ranging from primitive basalts to highly-evolved dacites and rhyolites (Green et al., 1988; Stasiuk and Russell JK, 1989; Read, 1990). Figure 3 illustrates the chemical diversity and petrologic classification of MMVC lavas (Le Bas et. al, 1986; Irvine and Baragar, 1971). Values of Mg# (molar MgO/ (MgO +FeO*)*100) (Fig. 4) are used to identify the primitive character of some of the MMVC volcanic rocks; within the Cascade arc Mg# > 60 have been considered “primitive” indicating limited crustal influence (Green and Harry, 1999; Schmidt et al., 2008; Mullen and Weis, 2013).

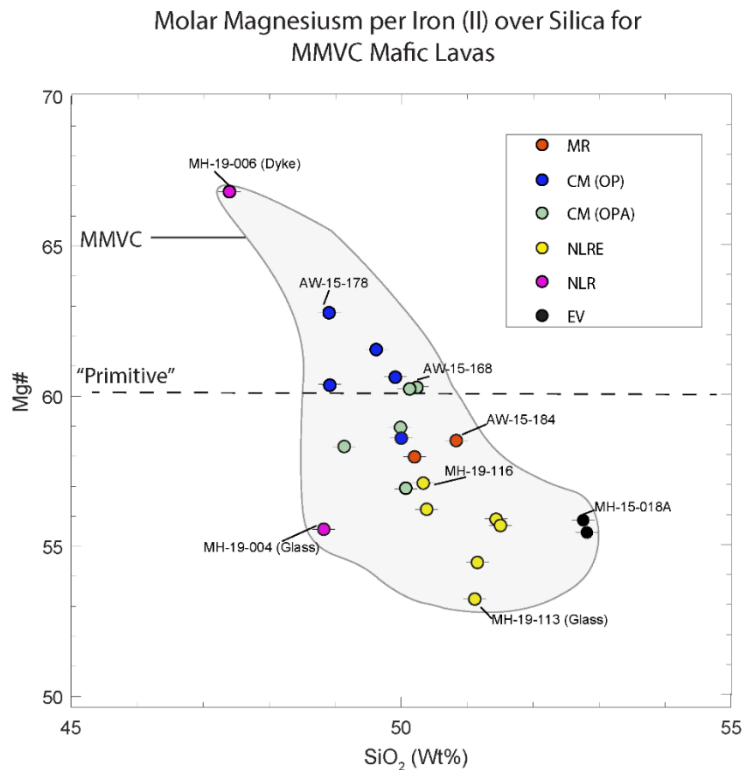


Figure 4: Mg# (molar MgO/ (MgO +FeO*)*100) vs Silica (SiO₂) wt. % for MMVC mafic lavas. Mg# depicts variations in the ratio of magnesium and iron (2+) in lavas, where the higher the number, the “more primitive” (i.e. less influenced by crustal signatures). FeO* is calculated from Fe(total), assuming $Fe^{2+} / \Sigma Fe \sim 89\%$. Prior Cascade arc studies indicate Mg#> 60 are primitive (Green and Harry, 1999; Schmidt et al., 2008; Mullen and Weis, 2013). MMVC mafic centres are: Mosaic Ridge (MR), Cracked Mountain (CM; OP, OPA), East Lillooet Ridge (NLRE), Lillooet River (LR), and Elaho Valley (EV). In the MMVC, the LR dyke sample (MH-19-006 – Supplementary Data) is most primitive, while basalts from the NLRE are least primitive.

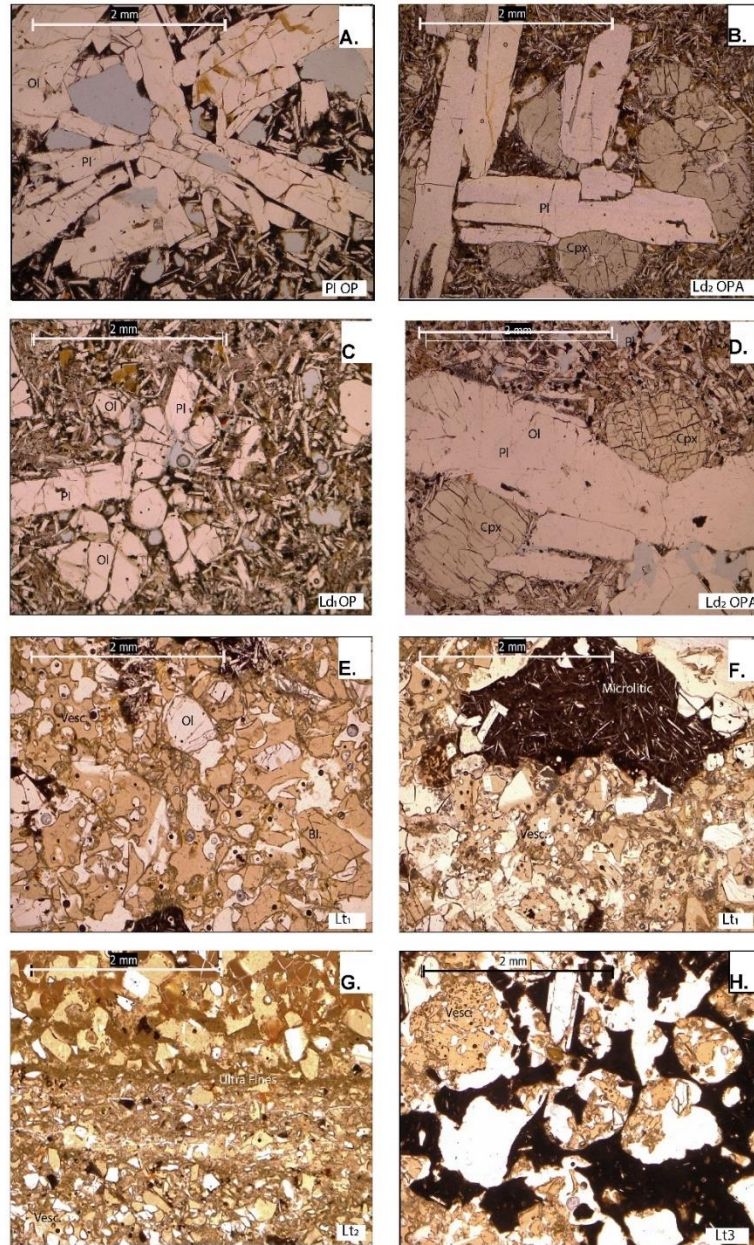


Figure 5: Plane-polarized photomicrographs at 4x magnification for CM samples. A) PI sample with olivine (Ol) and plagioclase (Pl) phenocrysts. B) Ld₂ (OPA dyke) with olivine, plagioclase, and augite (cpx) phenocrysts. C) Ld₁ (OP dyke) with olivine and plagioclase phenocrysts. D) Ld₂ (OPA dyke) with olivine, plagioclase, and augite (Cpx) phenocrysts. E) Lt₁ sample with blocky (Bl) and highly vesiculated (Vesc.) vitric juveniles. F) Lt₁ sample with microlitic juvenile lapilli clast, blocky, and highly vesiculated juveniles. G) Lt₂ sample with layers of ultra fines between coarser, blocky, and vesiculated vitric juveniles. H) Lt₃ sample with highly vesiculated, vitric spatter lapilli within an ash-sized vitric matrix.

The storage conditions of magmas (including depth and duration) are an important factor relevant to the exploration for and assessment of geothermal potential in volcanic systems. For example, more primitive (i.e. mafic) magmas within the MMVC most probably erupted after relatively short residence times within the upper crust. In contrast, less primitive or evolved magmas (i.e. intermediate to felsic) are commonly indicative of magmatic differentiation and suggest longer residence times within the crust before an eruption.

Cracked Mountain

The Cracked Mountain volcanic deposits comprise two petrographic suites based on their phenocryst assemblages (Figure 5). The majority of rocks are olivine + plagioclase porphyritic (OP; Figs. 5A, 5C) but several deposits contain a phenocryst assemblage of olivine + plagioclase + augite (OPA; Figs. 5B, 5D). Both petrographic suites (i.e. OP and OPA) are subalkaline but have different silica and alkali contents (Fig. 3B). The OP suite is more primitive, with Mg#’s ranging 60-63 versus 56-60 for the OPA suite (Fig. 4).

Other Volcanic Domains

Seven other isolated volcanic outcroppings were identified via field mapping, including: NLRE, NLRW, LR, MR, EV, DC, and PP (Fig. 1). The petrographic and chemical properties of these volcanic rocks are summarized here (Fig. 3, 4, 6, 7) and more fully described in the appendices.

The volcanic rocks outcropping on the Eastern edge of Lillooet Ridge (NLRE) (Fig. 1) comprise plagioclase + augite porphyritic subalkaline andesites (i.e. NLhcL and NLcjL; Figs. 3A, 6A, 6B), and olivine, plagioclase, and augite subalkaline basalts (i.e. NLpL, NLbjL, NLmtB, and associated intrusions; Figs. 3B, 7A, 7B) The NLRE basalts are the least primitive of the MMVC mafic lavas, with Mg#’s ranging from 53-58 (Fig. 4).

The volcanic rocks at the edge of the western Lillooet Ridge (NLRW) (Fig. 1) include andesites (NLijL and NLmcB), dacites (NLvjL, NLmcB), and high silica rhyolites (NLbcL) (Fig. 3A). The andesite lavas are plagioclase porphyritic featuring sieve textured phenocrysts and sometimes contain augite (Fig. 6C). Dacite lavas and breccias are plagioclase, hornblende, and biotite porphyritic (Figs. 6D, 6E). Rhyolite lavas are plagioclase, biotite, hornblende, and alkali-feldspar porphyritic (Fig. 6H).

The volcanic rocks exposed at the waterfall above the Lillooet River (LR) (Fig. 1) are olivine porphyritic alkaline basalts (NLmpB, and associated intrusions; Fig 3B, 7C, 7D). LR basalts are the most primitive lavas in the MMGC with Mg#’s of ~67 (Fig. 4).

The volcanic rocks covering the Mosaic Ridge (MR) (Fig.1) are olivine, plagioclase, and augite porphyritic subalkaline basalts (Ps-10x/f and associated intrusions; Fig. 3B, 7F). MR lavas are and non-primitive with Mg#’s ranging from 58-59 (Fig. 4).

The volcanic rocks exposed at the mouth of the Elaho Valley (EV) are olivine, plagioclase, and augite porphyritic subalkaline basaltic-andesites (Figs. 3B, 7E). EV lavas are highest in silica (< 52 wt. %) of MMVC mafic lavas, and are non-primitive, with Mg#’s ranging from 55-56 (Fig. 4).

The lavas exposed above and west of Devastator Creek (DC) (Fig. 1) are plagioclase, augite, and hornblende porphyritic subalkaline dacites (DCcjL; Figs. 3A, 6F).

The lavas exposed ~1 km W of Meager Peak, adjacent to Perkins Pillar (PP) (Fig. 1) are plagioclase and biotite porphyritic subalkaline dacites (Figs. 3A, 6G).

Table 2 summarizes each MMVC site of study, with petrographic properties (i.e. major phenocrysts), chemical classification, Mg#’s, and ages. Major elemental data for MMVC samples are provided in supplementary Excel files.

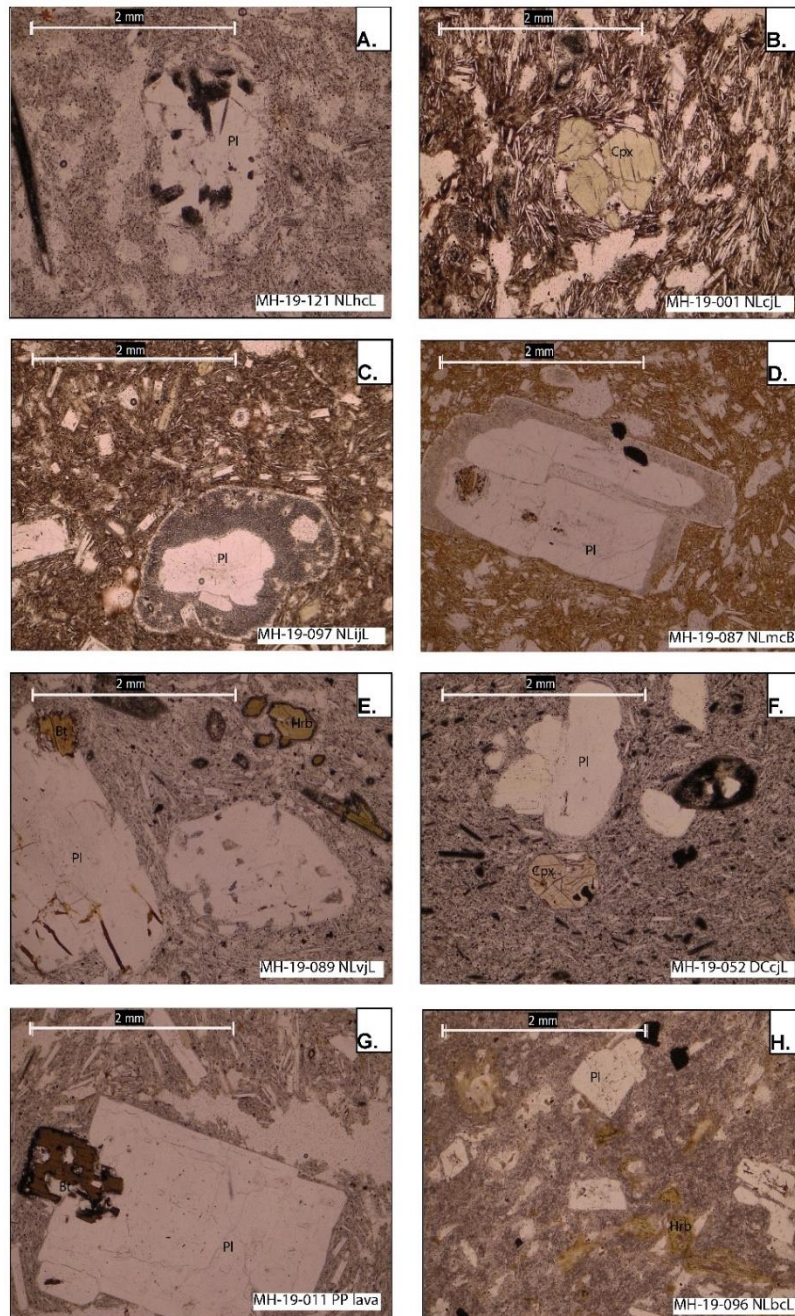


Figure 6: Plane-polarized photomicrographs at 4x magnification for MMVC intermediate-felsic samples. A) NLhcL sample with sparse plagioclase (Pl) phenocrysts. B) NLcJL sample with sparse augite (Cpx) phenocrysts. C) NLiJL sample with plagioclase and minor augite phenocrysts. D) NLmcB sample with sparse plagioclase phenocrysts. E) NLvjL sample with plagioclase, hornblende (Hrb), and biotite (Bt) phenocrysts. F) DCcJL sample with plagioclase and augite phenocrysts. G) PP lava sample with plagioclase and biotite (Bt) phenocrysts. H) NLbcL sample with plagioclase and hornblende phenocrysts.

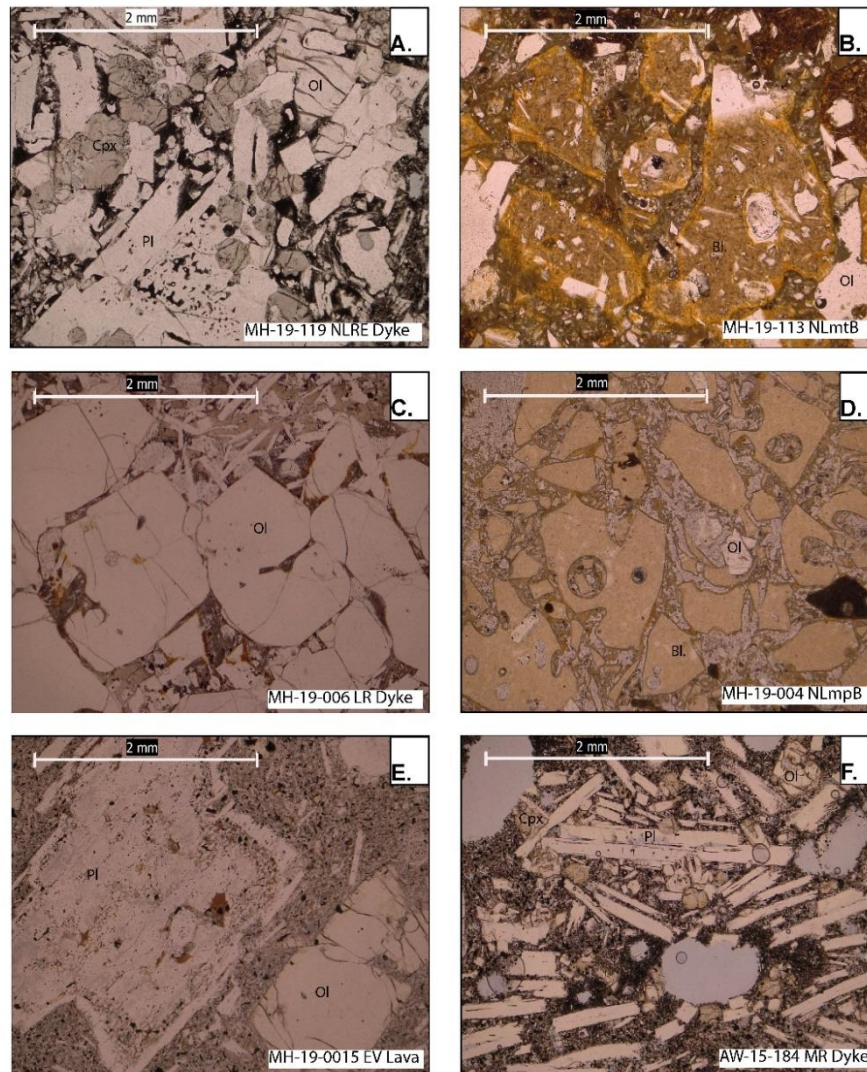


Figure 7: Plane-polarized photomicrographs at 4x magnification for MMVC mafic samples. A) NLRE dyke sample with olivine (Ol) and plagioclase (Pl), and augite phenocrysts (Cpx). B) NLmtB sample with olivine-rich, blocky (Bl) vitric juvenile components. C) LR dyke sample with coarse, glomeroporphyritic olivine phenocrysts. D) NLmpB sample with blocky vitric juvenile components. E) EV lava sample with olivine and plagioclase phenocrysts. F) MR dyke sample olivine, plagioclase, and augite phenocrysts.

Table 2: Petrographic and Geochemical Summary for MMVC Volcanics. Abbreviations are as in Table 1. Mg# as molar 100 MgO/ (MgO +FeO).

Domain	Phenocryst (Vol. %)	Rock Type	Mg#	Age
CM	OP: Ol (10%), Pl (10-15%)	Basalt	60-63	190 ± 61 ka
	OPA: Ol (10%), Pl (10-15%), Augite (2-5%)	Basalt	56-60	
NLRE	NLpL/NLbjL/ Dykes: Ol (10%), Pl (10-12%), Augite (5-7%)	Basalt	53-58	Pleistocene (?) Miocene (?)
	NLhcL/NLcjL: Pl (1-3%), Augite (1-2%) Hbl (1-2%)	Andesite	-	
	NLRW	NLijL: Pl (2-5%), Augite (1-3%)	Andesite	
	NLvjl/NLmcB: Pl (20-25%), Hbl (10%) Biotite (2-3%)	Dacite	-	
	NLbcL: Pl (10-15%), Biotite (5%), Hbl (1-2%), K-spar (1-2%)	Rhyolite	-	
LR	Dyke: Ol (20-25%)	Basalt	67	Pleistocene (?)
MR	Ps-10x/Dyke: Ol (10-15%), Pl (15%), Augite (10%)	Basalt	58-59	90 ± 60 ka
EV	EVbjL: Ol (5%), Pl (10-15%), Augite (3-4%)	Basaltic Andesite	55-56	140 ± 100 ka
PP*	PPbjL: Pl (15%), Biotite (5%), Hbl (1-2%), Augite (2%), Qtz (1-2%)	Dacite	-	Holocene (?)
DC*	DCcjL: Pl (20%), Augite (5%), Hbl (3-4%)	Dacite	-	Pleistocene (?)

MMVC Bedrocks

Undivided bedrock units include pre-MMVC crystalline and metamorphic rocks and our map separates those geological units from younger volcanic units, including the MMVC, and glacial and alluvial deposits (Fig. 2). We used the pre-existing maps of Read (1979) and Woodsworth (1977) in conjunction with our results from the 2019 and 2020 field seasons to create the bedrock interface map (Fig. 2). The youngest MMVC eruption, 2350 B.P Pebble Creek Formation (Hickson et al., 1999; Stewart et al., 2008) and youngest landslide (2010) (Roberti et al., 2018) are also distinguished (Fig. 2).

Elevations of Basement Outcroppings Volcanic Contacts, Magma-Crustal Storage

Cross-sections A-A', B-B', and C-C' show profile views of the NE-SW, NW-SE, and N-S MMVC respectively (Fig. 2). These profile views inform on locations and elevations where basement and volcanic outcroppings occur— information that is paramount when assessing locations for potential geothermal drilling. Section A-A' shows basement-volcanic outcrops at elevations of ~1,300 m in the SW MMVC, and as low as 600 m in the NE MMVC (Lillooet River). Section B-B' shows basement-volcanic outcrops at ~1,700 m in NW MMVC (MR), ~1,500 m on the NW Mount Meager Massif, and ~1,300 m on the SE Mount Meager Massif. Section C-C' shows basement-volcanic outcrops at elevations of ~1,900 in the N MMVC (NLRE), 1,600 m on the N Mount Meager Massif, ~1,400 m on the S Mount Meager Massif, and ~1,500 in the S MMVC (CM). Phase 2 will examine id gravity and MT data can help resolve extensions of vent complexes into the subsurface

Magma-Crustal Storage

Phenocryst assemblages in volcanic rocks provide critical quantitative information on pre-eruptive temperatures, H₂O contents, and pressures (i.e. depth) of the corresponding magmas. Different minerals (i.e. olivine, plagioclase, pyroxene, and spinel) are stable at different P-T conditions (Gualda and Ghiorso, 2015). Such thermodynamic models, in conjunction with the presence (or absence) of certain phenocrysts and estimates of magma composition, can uniquely constrain the conditions in the magma before the eruption and, thus, the depth of magma storage.

We used the thermodynamic model *Rhyolite-MELTS* (Gualda and Ghiorso, 2015) to constrain the pre-eruptive storage depths of crystallization for mafic volcanic rocks within and around the MMVC. This includes mafic volcanic rocks from Cracked Mountain, the North Lillooet Ridge, Mosaic Ridge, and the Elaho Valley map areas (Fig. 2). Major elemental compositions for representative samples were put into MELTS which recalculated FeO and Fe₂O₃ contents assuming an oxygen fugacity set by the QFM buffer and normalized on an anhydrous basis.

Forty-five isobaric crystallization simulations were conducted for each sample. Each isobaric simulation ran from liquidus conditions (< 1300°C) to a temperature where the system was ~95% crystallized (~950°C). The pressure range explored was from surface pressures (1 atm) to 0.4 GPa (~15 km depth) over increments of 50 MPa. Volatile content was also varied by changing the H₂O wt. % (0-2) in steps of 0.5%. The model results for each isobaric run showed stepwise changes in the mineral assemblage (i.e. olivine, plagioclase, clinopyroxene, orthopyroxene, and spinel), and increases in mineral abundances, as a function of decreasing temperature. This information was then used to generate mineral stability fields based on depth (a function of pressure) and volatile content (H₂O wt. %). Petrographic analysis of mineral occurrence and volume (%) for the modeled samples were then transposed with the generated mineral stability fields, and approximate ranges of crustal storage for each magma were achieved. These magma-crustal storage depths are depicted schematically in Figure 2.

The MMVC mafic occurrences are in the North (NLRE), West (MR), and Southwest (CM, EV) (Fig. 2). By combining our MMVC bedrock map and cross-sections (Fig. 2) with the *MELTS* thermodynamic models, we can constrain the regional depths of MMVC magma storage. Our models show that the two CM phenocrystic suites (i.e. OP and OPA), were stored at different depths. The OP magmas were stored at depths ranging from 2-4 km while OPA were 6-7 km (Fig. 2). NLRE basalts were stored at depths ranging from 5-12 km (Fig. 2). MR basalts were stored at depths ranging from 3-10 km (Fig. 2). EV basaltic andesites were stored at depths ranging from 7-10 km (Fig. 2). The depths of magma reservoirs are inherently related to geothermal viability, and our study finds that the CM-OP and MR lavas represent the shallowest stored magmas with depths as little as 2-3 km (Fig. 2).

Summary

The MMVC situated in the northern part of the GVB in southwest British Columbia is an active volcanic system and has untapped geothermal potential (Lewis and Souther, 1978; Jessop, 1998; Grasby and Salas, 2020). In support of the current evaluation of MMVC for its geothermal resource potential, we have conducted field mapping that builds previous published geological maps (i.e. (Read, 1979). Our field mapping has expanded bedrock mapping to the north, west, and southwest of the main MMVC. Sample collection, petrographic and geochemical analyses have given insight into MMVC magma sourcing, crustal residence times.

Our work has produced four new geologic maps for the MMVC:

1. Geological Map of Cracked Mountain, SW MMVC (Appendix 1) details the monogenetic, basaltic lithofacies. The paleo-eruptive environment (i.e. subglacial) confined the erupting lava above the

present-day Meager Creek and Elaho Valleys. The stratigraphy of CM lithofacies suggests that the eruption began explosively, with signatures of magmatic and phreatomagmatic fragmentation, followed by voluminous intrusive and effusive eruptions of lava. Petrographic and geochemical results show how two distinct magma batches (i.e. OP and OPA) fed the eruption. OP samples are chemically more primitive than OPA. Thermodynamic models show OP and OPA magmas were stored at depths of ~2-4 km and 6-7 km respectively, prior to the eruption.

2. Geological Map of Lillooet Ridge, N MMVC (Appendix 2) is the first detailed bedrock map for the region's three volcanic centres (Fig. 1): 1) NLRW, evolved intermediate to felsic andesites, dacites, and rhyolite lavas, likely Miocene in age. 2) NLRE, mafic to intermediate basalts and andesites. 3) LR, basalt. Petrographically and geochemically, the NLRE and LR basalts are distinct, with NLRE being non-primitive, plagioclase and augite phyric, and LR being highly primitive and olivine phyric. Thermodynamic models suggest the NLRE basalts were stored at depths of ~5-12 km prior to eruption.
3. Geological Map of W MMVC (Appendix 3) connects the SW MMVC mapping through the Mosaic Ridge, NW MMVC (Read, 1979). Basement-volcanic contacts are shown as high as the Job Glacier summit (~2,400 m). The newly discovered Devastator Creek lava (DCcJL), is chemically dacitic with plagioclase, augite, and hornblende phenocrysts. Petrographically and geochemically, the MR basalts (PS-10x/f) are non-primitive, and thermodynamic models suggest MR basalts were stored at depths of ~3-10 km.
4. Undivided Geological Map of MMVC (Fig. 2) shows the large-scale dispersion of volcanics, basement, and alluvium throughout the region. Basement-volcanic contacts are detailed throughout the Mount Meager Massif and surrounding complex, reaching elevations of: ~1,300 m SW, ~1,500 m S, ~1,300 m SE, ~1,700 m NW, ~1,900 m N, and ~600 m NE.

Our mapping results will be used in the continued exploration of geothermal potential within the MMVC. The identification of bedrocks across the MMVC should assist future geologists in generating subsurface models and our detailed contact locations can be used to assess potentially viable geothermal drill locations.

Acknowledgements

Thanks to Mahmud Muhammad, Sophie Leiter, Lindsey Abdale, Dr. Lucy Porritt, and Dr. Rene Barendregt for their assistance during the 2020 field season.

References

- Le Bas, M.J., Le Maitre, R.W., Streckeisen, A., and Zanettin, B., 1986, A chemical classification of volcanic rocks based on the total alkali-silica diagram: *Journal of Petrology*, v. 27, p. 745–750, doi:10.1093/petrology/27.3.745.
- Befus, K.S., Hanson, R.E., Miggins, D.P., Breyer, J.A., and Busbey, A.B., 2009, Nonexplosive and explosive magma/wet-sediment interaction during emplacement of Eocene intrusions into Cretaceous to Eocene strata, Trans-Pecos igneous province, West Texas: *Journal of Volcanology and Geothermal Research*, v. 181, p. 155–172, doi:10.1016/j.jvolgeores.2008.12.017.
- Brooks, E.R., Wood, M.M., and Garbutt, P.L., 1982, Origin and metamorphism of peperite and associated rocks in the Devonian Elwell Formation, northern Sierra Nevada, California.: *Geological Society of America Bulletin*, v. 93, p. 1208–1231, doi:10.1130/0016-7606(1982)93<1208:OAMOPA>2.0.CO;2.
- Doyle, M.G., 2000, Clast shape and textural associations in peperite as a guide to hydromagmatic interactions: Upper Permian basaltic and basaltic andesite examples from Kiama, Australia: *Australian Journal of Earth Sciences*, v. 47, p. 167–177, doi:10.1046/j.1440-0952.2000.00773.x.
- Edwards, B.R., Skilling, I.P., Cameron, B., Haynes, C., Lloyd, A., and Hungerford, J.H.D., 2009, Evolution of an englacial volcanic ridge: Pillow Ridge tinar, Mount Edziza volcanic complex, NCVP, British Columbia, Canada: *Journal of Volcanology and Geothermal Research*, v. 185, p. 251–275, doi:10.1016/j.jvolgeores.2008.11.015.
- Grasby, S.E., and Salas, C., 2020, Searching for Mount Meager’s Geothermal Heart: *EOS*, v. 101, doi:<https://doi.org/10.1029/2020EO140214>.
- Green, N.L., Harakal, J.E., Souther, I.J.G., and Read, P.B., 1988, Eruptive history and K-Ar geochronology of the late Cenozoic Garibaldi volcanic belt, southwestern British Columbia: *Geological Society of America Bulletin*, v. 100, p. 563–579, <https://pubs.geoscienceworld.org/gsa/gsabulletin/article-pdf/100/4/563/3380343/i0016-7606-100-4-563.pdf>.
- Green, N.L., and Harry, D.L., 1999, On the relationship between subducted slab age and arc basalt petrogenesis, Cascadia subduction system, North America: *Earth and Planetary Science Letters*, v. 171, p. 367–381, doi:10.1016/S0012-821X(99)00159-4.
- Gualda, G.A.R., and Ghiorso, M.S., 2015, MELTS-Excel: A Microsoft Excel-based MELTS interface for research and teaching of magma properties and evolution: *Geochemistry, Geophysics, Geosystems*, v. 16, p. 315–324, doi:10.1002/2014GC005545.
- Hickson, C.J., Russell, J.K., Stasiuk, M. V, and Swanson, D.A., 1999, Volcanology of the 2350 B.P. Eruption of Mount Meager Volcanic Complex, British Columbia, Canada: implications for Hazards from Eruptions in Topographically Complex Terrain 1: *Bulletin of Volcanology*, v. 60, p. 489–507.
- Houghton, B.F., and Smith, R.T., 1993, Recycling of magmatic clasts during explosive eruptions: estimating the true juvenile content of phreatomagmatic volcanic deposits: *Bulletin of Volcanology*, v. 55, p. 414–420.
- Irvine, T.N., and Baragar, W.R.A., 1971, A Guide to the Chemical Classification of the Common Volcanic Rocks: *Canadian Journal of Earth Sciences*, v. 8, p. 523–548, doi:10.1139/e71-055.

- Jessop, A.M., 1998, Geothermal Energy in Canada: Geoscience Canada, v. 25, p. 33–41.
- Kano, K., 1991, Miocene pillowed sills in the Shimane Peninsula, SW Japan: *Journal of Volcanology and Geothermal Research*, v. 48, p. 359–366, doi:10.1016/0377-0273(91)90051-Z.
- Lawrence', R.B., Armstrong, R.L., and Berman, R.G., 1984, Garibaldi Group Volcanic Rocks of the Salal Creek Area, Southwestern British Columbia: Alkaline Lavas on the Fringe of the Predominantly Calc-Alkaline Garibaldi (Cascade) Volcanic Arc: *Journal of Volcanology and Geothermal Research*, v. 21, p. 255–276.
- Lewis, T.J., and Souther, J.G., 1978, Meager Mountain, B.C.: a possible geothermal energy resource: *Geothermal Service of Canada*, v. 9, p. 1–17.
- Moitra, P., Gonnermann, H.M., Houghton, B.F., and Giachetti, T., 2013, Relating vesicle shapes in pyroclasts to eruption styles: *Bulletin of Volcanology*, v. 75, p. 1–14, doi:10.1007/s00445-013-0691-8.
- Moitra, P., Gonnermann, H.M., Houghton, B.F., and Tiwary, C.S., 2018, Fragmentation and Plinian eruption of crystallizing basaltic magma: *Earth and Planetary Science Letters*, v. 500, p. 97–104, doi:10.1016/j.epsl.2018.08.003.
- Mullen, E.K., and Weis, D., 2013, Sr-Nd-Hf-Pb isotope and trace element evidence for the origin of alkalic basalts in the Garibaldi Belt, northern Cascade arc: *Geochemistry, Geophysics, Geosystems*, v. 14, p. 3126–3155, doi:10.1002/ggge.20191.
- Read, P., 1979, Meager Creek Geothermal Area: p. 1 Sheet, doi:10.4095/129507.
- Read, P., 1990, Mt Meager Complex, Garibaldi Belt, Southwestern BC.: *Geoscience Canada*, v. 17, p. 167–170.
- Roberti, G., Ward, B., van Wyk de Vries, B., Friele, P., Perotti, L., Clague, J.J., and Giardino, M., 2018, Precursory slope distress prior to the 2010 Mount Meager landslide, British Columbia: *Landslides*, v. 15, p. 637–647, doi:10.1007/s10346-017-0901-0.
- Russell, J.K., and Stasiuk, M., 1990, The Bridge River Assemblage in the Meager Mountain volcanic complex, southwestern British Columbia; in *Current Research, Part E*, Geological Survey of Canada.:
- Schmidt, M.E., Grunder, A.L., and Rowe, M.C., 2008, Segmentation of the Cascade Arc as indicated by Sr and Nd isotopic variation among diverse primitive basalts: *Earth and Planetary Science Letters*, v. 266, p. 166–181, doi:10.1016/j.epsl.2007.11.013.
- Skilling, I.P., 1994, Evolution of an englacial volcano: Brown Bluff, Antarctica: *Bulletin of Volcanology*, v. 56, p. 573–591, doi:10.1007/BF00302837.
- Skilling, I.P., White, J.D.L., and McPhie, J., 2002, Peperite : a review of magma-sediment mingling: *Journal of Volcanology and Geothermal Research*, v. 114, p. 1–17.
- Stasiuk, M., and Russell JK, 1989, Petrography and chemistry of the Meager Mountain volcanic complex, southwestern British Columbia: *Geological Survey of Canada*, p. 189–196.

- Stewart, M.L., Russell, J.K., and Hickson, C.J., 2008, Geology, Pebble Creek formation, British Columbia: p. 1 sheet.
- Tuffen, H., McGarvie, D.W., Pinkerton, H., Gilbert, J.S., and Brooker, R.A., 2008, An explosive - Intrusive subglacial rhyolite eruption at Dalakvísl, Torfajökull, Iceland: *Bulletin of Volcanology*, v. 70, p. 841–860, doi:10.1007/s00445-007-0174-x.
- White, J.D.L., and Houghton, B.F., 2006, Primary volcanoclastic rocks: *Geology*, v. 34, p. 677–680, doi:10.1130/G22346.1.
- White, J.D.L., McPhie, J., and Skilling, I., 2000, Peperite: A useful genetic term: *Bulletin of Volcanology*, v. 62, p. 65–66, doi:10.1007/s004450050293.
- White, J.D.L., and Valentine, G.A., 2016, Magmatic versus phreatomagmatic fragmentation: Absence of evidence is not evidence of absence: *Geosphere*, v. 12, p. 1478–1488, doi:10.1130/GES01337.1.
- Wilson, A.M., 2019, Glaciovolcanism in the Garibaldi volcanic belt: University of British Columbia, 1–232 p.
- Wilson, A.M., and Russell, J.K., 2018, Quaternary glaciovolcanism in the Canadian Cascade volcanic arc—Paleoenvironmental implications: *Field Volcanology: A Tribute to the Distinguished Career of Don Swanson*. Geological Society of America, v. 538, doi:10.1130/2018.2538(06).
- Woodsworth, G., 1977, Geology of Pemberton (92J) Map Area: Geological Survey of Canada, p. 1 sheet.
- Zimanowski, B., Fröhlich, G., and Lorenz, V., 1991, Quantitative experiments on phreatomagmatic explosions: *Journal of Volcanology and Geothermal Research*, v. 48, p. 341–358, doi:10.1016/0377-0273(91)90050-A.

Appendix 1

Cracked Mountain Map Area, SW MMVC

Volcanic Lithofacies

Results from CM fieldwork identify ten volcanic lithofacies; Five are primary volcanoclastic units: Three lapilli tuffs (Lt), one Peperite (P), and one tuff breccia (Tb). Five are coherent volcanic lithofacies: three intrusions (i), and Two lavas (L).

Volcanoclastic units are subdivided based on grain size (l = lapilli, b = block), bed characteristics (i.e. massive, thinly bedded), and major components (i.e. ash-lapilli juveniles, spatter bombs, pillow fragments, and dense lava fragments). Intrusions are subdivided on the basis of margins (i.e. well defined, poorly defined/pillowed, peperitic), phenocryst assemblages (i.e. olivine-plagioclase-augite, olivine-plagioclase), and magnetic susceptibility (i.e. high = 10-20, low = 0-8). Lavas are subdivided based on dominant structures (p= pillows, j= columnar jointed).

Volcanoclastic Lithofacies:

CM lapilli tuffs (Lt₁₋₃) are stratigraphically lowest (i.e. oldest), underlying, or intruded by all other lithofacies. Thicknesses range from 0.5 m to < 6 m. The massive, moderately- to poorly-sorted Lt₁ is observed within crack exposures across the whole mountain and as surficial lithofacies in the centrally located, high elevations of CM (Map 1). Lt₁ is commonly cut by dykes and mingled with pillow lobes reminiscent of “peperites”, a rock formed by in-situ fragmentation of magma intruding and mingling with unconsolidated, typically wet sediments (Brooks et al., 1982; Skilling et al., 2002; White and Houghton, 2006). In some instances, soft-sediment deformation of Lt₁ is observed. The thinly bedded, well-sorted Lt₂ outcrop in the SE and N sections of CM (Map 1). Beds of ultra-fine ash are up to 5 cm thick and dip shallowly (>30 degrees). In some cases, microfractures offset laminated beds. Two small outcroppings of Lt₃ are located near the central and NE sections of the CM (Map 1). These outcrops display localized stratification of lapilli and bomb-sized, fluidal to blocky, highly vesiculated spatter clasts, supported by a well-sorted ash matrix. Texturally, all CM Lt are monolithic and dominated by vitric juvenile particles (Figs. 5E-5H). Highly vitric olivine and plagioclase microlitic juveniles (Fig. 5F) make up ~5-25% by volume within the Lt, and stand-alone crystals of olivine and plagioclase make up a lesser degree of the unit’s matrix. All three CM Lt show both highly vesiculated (<60%) and dense blocky juveniles (Figs. 5E-5H), suggesting both magmatic and phreatomagmatic fragmentation (Zimanowski et al., 1991; Houghton and Smith, 1993; Moitra et al., 2013, 2018; White and Valentine, 2016).

Peperites (Pi), termed after White et al., (2000) and Skilling et al., (2002) are the primary volcanoclastic deposits formed by the mingling of magma with wet, unconsolidated sediments. At CM, Pi is present along the margins of the peperitic intrusive bodies (Lpi) where quench fragmented, globular to blocky components of basalt are supported by ash-sized tuff matrix. We discern Pi from Lpi as volcanoclastic from coherent respectively. Lpi contains intact pillowed lobes (block and coarse lapilli), with minor interstitial sediments or preserved tuff lenses, while Pi is matrix-supported and contains finer scale (block to fine lapilli) vitric basalt components that are commonly jig-saw fragmented. The thickness of Pi varies from a few cm to 2-3 m away from the margins of Lpi. Pi rarely occurs at the present-day CM surface but is commonly exposed in stratigraphic exposers at all locations of the volcano.

CM Tuff Breccia (Tb) covers the largest surface area at CM (Map 1) and is highest in stratigraphy. The breccias are massive, with thicknesses ranging from 0.5 m to <9 m, and form flat-lying and slope/valley filling outcrops. Tb is clast-supported with monolithic, lapilli to block-sized, olivine and plagioclase porphyritic pillow and blocky lava fragments. Greater than 50% of clasts show rounded and chilled

margins. Minor, yellow ash-sized interstitial sediment is present between breccia clasts. Rarely, block and lapilli-sized, rounded Lt_1 lithics are entrained.

Coherent Lithofacies:

Pillow lavas (Lp), which are comprised of individually stacked radial and quenched lobes, make up ~20% of the edifice volume but form the dominant lithofacies at the edges of CM. Lp outcrop at the present-day, shallow dipping high elevations CM (Map 1), and range from 1-3 m. The Lp thickens substantially as you move to the margins of the edifice, forming nearly vertical walls (~ 30 m). Individual pillows are bulbous, up 50 cm in diameter. Lp is olivine and plagioclase \pm augite porphyritic. Interstitial quench-fragmented vitric sediment fills void spaces between intact pillows in some outcrops, while large radial columnar jointed pods, up to three meters in diameter, make up a lesser degree of the lithofacies. Stratigraphically, Lp is overlain by tuff breccia (TbP), is cut by dykes (Ld_2), and is observed to overlie outcroppings of lapilli tuff at the base of the edifice.

Pillowed lava (Lpi), are peperitic intrusions, outcropping as coherent bodies and lobes of lava exposed at the present surface of CM and within stratigraphic exposures across the whole edifice. Here we use the term “peperitic” as the deposit adjective after White and Houghton (2006), used in a genetic sense to describe the mingling of magma and unconsolidated sediment. We make the distinction of Lpi from a “peperite” (Pi) (e.g. (White et al., 2000; Skilling et al., 2002), a primary volcanoclastic rock (i.e magma and host sediment), as here we refer to the intrusive coherent lava body only (e.g. (Doyle, 2000; Tuffen et al., 2008). Lpi is reminiscent of “intrusive pillows” observed at other glaciovolcanic centres (e.g. (Skilling, 1994; Edwards et al., 2009) and submarine settings (e.g. (Kano, 1991; Befus et al., 2009), however individual pillow lobes are not always observed at each exposure. Instead, Lpi more commonly occurs as massive globular bodies up to 15-20 m across, with branching, mingled smaller pods, and lobes of subrounded lava with chilled margins. Lpi is often associated with the presence of peperitic dykes (Ld_1). In each occurrence, Lpi intrudes lapilli tuff (Lt_1) which we interpret as the host sediment for these peperitic intrusions.

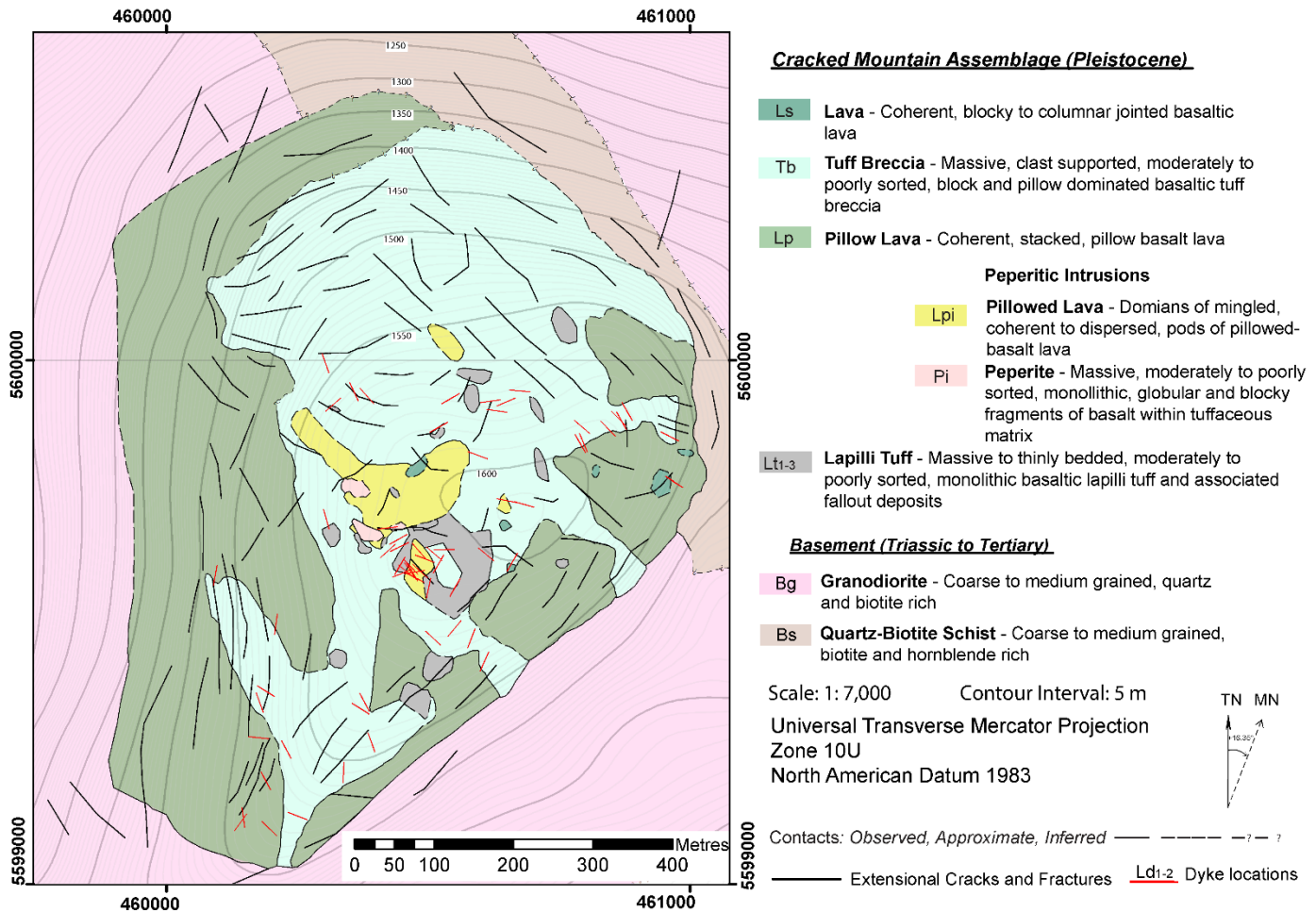
CM blocky and columnar jointed lava (Ls) outcrop near the highest elevations as well as sections of the eastern edge of the mountain (Map 1). Ls is 0.5 m to 2 m thick with crude to well-formed, subvertical to radial columnar joints up to 30 cm in diameter. Ls is holocrystalline, olivine, plagioclase \pm augite porphyritic, and ranges from medium to high magnetic susceptibility (~2-18). The coarse jointing, rather than pillowing, indicates subaerial cooling, and the stratigraphic location at the present-day surface suggests these outcrops represent remnant late-stage effusions during the CM eruption.

CM has nearly 50 subvertical intrusions (Ld_{1-2}) (Wilson and Russell, 2018) (Map 1). Petrographic study shows two different phenocrystic assemblages for the CM intrusions: olivine-plagioclase phyric (OP) (Fig. 5C) and olivine-plagioclase-augite phyric (OPA) (Figs. 5B, 5D). Further analyses with a hand-held KT-9 Kappa meter showed variation in magnetic susceptibility, with OP samples being low (0-8) and OPA medium to high (9-22). Ld_1 intrusions have poorly defined or pillowed margins, while Ld_2 intrusions have well-defined margins and high magnetic susceptibility. Ld_1 intrusions commonly feed Lpi and are cut by Ld_2 .

Basement Geology:

The biotite hornblende granodiorite (Bg), and quartz biotite-rich schist (Bs) (Map 1) unconformably underlie the Cracked Mountain assemblage and mark a topographic shallowing beneath the pillow lavas. The granodiorite is exposed along the southwest to the southeast edge of the Cracked Mountain volcano. The granodiorites dip to the SW and SE and have steeply dipping NE and SW joint orientations. The quartz biotite schist is well exposed along the southeast and eastern edge of the Cracked Mountain volcano. The

pillow lava and breccia contact with the schist can be followed along an NW trending extensional crack on the eastern edge of Cracked Mountain.



Map 1: Geologic map of Cracked Mountain, a glaciovolcanic landform with an age date of 190 ± 61.0 ka (Wilson, 2019 unpublished). Ten volcanic lithofacies are shown across the volcanic edifice. The volcanic edifice unconformably overlies basement granodiorites and mica-schists. Note: Full size PDF and map polygons are available on GeoScience BC website.

Appendix 2

North Lillooet Ridge, N MMVC Map Area

Volcanic Lithofacies

The NLRE is capped by two small N-S oriented, steep-sided flat-topped andesitic peaks (NLcjL, NLhcL) (Map 2, Fig. 3A). NLcjL is sparsely plagioclase and clinopyroxene porphyritic (Fig. 6B) and forms columnar jointed lavas that extend from the Northern peak ~1km SW. NLhcL is aphyric to plagioclase porphyritic (Fig. 6A) with hackly, irregular, horizontally oriented columnar. NLhcL extends SW for ~500 m. The edge of the Eastern Lillooet Ridge is marked by a transition to basaltic lithofacies (NLbjL, NLpL, NLmtB) (Map 2, Fig. 3B). NLbjL is black, highly vesicular, blocky, and olivine, plagioclase, and augite porphyritic. NLbjL outcrops at ~2,000 m elevation and continues ~100 m down the valley before transitioning to pillow lava (NLpL). NLpL resembles NLbjL in colour, vesicularity, and phenocrystic texture, but differs in the structural occurrence (i.e. pillow lobes and radial jointed pods). NLpL extends ~400 m S and ~1 km E-W. Massive, monolithic, vitric tuff breccia (NLmtB) outcrops within the NLpL in a series of stream cut valleys at ~1,900 m elevation. NLmtB is dominated by dense, blocky, and crystal-rich ash and lapilli-sized juveniles (Fig. 7B). Subvertical, olivine, plagioclase, and augite porphyritic (Fig. 7A) intrusions cut through NLmtB. At ~1,700 m elevation, NLpL transitions into NLmtB which continues ~400 m before the exposure is covered by alluvium (Map 2). No age dates exist for the NLRE volcanics. Based on degrees of weathering, the andesites (NLcjL, NLhcL) are likely Miocene-aged Pemberton Arc remnants (Woodsworth, 1977; Lawrence et al., 1984), while the less-altered basalts are likely Pleistocene in age.

Approximately 1.5 km S of the top of the East Lillooet Ridge and above the present-day Lillooet River, a waterfall flows down a cliff face of massive, pillow-dominated, basaltic tuff breccia (NLmpB). The NLmpB matrix material is dominated by ash- and lapilli-sized dense to blocky juvenile components with minor crystals of olivine (Fig. 7D). A series of subvertical, holocrystalline, olivine porphyritic (Fig. 7C) basaltic intrusions cut through the NLmpB cliff face. Petrographic and geochemical analysis has shown that there are differences between the basalts at the top of the NLRE and the basalts at the lower waterfall exposure. Namely, the lower waterfall basalts lack augite and plagioclase phenocrysts and are lower in silica and total alkali wt. % (Fig. 3B, Fig. 7). Thus, we have revised these lower waterfall basalts (i.e. NLmpB and intrusions) as separate from the NLRE and will further be referred to as Lillooet River basalts (LR) (Fig. 1). There are no age dates for the LR basalts. A basal till underlies the NLmpB cliff, suggesting the LR eruptions occurred after one of the recent Lillooet Valley glaciations during the Pleistocene.

The NLRW comprises four intermediate to felsic volcanic units (Map 2). NLijL is andesite lava, plagioclase, and augite porphyritic, and stretches ~1 km E-W (Map 2, Fig. 6C) with fine, hackly, and irregular columnar jointing. The eastern extent of NLijL contacts NLmcb, a monolithic, clast-supported dacite breccia. NLmcb clasts are aphyric to plagioclase porphyritic (Fig. 6D) and form stacked spires up to 10 m high. A dacite lava (NLvjL) cap a southern peak on the edge of the NLRW (Map 2) and form coarse vertical columnar joints up to 0.5 m in diameter. NLvjL is plagioclase, hornblende, and biotite porphyritic (Fig. 6E). In some locations, NLvjL overlies NLijL (Map 2). Rhyolite lava (NLbcL) outcrops at the SW extent of the NLRW (Map 2) above a waterfall at ~1,700m elevation. The lava is plagioclase, biotite, hornblende, and alkali feldspar porphyritic (Fig. 6H), and forms blocky and radial jointed columns. No age dates exist for NLRW volcanics, but the high degree of weathering coupled with highly evolved compositions suggest these may be remnant Miocene-aged Pemberton arc volcanics (Woodsworth, 1977; Lawrence et al., 1984).

Basement Geology

East Lillooet Basement Geology

The eastern Lillooet ridge basement rocks are predominantly monolithic, with the entirety of the East Lillooet Ridge volcanic assemblage overlying the pink, coarse-grained monzonite (Mqm) (Map 2). South-southwest dipping monzonite outcrops along the southward edge of the ridge and continues east, paralleling Salal Creek. To the NW, the monzonite is in contact with coarse-grained quartz and biotite-rich gneiss (uTrcsb) (Map 2); the contact with the monzonite dips S-SE whilst the fabric in the gneiss dips N-NW. The contact can be traced ~1.5 km before the monzonite is truncated by a glacial valley, while the gneiss continues northwest, partially overlain by portions of the present-day glaciers.

West Lillooet Basement Geology

The western Lillooet ridge basement rocks begin on the west side of the glacial valley that divides the ridge into eastern and western segments. East-southeast dipping coarse-grained gneiss (uTrcsb) (Map 2) overlies E-SE dipping coarse-grained granodiorite (Mgd) (Map 2). Stream cut incisions through the granodiorite expose thin outcroppings of the underlying, medium-grained, platy fractured amphibolite (Hpa) (Map 2). The granodiorite extends ~ 5 km west, reaching the glacial valley that bounds the North Lillooet ridge. Two east-west trending outcroppings of white marble (uTrcc) (Map 2) are thrust up through the granodiorite along small localized folds. Medium-grained biotite, hornblende, and quartz-rich diorite (Mqd) (Map 2) occur along the western edge of the ridge, bordering the westward glacial valley. Medium to coarse-grained hornblende, pyroxene, and plagioclase-rich amphibolite (Hpa) outcrops in a large section of the western edge of the ridge, unconformably underlies the NLvjL (Map 2).

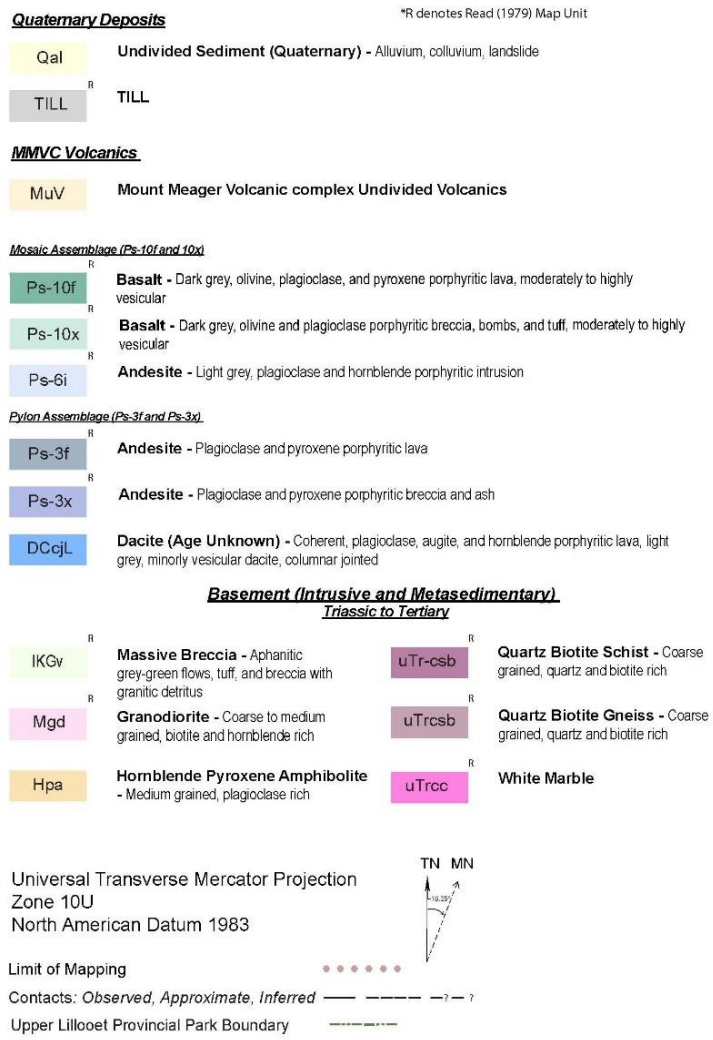
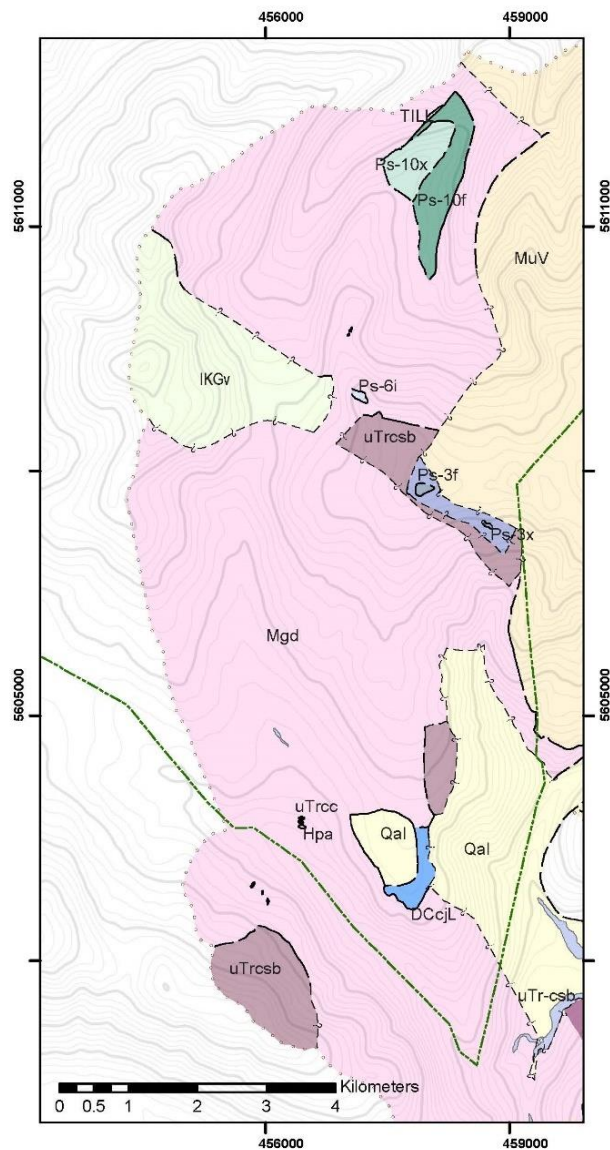
Map 2: Geologic map of North Lillooet Ridge, showing three newly defined young volcanic centres in the N MMVC: The East Lillooet Ridge volcanic assemblage (NLRE and LR) and West Lillooet Ridge volcanic assemblage NLRW. Volcanic rocks overly basement monzonite, granodiorite, diorite, amphibolite, marble, and mica-rich gneiss. Note: Full size PDF and map polygons are available on GeoScience BC website.

Appendix 3

West MMVC Geologic Descriptions

The W MMVC consists predominantly of basement rocks, reaching elevations as high as ~2,400 m within Job glacier (Map 3). Biotite-hornblende granodiorite (Mgd) is the major lithology, outcropping in Meager Creek and persisting N, underlying the Mosaic Ridge (MR) (Fig. 1) in the NW extent of the map (Map 3). Moderate occurrences of coarse-grained quartz and biotite gneiss (uTrcsb) outcrop in the SW corner of the ULPP and again at the summit of Job Glacier, but are absent in the NW region. A massive detrital breccia (IKGv) extends E from Polychrome Ridge and is found at elevations up to 2,400 m (Map 3).

The Devastator Creek lava (DCcjL) (DC) (Fig. 1, Map 3) unconformably overlies Mgd in the flat-lying plateau W of Devastator Creek and N of Meager Creek. DCcjL is coarsely-jointed and plagioclase, augite, and hornblende porphyritic (Fig. 6F). Chemically, DCcjL is dacite (Fig. 3A) of unknown age. Ice-confined, sparsely plagioclase and pyroxene porphyritic andesites (Ps-3f; Ps-3x) outcrop in the center of Job Glacier (Map 3) forming a steep-sided, flat-topped peak with outward-facing columnar joints. N of Job Glacier, thin outcroppings of highly-weathered, plagioclase, and hornblende porphyritic andesite (Ps-6i) intrude through the basement rocks (Map 3). The Mosaic Ridge (MR) (Figs. 1, 2) is host to the Mosaic Assemblage basalts (Ps-10f; Ps-10x) (Read, 1979, 1990; Green et al., 1988; Stasiuk and Russell JK, 1989) (Map 3). MR basalts are olivine, plagioclase, and augite porphyritic (Fig. 7F) occurring as 1) crudely jointed lava 2) massive, monolithic, tuff breccia 3) subvertical jointed intrusions. MR basalts have a whole rock K-Ar age of 0.09 ± 0.06 Ma (Green et al., 1988; Read, 1990).



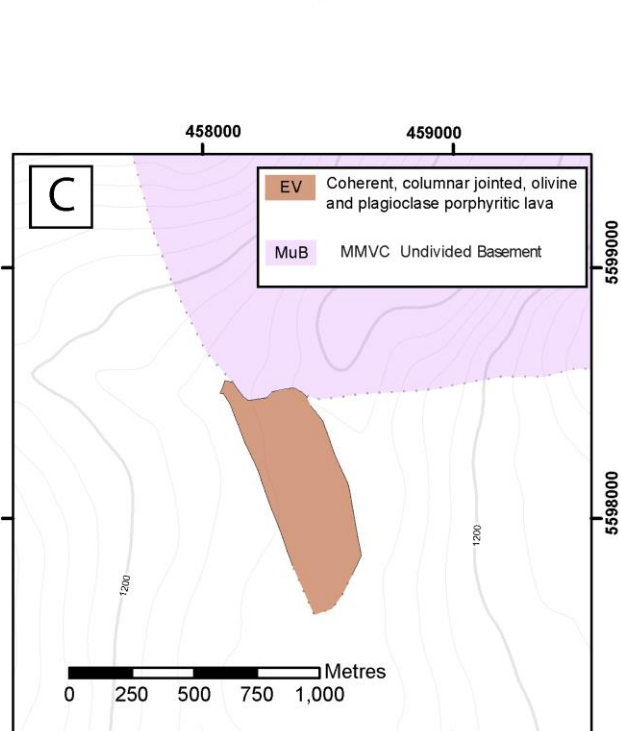
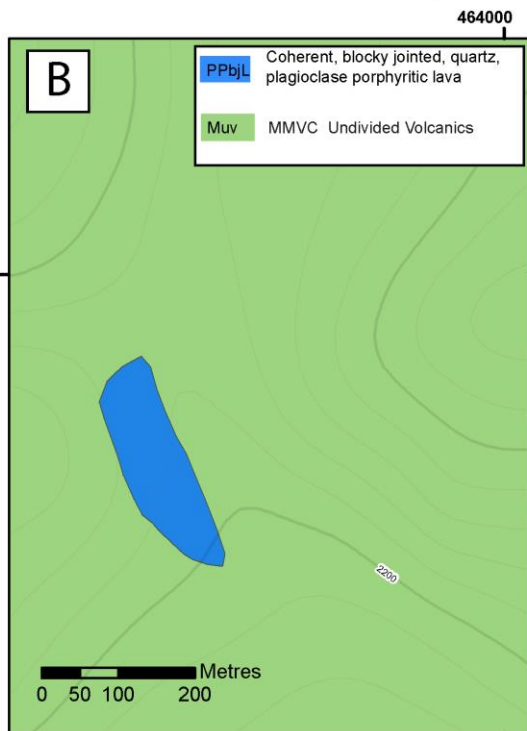
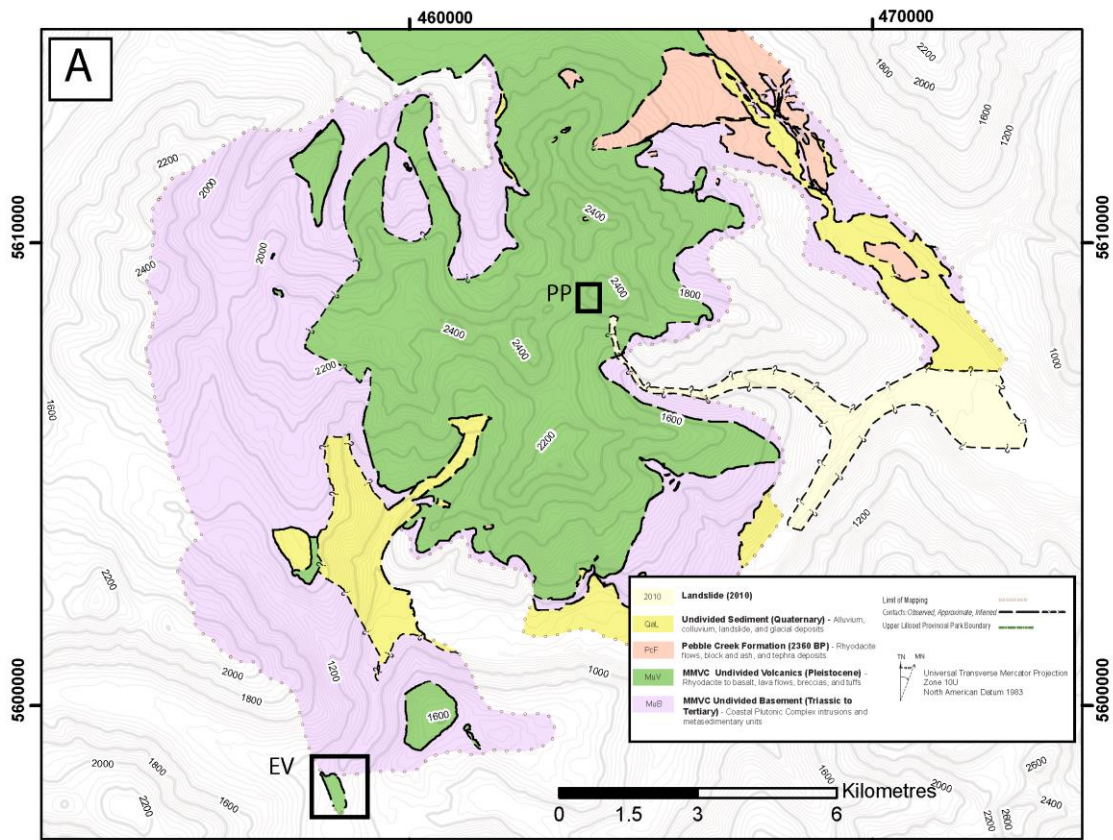
Map 3: Geological Map of W MMVC connects the SW MMVC through the Mosaic Ridge, NW MMVC (Read, 1979). The newly discovered Devastator Creek dacite (DCcJL) outcrops in the SW, overlaying the Mgd basement. Pylon assemblage lavas (Ps-3f/x) outcrop in the summit of Job glacier at elevations ~2,400 m. Mosaic Assemblage basalts (PS-10x/f) overlay glacial till and Mgd basement in the N section of the map. Undifferentiated volcanics (MuV) are depicted on the east edge of the map based on Read, 1979. Note: Full size PDF and map polygons are available on GeoScience BC website.

Appendix 4

Perkins Pillar and Elaho Valley- Volcanic Lithofacies

The Perkins Pillar lava (PP) (Fig. 1; Map 4) sits ~1 km W-NW of Mount Meager summit, at ~2,360 m elevation, and until recently, has been covered by alpine glacial ice. PP lava is plagioclase, biotite, and hornblende porphyritic, and is chemically dacitic (Figs. 3A, 6G). The age of the lava is unknown. Based on the stratigraphic location near Meager Peak, and fresh, unaltered phenocrysts, PPbjL is potentially quite young (i.e. Late-Pleistocene or Holocene).

The Elaho Valley (EV) (Figs. 1, 2; Map 4) hosts lavas that extend more than 20 km southward (Woodsworth, 1977; Green et al., 1988). Texturally, the lavas are olivine, plagioclase, and augite porphyritic, and chemically are basaltic andesite (Figs. 3B, 7E). Samples collected ~5 km S of the Elaho mouth returned the whole rock K-Ar age of 0.14 ± 0.10 Ma (Green et al., 1988).



Map 4: Geological maps showing the location of two ancillary lavas, adjacent to Perkins Pillar (Mt. Meager) and at the mouth of the Elaho Valley (SW MMVC). A) Undivided geologic map of MMVC with locations of Perkins Pillar lava (PP) and Elaho Valley Lavas (EV) (outline in black). B) Map showing the location of Perkins Pillar lava (PPbjL) at ~2300 m a.s.l. overlying undivided MMVC volcanics (MuV). C) Map showing the location and approximate source of Elaho Valley lavas (EV). Note the lavas extend ~20 km south (Green et. al. 1988) but were only mapped and sampled near the source in this study.

Chapter 3 - Fracture system analyses of the Mount Meager area

Chen, Z., Grasby, S.E., Liu, X.

Geological Survey of Canada

Introduction

A two week field geological and fracture study campaign were conducted in the Mount Meager area during the period of July 7-19, 2019. The main objectives of the study were: 1) to improve our understanding of the fracture systems and their control on geothermal reservoirs in a volcanic belt, 2) to search for geoscience indicators for geothermal resource 'sweet-spots' in the south Mount Meager geothermal area, and 3) determine the ability to extrapolate such indicators across the Garibaldi Volcanic Belt. The specific aim of the 2019 summer fieldwork was to assess the volcanic geothermal resource potential through field observation and data analysis with following three tasks:

- A) measuring fracture attributes, such as strike, dip direction, dip angle, spacing and density, for fracture reservoir model construction;
- B) collecting rock samples to obtain reservoir parameters (porosity, permeability and density) and rock thermal properties (such as thermal conductivity, thermal capacity); and
- C) collecting geological evidence and indicative features of geothermal anomalies in the Mount Meager volcanic complex.

Here we report on data collected. A subsequent study will link these field observation to the existing regional geological framework, and integrate previously defined fracture/fault system and interpreted fault/fracture zones from remotely sensed image data to constrain development of a geothermal reservoir model (Chen, et al., 2020a and b). The new data collected here provide insight for better understanding of the fracture system and its role in defining the geothermal reservoir and improving geothermal energy production strategies.

Methods

Traditional methods for geological fieldwork were used. The field party observed, identified and recorded geological and geomorphologic features, measured attitudes (strike, dip direction, dip angle, density and spacing) of fracture/fault planes, and collected rock samples for further laboratory analysis. The identified geological and geomorphologic features and evidence of geological processes were analyzed in relation to tectonic and volcanic activities of the region and to assess their association to reservoir development in and around each station. Fracture spacing in this study is defined as the perpendicular distance between two neighbouring fracture planes from the same fracture set (Fig. 1). Two major fracture sets were recognized in Figure 1 and fracture spacing was measured separately for each fracture set. Sanderson and Peacock (2019) provided details on the definition and quantitative methods of spacing data analysis. In addition, a drone was used to assist the fieldwork by taking aerial photos and searching for suitable sites for setting stations. Figure 2 is an aerial photo of a road cut cross section along the Lillooet River valley, showing a prominent fracture set with strike about parallel to the river. Outcrop photos were used to

digitize fracture traces allowing calculations of occurrence, length distribution, density, and spacing for construction of fractured reservoir model.

Data analysis methods included statistics of the measured fracture orientation, dip direction and angle, and estimation of fracture density and other parameters useful for geological synthesis and model development. Various graphic methods were applied to reveal geological trends, spatial variation of geological features and fractures, and correlation between geomorphologic and geological features. Laboratory physical and numerical fracture modelling results were used to guide field data interpretation (e.g., Guo et al., 2017).

Data Collection

Station locations were based on work objectives and one of the following criteria: 1) exposure of crystalline basement, or new volcanic bodies allowing observation and study of the rock, and to take samples for laboratory analysis and tests; b) exposure of measurable fracture sets and fault zones; c) exposure of specific geological or geomorphologic features, or sites that help determine the nature and character of the geothermal resource in the region, such as hot spring, evidence of permeable zone and ground-water circulation, and special geomorphologic features. Figure 3 shows some examples of the special feature station.

The study area is in a rain forest climate zone, where forest and vegetation cover most of the low lying areas, and snow and ice cover most of the higher regions, with often poorly exposed bedrock. The topography of the volcanic complex is extremely steep and glaciers cover large portion of the mountain. Figure 4 is a Google Earth map showing topographic characters of the Mount Meager volcanic complex and locations of observation stations. Most observation stations were along major logging roads and on mountain ridges, where fresh bedrock is best exposed. Access to the stations along the logging road was by moto vehicle, while access to stations on the mountain ridges relied on a helicopter for transportation. The 2010 Mount Meager landslide has destroyed the bridge close to the intersection of Capricorn Creek and Meager Creek. As such, a helicopter had to be used to access the observation stations in the southern Meager geothermal lease area.

We have made 55 observation stations (Table 1; Fig. 5) and taken 25 rock specimens for analysis. Depending on the condition of bedrock exposure, we have two types of stations, single outcrop and cross section. Stations #3 and 5 are cross sections, each extend for about 120 meters, and #40, 42, 43, 44, 45, 46, each for about 58 meters. The remaining stations are single outcrops. For the fracture study, more than 1207 fracture space data points were measured, and 251 attitudes of fracture plane were recorded.

Fracture measurements from previous fieldwork published in literature and technical reports were compiled to fill the data gaps geographically.

Results

Rock samples have been sent to relevant laboratories for different analysis and tests. Two major categories of analysis were conducted: a) petrology, such as type and characteristics of the rock (thin section and mineral composition); and b) petrophysical and thermal properties of the rock, such as density, permeability, porosity, thermal conductivity and heat capacity. The results will be released in a Geological Survey of Canada Open File when the analysis and tests are completed. In this report, we

present the field observation and data collection in the 2019 summer field campaign, and discuss preliminary results of data analysis with emphasis on measured fracture spacing and attitudes.

The fracture measurements (surface attitude, spacing and density) are listed numerically in Appendix 1 as a separate data file, and displayed graphically in various plots (Figs. 6, 7, 8 and 9). The dip-direction and dip-angle cross plot (Fig. 6) shows variation in fracture planes by station, depicting the pertinent trends of dip direction and angle in each site. The rose diagram (Fig. 7) displays the distribution of dip directions of the measured fractures. Fracture planes are projected on a stereo net for each station to reveal their spatial association (Fig. 8). It is noteworthy that for the same fracture set, we may have numerous fracture spacing measurements, but only one representative fracture attitude. In this case, when the data were plotted, the same representative fracture attitude was assigned for each spacing data point. This may cause visual inconsistency when comparing different figures of the same station if the number of measurements is involved in the plots.

The statistics of fracture spacing data are shown in Figures 9A and B as a histogram and cumulative distribution curve. Although varying over a large range from about 1 cm to over 200 cm, the majority of the fractures (>85%) have a spacing less than 50 cm. Fracture spacing measurements in basement rock and volcanic cover are plotted separately in Figs. 9C and D and 9E and F. Comparison of the cumulative distribution curves (Fig. 9F) suggests that fracture spacing is slightly greater in the volcanic cover layers than that in the basement rocks in the studied outcrops.

Discussion

Multiple groups of fracture sets were observed in most bedrock outcrop stations examined. The analysis of the fracture orientation shows interesting variations. Spatially, the orientation of major fracture group(s) varies depending on the location relative to the volcanic eruption center in the margin of the Mount Meager complex. From stations along the Lillooet River in the northeast side of the complex, the fractures striking NW-SE are most common, to the southeast the most apparent fracture orientation is NE-SW, while to the south E-W striking fractures prevail (Fig. 10), although other groups with different orientations coexist. Geographically, the primary circular drainage segments define the margin of the Mount Meager volcanic complex. For example, the Lillooet River marks the northern and northeastern margin and the Meager Creek defines the margin to the south and southeast. The secondary radial drainage segments, representing by a series of creeks, starting from glaciers in the mountain highs, intersect the primary circular branches, forming a typical volcanic drainage system. Geomorphic process study suggests that physical discontinuities in the form of fractures/faults within the rock mass strongly influence bedrock weathering and erosion (e.g., Scott, et al., 2018). A numerical model shows that drainage network patterns are highly sensitive to the mechanical weakness, narrow fracture spacing, and persistent low relief, associated with fault-weakened zones (Roy, et al., 2016). Associated geomorphologic features are the NW segment of the Lillooet River and NE and EW segments of the Meager Creek for the circular fracture group; while small creeks, appearing radial around the volcanic complex, belongs to the second group.

Within the volcanic complex, the E-W striking fractures dominate in the Mount Meager peak and around Perkin's Pillar in the east, coincident with the general trend of contacts of distinct volcanic assemblages of different ages (See Figure 2 of Reed, 1990). In the western part of the complex, the strike of prominent fracture set appears to be NS to NNW-SSE, where the observed fracture orientation is aligned well with clusters of earthquakes and mapped volcanic eruption centers (Fig. 10).

At least three types of fractures of different origins under distinct geological processes are recognized. The fracture groups related to regional tectonic deformation are consistent in character and are common in basement rocks. Their strikes are often in good spatial alignments with volcanic eruption centers and veins, and earthquake events. Fractures associated with volcanic doming and eruption activities may vary geographically. They are circular/radial segments and the strikes change spatially depending on their location relative to the eruption center. This is particularly true from the interpreted fault/fracture zones in Landsat images. Volcanic activity may overprint tectonic fractures. The pre-existing zones of weakness can be further complicated by reactivation and modification during volcanic activity. The gravitational fracture is common in volcanic areas and commonly appears parallel to slope. This type of fracture causes instability in the mountain ridge and peak, and can lead to slides and rock avalanche.

The southern Meager Creek geothermal reservoir is a fractured crystalline basement consisting of metamorphic rocks and quartz monzonite plutons. A volcanic complex of overlapping andesite, dacite and pyroclastic piles that become progressively younger from south to north overlies on the post-Miocene erosion surface of the basement (Fairbank et al., 1981; Lewis and Souther, 1978). Previous exploration has outlined the potential high temperature geothermal resource prospective area, and subsequent production tests confirmed the presence of a permeable zone that defines the fractured reservoir, although the obtained water flow rate did not justify a commercial power plant (GeothermEx Inc., 2004; 2009).

Regional structure studies in western Turkey and the western Great Basin of the United States shown that many geothermal fields appear to be associated with fault system (e.g., Faulds, 2010). Under a regional geological framework, we integrated the field observations with the previously mapped known fault and fracture systems and inferred that the NE striking fracture group, parallel to maximum horizontal compressional stress (Reiter et al., 2014), is most likely to be open in the subsurface for fluid flow. Our field observations and interpretation of remote sensing data suggest that the NE oriented fracture group is present in the southern Meager Creek area, forming a sharp boundary as NE trending land surface temperature anomalies, and a persistent feature of internal structure of many observed anomalies, and geographically in a good accordance with observed geophysical anomalies (Chen et al., 2020, 2021).

To improve the flow rate, we propose a geothermal production well strategy (Chen et al., 2020) by:

- a) utilizing a horizontal well to save development costs and reduce environmental footprints;
- b) orienting the horizontal wells to be perpendicular to the maximum horizontal compressional stress to maximize the interaction of open fractures to improve flow rates;
- c) drill the wells from a drilling pad placed in lower elevation in the Meager Creek valley to gain a few hundred meters of additional water head for water flow;
- d) Placing the horizontal legs at the northern end of geothermal reservoir could help maximize heat energy extraction as reservoir temperature increases toward to the volcanic edifice.

Summary and Future Work

Fractures are common in intrusive and metamorphic basement rocks and volcanic rocks that cover them in the study area. The fracture measurements (attitude, spacing and density) were plotted to depict general strike trends and mechanic relationships among the recorded groups at each station, to reveal their spatial relationship to volcanic eruption centers, and to show differences in character between

basement rock and volcanic cover collectively. Preliminary analysis suggests at least three types of fractures, each with distinct characters, that are likely related to different geological processes, such as regional deformation, volcanic activity, and slope stability related to gravitational forces.

The field fracture observations will be used in conjunction with remotely sensed interpretation, and other newly acquired geophysical/geological data to generate regional maps that describe spatial variation of fracture properties, such as fracture density, spacing, dip angle and direction of various groups, and to investigate their relationship with regional deformation belts, volcanic activities, and hazardous gravitational deformation. The results will provide insights for fractured reservoir modeling, and improve our understanding on the geothermal anomalies in the Mount Meager volcanic complex.

In addition, this field geological campaign provides a valuable dataset for validating remote sensing interpretation. However, there are still several key data and technical gaps for identifying and confirming geothermal anomalies in the region. Future field campaigns at Meager are necessary to address the data and technical gaps, particularly for confirming geothermal anomalies zones identified from remotely sensed physical data.

This study provides insights for a better understanding of the volcanic activities and their relationship with the development of the fault/fracture system in the reservoir, helping better define and characterize the geothermal resource prospect with an optimized resource development strategy.

Data

Raw data is provided as a separate excel spreadsheet data file for all the fracture measurements.

Acknowledgements

This is an output from Geoscience for New Energy Supply of Natural Resources Canada. Ms. Christine Deblonde of Geological Survey of Canada (Calgary) provided field GIS equipment, preparation of GIS maps for the fieldwork and the Google Earth map for this report.

Citations

Chen, Z, Grasby, Liu, X., S, Deblonde, C. and Yang, J., 2020. Bedrock fracture study of the Mount Meager Area: implications to geothermal reservoir characterization, Geoconvention 2020, Sept. 21-23, 2020, Calgary, Alberta, Canada. Virtual

Chen, Z., Grasby, E., Deblonde, C. and Liu, X., 2021. AI-enabled remote sensing data interpretation for geothermal resource evaluation as applied to the Mount Meager geothermal prospective area, GSC Open File.

Fairbank; B. D. Openshaw; R. E. Souther, J. G. and Stauder, J, J., 1981, Meager Creek geothermal project: an exploration case study, Geothermal Resources Council Bulletin July 1981, p3-7.

Faulds, J., Coolbaugh, M., Bouchot, V. Moeck, I. and Oğuz, K. 2010. Characterizing Structural Controls of Geothermal Reservoirs in the Great Basin, USA, and Western Turkey: Developing Successful Exploration Strategies in Extended Terranes, Proceedings World Geothermal Congress 2010. Bali, Indonesia, 25-29 April 2010.

GeothermEx Inc., 2004. Report on the south meager geothermal resource British Columbia, Canada, for Western Geopower Corp. 156p.

GeothermEx Inc., 2009. Report on the south meager geothermal resource British Columbia, Canada, for Western Geopower Corp. 20p.

Guo, L., Latham, J. P., and Xiang, J., 2017. A numerical study of fracture spacing and through-going fracture formation in layered rocks, International Journal of Solids and Structures. [Volumes 110–111](#), April 2017, Pages 44-57, <https://doi.org/10.1016/j.ijsolstr.2017.02.004>

Lewis, J.F., and Souther, J.G., 1978, Meager Mt., B.C.-Possible Geothermal Energy Resource: EMR, Earth Physics Branch, Geothermal Series No. 9, Ottawa, 17 pp.

Nemcok, M., Moore, J.M., Allis, R. & McCulloch, J, 2004. Fracture development within a stratovolcano: the Karaha-Telaga Bodas geothermal field, Java volcanic arc, in Cosgrove, J. W. & Enget.DER, T. (eds) 2004. The Initiation, Propagation, and Arrest of Joints and Other Fractures. Geological Society, London, Special Publications, 231, 223-242. 0305-8719/04/\$15 ©. The Geological Society of London 2004.

Read, P. B. ,1990. Mount Meager Complex, Garibaldi Belt, Southwestern British Columbia. Geosciences Canada 17 (3): 167- 170

Reiter, K., Heidbach, O., Schmitt, D., Haug, K., Ziegler, M. and Moeck, I., 2014. A revised crustal stress orientation database for Canada, Tectonophysics 636 (2014) 111–124.

Roy, S.G., Tucker, G.E., Koons, P.O., Smith, S.M., and Upton, P., 2016. A fault runs through it: Modeling the influence of rock strength and grain-size distribution in a fault-damaged landscape, Journal of Geophysical Research: Earth Surface, 10.1002/2015JF003662.

Sanderson, D.J., Peacock, D.C.P., 2019., Line sampling of fracture swarms and corridors, Journal of Structural Geology 122 (2019) 27–37.

Scott, D.N. and Wohl, E.E., 2018. Bedrock fracture influences on geomorphic process and form across process domains and scales, Earth surface processes and landforms, volume 44 issue 1, p. 27-45.

Table 1. List of observation stations and rock samples of the 2019 fieldwork.

Station #	Type	Lat	long	Sample #	Date	On note book	Location
1	Geology	50.67893	-123.499	20190707 #1	20190707	1	Road to the Pumice mine (blockedby slide)
2	Geology +old well site	50.6405	-123.419	20190707 #2	20190707	2	Road side close to field camp
3	Geology+fract	50.65094	-123.438	20190708 #1	20190708	1	Road side-xsection
4	Geology+fract	50.66806	-123.46	20190709 #1	20190709	1	Hot Spring, Keyhole
5	Geology+fract	50.64842	-123.436		20190709	#22	Road side xsection
6	Geology+fract	50.58818	-123.47	20190711 #1	20190711	1	East Meager geothermal prospect
7	Geology+fract	50.58996	-123.464	20190711 #2	20190711	2	East Meager geothermal prospect
8	Geology+fract	50.58985	-123.463		20190711	3	East Meager geothermal prospect
9	Geology+fract	50.58847	-123.465		20190711	4	East Meager geothermal prospect
10	Geology+fract	50.604	-123.489	20190712 #1	20190712	1	E. of Devastation Glacier
11	Geology+fract	50.6045	-123.493	20190712 #2	20190712	2	E. of Devastation Glacier
12	Geology+fract	50.6038	-123.493		20190712	3	E. of Devastation Glacier
13	Geology+fract	50.6298	-123.517		20190712	4	W. M Meager peak

14	Geology+fract	50.62965	-123.518	20190713 #1	20190713	1	W. M Meager peak
15	Geology+fract	50.64124	-123.493	20190713 #2	20190713	2	NE of M Meager peak
16	Geology+fract	50.64148	-123.496	20190713 #3	20190713	3	NE of M Meager peak
17	Geology+fract	50.64269	-123.487	20190713 #4	20190713	4	NE of M Meager peak
18	Geology+fract	50.64282	-123.487	20190713 #5	20190713	5	NE of M Meager peak
19	Geology+fract	50.64617	-123.554		20190713	6	NE of M Meager peak
20	Geology	50.62361	-123.487	20190714 #1	20190714	1	SE. M. Meager peak Ridge
21	Geology+fract	50.62262	-123.486	20190714 #2	20190714	2	SE. M. Meager peak Ridge
22	Geology	50.62309	-123.49		20190714	3	SE. M. Meager peak Ridge
23	Geology+fract	50.6245	-123.491		20190714	4	SE. M. Meager peak Ridge
24	Geology+fract	50.62402	-123.482		20190714	5	SE. M. Meager peak Ridge
25	Geology+fract	50.62428	-123.481		20190714	7	SE. M. Meager peak Ridge
26	Geology+fract	50.6238	-123.481		20190714	8	SE. M. Meager peak Ridge
27	Geology+fract	50.62579	-123.475		20190714	9	SE. M. Meager peak Ridge
28	Geology+fract	50.62663	-123.469		20190714	10	SE. M. Meager peak Ridge
29	Geology	50.62773	-123.47		20190714	11	SE. M. Meager peak Ridge
30	Geology+fract	50.62664	-123.467		20190714	11	SE. M. Meager peak Ridge
31	Geology+fract	50.60446	-123.494	20190715 #1	20190715	1	E. of Devastation Glacier
32	Geology	50.60428	-123.496	20190715 #2	20190715	2	E. of Devastation Glacier
33	Geology	50.604	-123.495		20190715	3	E. of Devastation Glacier
34	Geology+fract	50.6045	-123.489		20190715	4	E. of Devastation Glacier
35	Geology+fract	50.60437	-123.488		20190715	5	E. of Devastation Glacier
36	Geology+fract	50.60434	-123.485		20190715	6	E. of Devastation Glacier
37	Geology	50.56788	-123.515		20190715	7	MC1-2-3 well pad
38	Geology+fract	50.57021	-123.473		20190715	8	Hot Spring, Meager Creek east
39	Geology	50.57044	-123.473		20190715	9	Hot Spring, Meager Creek east
40	Geology+fract	50.57109	-123.527	20190716 #1	20190716	1	Along S Meager drilling trail
41	Geology+fract	50.5705	-123.523	20190716 #2	20190716	2	Along S Meager drilling trail
42	Geology+fract	50.57059	-123.523		20190716	3	Along S Meager drilling trail
43	Geology+fract	50.57073	-123.522		20190716	4	Along S Meager drilling trail
44	Geology+fract	50.57089	-123.522		20190716	5	Along S Meager drilling trail
45	Geology+fract	50.57132	-123.521		20190716	6	Along S Meager drilling trail
46	Geology	50.57153	-123.52		20190716	7	Along S Meager drilling trail
47	Geology	50.57495	-123.513		20190716	8	M-8 well pad
48	Geology	50.56968	-123.527		20190716	9	Along S Meager drilling trail
49	Geology	50.56975	-123.527		20190716	10	Along S Meager drilling trail
50	Geology+fract	50.66907	-123.454	20190717 #1	20190717	1	Road site bedrock outcrop
51	Geology	50.66301	-123.444	20190717 #2	20190717	2	Road side Pumice exposure
52	Geology	50.64228	-123.554	20190718 #1	20190718	1	N of Mount Job peak
53	Geology+fract	50.64195	-123.553	20190718 #2	20190718	2	N of Mount Job peak
54	Geology	50.68149	-123.513	20190718 #3, #	20190718	3	Pumice mine site
55	Geology	50.67759	-123.475	20190707#1	20190718	4	Keyhole Bridge

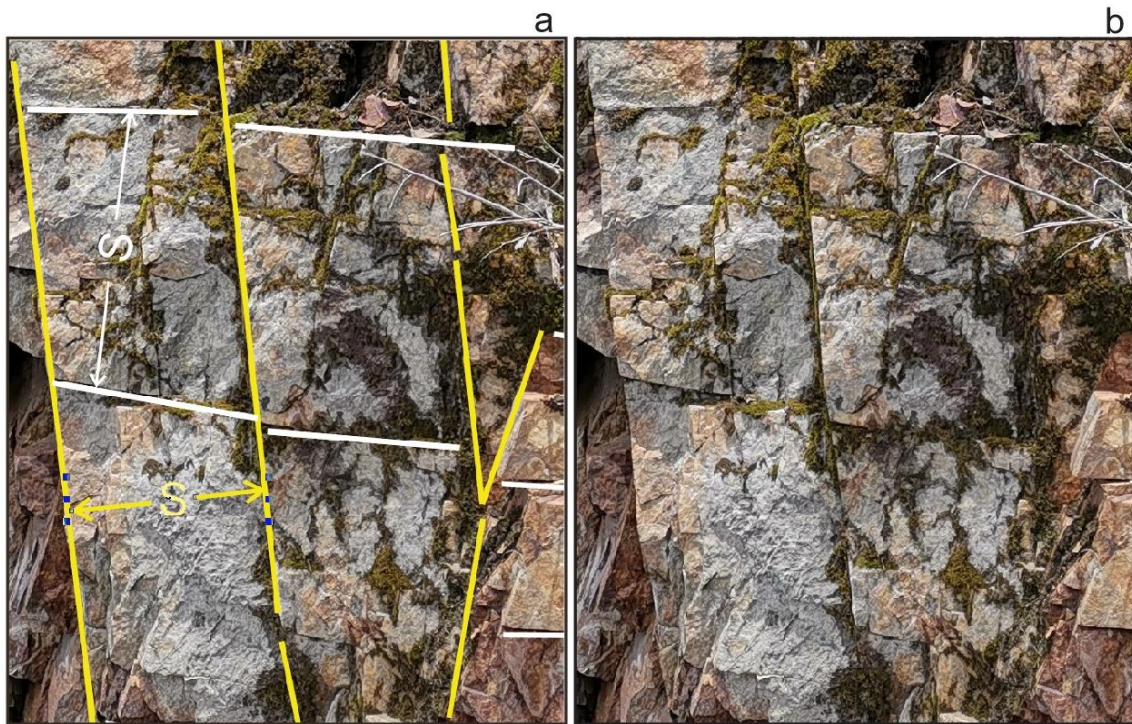


Figure 1. Definition of fracture spacing that measure the vertical distance between two neighbouring fractures of the same fracture set. Left (a): two major fracture sets are recognized and each has its own spacing measures. Right (b): original photo. Photo taken at St. # 5.



Figure 2. A drone photograph showing a bird's-eye view of the roadside cross-section station #3 along the Lillooet River (see location in Figure 3) as well as fracture pattern in the Cretaceous rock complex.



Figure 3. Example feature observation stations: A) the full diamond production test well site (CM-1 well, st. # 37), B) Keyhole hot spring (st. # 4), C) Pumice mine (St.# 54), D) water leaking from permeable intervals between two volcanic layers; E) contact boundaries between volcanic layers, and F) Keyhole fall cliff consisting of welded breccia of competent portion of the volcanic pile (from st. # 55).

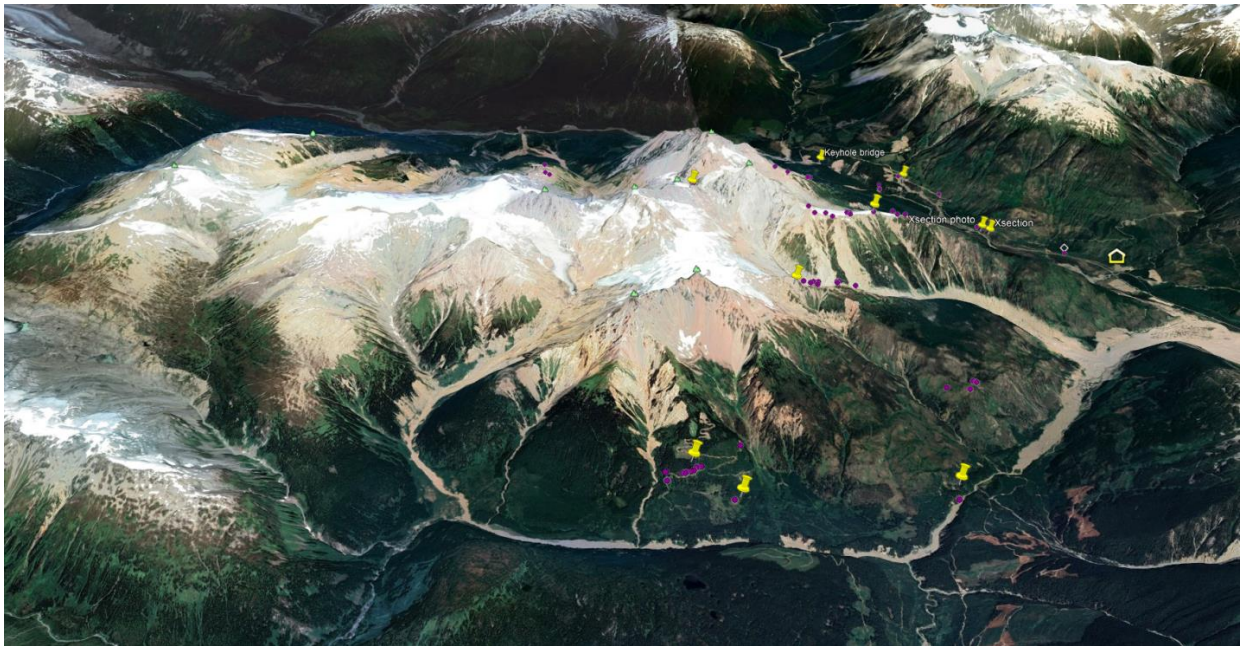


Figure 4 Google Earth view of the study area and locations of observation station (magenta) in the 2019 summer GSC Mount Meager fieldwork. Yellow marker indicates location of photo cross section that will be discussed in the next section.

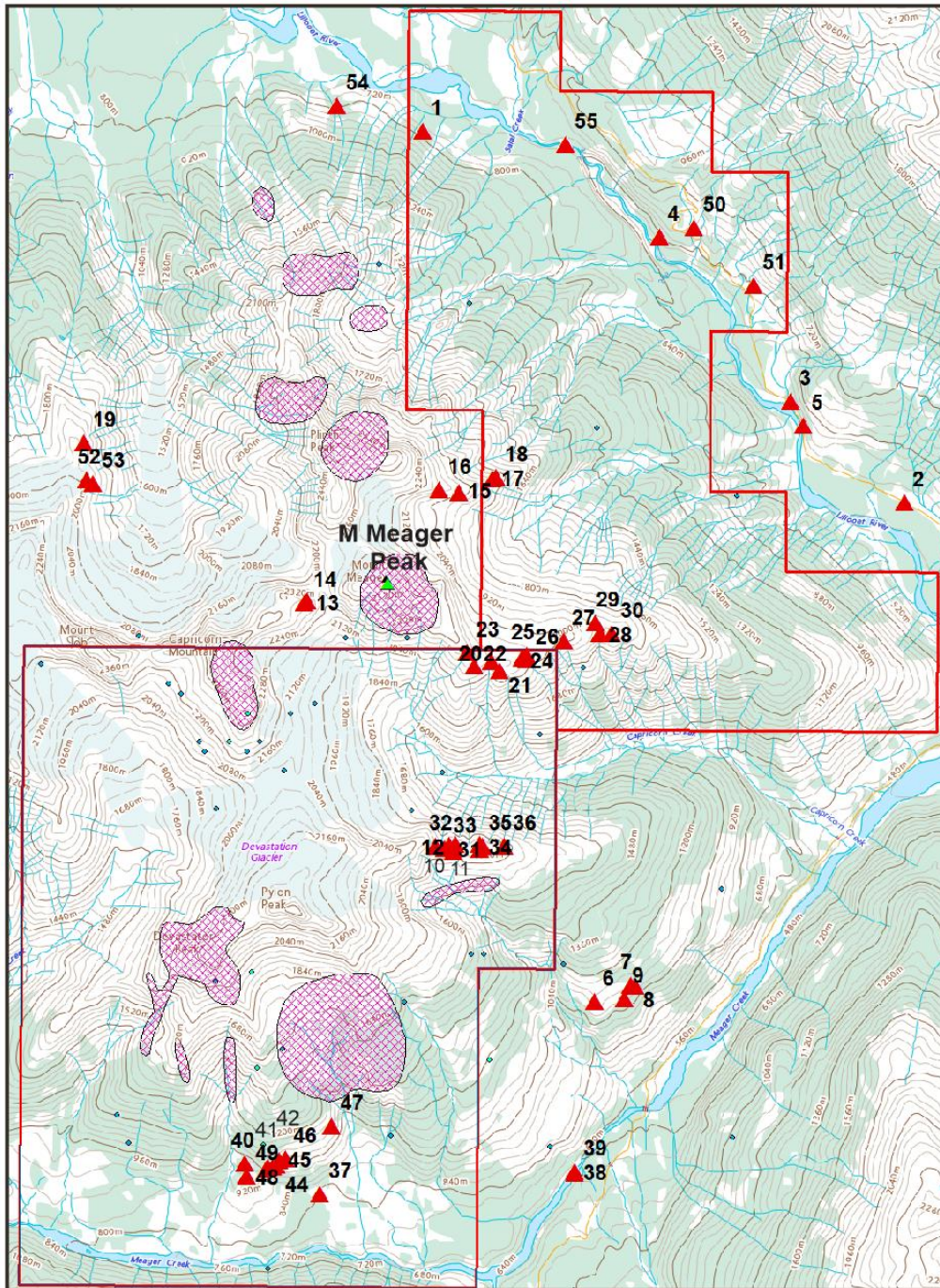


Figure 5. Map showing the locations of the observation station in this study, and regional geological elements and topographic features of the Mount Meager area. (Source of the extent of volcanic complex: GeothermEx Inc., 2004). Red polygons are geothermal energy resource lease blocks and blue dot indicates earthquake event.

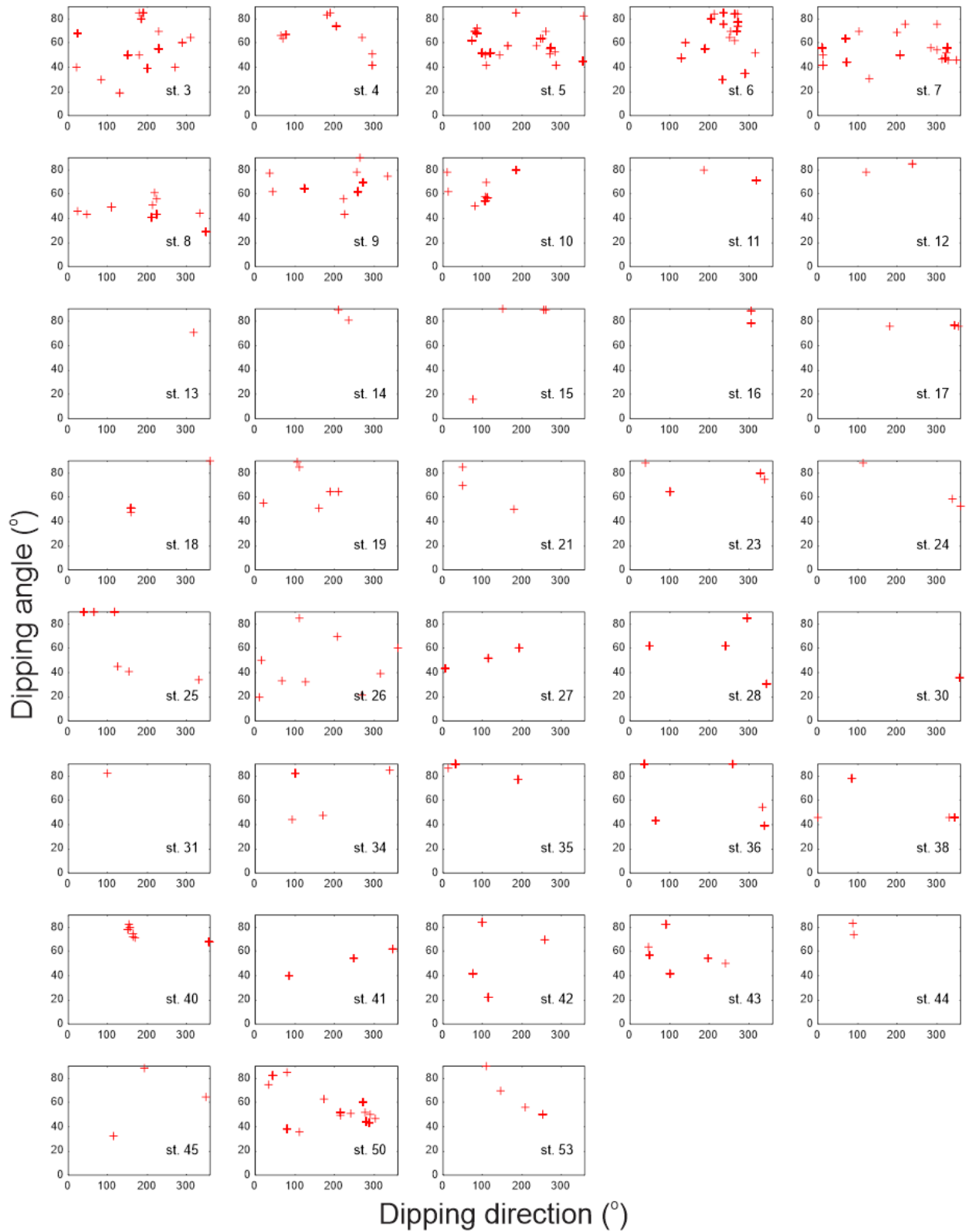


Figure 6. Plots showing the variation of observed fracture dipping direction and angles in various stations. St. in the lower-right is the station number.

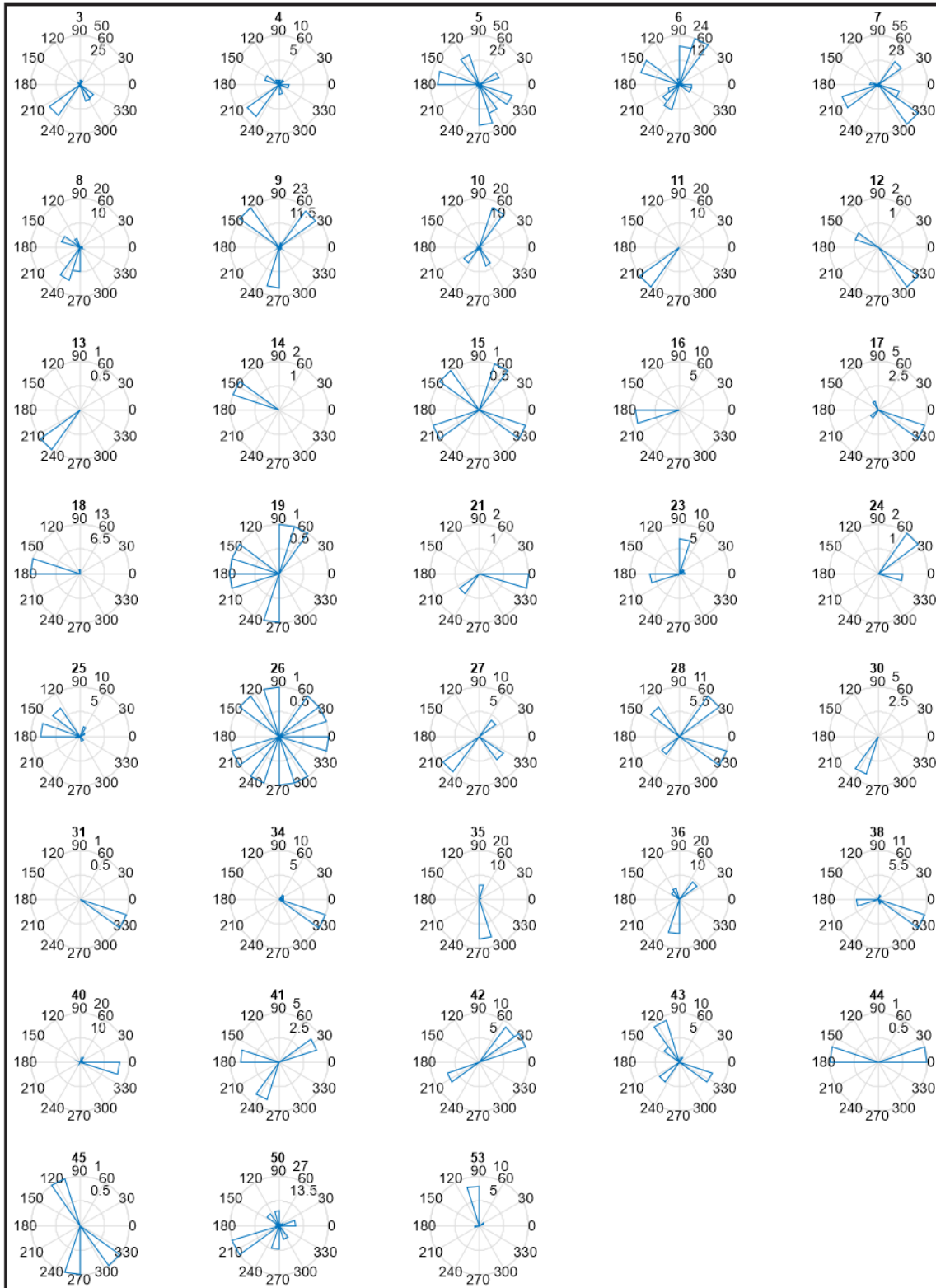


Figure 7. Rose diagrams showing the dip directions of the measured fracture sets in all stations with measurements. Please note that the plots were made directly using Matlab function `rose.m`, which are not comparable with geographic north with an anticlockwise angular axis.

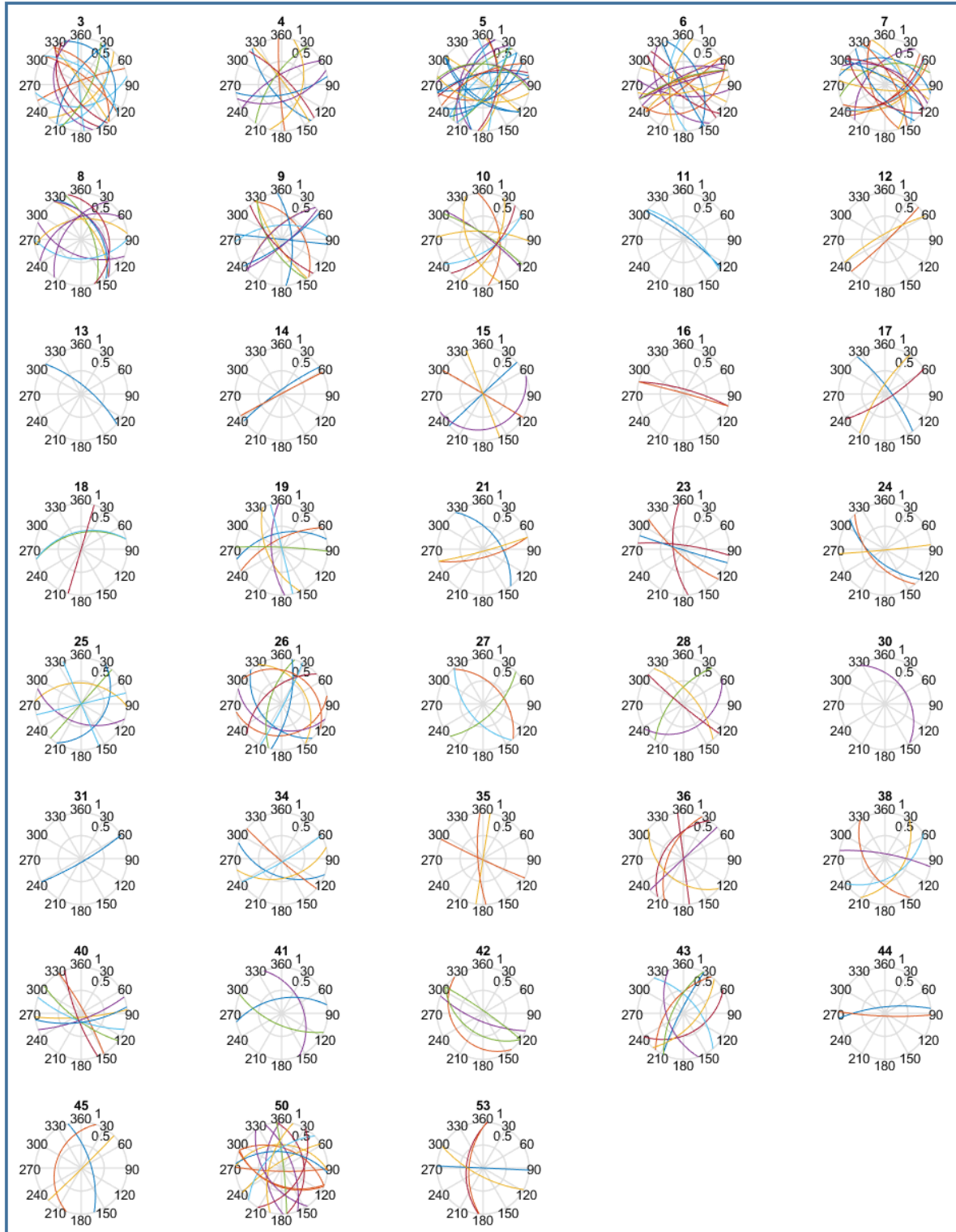


Figure 8. Fracture plane stereo nets for all stations with fracture measurements, showing occurrence and spatial relationship amount the fracture set in each station.

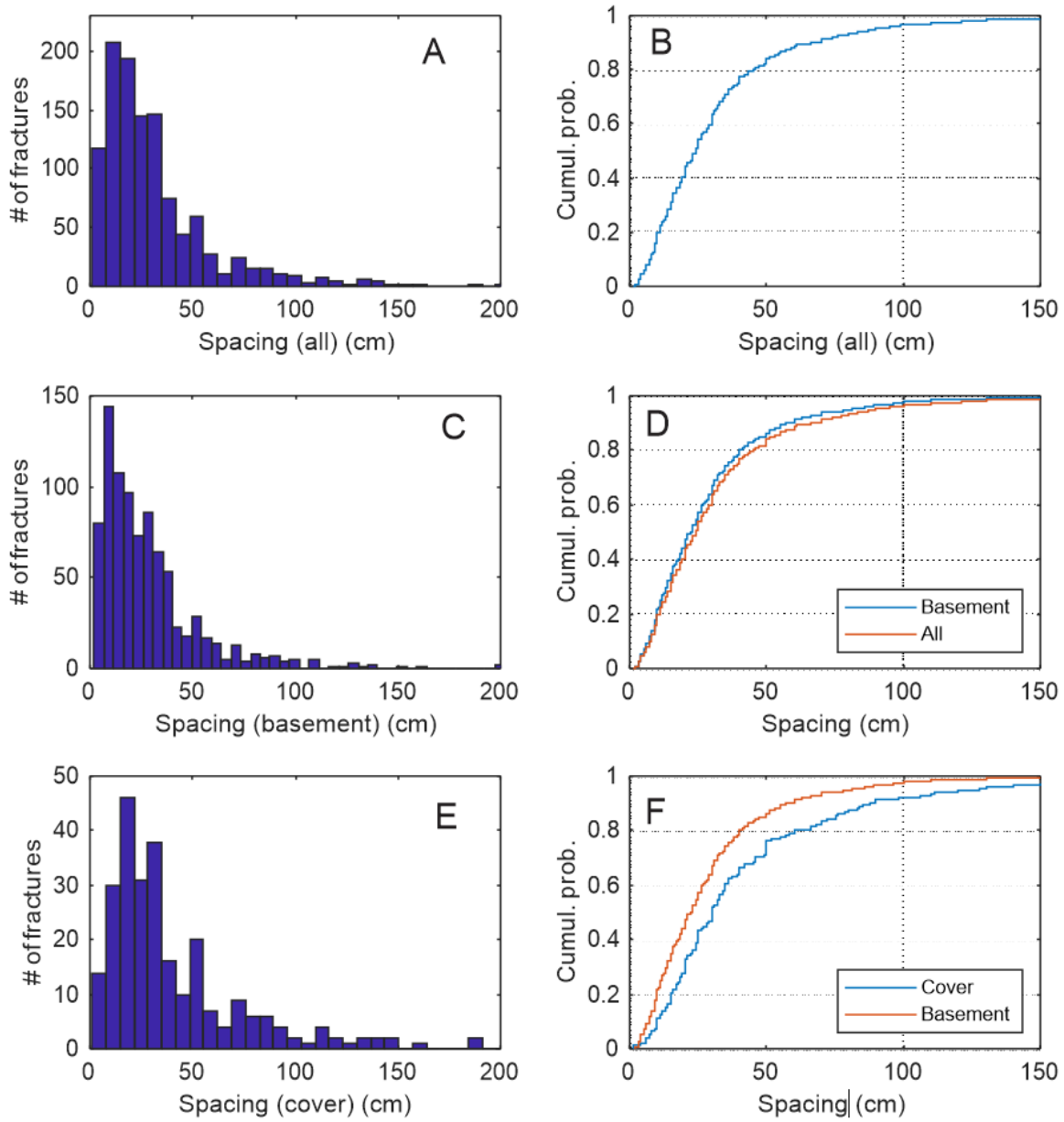


Figure 9. A) histogram of single fracture spacing of all measured fracture group; B) cumulative distribution of all measured single fracture spacing, from which 85% fracture measure have spacing <50 cm; C) histogram of single fracture spacing measured in basement rock; D) cumulative distribution of measured fracture spacing in basement rock; E) histogram of fracture spacing measured in volcanic cover; F) cumulative distribution of measured fracture spacing in volcanic cover.

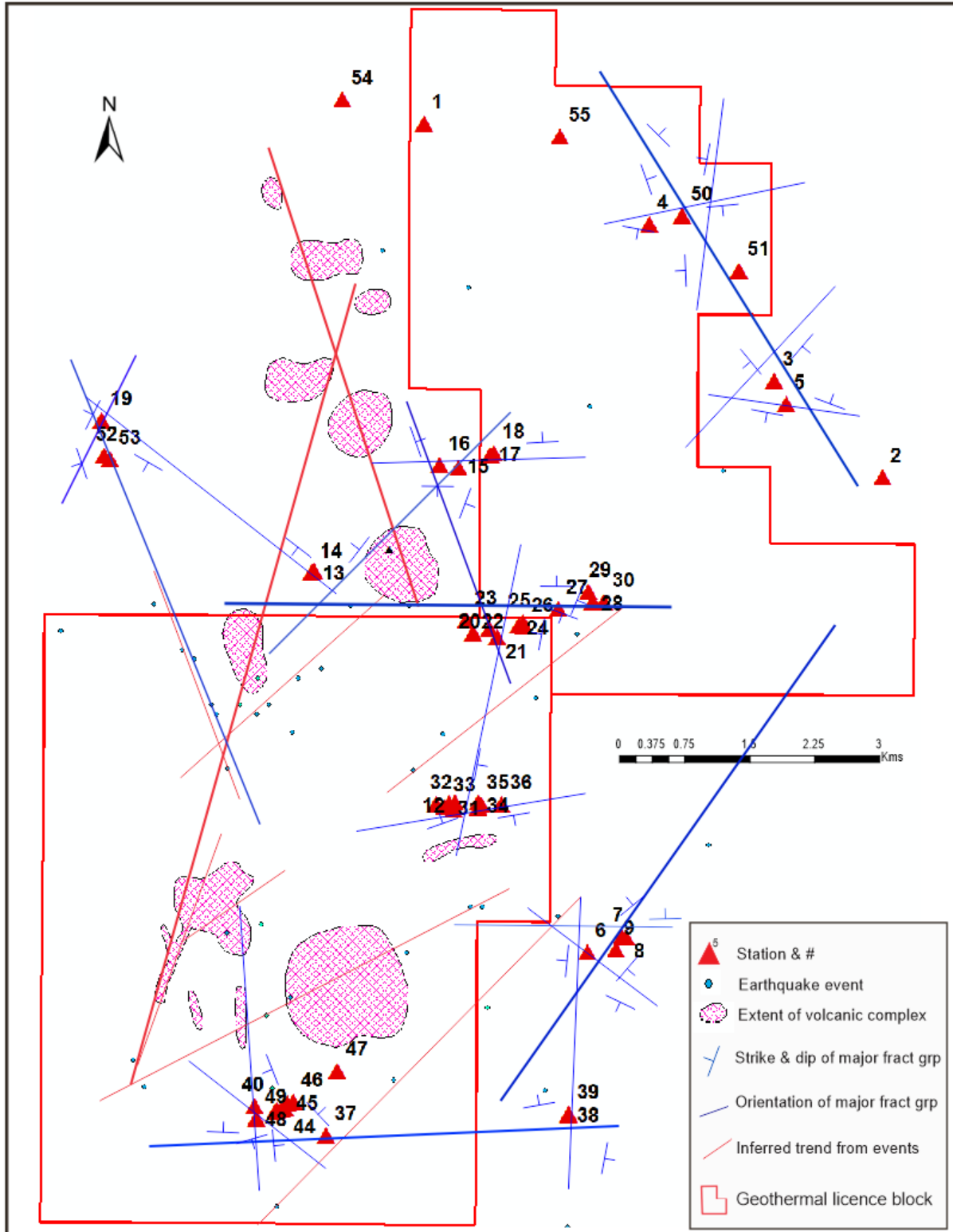


Figure 10. Summary map showing orientation and dip of major fracture groups in the Mount Meager area based on 2019 GSC field observation. The extent of volcanic complex is from GeothermEx Inc. (2004).

Chapter 4 - Gravity Survey at Mt. Meager Volcanic Complex: 2019-2020

Calahorrano-Di Patre, A.E.¹; Williams-Jones, G.

Physical Volcanology Group, Centre for Natural Hazards Research, Department of Earth Sciences, Simon Fraser University, Burnaby, B.C., Canada

Introduction

Geothermal resources, a precious commodity in the current energy climate, are being sought out by companies all over the world as a feasible alternative to carbon-based energy sources (Lebel, 2009). As such, critical information on subsurface processes and geological features needs to be collected by diverse geophysical methods to ensure the best return on investment (Domra Kana et al., 2015). Mapping of subsurface structures is not only useful for imaging an already known reservoir (e.g., the geothermal resource on the southern flank of Mt. Meager), but also to detect new potential project areas and to identify best avenues for efficient extraction (Domra Kana et al., 2015).

Bouguer gravity anomaly maps are one of the valuable geophysical techniques that image subsurface geology. Gravity measurements provide information on density changes below the ground, complementing the information from other geophysical data such as magnetotelluric and passive seismic surveys. Bouguer anomalies are defined as the difference between the observed gravity and the theoretical gravity at the ellipsoid in the same site, considering the influence of elevation, the infinite Bouguer slab, and terrain effects (Hinze et al., 2005; Vajda et al., 2020). Bouguer anomalies - as defined in the geophysical sense - are used to determine variations in mass that reflect the subsurface geology. Inverse modelling of Bouguer anomalies in volcanic areas can help determine the shape and size of hydrothermal reservoirs, elucidate internal magmatic pathways, and better understand the extent of hazards such as landslide-prone areas (MacQueen et al., 2016; Miller et al., 2017; Zurek et al., 2015).

As part of the Mount Meager field program, 81 gravity sites were surveyed in 2019 around the Meager massif, with the preliminary results presented in the Geological Survey of Canada Open File 8732 (Grasby et al., 2020). Due to logistical issues, no measurements were taken in 2019 in the western area of the massif, which forms part of the Upper Lillooet Provincial Park. Despite the 2020 constraints resulting from the COVID-19 pandemic, additional gravity measurements were performed in two different short, physically distanced surveys during the summer of 2020: the first survey spanned from August 4 to August 5, and the second survey from September 14 to September 17. Gravity measurements were also performed at selected stations in July 2020 to link the gravity sites at Mt. Meager with the network of absolute gravity stations from NRCAN/GSC.

The two gravity surveys performed at the Mount Meager Volcanic Complex complemented the results from other geophysical techniques employed in the area to investigate the overarching structure of the massif and surrounding area and constrain its tectonic controls.

Methods

Gravity measurements for all the surveys were collected with a LaCoste & Romberg relative gravity meter (G-127). The gravity meter consists of a zero-length spring which is extended or shortened depending on changes of the gravity field (Lowrie, 2007). G-127 has an Alliod equipped feedback system that allows for

continuous recording of gravity measurements sent through Bluetooth to a handheld receiver. A relative gravity meter does not measure the true value of Earth’s gravity; however, it is capable of measuring the difference in the gravitational field between two sites up to a 1 μGal resolution (1 $\text{mGal} = 0.00001 \text{ m/s}^2$). For this reason, relative gravity meters measure sites in survey loops, where several sites are measured on the same day in a predetermined order, and it is vital to establish one or more reference sites for each survey loop (Battaglia et al., 2008; Lowrie, 2007; Van Camp et al., 2017). Any sites measured with a relative gravity meter need to be “linked” to a site where the gravitational field has been measured by an absolute gravity meter. Since gravity measurements are very sensitive to ambient seismic noise (such as vehicle traffic) and drift or tare effects from transport, survey loops need to consider travel time between stations, and repeatedly measure sites during loops to decrease the potential error in measurements (e.g., Calahorrano-Di Patre et al., 2019).

Relative gravity data needs to be corrected for time-dependent effects, the most relevant of these being Earth tides and daily instrumental drift (Battaglia et al., 2008; Van Camp et al., 2017). Other time dependent effects such as ocean tides are too small in comparison to our survey error and therefore are not considered. For an in-depth explanation of these effects, see Chapter 4 of the Geological Survey of Canada Open File 8732 (Grasby et al., 2020). All measurements presented in this report have been corrected for time-dependent effects using the Matlab suite of programs gTOOLS (Battaglia et al., 2012). gTOOLS computes and corrects the Earth tide effect on measurements, calculates the linear instrumental drift, and computes the weighted least-square adjusted gravity values as well as the accumulated errors on the data.

Once the corrected relative gravity measurements have been obtained, and the absolute gravity has been calculated for each site by adding or subtracting the difference between the measured site and the absolute station, the Bouguer gravity anomalies can be inferred. In order to determine spatial subsurface mass changes, it is necessary to remove from the gravity data the effects of topographical and spatial features. As such, the contribution of elevation changes from station to station (free-air effect), latitude variations, infinite Bouguer slab, and terrain need to be removed from the data. To do so, we used the open-source program GSOLVE, a Python GUI program created to calculate gravity anomalies from relative gravity measurements (McCubbine et al., 2018), with different modules that compute sequentially the spatial corrections. An in-depth description of the spatial corrections was presented in Chapter 4 of the Geological Survey of Canada Open File 8732 (cf. Hinze et al., 2005; Li & Götze, 2001; Lowrie, 2007; Vajda et al., 2020). For this report, we list only the relevant equations (Table 1).

Table 1. Spatial effects to be removed from absolute gravity data and their equations.

Spatial effect	Correction on Data
Free-air effect (δg_{FA})	$-0.3086H \text{ mGal m}^{-1}$
Normal Gravity - Latitude Correction ($\gamma(\varphi)$)	$\gamma_a \frac{1+k\sin^2(\varphi)}{\sqrt{1-e^2\sin^2(\varphi)}} \text{ mGal}$
Bouguer Slab Correction (δg_{Bs})	$-0.0419\rho H \text{ mGal}$
Terrain Correction (δg_{TC})	Nagy prism formula (Nagy, 1966)

Where H is the station elevation above the ellipsoid, and ρ is the rock density in g/cm^3 . The typical value of 2.67 g/cm^3 will be used for the preliminary results, however, other rock densities collected by the geologic mapping team on site will be used in the future to further reduce the data. The normal gravity refers to the theoretical value of the gravitational field on the reference ellipsoid (either GRS80 or GRS67). For this report, the reference ellipsoid used is GRS80, and φ is the ellipsoidal latitude of the station, γ_a is

the normal gravitational acceleration at the equator (978032.67715 mGal for GRS80), k is the normal gravity constant (0.001931851353 for GRS80), and e^2 is the square of the first numerical eccentricity of the ellipsoid (0.00669438002290 for GRS80)(Moritz, 1980). A complete Bouguer anomaly is then defined by:

$$\Delta g_{BA} = g - \gamma(\varphi) - \delta g_{FA} + \delta g_{BS} + \delta g_T$$

GSOLVE calculates the terrain correction from a Digital Elevation Model (DEM) by using the Nagy prism formula (Nagy, 1966). GSOLVE allows for calculations of terrain corrections inside a selected range annulus (with a minimum and maximum radius) around several points (McCubbine et al., 2018). Although in the past, different resolution DEMs were used to correct the topography effect around stations in Mt. Meager, for consistency only one DEM is used to correct all data points in the report; an internal annulus radius of 6.25 m and a maximum radius of 25,000 m. The DEM used for calculating the terrain correction is an ALOS Palsar Radiometric Terrain Corrected GeoTiff, with a 12.5 m spatial resolution on single polarization mode (FBS). All the elevations are in relation to the ellipsoid GRS80.

Data Collection

Linking Absolute Measurements to Relative Sites

Gravity sites from the 2019 field program at Mt. Meager were referenced to the station BASE, located in the base camp at the Innergex Power Plant (Lat: 50.63556755°, Long: -123.4055742°, Figure 1). In order to determine the true gravity field values at the stations, the BASE site was linked to the absolute gravity site CGSN-9929-2008 (shortened to ABSW for this study), located in West Vancouver and last surveyed by NRCAN in 2019. Since the travel time between Mt. Meager and West Vancouver is long enough to potentially cause an increase in the error of the data, and taking into account logistical constraints, three more gravity sites were surveyed between West Vancouver and Mt. Meager: SFU1 (located near the RCMP office in Squamish), SFU2 (located in front of the Whistler Fire Department in Whistler Village), and SFU3 (located near the Village of Pemberton). At all the SFU sites, a metal rod was installed to mark the measured point and make it available for future surveys (Table 2).

Survey loops were performed using the step-method, where stations were measured consecutively, and sites were measured twice or more in one day (e.g., ABSW-SFU1-ABSW-SFU1-SFU2-SFU1-ABSW). The reference station for the survey loop was measured at the beginning and end of day. The survey consisted of two daily-loops: stations ABSW, SFU1, and SFU2 were measured on July 16, 2019 while stations SFU1, SFU2, and SFU3 were measured on July 17. At each station, the accurate position of the site was recorded using a differential GPS Leica receiver, which continuously measured over the span of 2.5 hours to achieve less than 10 cm error in the position. The GPS data was processed using the Precise Point Positioning (PPP) online service from Natural Resources Canada. The processing mode was static, using the ITRF reference frame with the CGVD2013 datum. The sites locations are presented in Table 2, where the elevation is the ellipsoidal height.

Table 2. GPS locations of stations linked to ABSW in Squamish, Pemberton, and Whistler. ABSW is the measured absolute gravity site CGSN-9929-2008.

STAT	LAT (deg)	LONG (deg)	ELEV (m)	Sigma X (m)	Sigma Y (m)	Sigma H (m)
SFU2	50.11626	-122.95407	657.668	0.015	0.015	0.079
SFU3	50.32400	-122.75200	328.726	0.010	0.011	0.049
ABSW	49.3516344	-123.24916	148.885	0.013	0.013	0.060
SFU1	49.7183925	-123.146989	-11.813	0.012	0.016	0.048

July and August 2019 Meager Survey

A total of 81 survey gravity stations, aside from the Innergex base station, were measured around the Mount Meager Volcanic Complex during July and August 2019. The survey grid was established considering the desired resolution of the results and on assumptions based on previously released data (Witter, 2019).

Station density varied between spacings of 250 to 500 m in order to image shallower and smaller structures like the hydrothermal system, to an average of 1 to 2 km distance between measured sites to capture the gravity signature of deeper and larger structures. Closely spaced stations at Mt. Meager were located near points of interest (such as the South Meager geothermal area and the ridges below Pylon Peak and Mt. Meager) while stations were surveyed at a wider spacing farther away from the edifice or at points located on sharp topographic features such as the ridge below Capricorn Mountain. Most of the surveyed sites were reached via helicopter, except for those located along the North Lillooet Forest Service road. To reduce travel times and surveying costs, gravity stations were located close to the measurement sites of other geophysical methods (MT, AMT, and seismic stations) when possible. The resulting network is shown in Figures 3 and 4. A picture of one of the measurements is shown in Figure 6.

In order to correct for drift and other temporal effects, a base (BASE) station was established at the Innergex Power Plant (Lat: 50.63556755°, Long: -123.4055742°, Figure 1) which was measured at the beginning and the end of each day. Gravity sites in the rest of the survey area were sequentially measured in between these two BASE measurements. To ensure high precision measurements that reflect reality and to avert and correct the effect of instrumental tares in the data, a protocol of measurement stabilization was implemented: in each station, measurements were recorded when a difference of less than 10 μGal between 5 consecutive measurements was achieved. Selected gravity sites were measured in different daily loops of the survey to check for repeatability. Additionally, to avoid excessive instrumental drift, days where more than 5 hours would be spent between the beginning and end of the day had an extra repeated BASE measurement between occupations of survey stations. Repeatability of measurements based on the doubled-surveyed sites was within 25 to 30 μGal , while the closure of daily loops (the gravity difference between two BASE measurements in a day) generally did not surpass 40 to 50 μGal . Two long days (>5 hrs) in which the end of the day closure reached 100 μGal and 150 μGal respectively, are notable exceptions; however, these values are still within an acceptable measurement error for a Bouguer gravity survey.

The precise position of the gravity sites was measured with a Juniper Geode sub-meter GNSS receiver. The Geode is a novel hand-held GNSS, which uses a SBAS correction signal to achieve a 30 cm horizontal accuracy (Juniper Systems, 2019). The Geode has a receiver type GNSS single frequency with carrier phase tracking, 162 channels, and 3 channel SBAS parallel tracking. The data collected is in NMEA 0183, crescent binary format. The Geode was mounted on a one-meter vertical pole beside the gravity meter to improve the line of sight (except in chosen stations where the usage of the pole was not possible or unnecessary). GNSS measurements were collected at a frequency of 1 Hz and stored for the totality of the gravity reading. The time-series of x,y,z positions were then post-processed to remove data outliers, and the average values of stabilized and low-error measurements were chosen as the site position.

August 04-05 and September 14-17, 2020 Meager Survey

Due to COVID-19 constraints in 2020, the SFU team did not stay overnight at the Innergex base camp (located near station BASE), and instead stayed in an hotel close to the SFU2 site in Whistler. As such, each survey loop began and ended at station SFU2, where 5 minutes of measurements were collected with a

frequency of 1 second. After the gravity team measured the reference station (SFU2), they were transported by helicopter from the No-Limits Heli adventure helicopter pad (Lat: 50.168726, Lon: -122.905241) to the BASE station at Mt Meager for another 5 minutes of gravity measurements. Other stations were then measured around the massif, by optimizing spatial coverage of the previously non-surveyed area and flying time. In a similar manner to the 2019 survey, to ensure that measurements reflect reality and tares are averted, a protocol of measurement stabilization was implemented: at each station, measurements were recorded when a difference of less than 10 μGal between 5 consecutive measurements was achieved. Gravity sites were predominantly reached by helicopter, while ridges were traversed by foot. Average site spacing in the network was 1 km, however, measurements located on ridges near points of interest (where shallower features were suspected) were surveyed with a distance of 500 m between each other. Gravity survey loops usually ended with one measurement at the BASE station, and then after the flight back to Whistler, a final measurement at the reference station SFU2. As a notable exception, the BASE measurement at the end August 4 was skipped due to fluctuations of the battery power of the instrument. A longer measurement was taken at SFU2 (after changing the problematic battery) to take into consideration any potential drift due to power loss in the gravity meter. Stations G082 to G096 were measured on August 4 and 5.

During the September survey, besides the constraints imposed by the COVID-19 pandemic, helicopter flights were severely disrupted by smoke coming from the Washington and California Wildfires. As such, on September 14 and 15, it was not possible to fly towards Mt. Meager. As an alternative, gravity sites were measured alongside the road leading from station SFU2 to BASE, resulting in a loop connecting the two stations, and adding stations to the broader Garibaldi Volcanic Belt Project (L001 to L009). On September 16 and 17, the same framework used in the August survey was employed for measuring stations G097 to G113.

In comparison with measurements from the 2019 survey, the survey closures (the difference between the first and last measurement of the day in the same station) were much larger, although within the limits of error for a Bouguer survey (100-150 μGal closure). The reason for these larger differences is likely due to the extended travel time between the reference station SFU2 and the BASE station at Mt. Meager (30 min. helicopter flight), or perhaps power issues as seen on August 04. Although the survey closures were large, the drift for all the survey loops was still linear, and as such could be removed without issue from the data. It would be impossible to prove the validity of the loops beyond a doubt without a secondary reference station near Mt. Meager, hence the need to measure the BASE site twice for each survey loop in addition to reference station SFU2.

Similar to the 2019 survey, GPS measurements at each station were obtained with the Juniper Geode sub-meter GNSS receiver. In order to improve its line of sight, the Geode was mounted on a one-meter vertical pole beside the gravity meter or on a camera tripod levelled to be horizontal to the ground. GNSS measurements were again collected at a frequency of 1 Hz and stored for the totality of the gravity reading. The measurements were then post-processed to remove outliers in the data, and the average of the readings were used as the elevation of the gravity site, removing the length of the pole or tripod. The maps of measured gravity sites at the area around Mt. Meager are shown in Figures 3 to 5. In Figure 5, stations measured during 2020 are highlighted in red.

Results

Absolute gravity link

The results from GTOOLS processing of gravity data for the July loop of stations ABSW, SFU1, SFU2, and SFU3 are shown in Figures 7-16. Note that the errors on the individual measurements are slightly larger

than for Mt. Meager sites, as these stations are located near areas of high vehicle traffic. Once the corrected differences between stations were processed, the absolute gravity is found by adding the difference station ABSW and the other measured sites. The results are summarized in Tables 3-6.

Table 3. Relative gravity difference between stations ABSW, SFU1, and SFU2 measured on July 16. The small value of ABSW is related to the residual of the drift correction. The NaN error value is displayed when GTOOLS cannot calculate deviation from the linear drift as there is only one measurement at the selected station for that survey loop.

SITE	DATE (dd-mmm-yy)	LSGRAVITY	STDEV (mGal)	STDERROR (mGal)
ABSW	16-jul-20	0.0013	0.0043	0.0025
SFU1	16-jul-20	-16.7246	0.004	0.0023
SFU2	16-jul-20	-98.488	NaN	NaN

Table 4. Relative gravity difference between stations SFU1, SFU2, and SFU3 measured on July 17. The small value of SFU1 is related to the residual of the drift correction. It must be noted that these are differences related to SFU1.

SITE	DATE (dd-mmm-yy)	LSGRAVITY (mGal)	STDEV (mGal)	STDERROR (mGal)
SFU1	17-jul-20	0.0064	0.0303	0.0214
SFU2	17-jul-20	-81.7231	0.0244	0.0141
SFU3	17-jul-20	-18.0402	0.0331	0.0234

Table 5. Relative gravity difference between stations BASE, SFU2, and SFU3, measured over several surveys during the summer. All the measurements are in relation to SFU2.

SITE	DATE (dd-mmm-yy)	LSGRAVITY (mGal)	STDEV (mGal)	STDERROR (mGal)
BASE	14-sep-20	19.6662	NaN	NaN
SFU2	14-sep-20	0.0019	0.036	0.0255
SFU3	14-sep-20	63.6274	0.0362	0.0256
BASE	16-sep-20	19.8266	0.0321	0.0227
SFU2	16-sep-20	0.0043	0.0319	0.0225
BASE	04-aug-20	19.7669	NaN	NaN
SFU2	04-aug-20	-0.0001	0.0005	0.0003
BASE	05-aug-20	19.7283	0.0292	0.0207
SFU2	05-aug-20	0.0094	0.0282	0.0199

Table 6. Absolute gravity values for stations linked directly or indirectly to ABSW (CGSN - 9929-2008), using the average relative gravity differences presented in Tables 1-3.

SITE	Absolute Gravity (mGal)
ABSW	980919.501
SFU1	980902.761
SFU2	980821.014
SFU3	980884.697
BASE	980840.757

Bouguer Anomaly Map of Mt. Meager

After applying the temporal and spatial corrections detailed in the Methods section using equation 1, the Bouguer gravity anomalies can be estimated for all the measured stations (the step by step corrections on the data are presented in Tables 7-9). In order to visualize the final results of Table 9, the Bouguer gravity anomalies measured at each station were interpolated with ArcGIS for the area presented in Figure 16 using empirical Bayesian kriging. Empirical Bayesian kriging uses an intrinsic random function as the kriging model, thus negating the danger of assuming a tendency toward an overall mean (Krivoruchko & Gribov, 2019). The power semivariogram was selected for the interpolation since it did not cause sudden “eyes” in the data (in contrast with the thin plate spline variogram) and minimized ragged lines and angles in the interpolation (which was prominent with the linear semivariogram). In Figure 16, data from station G046 was not considered for the kriging, as the measurement at the site differs by more than 100 mGal from the nearby stations and thus it is an obvious outlier. It is noteworthy that the interpolation is stable, as removing random data points did not cause a substantial change in the result.

Although the Pemberton Meadow stations L001-L009 and stations SFU2 and SFU3 were also corrected for spatial effects, they were not included in the interpolation since the straight line and poor station density over a large area disrupted the kriging. All the results are presented in Table 9.

Figure 16 presents the gravity anomalies at Mt. Meager and the surrounding areas. The addition of survey stations in the survey of 2020 on the western and northern flanks of the complex help immensely to elucidate the previously ambiguous low gravity regions discussed in the 2019 preliminary gravity map (Chapter 4 of the GSC Open File 8732; Grasby et al., 2020). Some key information that can be extracted from Figure 16:

1. There is a low gravity region around the area associated with the South Meager Geothermal Project. Future inverse modelling will focus on this anomaly to image shallow sources.
2. The negative anomaly on the northern flank of Meager, already observed in the 2019 map (Chapter 4 of the GSC Open File 8732; Grasby et al., 2020), is much larger than previously estimated. The addition of several stations around the area shows that it is not only due to the influence of the river sediments as previously hypothesized. Reprocessing of the terrain corrections with more representative rock densities might change the values of the gravity anomaly and might be an avenue to investigate in future studies.
3. Large positive anomalies in the mountains surrounding Mt. Meager and on the south-western flank of the massif confirm that the low-density areas are constrained to only certain parts of Mt. Meager. Moreover, the large gravity anomalies around the area, consistent with the volcanic setting, are promising and modelling of the data will help clearly distinguish the subsurface geological features.

Conclusions and Possible Future Work

Gravity measurements were collected at 113 survey stations around the Mt. Meager Volcanic Complex during the Summer Field Seasons of 2019 and 2020, with an additional 9 surveyed sites located along the Lillooet Forest Road and Pemberton Meadows, and three reference stations located near Mt. Meager, Pemberton, and Whistler. The network of gravity sites around the Mt. Meager Volcanic Complex was designed to enable detection of both shallow and deep subsurface mass variations. The 2020 surveyed sites allow for spatial coverage of the western side of the volcanic complex, and a tighter network of sites on the northern flank, while sites surveyed in 2019 cover mainly the eastern flanks of Mt. Meager, focusing on the area related to the South Meager Geothermal Project. All the Mt. Meager sites were linked to the

absolute gravity station CGSN-9929-2008, last surveyed by NRCAN in 2019, allowing for the conversion of relative “instrumental dial” measurements to true gravity values. The established reference stations in Squamish, Pemberton, and Whistler will be valuable assets for future gravity measurements in the Garibaldi Volcanic Belt. All measurements were collected with a relative LaCoste & Romberg gravity meter and corrected for temporal effects - such as tide and drift - with the gTOOLS suite of programs. Spatial corrections were performed using the Python-based program GSOLVE, which not only performs the simple Bouguer corrections (free air, latitude, and Bouguer slab correction), but also calculates Terrain corrections based on DEMs of the area.

The Bouguer gravity anomaly map presented in this report shows two regions of relatively low gravity: the area of the South Meager Geothermal Project, as well as the northern flank below Plinth Peak and on the opposite mountain. A positive gravity anomaly was also detected on the mountains south of Mt. Meager, and on the south-western flank of the volcanic complex. These results differ from the preliminary 2019 map due to the addition of data from the 2020 survey stations, as well as the switch from two different resolution DEMs to just one for the Terrain correction. The methodology and processing of gravity data collection and the reduction of measurements has been refined so that the Bouguer gravity anomaly map is as accurate as possible considering the amount of data available.

This Bouguer gravity anomaly map has sufficient data density to allow for simple forward and inverse modelling. Open-source software packages such as GRAV3D (UBC-GIF, 2017) and SimPEG (Cockett et al., 2015) have the capabilities for performing such modelling with the available gravity anomaly values, as well as a number of other proprietary codes (e.g., Geosoft). Considering the different datasets collected alongside the gravity surveys, it would be possible (and advisable) for these inverse models to be informed by results from other geophysical methods such as MT and passive seismic data. Finally, since the raw gravity data and all the steps for reducing the corrections are presented here, additional analysis can be surmised by other researchers in the future if necessary, and supplementary maps can be created from the already provided data (e.g., isostatic maps) which can further develop the understanding of subsurface structures at the Mt. Meager Volcanic Complex.

The work done during the 2019 and 2020 gravity surveys at the Mt. Meager Volcanic Complex has provided invaluable data for the analysis of sub-surface structures. This is the first complete gravity survey at Mt. Meager, with stations located with tight spacing around areas of interest as well as stations surveyed far away of Meager for reference. The step-by-step analysis and the strict methodology used during survey ensures that the collected data will have value beyond this report. At the conclusion of this multidisciplinary project at the Mt. Meager Volcanic Complex, the initial objectives proposed by the gravity team - the collection of a robust dataset of gravity values and subsequent generation of a Bouguer gravity anomaly map - have thus been achieved, with numerous possibilities for further work with the obtained datasets.

Data

Table 7. Gravity differences between reference and survey stations collected during the Summer 2019 and Summer 2020 surveys at the MMVC, corrected for temporal effects. The sites measured during the Summer 2020 start from G082 to G113 for the Mt. Meager Area, and L001-L009 for the Pemberton Meadows/Lillooet Forest road. The "absolute gravity" values were obtained by linking the BASE station to the absolute gravity station CGSN- 9929-2008 (ABSW).

Name	Absolute Gravity (mGal)	Standard Error (mGal)	Number of Observations	Latitude (deg)	Longitude (deg)	Elevation (m.a.e)
BASE	980840.766	0.012	40	50.6355675	-123.405574	473.662018
G001	980773.797	0.025	1	50.6850914	-123.478499	724.867
G002	980856.026	0.024	1	50.6224858	-123.400172	412.655
G003	980840.055	0.025	1	50.6386853	-123.414103	460.908
G004	980834.517	0.025	1	50.643601	-123.429881	449.924
G005	980823.118	0.026	1	50.6509293	-123.438205	467.457
G006	980807.231	0.026	1	50.6603613	-123.445788	534.014
G007	980680.295	0.024	1	50.5777116	-123.519648	1366.765
G008	980688.798	0.024	1	50.5765999	-123.520833	1320.512
G009	980693.261	0.024	1	50.5760687	-123.520368	1301.63
G010	980780.847	0.025	1	50.6834902	-123.492292	674.288
G011	980474.258	0.025	1	50.6241061	-123.539689	2334.709
G012	980601.427	0.024	1	50.5838289	-123.53668	1759.159
G013	980637.37	0.024	1	50.5142708	-123.436377	1718.323
G014	980864.874	0.025	1	50.5785118	-123.292751	336.636
G015	980728.182	0.025	1	50.574957	-123.512911	1105.828
G016	980737.195	0.024	1	50.5729998	-123.514609	1064.288
G017	980753.729	0.024	1	50.5713607	-123.526785	974.189
G018	980764.987	0.024	1	50.568274	-123.527122	921.589
G019	980772.981	0.025	1	50.565991	-123.526444	877.908
G020	980537.228	0.025	1	50.6238385	-123.487432	2088.079
G021	980546.564	0.025	1	50.6241532	-123.480505	2039.521
G022	980551.704	0.024	1	50.6252219	-123.476855	2010.219
G023	980857.657	0.025	1	50.5928136	-123.353948	361.198
G024	980589.524	0.025	1	50.6040269	-123.484401	1823.743
G025	980581.768	0.024	1	50.6038172	-123.490423	1865.72
G026	980574.288	0.024	1	50.6040963	-123.494321	1895.409
G027	980533.477	0.024	1	50.6036941	-123.504756	2078.366
G028	980535.371	0.024	1	50.6035259	-123.502292	2062.542
G029	980617.25	0.025	1	50.600813	-123.482481	1705.59
G030	980623.797	0.025	1	50.6014367	-123.478024	1673.244
G031	980647.067	0.026	1	50.5474184	-123.558379	1595.727
G032	980747.693	0.025	1	50.5711684	-123.519046	1012.591
G033	980753.677	0.024	1	50.5713681	-123.514333	971.615
G034	980760.11	0.024	1	50.572234	-123.511486	931.316
G035	980786.592	0.026	1	50.5680744	-123.514271	790.921
G036	980668.13	0.026	1	50.6002693	-123.671419	1629.552
G037	980683.545	0.025	1	50.5800316	-123.620082	1479.397
G038	980781.966	0.024	1	50.7326077	-123.707255	803.301
G039	980691.796	0.024	1	50.7354588	-123.470546	1199.056
G040	980758.904	0.024	1	50.6814083	-123.513102	788.92

G041	980782.449	0.025	1	50.5672608	-123.517827	812.057
G042	980789.199	0.026	1	50.5658239	-123.513271	776.225
G043	980690.902	0.025	1	50.5845516	-123.491057	1339.53
G044	980709.463	0.024	1	50.5804927	-123.490749	1241.694
G045	980723.956	0.024	1	50.5791589	-123.487863	1167.353
G046	980836.796	0.024	1	50.5761578	-123.487899	1097.519
G047	980500	0.025	1	50.6313709	-123.51538	2235.599
G048	980510.812	0.025	1	50.6443647	-123.525915	2158.968
G049	980582.93	0.026	1	50.6380028	-123.534621	1833.293
G050	980563.623	0.025	1	50.7338787	-123.57778	1961.941
G051	980491.29	0.024	1	50.6180723	-123.572071	2332.977
G052	980552.77	0.023	1	50.6420909	-123.5538	1987.437
G053	980775.348	0.023	1	50.6852253	-123.528212	727.959
G054	980625.274	0.023	1	50.660085	-123.509751	1560.251
G055	980684.681	0.023	1	50.6494019	-123.476593	1276.142
G056	980661.266	0.023	1	50.6388679	-123.477491	1454.857
G057	980855.271	0.023	1	50.6142801	-123.383482	395.069
G058	980855.497	0.024	1	50.6036539	-123.372217	388.592
G059	980559.365	0.026	1	50.637637	-123.527805	1945.765
G060	980792.957	0.025	1	50.5609998	-123.536435	750.618
G061	980804.776	0.024	1	50.5617325	-123.505065	676.509
G062	980813.922	0.024	1	50.5592999	-123.489066	642.663
G063	980820.219	0.024	1	50.5686921	-123.474703	604.481
G064	980781.09	0.026	1	50.6687334	-123.451725	688.134
G065	980749.182	0.026	1	50.6757162	-123.464423	866.522
G066	980623.701	0.025	1	50.4855654	-123.497967	1790.601
G067	980528.07	0.019	2	50.5618362	-123.417272	2219.48
G068	980579.207	0.023	1	50.5946119	-123.50125	1875.484
G069	980595.904	0.024	1	50.5948547	-123.497167	1796.456
G070	980611.957	0.025	1	50.5943342	-123.493999	1722.517
G071	980601.989	0.024	1	50.6960858	-123.354437	1822.096
G072	980834.558	0.019	2	50.5998121	-123.435066	513.288
G073	980781.301	0.024	1	50.5647985	-123.533194	827.25
G074	980755.523	0.023	1	50.6578543	-123.426729	927.987
G075	980777.772	0.024	1	50.5711023	-123.50479	840.253
G076	980798.579	0.025	1	50.5627124	-123.495724	741.378
G077	980757.674	0.024	1	50.6047057	-123.448477	969.526
G078	980736.299	0.024	1	50.5881996	-123.469845	1104.033
G079	980621.328	0.025	1	50.580354	-123.422903	1720.35
G080	980771.351	0.024	1	50.57124	-123.56768	893.33
G081	980747.464	0.025	1	50.62372	-123.42645	1029.84204
G082	980486.867	0.022	1	50.6205317	-123.594895	2395.218
G083	980467.479	0.022	1	50.6338258	-123.642442	2498.656
G084	980474.894	0.023	1	50.6334236	-123.646108	2477.333
G085	980530.739	0.023	1	50.6184857	-123.648659	2263.17
G086	980538.896	0.023	1	50.6164457	-123.64562	2225.111
G087	980565.61	0.023	1	50.6119834	-123.644135	2104.423
G088	980712.844	0.022	1	50.7018368	-123.507006	1058.429
G089	980694.672	0.022	1	50.7111497	-123.470551	1179.619
G090	980726.775	0.022	1	50.6958293	-123.472562	1011.009

G091	980576.921	0.022	1	50.6478086	-123.607012	1923.072
G092	980547.526	0.022	1	50.660246	-123.63977	2085.647
G093	980601.363	0.022	1	50.6441597	-123.664783	1904.482
G094	980595.732	0.022	1	50.59375	-123.595113	1900.059
G095	980555.37	0.022	1	50.605985	-123.557759	1997.517
G096	980585.61	0.022	1	50.6827492	-123.690938	1987.03
G097	980519.303	0.022	1	50.7213567	-123.499083	2088.373
G098	980527.622	0.022	1	50.7503192	-123.545966	2153.383
G099	980566.966	0.022	1	50.6066707	-123.599904	2045.388
G100	980581.072	0.022	1	50.601864	-123.601561	1995.417
G101	980589.987	0.022	1	50.5984646	-123.602367	1951.98
G102	980677.917	0.022	1	50.5944289	-123.553635	1377.241
G103	980534.793	0.023	1	50.6407237	-123.57595	2072.928
G104	980614.2	0.026	1	50.6458854	-123.595356	1728.783
G105	980583.489	0.025	1	50.6358287	-123.595605	1898.11
G106	980512.624	0.024	1	50.6296735	-123.604647	2267.633
G107	980555.565	0.024	1	50.6401242	-123.607345	2058.218
G108	980625.505	0.024	1	50.6439343	-123.620405	1687.827
G109	980656.211	0.024	1	50.6594189	-123.607129	1487.499
G110	980824.903	0.024	1	50.5790195	-123.461124	567.634
G111	980495.167	0.025	1	50.6327336	-123.566942	2282.452
G112	980586.686	0.025	1	50.6500354	-123.553859	1816.908
G113	980780.964	0.026	1	50.6937706	-123.56521	721.688
L001	980884.499	0.018	2	50.5054465	-122.981662	239.187
L002	980870.461	0.021	1	50.5712804	-123.241178	304.498
L003	980886.018	0.022	1	50.5415845	-123.125229	263.025
L004	980889.41	0.024	1	50.5010625	-122.967937	235.697
L005	980897.5	0.024	1	50.4612412	-122.933682	227.553
L006	980896.124	0.025	1	50.4272654	-122.9077	223.979
L007	980898.659	0.025	1	50.3745946	-122.864306	219.017
L008	980899.482	0.025	1	50.3510245	-122.83212	213.752
L009	980879.984	0.026	1	50.2878312	-122.844391	375.716
SFU2	980821.02	0.011	10	50.1162648	-122.954073	657.668
SFU3	980884.681	0.013	2	50.3240894	-122.75194	328.726

Table 8. Raw averaged gravity readings collected with the LaCoste & Romberg relative gravity meter alongside their time and date of acquisition, as well as the calculated tide effect and residual from drift correction.

Name	Dial (mGal)	Day	Month	Year	Hour	Minute	Tidal Effect (mGal)	Loop	Residual (mGal)
BASE	4338.6455	10	7	2019	15	20	-0.03253314	1	-0.00014642
G001	4271.6672	10	7	2019	16	32	-0.0380497	1	-5.457E-10
G002	4353.9533	10	7	2019	21	30	0.03307308	1	1.6289E-09
G003	4337.9905	10	7	2019	22	22	0.04375975	1	-1.2651E-09
G004	4332.4556	10	7	2019	23	6	0.04945584	1	9.1586E-10
G005	4321.057	10	7	2019	23	35	0.05156899	1	-1.9099E-10
G006	4305.17	11	7	2019	0	2	0.05250124	1	2.8194E-11
BASE	4338.7042	11	7	2019	0	33	0.05251044	1	0.00014642
BASE	4338.8798	11	7	2019	14	5	-0.01307142	2	2.9037E-05
G007	4178.3546	11	7	2019	16	35	-0.06183641	2	6.5393E-10
G008	4186.8568	11	7	2019	18	2	-0.0602344	2	9.5406E-10
G009	4191.3317	11	7	2019	19	1	-0.04611039	2	9.4496E-10
G010	4278.9711	11	7	2019	21	21	0.01095659	2	-8.713E-10
BASE	4338.9218	11	7	2019	22	52	0.04546867	2	-2.9039E-05
BASE	4338.8	12	7	2019	15	32	-0.04929551	3	-4.9406E-05
G011	3972.2788	12	7	2019	18	18	-0.0841643	3	-8.4265E-10
G012	4099.4576	12	7	2019	18	52	-0.07912221	3	-8.6402E-11
G013	4135.4125	12	7	2019	19	22	-0.0712459	3	7.667E-10
G014	4363.0617	12	7	2019	23	18	0.04243676	3	-9.8771E-10
BASE	4339.0111	13	7	2019	1	50	0.07893553	3	4.9404E-05
BASE	4338.8996	13	7	2019	14	4	0.01302498	4	-0.00012944
G015	4226.2322	13	7	2019	16	28	-0.06935454	4	5.0386E-10
G016	4235.2133	13	7	2019	18	16	-0.10045371	4	-4.6384E-10
G017	4251.7485	13	7	2019	19	3	-0.09929306	4	4.311E-10
G018	4263.0379	13	7	2019	20	44	-0.06698131	4	-6.0936E-10
G019	4271.0552	13	7	2019	21	28	-0.04339723	4	5.979E-09
BASE	4338.9207	13	7	2019	23	44	0.03679111	4	0.00012944
BASE	4338.8552	14	7	2019	14	6	0.03123451	5	-0.00021105
G020	4035.2664	14	7	2019	15	35	-0.02361107	5	-2.4334E-09
G021	4044.5679	14	7	2019	16	34	-0.06018435	5	6.2437E-10
G022	4049.6764	14	7	2019	17	45	-0.09452559	5	6.5024E-09
BASE	4338.8874	15	7	2019	0	21	0.03700748	5	0.00021104
BASE	4338.8975	15	7	2019	14	6	0.05043854	6	-0.00039593
G023	4355.7118	15	7	2019	15	52	-0.01293815	6	-2.1801E-09
G024	4087.5479	15	7	2019	16	32	-0.03911985	6	-4.1382E-10
G025	4079.7494	15	7	2019	17	30	-0.07446967	6	1.9527E-09
G026	4072.2443	15	7	2019	18	10	-0.09398052	6	-1.0727E-09
G027	4031.4108	15	7	2019	19	1	-0.11019938	6	1.0295E-09
G028	4033.2946	15	7	2019	19	45	-0.11485461	6	-1.6021E-09
G029	4115.1884	15	7	2019	21	36	-0.08683203	6	2.2492E-09
G030	4121.7558	15	7	2019	22	25	-0.05983372	6	-1.0377E-09

G031	4145.058	15	7	2019	23	26	-0.02029889	6	4.3383E-09
BASE	4338.7872	16	7	2019	0	20	0.01583842	6	0.00039592
BASE	4338.8424	16	7	2019	14	6	0.06645851	7	4.7443E-05
G032	4245.7095	16	7	2019	16	23	-0.00897479	7	-1.6926E-09
G033	4251.6323	16	7	2019	18	26	-0.08451204	7	1.0377E-09
G034	4258.0491	16	7	2019	20	19	-0.1133238	7	-5.6662E-10
G035	4284.6006	16	7	2019	22	52	-0.06208851	7	1.9108E-09
BASE	4338.8248	16	7	2019	23	57	-0.01981256	7	-4.7446E-05
BASE	4338.8474	18	7	2019	13	14	0.08356084	8	-0.00024142
G036	4166.211	18	7	2019	14	29	0.07747135	8	1.658E-09
G037	4181.6138	18	7	2019	15	28	0.06056551	8	-2.7394E-09
G038	4279.9595	18	7	2019	18	13	-0.02827419	8	4.8112E-10
G039	4189.7664	18	7	2019	19	1	-0.05562152	8	-2.7012E-10
G040	4256.856	18	7	2019	19	51	-0.0779296	8	1.618E-09
G041	4280.3909	18	7	2019	21	7	-0.0949249	8	-1.3215E-09
G042	4287.1541	18	7	2019	22	22	-0.0870196	8	4.4574E-09
BASE	4338.7584	18	7	2019	23	37	-0.05695134	8	0.00024142
BASE	4338.8466	19	7	2019	14	10	0.07766311	9	6.3312E-05
G043	4188.9701	19	7	2019	15	51	0.06097803	9	2.3165E-09
G044	4207.4956	19	7	2019	17	25	0.02107212	9	-4.2655E-10
G045	4221.9376	19	7	2019	19	10	-0.03499715	9	5.6752E-10
G046	4334.7519	19	7	2019	20	19	-0.06461062	9	-4.4747E-10
G047	3997.944	19	7	2019	21	31	-0.07948708	9	-4.4793E-10
G048	4008.757	19	7	2019	21	59	-0.07990182	9	8.622E-10
G049	4080.8805	19	7	2019	22	32	-0.07645811	9	-8.2582E-09
BASE	4338.7291	19	7	2019	23	14	-0.06594328	9	-6.3308E-05
BASE	4338.8434	20	7	2019	14	9	0.06827375	10	-0.0042957
G050	4061.7046	20	7	2019	15	17	0.06748009	10	2.5348E-09
G051	3989.3558	20	7	2019	16	41	0.0512152	10	-2.9377E-10
G052	4050.771	20	7	2019	19	20	-0.01515646	10	-6.23E-10
G053	4273.3267	20	7	2019	20	16	-0.03832072	10	6.1482E-10
G054	4123.241	20	7	2019	20	53	-0.05035653	10	1.4779E-09
G055	4182.6406	20	7	2019	21	29	-0.05836827	10	2.3556E-09
G056	4159.2225	20	7	2019	22	3	-0.06203027	10	1.3933E-09
BASE	4338.74	20	7	2019	22	34	-0.06182378	10	0.01669594
G057	4353.2344	20	7	2019	23	16	-0.0562274	10	-2.0673E-09
G058	4353.4886	21	7	2019	0	41	-0.02859537	10	2.02E-09
BASE	4338.7681	21	7	2019	1	29	-0.00660488	10	-0.01240025
BASE	4338.7955	21	7	2019	13	39	0.05047957	11	-0.00030036
G059	4057.4019	21	7	2019	14	39	0.05589665	11	-1.0295E-09
G060	4290.996	21	7	2019	16	20	0.05432029	11	2.6557E-10
G061	4302.7898	21	7	2019	18	23	0.02559689	11	2.7285E-11
G062	4311.9005	21	7	2019	20	14	-0.01405577	11	-1.7826E-10
G063	4318.175	21	7	2019	21	55	-0.03943982	11	-9.4224E-10
G064	4279.0574	22	7	2019	0	6	-0.03255225	11	-1.2797E-09
G065	4247.1589	22	7	2019	0	37	-0.02417046	11	-1.2315E-09

BASE	4338.7548	22	7	2019	1	8	-0.01382987	11	0.00030036
BASE	4338.7545	22	7	2019	13	5	0.03062889	12	-0.00792856
G066	4121.7053	22	7	2019	13	49	0.03308707	12	6.6939E-10
G067	4026.1047	22	7	2019	15	21	0.04110757	12	0.00996448
G068	4077.2454	22	7	2019	18	43	0.02810232	12	-5.1887E-10
G069	4093.9326	22	7	2019	20	5	0.00834512	12	8.1218E-10
G070	4109.9767	22	7	2019	21	45	-0.01418895	12	5.276E-09
BASE	4338.7875	22	7	2019	23	7	-0.02153133	12	-0.00203593
BASE	4338.7525	23	7	2019	14	11	0.01537315	13	-0.00710751
G071	4100.0044	23	7	2019	16	12	0.02460896	13	2.0564E-09
G072	4332.5981	23	7	2019	17	1	0.0278967	13	0.01577546
G067	4026.0981	23	7	2019	19	35	0.02405656	13	-0.00996449
G073	4279.3367	23	7	2019	21	39	0.00813976	13	1.5953E-09
BASE	4338.8076	23	7	2019	23	31	0.00010111	13	0.00129654
BASE	4338.7439	24	7	2019	13	46	-0.00177056	14	0.00613249
G074	4253.5202	24	7	2019	16	42	0.00359705	14	1.4516E-09
G072	4332.5486	24	7	2019	17	23	0.00869379	14	-0.01577546
G075	4275.7903	24	7	2019	18	12	0.01480011	14	-2.7539E-09
G076	4296.6057	24	7	2019	18	48	0.01871603	14	9.7625E-09
BASE	4338.8143	24	7	2019	19	51	0.02346888	14	0.00964296
BASE	4338.6976	27	8	2019	13	37	0.02800003	15	-0.00022308
G077	4255.5038	27	8	2019	16	17	-0.07366141	15	1.628E-09
G078	4234.1127	27	8	2019	16	50	-0.08983839	15	-1.8372E-10
G079	4119.1243	27	8	2019	18	59	-0.10711435	15	-3.9827E-09
BASE	4338.5834	27	8	2019	20	0	-0.08635199	15	0.00022308
BASE	4338.6928	29	8	2019	14	35	0.07343146	16	-0.00049929
G080	4269.2192	29	8	2019	16	15	0.00661663	16	1.1141E-09
G081	4245.3098	29	8	2019	16	48	-0.018811	16	-2.2583E-09
BASE	4338.5879	29	8	2019	17	27	-0.04706781	16	0.00049928
SFU2	4320.7775	4	8	2020	15	41	0.05423084	17	-0.01022389
BASE	4340.4507	4	8	2020	18	19	-0.03921763	17	0.01275996
G082	3986.4835	4	8	2020	20	39	-0.09213026	17	-3.3519E-09
G083	3967.0956	4	8	2020	21	30	-0.09107387	17	-1.1669E-09
G084	3974.5157	4	8	2020	21	59	-0.08517111	17	9.6225E-10
G085	4030.3741	4	8	2020	22	40	-0.07088815	17	-1.2374E-09
G086	4038.5446	4	8	2020	23	9	-0.057159	17	3.6198E-10
G087	4065.2773	4	8	2020	23	43	-0.03824411	17	-1.437E-09
SFU2	4320.8026	5	8	2020	3	48	0.08375296	17	-0.00253607
SFU2	4320.8444	5	8	2020	13	34	0.08348522	18	0.01171818
BASE	4340.6045	5	8	2020	15	10	0.07687945	18	-0.01248926
G088	4212.7034	5	8	2020	16	8	0.05870877	18	1.6653E-09
G089	4194.5324	5	8	2020	16	43	0.04299445	18	4.2382E-10
G090	4226.6335	5	8	2020	17	14	0.02696859	18	-7.0759E-10
G091	4076.7763	5	8	2020	17	46	0.00937591	18	-1.3629E-09
G092	4047.3783	5	8	2020	18	17	-0.00821678	18	-5.3933E-10
G093	4101.2123	5	8	2020	18	50	-0.02643089	18	8.1218E-10

G094	4095.58	5	8	2020	19	25	-0.04420175	18	1.1078E-09
G095	4055.2197	5	8	2020	19	57	-0.05751478	18	-1.5857E-09
G096	4085.4666	5	8	2020	20	36	-0.06864384	18	5.1186E-09
BASE	4340.6326	5	8	2020	21	32	-0.07490192	18	-0.01014525
SFU2	4320.9678	5	8	2020	23	4	-0.05722467	18	0.01091631
SFU2	4320.7086	14	9	2020	12	48	0.05689238	19	0.0403806
SFU3	4384.2598	14	9	2020	15	26	-0.02947144	19	-0.0246301
L001	4384.1421	14	9	2020	20	51	-0.04141545	19	-0.03310773
BASE	4340.4518	14	9	2020	21	57	0.00129722	19	-0.05029131
L002	4370.2326	14	9	2020	22	35	0.0274209	19	5.1296E-10
L003	4385.8241	14	9	2020	23	13	0.0516513	19	9.577E-10
L001	4384.3638	14	9	2020	23	44	0.0689534	19	0.03310773
SFU3	4384.5565	15	9	2020	0	35	0.09031622	19	0.00911166
SFU2	4320.9355	15	9	2020	1	26	0.10106935	19	0.02542914
SFU2	4320.8984	15	9	2020	14	14	0.05519984	20	2.3775E-05
L004	4389.1942	15	9	2020	20	22	-0.06933839	20	2.3247E-09
L005	4397.2999	15	9	2020	20	52	-0.05551182	20	4.0927E-11
L006	4395.9381	15	9	2020	21	13	-0.04378144	20	-1.1396E-09
L007	4398.4872	15	9	2020	21	33	-0.03135724	20	2.4647E-10
L008	4399.3274	15	9	2020	21	56	-0.01583246	20	4.5384E-10
L009	4379.8576	15	9	2020	22	32	0.00953518	20	-1.4188E-10
SFU2	4320.9283	15	9	2020	23	17	0.04057823	20	-2.3775E-05
SFU2	4320.939	16	9	2020	14	58	0.07084696	21	-0.01917817
BASE	4340.6856	16	9	2020	18	17	-0.04763338	21	0.02011607
G097	4019.213	16	9	2020	19	32	-0.06714656	21	-1.703E-09
G098	4027.5474	16	9	2020	20	9	-0.06608443	21	-1.2496E-09
G099	4066.935	16	9	2020	21	14	-0.04799826	21	-1.4415E-10
G100	4081.0795	16	9	2020	21	55	-0.02656662	21	2.1E-09
G101	4090.0246	16	9	2020	22	25	-0.00771526	21	-4.6521E-10
G102	4178.0159	16	9	2020	23	21	0.03068966	21	-5.3569E-10
G103	4034.9337	17	9	2020	0	1	0.05702899	21	-3.7558E-09
BASE	4340.9932	17	9	2020	0	38	0.0784368	21	0.04945725
SFU2	4321.2009	17	9	2020	1	48	0.10432453	21	-0.05039515
BASE	4341.3264	17	9	2020	15	36	0.0867165	22	-0.00015534
G104	4114.7418	17	9	2020	16	28	0.06057988	22	-4.4747E-10
G105	4084.0077	17	9	2020	17	17	0.03086665	22	4.2819E-09
G106	4013.1231	17	9	2020	17	58	0.00592635	22	-4.4724E-09
G107	4056.0513	17	9	2020	18	31	-0.01209848	22	-8.4492E-10
G108	4125.9798	17	9	2020	19	7	-0.02801266	22	-2.9513E-09
G109	4156.6802	17	9	2020	19	57	-0.04105632	22	5.3251E-09
G110	4325.3862	17	9	2020	21	12	-0.03748901	22	7.9308E-10
G111	3995.6698	17	9	2020	21	52	-0.02392276	22	-2.5248E-09
G112	4087.2176	17	9	2020	22	38	-0.00095022	22	9.8589E-10
G113	4281.5192	17	9	2020	23	10	0.01814303	22	2.0746E-09
BASE	4341.3477	17	9	2020	23	43	0.03895275	22	0.00015533

Table 9. Spatial corrections calculated for base and survey stations, alongside the measured absolute gravity. The Free air anomaly is the result of subtracting the ellipsoidal (normal) gravity and the free air effect from the absolute gravity. The Bouguer anomalies have been calculated by summing the Bouguer Slab correction and the Terrain Correction with the Free air anomaly. All the corrections are in relation with the GRS80 ellipsoid. The density value used for the Bouguer and Terrain corrections is 2.67 g/cm³. The values in the last column (Bouguer anomalies) have been interpolated with Empirical Bayesian Kriging and plotted in Figure17.

Name	Absolute Gravity	Ellipsoidal gravity	Free air effect	Free air anomaly	Bouger Slab Correction	Terrain Correction (mGal)	Bouguer Anomalies
BASE	980840.766	981126.94	-146.172099	-140.001718	-52.9899909	22.5959681	-170.39574
G001	980773.797	981131.339	-223.693956	-133.847947	-81.0930459	19.1885512	-195.752442
G002	980856.026	981125.778	-127.345333	-142.406217	-46.1649528	22.4493517	-166.121818
G003	980840.055	981127.217	-142.236209	-144.925591	-51.5631607	24.1372686	-172.351483
G004	980834.517	981127.654	-138.846546	-154.289965	-50.3343477	26.0827152	-178.541598
G005	980823.118	981128.305	-144.25723	-160.929296	-52.295817	30.6980293	-182.527084
G006	980807.231	981129.142	-164.79672	-157.11465	-59.7417482	27.4774628	-189.378935
G007	980680.295	981121.799	-421.783679	-19.7200539	-152.904101	15.93852	-156.685635
G008	980688.798	981121.7	-407.510003	-25.3919229	-147.729639	15.9641226	-157.157439
G009	980693.261	981121.653	-401.683018	-26.7086959	-145.617253	16.3947607	-155.931188
G010	980780.847	981131.197	-208.085277	-142.264423	-75.4346214	19.2753579	-198.423686
G011	980474.258	981125.922	-720.491197	68.8276897	-261.1909	28.8092113	-163.553999
G012	980601.427	981122.342	-542.876467	21.9610605	-196.802395	25.3524131	-149.488921
G013	980637.37	981116.159	-530.274478	51.4854022	-192.233949	9.57009191	-131.178455
G014	980864.874	981121.87	-103.88587	-153.109979	-37.6604792	29.4204671	-161.349991
G015	980728.182	981121.554	-341.258521	-52.1133854	-123.712296	19.4911765	-156.334505
G016	980737.195	981121.38	-328.439277	-55.7456703	-119.065091	18.4621854	-156.348576
G017	980753.729	981121.234	-300.634725	-66.8705443	-108.985446	16.7767844	-159.079206
G018	980764.987	981120.96	-284.402365	-71.5705461	-103.100926	15.0455432	-159.625929
G019	980772.981	981120.757	-270.922409	-76.8535823	-98.2142017	15.4838478	-159.583936
G020	980537.228	981125.898	-644.381179	55.7114414	-233.599662	26.6195197	-151.268701
G021	980546.564	981125.926	-629.396181	50.0344824	-228.167333	29.3897688	-148.743082
G022	980551.704	981126.021	-620.353583	46.0369383	-224.88923	30.3855611	-148.466731
G023	980857.657	981123.141	-111.465703	-154.018184	-40.4083039	31.928493	-162.497995
G024	980589.524	981124.137	-562.80709	28.1937283	-204.027601	24.2317097	-151.602163
G025	980581.768	981124.119	-575.761192	33.4104659	-208.723694	22.8873694	-152.425858
G026	980574.288	981124.144	-584.923217	35.0676864	-212.045091	24.956564	-152.020841
G027	980533.477	981124.108	-641.383748	50.7529569	-232.51304	25.7470206	-156.013062
G028	980535.371	981124.093	-636.500461	47.7786185	-230.742761	28.7667397	-154.197403
G029	980617.25	981123.852	-526.345074	19.743313	-190.80947	18.5759899	-152.490167
G030	980623.797	981123.907	-516.363098	16.2529116	-187.190826	18.8657808	-152.072134
G031	980647.067	981119.106	-492.441352	20.4022785	-178.518767	15.7433959	-142.373092
G032	980747.693	981121.217	-312.485583	-61.0385955	-113.281593	17.4746163	-156.845572
G033	980753.677	981121.235	-299.840389	-67.7175346	-108.697485	18.9801794	-157.43484
G034	980760.11	981121.312	-287.404118	-73.7977655	-104.189115	19.2787513	-158.708129
G035	980786.592	981120.942	-244.078221	-90.2719509	-88.482705	18.7001792	-160.054477

G036	980668.13	981123.803	-502.879747	47.2062994	-182.302871	8.02876886	-127.067803
G037	980683.545	981122.005	-456.541914	18.0819883	-165.504581	9.12934215	-138.29325
G038	980781.966	981135.558	-247.898689	-105.693573	-89.8676928	31.8482471	-163.713019
G039	980691.796	981135.811	-370.028682	-73.9867075	-134.141992	15.8403229	-192.288376
G040	980758.904	981131.012	-243.460712	-128.647081	-88.2588472	20.1512292	-196.754699
G041	980782.449	981120.87	-250.60079	-87.8200649	-90.8472528	16.8353007	-161.832017
G042	980789.199	981120.742	-239.543035	-92.0001071	-86.8386194	17.454908	-161.383819
G043	980690.902	981122.407	-413.378958	-18.1256761	-149.85724	16.3068793	-151.676036
G044	980709.463	981122.046	-383.186768	-29.3961403	-138.912033	14.7761353	-153.532038
G045	980723.956	981121.927	-360.245136	-37.7262229	-130.595282	14.0246043	-154.296901
G046	980836.796	981121.661	-338.694363	53.8297328	-122.782743	15.6628857	-53.2901246
G047	980500	981126.567	-689.905851	63.3388799	-250.103167	19.2797486	-167.484538
G048	980510.812	981127.721	-666.257525	49.3481709	-241.530227	27.5033486	-164.678708
G049	980582.93	981127.156	-565.75422	21.5280522	-205.095988	15.4712106	-168.096725
G050	980563.623	981135.671	-605.454993	33.406891	-219.488225	16.6965984	-169.384736
G051	980491.29	981125.385	-719.956702	85.8613031	-260.997136	22.7820327	-152.3538
G052	980552.77	981127.519	-613.323058	38.5737007	-222.34054	18.7580379	-165.008801
G053	980775.348	981131.351	-224.648147	-131.354651	-81.4389572	16.9256965	-195.867912
G054	980625.274	981129.118	-481.493459	-22.3503727	-174.54996	19.7717254	-177.128607
G055	980684.681	981128.169	-393.817421	-49.6704186	-142.765834	20.0560221	-172.38023
G056	980661.266	981127.233	-448.96887	-16.9981593	-162.759217	17.8480736	-161.909303
G057	980855.271	981125.048	-121.918293	-147.859152	-44.1975542	27.0370023	-165.019704
G058	980855.497	981124.104	-119.919491	-148.687725	-43.4729528	27.8364743	-164.324204
G059	980559.365	981127.124	-600.463079	32.7044045	-217.678568	14.6370544	-170.337109
G060	980792.957	981120.313	-231.640715	-95.7156257	-83.9738875	21.1435602	-158.545953
G061	980804.776	981120.378	-208.770677	-106.831799	-75.6830914	22.9967452	-159.518145
G062	980813.922	981120.162	-198.325802	-107.914437	-71.8966378	20.5984653	-159.21261
G063	980820.219	981120.997	-186.542837	-114.235236	-67.6251029	22.7371294	-159.12321
G064	980781.09	981129.886	-212.358152	-136.437872	-76.983615	24.4163451	-189.005142
G065	980749.182	981130.506	-267.408689	-113.915549	-96.9404157	19.9831943	-190.872771
G066	980623.701	981113.606	-552.579469	62.6739904	-200.319906	8.49433884	-129.151576
G067	980528.07	981120.388	-684.931528	92.6138368	-248.299886	30.0797368	-125.606312
G068	980579.207	981123.301	-578.774362	34.6806635	-209.816022	21.9153904	-153.219968
G069	980595.904	981123.322	-554.386322	26.9680434	-200.974922	21.0998272	-152.907051
G070	980611.957	981123.276	-531.568746	20.2497255	-192.703144	21.3691057	-151.084313
G071	980601.989	981132.315	-562.298826	31.9725127	-203.843346	19.3665129	-152.50432
G072	980834.558	981123.763	-158.400677	-130.804145	-57.4230684	30.9044335	-157.32278
G073	980781.301	981120.651	-255.28935	-84.0606441	-92.5469393	17.1333131	-159.47427
G074	980755.523	981128.92	-286.376788	-87.0198939	-103.81669	21.5244866	-169.312097
G075	980777.772	981121.211	-259.302076	-84.1372195	-94.0016239	18.6259102	-159.512933
G076	980798.579	981120.466	-228.789251	-93.0973236	-82.940181	16.1929561	-159.844548
G077	980757.674	981124.198	-299.195724	-67.3279579	-108.463782	21.0853456	-154.706395
G078	980736.299	981122.731	-340.704584	-45.7272622	-123.511484	17.8498484	-151.388898
G079	980621.328	981122.034	-530.90001	30.1944335	-192.460716	27.3361916	-134.93009
G080	980771.351	981121.224	-275.681638	-74.1909002	-99.9395071	17.5576425	-156.572765
G081	980747.464	981125.887	-317.809254	-60.6139521	-115.211519	23.343269	-152.482202

G082	980486.867	981125.604	-739.164275	100.427356	-267.960223	23.0388293	-144.494038
G083	980467.479	981126.785	-771.085242	111.779164	-279.532143	32.8604089	-134.89257
G084	980474.894	981126.749	-764.504964	112.649621	-277.146675	30.9681472	-133.528907
G085	980530.739	981125.422	-698.414262	103.731131	-253.187617	20.0114918	-129.444995
G086	980538.896	981125.241	-686.669255	100.324382	-248.929843	17.5118044	-131.093656
G087	980565.61	981124.844	-649.424938	90.1905687	-235.428114	13.535871	-131.701675
G088	980712.844	981132.826	-326.631189	-93.3508338	-118.409628	19.4947739	-192.265687
G089	980694.672	981133.653	-364.030423	-74.9505808	-131.967516	16.141839	-190.776258
G090	980726.775	981132.293	-311.997377	-93.5201489	-113.10461	15.330098	-191.294661
G091	980576.921	981128.027	-593.460019	42.3537227	-215.139834	13.3891228	-159.396988
G092	980547.526	981129.132	-643.630664	62.0245294	-233.327587	20.9088097	-150.394248
G093	980601.363	981127.703	-587.723145	61.3829988	-213.060115	12.7730493	-138.904067
G094	980595.732	981123.224	-586.358207	58.8660988	-212.565301	11.8150634	-141.884138
G095	980555.37	981124.311	-616.433746	47.4923829	-223.468219	19.7358731	-156.239963
G096	980585.61	981131.131	-613.197458	67.6765733	-222.295007	15.7663359	-138.852098
G097	980519.303	981134.559	-644.471908	29.2155919	-233.632553	27.6589213	-176.758039
G098	980527.622	981137.131	-664.533994	55.0253374	-240.905416	16.21454	-169.665539
G099	980566.966	981124.372	-631.206737	73.8004467	-228.823692	11.1430212	-143.880224
G100	980581.072	981123.945	-615.785686	72.912528	-223.233286	10.2226529	-140.098105
G101	980589.987	981123.643	-602.381028	68.7249532	-218.373859	10.1088695	-139.540036
G102	980677.917	981123.284	-425.016573	-20.3508652	-154.076082	16.8131635	-157.613784
G103	980534.793	981127.398	-639.705581	47.1006897	-231.904674	23.8797382	-160.924246
G104	980614.2	981127.856	-533.502434	19.845986	-193.404141	9.47969609	-164.078458
G105	980583.489	981126.963	-585.756746	42.282725	-212.34726	10.0867982	-159.977737
G106	980512.624	981126.416	-699.791544	85.999378	-253.686907	18.0907148	-149.596814
G107	980555.565	981127.345	-635.166075	63.3864378	-230.259022	13.4444984	-153.428086
G108	980625.505	981127.683	-520.863412	18.685295	-188.82227	11.1689781	-158.967997
G109	980656.211	981129.059	-459.042191	-13.8054674	-166.410976	12.8131066	-167.403336
G110	980824.903	981121.915	-175.171852	-121.840122	-63.5029185	26.9191322	-158.423908
G111	980495.167	981126.688	-704.364687	72.8436459	-255.344753	20.3115528	-162.189554
G112	980586.686	981128.225	-560.697809	19.1586917	-203.262949	17.4519076	-166.652349
G113	980780.964	981132.11	-222.712917	-128.432791	-80.7374016	15.3859457	-193.784247
L001	980884.499	981115.374	-73.8131082	-157.062327	-26.7585673	27.0904998	-156.730395
L002	980870.461	981121.227	-93.9680828	-156.798049	-34.0651048	29.9235296	-160.939624
L003	980886.018	981118.587	-81.169515	-151.39994	-29.4253958	24.839395	-155.985941
L004	980889.41	981114.985	-72.7360942	-152.838509	-26.3681305	29.0963244	-150.110315
L005	980897.5	981111.443	-70.2228558	-143.720246	-25.4570368	21.3148729	-147.86241
L006	980896.124	981108.421	-69.1199194	-143.176825	-25.0572027	26.2872019	-141.946826
L007	980898.659	981103.734	-67.5886462	-137.486363	-24.5020888	21.2975772	-140.690875
L008	980899.482	981101.636	-65.9638672	-136.19032	-23.9130775	15.2056171	-144.897781
L009	980879.984	981096.01	-115.945958	-100.080239	-42.0324761	21.7841183	-120.328596
SFU2	980821.02	981080.725	-202.956345	-56.7482362	-73.5752922	9.85121759	-120.472311
SFU3	980884.681	981099.238	-101.444844	-113.112636	-36.7755638	12.2787702	-137.609429

References

- Battaglia, M., Gottsmann, J., Carbone, D., & Fernández, J. (2008). 4D volcano gravimetry. *Geophysics*, 73(6), WA3–WA18. <https://doi.org/10.1190/1.2977792>
- Battaglia, M., Poland, M. P., & Kauhikaua, J. P. (2012). GTOOLS: an Interactive Computer Program to Process Gravity Data for High-Resolution Applications. *American Geophysical Union, Fall Meeting 2012, Abstract #GP43B-1143*.
- Calahorrano-Di Patre, A., Williams-Jones, G., Battaglia, M., Mothes, P., Gaunt, E., Zurek, J., Ruiz, M., & Witter, J. (2019). Hydrothermal fluid migration due to interaction with shallow magma: Insights from gravity changes before and after the 2015 eruption of Cotopaxi volcano, Ecuador. *Journal of Volcanology and Geothermal Research*, 387, 106667. <https://doi.org/10.1016/j.jvolgeores.2019.106667>
- Cockett, R., Kang, S., Heagy, L. J., Pidlisecky, A., & Oldenburg, D. W. (2015). SimPEG: An open source framework for simulation and gradient based parameter estimation in geophysical applications. *Computers & Geosciences*, 85, 142–154. <https://doi.org/10.1016/j.cageo.2015.09.015>
- Domra Kana, J., Djongyang, N., Raïdandi, D., Njandjock Nouck, P., & Dadjé, A. (2015). A review of geophysical methods for geothermal exploration. *Renewable and Sustainable Energy Reviews*, 44, 87–95. <https://doi.org/10.1016/j.rser.2014.12.026>
- Grasby, S. E., Ansari, S. M., Bryant, R., Calahorrano-Di Patre, A., Chen, Z., Craven, J. A., Dettmer, J., Gilbert, H., Hanneson, C., Harris, M., Hormozzade, F., Liu, J., Montezadian, D., Muhammad, M., Russell, J. K., Salvage, R. O., Savard, G., Su, H., Tschirhart, V., ... Williamson, A. R. (2020). *The Garibaldi Volcanic Belt geothermal energy project - Mount Meager 2019 field program*. <https://doi.org/10.4095/326565>
- Grasby, S. E., Ansari, S. M., Calahorrano-Di Patre, A., Chen, Z., Craven, J. A., Dettmer, J., Gilbert, H., Hanneson, C., Harris, M., Liu, J., Muhammad, M., Russell, K., Salvage, R. O., Savard, G., Tschirhart, V., Unsworth, M. J., & Vigouroux-Caillibot, N. Williams-Jones, G. (2020). Geothermal Resource Potential of the Garibaldi Volcanic Belt, Southwestern British Columbia (Part of NTS 092J). In *Geoscience BC Summary of Activities 2019: Energy and Water, Geoscience BC* (pp. 103–108).
- Hinze, W. J., Aiken, C., Brozena, J., Coakley, B., Dater, D., Flanagan, G., Forsberg, R., Hildenbrand, T., Keller, G. R., Kellogg, J., Kucks, R., Li, X., Mainville, A., Morin, R., Pilkington, M., Plouff, D., Ravat, D., Roman, D., Urrutia-Fucugauchi, J., ... Winester, D. (2005). New standards for reducing gravity data: The North American gravity database. *Geophysics*, 70(4), 25–32. <https://doi.org/10.1190/1.1988183>
- Juniper Systems. (2019). *Geode Owner's Manual*. Juniper Systems Inc.
- Krivoruchko, K., & Gribov, A. (2019). Evaluation of empirical Bayesian kriging. *Spatial Statistics*, 32, 100368. <https://doi.org/10.1016/j.spasta.2019.100368>
- Lebel, D. (2009). Geoscience Needs for Geothermal Energy Development in Western Canada : Findings and Recommendations. In *Petroleum Geology Open File*.
- Li, X., & Götze, H. (2001). Ellipsoid, geoid, gravity, geodesy, and geophysics. *GEOPHYSICS*, 66(6), 1660–1668. <https://doi.org/10.1190/1.1487109>
- Lowrie, W. (2007). *Fundamentals of Geophysics*. In *Cambridge University Press*. Cambridge University Press. <https://doi.org/10.1017/CBO9780511807107>
- MacQueen, P., Zurek, J., & Williams-Jones, G. (2016). Connected magma plumbing system between Cerro Negro and El Hoyo Complex, Nicaragua revealed by gravity survey. *Journal of Volcanology*

- and Geothermal Research*, 327, 375–384. <https://doi.org/10.1016/j.jvolgeores.2016.09.002>
- McCubbine, J., Tontini, F. C., Stagpoole, V., Smith, E., & O'Brien, G. (2018). Gsolve, a Python computer program with a graphical user interface to transform relative gravity survey measurements to absolute gravity values and gravity anomalies. *SoftwareX*, 7, 129–137. <https://doi.org/10.1016/j.softx.2018.04.003>
- Miller, C. A., Le Mével, H., Currenti, G., Williams-Jones, G., & Tikoff, B. (2017). Microgravity changes at the Laguna del Maule volcanic field: Magma-induced stress changes facilitate mass addition. *Journal of Geophysical Research: Solid Earth*, 122(4), 3179–3196. <https://doi.org/10.1002/2017JB014048>
- Moritz, H. (1980). Geodetic reference system 1980. *Bulletin Géodésique*, 54(3), 395–405. <https://doi.org/10.1007/BF02521480>
- Nagy, D. (1966). THE GRAVITATIONAL ATTRACTION OF A RIGHT RECTANGULAR PRISM. *GEOPHYSICS*, 31(2), 362–371. <https://doi.org/10.1190/1.1439779>
- UBC-GIF. (2017). *A Program Library for Forward Modelling and Inversion of Gravity Data over 3D Structures*. UBC-Geophysical Inversion Facility, Department of Earth and Ocean Sciences, University of British Columbia, Vancouver, British Columbia.
- Vajda, P., Foroughi, I., Vaníček, P., Kingdon, R., Santos, M., Sheng, M., & Goli, M. (2020). Topographic gravimetric effects in earth sciences: Review of origin, significance and implications. *Earth-Science Reviews*, 211(September). <https://doi.org/10.1016/j.earscirev.2020.103428>
- Van Camp, M., de Viron, O., Watlet, A., Meurers, B., Francis, O., & Caudron, C. (2017). Geophysics From Terrestrial Time-Variable Gravity Measurements. *Reviews of Geophysics*, 55(4), 938–992. <https://doi.org/10.1002/2017RG000566>
- Witter, J. (2019). South Meager Geothermal Project: New Perspectives from Recently Unearthed Data. In *GeoscienceBC*.
- Zurek, J., Williams-Jones, G., Trusdell, F., & Martin, S. (2015). The origin of Mauna Loa's Nīnole Hills: Evidence of rift zone reorganization. *Geophysical Research Letters*, 42(20), 8358–8366. <https://doi.org/10.1002/2015GL065863>

Acknowledgements

Our gratitude goes to Dr. Jeffrey Zurek, for expert advice and conversations during processing of the data.

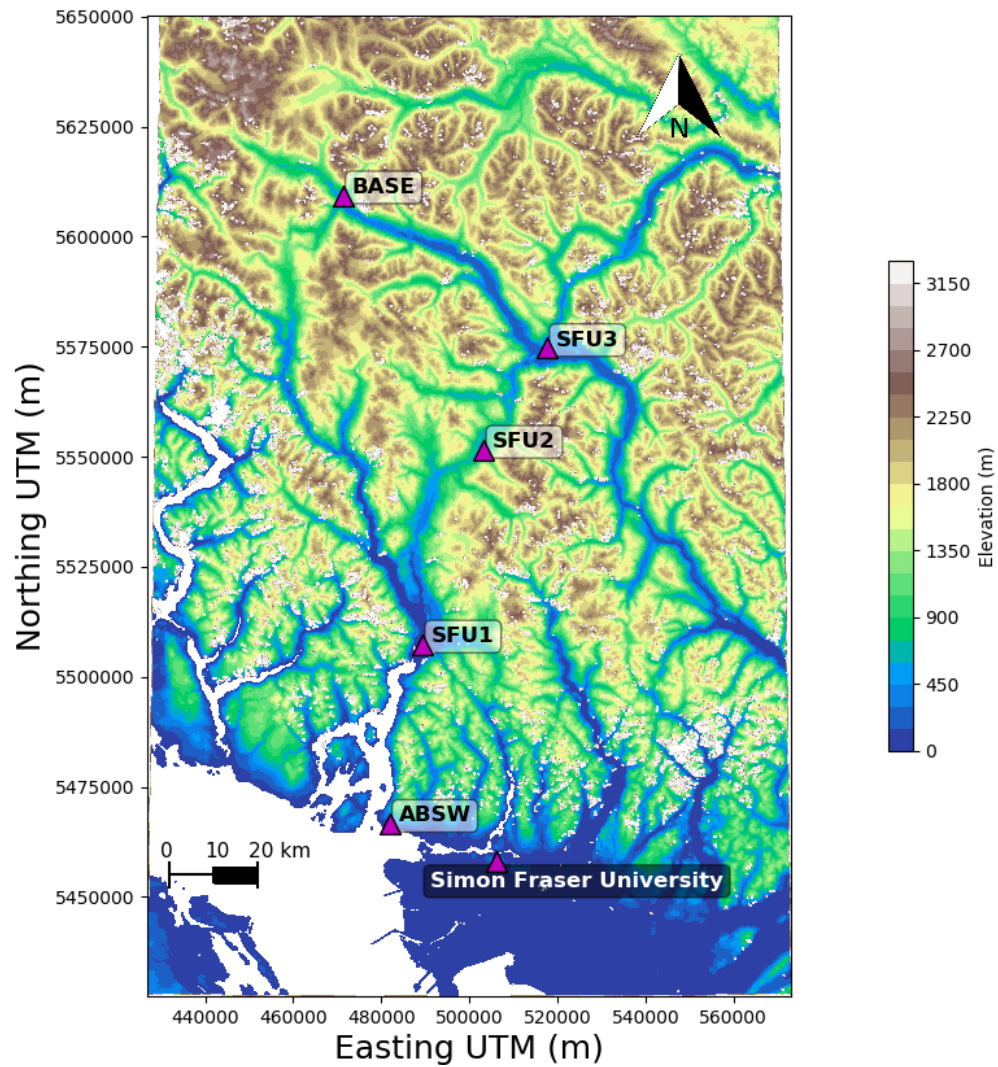


Figure 1. Gravity stations (magenta triangles) linked to absolute gravity stations ABSW (located in West Vancouver). Station BASE was the main reference station for the 2019 Meager gravity survey, and the secondary reference station for the 2020 Meager survey. The DEM pictured was downloaded from the GMTSAR DEM generator, which generates DEMs from the Shuttle Radar Topography Mission (SRTM1). This map elevation is based on mean sea level. This DEM was not used for processing or further plotting of data.



Figure 2. Gravity measurements at stations SFU3 (left), ABSW (top) and SFU1 (right).

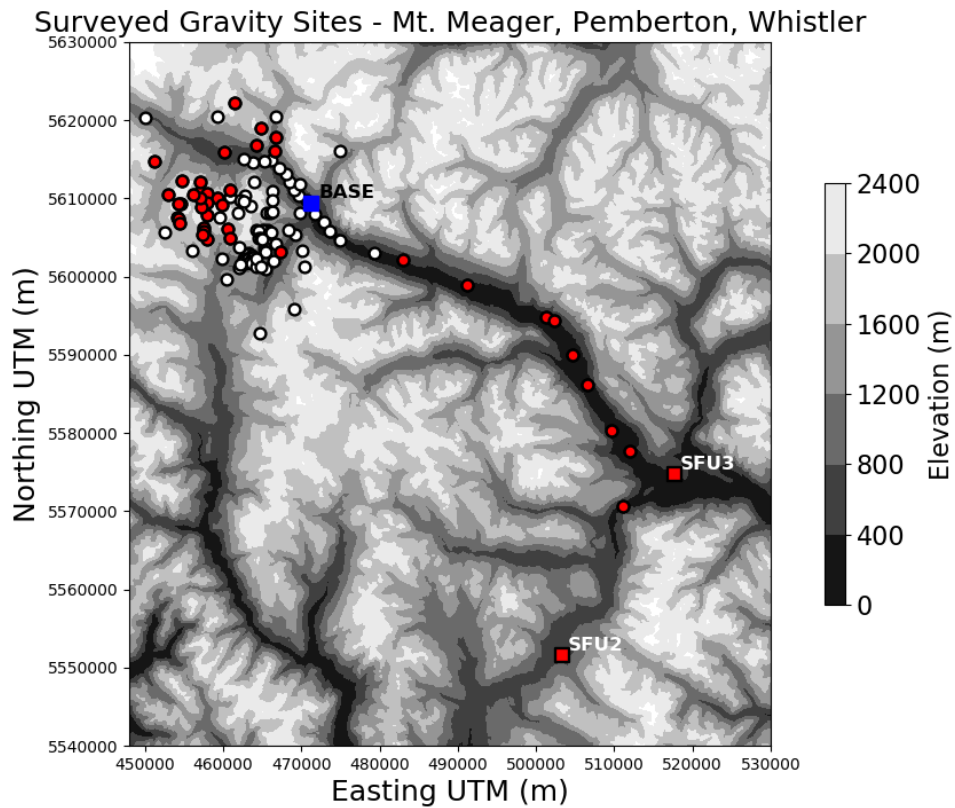


Figure 2. Measured gravity sites around Mt. Meager, Pemberton, and Whistler. Stations highlighted in red were surveyed in August and September 2020. Sites indicated by a red square are reference stations.

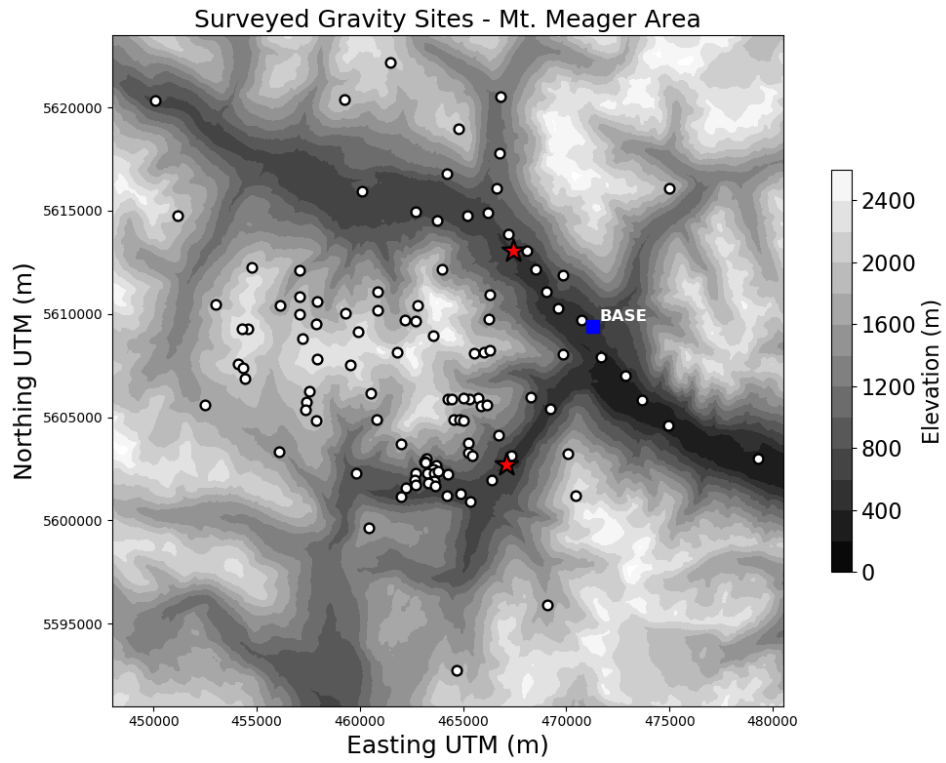


Figure 3. All gravity sites surveyed around Mt. Meager between July 2019 and September 2020. Red stars represent hot springs (northern star is Keyhole and southern star is Meager Creek). The blue square is the reference station BASE located at the Innergex power plant.

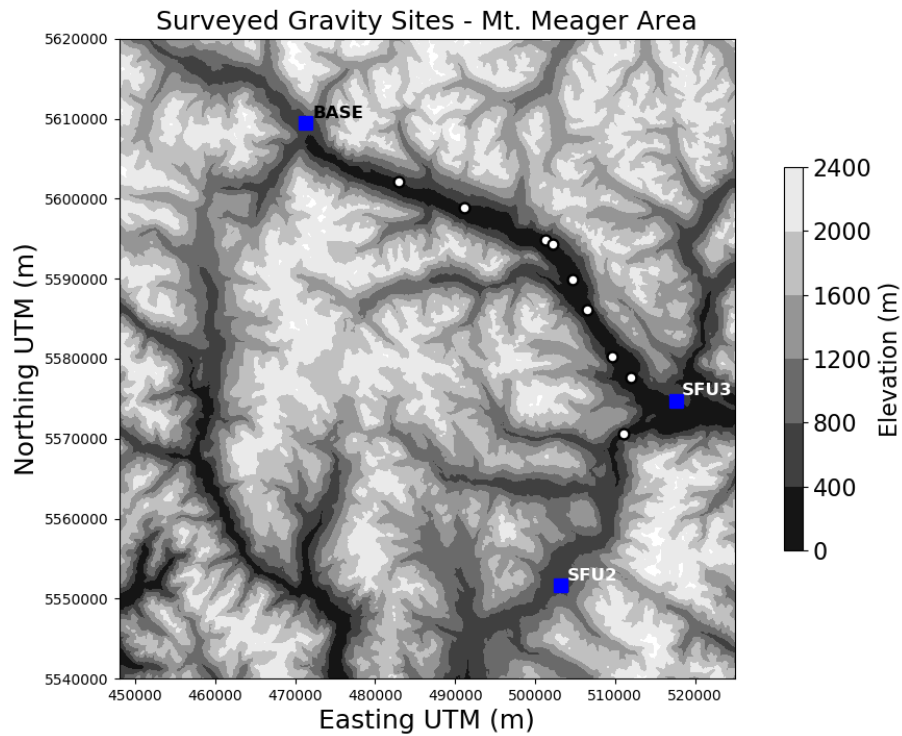


Figure 4. Gravity sites surveyed on the Pemberton Meadows and Lillooet forest road on September 14 and 15 (sites L001-L009). These stations will serve as a comparison for Mt. Meager measurements, and as initial datasets for the larger Garibaldi Volcanic Belt project.



Figure 5. Gravity measurements at station G109 during the September 2020 survey. In the picture, the LaCoste & Romberg relative gravity meter is on top of a flat rock, while the Geode GPS antenna is reposing on top of a levelled camera tripod.

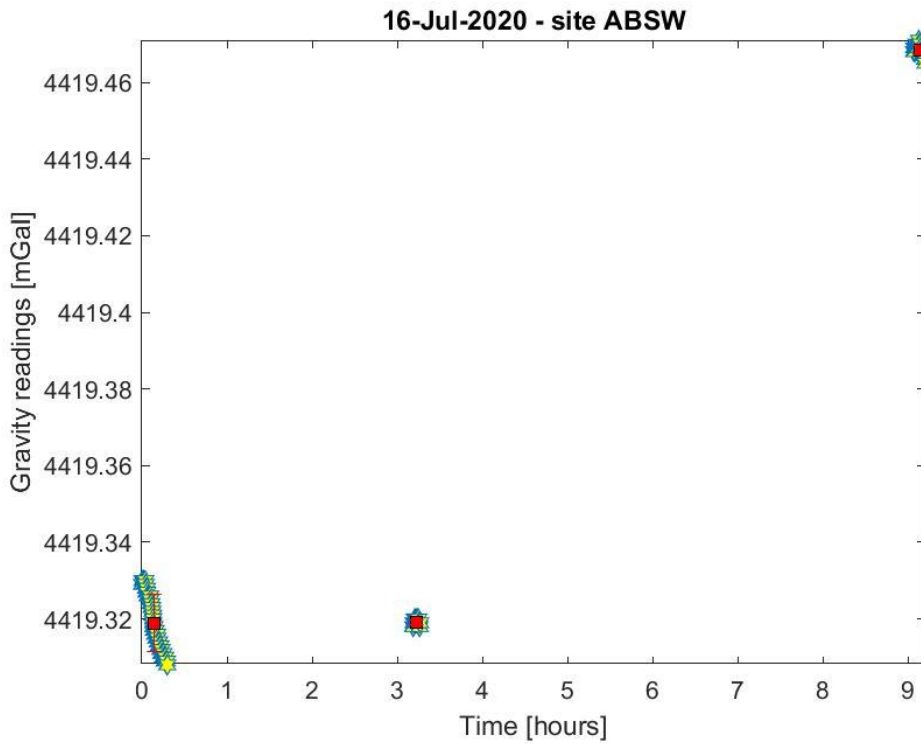


Figure 6. GTOOLS filtered data from all the measurements at ABSW on July 16, 2020. Data has yet to be corrected for Earth tide and drift.

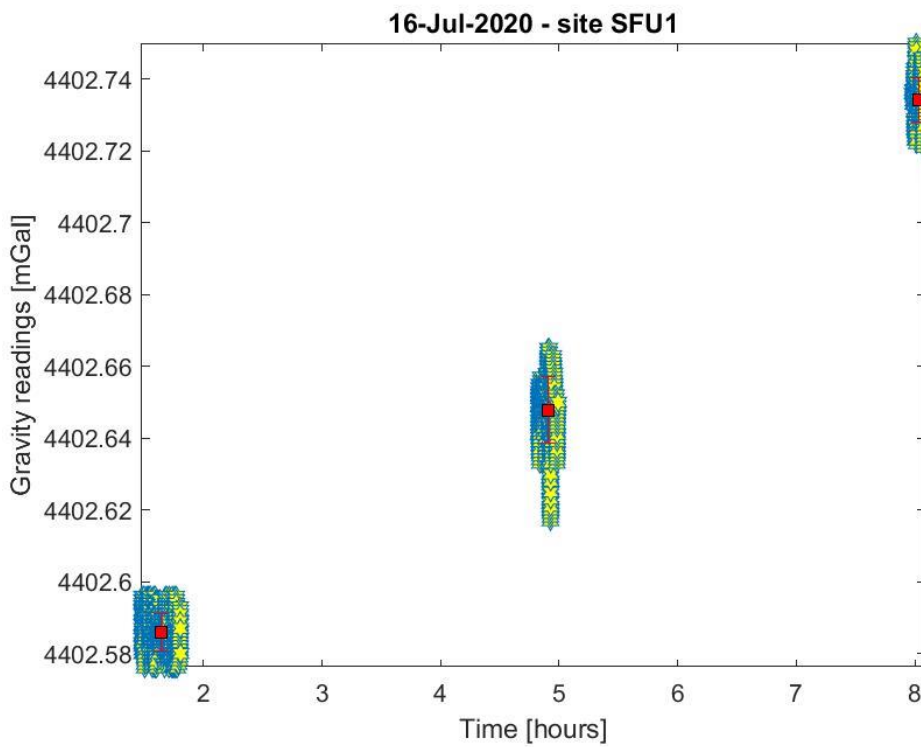


Figure 7. GTOOLS filtered data from all the measurements at SFU1 on July 16, 2020. Data has yet to be corrected for Earth tide and drift.

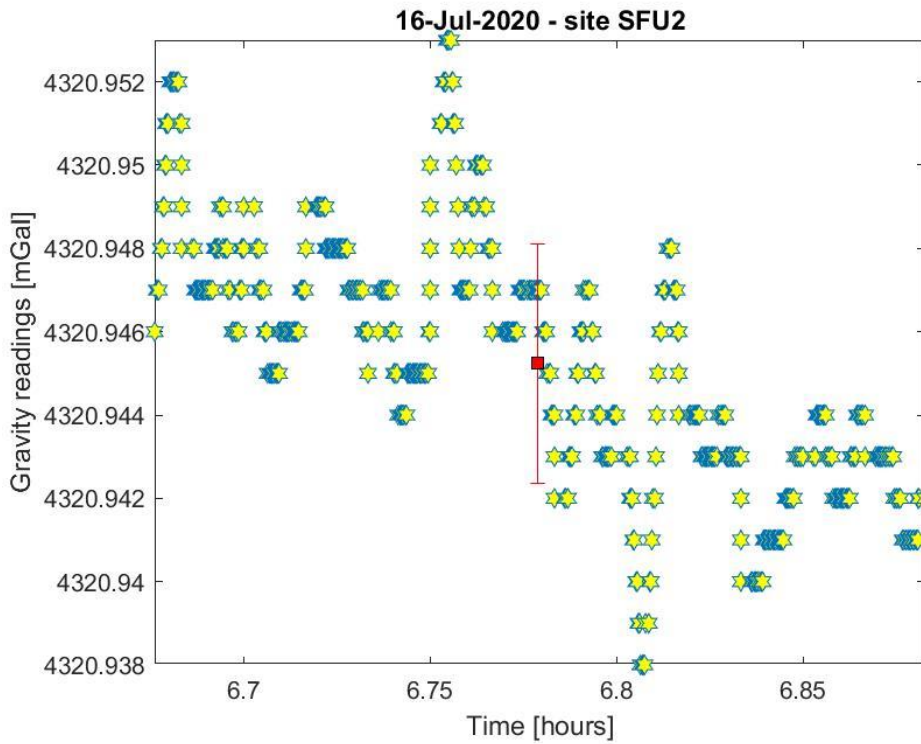


Figure 8. GTOOLS filtered data from the measurement at SFU2 on July 16, 2020. Data has yet to be corrected for Earth tide and drift.

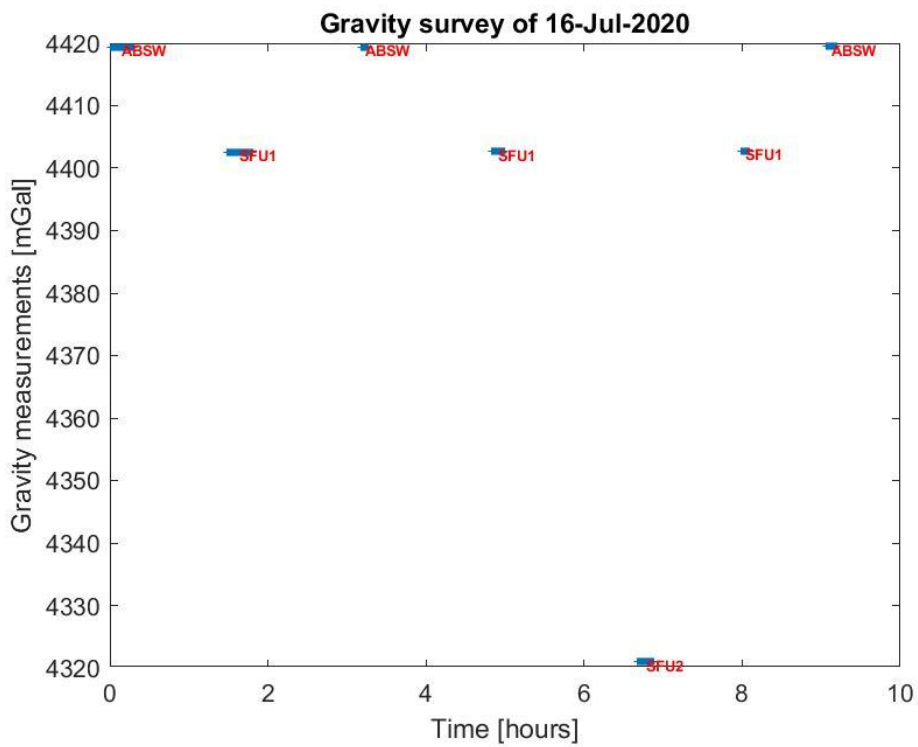


Figure 9. All measurements filtered for the survey loop on July 16, 2020. Data has yet to be corrected for Earth tide and drift.

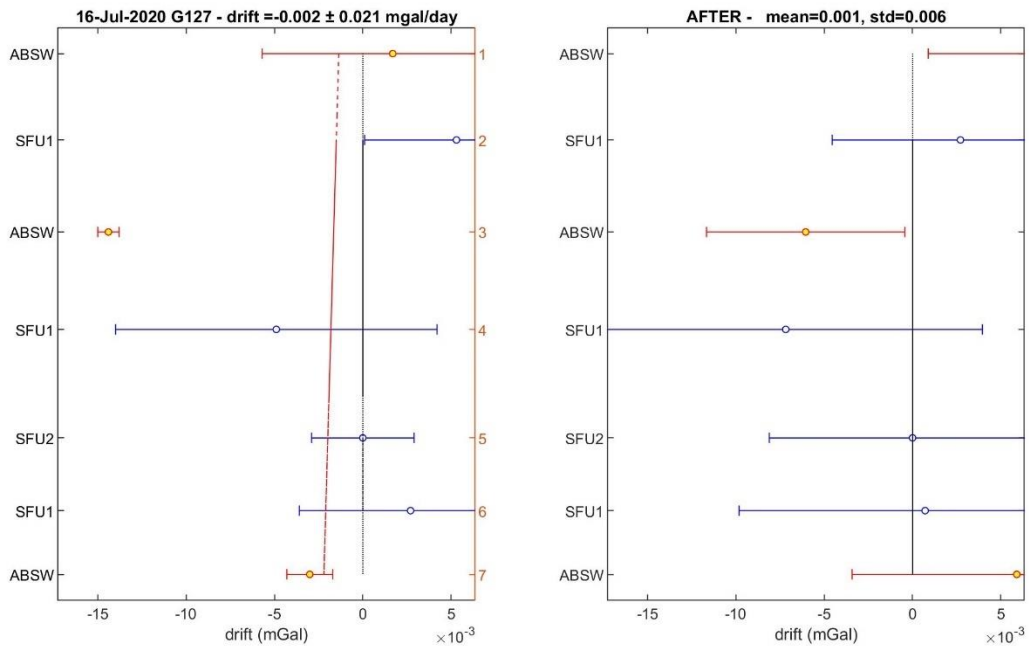


Figure 10. Gravity data from the survey loop on July 16, 2020 after filtering, Earth tide, and drift correction.

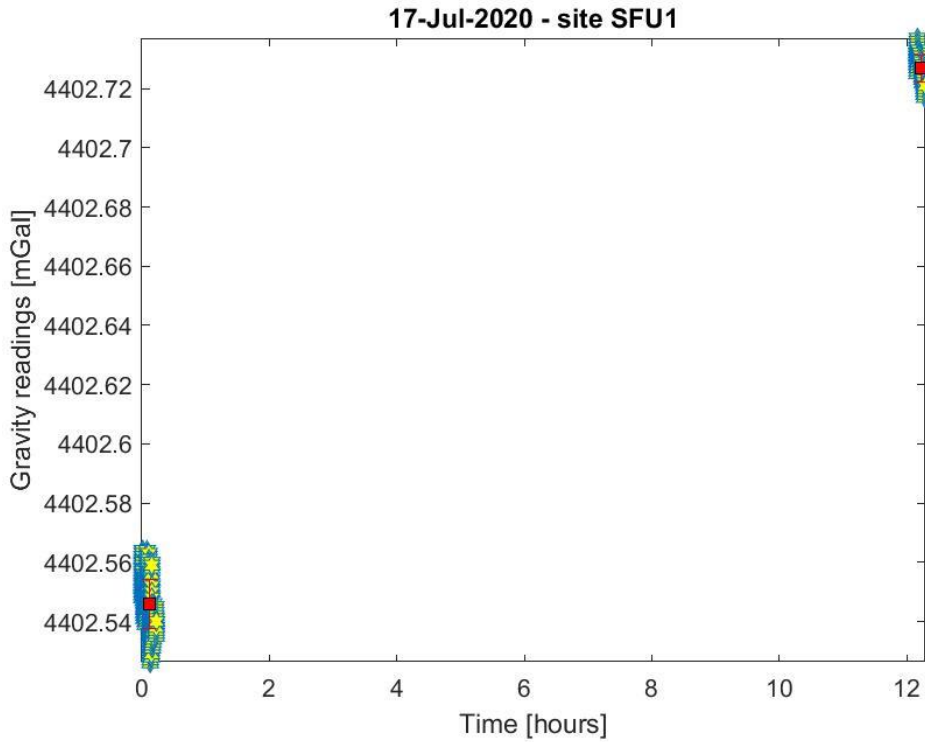


Figure 11. GTOOLS filtered data from all measurements at SFU1 on July 17, 2020. Data has yet to be corrected for Earth tide and drift.

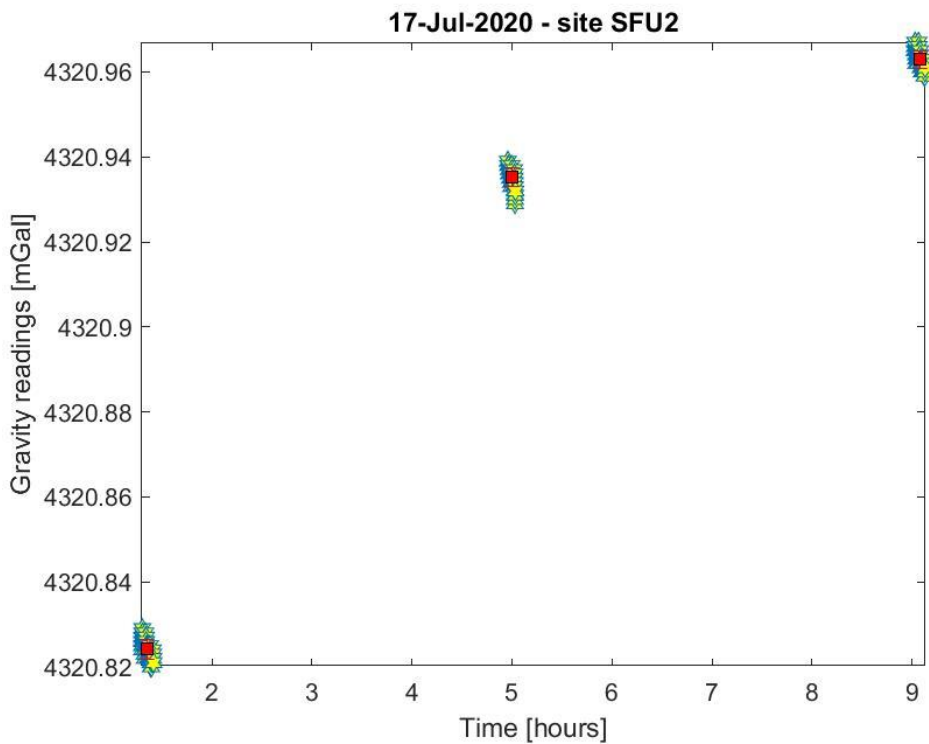


Figure 12. GTOOLS filtered data from all measurements at SFU2 on July 17, 2020. Data has yet to be corrected for Earth tide and drift.

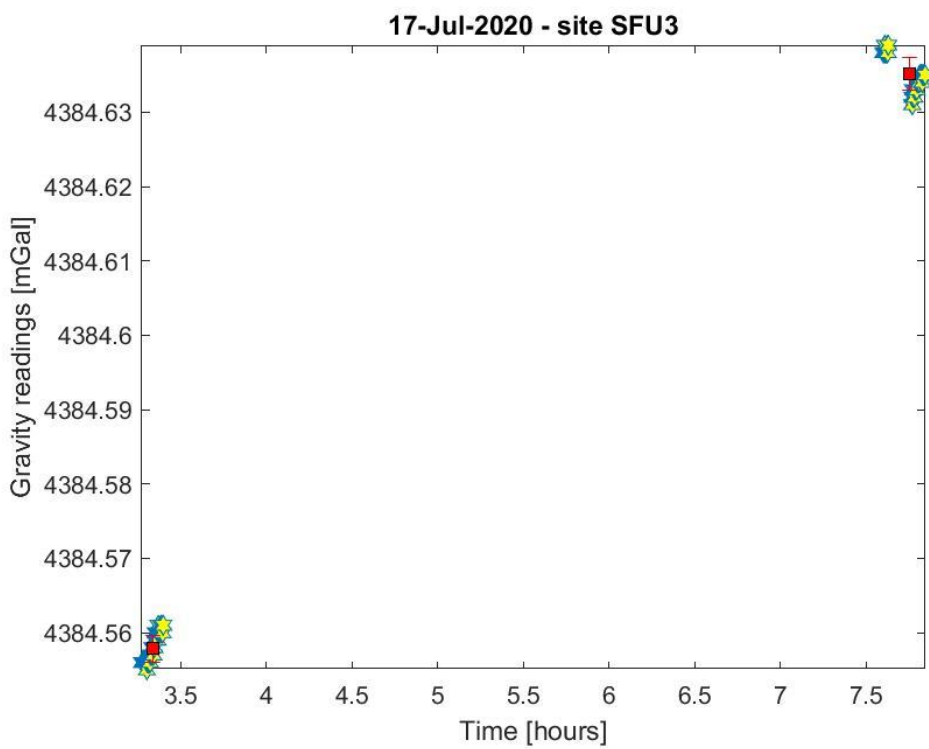


Figure 13. GTOOLS filtered data from all measurements at SFU3 on July 17, 2020. Data has yet to be corrected for Earth tide and drift.

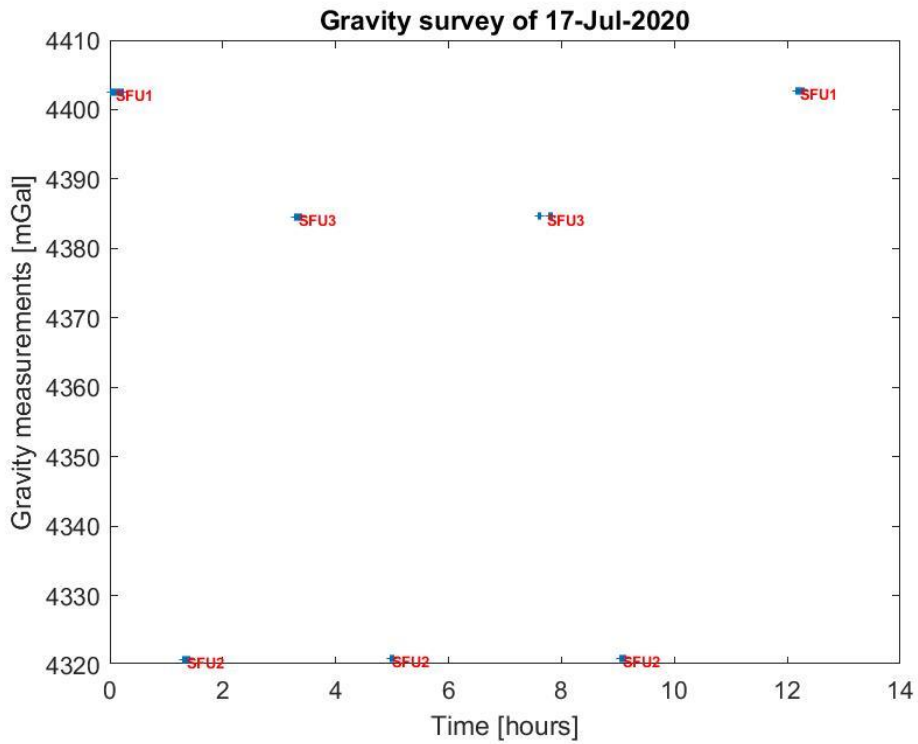


Figure 14. All measurements filtered for the survey loop on July 17, 2020. Data presented here has yet to be corrected for Earth tide and drift.

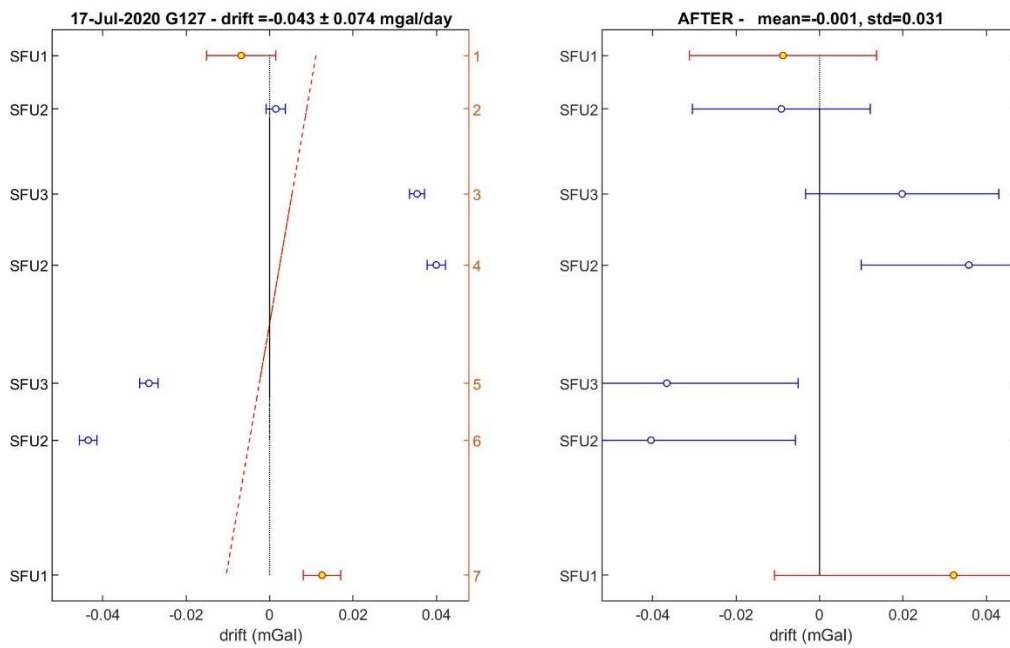


Figure 15. Gravity data from the survey loop on July 17, 2020 after filtering, Earth tide, and drift correction.

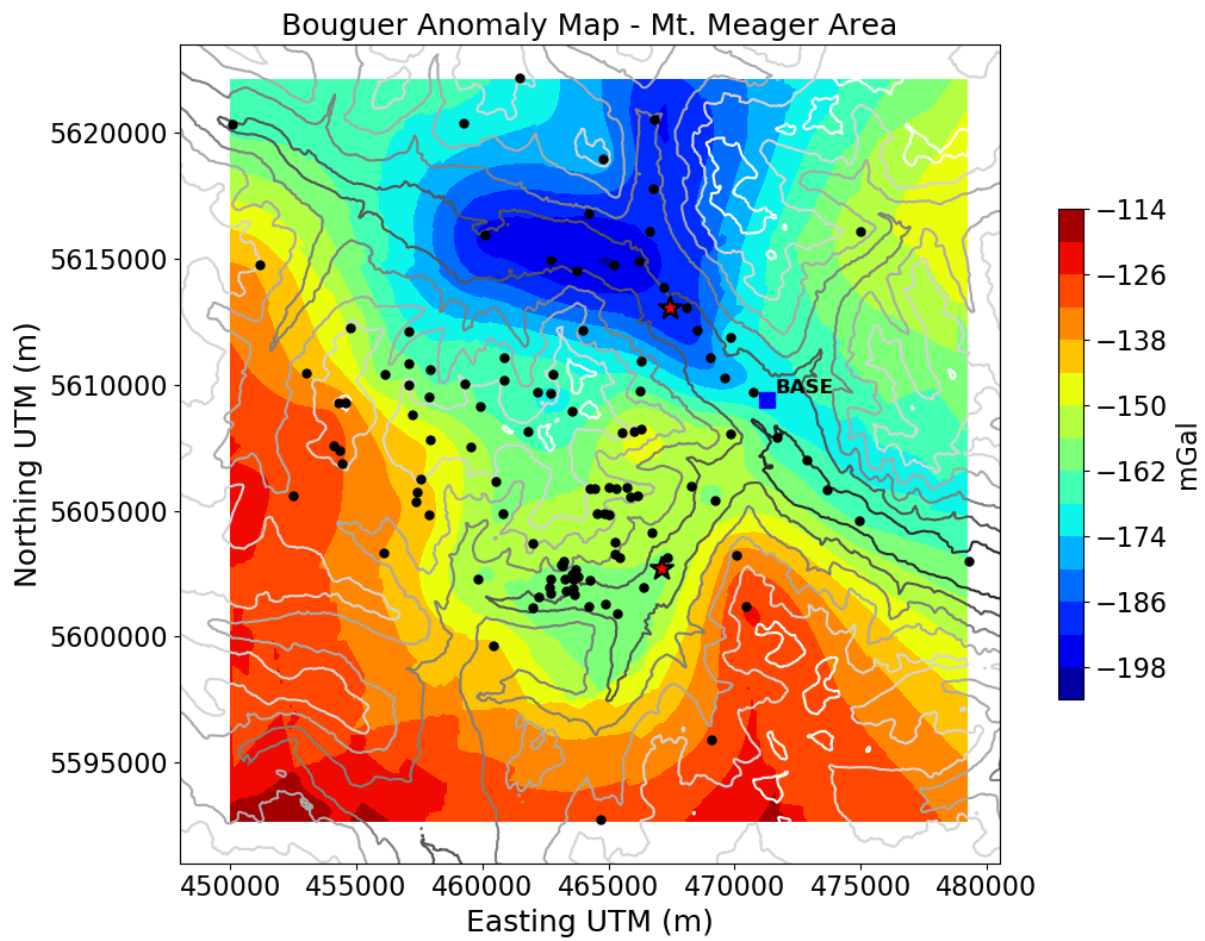


Figure 16. Bouguer gravity anomaly map of the Mt. Meager massif and surrounding area. Gravity sites are shown as black dots, the reference station BASE is a blue square, and Keyhole and Meager hot springs are noted with a red star. The topography is contoured with similar colours as in Figure 3.

Chapter 5 - Final report on the 2019-2020 broadband magnetotelluric study at Mount Meager: Implications for structure of the hydrothermal and magmatic system

Unsworth, M.J., Hanneson, C.¹, Williamson A.R. , Vestrum Z.E.

Department of Physics, University of Alberta, Edmonton, Alberta, Canada

The University of Alberta is furnishing this report "as is". The University of Alberta does not provide any warranty of the contents of the report whatsoever, whether express, implied, or statutory, including, but not limited to, any warranty of merchantability or fitness for a particular purpose or any warranty that the contents of the report will be error-free.

Introduction

Magmatism is a fundamental geological process that is important in many areas of Earth science. It occurs when crustal or mantle rocks melt to form partially molten rock, which rises due to its low density. The majority of the molten rock solidifies below the surface of the Earth to form plutonic, or intrusive, rocks. Molten rock that reaches the surface and erupts produces a volcano with associated volcanic, or extrusive, rocks. Magmatic systems are characterized by complicated interactions between the host rock, magma, and hydrothermal fluids. A number of fundamental scientific questions can be addressed by studying magmatic systems. A key question is how magmatic systems can transform mafic input into volcanic rocks with a broad range of compositions. Over geological time, this process has produced the bimodal distribution of oceanic and continental crust observed on Earth today.

From a practical point of view, there are a number of compelling reasons for studying magmatic systems, with a specific focus on active volcanoes. These studies are important for understanding the nature of future eruptions, landslides, and the potential to generate geothermal energy from the hot water found in hydrothermal systems.

Mount Meager is Canada's most active volcano and one of Canada's most promising geothermal resources. There are many aspects of the history and structure of Mount Meager that are not well understood. These questions need to be addressed in order to fully understand (1) the hazards associated with future volcanic eruptions and landslides and (2) the nature of the geothermal resource that could be developed from the high temperature reservoir that was discovered in the 1980s. The following three questions are all important for Mount Meager in the Garibaldi Belt of British Columbia. Questions that need to be answered are:

(1) What is the nature of the geothermal resources that can be used for energy production?

It is important to quantify the geothermal resources beneath a volcano to determine how much thermal energy could be extracted, either for direct use or electricity generation. Geophysical data can be used to characterize the geothermal reservoir and the pathways that transport fluids

from sources at depth. These data can contribute significantly to the development of a power plant by reducing the exploration risk.

(2) What is the size, location and composition of the magma body beneath Mount Meager?

Determining the size and composition of magma bodies beneath the volcano can give information about size of future eruptions, on timescales from days to millennia. The last eruption at Mount Meager occurred 2400 years ago, and recently active fumaroles indicate that the volcano is certainly not extinct. Understanding the nature of the entire magmatic system assists in the development of geothermal energy by defining the deeper source of heat and fluids feeding the present-day reservoirs. It could also lead to the discovery of concealed geothermal systems.

(3) Are there structures within the volcanic edifice that could cause major landslides?

Volcanic processes, such as hydrothermal circulation, can greatly decrease the strength of a volcanic edifice, and lead to sector collapses and major landslides. Mount Meager was the location of the largest recorded landslide in Canadian history in 2010 (Guthrie et al., 2012). Understanding the internal structure of the volcanic edifice is essential to determining the long-term risk of large events. This is also relevant to geothermal development, as it can guide plans to reduce the risks associated with constructing infrastructure on a restless volcano.

Information used to address these questions can be obtained from surface observations of erupted lavas, hydrothermal fluids, and gases. However, these methods are limited in what they can tell us about the structure of a volcanic system at depth. Geophysical methods are required to investigate the subsurface structure of these regions and a range of techniques can be used, as described elsewhere in this report. Each geophysical method measures a specific parameter that can be used to characterize the subsurface rock structure.

In many studies, geophysical exploration with the magnetotelluric (MT) method has been used to image the structure of active volcanoes and associated geothermal fields. This method measures the subsurface resistivity, a parameter that is sensitive to the presence of fluids. The MT method was used at Mount Meager during exploration in 2019 and 2020 by groups from the University of Alberta and Natural Resources Canada. This final report describes the work conducted by the University of Alberta at Mount Meager in 2019 and 2020.

Previous magnetotelluric studies at Mount Meager

Electrical resistivity is a useful parameter to measure in volcanic and geothermal studies because it is highly sensitive to the presence of magma, hydrothermal fluids, and the clay alteration produced by interactions of fluids with the host rock. A range of geophysical methods can be used to measure electrical resistivity. Electrical methods, such as direct current (DC) resistivity, use the injection of electric currents from metal electrodes, and have been used to image the near surface structure of many volcanos and geothermal systems worldwide (Eysteinnsson et al., 1994). Exploration at Mount Meager in the 1970s and 1980s included a number of DC resistivity surveys (Shore, 1975; Shore, 1981). A challenge of the DC resistivity method is that the depth of exploration is proportional to the current electrode spacing used. Thus, deeper sounding requires the deployment of large dipoles and this can be logistically challenging in rugged terrain. Deeper exploration is most efficient with electromagnetic (EM) methods that probe the resistivity structure with either naturally occurring electromagnetic signals or electromagnetic signals

generated by a transmitter. The depth of exploration in these studies is controlled by the frequency of the EM signal, with the depth of investigation increasing as frequency decreases.

For imaging structure below a depth of 1-2 km, EM methods using natural signals are the most efficient, since it is expensive and logistically complicated to generate powerful, low-frequency EM signals. The most suitable natural source EM method is magnetotellurics (MT), which is an established method that measures electric and magnetic fields at points on the surface. The magnetotelluric (MT) method was developed in the 1950s and 1960s and has become a widely used tool in volcano studies and geothermal exploration (Pellerin et al., 1996; Spichak and Manzella, 2009; Munoz, 2014). As shown in Figure 1, EM waves originate in the atmosphere and travel toward the Earth. At the Earth's surface, most of the energy is reflected back into the atmosphere, but a small fraction of the energy enters the Earth. The depth to which this transmitted signal travels in the Earth depends on both the resistivity of the Earth and frequency of the signal through the skin depth equation. It can be shown mathematically that the resistivity of the Earth can be calculated from the ratio of the horizontal electric field and orthogonal horizontal magnetic field at the surface. This gives a value of resistivity that is an average from the surface to a depth equal to one skin depth. By measuring EM signals at different frequencies, the variation of resistivity with depth can be determined. The instrument used in MT is basically a sensitive radio receiver that measures the electric and magnetic field components of these natural EM signals at the surface of the Earth. The instrument is shown schematically in Figure 2. Additional details of the magnetotelluric method are described by Vozoff (1991) and Simpson and Bahr (2005). Several prior studies have used MT exploration at Mount Meager and are summarized below.

The first MT studies at Mount Meager were reported from an exploration program described by Pham (1977), Pham (1978) and Pham (1980). In total 17 MT soundings were collected, and it was proposed that a shallow conductor was present at a depth of 2-4 km and likely due to the presence of partial melt. MT exploration continued with a survey of 7 MT soundings in 1982 reported by Flores-Luna (1986). A combination of 1-D, 2-D and 3-D analysis was undertaken and reported a north-dipping conductor (Flores-Luna, 1986). This study discounted the presence of the shallow conductor at a depth of 2-4 km reported by Pham (1978). Jones and Dumas (1993) presented a more detailed analysis of the previously collected MT data, combined with new Lithoprobe data that were collected in the Garibaldi Belt. This study applied novel techniques to remove galvanic distortion from the MT data and gave evidence for both a shallow conductor that was possibly a geothermal reservoir and a deeper regional conductor at 10-15 km depth.

In the studies listed above, the MT instruments that were used were bulky, and this limited data collection to vehicle accessible locations, mostly along Meager Creek. The MT data analysis techniques available at that time were hampered by the small number of stations. The analysis reported a low resistivity layer that was identified as a geothermal reservoir. A more recent analysis of the Lithoprobe MT data, combined with more recent MT measurements made in 2006 by the University of Alberta produced the two 2-D resistivity models shown by Rippe et al. (2013). The northern profile, named ABC-N, passes close to Mount Meager.

In 2000, a more detailed commercial MT survey collected 30 stations on the south slope of the Mount Meager volcanic complex (Candy, 2001). This gave a clearer impression of the geometry of the low resistivity layer. However, the combined MT dataset from surveys in the 1980s and 2000 was insufficient to reliably image the 3-D structure of the geothermal system, the magmatic system, or subsurface structures that may control the strength of the volcanic complex.

To address the shortcomings of the previously collected MT data, a research program was initiated in 2019 that included a systematic component of MT exploration (Grasby et al., 2020). This new study was motivated by the fact that (1) previous MT studies had identified a significant low resistivity target, but had insufficient station coverage to adequately define the geometry of the target and (2) since 2000 the MT method has advanced greatly and can now generate fully 3-D resistivity models because of improved instrumentation, new inversion algorithms, and accessibility to greater computer processing power.

Fieldwork took place in 2019 and 2020 and two types of MT instrument were used in the field.

- A group from Natural Resources Canada used audio-magnetotelluric (AMT) instruments that record high frequencies and image the near surface structure.
- The group from the University of Alberta used a separate broadband magnetotelluric (BBMT) system to measure lower frequencies and image structure to mid-crustal depths

Details of the data collection and analysis are described in the remainder of this report.

Data collection at Mount Meager in 2019 and 2020

The hydrothermal and magmatic systems at Mount Meager were investigated using a combination of broadband magnetotelluric (BBMT) data and audio-magnetotelluric (AMT) data.

Audio-magnetotelluric data collection at Mount Meager

The goal of the AMT survey was to determine permeability variations in the subsurface and link these to flow rates observed at the surface and in boreholes. Since the target was in the upper 1-2 km, this only required high frequency MT measurements in the band 10000 – 1 Hz. A detailed survey of the geothermal reservoir previously detected on the south side of Pylon Peak was carried out using higher frequency audio-magnetotelluric (AMT) data by the group from Natural Resources Canada and is described by Craven et al. (Grasby et al., 2020, Chapter 6).

Broadband magnetotelluric data collection at Mount Meager in 2019 and 2020

A more regional MT survey, aimed at studying the deeper parts of the geothermal system and magmatic system was undertaken by the University of Alberta using broadband MT instruments in 2019 and 2020. The University of Alberta MT research group has used this approach on a number of active volcanos in the Andes in recent years and been able to define the location, size and composition of magma bodies (Comeau et al., 2015; Cordell et al., 2018).

At Mount Meager, the broadband MT survey was designed to image fluid pathways that carried fluids to the geothermal reservoir and the fumaroles on the Job Glacier. It was also planned that these measurements might define the size and content of any magma bodies present beneath the volcano. With the deeper exploration targets, lower frequencies were used in the broadband magnetotelluric survey than in the AMT survey.

At Mount Meager the electric fields were measured with dipoles 30-90 metres in length and connected to the ground with porous pot electrodes. One pair of electrodes measured the north-south electric field component and a second pair measured the east-west electric field component. The three orthogonal components of the magnetic field were measured with induction coils. Figures 3 to 6 show the University of Alberta field crew installing and operating the broadband MT instruments at Mount Meager in July 2019 and August 2020.

The duration of the measurement depends on the frequencies to be recorded. Logistics makes it efficient to record MT data for one day at each site, with recording continuing overnight. This typically gives measurements in the frequency band 1000 – 0.001 Hz. From the physics of EM signal propagation in the Earth, these frequencies typically sample from the surface to a depth of 30 – 60 km. Commercial MT instruments are manufactured by a number of companies and have been developed to be very efficient. All BBMT data collection at Mount Meager in July 2019 and August 2020 used V5-2000 instruments manufactured by Phoenix Geophysics, a Canadian company based in Toronto.

Each phase of data collection began with instrument calibration that is an important check on the functioning of the instruments and induction coils. Calibrations were repeated at the end of data collection to confirm that the instrument responses had not changed. The calibration files are included in the data archive, and figures showing the responses are included in Appendix C.

During the July 2019 broadband MT survey, data were collected at 23 points. A total of 20 stations were accessed by helicopter while 3 were accessed by truck. The station deployment is shown in Figure 7 and details of each station are listed in Table 1. Recording times are shown in Figure 8(a). Since MT is a natural source EM method, the data quality depends on the signal strength which is out of the control of the user. During the 2019 survey, the signal levels were generally low as shown by the k-index plotted in Figure 8(a). These low signal levels were as expected since 2019 coincided with low sunspot numbers near the minimum of the approximately 11-year solar cycle. However, given the low levels of human-caused electromagnetic noise in the study area, the MT data were generally of good quality, as explained in the following section.

In August 2020, broadband MT data were collected at 12 points, with 11 stations accessed by helicopter and 1 accessed by truck. The station deployment is shown in Figure 7 and details of each station are listed in Table 2. Time series data were recorded at each station for up to three days as shown in Figure 8(b). In the field, the MT data were recorded in geomagnetic coordinates with the x-axis oriented to geomagnetic north and the y-axis oriented geomagnetic east.

In both 2019 and 2020, standard MT data collection techniques were used, generally without problems. High contact resistances were obtained at some sites, as expected with high resistivity crystalline rocks or ice present in the subsurface.

Analysis of the 2019-2020 broadband MT data

Time series analysis for the Mount Meager data

Time series data from both the 2019 and 2020 MT stations were processed using the statistically robust algorithm of Egbert and Booker (1986). In the first processing step, the time series were processed to calculate the spectra of the electric and magnetic field components as functions of frequency. Since measurements were usually made simultaneously at multiple stations, the remote reference method of Gamble et al. (1979) was used to separate signal from noise when appropriate. In the second step, the spectra were used to compute the apparent resistivity and phase, as functions of frequency. These quantities are important because they depend only on Earth resistivity structure, and not on the characteristics of the EM signals.

Two typical soundings from the 2019 survey are shown in Figure 9 and all 23 soundings are shown in Appendix A. Two typical soundings from the 2020 survey are shown in Figure 10 and all 12 soundings are shown in Appendix B.

Characteristics of the 2019-2020 Mount Meager apparent resistivity and phase data

Apparent resistivity can be considered as an average resistivity of the Earth from the surface to the maximum depth to which the EM signal penetrates. Thus, when apparent resistivity is plotted as a function of decreasing frequency, this corresponds to increasing depth in the Earth.

In each sounding there are two curves for apparent resistivity. The first is calculated from the north-south electric field and the east-west magnetic field, which is referred to as the XY component of the data. The second is calculated from the east-west electric field and the north-south magnetic field, which is referred to as the YX component of the data. By looking at both the XY and YX components of the data, information can be determined about whether the subsurface resistivity structure is 1-D, 2-D or 3-D.

Inspection of MT sounding curves can determine the quality of the data. A number of tests can be applied to the data.

- (1) The apparent resistivity and phase curves should be smooth, as a function of frequency. This is generally the case for the Mount Meager data in the frequency band 100 – 0.001 Hz. The accuracy of the apparent resistivity and phase decreases as frequency decreases. This is because for a given recording time, there will be less estimates of the low frequency signals than the high frequency signals. The XY component at station MGR204 has poor quality data, especially at low frequency, likely caused by a noisy time series of the north-south electric field. Also, this recording was made on a day with weak signal levels, when the k-index was 0 or 1 (Figure 8b).
- (2) The apparent resistivity and phase should be mutually consistent. It can be shown mathematically that when apparent resistivity increases with decreasing frequency, the phase angle should be in the range 0-45°. Similarly, when the apparent resistivity decreases with decreasing frequency, the phase angle should be in the range 45-90°. This observation provides a self consistency test for MT data and is generally valid for the stations collected at Mount Meager in both 2019 and 2020.

Visual inspection of the apparent resistivity curves in Appendices A and B shows a number of features.

- (1) At high frequency (> 1 Hz) the apparent resistivity is quite variable. These high frequency signals measure near surface structure, implying that the actual resistivity is spatially quite variable. This is as expected in volcanic environments where materials with a wide range of resistivity are found. Regions with recently extruded lava can have a resistivity in excess of 1000 Ωm . In contrast, an area where the rock has undergone hydrothermal alteration to form clay minerals can have a resistivity less than 1 Ωm .
- (2) At low frequency (< 1 Hz) all of the MT curves show a decreasing apparent resistivity in both the XY and YX components. This implies that there is a low resistivity layer at depth beneath the entire survey area. The preliminary 3-D resistivity model presented later in this report confirms this observation. An inversion of the MT data is needed to determine the actual depth and horizontal extent of the layer.
- (3) Electric and magnetic fields are each measured in two orthogonal directions. Thus, apparent resistivity / phase can be computed from the E_x and H_y components OR from the E_y and H_x components. These are referred to as the XY and YX data components in Figures 9 and 10 and Appendices A and B. If the XY and YX components are identical for all co-ordinate systems, then

this would imply that the subsurface resistivity structure was 1-D. This is clearly not the case for the MT data collected at Mount Meager in 2019 and 2020. The sounding curves shown in Appendices A and B give evidence of a 3-D resistivity structure, which requires a 3-D approach to inversion.

- (4) The XY and YX curves are often offset and parallel at high frequency (100-1 Hz) showing the presence of complicated effects due to 3-D resistivity structure in the near-surface. These offsets are sometimes referred to as static shifts and can greatly complicate MT data analysis in volcanic environments (Arnason, 2015).

Apparent resistivity at a given frequency can also be plotted as a map to illustrate spatial variations. Figure 11 shows apparent resistivity and phase at two frequencies in map view. In this figure the average of the XY and YX apparent resistivity is plotted. At the relatively high frequency of 4 Hz shown in Figure 11(a-b), the EM signals are only penetrating to a depth of 1-2 km, and the lowest apparent resistivity is observed at the station nearest Mount Meager and the fumaroles. At the lower frequency of 0.02 Hz shown in Figure 11(c-d) the EM signals are penetrating deeper and the resistivity is lower, with the lowest resistivity observed around Mount Meager.

Characteristics of the Mount Meager induction vector data

MT instruments also measure the vertical component of the magnetic field. Measurement of the vertical magnetic field at Mount Meager is shown in Figures 4 and 6. This quantity is sensitive to horizontal changes in resistivity structure and complements the apparent resistivity and phase data described above. The vertical magnetic field data at a set of stations can be conveniently plotted as induction vectors. When plotted in the Parkinson convention, the in-phase component of induction vectors point at conductors (regions of low resistivity). If plotted in the Weise convention, the in-phase component of these vectors points away from conductors. Figure 12 shows the in-phase components of the induction vectors in the Weise convention.

At a frequency of 4 Hz, the EM signals sample the near surface resistivity structure, and the induction vectors plotted in Figure 12(a) illustrate a radial pattern, pointing away from Mount Meager. This indicates that the Mount Meager complex has a low resistivity close to the surface. This is likely caused by hydrothermal fluids and extensive near-surface clay alteration.

At a lower frequency of 0.02 Hz, the EM signals sample deeper resistivity structure, and the induction vectors plotted in Figure 12(b) generally point southwest. This indicates that the resistivity at depth is relatively low to the northeast of the survey area. These observations agree with the induction vector patterns presented by Unsworth et al. (Grasby et al., 2020, Chapter 5).

3-D magnetotelluric inversion of the Mount Meager broadband MT data

The apparent resistivity, phase and vertical magnetic field data were then converted into a model of subsurface resistivity. This used a computer algorithm to implement a process called inversion, which seeks a resistivity model whose response fits the measured MT data to a given statistical tolerance. This process is non-unique, meaning that many resistivity models can be found which all fit a given MT dataset to within the same statistical tolerance. To overcome this limitation, conditions are imposed on the resistivity model. The most common approach is to require the resistivity model to be as spatially smooth as possible. However other approaches can be used, such as imposing constraints from other geophysical surveys or geological information from drilling. Depending on the characteristics of the measured MT

data, this can be done in 1-D, 2-D or 3-D. In the past, only 1-D and 2-D inversions were practical because of limitations in computer speed and memory. However, in recent years fully 3-D inversions have become practical for large MT datasets. Given the expected 3-D nature of a volcano such as Mount Meager, the focus was on 3-D inversion.

The MT soundings collected in 2019 and 2020 were combined with selected stations from the 1982 and 2000 surveys to give the array of 66 stations shown in Figure 13. These data were then edited to remove noisy points and interpolated onto a set of 29 frequencies in the bandwidth 0.001-400 Hz. The ModEM inversion algorithm of Kelbert et al. (2014) was then used to generate a 3-D resistivity model that fits the measured MT data to within a specified tolerance. This is a complicated process, with many inversions needed to be run in order to explore how the final 3-D model depends on the choice of data, inversion control parameters, and the degree of model smoothing. Each run typically takes several weeks on a high-performance computer cluster. Some initial 3-D resistivity models have been obtained, and they show a consistent set of features. Figures 14, 15 and 16 show a preliminary resistivity model as both horizontal and vertical slices, and this is discussed in the following section.

The preliminary 3-D resistivity model for Mount Meager is shown in Figures 14, 15 and 16. While this is a preliminary resistivity model, some significant model features can be identified as follows.

- (1) From the surface to sea-level the resistivity of the Mount Meager complex is generally high, with a number of low resistivity features with resistivities in the range 1-10 Ωm . These appear to correlate with the location of the fumaroles on the north side of the massif, and with the geothermal resources on the south side of the massif above Meager Creek.
- (2) From sea level to a depth of 5 km the crust has a relatively high resistivity in the range 100-1000 Ωm . A few isolated conductors are observed within this layer.
- (3) From 5 – 10 km a pronounced low resistivity layer is observed under most of the Mount Meager Massif with a resistivity in the range 0.1-10 Ωm . The lowest resistivities are centered beneath the geothermal reservoir in Meager Creek. The cause of this low resistivity is likely a combination of saline fluids, clay alteration, and partial melt. A careful analysis constrained by laboratory experiments on rock resistivity is needed to determine the cause of low resistivity. This work is currently in progress.

Summary and Future Work

Summary

The results above have presented the first 3-D resistivity model of the crustal structure beneath Mount Meager. The model shows a low resistivity layer at a depth of 5 km below sea level that is caused by a combination of saline fluids, clay alteration, and partial melt. A number of shallower low resistivity features can be identified and interpreted as shallow geothermal reservoirs or zones of hydrothermal alteration.

Ongoing data analysis

Additional data analysis is required and will include the following tasks.

- (1) Additional 3-D MT inversions to investigate how well the measured MT data can resolve the various resistivity features. This will include editing the 3-D resistivity model and restarting the inversion from the edited model. The statistical approach introduced by Lee et al. (2020) for the Krafla geothermal field will be used. Synthetic MT inversions will be used to test 3-D resistivity model resolution.
- (2) Determine the cause of the regions with low resistivity using laboratory studies of rock resistivity being conducted (Chapter 3). A key aspect of the data analysis will be to address the cause of zones of high and low resistivity found beneath Mount Meager. Resistivity contrasts in this type of environment can be caused by saline fluids, molten rock or minerals formed by hydrothermal alteration. External constraints are often needed to distinguish between these alternatives. It was once assumed that both geothermal reservoirs and magma bodies always had a low resistivity. However, careful laboratory experiments in recent years have shown that these assumptions are not always valid (Pommier and Le Trong, 2011). The resistivity of molten rock depends on the composition, and a high silica content can often produce molten rock with a relatively high resistivity making detection with electromagnetic methods challenging (Cordell et al., 2018; Lee et al., 2020). Similarly, in high temperature geothermal fields, the clay alteration minerals formed do not necessarily have a low resistivity, resulting in a reservoir that can be relatively resistive compared to the surrounding rock (Arnason et al., 2000). Analysis of the new 3-D resistivity models from Mount Meager will benefit greatly from the other available geological and geophysical datasets, including those collected in the 2019-2020 field campaigns and in previous exploration.
- (3) Systematic comparison of the 3-D resistivity model with other available geophysical datasets. This will include the resistivity models obtained from DC resistivity exploration (Shore, 1981) and the seismic and gravity studies that took place in 2019 (Grasby et al., 2020).

Data

The measured MT time series data have been provided as requested and consist of the following files:

- (a) A summary of the data acquisition is provided in an Excel file for each year of data collection listing recording dates, locations, and recording parameters.
- (b) The time series data files are sorted by recording date, with one folder being provided for each day. This means that synchronous recordings are in the same folder, which facilitates the use of remote reference processing to improve the quality of the response. For each recording, there are four files:

The run information is contained in a file with extension TBL. Data were recorded with three sample rates and each is contained in a single file with extension TS3, TS4 or TS5.

- (c) The calibration files recorded in 2019 and 2020. The instrument calibrations are contained in the files with extension CLB. Induction coil calibrations are contained in files with the extension CLC.

These time series data can be viewed using the program SyncTSV provided by Phoenix Geophysics. The data files can be processed using the SSMT software package, also produced by Phoenix Geophysics.

References

- Arnason K, The Static Shift problem in MT Soundings, Proceedings of the World Geothermal Congress, Melbourne, Australia, 19-25 April 2015.
- Arnason K, Karlsdottir R, Eysteinnsson H, Flovenz OG, and Gudlaugsson ST, The resistivity structure of high-temperature geothermal systems in Iceland, World Geothermal Congress, 2000.
- Comeau M, MJ Unsworth, F Ticona, and M Sunagua, Magnetotelluric images of magma distribution beneath Volcan Uturuncu, Bolivia: Implications for magma dynamics, *Geology*, 43(3), 243-246, March 2015.
- Candy C, Crew Development Corporation report on a magnetotelluric survey: South Meager Geothermal Project, Pemberton, British Columbia, Frontier Geosciences project FG1-581, 2001.
- Cordell DR, MJ Unsworth, and D Diaz, Imaging the Laguna del Maule Volcanic Field, central Chile using magnetotellurics: Evidence for crustal melt regions laterally-offset from surface vents and lava flows, *Earth and Planetary Science Letters*, 488, 168-180, 2018.
- Egbert GD and JR Booker, Robust estimation of geomagnetic transfer functions, *Geophysical Journal of the Royal Astronomical Society*, 87, 173-194, 1986.
- Eysteinnsson H, K Arnason, and OG Flovenz, Resistivity methods in geothermal prospecting in Iceland, *Surveys in Geophysics*, 15, 263-275, 1994.
- Flores-Luna CF, Electromagnetic induction studies over the Meager Creek Geothermal Area, British Columbia: Research in Applied Geophysics No. 37, University of Toronto, 1986.
- Gamble TB, WM Goubau, and J Clarke, Magnetotellurics with a remote reference, *Geophysics*, 44, 53-68, 1979.
- Grasby SE, SM Ansari, R Bryant, A Calahorrano-DiPatre, Z Chen, JA Craven, J Dettmer, H Gilbert, C Hanneson, M Harris, F Hormozzade, J Liu, D Montezadian, M Muhammad, JK Russell, RO Salvage, G Savard, V Tschirhart, MJ Unsworth, N Vigouroux-Caillibot, G Williams-Jones, and AR Williamson, Garibaldi Geothermal Energy Project, Mount Meager 2019 – Field Report, Geoscience BC Report 2020-09.
- Guthrie RH et al., The 6 August 2010 Mount Meager rock slide-debris flow, Coast Mountains, British Columbia: characteristics, dynamics, and implications for hazard and risk assessment, *Nat. Hazards Earth Syst. Sci.*, 12, 1277–1294, 2012.
- Jones, AG and I Dumas, Electromagnetic images of a volcanic zone, *Physics of the Earth and Planetary Interiors*, 81, 289-314, 1993.
- Kelbert A, N Meqbel, GD Egbert, and K Tandon, ModEM: A modular system for inversion of electromagnetic geophysical data, *Computers and Geosciences*, 66, 40-53, 2014.
- Lee BM, MJ Unsworth, K Arnason, and DR Cordell, Imaging the magmatic system beneath the Krafla geothermal field, Iceland: A new 3-D electrical resistivity model from inversion of magnetotelluric data, *Geophysical Journal International*, 2020.
- Munoz G, Exploring for Geothermal Resources with Electromagnetic Methods, *Surveys in Geophysics*, 35, 101-122, 2014.
- Pellerin L, JM Johnston, and GW Hohmann, A numerical evaluation of electromagnetic methods in geothermal exploration, *Geophysics*, 61, 121-130, 1996.
- Pommier A and E Le Trong, SIGMELTS: A web portal for electrical conductivity calculations in geosciences, *Computers and Geosciences*, 37, 1450-1459, 2011.

- Rippe D, MJ Unsworth and CA Currie, Magnetotelluric constraints on the fluid content of the upper mantle beneath the southern Canadian Cordillera: implications for rheology, *Journal of Geophysical Research*, 118(10), doi:10.1002/jgrb.50255, October 2013.
- Shore GA, Deep Resistivity Surveys and Supplementary Geophysics at Meager Creek selected area, Pemberton BC, report prepared for British Columbia Hydro and Power Authority, report G.T. 4, 1975.
- Shore GA, Report on DC resistivity survey in the Meager Creek Geothermal Area 1980, report prepared for British Columbia Hydro and Power Authority, report G.T. 26, 1981.
- Simpson F and K Bahr, *Practical magnetotellurics*, Cambridge University Press, 2005.
- Spichak V and A Manzella, Electromagnetic sounding of geothermal zones, *Journal of Applied Geophysics*, 68, 459-478, 2009.
- Pham van Ngoc, Magnetotelluric reconnaissance survey in the Lilloet Valley, BC, Earth Physics Branch Open File 77-20, Earth Physics Branch, Department of Energy, Mines and Resources, Ottawa, 40 pp., 1977.
- Pham van Ngoc, Magnetotelluric prospecting in the Mount Meager Geothermal Region, Earth Physics Branch Open File 78-6E, Earth Physics Branch, Department of Energy, Mines and Resources, Ottawa, 31 pp., 1977.
- Pham van Ngoc, Magnetotelluric survey of Mount Meager and the region of the Squamish Valley, Earth Physics Branch Open File 80-8E, Earth Physics Branch, Department of Energy, Mines and Resources, Ottawa, 77 pp., 1980.
- Vozoff K, The magnetotelluric method, in *Electromagnetic Methods in Applied Geophysics*, Vol. 2B, 641-711, Society of Exploration Geophysicists, 1991.

Acknowledgements

This research was supported by an NSERC Discovery Grant to Martyn Unsworth, and an award from the Future Energy Systems program at the University of Alberta. The 3-D inversions were performed on the high-performance computer clusters operated by Compute Canada. Gary Egbert, Anna Kelbert and Naser Meqbel are thanked for allowing the use of the ModEM inversion program. Jim Craven at the Geological Survey of Canada is thanked for his help in preparing the MT instruments for use in the field at Mount Meager in 2019 and 2020. Steve Grasby is thanked for his leadership of the project and assistance in securing funding and planning field logistics. Cliff Candy at Frontier Geosciences is thanked for making the 2000 Geosystem data available for this research.

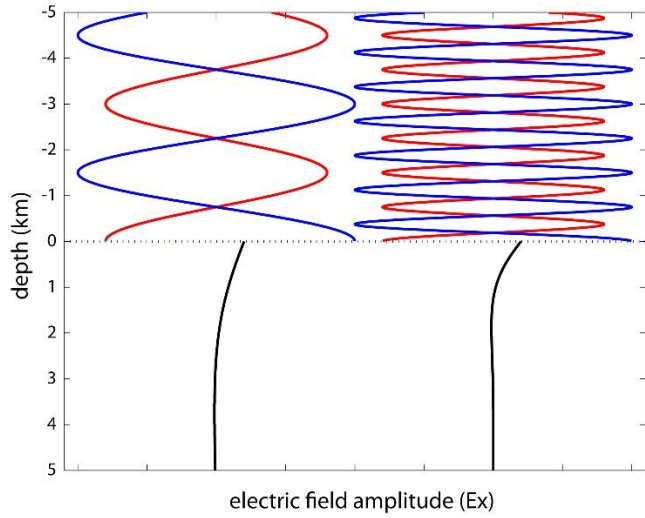


Figure 1: Schematic of the electromagnetic (EM) signals used in magnetotelluric exploration. The blue lines show a low frequency signal (left) and high frequency signal (right) incident on the surface of the Earth. Most of the energy is reflected back into the atmosphere (red), and a small fraction is transmitted into the Earth (black). Within the Earth the EM energy travels by diffusion. Note that the low frequency signal travels deeper into the Earth than the high frequency. An animated version of this figure can be viewed at <https://sites.ualberta.ca/~unsworth/MT/MT.html>

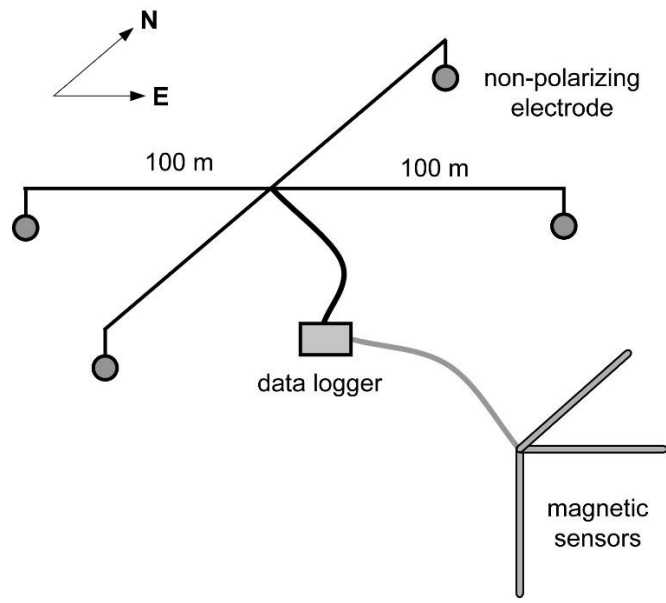


Figure 2: Schematic diagram of a broadband magnetotelluric station used to measure the electric and magnetic fields. The electric fields are measured in the north-south and east-west directions using pairs of non-polarizing electrodes. The magnetic fields are measured in north-south, east-west and vertical directions using induction coils.



Figure 3: Photographs of the University of Alberta field crew installing and operating Phoenix Geophysics MT instruments at Mount Meager in July 2019. (a) Helicopter departing from station MGR108 (b) Data being recorded at station MGR108 with a Phoenix Geophysics MTU5A instrument (c) Field crew at station MGR 116 (d) Data collection from the instrument at station MGR116.

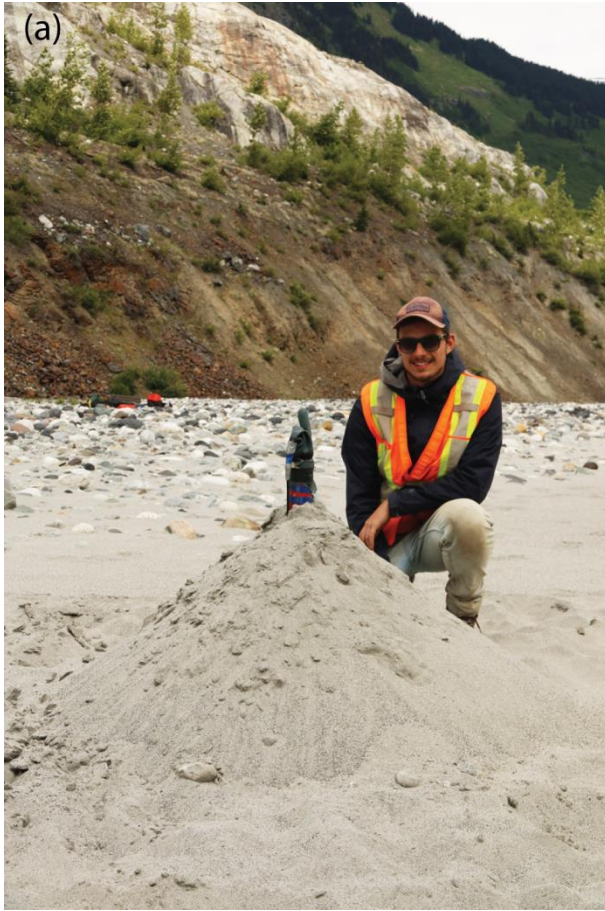


Figure 4: (a) Installation of the induction coil measuring the vertical magnetic field at station MGR111 (b) field camp at the foot of Mount Meager.

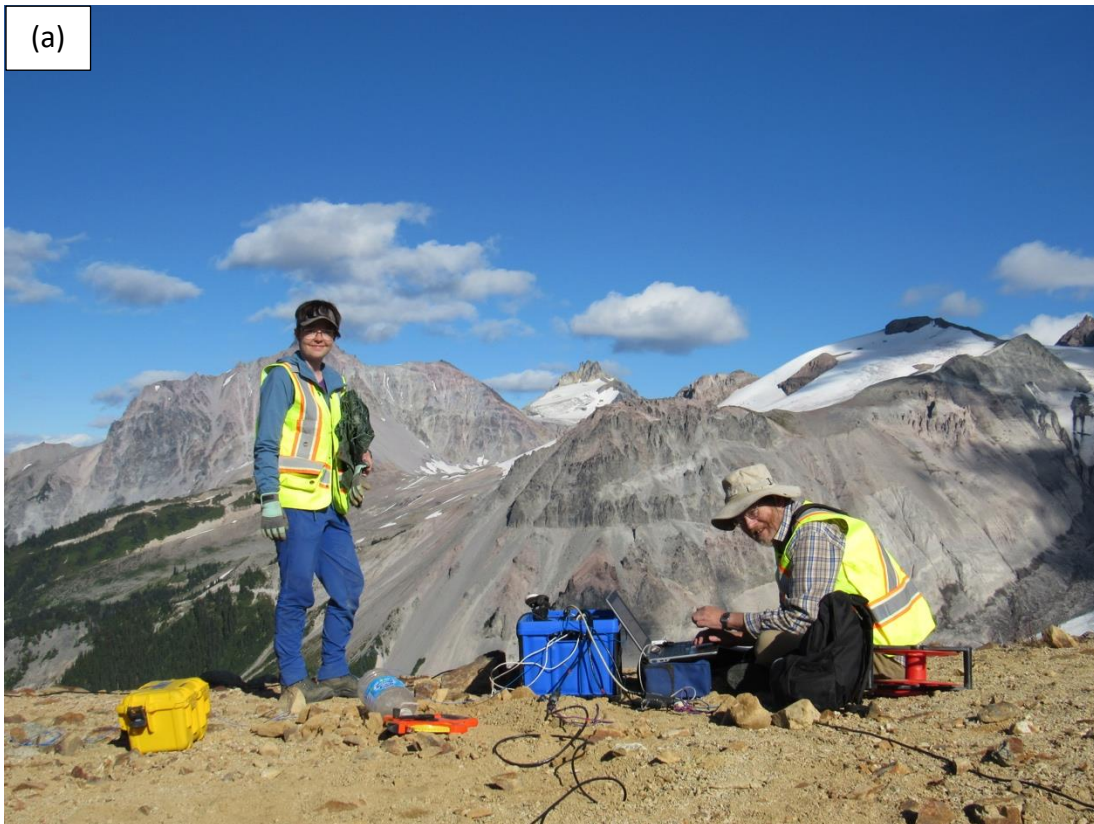


Figure 5: Photographs of the University of Alberta field crew operating a Phoenix Geophysics MT instrument at site MGR205 on August 8, 2020 with Mount Meager in the background. (a) Zoë Vestrum and Martyn Unsworth and (b) Cedar Hanneson and Zoë Vestrum.



Figure 6: Installation of the induction coil measuring the vertical magnetic field at station MGR207 on August 9, 2020.

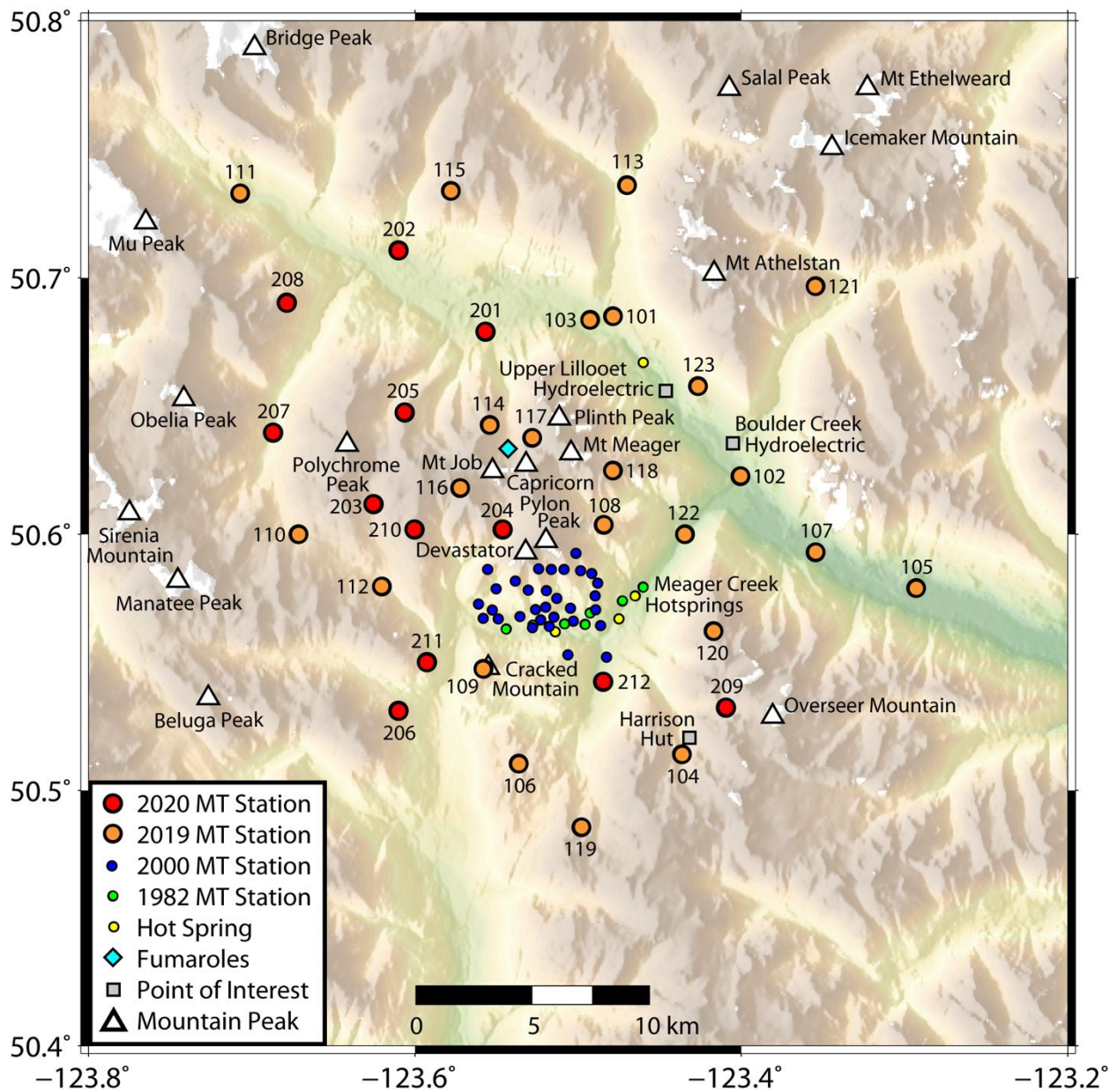


Figure 7: Map of the Mount Meager area showing previously collected MT data, and data collected in 2019 and 2020 by the University of Alberta. Details of the 2019 deployments are presented in Table 1 and details of the 2020 deployments are presented in Table 2. The AMT sites installed by NRCan in 2019 are not shown.

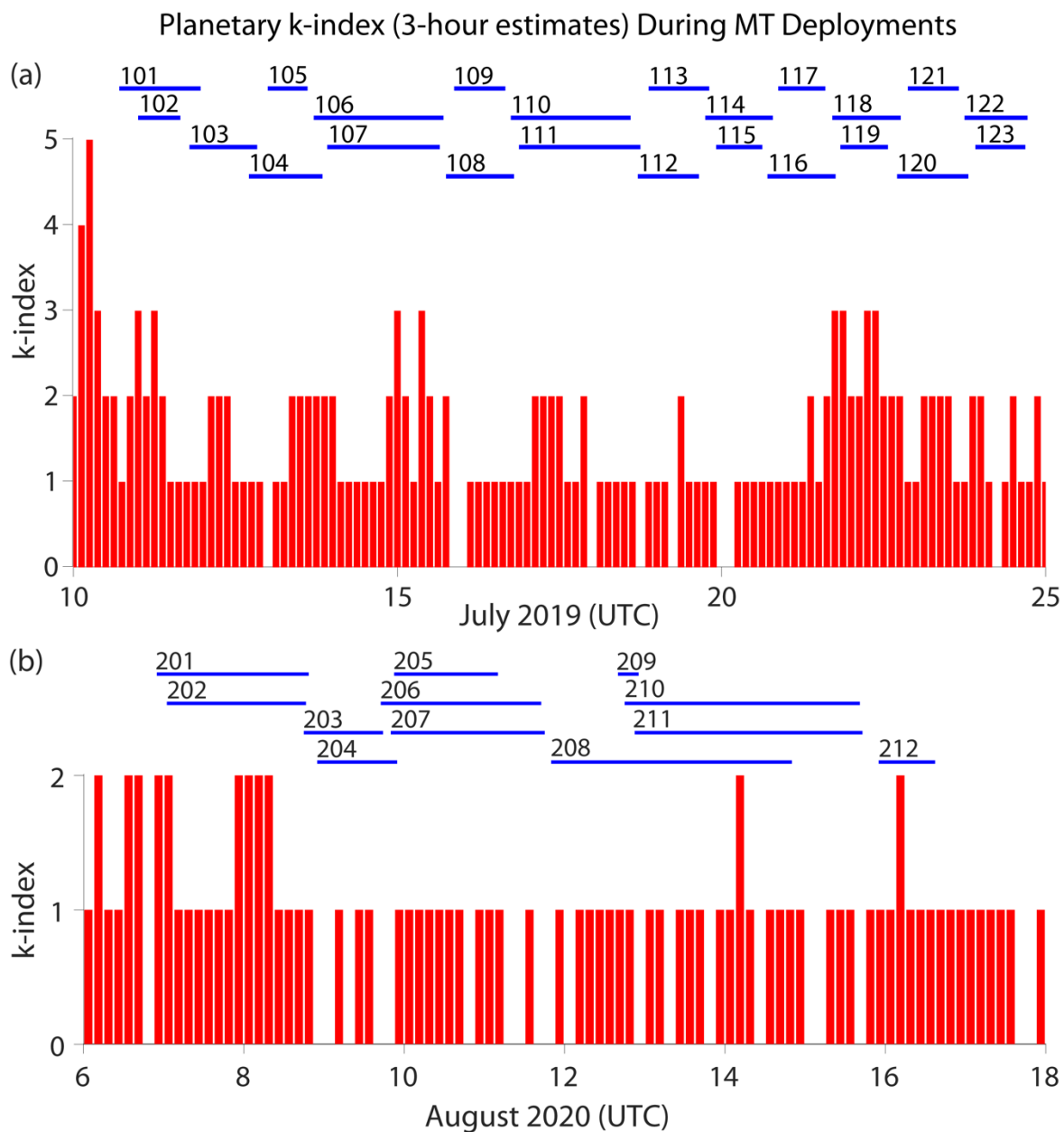


Figure 8: (a) The k-index as a function of date during the July 2019 survey at Mount Meager. The recording times of the 23 magnetotelluric stations are shown in blue. (b) The k-index as a function of date during the August 2020 survey at Mount Meager. The recording times of the 12 magnetotelluric stations are shown in blue. Two recordings were made at MGR205; only the second one was used, and it is shown. Two recordings were made at MGR209; only the first one was used, and it is shown. Only one recording was made at each of the other ten sites. Details are included in the supplemental spreadsheets.

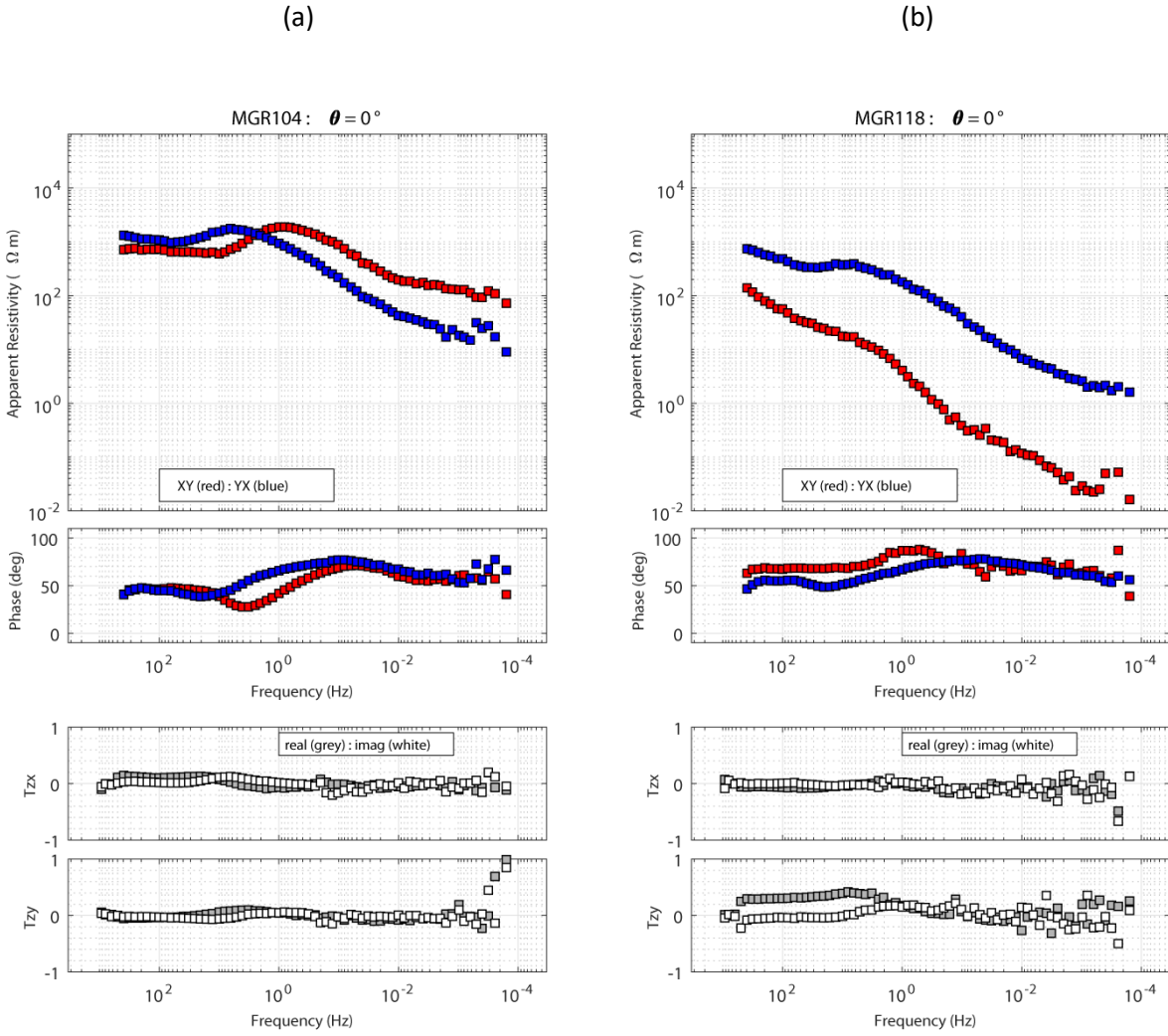


Figure 9: Apparent resistivity, phase, and tipper curves at two representative stations recorded at Mount Meager by the University of Alberta in July 2019. (a) MGR104 and (b) MGR118

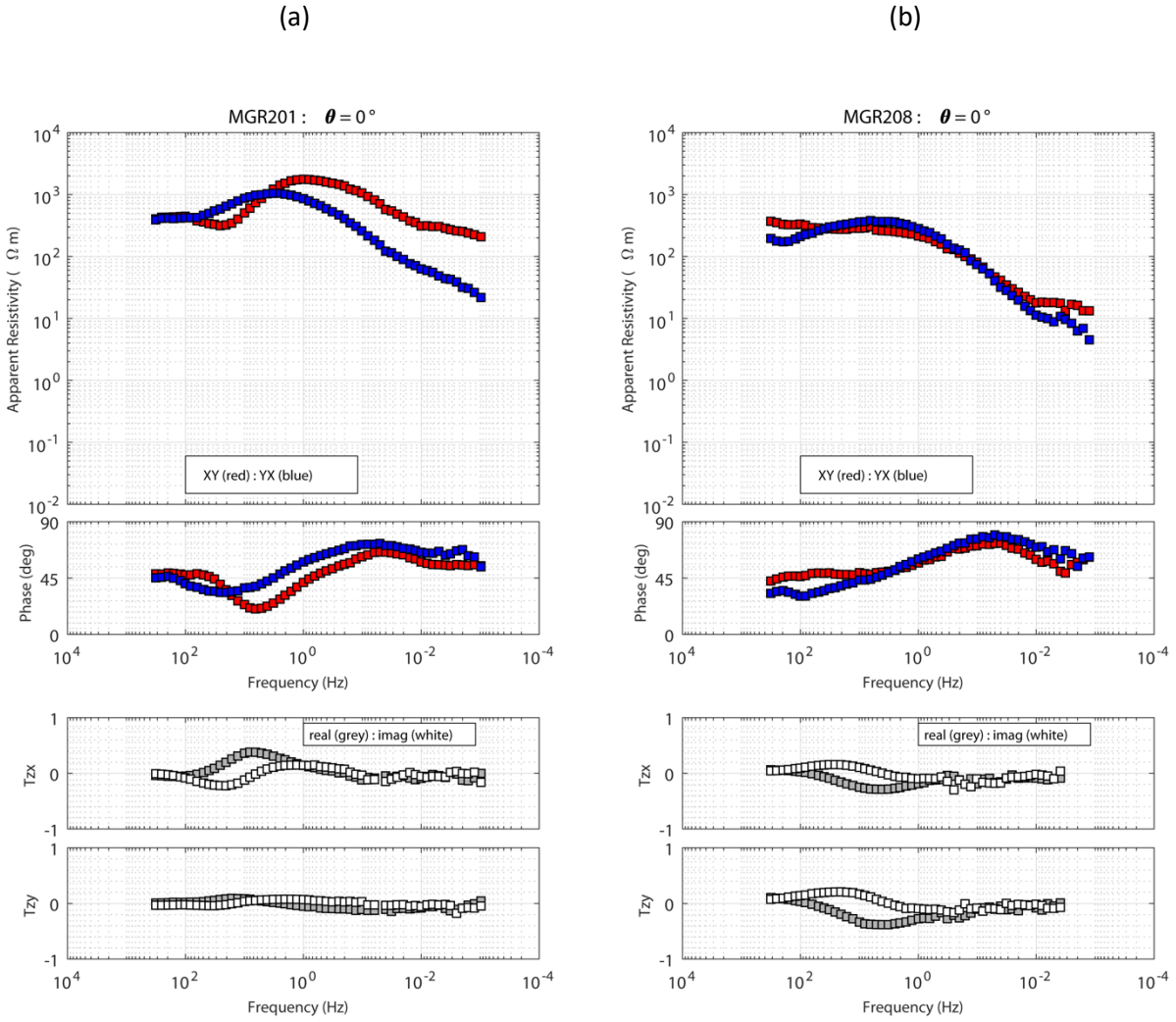


Figure 10: Apparent resistivity, phase, and tipper curves at two representative stations recorded at Mount Meager by the University of Alberta in August 2020. (a) MGR201 and (b) MGR208

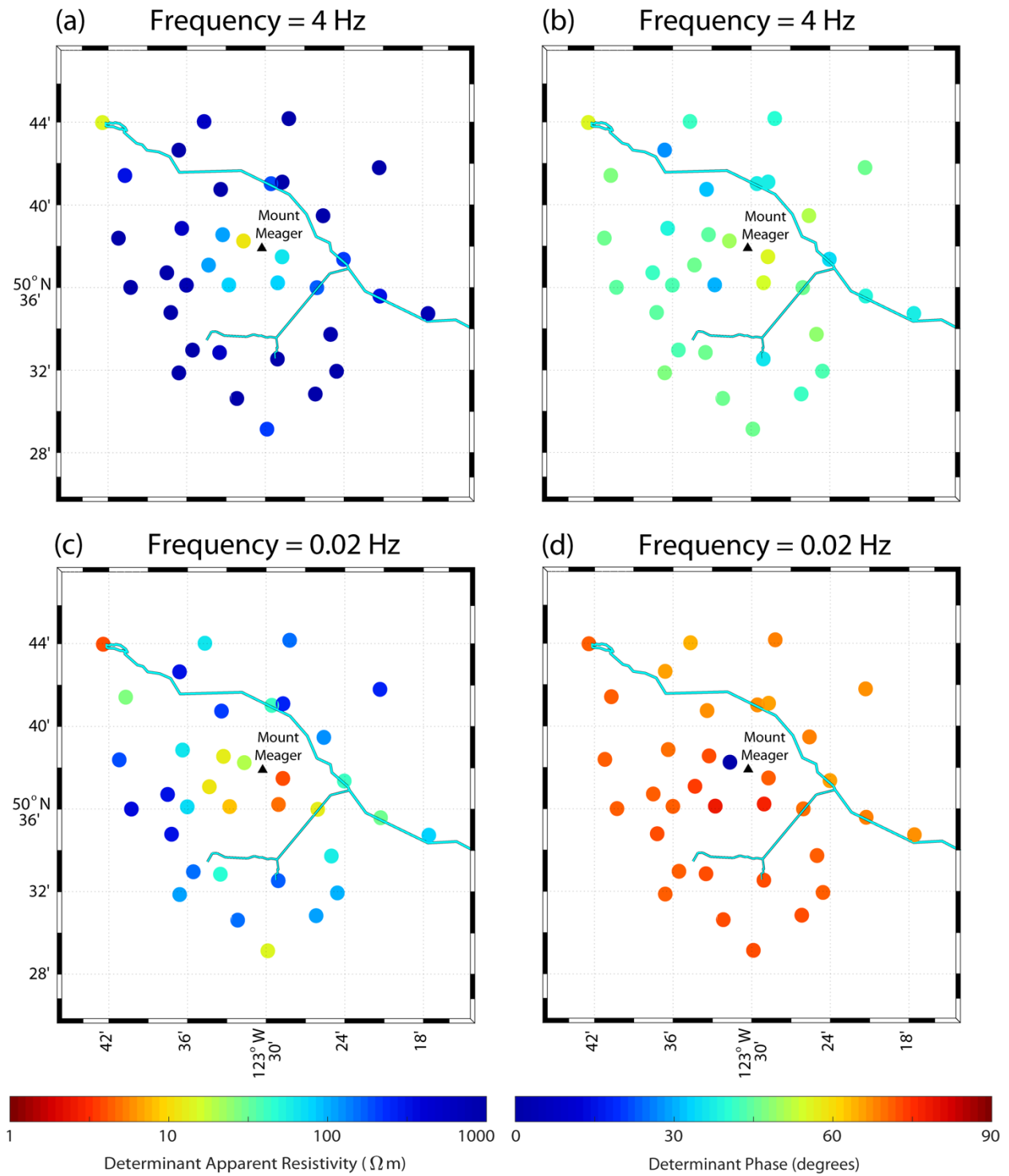


Figure 11: Maps of apparent resistivity and phase at two representative frequencies, including 2019 and 2020 data. (a) and (c) show the average value of the apparent resistivity computed from the north-south and east-west electric fields. (b) and (d) show the corresponding phases.

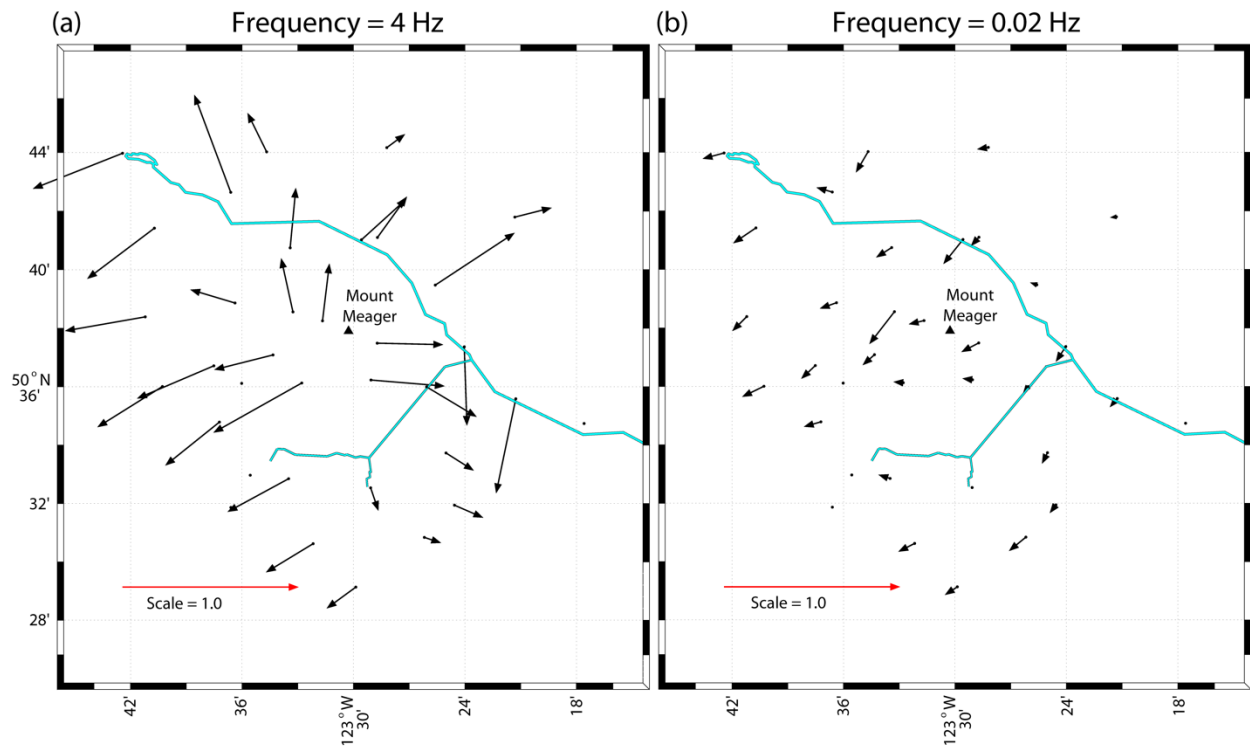


Figure 12: Maps of induction vectors at two representative frequencies, including 2019 and 2020 data. Induction vectors are plotted in the Weise convention and point away from zones of low resistivity (high conductivity). (a) shows data at a frequency of 4 Hz and vectors point away from the Mount Meager volcanic complex, showing that at shallow depth it is characterized by low resistivity. (b) shows induction vectors at a lower frequency of 0.02 Hz which penetrates deeper into the Earth. These vectors mostly point southwest, indicating that conductivity increases to the northeast.

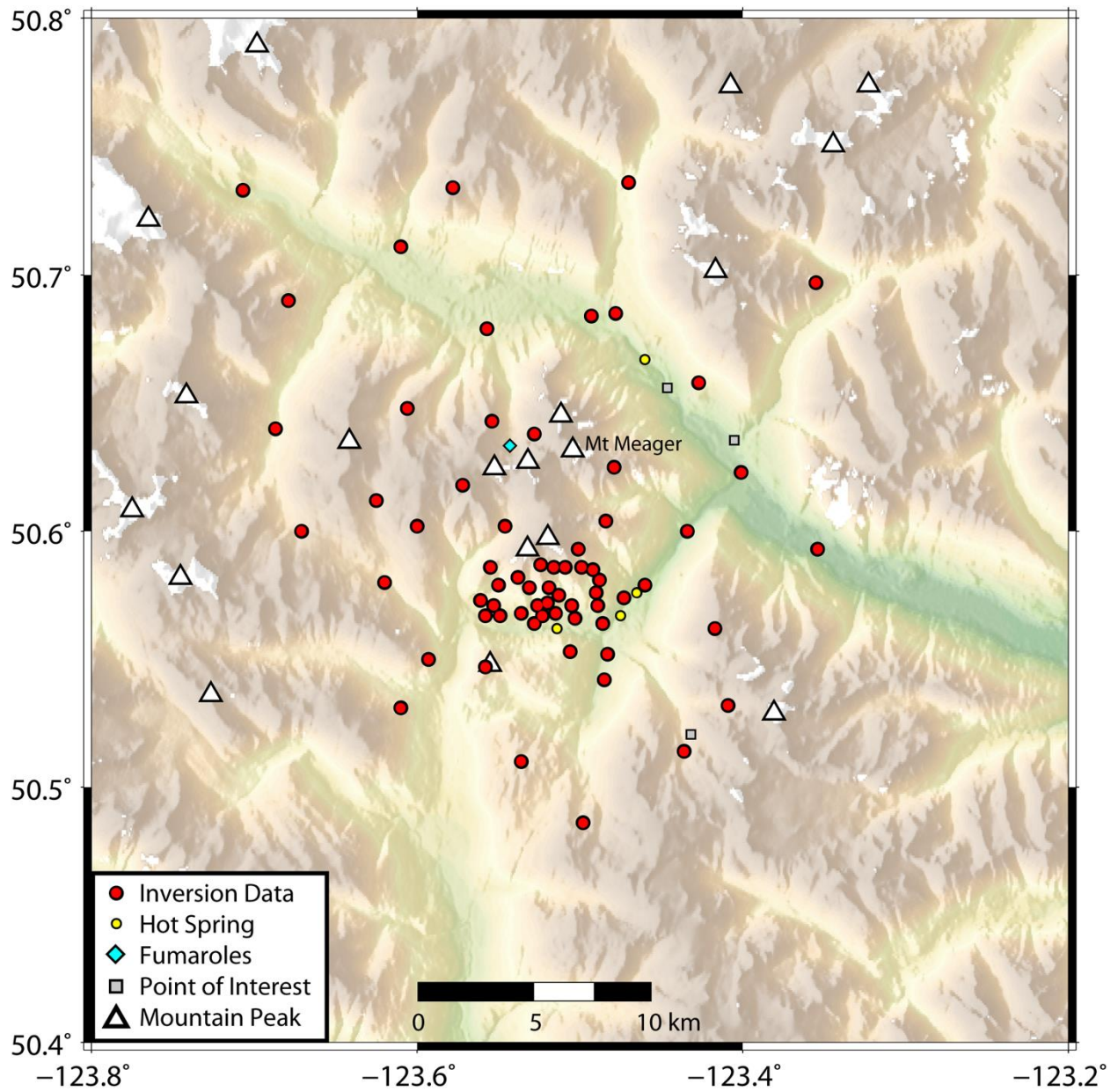


Figure 13: Map of all MT stations used in the 3-D inversion. This uses a combination of the four broadband MT datasets collected in 1982, 2000, 2019 and 2020 that were shown in Figure 5.

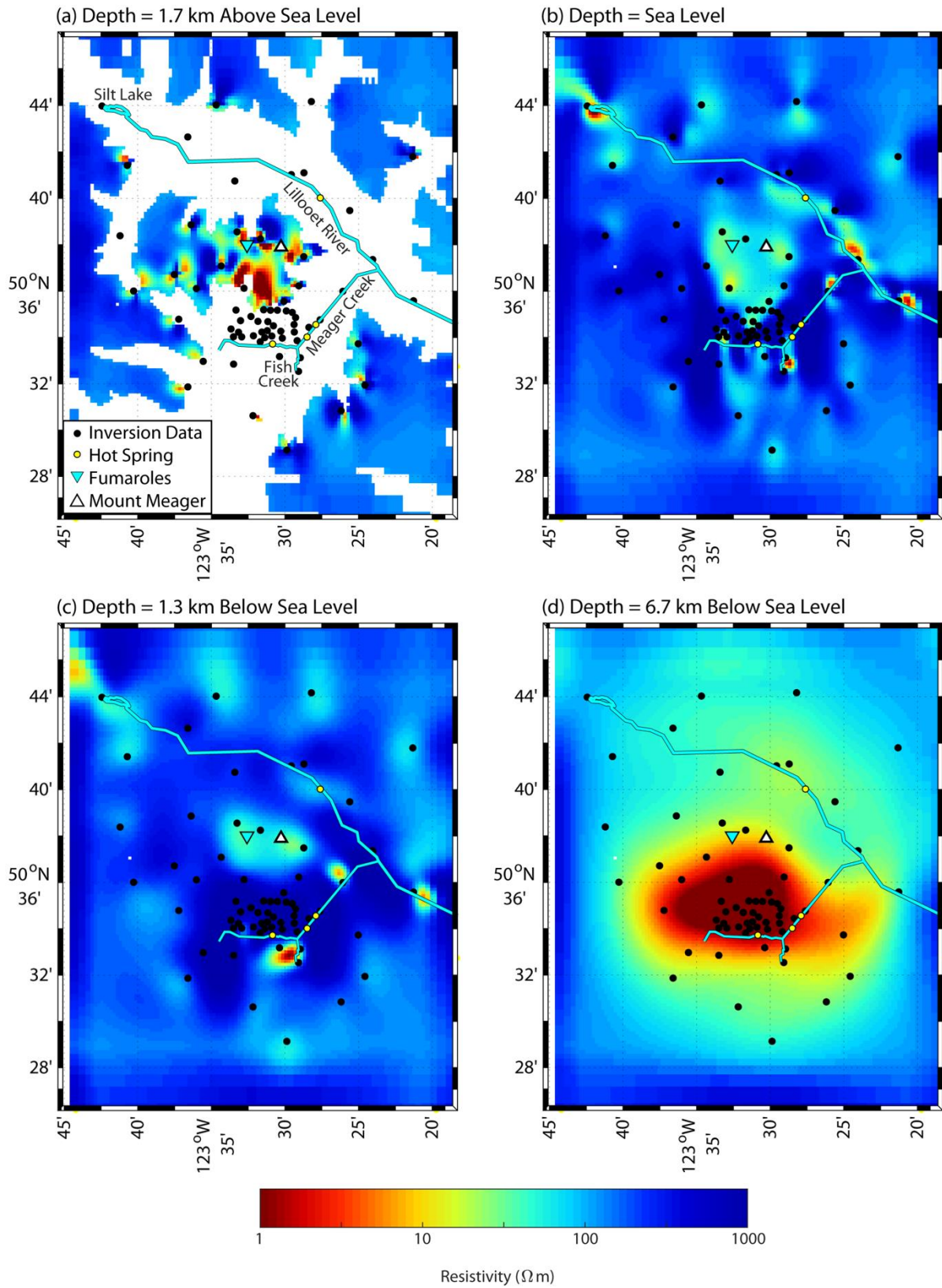


Figure 14: Horizontal slices of the preliminary 3-D resistivity model obtained using the 3-D ModEM inversion and data from 66 MT sites (listed in Table 3).

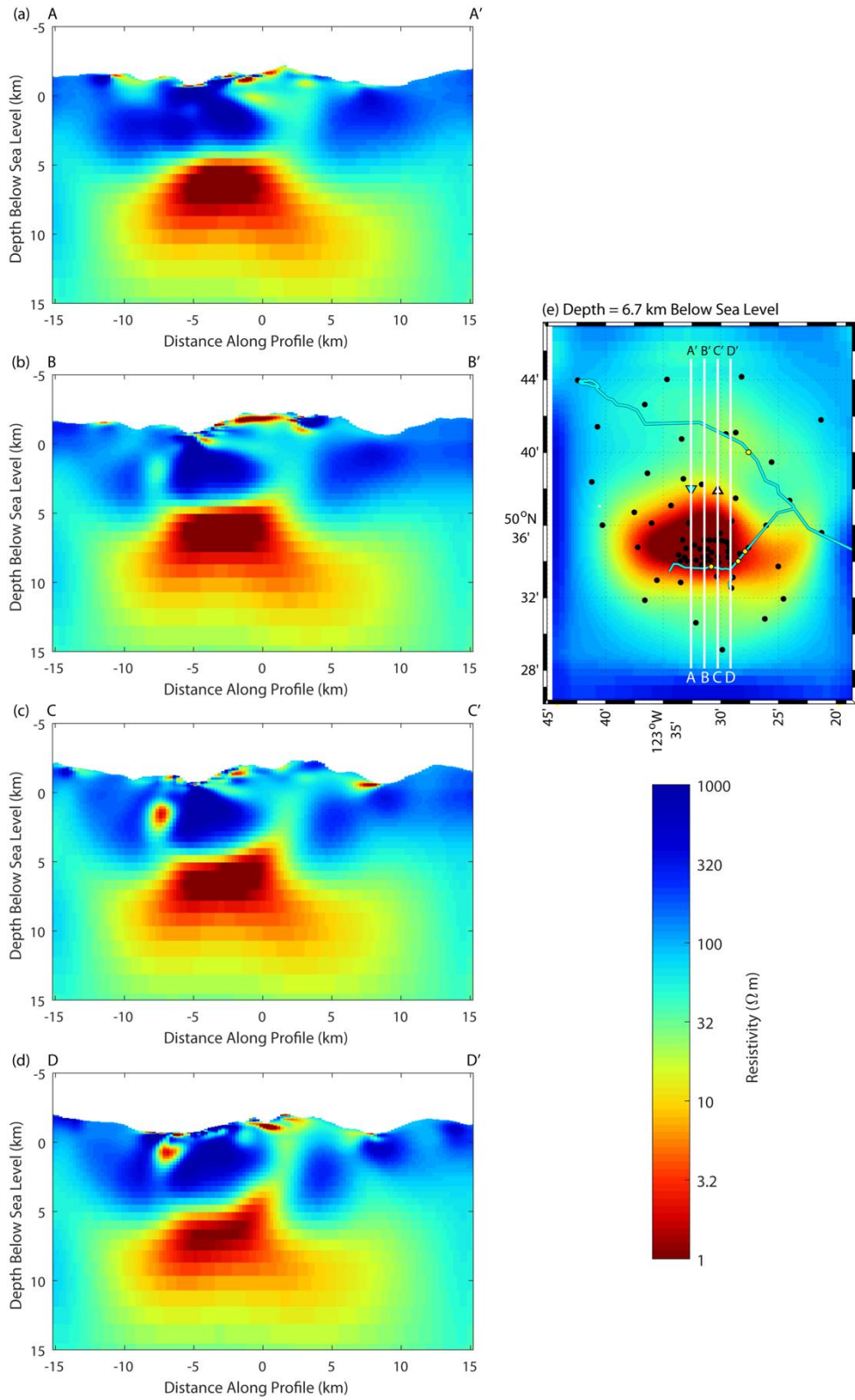


Figure 15: Vertical north-south slices of the preliminary 3-D resistivity model obtained using the 3-D ModEM inversion and data from 66 MT sites (listed in Table 3). (a)-(d) show four north-south transects with locations shown in (e).

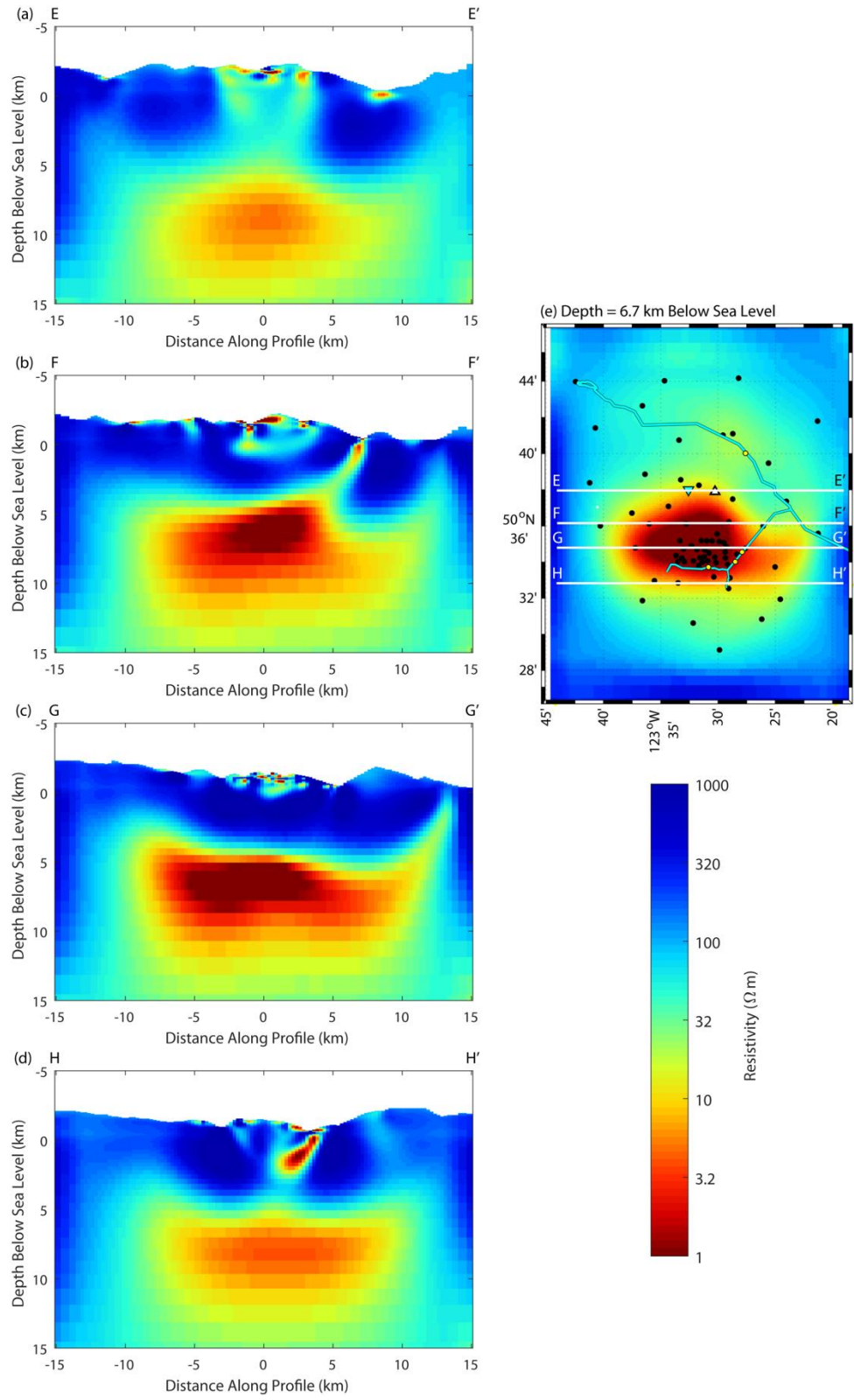


Figure 16: Vertical east-west slices of the preliminary 3-D resistivity model obtained using the 3-D ModEM inversion and data from 66 MT sites (listed in Table 3). (a)-(d) show four east-west transects with locations shown in (e).

Date of Deployment	Station Name	Latitude (°N)	Longitude (°W)	Elevation (m)	N-S Line (m)	E-W Line (m)	Helicopter (H) or Truck (T)
2019/07/10	MGR101	50.685	123.478	726	27	35	T
2019/07/10	MGR102	50.623	123.401	411	53	58	T
2019/07/11	MGR103	50.684	123.493	675	60	77	H
2019/07/12	MGR104	50.514	123.436	1713	57	51	H
2019/07/12	MGR105	50.579	123.293	343	52	57	T
2019/07/13	MGR106	50.510	123.536	1613	47	75	H
2019/07/13	MGR107	50.593	123.354	363	53	59	H
2019/07/15	MGR108	50.604	123.484	1827	52	57	H
2019/07/15	MGR109	50.547	123.558	1597	52	75	H
2019/07/16	MGR110	50.600	123.671	1628	64	54	H
2019/07/16	MGR111	50.733	123.707	805	53	62	H
2019/07/18	MGR112	50.580	123.620	1484	53	88	H
2019/07/18	MGR113	50.736	123.470	1200	61	52	H
2019/07/19	MGR114	50.643	123.554	1970	52	52	H
2019/07/19	MGR115	50.734	123.578	1960	55	54	H
2019/07/20	MGR116	50.618	123.572	2335	40	52	H
2019/07/20	MGR117	50.638	123.528	1946	66	47	H
2019/07/21	MGR118	50.625	123.479	2028	52	73	H
2019/07/21	MGR119	50.486	123.498	1789	63	56	H
2019/07/22	MGR120	50.562	123.417	2213	57	54	H
2019/07/22	MGR121	50.697	123.355	1823	54	88	H
2019/07/23	MGR122	50.600	123.434	508	88	54	H
2019/07/23	MGR123	50.658	123.427	925	44	38	H

Table 1: Details of MT soundings recorded at Mount Meager in July 2019 by the University of Alberta.

Date of Deployment	Station Name	Latitude (°N)	Longitude (°W)	Elevation (m)	N-S Line (m)	E-W Line (m)	Helicopter (H) or Truck (T)
2020/08/06	MGR201	50.679	123.557	831	58	44	H
2020/08/06	MGR202	50.711	123.610	812	30	30	H
2020/08/08	MGR203	50.612	123.625	1752	57	52	H
2020/08/08	MGR204	50.602	123.546	1520	44	42	H
2020/08/08	MGR205	50.648	123.606	1912	56	46	H
2020/08/09	MGR206	50.531	123.610	1477	67	60	H
2020/08/09	MGR207	50.640	123.687	1281	50	56	H
2020/08/11	MGR208	50.690	123.679	1756	60	55	H
2020/08/12	MGR209	50.532	123.409	1810	60	59	H
2020/08/12	MGR210	50.602	123.600	1970	50	52	H
2020/08/12	MGR211	50.550	123.593	1545	60	37	H
2020/08/15	MGR212	50.543	123.485	757	32	32	T

Table 2: Details of MT soundings recorded at Mount Meager in August 2020 by the University of Alberta.

Station Name	Year Deployed	Station Name	Year Deployed	Station Name	Year Deployed
MGR101	2019	MGR201	2020	mt16	2000
MGR102	2019	MGR202	2020	mt17	2000
MGR103	2019	MGR203	2020	mt19	2000
MGR104	2019	MGR204	2020	mt20	2000
MGR106	2019	MGR205	2020	mt21	2000
MGR107	2019	MGR206	2020	mt22	2000
MGR108	2019	MGR207	2020	mt23	2000
MGR109	2019	MGR208	2020	mt24	2000
MGR110	2019	MGR209	2020	mt27	2000
MGR111	2019	MGR210	2020	mt28	2000
MGR112	2019	MGR211	2020	mt29	2000
MGR113	2019	MGR212	2020	mt30	2000
MGR114	2019	mt01	2000	mt31	2000
MGR115	2019	mt02	2000	mt32	2000
MGR116	2019	mt03	2000	mt33	2000
MGR117	2019	mt06	2000	mt34	2000
MGR118	2019	mt07	2000	mt35	2000
MGR119	2019	mt11	2000	mt37	2000
MGR120	2019	mt12	2000	me4	2000
MGR121	2019	mt13	2000	fl03	2000
MGR122	2019	mt14	2000	meager82_6	1982
MGR123	2019	mt15	2000	meager82_7	1982

Table 3: MT stations that were used in the 3-D inversion and the year in which they were deployed.

Appendix A: MT sounding curves from Mount Meager in 2019

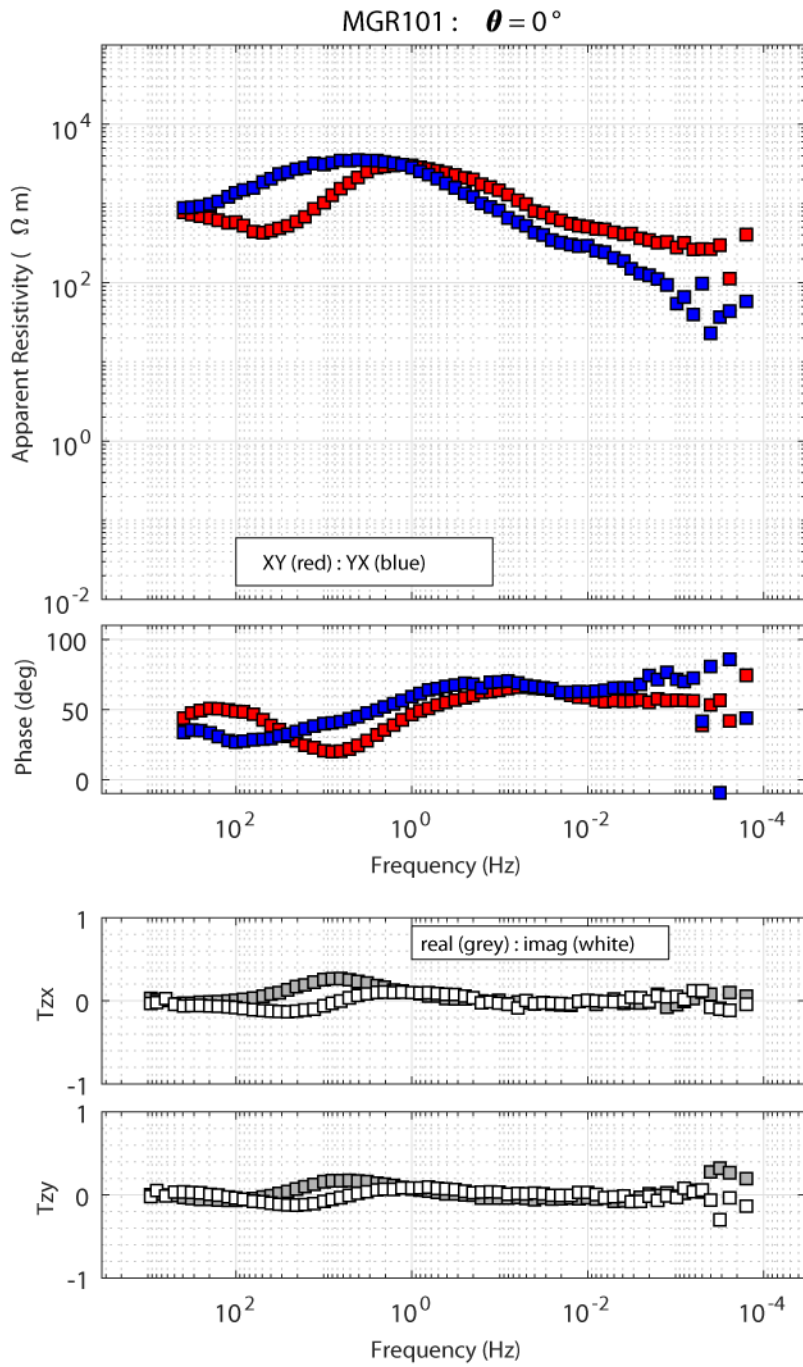


Figure A1: MT sounding MGR101.

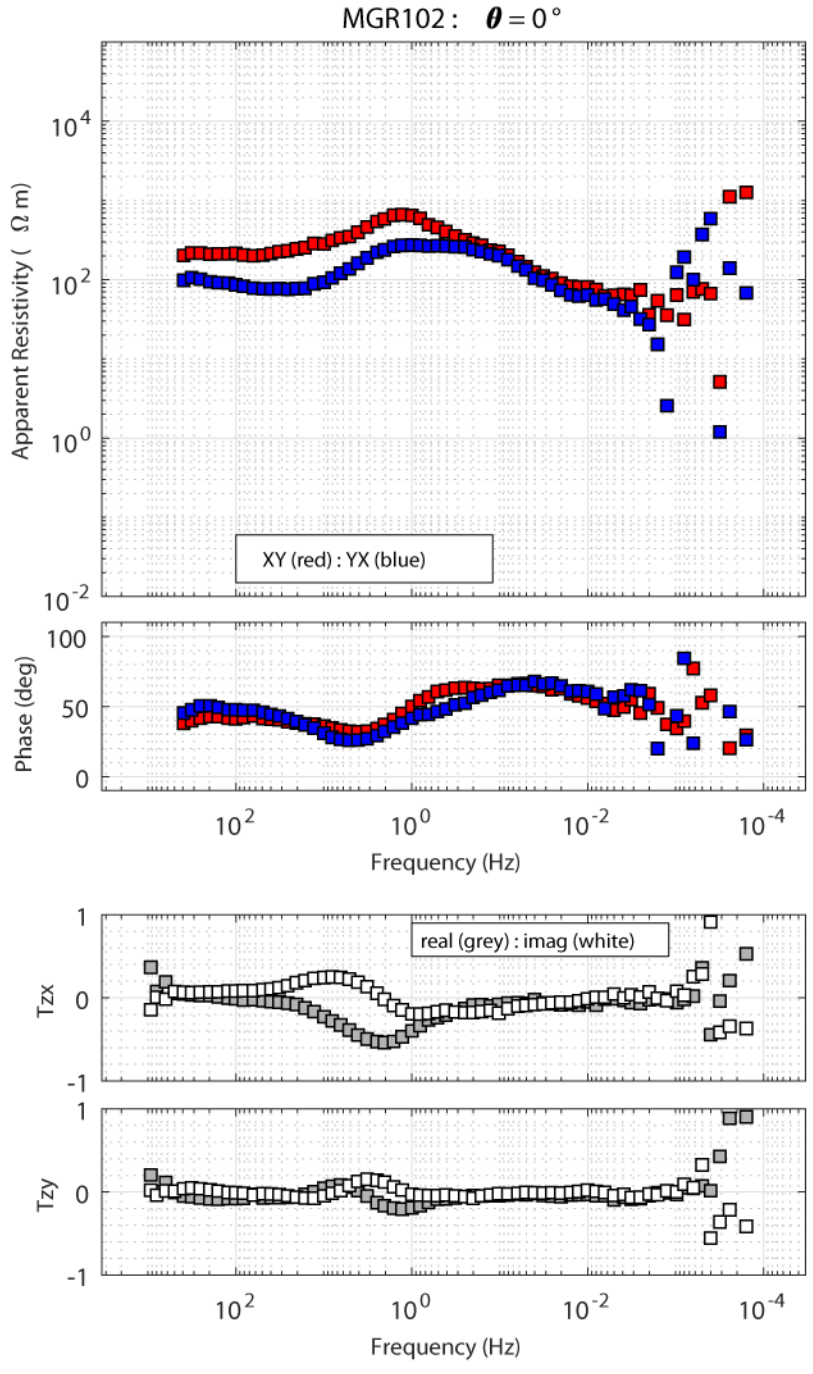


Figure A2: MT sounding MGR102.

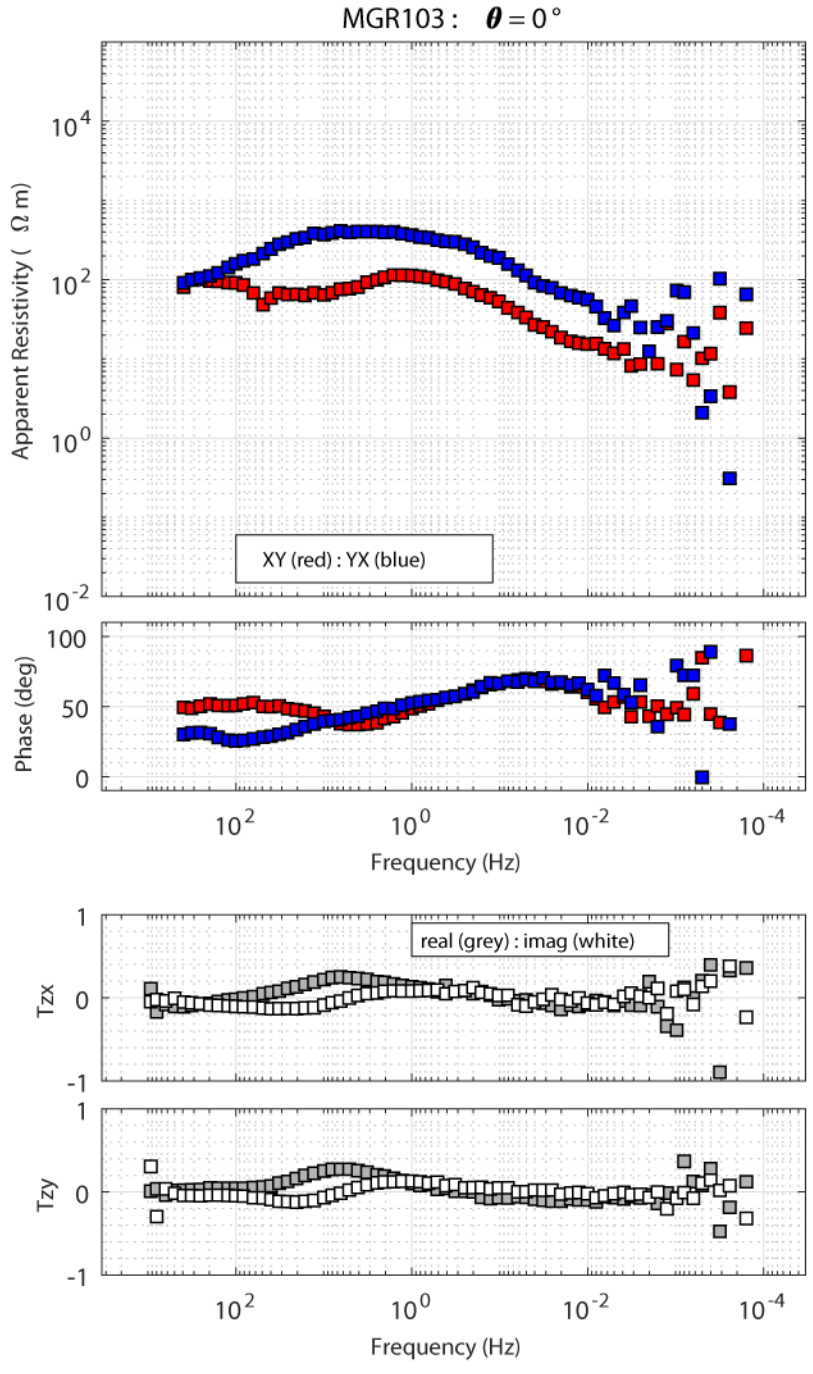


Figure A3: MT sounding MGR103.

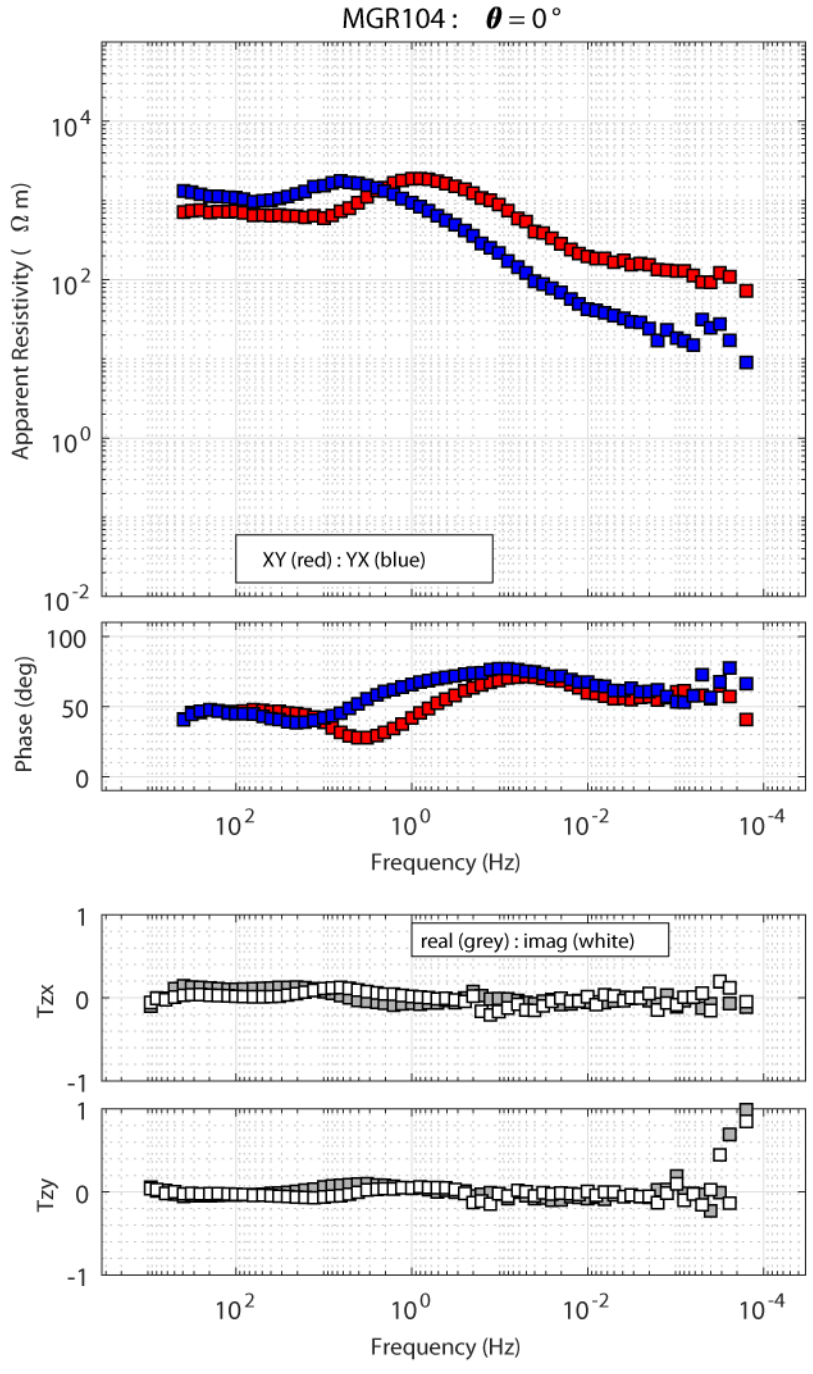


Figure A4: MT sounding MGR104.

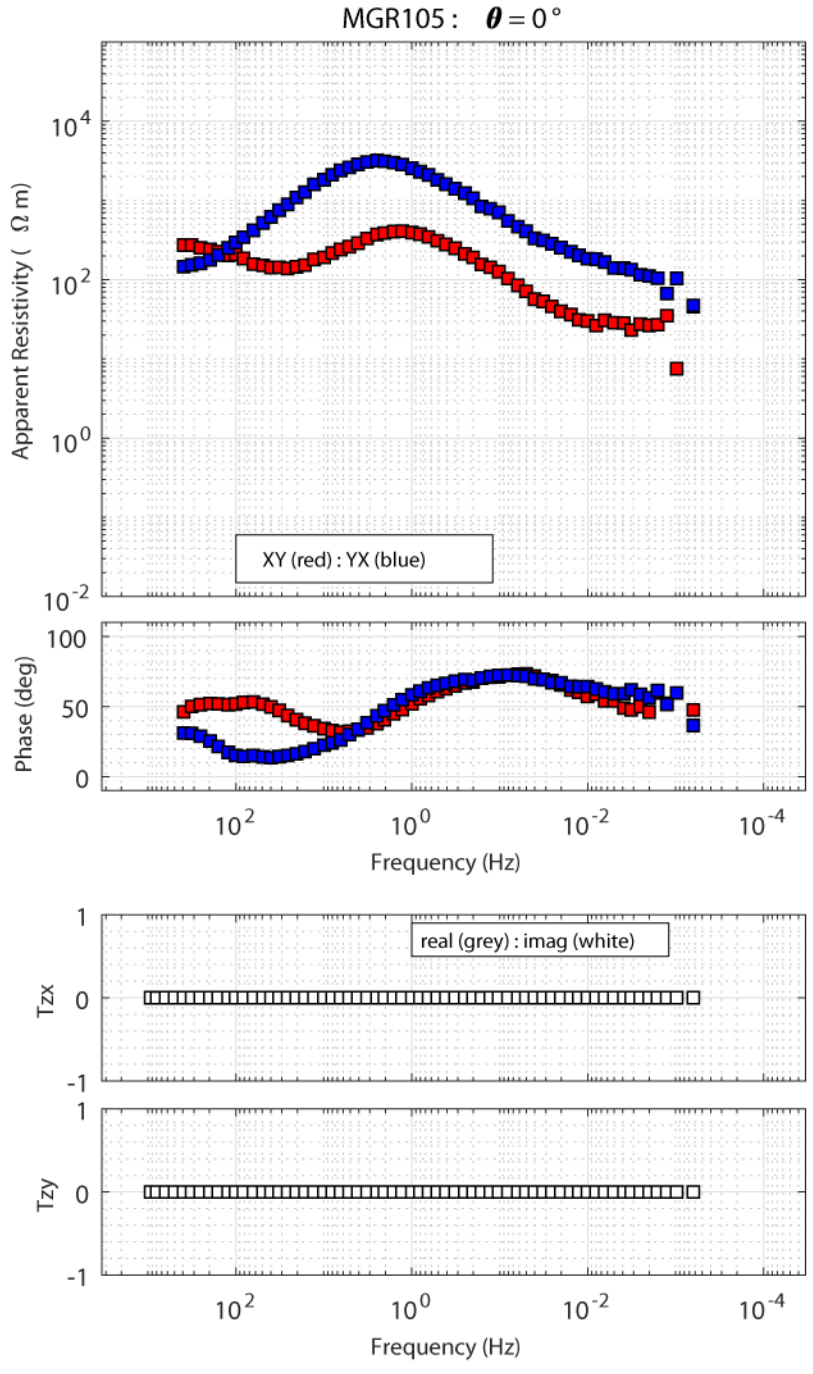


Figure A5: MT sounding MGR105. The vertical component of the magnetic field was not measured.

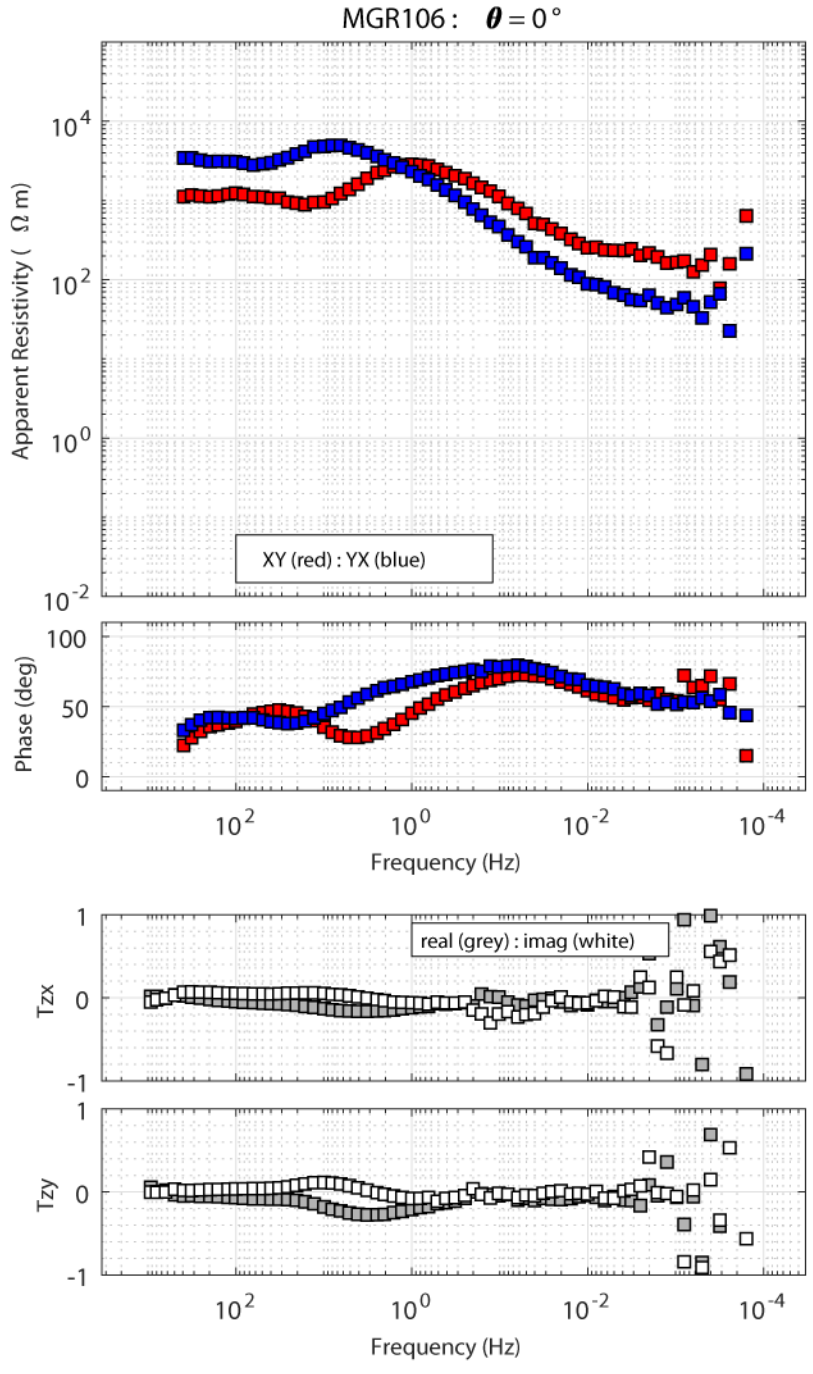


Figure A6: MT sounding MGR106.

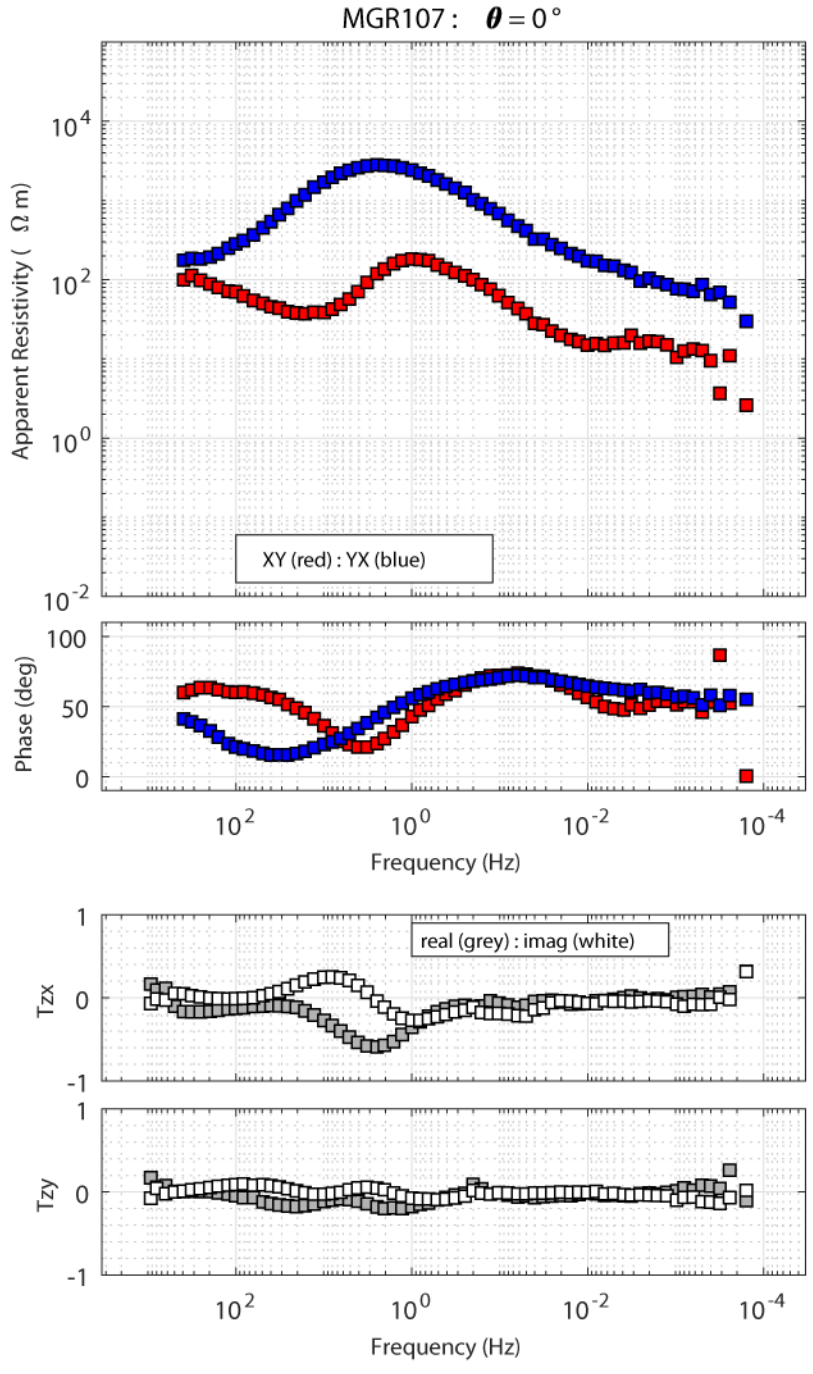


Figure A7: MT sounding MGR107.

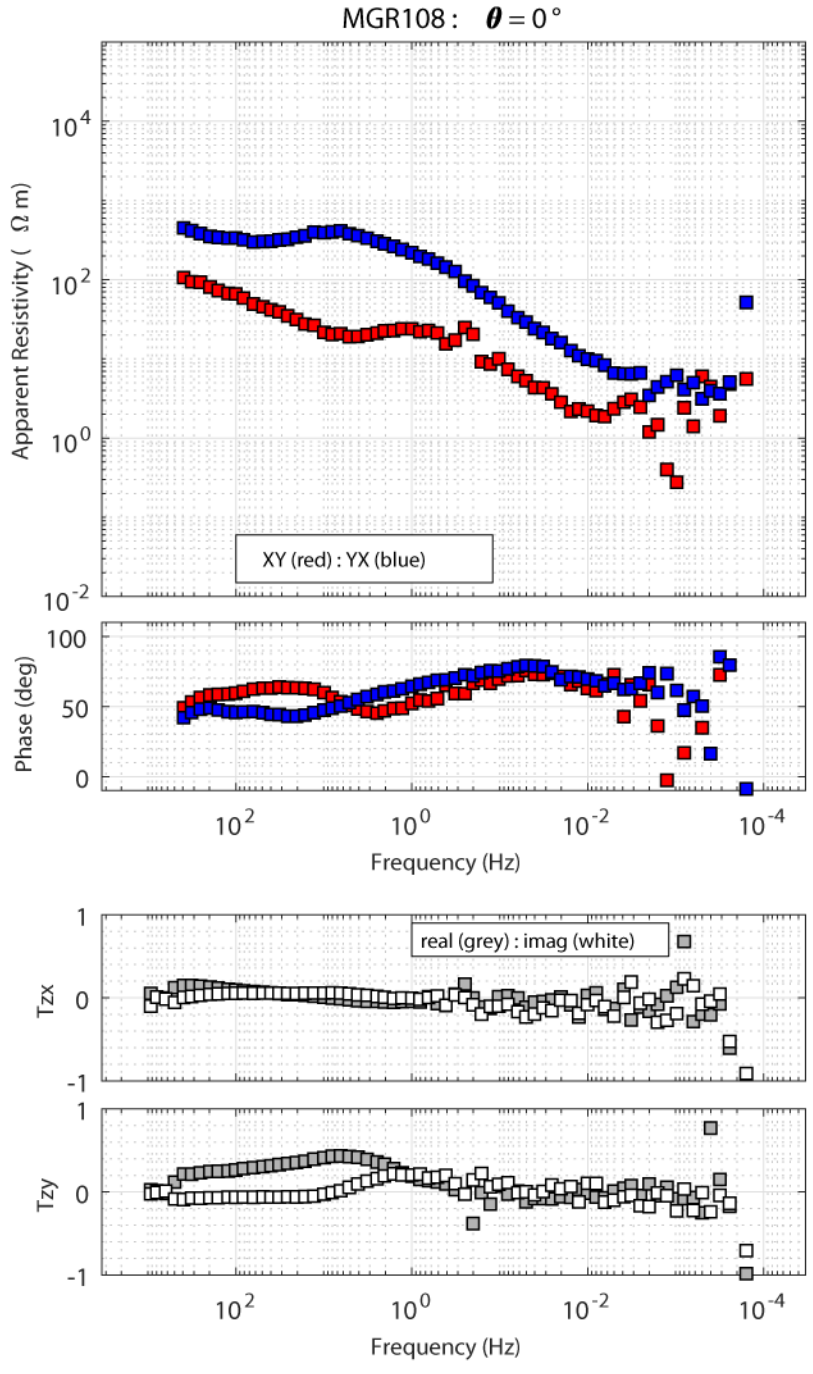


Figure A8: MT sounding MGR108.

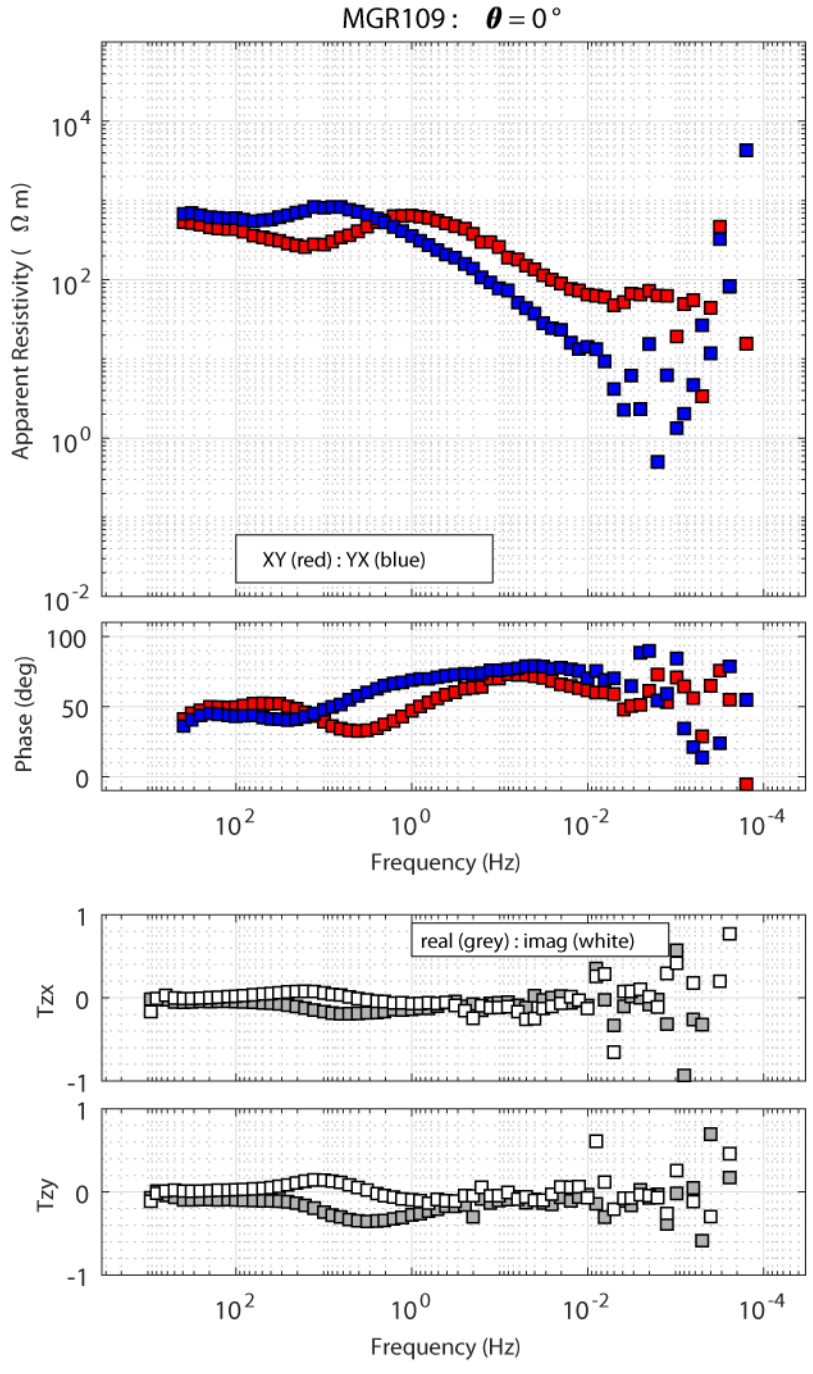


Figure A9: MT sounding MGR109.

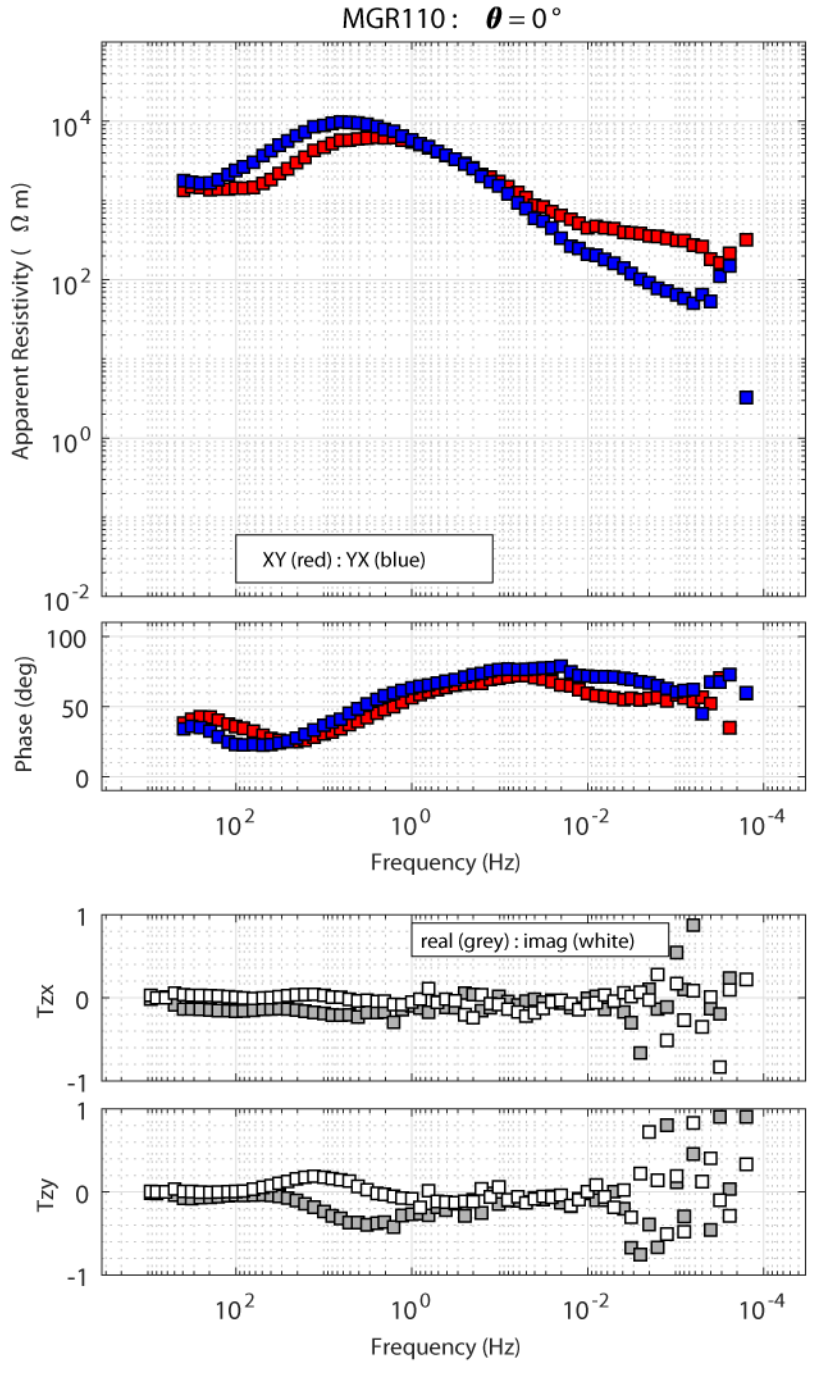


Figure A10: MT sounding MGR110.

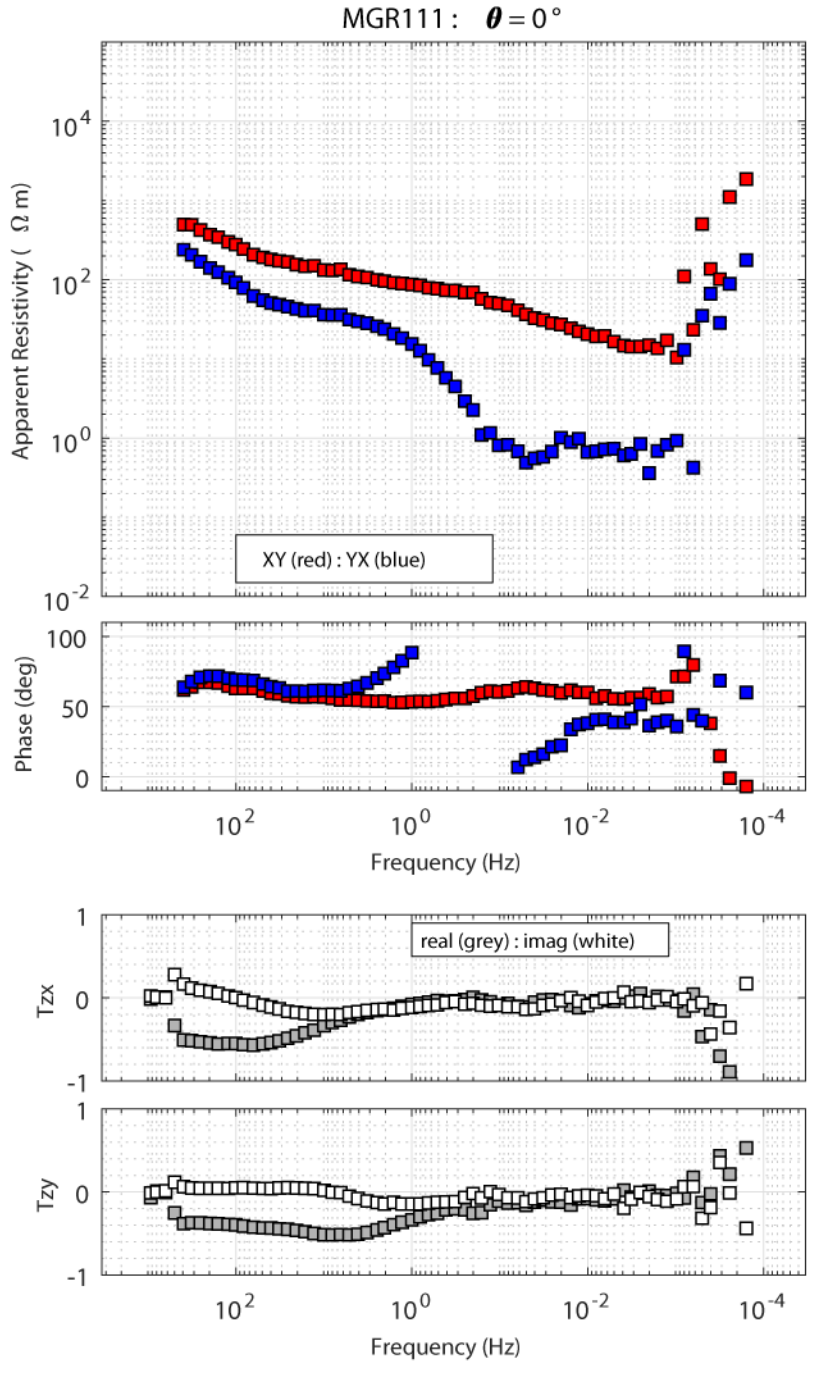


Figure A11: MT sounding MGR111.

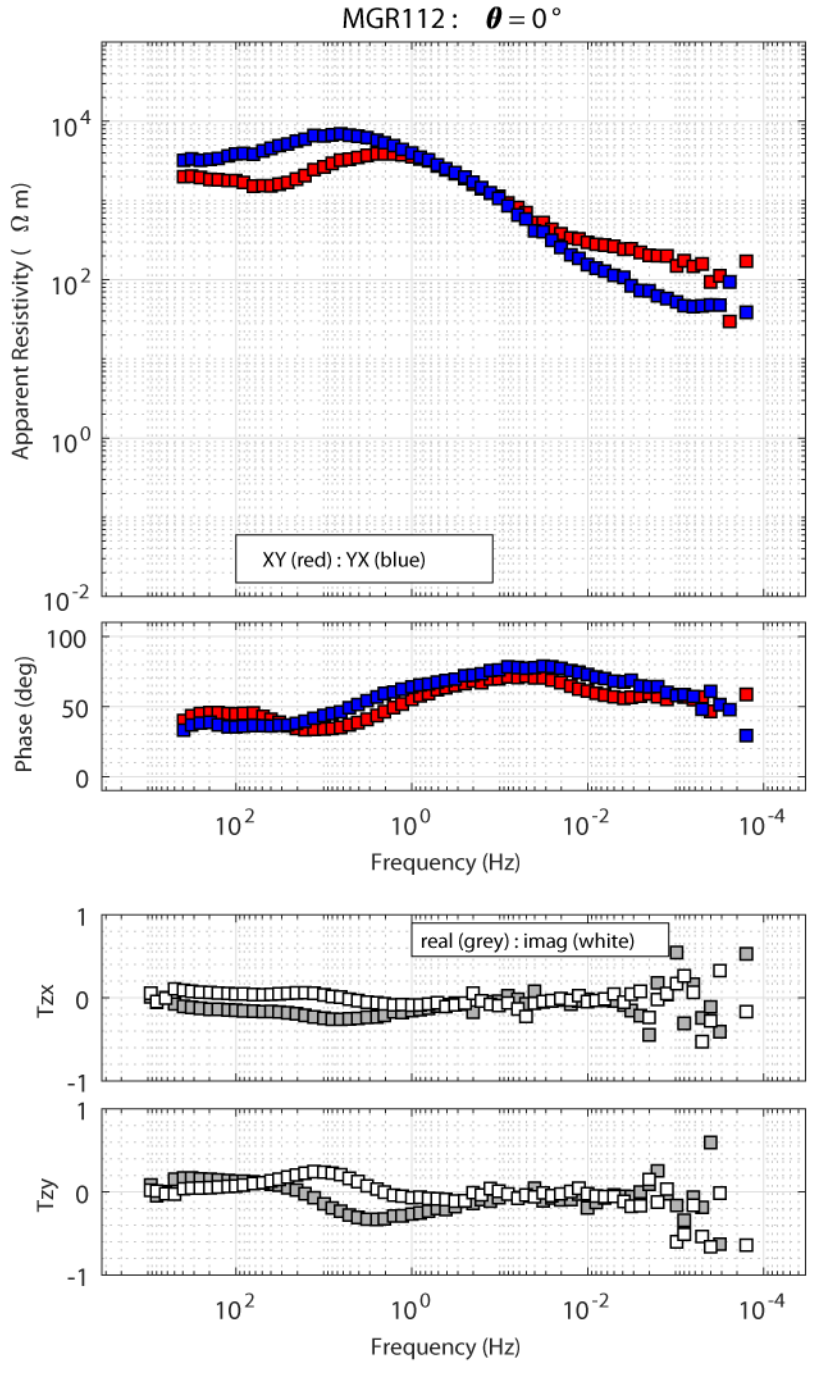


Figure A12: MT sounding MGR112.

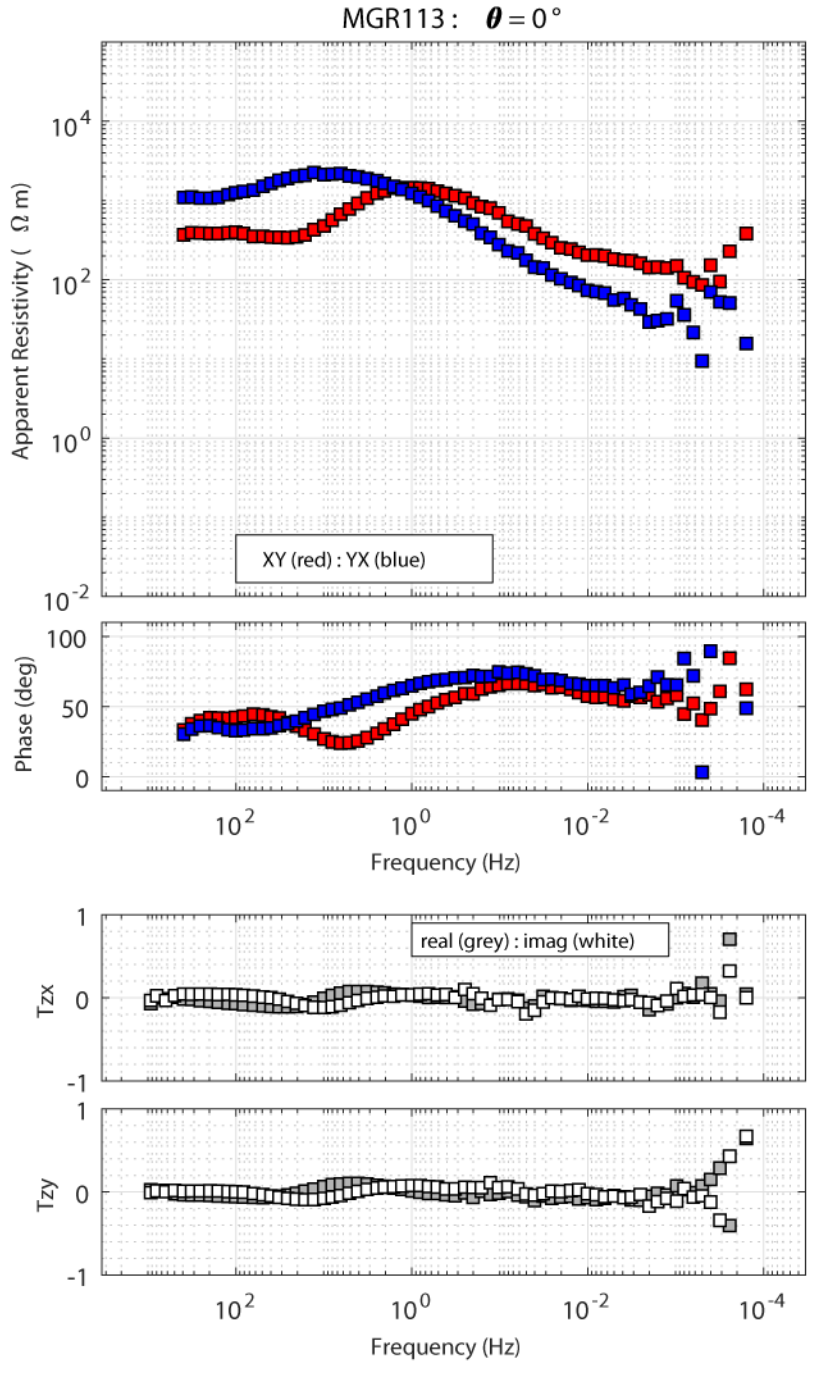


Figure A13: MT sounding MGR113.

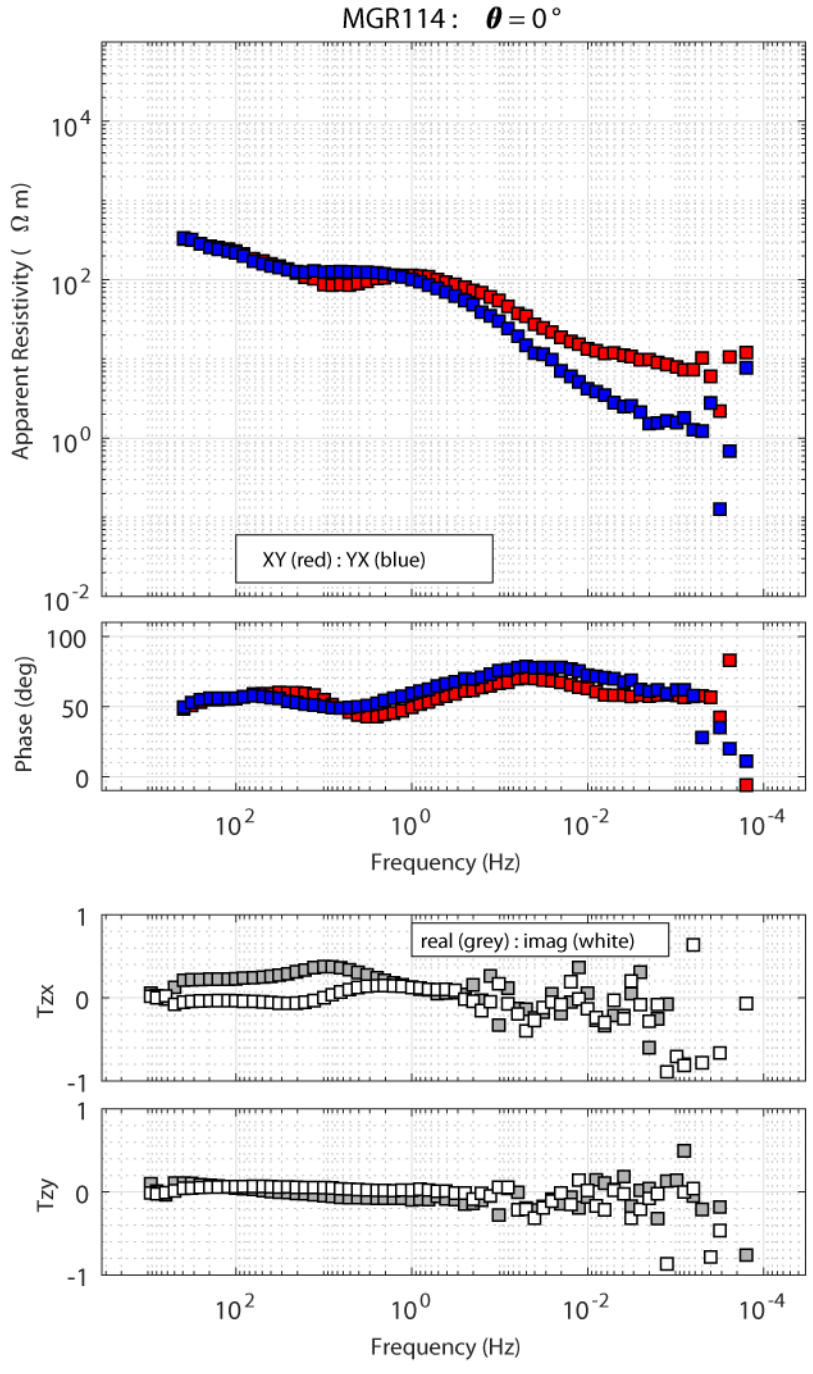


Figure A14: MT sounding MGR114.

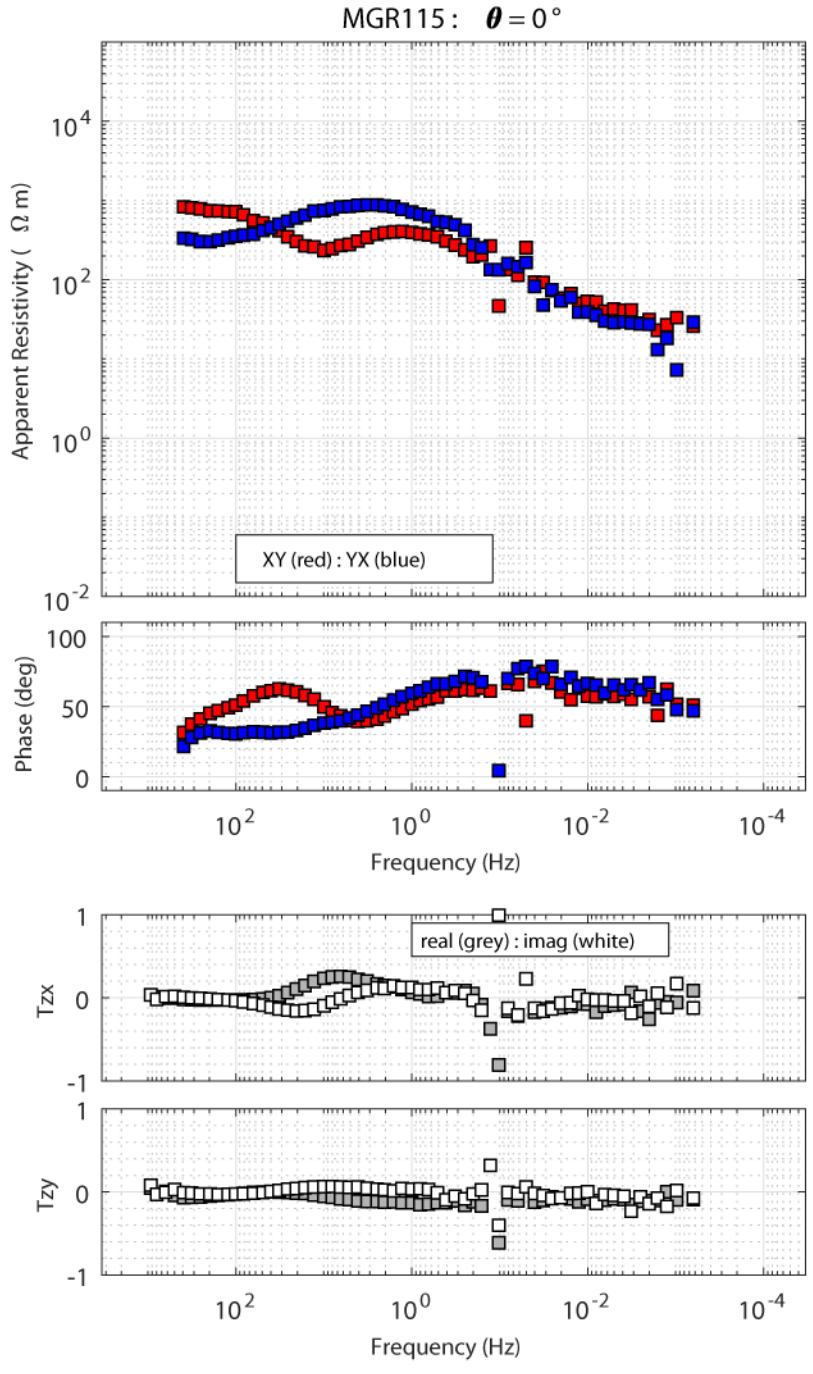


Figure A15: MT sounding MGR115.

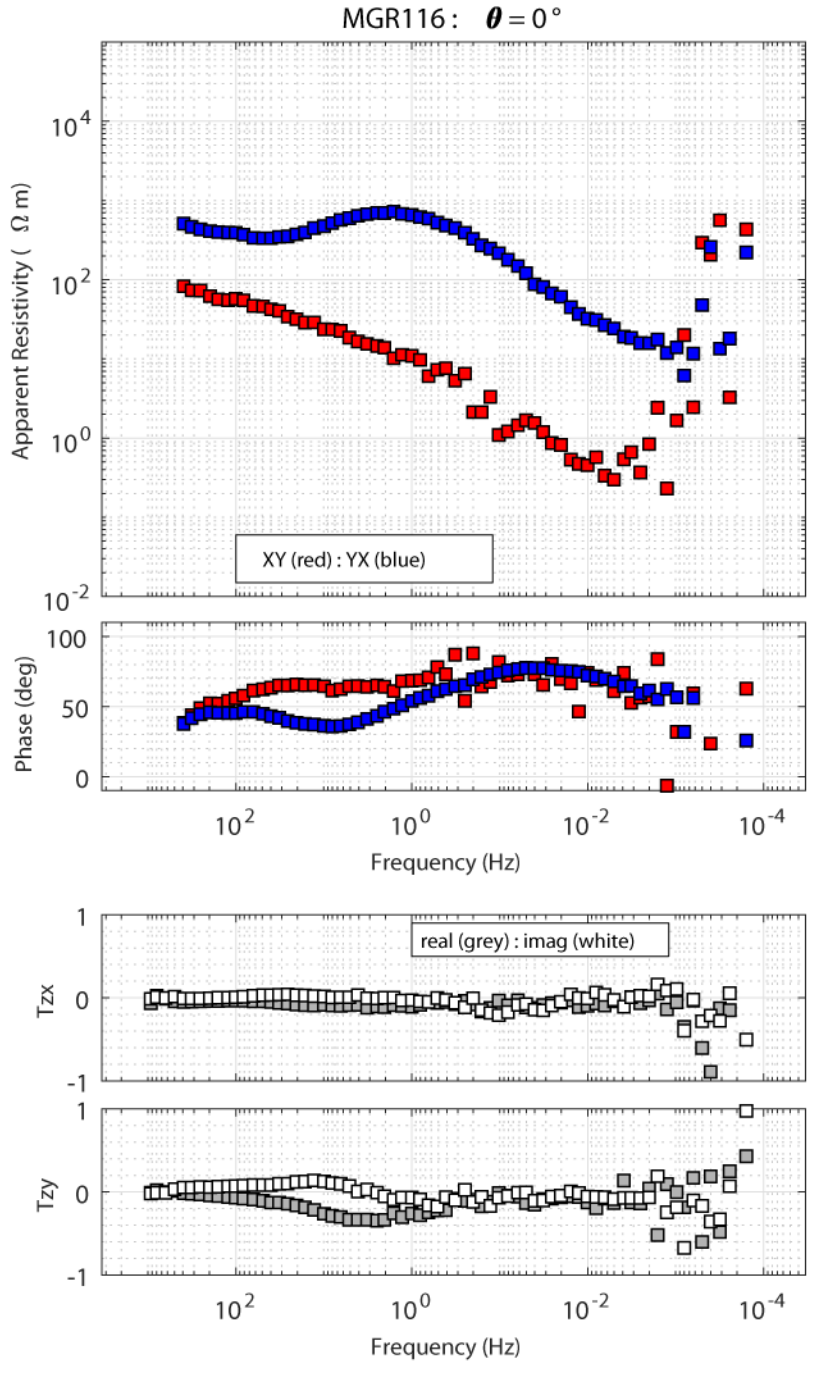


Figure A16: MT sounding MGR116.

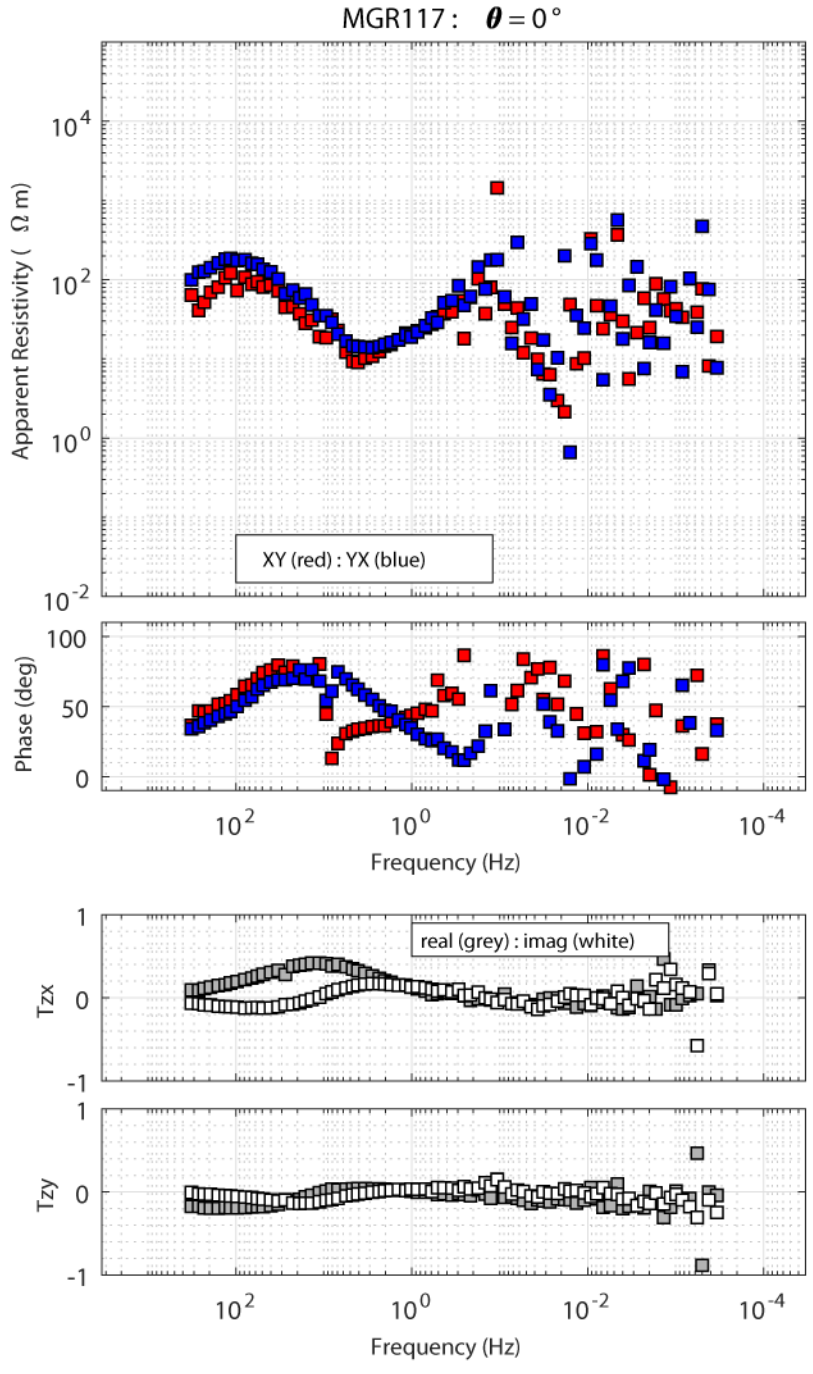


Figure A17: MT sounding MGR117.

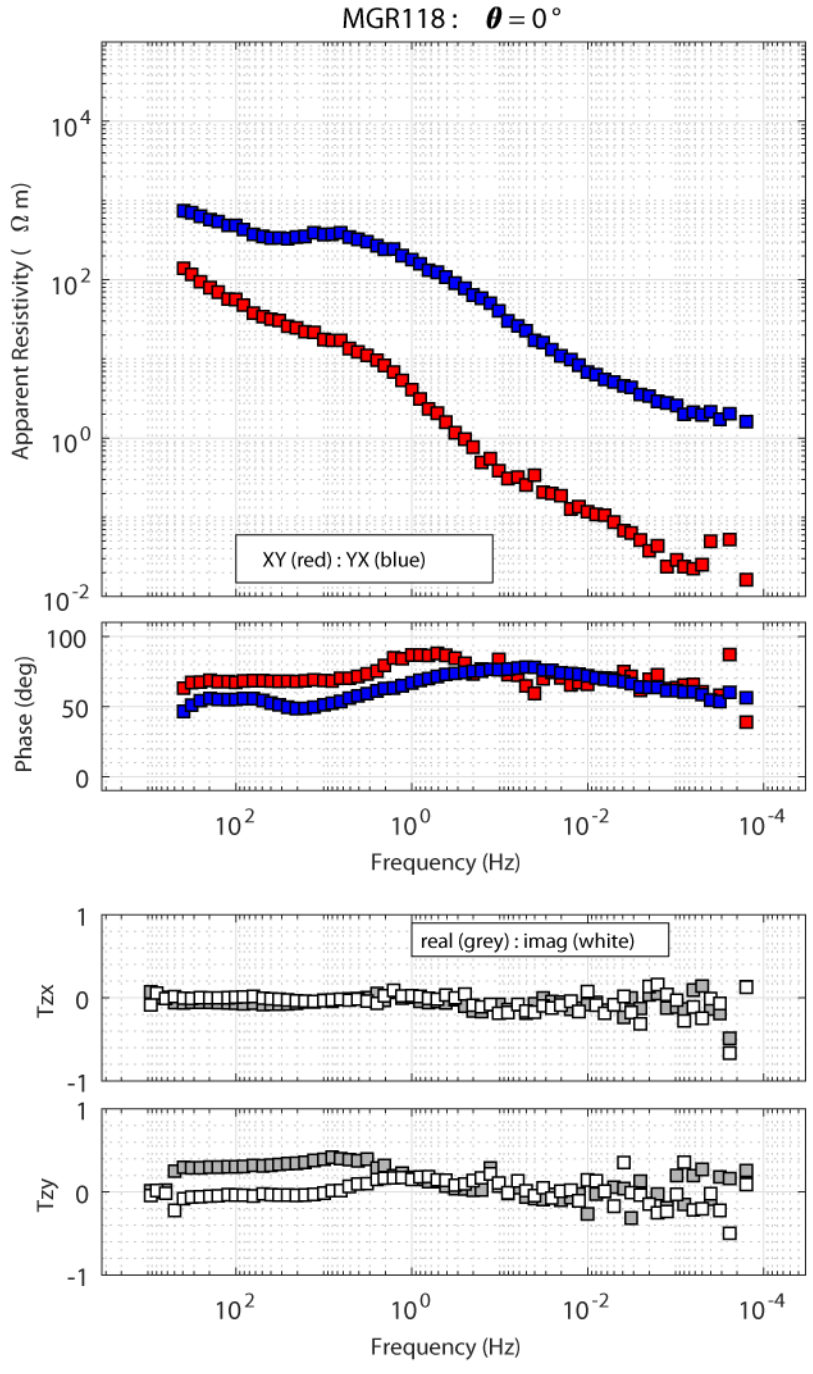


Figure A18: MT sounding MGR118.

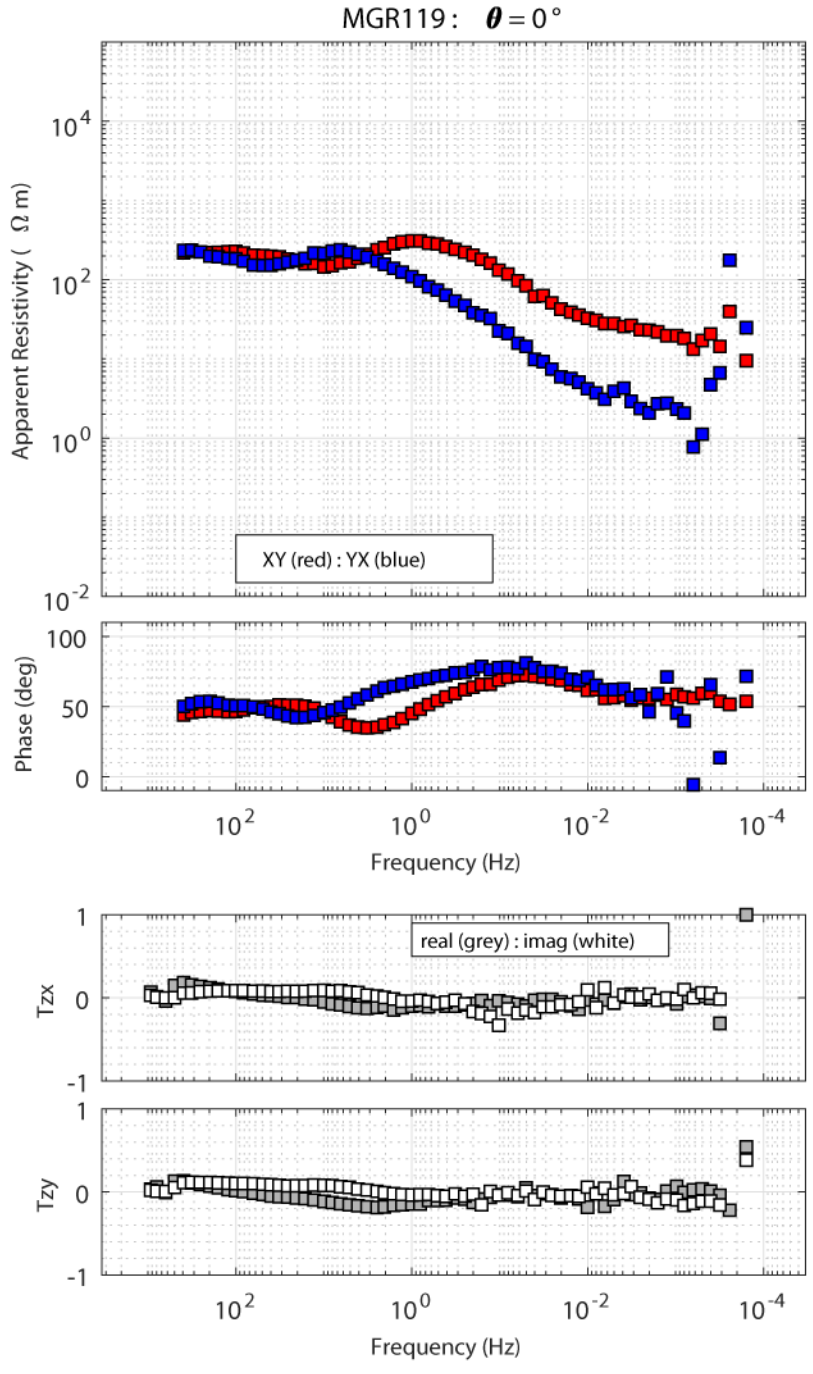


Figure A19: MT sounding MGR119.

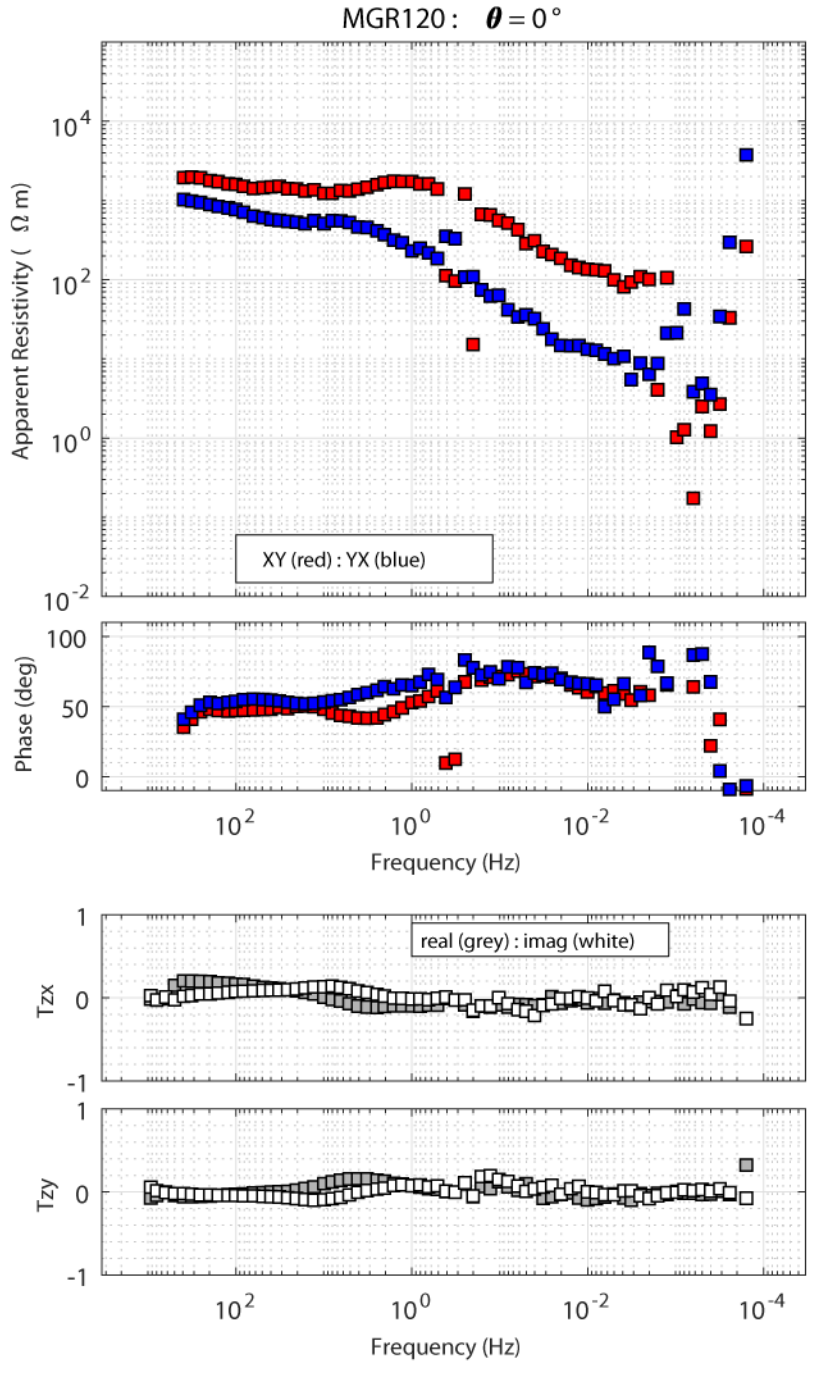


Figure A20: MT sounding MGR120.

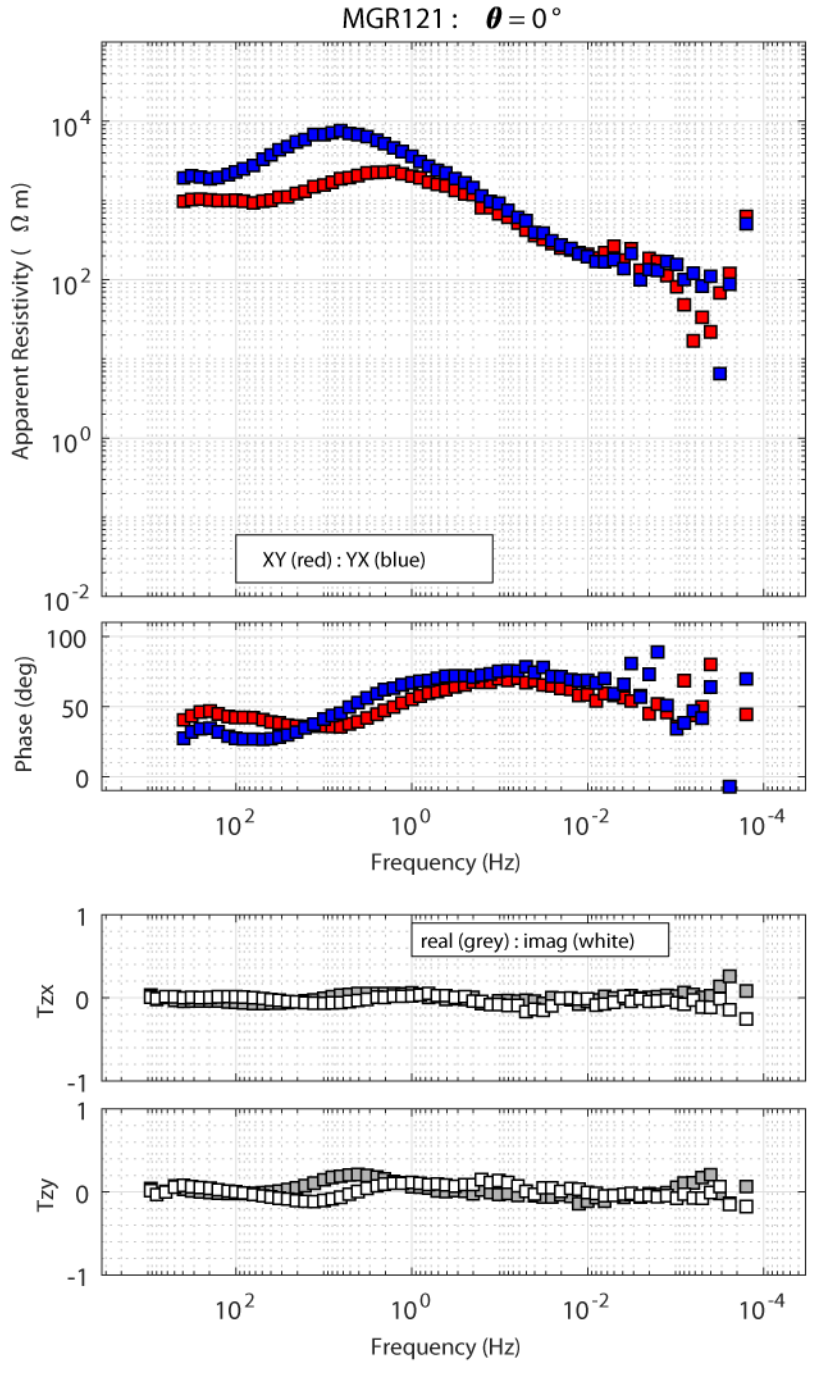


Figure A21: MT sounding MGR121.

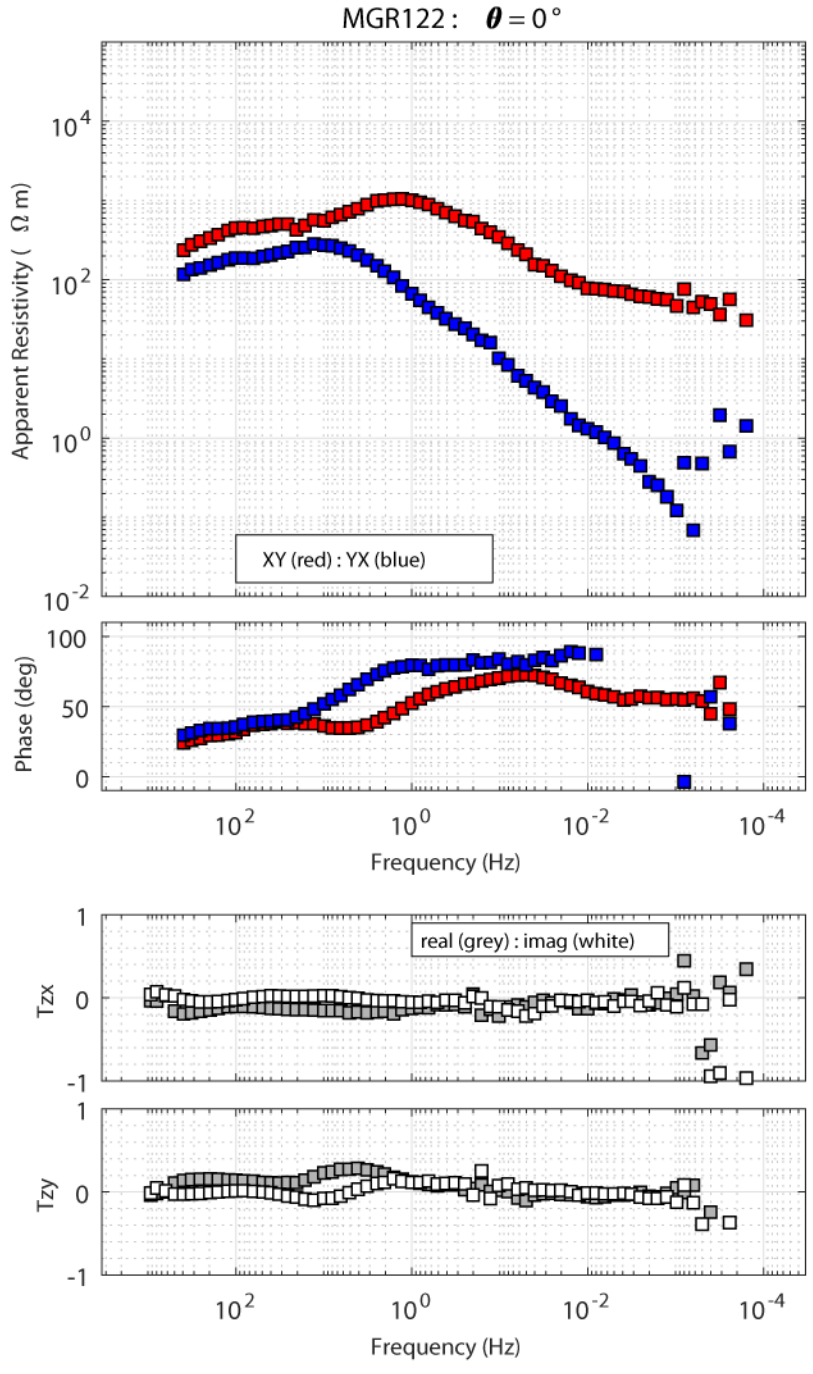


Figure A22: MT sounding MGR122.

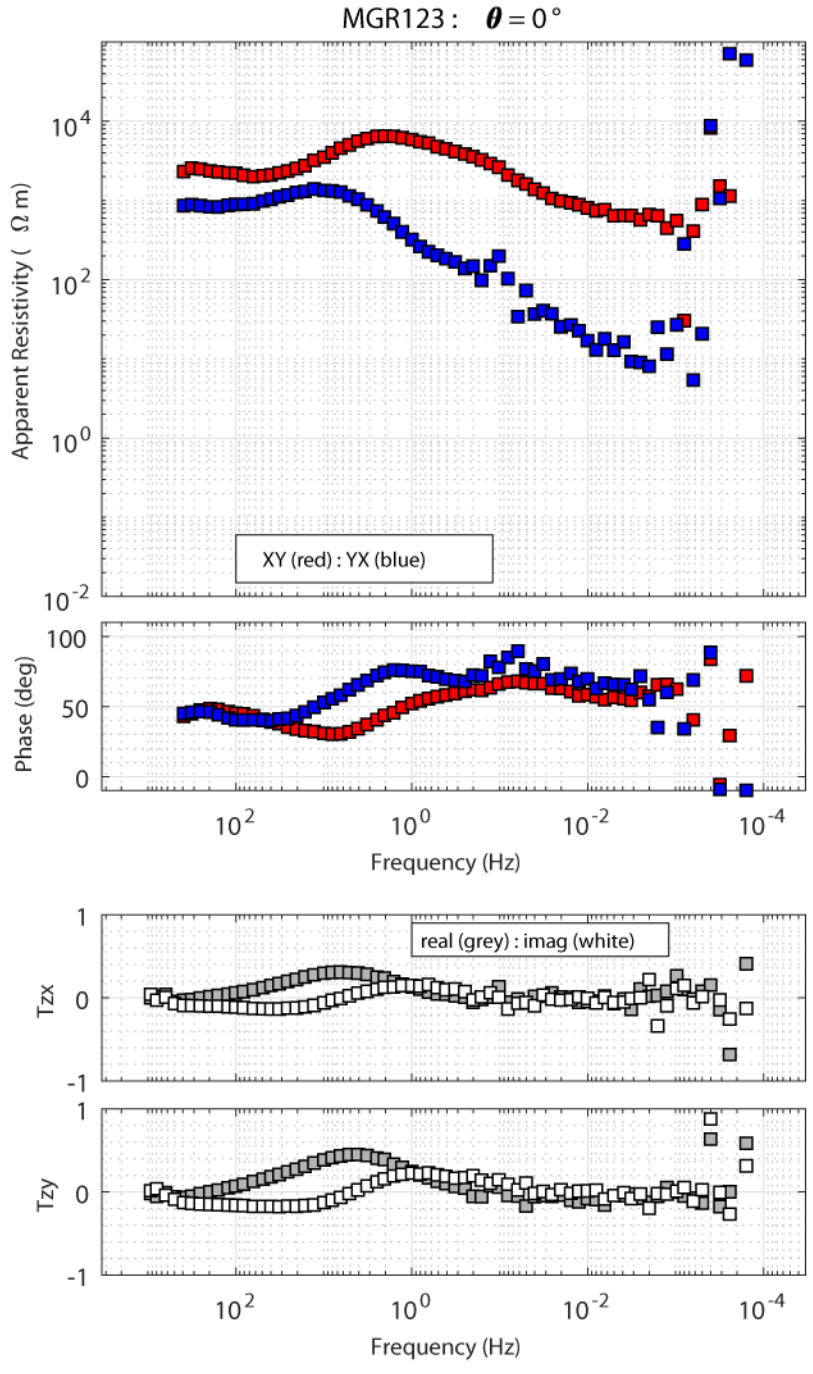


Figure A23: MT sounding MGR123.

Appendix B: MT sounding curves from Mount Meager in 2019

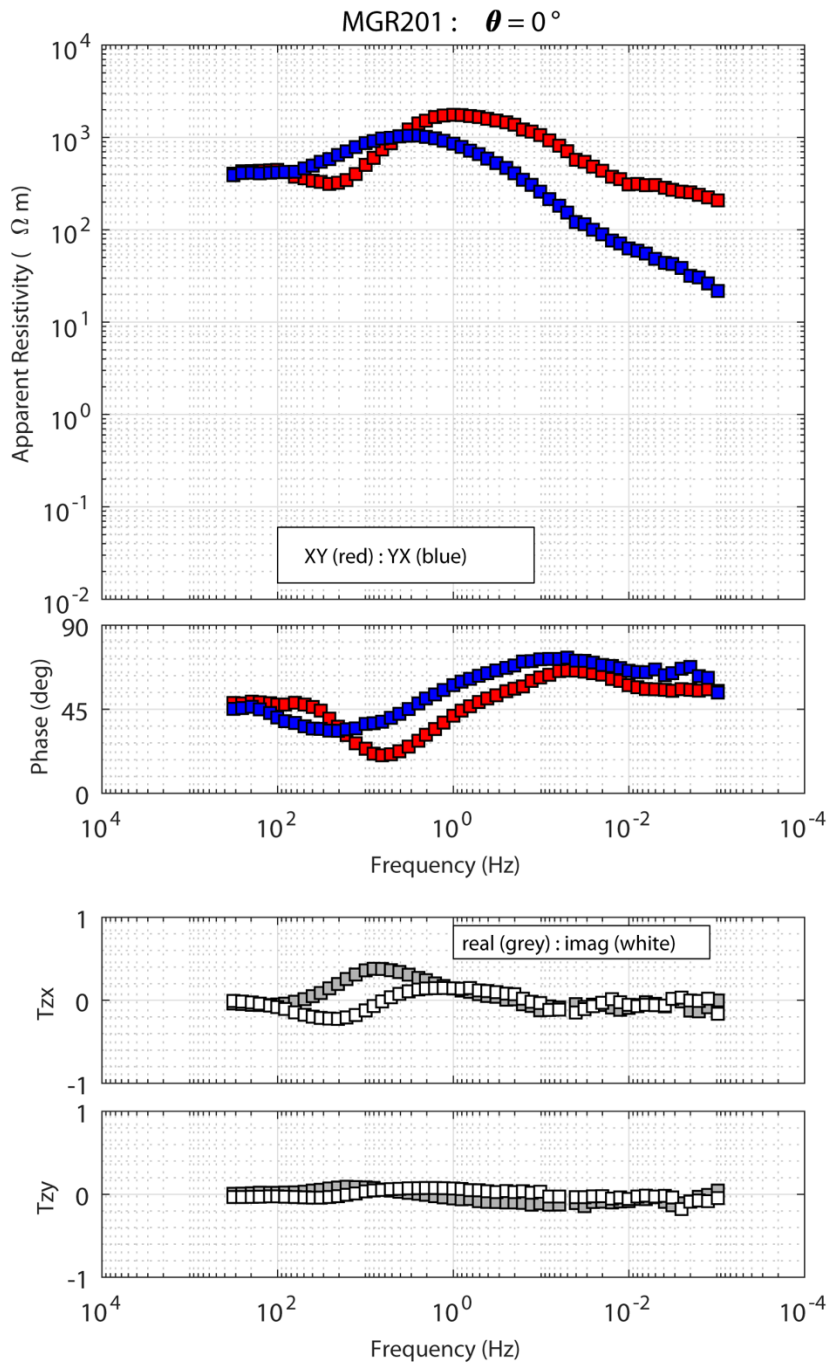


Figure B1: MT sounding MGR201.

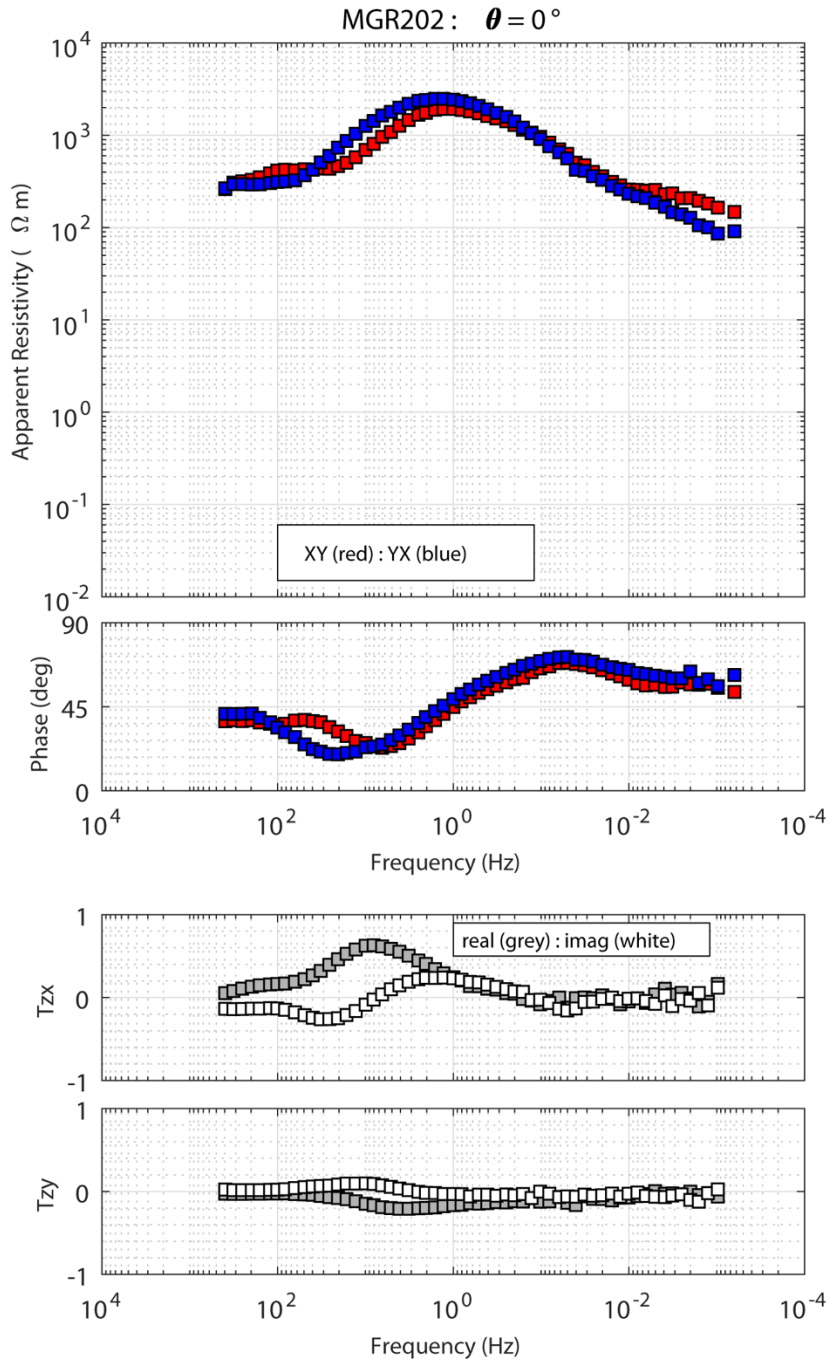


Figure B2: MT sounding MGR202.

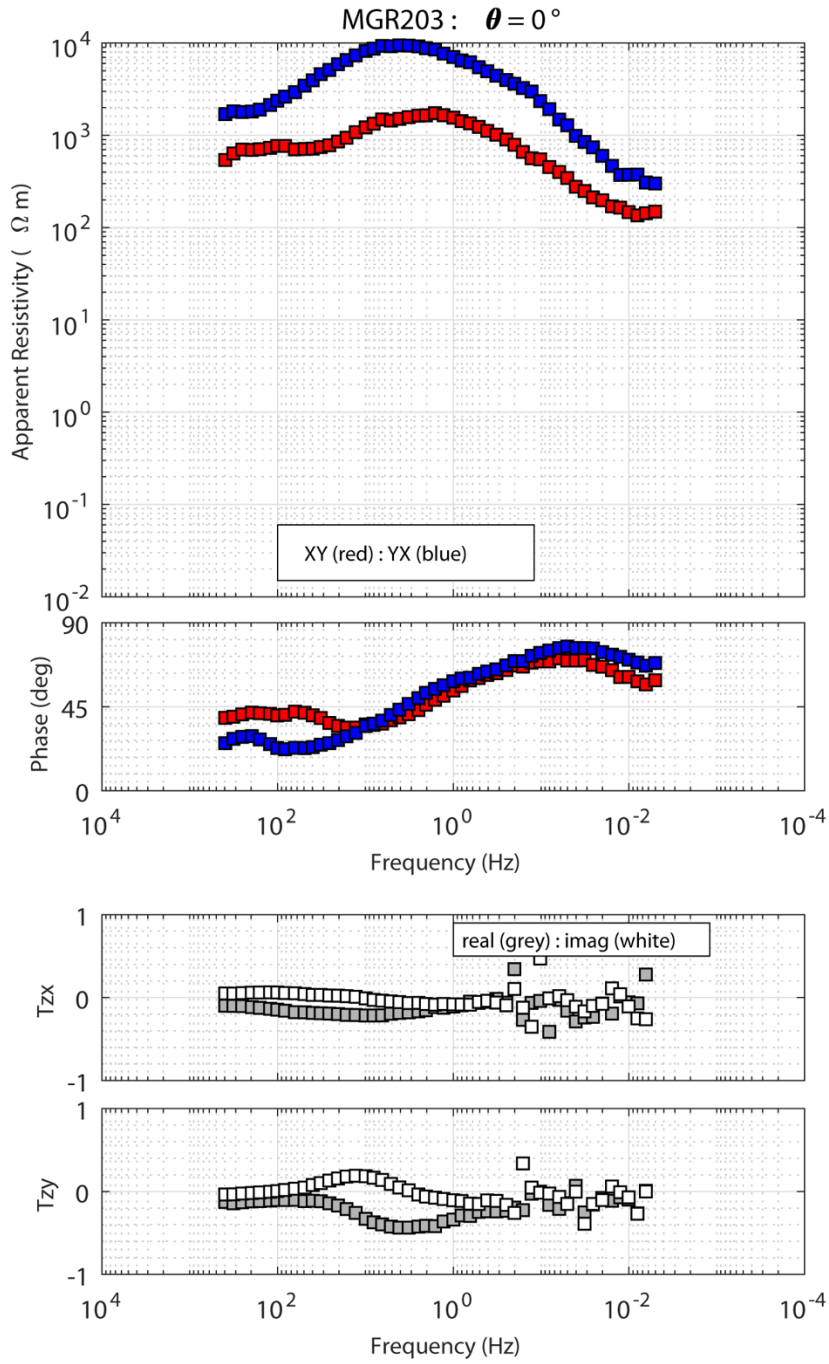


Figure B3: MT sounding MGR203.

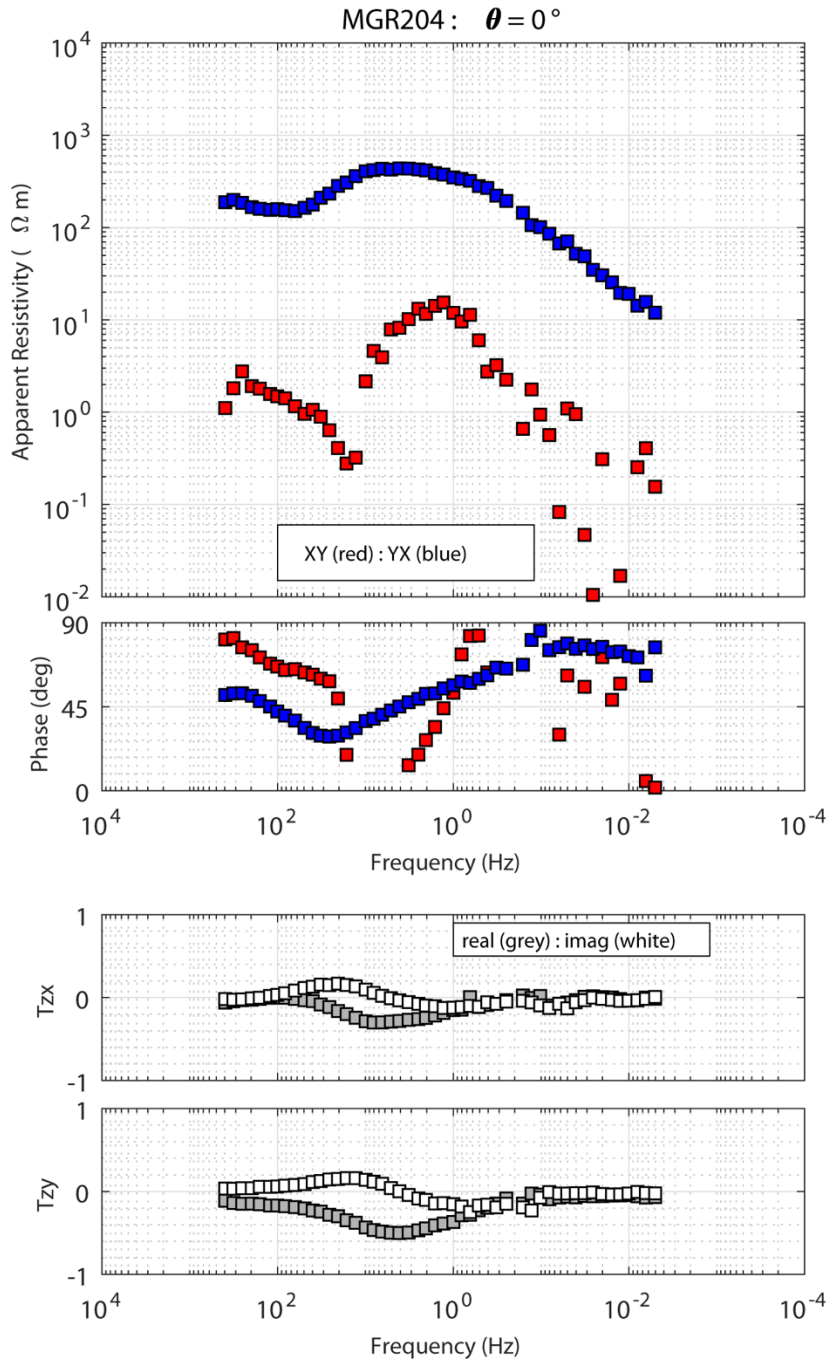


Figure B4: MT sounding MGR204.

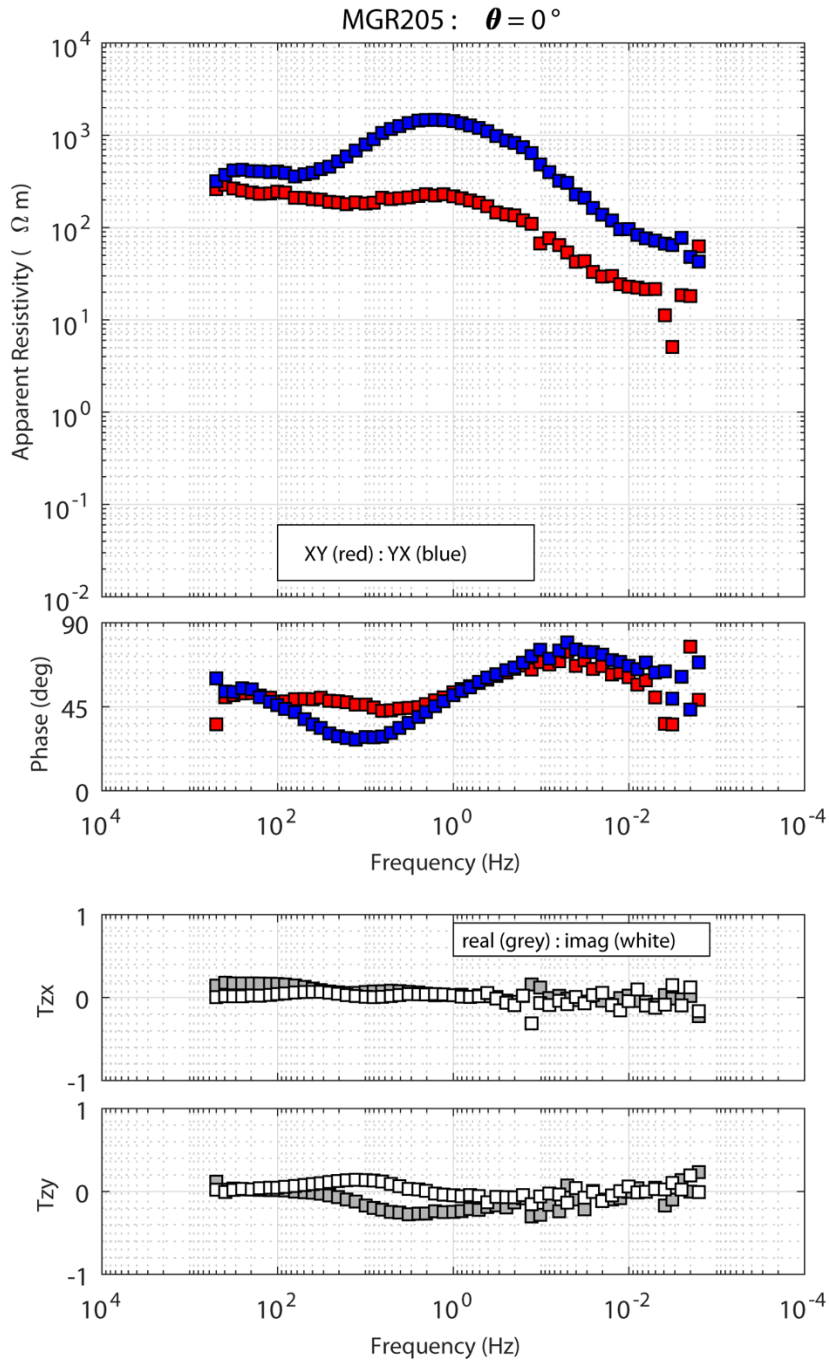


Figure B5: MT sounding MGR205.

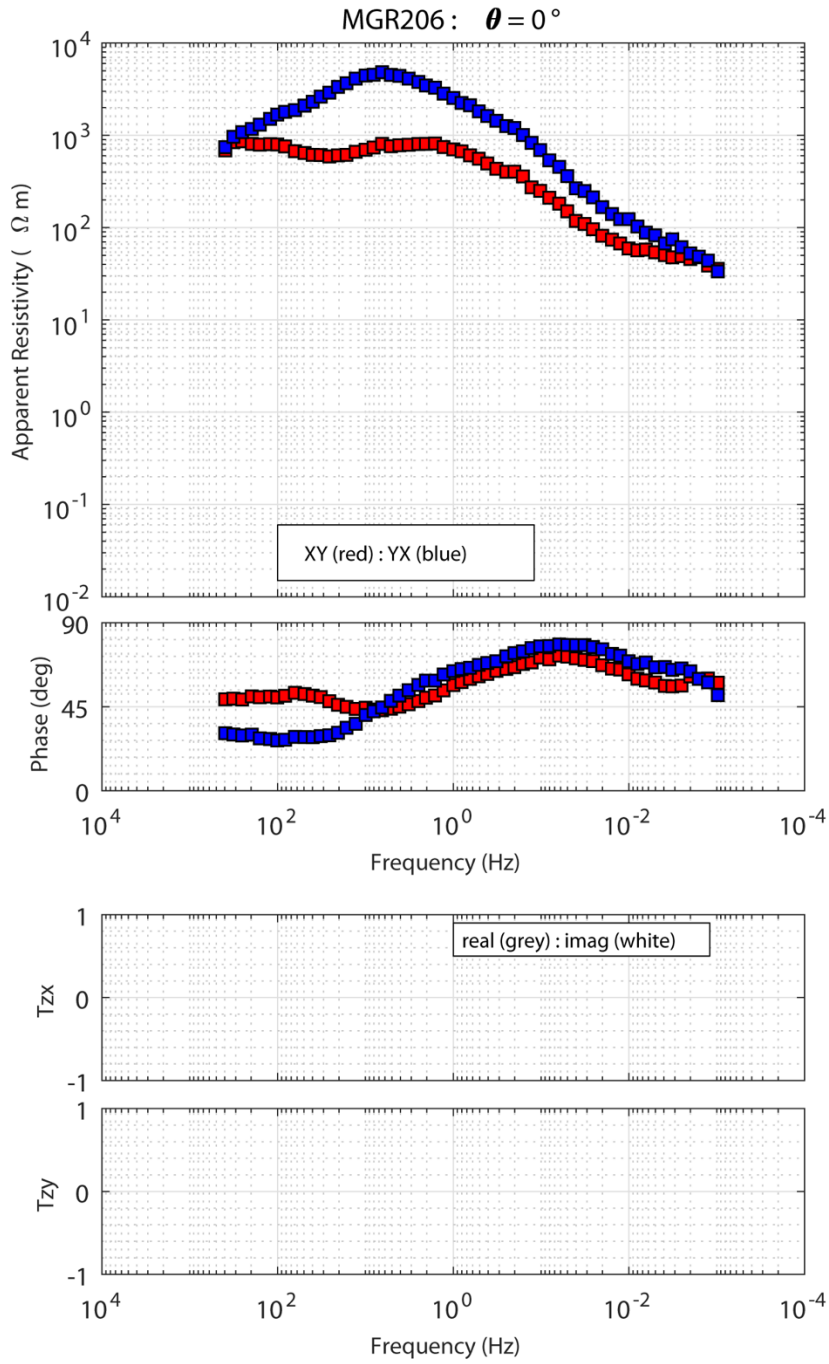


Figure B6: MT sounding MGR206. The vertical component of the magnetic field was not measured.

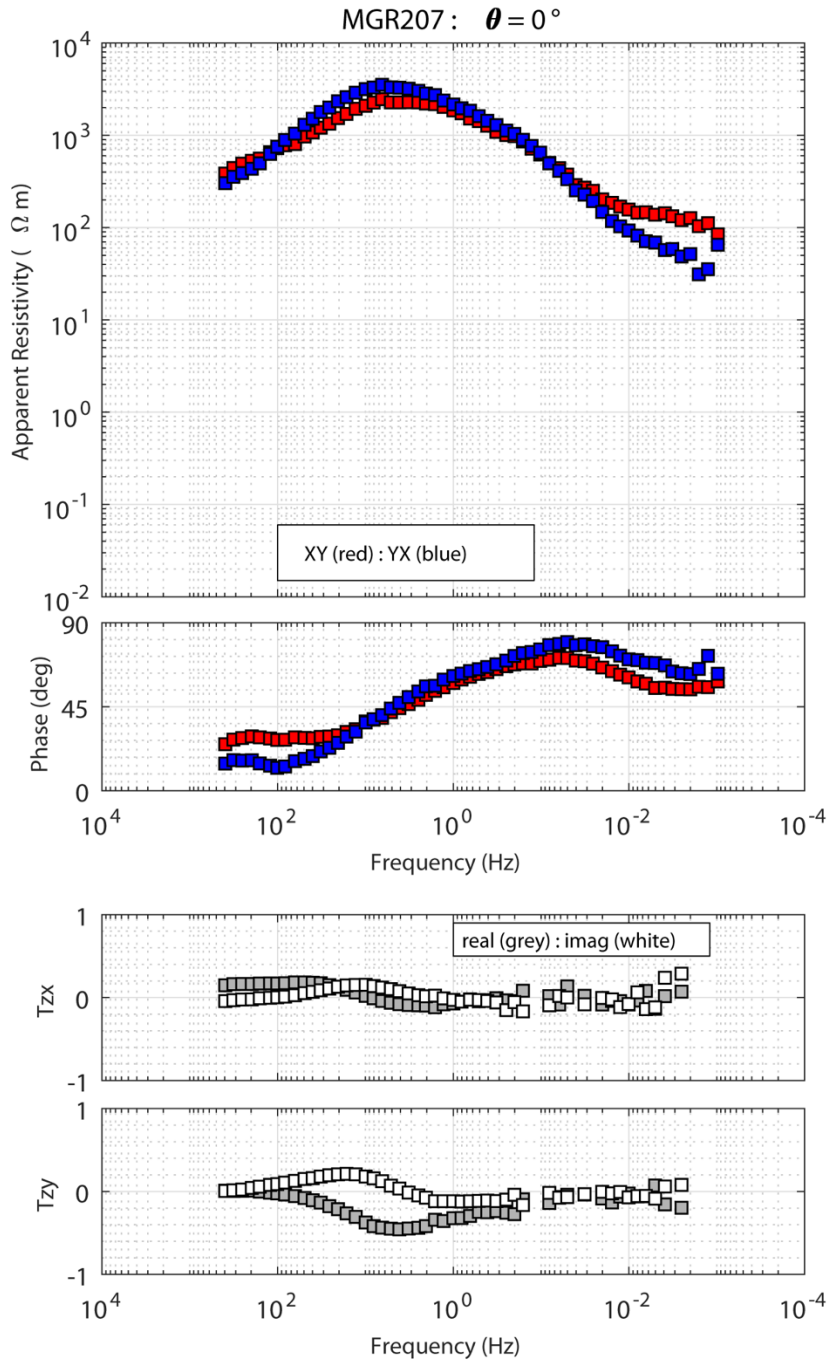


Figure B7: MT sounding MGR207.

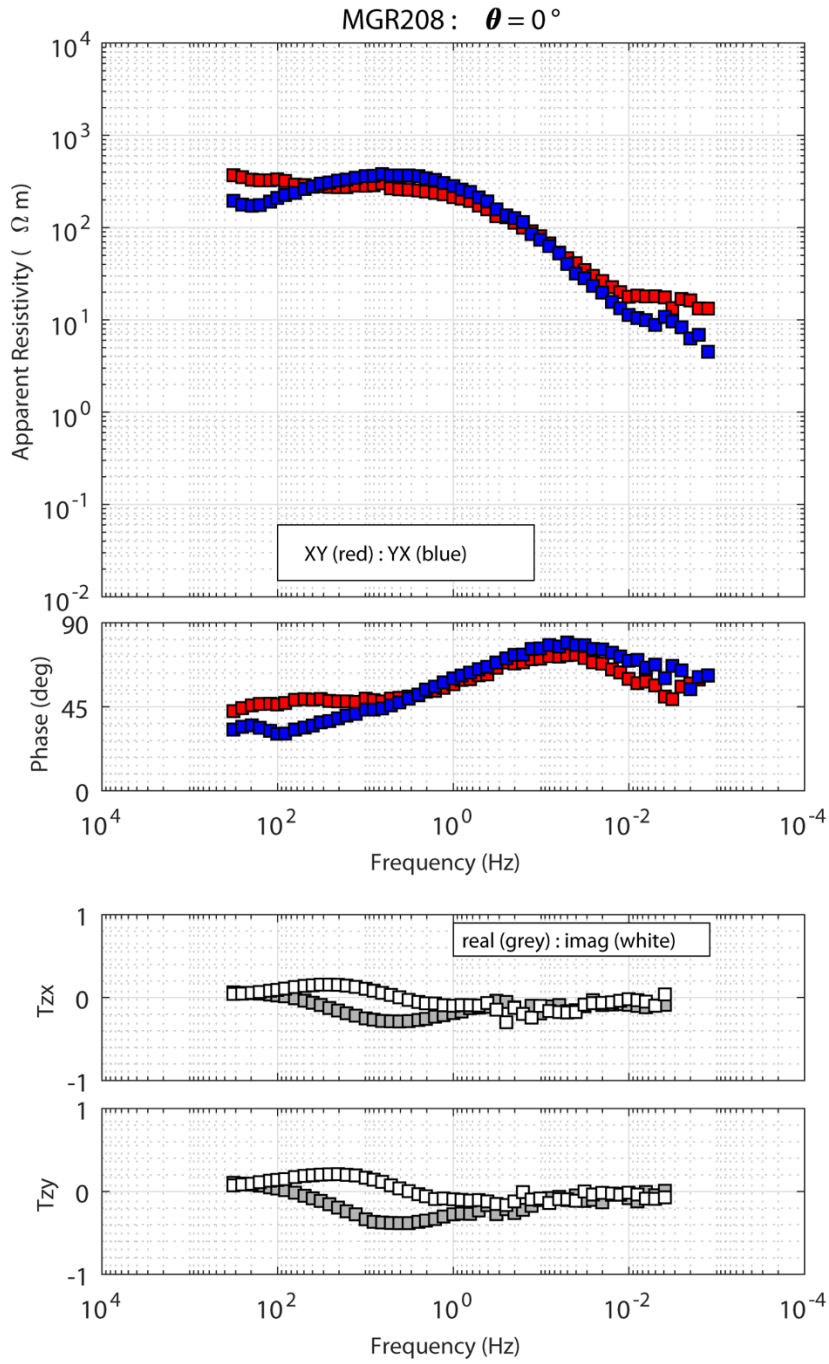


Figure B8: MT sounding MGR208.

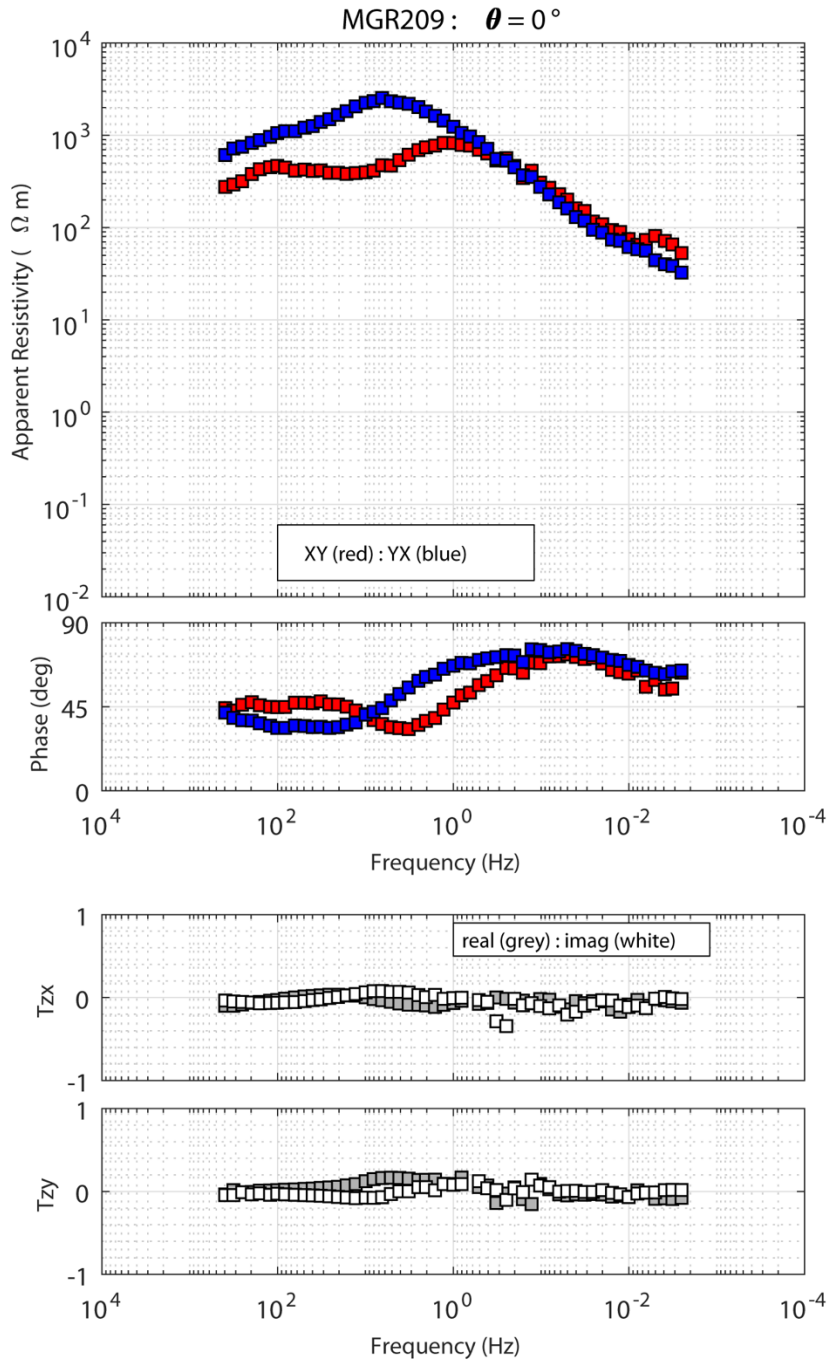


Figure B9: MT sounding MGR209.

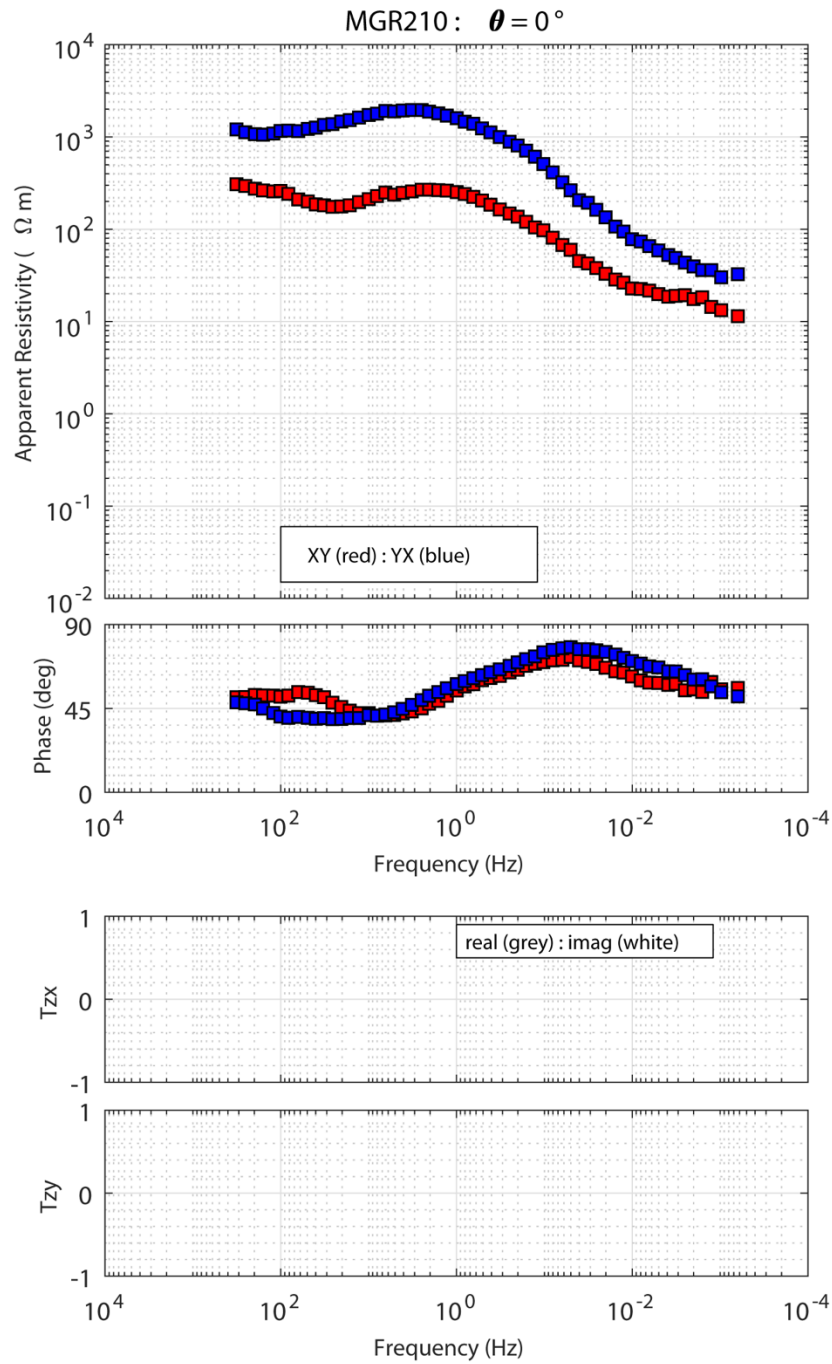


Figure B10: MT sounding MGR210. The vertical component of the magnetic field was not measured.

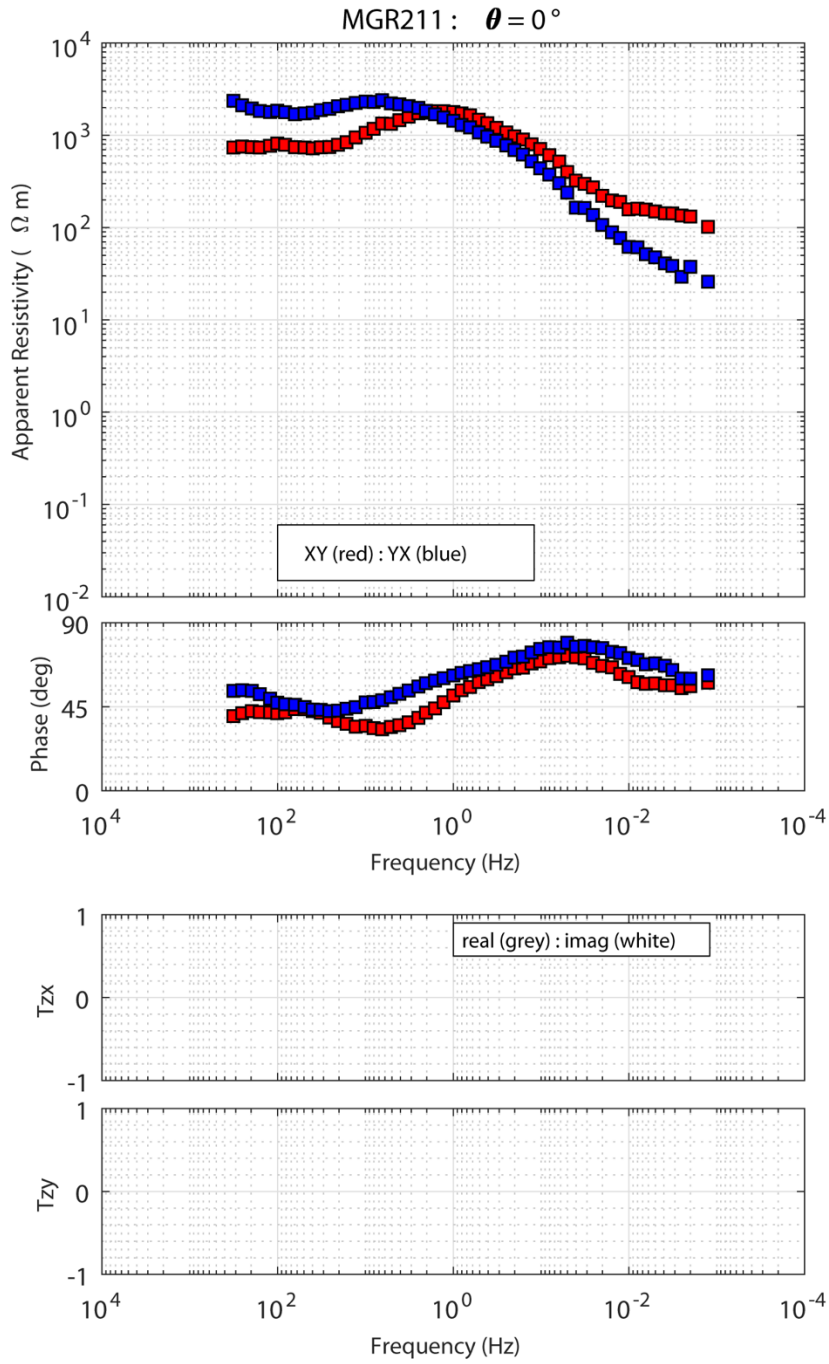


Figure B11: MT sounding MGR211. The magnetic field was not measured at this location, so the horizontal components of the magnetic field measured simultaneously at site MGR210, ~6 km away, were used.

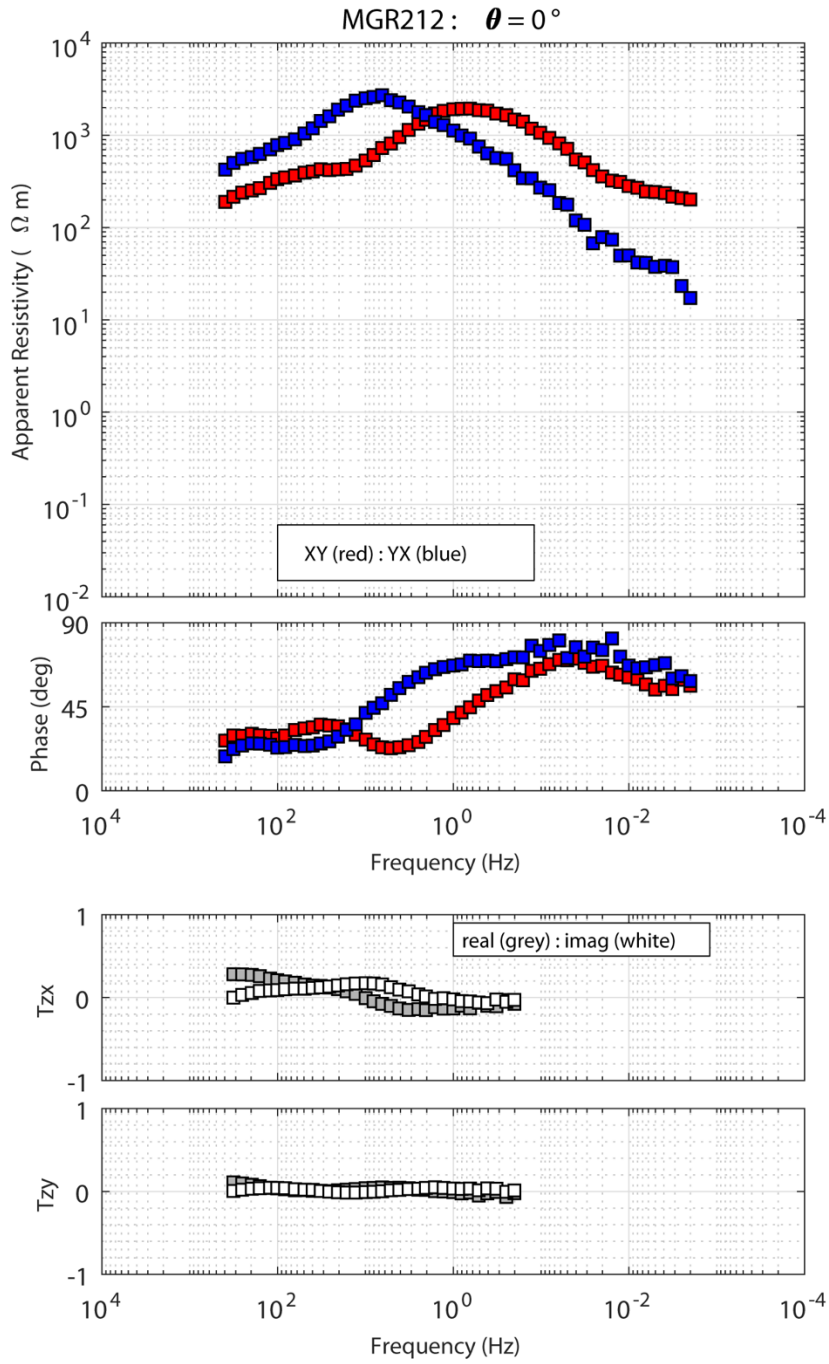


Figure B12: MT sounding MGR212.

Appendix C: MT instrument calibration

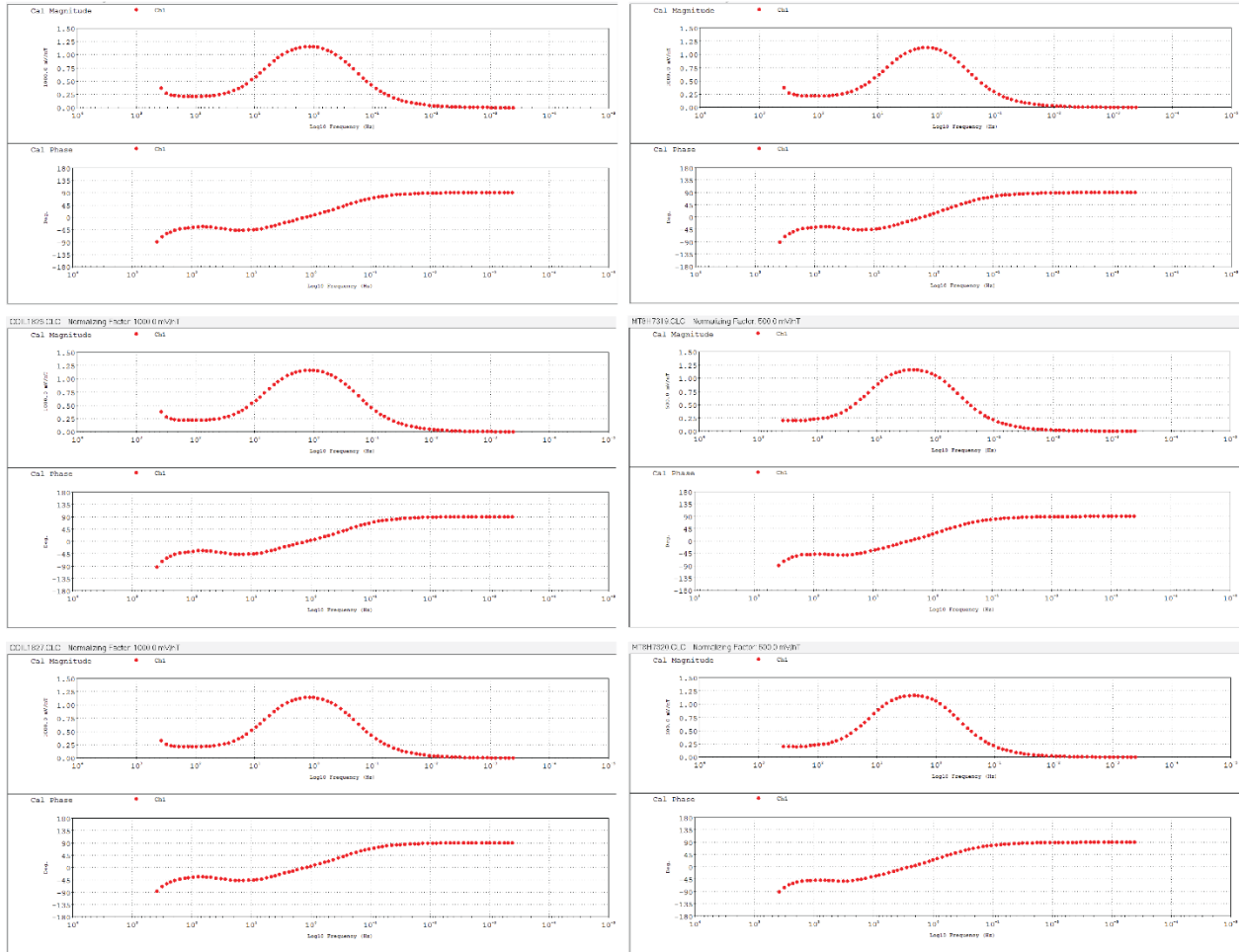


Figure C1: Calibration responses of the MTC50 induction coils on July 24, 2019. These responses are provided in the CLC files provided as part of this report. Calibration performed near Mount Meager.

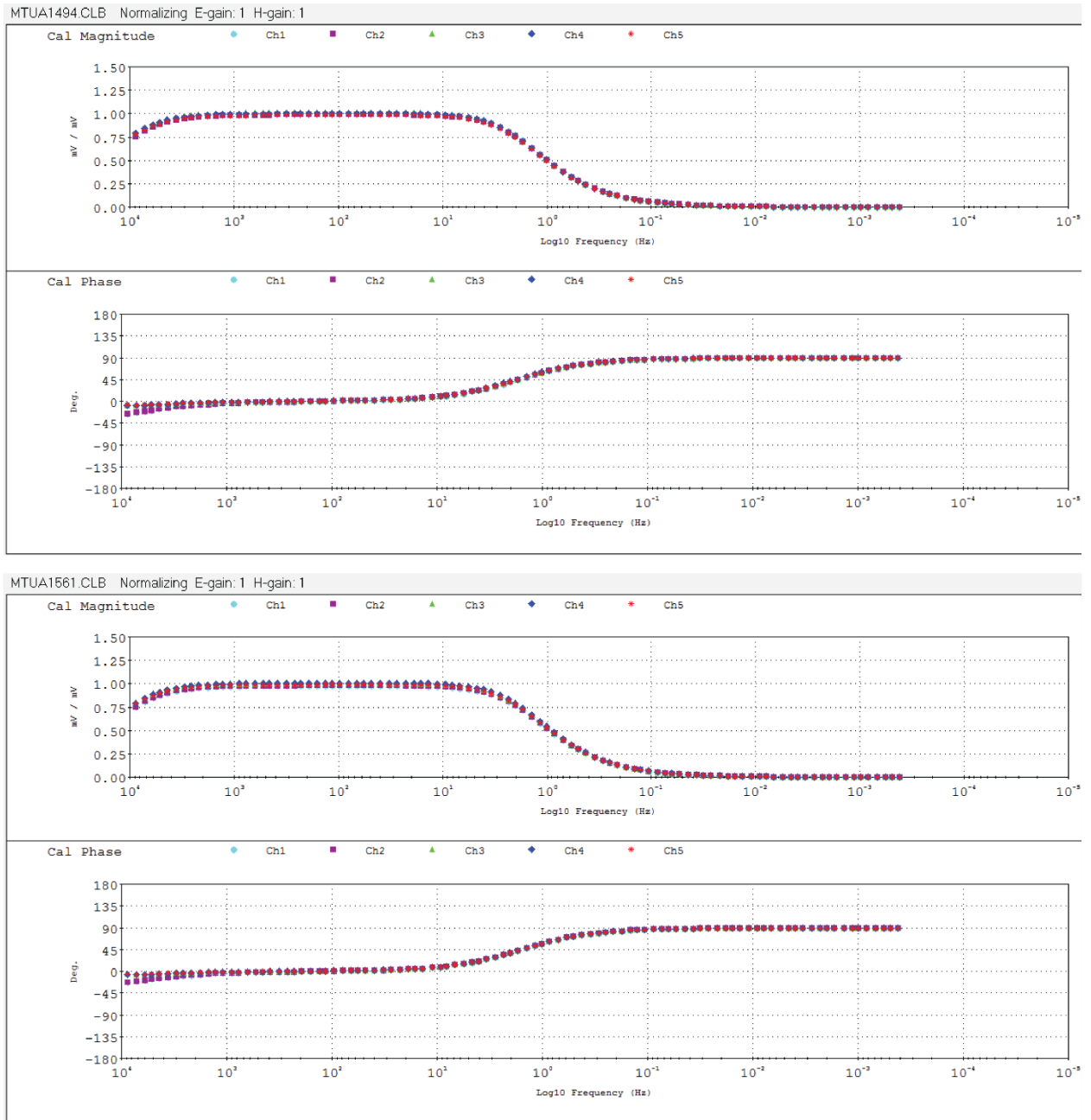


Figure C2: Calibration responses of the electric fields of the MTU5A instruments on July 24, 2019. These responses are provided in the CLB files provided as part of this report. Calibration performed near Mount Meager.

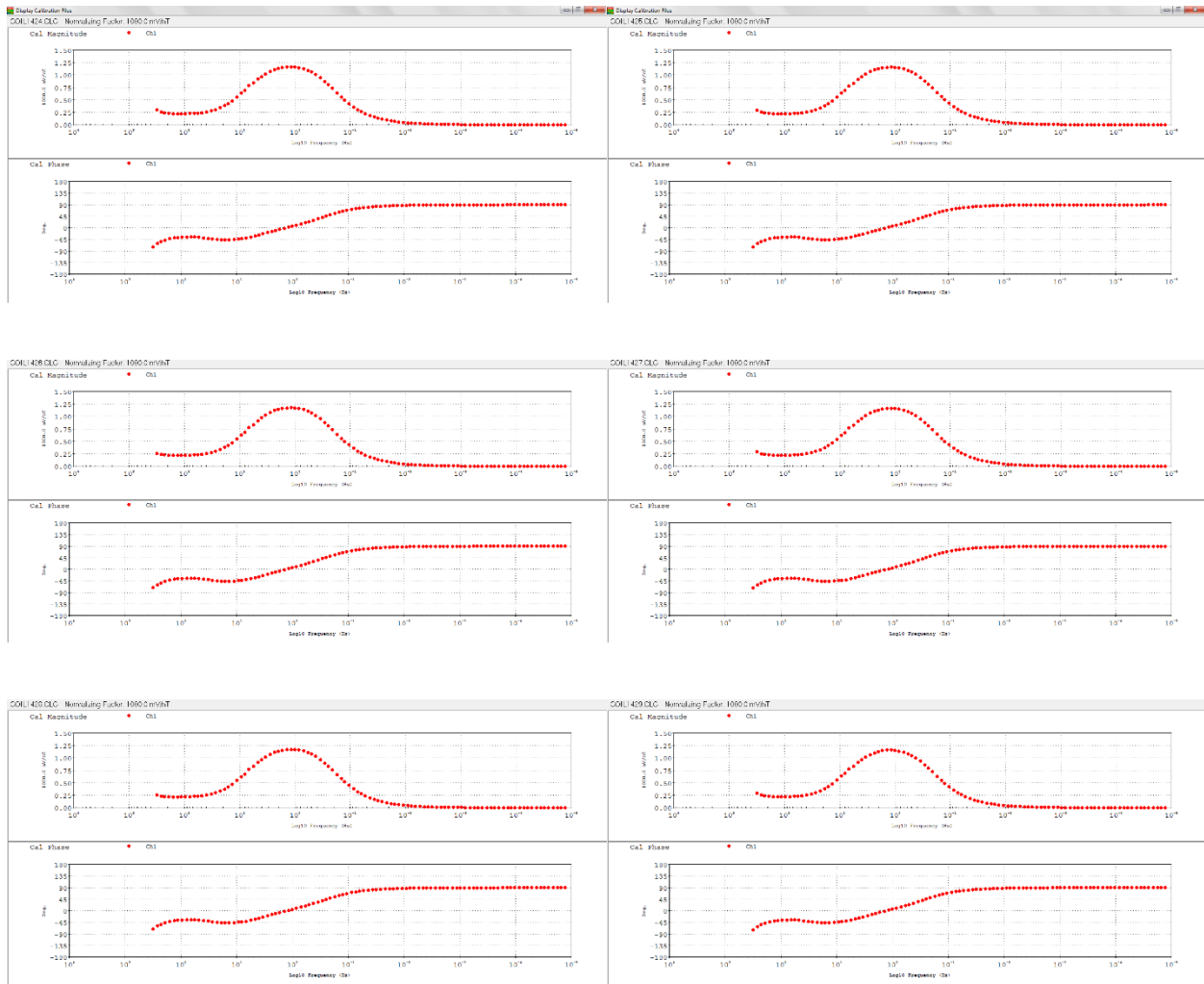


Figure C3: Calibration responses of the MTC-50 induction coils on November 2, 2020. These responses are provided in the CLC files provided as part of this report. Calibration performed in Edmonton.

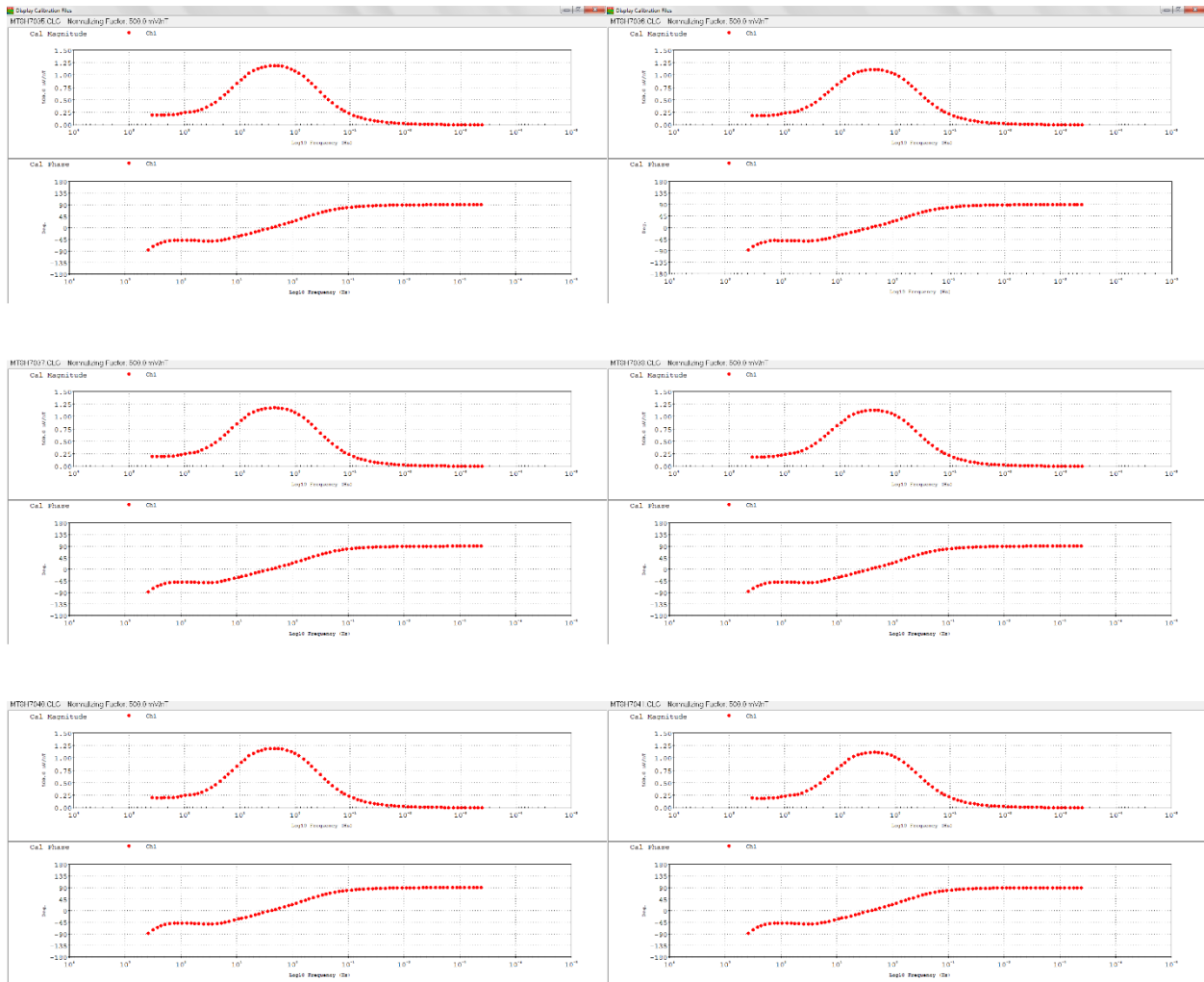


Figure C4: Calibration responses of the MTC-80 induction coils on November 2, 2020. These responses are provided in the CLC files provided as part of this report. Calibration performed in Edmonton.

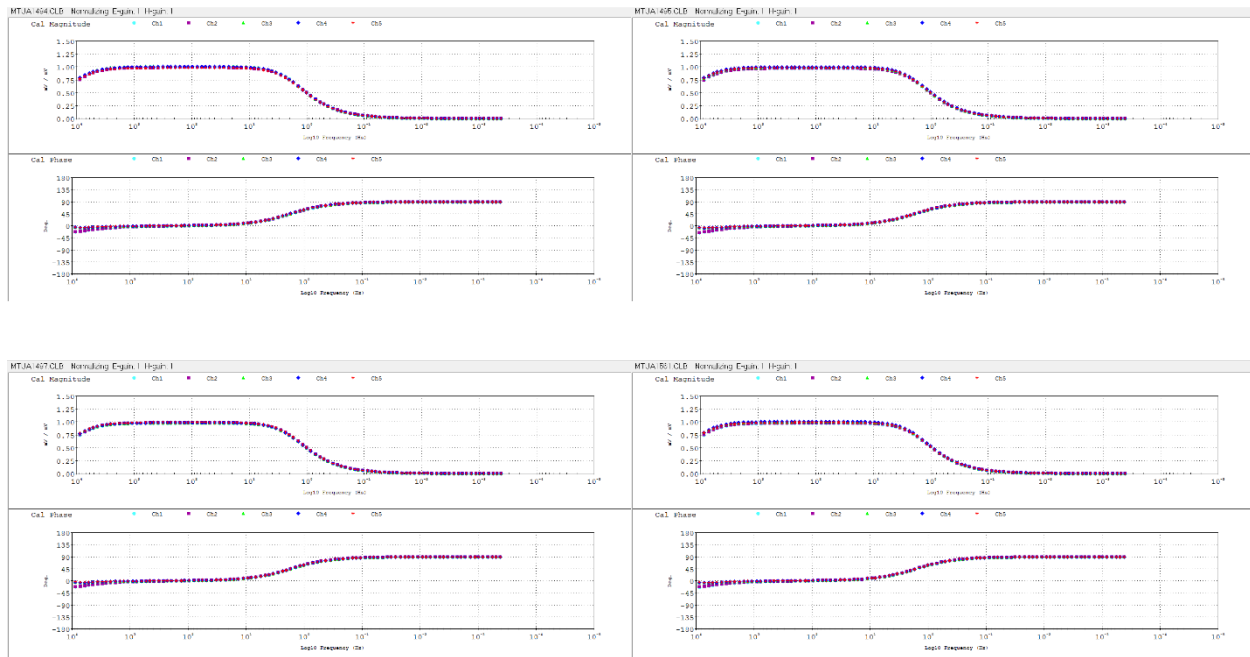


Figure C5: Calibration responses of the electric fields of the MTU-5A instruments on November 2, 2020. These responses are provided in the CLB files provided as part of this report. Calibration performed in Edmonton.

Chapter 6 - Overview of the 2019 Audiomagnetotelluric Survey of the Mount Meager Geothermal Reservoir

Craven, J.A.¹; Hormozzade, F.^{1,2}, Tschirhart, V.¹; Ansari, M.¹, Bryant, R.¹, and Montezadian, D.²

¹Geological Survey of Canada

²Carleton University

Introduction

This report documents the collection and basic processing of data from 84 magnetotelluric (MT) sites (Figure 1) acquired during the summer of 2019 as part of a Geothermal Resource Assessment of the Garibaldi Belt science program at Mount Meager. An MT survey is an electromagnetic exploration method used in both geothermal exploration and studies of the magmatic systems of active volcanoes (Chave and Jones, 2012). Ambient low frequency electromagnetic (EM) waves act as a (natural) transmitter in an EM geophysical survey where an active source is typically deployed. The MT amplitude and phase properties are associated with the diffusion of the ambient fields into the subsurface and can be measured by comparatively easy to deploy receivers and used to infer the resistivity of the subsurface. Resistivity is a property of a rock matrix that is also sensitive to the presence of fluids within interconnected pore spaces (i.e., permeability) and to any clay alteration products commonly found in geothermal reservoirs. Because temperature is a strong control on the presence of key clay alteration products, a subsurface map of resistivity can also serve as a proxy for a subsurface temperature map.

Geothermal exploration at Mount Meager using magnetotellurics began in the 1980s. At that time MT instruments were bulky requiring AC power sources that lengthened installation times to upwards of half a day per site and constrained the stations collected to vehicle accessible locations primarily along Meager Creek (Flores Luna et al, 196) and Pham (1977). Unfortunately, the MT data from four widely spaced sites documented by Pham (1977) has been lost. The analysis of the eight road sites from the 1982 survey was compromised by the small number of sites, a problem compounded by the data analysis techniques available at the time that were limited to simple 1-D layered earth models, low resolution 2-D models, or unrealistic thin sheet 3-D models. Even so, careful analysis of the data detected a dipping low resistivity layer identified as a fault controlled geothermal reservoir (Flores Luna et al, 1986) and later, when aided by off-line legacy data the reservoir was shown to be affected by clay alteration (Jones and Dumas, 1993). Important geometrical information and fundamental relationships to the permeability of the reservoir were not established.

Methods

MT surveys involve the measurement of natural electric and magnetic fields at the surface of the Earth. In general, electromagnetic geophysical surveys utilize a generator and complicated grounded electrodes or antennas to form transmitters, but the use of natural signals by MT as a transmitter avoids these complications. Because the depth of investigation of EM surveys depends on the frequency of the fields and the natural spectrum covers a broad range of frequencies, the same

instrument can measure the subsurface resistivity at different depths simply by recording different ranges of frequencies. Typical MT measurements are made in the range 10000 – 0.001 Hz. When exclusively in the higher frequency range of 1000 – 1 Hz the data is often referred to as audiomagnetotellurics (AMT). The frequency range of approximately 400-0.001 Hz is often referred to as broadband MT (BBMT). In general, results from AMT surveys are often at higher resolution than BBMT, but are less depth penetrating.

As stated earlier, MT uses ambient or natural EM fields as effective sources. This has advantages as pointed out above, but also some disadvantages. One disadvantage is that times of low ambient signal may dominate a particular recording interval. MT data are typically acquired overnight when signal strength is higher to ensure high quality data. During the Meager project, to maximize the number of sites, steel electrodes, and a comparatively short ½ hour daytime AMT recording interval was utilized at sites shown in Figure 1. Any resulting decrease in data quality was minimized through careful data editing (described in detail below) and part-way through the project the installation of a permanent site recording (only) daytime broadband magnetic fields. The broadband magnetic field data at the permanent site could be processed with the local electric fields collected at each AMT site to enable better AMT processing down to frequencies where AMT and BBMT recording overlap at 1 Hz or so (when the response of the electrodes used for the AMT starts to fall-off). Such processing is possible at only the longer periods because of the planar nature of the fields. This recording method, whilst able to produce high quality AMT data does generate a large data set requiring considerable manual editing to remove bursts of high frequency noise plus subsequent manual merging of the locally processed AMT data with the permanent MT coil processed data.

Prior to editing, the MT metadata were evaluated. In this step, the dipole length, declination, azimuth and calibrations were checked. In order to ensure high data quality data unaffected by man-made or non-planar natural noise sources, the MT data from the survey were processed and edited manually using the EMPower software utilizing a consistent workflow and parameters. The time series were converted to impedances, apparent resistivity and phase; all of which are functions of frequency. To get the final responses, the cross powers were edited such that inconsistent data from different recordings were removed from the calculations of resistivity, phase and other geophysical parameters. The key tools utilized in the EMPower software were the Polar Editor and Time Editor, in which masks were created to remove the bad data selected by visual inspection. This procedure was used on both the and AMT (example shown in Figure 2) and BBMT (Figure 3) processed data sets and the merged data (Figure 4) for each site was exported from the EMPower software.

Data Collection

The collection of the MT data at 84 sites (Figure 1) was conducted in the summer 2019. The recordings were made using AMT sensors and steel electrodes connected to newly acquired MTU-5C recorders. Declination was calculated using online calculators and found to vary between 16.37 to 16.41 degrees. Direct site access was generally impossible via truck, quad or helicopter and so the sites had to be backpacked. The AMT coils were cumbersome to carry, so the crews switched to open top portage style bags. The sites recorded along the Lillooet River were made primarily to test varying bags for portability and to train crews on data acquisition prior to deployment on the mountainside. As mentioned above, to ensure high quality at the lower end of the AMT frequency spectrum,

broadband MT sensors were deployed part way through the survey at a permanent site to be processed with the local AMT electric field data. A summary of AMT recording is presented in Tables 1 and 2 below. The permanent magnetic field-only recordings are listed in Table 3.

Results

The primary results documented here are the vetting, checking, editing and basic processing of time series from 84 AMT sites collected in the summer of 2019 at Mount Meager and the creation of an edited merged high quality data set consisting of impedances in the AMT frequency domain.

Summary and Future Work

AMT data were collected at 84 stations and processed to response functions that can be used to formulate models of subsurface structure, both in terms of the geothermal reservoir and the underlying magmatic systems. These inversion models will provide important information about subsurface electrical resistivity structure which can be used to address question related to the viability of the geothermal resource of Mount Meager.

Data

The raw data consist of time series (.JSON) and calibration (.CAL) files. More information about the format of time series can be found at

<http://empower.phoenix-geophysics.com/releases/LATEST/manuals/Time-series%20JSON%20format.pdf>.

After manual editing and merging, EDI files were exported from the EMPower software for further use in modeling and interpretation. The 200 GB data set can be downloaded here or will be made available as a vetted data set in a subsequent GSC Open File report.

Citations

Chave, A., & Jones, A. (2012). *The magnetotelluric method: theory and practice*. Cambridge;: Cambridge University Press.

Flores-Luna, C., Kurtz, R.D., DeLaurier, J. (1985). Magnetotelluric exploration in the Meager Mountain Geothermal Area, Canada. *Acta Geodaet, 20, Geophys. Mont. Acad. Sci*, pp. 165-171.

Flores-Luna, C. (1986). *Electromagnetic induction studies over the Meager Creek geothermal area, British Columbia*. PhD Thesis, Department of Physics, University of Toronto. 221 pp.

Jones, A. G. and Dumas, I. (1993). Electromagnetic images of a volcanic zone, *Phys. Earth and Planet. Inter.* 81, pp. 289–314.

Pham, van Ngoc (1977). *Magneto-Telluric survey of the Mount Meager region of the Squamish Valley*, Earth Physics Branch, Open File Number 77-20-E, pp. 64, <https://doi.org/10.4095/314797>.

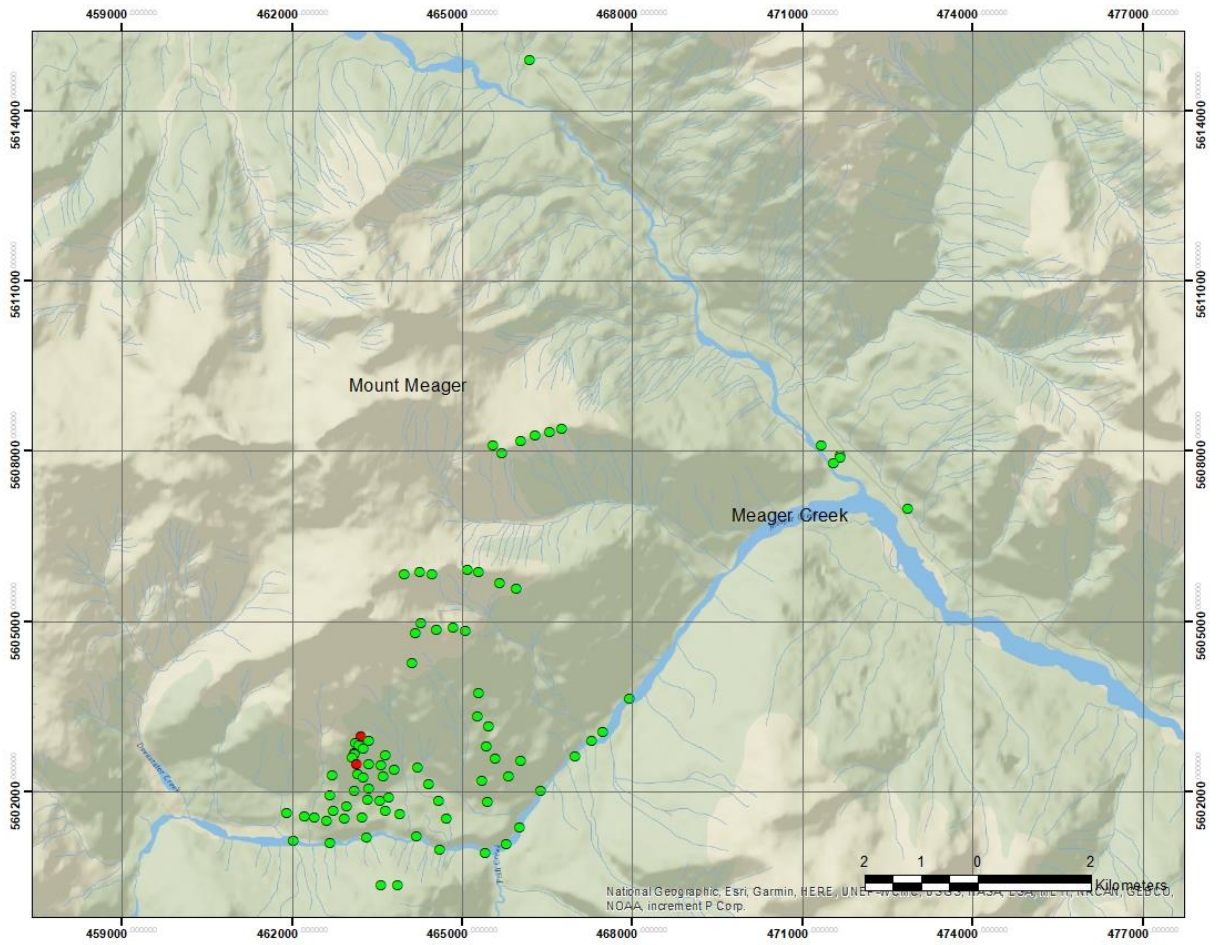


Figure 1. Station locations for the 84 AMT MTU-5C sites. MTU-5A AMT site (not discussed) are shown in red.

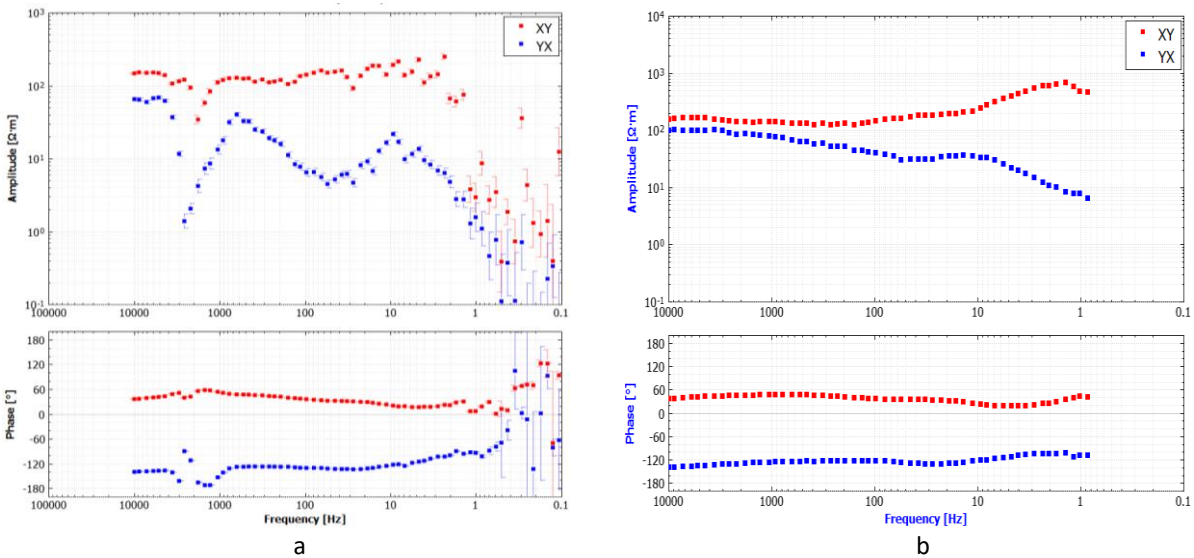


Figure 2. AMT apparent resistivity and phase responses of Zxy (red dots) and Zyx (blue dots) for site number 84, a) before editing and b) after editing.

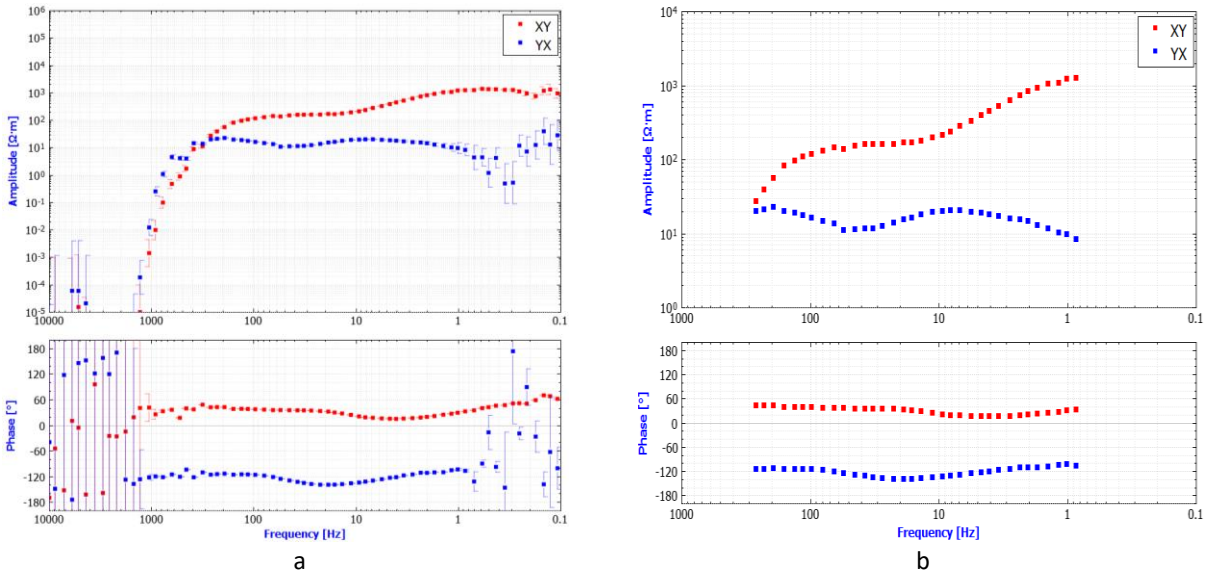


Figure 3. MT apparent resistivity and phase responses of Z_{xy} (red dots) and Z_{yx} (blue dots) for site number 84, a) before editing and b) after editing.

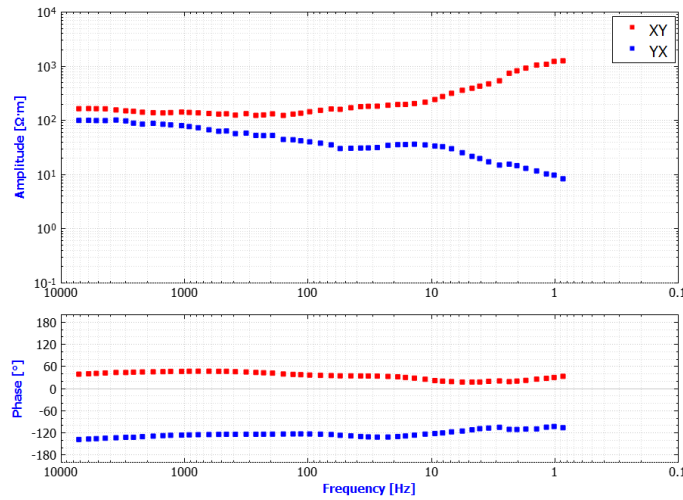


Figure 4. MT apparent resistivity and phase responses of Z_{xy} (red dots) and Z_{yx} (blue dots) for site number 84 (Merged)

Table 1. Site coordinates and configurations of the Mount Meager MT survey

Site Name	Latitude	Longitude	Elevation (m)	Hz azimuth (°)	Ex azimuth (°)	Declination (°)
01	50.62262	-123.4006	393.516674	0	0	16.39
01b	50.62227	-123.4006	390.657858	0	0	16.39
02	50.62131	-123.4021	394.649283	0	0	16.38
03	50.62424	-123.4052	395.127848	0	0	16.39
04	50.68503	-123.4786	705.010088	0	0	16.41
06	50.57658	-123.5208	1303.957128	0	0	16.39
07	50.57694	-123.5177	1317.964034	0	0	16.39
08	50.57627	-123.5201	1294.815007	0	0	16.39
09	50.5756	-123.5189	1263.50623	0	0	16.39
10a	50.57489	-123.5213	1231.130754	0	0	16.39
10b	50.57486	-123.5211	1234.050084	0	0	16.39
11	50.57428	-123.5218	1197.923076	0	0	16.39
13	50.57318	-123.5176	1095.395138	0	20	16.39
14	50.57469	-123.5133	1080.166357	0	0	16.39
15	50.57296	-123.5146	1049.414719	0	0	16.39
16	50.57153	-123.5203	1016.039198	0	0	16.39
17	50.57132	-123.5267	1005.012571	0	0	16.39
18	50.56817	-123.5273	906.876575	0	0	16.39
19	50.56583	-123.5263	859.448098	0	0	16.39

Site Name	Latitude	Longitude	Elevation (m)	H _z azimuth (°)	Ex azimuth (°)	Declination (°)
20	50.62386	-123.4872	2069.493576	0	0	16.4
21	50.62457	-123.4802	2028.923018	0	0	16.4
22	50.62268	-123.485	2063.22173	0	0	16.4
23	50.62543	-123.4766	1991.358404	0	0	16.4
24	50.62595	-123.4732	1983.236051	0	0	16.39
25	50.62649	-123.47	1897.97168	0	0	16.39
26	50.60339	-123.509	2161.918937	0	0	16.39
27	50.60404	-123.4934	1871.827809	0	10	16.39
28	50.60372	-123.5051	2065.118357	0	30	16.39
29	50.60375	-123.4904	1847.917505	0	0	16.39
30	50.60328	-123.5021	2036.358392	0	0	16.39
31	50.60206	-123.4852	1764.996737	0	0	16.39
32	50.60125	-123.4811	1678.366567	0	0	16.39
33	50.56645	-123.5229	842.104667	0	0	16.39
34	50.57106	-123.5188	991.706354	0	0	16.39
35	50.56453	-123.5235	827.787039	0	0	16.39
36	50.57134	-123.514	954.445102	0	30	16.39
37	50.56483	-123.5191	787.993877	0	0	16.39
38	50.57238	-123.5113	920.069013	0	0	16.39
39	50.56528	-123.5098	762.699639	0	0	16.38

Site Name	Latitude	Longitude	Elevation (m)	H _z azimuth (°)	Ex azimuth (°)	Declination (°)
40	50.56905	-123.521	863.277112	0	0	16.39
41	50.56576	-123.5132	764.776517	0	0	16.39
42	50.56926	-123.5176	870.880817	0	0	16.39
43	50.56795	-123.5125	781.913085	0	30	16.39
44	50.56762	-123.5176	800.961316	0	0	16.39
45	50.58457	-123.4904	1308.875694	0	0	16.39
46	50.56743	-123.5148	779.654134	0	0	16.39
47	50.58084	-123.4905	1230.23032	0	0	16.38
48	50.57926	-123.4877	1149.420276	0	0	16.38
49	50.57608	-123.4883	1084.146812	0	0	16.38
50	50.57421	-123.486	977.751247	0	0	16.38
51	50.57398	-123.4796	879.325601	0	0	16.38
52	50.57136	-123.4826	840.89468	0	0	16.38
53	50.57068	-123.4894	887.855708	0	0	16.38
54	50.56737	-123.4878	735.966065	0	0	16.38
55	50.61429	-123.3835	388.993311	0	0	16.37
56	50.56066	-123.5271	707.043132	0	0	16.38
57	50.56103	-123.5361	734.115083	0	0	16.38
58	50.56157	-123.518	689.920022	0	0	16.38
59	50.56176	-123.5056	664.237897	0	0	16.38

Site Name	Latitude	Longitude	Elevation (m)	H _z azimuth (°)	Ex azimuth (°)	Declination (°)
60	50.55976	-123.4996	645.484607	0	0	16.38
61	50.55933	-123.4883	624.672987	0	0	16.38
62	50.56067	-123.4831	612.469875	0	0	16.38
63	50.56912	-123.4746	586.999872	0	0	16.38
64	50.56338	-123.4799	604.924088	0	0	16.38
65	50.58921	-123.5069	1813.951535	0	30	16.38
66	50.59398	-123.5063	1991.654962	0	0	16.38
67	50.55405	-123.5102	1261.817131	0	0	16.38
68	50.59556	-123.5047	1974.529782	0	0	16.38
69	50.5541	-123.5144	1243.562765	0	0	16.38
70	50.59466	-123.5009	1854.255011	0	0	16.39
71	50.57706	-123.462	540.825906	0	0	16.38
72	50.59501	-123.4969	1777.553747	0	0	16.39
73	50.58388	-123.4526	516.950066	0	0	16.39
74	50.59446	-123.4938	1702.225255	0	0	16.39
75	50.56413	-123.528	817.660964	0	0	16.38
76	50.57469	-123.4661	561.961008	0	0	16.39
77	50.56464	-123.5309	813.770478	0	0	16.38
78	50.57851	-123.4592	530.709255	0	0	16.39
79	50.56746	-123.5002	751.807959	0	0	16.39

Site Name	Latitude	Longitude	Elevation (m)	Hz azimuth (°)	Ex azimuth (°)	Declination (°)
80	50.56535	-123.5378	797.376991	0	0	16.38
81	50.56458	-123.4981	749.238919	0	0	16.38
82	50.56486	-123.5334	816.772403	0	0	16.38
84	50.57274	-123.5055	845.321417	0	0	16.38
86	50.57015	-123.5027	809.924889	0	0	16.38

Table 2. Detailed configuration of the Magnetic and Electric field measurements of sites named in Table 1.

Data File	Site Name	Start Time	End Time	MTU box number	Hx id	Hy id	Hz id	Ex line length	Ey line length	Processing note comment
10227_2019-07-07-231456	01	Sun Jul 07 2019 23:14:56 UTC	Mon Jul 08 2019 00:14:08 UTC	227	1148	1146	1173	28.1	28.3	
10229_2019-07-07-231300	01b	Sun Jul 07 2019 23:13:00 UTC	Mon Jul 08 2019 00:18:23 UTC	229	1141	1142	1143	25.87	29	
10227_2019-07-08-185238	02	Mon Jul 08 2019 18:52:38 UTC	Mon Jul 08 2019 20:03:15 UTC	227	1141	1142	1143	22.25	21.38	
10230_2019-07-08-185715	03	Mon Jul 08 2019 18:57:15 UTC	Mon Jul 08 2019 19:56:27 UTC	230	1170	1171	1173	24.9	24.8	
10229_2019-07-09-183437	04	Tue Jul 09 2019 18:34:37 UTC	Tue Jul 09 2019 20:42:01 UTC	229	1141	1142	None	27.5	38.5	
10230_2019-07-11-194326	06	Fri Jul 12 2019 00:53:26 UTC	Fri Jul 12 2019 03:56:36 UTC	230	1170	1173	None	21.3	20.9	
10227_2019-07-11-171743	07	Thu Jul 11 2019 17:17:43 UTC	Thu Jul 11 2019 18:50:43 UTC	227	1141	1142	1143	24.7	21.8	
10229_2019-07-11-184750	08	Fri Jul 12 2019 00:31:50 UTC	Fri Jul 12 2019 03:42:19 UTC	229	1148	1146	1327	22.43	23.08	
10229_2019-07-12-170419	09	Fri Jul 12 2019 17:04:19 UTC	Fri Jul 12 2019 18:04:40 UTC	229	1148	1146	1327	27.8	23.2	
10227_2019-07-11-202714	10a	Fri Jul 12 2019 00:31:14 UTC	Fri Jul 12 2019 03:54:24 UTC	227	1141	1142	None	24.6	23.05	
10227_2019-07-12-184456	10b	Fri Jul 12 2019 18:44:56 UTC	Fri Jul 12 2019 19:48:48 UTC	227	1141	1142	None	24.6	23.05	

Data File	Site Name	Start Time	End Time	MTU box number	Hx id	Hy id	Hz id	Ex line length	Ey line length	Processing note comment
10230_2019-07-12-170609	11	Fri Jul 12 2019 17:06:09 UTC	Fri Jul 12 2019 18:46:52 UTC	230	1170	1171	1173	25.2	27.3	
10229_2019-07-12-203316	13	Fri Jul 12 2019 20:33:16 UTC	Fri Jul 12 2019 21:41:30 UTC	229	1170	1171	1173	13.1	14.1	
10227_2019-07-13-170047	14	Sat Jul 13 2019 17:00:47 UTC	Sat Jul 13 2019 18:03:56 UTC	227	1141	1142	1143	15.5	11.76	
10230_2019-07-13-163351	15	Sat Jul 13 2019 16:33:51 UTC	Sat Jul 13 2019 17:32:48 UTC	230	1148	1146	1327	20.2	18.4	
10230_2019-07-13-184937	16	Sat Jul 13 2019 18:49:37 UTC	Sat Jul 13 2019 19:50:31 UTC	230	1148	1146	None	18.4	19.4	
10227_2019-07-13-194535	17	Sat Jul 13 2019 19:45:35 UTC	Sat Jul 13 2019 20:50:40 UTC	227	1141	1142	1143	27.3	30.3	Hx installed backwards
10230_2019-07-13-210600	18	Sat Jul 13 2019 21:06:00 UTC	Sat Jul 13 2019 22:06:16 UTC	230	1148	1146	1327	19.5	17.8	
10227_2019-07-13-215820	19	Sat Jul 13 2019 21:58:20 UTC	Sat Jul 13 2019 22:45:10 UTC	227	1142	1141	1143	18.55	28.64	
10227_2019-07-14-160715	20	Sun Jul 14 2019 16:07:15 UTC	Sun Jul 14 2019 17:15:24 UTC	227	1141	1142	1143	24.19	32.17	
10230_2019-07-14-161300	21	Sun Jul 14 2019 16:13:00 UTC	Sun Jul 14 2019 17:12:55 UTC	230	1148	1146	1327	30	30.8	
10227_2019-07-14-181854	22	Sun Jul 14 2019 18:18:54 UTC	Sun Jul 14 2019 19:19:25 UTC	227	1141	1142	1143	27.7	25.56	
10230_2019-07-14-181532	23	Sun Jul 14 2019 18:15:32 UTC	Sun Jul 14 2019 19:15:58 UTC	230	1148	1146	1327	31.2	23.7	

Data File	Site Name	Start Time	End Time	MTU box number	Hx id	Hy id	Hz id	Ex line length	Ey line length	Processing note comment
10230_2019-07-14-210330	24	Sun Jul 14 2019 21:03:30 UTC	Sun Jul 14 2019 22:03:05 UTC	230	1141	1142	1143	21.5	28.6	
10230_2019-07-14-224200	25	Sun Jul 14 2019 22:42:00 UTC	Sun Jul 14 2019 23:41:44 UTC	230	1141	1142	1143	32	26.6	
10230_2019-07-15-154934	26	Mon Jul 15 2019 15:49:34 UTC	Mon Jul 15 2019 16:47:38 UTC	230	1148	1146	1327	21.8	28.75	
10227_2019-07-15-161626	27	Mon Jul 15 2019 16:16:26 UTC	Mon Jul 15 2019 17:14:19 UTC	227	1141	1142	1143	29.06	33.78	
10230_2019-07-15-174619	28	Mon Jul 15 2019 17:46:19 UTC	Mon Jul 15 2019 18:41:50 UTC	230	1148	1146	1327	19.39	24.56	
10227_2019-07-15-180236	29	Mon Jul 15 2019 18:02:36 UTC	Mon Jul 15 2019 19:04:57 UTC	227	1141	1142	1143	31.06	32.12	
10230_2019-07-15-193625	30	Mon Jul 15 2019 19:36:25 UTC	Mon Jul 15 2019 20:30:20 UTC	230	1148	1146	1327	26.3	19.7	
10227_2019-07-15-201345	31	Mon Jul 15 2019 20:13:45 UTC	Mon Jul 15 2019 21:19:12 UTC	227	1141	1142	1143	33.55	24.58	
10230_2019-07-15-213359	32	Mon Jul 15 2019 21:33:59 UTC	Mon Jul 15 2019 22:30:34 UTC	230	1148	1146	1327	24.1	25.2	
10230_2019-07-16-180821	33	Tue Jul 16 2019 18:08:21 UTC	Tue Jul 16 2019 19:15:31 UTC	230	1141	1142	1143	22.93	23.08	
10229_2019-07-16-165427	34	Tue Jul 16 2019 16:54:27 UTC	Tue Jul 16 2019 17:54:52 UTC	229	1170	1171	1173	10.98	22.1	
10230_2019-07-16-203307	35	Tue Jul 16 2019 20:33:07 UTC	Tue Jul 16 2019 21:28:36 UTC	230	1141	1142	1143	18.45	23.28	

Data File	Site Name	Start Time	End Time	MTU box number	Hx id	Hy id	Hz id	Ex line length	Ey line length	Processing note comment
10229_2019-07-16-184312	36	Tue Jul 16 2019 18:43:12 UTC	Tue Jul 16 2019 19:44:40 UTC	229	1170	1171	None	15.8	11.4	
10230_2019-07-16-221551	37	Tue Jul 16 2019 22:15:51 UTC	Tue Jul 16 2019 22:29:47 UTC	230	1141	1142	None	17.14	14.92	
10229_2019-07-16-202850	38	Tue Jul 16 2019 20:28:50 UTC	Tue Jul 16 2019 21:29:13 UTC	229	1170	1171	1173	26.07	15.11	
10227_2019-07-18-171319	39	Thu Jul 18 2019 17:13:19 UTC	Thu Jul 18 2019 18:08:30 UTC	227	1141	1142	1143	16.29	28.63	
10229_2019-07-18-170502	40	Thu Jul 18 2019 17:05:02 UTC	Thu Jul 18 2019 17:58:31 UTC	229	1170	1171	1173	12.2	25	
10227_2019-07-18-185221	41	Thu Jul 18 2019 18:52:21 UTC	Thu Jul 18 2019 19:48:39 UTC	227	1141	1142	1143	24.57	31.26	
10229_2019-07-18-183603	42	Thu Jul 18 2019 18:36:03 UTC	Thu Jul 18 2019 19:33:38 UTC	229	1170	1171	1173	14.3	18.45	
10227_2019-07-18-204045	43	Thu Jul 18 2019 20:40:45 UTC	Thu Jul 18 2019 21:38:58 UTC	227	1141	1142	1143	26.1	23.89	
10229_2019-07-18-203426	44	Thu Jul 18 2019 20:34:26 UTC	Thu Jul 18 2019 21:32:18 UTC	229	1170	1171	None	29.25	15.67	
10229_2019-07-19-155042	45	Fri Jul 19 2019 15:50:42 UTC	Fri Jul 19 2019 16:30:15 UTC	229	1141	1142	1143	26.46	20.6	
10229_2019-07-18-221107	46	Thu Jul 18 2019 22:11:07 UTC	Thu Jul 18 2019 22:49:57 UTC	229	1170	1171	1173	27.6	27.6	
10229_2019-07-19-173035	47	Fri Jul 19 2019 17:30:35 UTC	Fri Jul 19 2019 18:10:17 UTC	229	1141	1142	1143	18.11	10.91	

Data File	Site Name	Start Time	End Time	MTU box number	Hx id	Hy id	Hz id	Ex line length	Ey line length	Processing note comment
10229_2019-07-19-190217	48	Fri Jul 19 2019 19:02:17 UTC	Fri Jul 19 2019 19:40:31 UTC	229	1141	1143	1142	11.23	19.23	
10229_2019-07-19-201917	49	Fri Jul 19 2019 20:19:17 UTC	Fri Jul 19 2019 20:50:26 UTC	229	1141	1142	1143	19.77	25.93	
10229_2019-07-19-213734	50	Fri Jul 19 2019 21:37:34 UTC	Fri Jul 19 2019 22:14:55 UTC	229	1141	1142	1143	21.65	18.72	
10229_2019-07-20-175841	51	Sat Jul 20 2019 17:58:41 UTC	Sat Jul 20 2019 18:41:23 UTC	229	1141	1142	1143	19.1	21.4	
10229_2019-07-20-192633	52	Sat Jul 20 2019 19:26:33 UTC	Sat Jul 20 2019 20:08:36 UTC	229	1141	1142	1143	20.33	13.06	
10229_2019-07-20-205918	53	Sat Jul 20 2019 20:59:18 UTC	Sat Jul 20 2019 21:38:19 UTC	229	1141	1142	1143	24.26	27.67	
10229_2019-07-20-223614	54	Sat Jul 20 2019 22:36:14 UTC	Sat Jul 20 2019 23:18:11 UTC	229	1141	1142	None	13.03	20.61	
10227_2019-07-21-002259	55	Sun Jul 21 2019 00:22:59 UTC	Sun Jul 21 2019 01:01:06 UTC	227	1170	1171	1173	19	25.6	
10229_2019-07-21-164745	56	Sun Jul 21 2019 16:47:45 UTC	Sun Jul 21 2019 17:27:08 UTC	229	1170	1171	1173	21.69	24.01	
10227_2019-07-21-163530	57	Sun Jul 21 2019 16:35:30 UTC	Sun Jul 21 2019 17:16:58 UTC	227	1141	1142	1143	26.56	26.96	
10229_2019-07-21-180858	58	Sun Jul 21 2019 18:08:58 UTC	Sun Jul 21 2019 18:49:12 UTC	229	1170	1171	1173	28.73	31.06	
10227_2019-07-21-184337	59	Sun Jul 21 2019 18:43:37 UTC	Sun Jul 21 2019 19:29:50 UTC	227	1141	1142	1143	26.35	31.85	

Data File	Site Name	Start Time	End Time	MTU box number	Hx id	Hy id	Hz id	Ex line length	Ey line length	Processing note comment
10229_2019-07-21-193505	60	Sun Jul 21 2019 19:35:05 UTC	Sun Jul 21 2019 20:17:28 UTC	229	1170	1171	1173	14.12	25.66	
10227_2019-07-21-201822	61	Sun Jul 21 2019 20:18:22 UTC	Sun Jul 21 2019 21:00:28 UTC	227	1141	1142	1143	21.34	28.48	
10229_2019-07-21-210517	62	Sun Jul 21 2019 21:05:17 UTC	Sun Jul 21 2019 21:43:53 UTC	229	1170	1171	1173	31.73	27.36	
10227_2019-07-21-220724	63	Sun Jul 21 2019 22:07:24 UTC	Sun Jul 21 2019 22:48:20 UTC	227	1141	1142	1143	27.92	18.68	
10229_2019-07-21-222418	64	Sun Jul 21 2019 22:24:18 UTC	Sun Jul 21 2019 23:05:26 UTC	229	1170	1171	1173	29.3	22.64	
10229_2019-07-22-150925	65	Mon Jul 22 2019 15:09:25 UTC	Mon Jul 22 2019 15:51:45 UTC	229	1170	1171	1173	17.93	13.03	
10227_2019-07-22-150100	66	Mon Jul 22 2019 15:01:00 UTC	Mon Jul 22 2019 15:40:38 UTC	227	1141	1142	1143	24.06	13.8	Hx installed backwards
10229_2019-07-22-181916	67	Mon Jul 22 2019 18:19:16 UTC	Mon Jul 22 2019 19:03:57 UTC	229	1170	1171	1173	20.69	18.25	
10227_2019-07-22-162235	68	Mon Jul 22 2019 16:22:35 UTC	Mon Jul 22 2019 17:06:30 UTC	227	1141	1142	1143	20.1	17.21	
10229_2019-07-22-195223	69	Mon Jul 22 2019 19:52:23 UTC	Mon Jul 22 2019 20:33:07 UTC	229	1170	1171	1173	7.99	12.43	
10227_2019-07-22-184338	70	Mon Jul 22 2019 18:43:38 UTC	Mon Jul 22 2019 19:24:53 UTC	227	1141	1142	1143	23.43	23.02	
10229_2019-07-23-155738	71	Tue Jul 23 2019 15:57:38 UTC	Tue Jul 23 2019 16:58:00 UTC	229	1141	1142	1143	17.92	19.08	

Data File	Site Name	Start Time	End Time	MTU box number	Hx id	Hy id	Hz id	Ex line length	Ey line length	Processing note comment
10227_2019-07-22-201716	72	Mon Jul 22 2019 20:17:16 UTC	Mon Jul 22 2019 21:01:04 UTC	227	1141	1142	1143	23.3	14.58	
10229_2019-07-23-175120	73	Tue Jul 23 2019 17:51:20 UTC	Tue Jul 23 2019 18:33:10 UTC	229	1141	1142	1143	25.99	24.46	
10227_2019-07-22-214849	74	Mon Jul 22 2019 21:48:49 UTC	Mon Jul 22 2019 22:17:23 UTC	227	1141	1142	1143	19.23	18.32	
10229_2019-07-23-200523	75	Tue Jul 23 2019 20:05:23 UTC	Tue Jul 23 2019 21:07:32 UTC	229	1141	1142	1143	11.64	24.96	
10227_2019-07-23-154701	76	Tue Jul 23 2019 15:47:01 UTC	Tue Jul 23 2019 16:43:34 UTC	227	1170	1171	1173	20.13	26.26	
10229_2019-07-23-215354	77	Tue Jul 23 2019 21:53:54 UTC	Tue Jul 23 2019 22:47:12 UTC	229	1141	1142	None	15.22	22.81	
10227_2019-07-23-172728	78	Tue Jul 23 2019 17:27:28 UTC	Tue Jul 23 2019 18:27:00 UTC	227	1170	1173	1171	23.87	23.29	
10229_2019-07-24-153403	79	Wed Jul 24 2019 15:34:03 UTC	Wed Jul 24 2019 16:31:47 UTC	229	1141	1142	1143	18.03	16.57	
10227_2019-07-23-193856	80	Tue Jul 23 2019 19:38:56 UTC	Tue Jul 23 2019 20:40:18 UTC	227	1170	1171	1173	17.8	21.53	
10229_2019-07-24-172440	81	Wed Jul 24 2019 17:24:40 UTC	Wed Jul 24 2019 18:13:37 UTC	229	1141	1142	1143	12.98	9.55	
10227_2019-07-23-211852	82	Tue Jul 23 2019 21:18:52 UTC	Tue Jul 23 2019 22:26:42 UTC	227	1170	1171	None	12.68	17.29	
10227_2019-07-24-152346	84	Wed Jul 24 2019 15:23:46 UTC	Wed Jul 24 2019 16:23:03 UTC	227	1170	1171	1173	20.02	16.13	

Data File	Site Name	Start Time	End Time	MTU box number	Hx id	Hy id	Hz id	Ex line length	Ey line length	Processing note comment
10227_2019-07-24-165932	86	Wed Jul 24 2019 16:59:32 UTC	Wed Jul 24 2019 17:56:49 UTC	227	1170	1171	1173	13.15	16.33	

Table 3. Detailed configuration of the Magnetic field measurements at the permanent site.

Data File	Site Name	Start Time	End Time	Latitude (°)	Longitude (°)	Elevation (m)	MTU box number	Hx id	Hy id	Hz id	Ex line length	Ey line length	Hz azimuth	Ex azimuth	Declination (°)
10227_2019-07-16-175805	MT Magonly 1	Tue Jul 16 17:58:05 2019	Tue Jul 16 23:20:25 2019	50.567	-123.523	847.215	227	1501	1494	None	Not installed	Not installed	0	0	16.39
10230_2019-07-18-161149	MT Magonly 2	Thu Jul 18 16:11:49 2019 GMT	Thu Jul 18 23:17:11 2019 GMT	50.567	-123.523	842.938	230	1501	1494	None	Not installed	Not installed	0	0	16.39
10230_2019-07-19-150815	MT Magonly 3	Fri Jul 19 15:08:15 2019 GMT	Fri Jul 19 23:07:30 2019 GMT	50.567	-123.523	842.47	230	1501	1494	None	Not installed	Not installed	0	0	16.39
10230_2019-07-20-160909	MT Magonly 4	Sat Jul 20 16:09:09 2019 GMT	Sun Jul 21 00:03:55 2019	50.567	-123.523	843.352	230	1501	1494	None	Not installed	Not installed	0	0	16.39

Data File	Site Name	Start Time	End Time	Latitude (°)	Longitude (°)	Elevation (m)	MTU box number	Hx id	Hy id	Hz id	Ex line length	Ey line length	Hz azimuth	Ex azimuth	Declination (°)
10230_2019-07-21-154727	MT Magonly	Sun Jul 21 15:47:27 2019 GMT	Sun Jul 21 23:25:55 2019 GMT	50.567	-123.523	843.19	230	1501	1494	None	Not installed	Not installed	0	0	16.39
10230_2019-07-22-140407	MT Magonly 5	Mon Jul 22 14:04:07 2019 GMT	Mon Jul 22 22:30:32 2019 GMT	50.567	-123.523	843.474	230	1501	1494	None	Not installed	Not installed	0	0	16.38
10230_2019-07-23-151812	MT Magonly 6	Tue Jul 23 15:18:12 2019 GMT	Tue Jul 23 23:18:13 2019 GMT	50.567	-123.523	843.666	230	1501	1494	None	Not installed	Not installed	0	0	16.38
10230_2019-07-24-143210	MT Magonly 7	Wed Jul 24 14:32:10 2019	Wed Jul 24 19:04:15 2019	50.567	-123.523	843.09	230	1501	1494	None	Not installed	Not installed	0	0	16.38

Chapter 7 - Mount Meager Passive Seismic Monitoring

Hersh Gilbert¹, Jan Dettmer¹, Genevieve Savard¹, Sara Klaasen², Andreas Fichtner², and Hongyi Su¹

¹Department of Geoscience, University of Calgary

²Department of Earth Sciences, ETH Zürich

Introduction

Our investigation of the subsurface structure of the Mount Meager geothermal system included the deployment of 59 seismic sensors and a distributed acoustic sensing (DAS) system to monitor earthquakes. The seismic sensors were configured to attain uniform sampling of Mount Meager in the area between Meager Creek and the Lillooet River, just outside of the Upper Lillooet Provincial Park (Fig. 1). The DAS system was located on a ridge with little exposure to rock fall. The system consisted of 3-km of optical fibre, a DAS interrogator unit (IU) and a power source (generator-charged battery bank). Sampling the entire Mt. Meager volcanic complex allows us to characterize crustal structures and processes associated with the area of high geothermal heat and how those vary across the complex. Specifically, these observations are used to detect sources of seismic signals (e.g., earthquakes, surface processes) and to identify the distribution of low seismic wave velocities that can mark the pathways of geothermal fluids as well as the presence of magma in the subsurface. The snapshot of local seismicity from our brief earthquake monitoring deployment provides constraints on the subsurface geometry of faults and fractures within Mount Meager that allow for fluid circulation through this geothermal system. Knowledge of the locations of potential geothermal heat sources and the plumbing system through which that heat is transported to the surface will aid future efforts in geothermal exploration.

During installation, the geophone instruments were almost completely buried to protect them from animals and the environment. The instruments were occasionally visited, and moved, by wildlife (likely bears based on claw marks). Although this disturbed the sensor once it was moved, for all cases we were able to retrieve the instrument and make use of the data from the recording period prior to the sensor being disturbed.

Methods

The local earthquakes we detected were too small to be identified by networks that relied on more sparsely spaced stations for event detection. The events we detected were identified using the short time average over long time average (STA/LTA) method, and the fingerprint and similarity thresholding (FAST) method (Yoon et al., 2015), which is a machine learning tool designed to recognize similar “earthquake fingerprints”. The FAST method involves creating a spectrogram from the continuous seismic time series and extracting spectral images. Each spectral image is then converted to a binary fingerprint based on selected wavelet coefficients. By recognizing patterns of similar wavelet coefficients, the FAST method can discern subtle signals in the seismic time series that may have been produced by earthquakes. Through this approach earthquakes can be detected in noisy records with very low signal-to-noise ratio that may otherwise go unnoticed.

To explore the completeness of our earthquake catalog derived from geophone data, we tested additional event detection schemes. We tested QuakeMigrate (Winder et al., 2020), which employs a waveform migration and stacking algorithm to identify sources of coherent signals and SCAMP (Zimmerman et al., 2019), which is an algorithm that makes use of GPUs for efficient operation and relies on the concept of the Matrix Profile for event detection. Using all the FAST, QuakeMigrate, and SCAMP approaches to event detection at Mount Meager we were able to detect and locate ~10 events that appear to be small

earthquakes during the summer and fall of 2019. While we only detected a small number of earthquakes with geophones during our recording period (a rate of approximately one per week), we detected signals with lower frequency content more commonly, at a rate of over one low frequency event per day.

The DAS data permitted the detection of >3000 events in only 1 month of recording with standard STA/LAT methods. However, the classification of these events is still ongoing and includes both events due to surface processes and earthquakes. A beamforming technique for the DAS data was developed (Klaasen et al., 2021) and applied to ~1000 of these events. The beamforming provides estimates for the azimuth at which detected events occur with respect to the location of the DAS array. DAS instruments have a highly directive response to strain transients (i.e., they measure axial strain and are broadside insensitive to compressional-wave signals). The beamforming algorithm uses the signal-to-noise ratio (SNR) of various channels and includes only those channels in the beamforming that exceed a certain threshold. Thereby, the SNR is used to implicitly account for the directivity of the array. The beamforming only provides effective bearings for the origin of events since the process assumes plane waves and a uniform half space. Nonetheless, the results can be used to identify where clusters of seismicity occur.

Data Collection

Our earthquake monitoring spanned three recording intervals from the beginning of July until the middle of October 2019. During this time, the geophone and DAS networks detected a variety of seismic signals associated with small earthquakes and surface processes. The small local earthquakes were located within the volcanic complex and detection was possible because sensors were sufficiently sensitive to low-amplitude signals that we were able to identify the pulse of faint seismic energy propagating across the array. Initial locations for a handful of these earthquakes place them directly below the recording array between Capricorn Mountain and Pylon Peak at a depth of just over 4 km (Fig. 1). Based on the signal duration and frequency content of these events, it appears their magnitudes are less than 1. In addition, the instruments recorded several regional and distant earthquakes from around the world.

Observations from Geophone Network

Tectonic Events:

Of particular interest for several of the earthquakes detected here, multiple events that occurred on July 13th, 2019 exhibited nearly identical waveforms (Fig. 2). Such similarities in earthquake records are indicative of repeating events where a single asperity repeatedly ruptures. Using these detections of repeating events as templates, we will continue to scan the data recorded by the Mount Meager array to identify whether additional events occurred using cross correlation techniques that are well suited for detecting highly similar waveforms. Repeating events with similar waveforms are especially useful for learning about geothermal systems because the repeating nature of these signals can be used to better understand how fluids migrate through cracks and fractures in the shallow crust.

Low frequency signals:

In addition to the signals observed at Mount Meager that appear to be related to small earthquakes, we also detect low frequency signals at a rate of one-to-two a day or more. Locating these lower frequency events are especially challenging due to the emergent nature of their arrivals (Fig. 3). Emergent signals are those where energy gradually builds over time which is characteristic of surface processes such as rock fall. Using the QuakeMigrate software package (Winder et al., 2020), we identified the source location of several of these LF events to be near the surface towards the upper portion of Job glacier. The source of the low frequency events appears to originate from very shallow depths. However, despite their shallow location, their arrivals are often only visible at the closest stations, suggesting that the waves have been attenuated in the shallow structure. Comparing the spectrogram of these signals to those from the

earthquakes illustrates that the energy produced by these events is associated with lower frequency energy (Fig. 4) than the earthquakes detected within Mount Meager.

Observations from DAS System

The DAS system provided an extremely rich, novel data set which has not previously been considered on a glacier-clad volcano. The system consisted of a 3-km long fibre, half of which was located on a ridge and the other half on the firn section of a small glacier. The resulting array had an aperture of 200 by 700 m and included 370 channels where strain-rate data were recorded. Data were recorded from 18 September 2019 to 17 October 2019. During this period, standard detection techniques (STA/LTA) led to the discovery of >3000 events in the frequency band from 5 to 45 Hz (referred to as high-frequency events in the following). In addition, peculiar long-period signals (0.01 to 1 Hz) were discovered and are hypothesized to be tremor associated with a geothermal system. These results are discussed in below and are fully documented in a submitted manuscript (Klaasen et al. 2021).

High-frequency Events:

The system permitted detecting >3000 events of this type. The large number of these events suggests that the DAS system presents a highly sensitive instrument with the potential to outperform traditional seismic sensors. Figure 5 shows summary statistics of the event catalog. It is particularly interesting to note that the events follow power-law scaling that is typical for seismic signals of natural origin. Specific consideration of the signal time series for individual events revealed that two groups of events are observed: Those with impulsive onset and those with emergent onset (Klaasen et al. 2021). This is consistent with the observations made with the geophone network. The emergent events are interpreted as surface events while impulsive events are more likely associated with ruptures. Ruptures can be due to fault ruptures of rocks (earthquakes) or may also be due to glacial processes. The precise locations of these events are not possible to determine due to the complex topography and unknown seismic velocity structure of the Meager complex. Beamforming of the signals showed that most events originate beneath the main peaks of the massif (Klaasen et al. 2021).

Tremor

The DAS system has exceptional capability to record low-frequency strain signals. While the environment at the deployment site was challenging and caused significant instrument drift, robust signals were extracted to 0.01 Hz. In this low-frequency portion of the signal, signals of extremely long duration (>10 hours) were observed throughout the recording period (Klaasen et al. 2021). The current hypothesis is that these signals are tremor associated with the geothermal system. However, the limited aperture of the array did not permit locating these events to date. More work is also required to distinguish tremors associated with magma and ice movements.

Summary and Future Work

The sound of rocks tumbling down the side of the mountain was a constant reminder during the installation and removal of the seismic network that the landscape around Mount Meager is highly unstable. The seismic sensors picked up several of these rock fall events, and they appear to have distinct signatures that distinguishes them from the earthquakes we recorded. Instead of exhibiting clear abrupt P- and S-waves arrivals, as observed for the earthquakes (Fig. 2), the rock falls show up as a much more emergent signal. Constraining the source of these low-frequency signals is an area of our ongoing efforts.

Our ongoing analysis is focused on examining the correlated signals in the ambient seismic noise recorded by the monitoring array. These correlated signals in the ambient noise possess information

about the structure of the subsurface and will allow us to constrain the sources of heat in the geothermal system.

Data

Our passive earthquake monitoring network recorded close to 650 Gb of three-component continuous seismic data during the summer and fall of 2019. In addition to the short-period Inova Hawks, that comprised much of the monitoring network, we also collected six weeks of broadband data at the DAS deployment location on the East ridge of Mount Meager. The 1-month DAS recording produced 1.7 TB of data on 370 channels along the 3-km fibre.

Peer-reviewed Publications

Klaasen, S. A., Paitz, P., Lindner, N., Dettmer, J., Fichtner, A., 2021, Distributed Acoustic Sensing in Volcano-Glacial Environments-Mount Meager, British Columbia, submitted to J. Geoph. Res. Solid Earth.

Conference Presentations

Dettmer, J., Gilbert, H., Grasby, S. E., Paitz, P., Fichtner, A., Flowers, G. E., Williams-Jones, G. (2019) A distributed acoustic sensing and geophone array to study the Mt. Meager Volcano, American Geophysical Union, Fall Meeting 2019, abstract S31A-06.

Gilbert, H., Su, H., Dettmer, J., Grasby, S. E. (2019) A novel nodal seismic investigation into the Mt. Meager geothermal system, American Geophysical Union, Fall Meeting 2019, abstract #T21F-0405.

Gilbert, H., Su, H., Savard, G., Dettmer, J. (2020) Geothermal prospecting – examining the structure of Mt. Meager, GeoConvention, Calgary Alberta.

Klaasen, S., Fichtner, A., Paitz, P., Dettmer, J. (2020) Distributed Acoustic Sensing for the Exploration of the Mount Meager Volcanic Complex, British Columbia, Canada, American Geophysical Union, Fall Meeting 2020, abstract S012-0019.

Klaasen, S., Paitz, P., Dettmer, J., Fichtner, A. (2021) Combining Distributed Acoustic Sensing and Beamforming in a Volcanic Environment on Mount Meager, British Columbia, EGU General Assembly 2021.

Klaasen, S., Paitz, P., Dettmer, J., Fichtner, A. (2021) Combining Distributed Acoustic Sensing and Beamforming in a Volcanic Environment on Mount Meager, British Columbia, Seis. Soc. Am. Annual Meeting 2021.

Citations

Klaasen, S. A., Paitz, P., Lindner, N., Dettmer, J., Fichtner, A., 2021, Distributed Acoustic Sensing in Volcano-Glacial Environments-Mount Meager, British Columbia, submitted to J. Geoph. Res. Solid Earth.

Winder, T., Bacon, C.A., Smith, J.D., Hudson, T., Greenfield, T. and White, R.S., 2020. QuakeMigrate: a modular, open-source python package for automatic earthquake detection and location. AGU Fall Meeting, 2020. Abstract# S38-0013.

Yoon, C., O'Reilly, O., Bergen, K. J., G. C. Beroza, 2015, Earthquake detection through computationally efficient similarity search, Science Advances, e1501057.

Zimmerman, Z., et al. "Matrix Profile XIV: Scaling Time Series Motif Discovery with GPUs to Break a Quintillion Pairwise Comparisons a Day and Beyond." Proceedings of the ACM Symposium on Cloud Computing. 2019.

Acknowledgements

The DAS project draws upon research supported by the Government of Canada's New Frontiers in Research Fund (NFRF). The field work was supported by OptaSense, in particular, Carson Laing, Jason France, and Martin Karrenbach. We are grateful to University of Calgary graduate students Jacquelyn Smale, Katherine Biegel, and Pejman Shahsavari who assisted in the deployment and removal of the seismic instruments. We thank Jeff Crompton (SFU/UAF) for carrying out steam drilling.

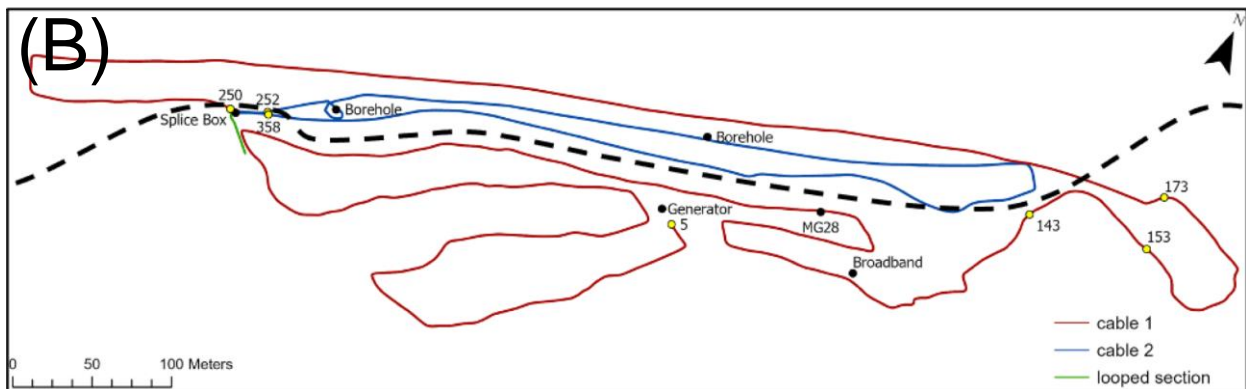
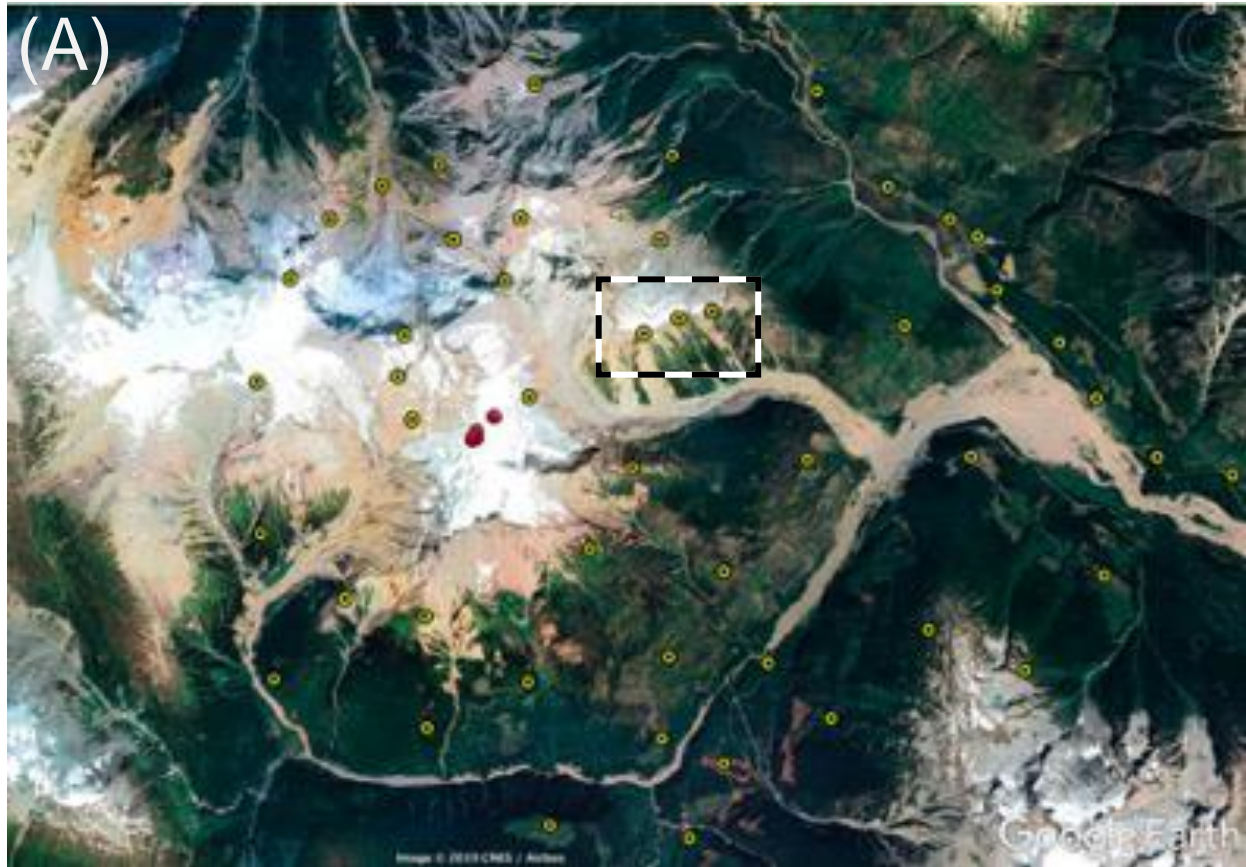


Figure 1. (A) Google Earth map of Mount Meager seismic stations (yellow circles) and some of the detected and located events (red dots) that occurred on July 13, 2019. The events appear to have occurred at a depth of just over 4 km. The dashed rectangle indicated the location of the DAS system. (B) The DAS system configuration consisting of 3-km optical fibre. The dashed line indicates the boundary between firn (top) and ridge (bottom).

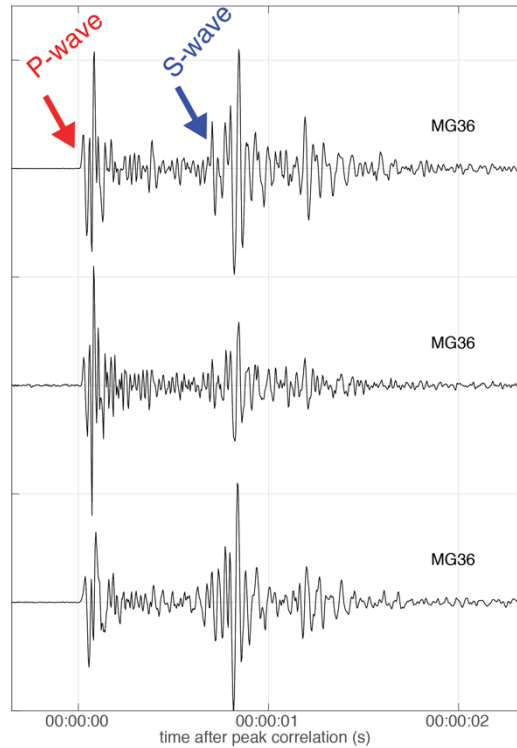


Figure 2. Seismograms illustrating repeating earthquake signals with impulsive onset from events that occurred on July 13, 2019. Example waveforms from a station near Job Glacier on the north side of Mount Meager. These well recorded events were located towards the central portion of the Mount Meager array (locations noted on Figure 1). The short time between the arrivals of the P and S waves exhibited on these waveforms (less than 1 s) support our findings that these are indeed local events and are located within the recording array.

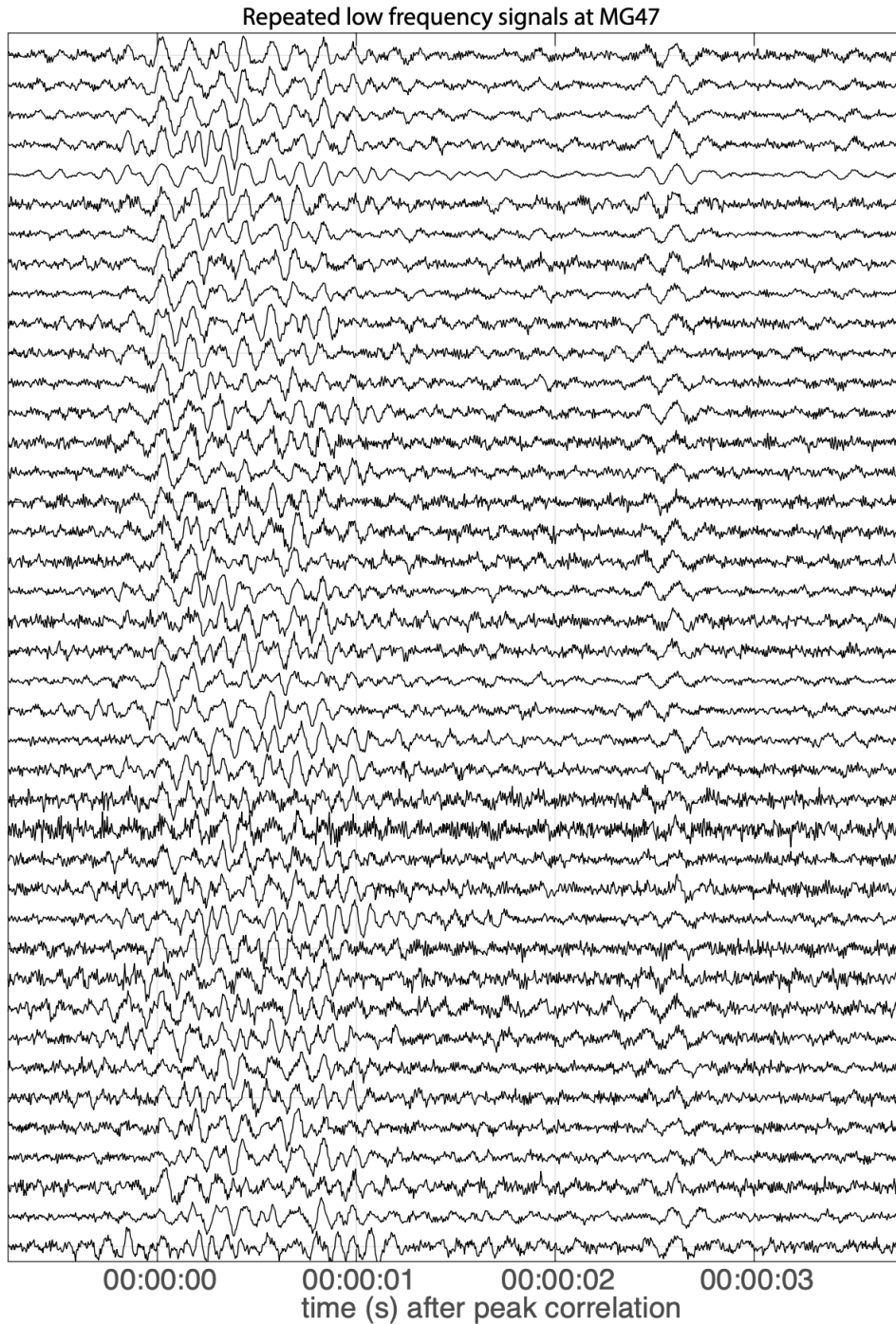


Figure 3. Example of several seismograms illustrating repeating low frequency (LF) signals from events that occurred during the deployment of the geophone array. Waveforms presented here were recorded by a station to the south of Job Glacier. The repetitive signals exhibit similar waveforms and emergent onset that possess pulses of energy that reach as long as three second. Note that the duration of these LF signals is a longer than the earthquakes presented in Fig. 2.

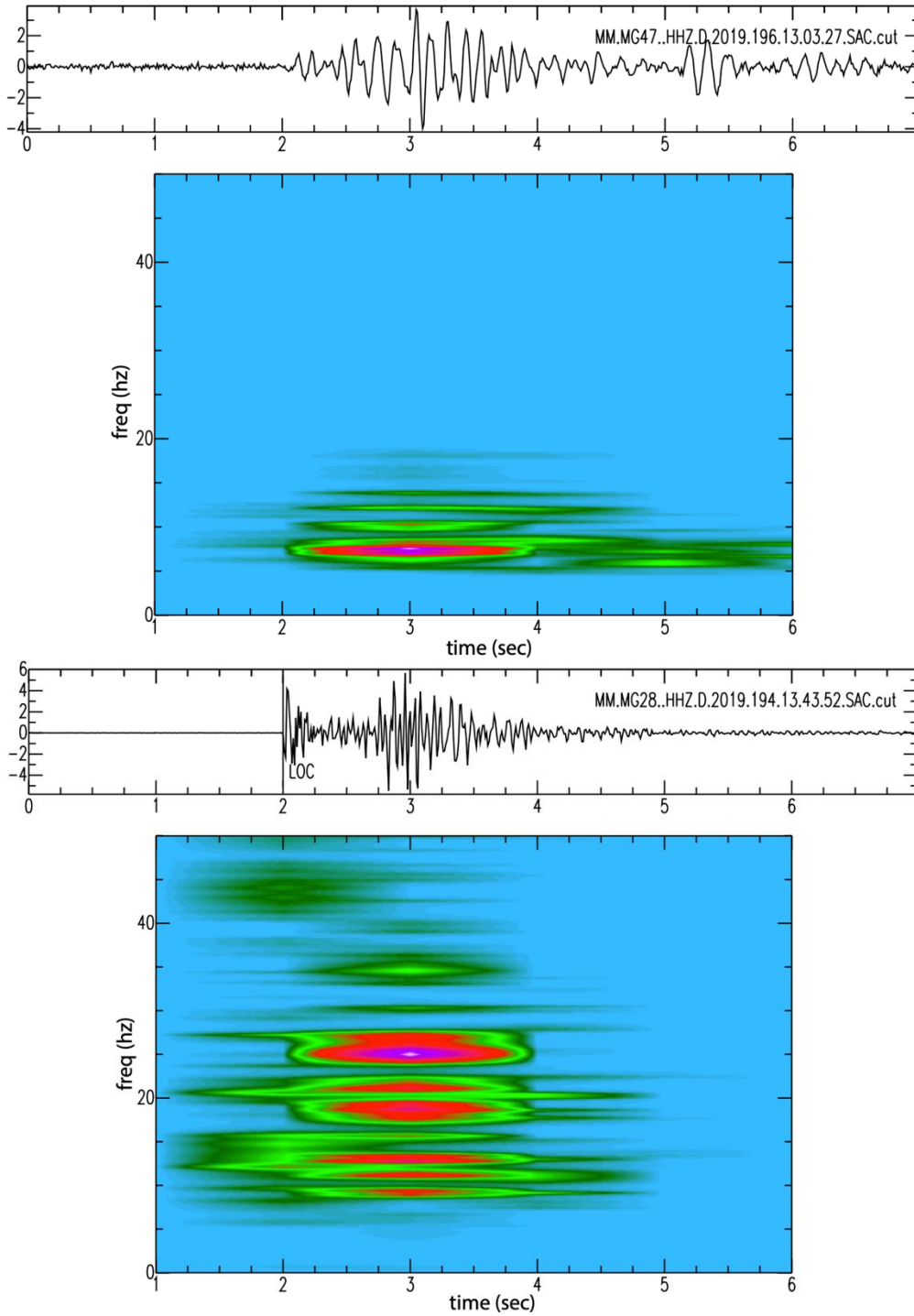


Figure 4. Clear differences in the spectral signal of the low frequency (LF) events (top) compared to the earthquake signals (bottom). The peak energy in the LF events on the left is between 5 and 10 Hz while the peak energy of the earthquakes is distributed over a broader frequency range between 10 and 30 Hz.

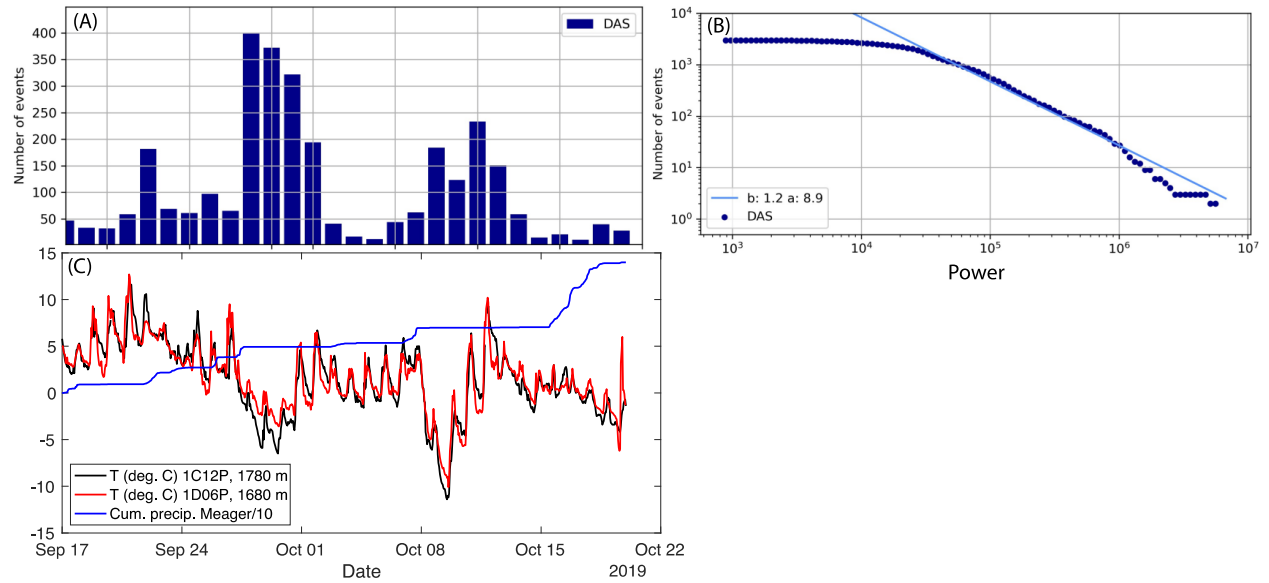


Figure 5. High-frequency events observed by the DAS system. (A) Number of events as a function of time, (B) frequency-power distribution indicating natural origin of the events, and (C), weather data from representative weather stations (weather data from the PCIC, pacificclimate.org).

Chapter 8- Applications of structural geology to the exploration of geothermal systems, Mt. Meager, BC

Mahmud Muhammad¹, Glyn Williams-Jones ¹, René W. Barendregt²

¹Department of Earth Sciences, Simon Fraser University, Burnaby, British Columbia, Canada

²Department of Geography and Environment, The University of Lethbridge, Lethbridge, Alberta, Canada

Introduction

Geothermal energy with its limited environmental impact is considered a particularly appealing energy source. However, development costs and large uncertainties regarding the presence of a good quality subsurface reservoir (e.g., sufficient geothermal heat storage and geothermal fluid pathways), can bring substantial economic risk. For instance, unproductive or failed boreholes can in fact negatively sway the economic plan. The usual mitigation steps for such uncertainties include evaluating reservoir capacity, zones of permeability, fracture, or fault patterns, which ultimately can reduce the exploration risk.

Various authors studied the role of structural geology in geothermal exploration (Philipp et al., 2007; Moeck, 2014; Filipovich et al., 2020; Liotta et al., 2021). The aforementioned studies all agree regarding the essential role of structural geology in maximizing the likelihood of a successful geothermal project; specifically, in reservoirs that require permeability enhancement (i.e., Enhanced Geothermal Reservoir Projects).

Philipp et al. (2007) studied the influence of structural geology and particularly the role of constraining the stress field to simulate an enhanced geothermal system in Buntsandstein, northern Germany. They found that the stress field controls the fault slip and fluid transport. Hence, the stress field can determine if and how fractures propagate or if fractures are opened rather than closed. For instance, if the maximum horizontal compressive stress becomes parallel to the strike of the fractures; fractures tend to open and thus fluid transport is enhanced. Alternatively, if the maximum horizontal compressive stress is perpendicular to strike of the fractures, various fractures may close reducing fluid transport. Therefore, it is important to understand the major geologic structures and timing of the latest tectonic activity that shaped the subsurface geothermal reservoir. This will help to assess not only the reservoir quality but also define the geothermal fluid pathways.

The Mount Meager Volcanic Complex (MMVC) comprises the northern most volcanic centre of the Garibaldi Volcanic Belt (GVB) (Fig. 1). MMVC contains basement complex and young volcanic rocks. The basement complex includes older unknown age high-grade metamorphic rocks, late Triassic Cadwallader group, late Jurassic to late Cretaceous intrusive rocks, late Cretaceous sedimentary rocks of the Gambier group and Paleogene to Miocene intrusive rocks (Fig. 2). The young volcanic rocks were emplaced during three different stages (Read, 1990): 1) Pliocene to Pleistocene rhyodacite (2-1 Ma); 2) early Pleistocene to late Pleistocene dacite to andesite-basalt (1-0.3 Ma); and 3) Late Pleistocene to Holocene and recent rhyodacite to dacite composition (0.3-0 Ma).

During the last >1.9 Ma, volcanic eruptions at Mt. Meager become younger from south to north, and a relatively young east-west striking extensional fault has been mapped along Meager Creek. The existence of this fault is well-documented through bedrock exposure mapping, fracture data, drilled core and refraction seismic data (Fairbank et al., 1980, 1981). Although, the Meager Creek fault zone is mapped as an extensional fault, the presence of mylonite found in drill holes suggests a compressional component (Fairbank et al., 1980, 1981). This may indicate the Meager Creek fault zone experienced multiple episodes

of deformation. In general, three types of faulting have been identified at Mt. Meager and include those related to tectonic stress such as the Owl Creek Fault (Fig. 2), faults related to volcanism, and faults related to mass creep and gravitational failure (Fairbank et al., 1980, 1981). For geothermal exploration, the most important structures are those controlled by regional tectonics followed by fault structures related to volcanism and they can play a major role in facilitating pathways for geothermal fluids.

Geologic mapping, seismic section profiles and Bouguer gravity modelling (Bustin et al., 2013) (Fig. 2) ~15 km south-southeast of Mt. Meager suggest that the Owl Creek Fault may have been active during the emplacement of at least the Miocene granitic intrusions (e.g., Salal Pluton; Fig. 2; also see Fig. 12 that shows the proximity of Owl Creek Fault to the North Lillooet ridge). We therefore need to understand the kinematic history (whether magmatism was emplaced syn or post tectonic deformation) and the kinematic compatibility (whether the current deformation or faulting is geometrically compatible) with the different periods of magmatic emplacement.

The aim of this work is to document the major structural geology features controlling the geothermal fluid pathway through 1) classic structural field geology mapping of faults, folds, and fractures of basement and young volcanic units (summer 2019 field work); 2) Paleomagnetic directions of basement and young volcanic units (summer 2020 field work); and 3) Geochronological dating for the drilled paleomagnetism samples to reconstruct the displaced structural geology features and define sequence of events (in progress); at this stage we use published geochronology age dates from (Woodsworth, 1977; Read, 1990) as well as, ages of paleomagnetic polarity (Fig. 9; Table 1).

Structural geology field mapping is the base and complementary tool for other geologic and geophysical exploration techniques. This is especially important in industries that require drilling deep exploration and production wells such as hydrocarbon and geothermal exploration. Structural studies can provide knowledge about the surface projection of subsurface fracture system which is essential to determine the efficiency of the geothermal fluid pathway. Additionally, it helps minimize the drilling risk through understanding the fault system and sequence of deformation of the bedrock that hosted the geothermal system.

Paleomagnetic directional data can be used to determine displacement, rotation and/or tilting of fault blocks. This technique is more convenient and accurate where structural data can be measured such as in sedimentary rocks. However, its application becomes more difficult in basement rocks where accurate bedding measurements are not feasible. A more detailed explanation of paleomagnetism techniques as it applies to structural geology and petrophysics can be found in the literature (Beck et al., 1986; Enkin, 2003; Butler, 2004; Richards et al., 2004a, 2004b). Here we carried out a pilot paleomagnetic study of the structural units of importance in the Mount Meager geothermal study.

The work in the MMVC involved: 1) obtaining post-deformational paleomagnetic directions and comparing these with the expected Geocentric Axial Dipole (GAD) field direction for the sampling latitude, and 2) establishing the age of measured geomagnetic polarities. Furthermore, radiometric dating of young volcanic rocks (Chapter 2) assisted in identifying displaced fault blocks and making assumptions about their reconstruction to a pre-deformation stage.

Methods and data collection

In this study, we conducted two years of field campaigns during summer 2019 and summer 2020. During the summer of 2019, further exploration of Mount Meager's geothermal potential was initiated with two weeks of geology field mapping, north of Mount Meager on the northern Lillooet ridge. We mapped both young volcanic rocks and basement rocks and collected structural data such as faults, folds, fractures, and attitude of bedding and planar features. During the summer 2020, we conducted additional field

campaigns which included a paleomagnetic study of young volcanic rocks with the goal of constraining and verifying whether tilting and/or rotation within basement rocks predates or postdates the youngest Quaternary volcanism within MMVC. Additionally, four rock samples have been sent to the Geochronology lab at Oregon State University (USA) in order to enable a better differentiation between fractures and faults related to volcanism, and those controlled by regional tectonics.

Summer 2019 structural geology mapping on North Lillooet Ridge

The Mt. Meager terrain is extremely rugged, covered by thick forests and vegetation at lower elevations and steep and unstable topography at higher elevations. Helicopter support was used to access remote locations, which helped extend the mapping. The mapping campaign produced 846 GPS site locations at which data were collected including: outcrop descriptions, contact relationships, sample locations, and structural measurements (e.g., foliations, fault orientations, etc.). Our structural geology mapping included two areas outside the bounds of the Read (1979) map: North Lillooet Ridge (Fig. 3A, B) and Southwestern Meager (Fig. 3B).

The 2019 mapping was conducted concurrently with the bedrock mapping by Harris et al. (2020); and designed to inform on the subsurface rock types and structures underlying the MMVC and to better characterize the peripheral volcanic centres. To do this we traversed the terrain by foot, locating outcrops, recording lithological field descriptions, collecting samples, taking structural measurements, and following discernable unit contacts. We spent six weeks mapping in the field, compiling rock measurements, descriptions, and samples.

Classic structural geology techniques were used including plotting attitude of structures on stereonet, analyzing structural trends, and spatial correlation between rock units versus structural features including fractures/veins, faults, folds, and the attitudes of basement and young volcanic units. We also considered syn- (i.e., intrusion and extrusion) and post- (i.e., faulting, mass movement, and glaciation) depositional processes. The data and field observations were used to study the potential kinematic compatibility of the mapped structures: 1) relative to spatial and cross-cutting relationship of structures such as faults, folds, and attitude of rock units, and 2) relative to the modern regional tectonic trend within Garibaldi Volcanic Belt including the Mount Meager Volcanic Complex.

Our fieldwork employed various field tools such as the Fieldmove Clino mapping application for recording bedding, joint and fracture orientations, dike trends and dips, and fault slickensides. Additionally, Gaia GPS was used to pinpoint site and sample locations with detailed tagged descriptions for each locality. Both field technologies enabled the efficient transfer of field data to laboratory computers.

Summer 2020 Paleomag

Samples for paleomagnetic analysis were collected from both basement and younger volcanic rocks at two ridges, the east Lillooet ridge and west Lillooet ridge north of the Mt. Meager massif. A portable gasoline-powered rock drill with water swivel attachment was used to drill 2.5 cm diameter cylindrical cores. Due to time and budget limitations, five sites were initially chosen for this pilot study. Eight cores were collected at each site over an area of 5-10 m to reduce the potential errors from lightening or minor local movements along joints, etc. Additionally, all samples were oriented using both a solar and magnetic compass to preclude orientation error due to compass deflection by strongly magnetized rocks at the outcrop. The samples were analyzed at the paleomagnetic laboratory of the University of Lethbridge, Alberta. Magnetic susceptibility was measured with a Sapphire Instruments (SI-2B) susceptibility meter. The magnetization of each sample was measured with an AGICO JR-6A spinner magnetometer prior to demagnetization and again after each level of stepwise demagnetization. Samples were kept in magnetic shields following field collection and between laboratory measurements. Most samples were subjected

to alternating field demagnetization with one-third of the collection subjected to thermal demagnetization. Alternating field demagnetization was performed using an ASC Scientific D-2000 demagnetizer with a three-axis manual tumbler and carried out at 10 milli-tesla (mT) steps (up to 100 mT).

Thermal demagnetization was carried out at 100, 200, 300, 400, 500, and 550 °C, using an ASC Model TD48 dual-chamber thermal demagnetizer to determine whether or not alternating field demagnetization was sufficient to resolve the primary remanence. AF Demagnetization was sufficient to resolve the primary remanence for most samples but for basement rocks (granodiorites), thermal demagnetization was required. Directions of characteristic remnant magnetization were determined for each sample by principal component analysis (Kirschvink, 1980) using Remasoft version 3.0 (Chadima and Hroudá, 2006). Mean characteristic remanent magnetization directions were calculated for each site and an overall mean was also calculated.

North Lillooet Ridge Structure

The main structural feature observed was the presence of a potential major E-W striking strike-slip fault between the western and eastern ridges (Figs. 3A, C). It is difficult to constrain the timing of deformation and/or timing of strike-slip movement due to the lack of clear offset of the young volcanic rocks. However, an approximate age based on the presence of other kinematic indicators mapped on both ridges can be provided. The kinematic indicators include bedding attitudes, minor folds, faults, veins and joints, and spatial relationship between outcrops of intact volcanic rocks and displaced volcanic rocks.

East Lillooet Ridge Structure

On the eastern ridge, two faults were mapped – the first is an ~ 33-m-long left-lateral strike-slip fault, striking E-W with a few metres of offset. The second fault, cut by the first, is ~300-m-long striking NS, with signs of multiple deformation events including normal, reverse and strike-slip. Additionally, nine minor folds were mapped, mostly trending in the E-W direction except for one minor fold trending NE-SW (Fig. 4). Three sets of joints/fractures were mapped striking NW-SE, E-W, and NNE-SSW. The overall strike of beddings of the basement rocks are E-W and ENE-WSW (Fig. 4). Spatially, the 300-m-long N-S striking fault appears to cut through the young volcanic rocks. However, the fault surface predominantly crops out at the centre of the ridge and ends at the north side between the beginning of intact young volcanic rocks and most likely displaced volcanic rocks; the fault surface outcrops further south in an area covered with air-fall pumice deposits (Fig. 4).

West Lillooet Ridge Structure

On the western ridge, four minor faults (two fault set) were mapped from the far west to the centre close to eastern ridge, striking NNE-SSW (reverse), NE-SW (normal), NE-SW (reverse), and NE-SW (reverse), respectively (Fig. 5). Additionally, two minor folds were mapped trending N-S and NNE-SSW. Also, three sets of joints and veins were identified in the field striking NNW-SSE, NE-SW and ENE-WSW (Fig. 5). In general, three striking trends were identified for the beddings of basement rocks on the west ridge include NNW-SSE, NE-SW and ENE-WSW (Fig. 5). The ridge mostly consisted of older basement rocks except the W and SSW face of the ridge crops out at least three different volcanic units including rhyodacite at the top of cliff, and basaltic-andesitic at the slope below the cliff and dacite at the western most part of the ridge which underlays Quaternary alluvium deposits (Fig. 10). The most important lithologic feature is the presence of at least two brecciated units within the basaltic-andesitic unit. The first breccia unit, which lies topographically above the second brecciated unit, includes mixed clasts of young volcanic units and older basement rocks.

Southwest Meager structure

The structural data recorded in the field include bedding of basement units, joints, fractures, veins and fault and fold data. Relative crosscutting relations were interpreted in the field where feasible. We cannot assign timing of deformation for the rock units due to lack of age constraints of the different basement rocks. Instead, a relative timing of deformation based on the kinematic compatibility of the crosscutting relationship was assigned to different structural features. Two major sets of joints/veins, striking NE-SW and ENE-WSW, and a few NW-SE striking veins have been identified in the field (Fig. 6). The NW-SE striking veins, where found, cut the major sets striking NE-SW and ENE-WSW (Fig. 8). Different types of faulting were mapped including reverse, oblique-slip normal and strike-slip. The faults strike NS, NE-SW and NW-SE, respectively.

Structural geology Synthesis

Tectonically, the Garibaldi Volcanic Belt (including the MMVC), coincides with Coast Plutonic Belt uplift and was produced by episodic accretion of multiple plates. The most recent tectonic phase includes the late Cenozoic subduction of the Juan de Fuca plate beneath the continental margins of SW British Columbia and northwestern Washington. This was later accompanied by Neogene-Quaternary volcanism and formed the NW-SE trending Garibaldi Volcanic Belt (Fig.1). Additionally, the GVB has recognized geothermal potential (Ghomshei et al., 1986, 1992, 2004, 2005; Arianpoo, 2009) and thus understanding the natural hazards, tectonic evolution and their influences on the quality of the geothermal activity is essential.

The current regional maximum horizontal principle stress within the Coast Plutonic Belt and the GVB is approximately ENE-WSW (Leonard et al., 2010; Balfour et al., 2011), perpendicular to the Juan de Fuca and SW BC subduction front (Fig.1). Thus, we can expect that trends of regional compressional structures such as the folds and reverse faults within the MMVC should be compatible with the regional horizontal maximum stress; possibly NNW-SSE trending structures.

Considering the proximity of Mt. Meager to the Nootka Fault, stress partitioning between the interaction of Juan de Fuca and North American plates and Explorer and North American plates should be recognized (Fig.1). The subduction rate between Explorer plate and the North American plate is less than that of the Juan de Fuca and North American plates (Riddihough and Hyndnan, 1976) and could lead to spatial and temporal stress partitioning. This may lead to volume change of discrete basement blocks through transpression (tri-axial deformation in the case of temporal stress partitioning or pure shear deformation during spatial stress partitioning) or rotation of discrete basement blocks (for simple shear deformation) (Fig.7) (Muhammad, 2016). In either case, it influences the style and geometry of fracture patterns and consequently the flow of subsurface hydrothermal fluids, basement rock stability, and the stability of any shallow magmatic systems. Considering the regional horizontal maximum stress direction, the major regional compressional structures such as folds should trend approximately NNW-SSE to satisfy the kinematic compatibility; major compressional faults should strike parallel to the trend of the folds (Fig.7) (Muhammad, 2016).

North Lillooet Ridge Structural Synthesis

The potential major left-lateral strike-slip fault structure between the western and eastern Lillooet ridges strikes roughly E-W (Fig. 3). On the western ridge, one normal and three reverse faults strike NNE-SSW and NE-SW, oblique and perpendicular to the strike of the strike-slip fault. Additionally, two minor folds trend N-S and NNE-SSW, oblique or perpendicular to the strike of the strike-slip fault (Fig.5). This spatial and kinematic distribution agrees with the strike-slip model. On the eastern ridge, the 300-m-long N-S striking fault has a fault surface with dip direction that alternates between east and west direction along strike (Fig. 4d). This fault is cut and offset a few metres by a 33-m-long E-W striking fault. The fault offset

in the field indicates a left-lateral strike-slip fault. Additionally, 8 minor folds, trend E-W and 1 minor fold trends NE-SW.

The kinematic relationship between these structures relative to the major strike-slip fault is as follows: 1) the 300-m-long N-S striking fault is kinematically compatible with the regional maximum horizontal stress direction and the presence of a strike-slip fault between west and east ridges; 2) the 33-m-long E-W striking strike-slip fault is also compatible kinematically with other structures and may be considered as a strand of the major strike-slip fault between the east ridge and west ridge; 3) the NNE-SSW trending minor fold, being oblique to strike of the major strike-slip fault, is also kinematically compatible with the strike-slip model; although, The two minor folds on the western ridge (see figure 5B show more northerly trend of NNE-SSW direction)) should have a fold axis orientation (trend) NW-SE. But as it explained could have been affected by the possible rotation of the fault blocks and possible subsequent deformation stages. 4) the other 8 minor folds trending E-W are not kinematically compatible with the other structures and thus not compatible with the modern regional horizontal stress direction (Figs. 4A; 7A). This inconsistency may be due to the rate of uplift, direction of modern plate movement within SW BC, and most importantly, movement of individual basement blocks in the region. The Garibaldi Volcanic Belt is tectonically active with very high rates of uplift (Parrish, 1982; Ryder et al., 1991; Roberti, 2018).

The presence of normal and reverse dip-slip slickenlines along a single fault surface (300-m-long N-S striking fault) may suggest the influence of glacial unloading. Our mapping of the attitude of basement beddings between the western ridge and eastern ridge (both ridges are less than 5 km apart) shows more than 50° change in strike (Figs. 4, 5); this suggests either tilting of basement units due to glacial unloading or basement block rotation. While this data is insufficient to constrain rotation of individual basement blocks, the change in strike orientation of the basement units along with the strike-slip structure makes basement block rotation feasible. Therefore, we consider that the inconsistency in the trend of the minor folds on the eastern ridge may be related to tilting of basement blocks due to glacial unloading and perhaps rotation of individual basement blocks. However, to confirm this, we would need to study paleomagnetic inclination of young volcanic rocks to validate any rotation of basement blocks as well as define timing of rotation.

Southwest Meager structural synthesis

A geometrical relationship between bedding of the units and minor folds indicates the presence of a major fold (trending NNW-SSE) (Fig. 6B) within the SW contact of the MMVC. Although we lack stratigraphic evidence, we have assigned this fold to be an anticline based on the patterns and geometry of the minor folds (S-shape, M-shape, and Z-shape minor folds) at the limbs of major fold (Figs. 8). Geometrically, buckling within compressional systems can define deformation history and thus aids in identifying the hinge zone and limbs. For example, in the case of an anticline, Z-folds represent the left limb, S-folds represent the right limb and M-folds indicate the hinge zone (Fig. 8). The coincidence of the fold hinge area with a paleo-glacial valley and the cross-cutting relationship between veins within the major fold hinge zone may indicate that the fold crest has undergone possible erosion by glaciation and outer arc extension (collapse) presumably due to glacial unloading (Fig. 8). Within the major fold hinge zone, an ESE-WNW striking vein cuts the NE-SW and ENE-WSW striking veins (Fig. 8). Thus, the ESE-WNW striking set must postdate the formation of folding. In general, three sets of faults were identified within southwest contact of Mt. Meager: 1) a reverse fault, which roughly strikes NS (Fig. 8); 2) a NE-SW striking normal fault (Fig. 8B) and 3) an approximately NW-SE striking fault with major strike-slip component (Fig. 10a). Adjacent to the NW-SE striking strike-slip fault with a few metres of lateral offset, a ubiquitous (possibly Quaternary age) NE-SW striking fault scarp (possible normal) is mapped (Fig. 8). Strike-slip and normal faults of southwestern Meager have similar structural trends with strike-slip and normal faults on

the North Lillooet Ridge; both are most likely related to structural collapse due to glacial unloading and movement between individual basement blocks.

Paleomagnetic study and Discussion

The North Lillooet ridge includes basement rocks such as granodiorite as old as 47 to 55 Ma, mostly outcropping on the western ridge (Fig. 1) and pink granitic rocks as old as 8 Ma (possibly Salal pluton), outcropping on the eastern ridge (Woodsworth, 1977). Additionally, younger undated basaltic and andesitic lava occur on the eastern ridge and dacite, rhyodacite and andesite lavas are located on western ridge. Although the younger lava on the North Lillooet ridge is not yet dated, the ages indicated on the regional geology map for the young volcanic lava (Woodsworth, 1977; Read, 1990) on Mt. Meager suggest ages of < 2 Ma as follow: 1) Pliocene to Pleistocene rhyodacite (2-1) Ma; 2) early Pleistocene to late Pleistocene dacite to andesitic-basalt (1-0.3) Ma; and 3) Late Pleistocene to Holocene and recent rhyodacite to dacite composition (0.3-0) Ma. Hence, the expected age range for the young lava at North Lillooet ridge should lie between 2 Ma to 0 Ma.

Sites 1, 2, 3 and 4 are stably magnetized (Fig. 10). Sites 1-3 are reversely magnetized and given the suggested ages, would fall within the Matuyama Reversed Chron. Site 4 is normally magnetized, and given its suggested age, falls within the Brunhes Normal Chron. Site 5 does not provide a reliable directional mean following AF demagnetization. It is weakly magnetized, and exhibits a soft, multi-domain remanence upon AF demagnetization. Two samples were thermally demagnetized and show a stable component between 400-550°C (See Appendix). More samples will need to be collected for thermal demagnetization. Hence, site 5 is excluded, pending further sampling.

While absolute ages are not yet available for these paleomagnetic sites, approximate ages for the samples based on the dated rocks nearby (Woodsworth, 1977; Read, 1979, 1990), as well as outcrop field relationships and polarity data allow for some preliminary estimates. Sites 1 and 2 collected on the eastern ridge in the andesitic lava are reversely magnetized; they are thought to be associated with the nearby andesitic lavas of similar chemistry which have an age range of 0.78-0.9 Ma or 1.06-1.78 Ma and therefore sites 1 and 2 fall within the Late Matuyama reversed Chron (1.78-0.78 Ma). These two sites may show a slight rotation of approximately 10 to 20 degrees anticlockwise, although it is not impossible that secular variation may account for this southeasterly declination (Fig.10; Table 1). Site 3 samples are from the pink granite basement rocks on the eastern ridge and are reversely magnetized. Based on field observations, this site is tentatively correlated to the Salal pluton (8 Ma). Similar to sites 1 and 2, site 3 shows a possible anticlockwise rotation of 10-20 degrees (Fig. 10; Table 1). However, given the nearly identical directions of Sites 1 to 3 and the proximity of site 3 (basement rock) to sites 1 and 2 (andesitic lava), it is possible that the basement rocks were thermally remagnetized (reset) by the eruption of the andesitic lava.

Site 4 samples collected on the western ridge in the dacitic lava reveal normal geomagnetic polarity. The nearby dacitic lavas have age ranges of 2-1.78 Ma or 0.3-0 Ma. Unlike other sites, this site does not show any rotation but does show significant tilting (shallowing of the paleomagnetic inclination by approximately 30 degrees northward) (Fig. 10; Table 1).

The preliminary paleomagnetic data (including possible rotation and significant tilting) is compatible with the presence of a suggested left-lateral strike slip fault between the west and east ridges at the North Lillooet ridge, north of the Mt. Meager massif (Fig. 3). The western ridge which shows no rotation, but significant tilting (~30° northward), resembles the footwall of the fault; and the eastern ridge which may show approximately 10-20° anticlockwise rotation to the east, resembles the hanging wall of the fault. The current paleomagnetic data, along with the structural geologic fieldwork including cross-cutting relationships of faults with the basement and younger lava flows, indicates that both dacitic and andesitic

lava flows on the North Lillooet ridge either predate faulting or were emplaced during faulting. Therefore, Mt. Meager, more specifically, North Lillooet ridge was tectonically active at least between 300-700 ka or between 2-1.2 Ma. These dates will be refined once we receive results from the geochronology analyses. Our data compares favorably with the regional geology map (Bustin et al., 2013; Fig. 2) which suggests that young volcanic rocks become younger from south to north on Mt. Meager.

The most distinctive regional tectonic fault is the Owl Creek fault. The mapped crosscutting relationships and position of metamorphic rocks (unknown age, unit m on Fig. 2) are of various ages, i.e., units Eg (55 to 45 Ma) and unit Czg (37 to 8 Ma) and this likely suggests that the Owl Creek fault was active on several occasions between 55 Ma to 8 Ma. Additionally, the tilting and rotation of basement and young volcanic rocks was most likely controlled by a newer fault strand of the Owl Creek fault and movement on the left-lateral strike slip fault between the east and west ridges of North Lillooet Ridge. In conclusion, potential geothermal fluid pathways, at least north of the Mount Meager Volcanic Complex, are likely to be controlled by the kinematics of the Owl Creek fault and the mapped left-lateral strike-slip fault between the east and west ridges of North Lillooet ridge, north of the Mount Meager massif (Figs. 2, 3, 4 and 5).

Summary and Results

In summer 2019, we carried out an intense two weeks of field geology mapping, north of Mount Meager, at the northern Lillooet ridge. We also mapped a small part of southwestern contact of Mount Meager, adjacent to Peter Reads (1990) geology map. We mapped both young volcanic rocks and basement rocks and collected structural data such as faults, folds, fractures and attitude of beddings and planar features. Interpretation of our data on the North Lillooet ridge indicates the presence of major strike-slip movement, at least two stages of deformation, and basement block tilting or potential basement block rotation. Strike-slip and normal faults of southwestern Meager has similar structural trends with strike-slip and normal faults on the North Lillooet ridge.

In summer 2020, paleomagnetic samples were drilled at the following five sites (Fig. 10): On the eastern ridge, site 1 and site 2 were drilled on the undated andesitic lava, with site 1 stratigraphically located above site 2; site 3 was drilled on pink granite basement rock which was in sharp contact with the andesitic lava. On the western ridge, site 4 was drilled on the large vertically jointed dacite lava flow; site 5 was drilled on older basement granodiorite rocks.

To summarize, we can list results of this work in the following points:

1. This field geology data, including outcrop scale, structural geology (faults, folds, joints, and attitude of basement units) mapped on the north Lillooet Ridge, north of the Mt. Meager massif indicate the presence of an E-W striking left-lateral strike-slip fault between east and west ridges at North Lillooet Ridges. Although, the two minor folds on the western ridge (see figure 5B show more northerly trend of NNE-SSW direction)) should have a fold axis orientation (trend) NW-SE. But as it explained could have been affected by the possible rotation of the fault blocks and possible subsequent deformation stages
2. Our preliminary paleomagnetic directional study for the young volcanic rocks (between 2 Ma to 0 Ma) agrees with the presence of a left-lateral strike slip fault and suggests an anticlockwise rotation of approximately 10 to 20 degrees on the eastern ridge and more than 40 degree tilting on the western ridge (Table 1 and Fig. 11).
3. The current paleomagnetic data, along with the structural geologic fieldwork including cross-cutting relationships of faults within the basement and younger lavas, indicates that both dacitic and andesitic lava flows on the North Lillooet ridge either predate faulting or were deposited during faulting.

4. If our preliminary pilot paleomagnetic results are accurate, Mt. Meager, and more specifically, North Lillooet ridge, was tectonically active at least between 300-700 ka or between 2-1.2 Ma.

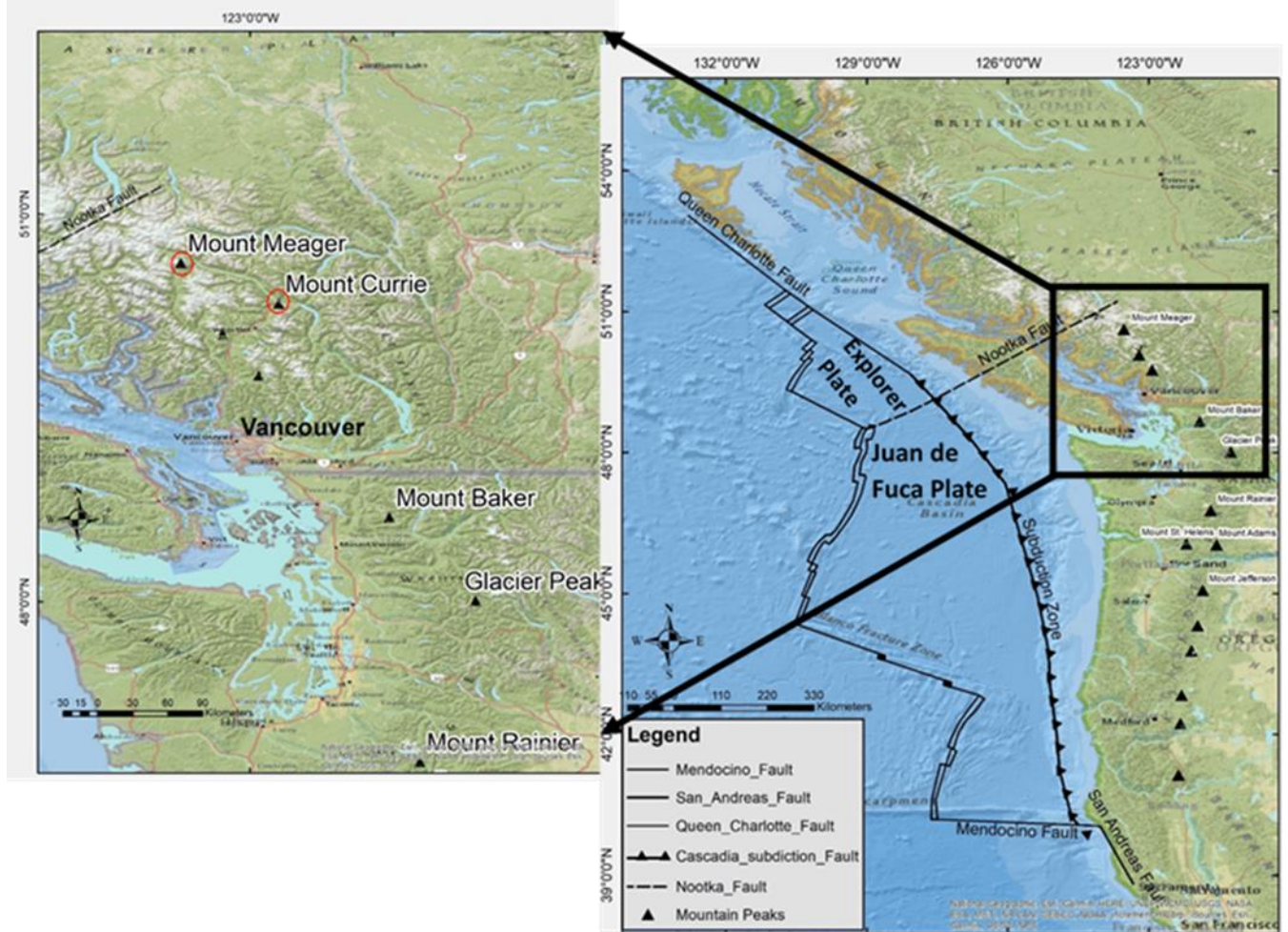


Figure 1. Regional Tectonic Map of US and Canadian segments of the Cascade Volcanic Arc (Leonard et. al 2010). Note change of plate boundaries starting from northern California to the northern Garibaldi Volcanic Belt (GVB), north of Mt. Meager. The age of subduction changes from 10 Ma south of GVB below Glacier Peak to 5 Ma beneath Mt. Meager the northern most part of the GVB.

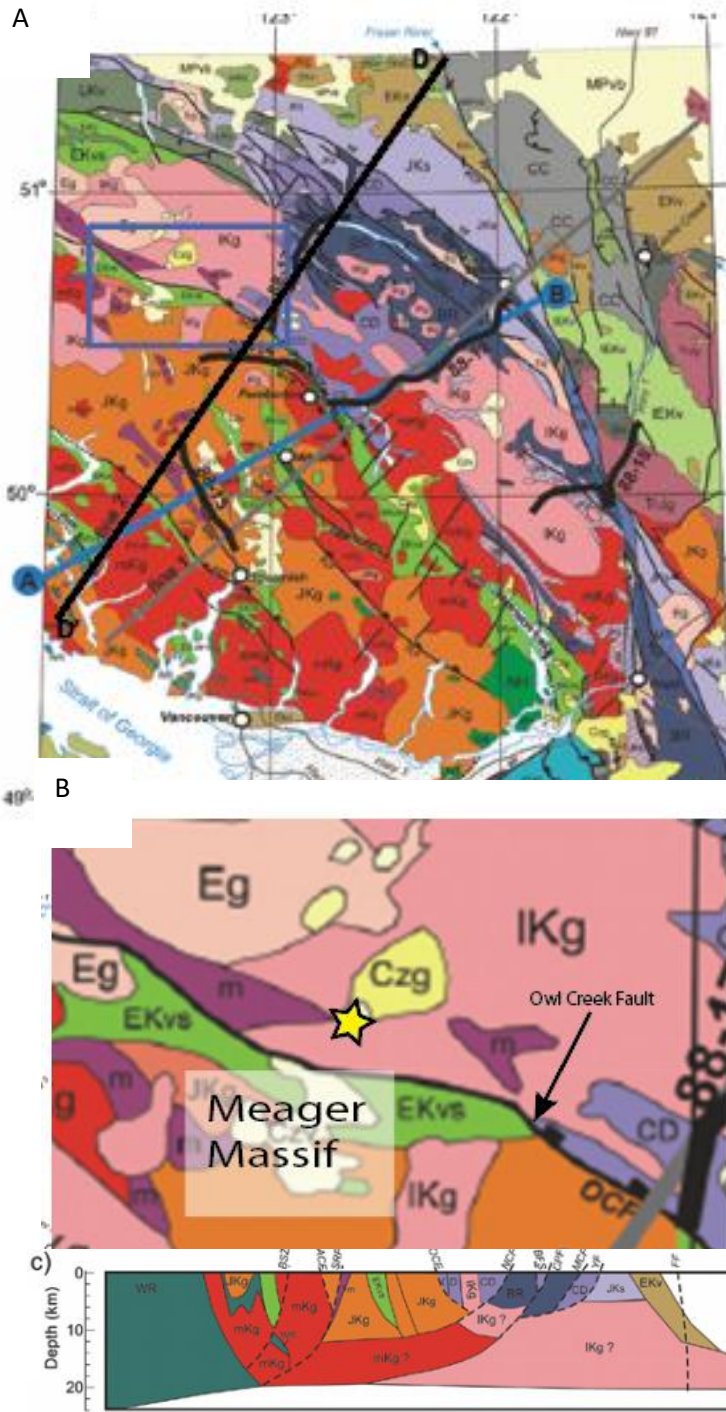


Figure 2. A) Geology of the southern Coast Mountains and surrounding areas (after Bustin et al., 2013). B) Subset showing Mt. Meager geology and Owl Creek Fault. EKvs: Lower Cretaceous Gambier group; CD: Cadwallader Group; Czg: Plutonic rocks (37 to 8 Ma); m: protolith unknown (metamorphic rock); Eg: Plutonic rock (55 to 45 Ma); IKg: plutonic rocks (85 to 65 Ma). Note: juxtaposition of CD to EKvs indicate that OCF must be active prior to or coeval with the Miocene intrusions. C) Bouguer gravity modelling along line D-D' (from Bustin et al., 2013). The yellow star represents approximate location of North Lillooet ridge

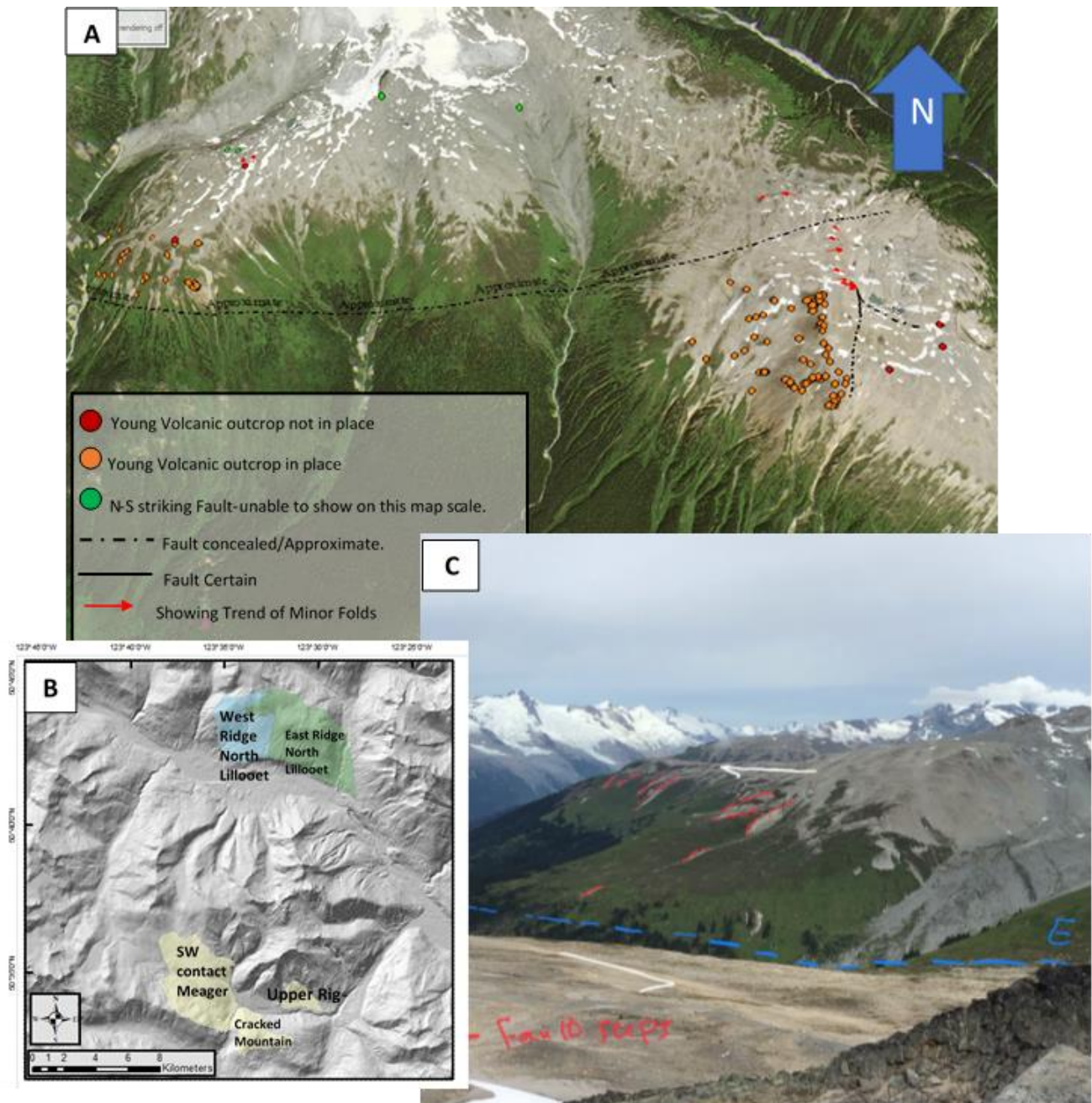


Figure 3. A) 3-meter PlanetScope satellite image draped over 1.5 m Digital Elevation Model (from historical aerial photos); orange dots represent outcrops of coherent young volcanic rocks; red dots represent outcrops of young volcanic rocks which most likely not in place; green dots represent locations of N-S striking minor faults on the western ridge; red arrows represent trend of minor folds; solid lines represent certain faults; dash-dot lines represent concealed-approximate fault trace. B) Map shows Locations of field mapping. C) Field photograph showing the patterns and geometry of fault steps. Note the geometry and arrangement of the fault steps indicate a left-lateral movement of the fault.

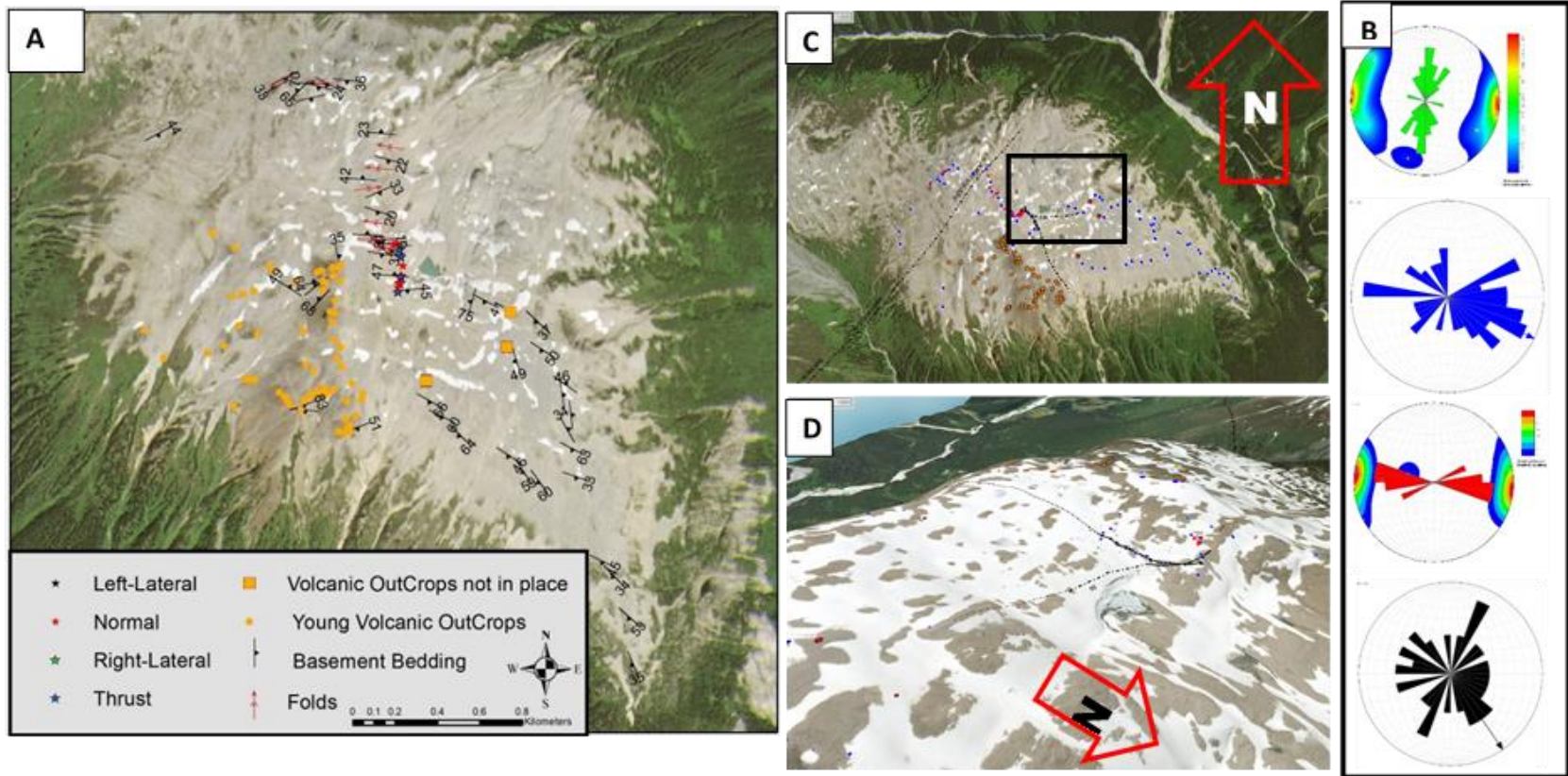


Figure 4. A) Geology Map of Eastern ridge of Northern Lillooet Ridges show: Outcrops of young volcanic rocks, older basement rocks and location and type of faults on the west ridge. Orange dots represent outcrops of young intact volcanic rocks; orange-square shapes represent outcrops of non-intact young volcanic rocks; black dots represent outcrops of older basement rocks. B) Stereographic plot of structural data of eastern Ridge; green, shows strike orientation of faults; blue, strike orientation of basement beddings; black strike orientation of joint, fractures and veins; red trend of minor folds. Stereographic Contours show the density of the data per cluster for poles of strike of structural features such as fault, joints/fractures and beddings. C) 3 m Planetscope satellite image draped over 1.5 m DEM; orange dots represent outcrops of coherent young volcanic rocks; red dots represent outcrops of young volcanic rocks which most likely not in place solid lines represent certain faults; dash-dot lines represent concealed-approximate fault trace. D) A 3D view constructed from draping 30 cm World imagery over 1.5 m DEM; notice the spatial relationship and topography between outcrops of coherent young volcanic and outcrops of young volcanic most likely not in place relative to the mapped fault structures.

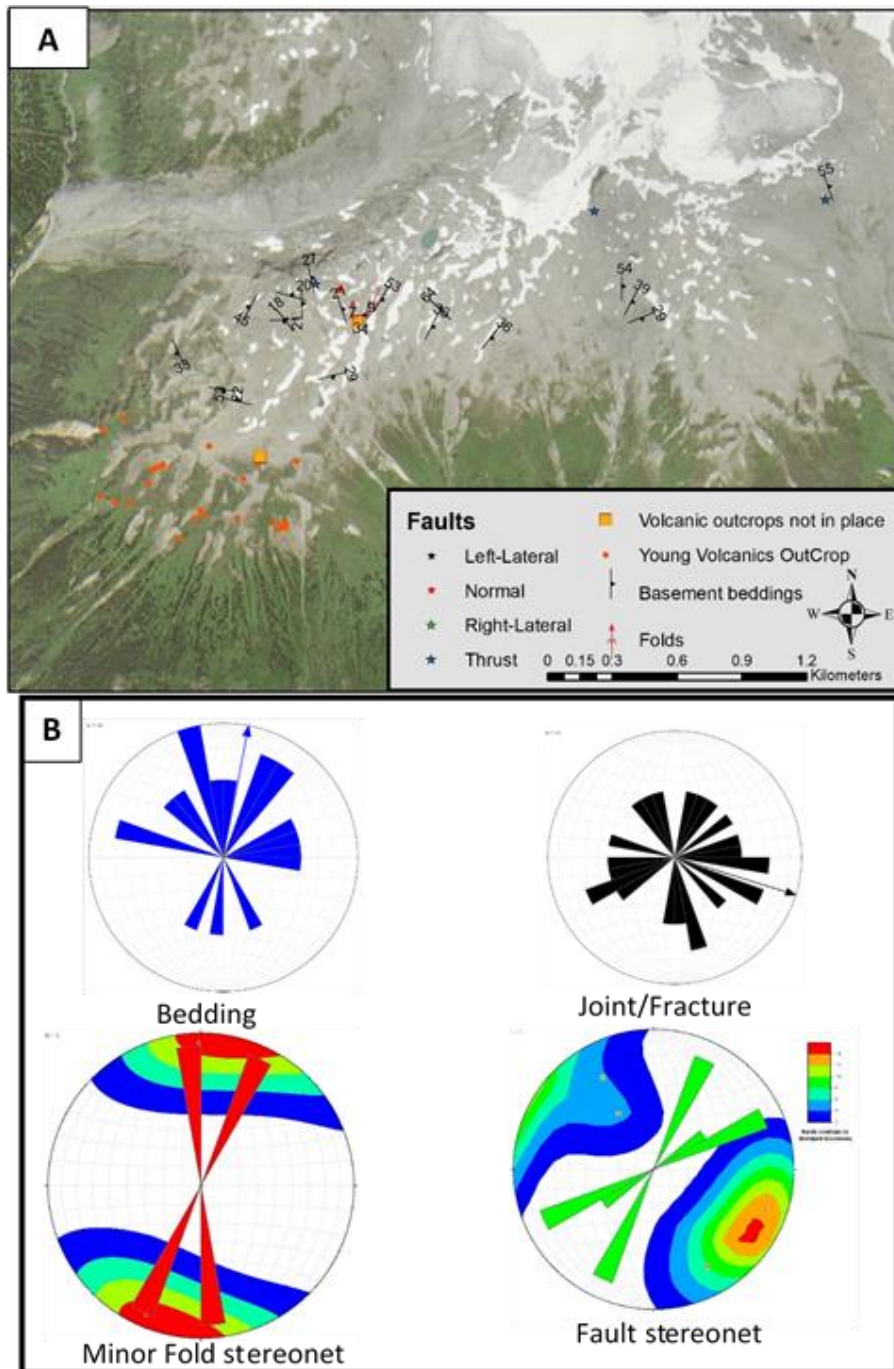


Figure 5. A) Geology Map of western ridge of Northern Lillooet Ridges show: Outcrops of young volcanic rocks, older basement rocks and location and type of faults on the west ridge. Orange dots represent outcrops of young intact volcanic rocks; orange-square shapes represent outcrops of non-intact young volcanic rocks; black dots represent outcrops of older basement rocks. B) Rose diagram for strike and trend of measured structural data; green, shows strike orientation of faults; blue, strike orientation of basement units; black strike orientation of joint, fractures and veins; red trend of minor folds. Stereographic Contours show the density of the data per cluster for poles of strike of structural features such as fault, joints/fractures and beddings.

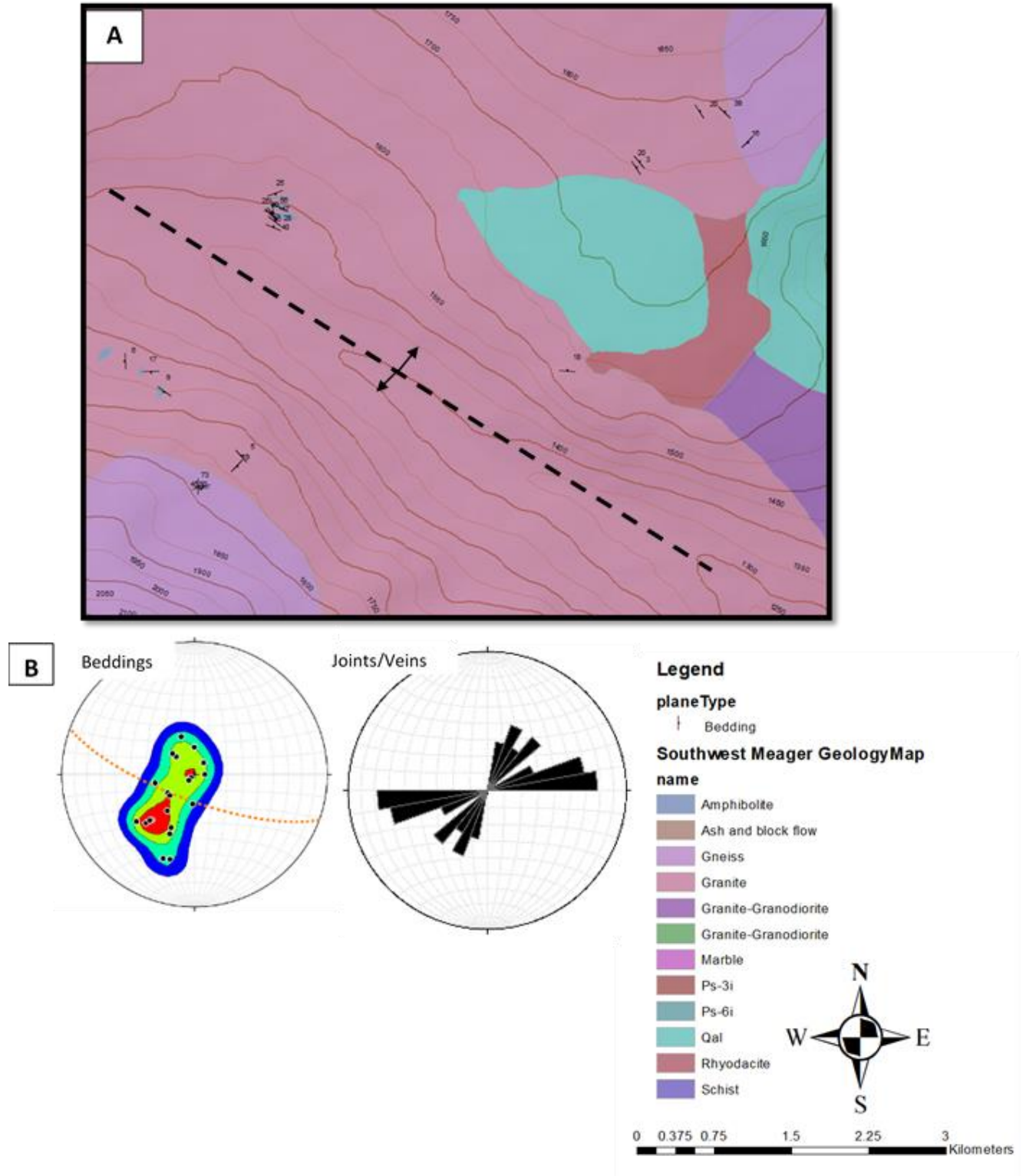


Figure 6. Geology Map of southwestern contact of Mt. Meager. B) Stereograph of basement beddings of southwestern contact of Mt. Meager: Orange dotted plane represents axial plane (striking NW-SE) of calculated fold structure; contours were drawn for poles of bedding planes for the major fold limbs.

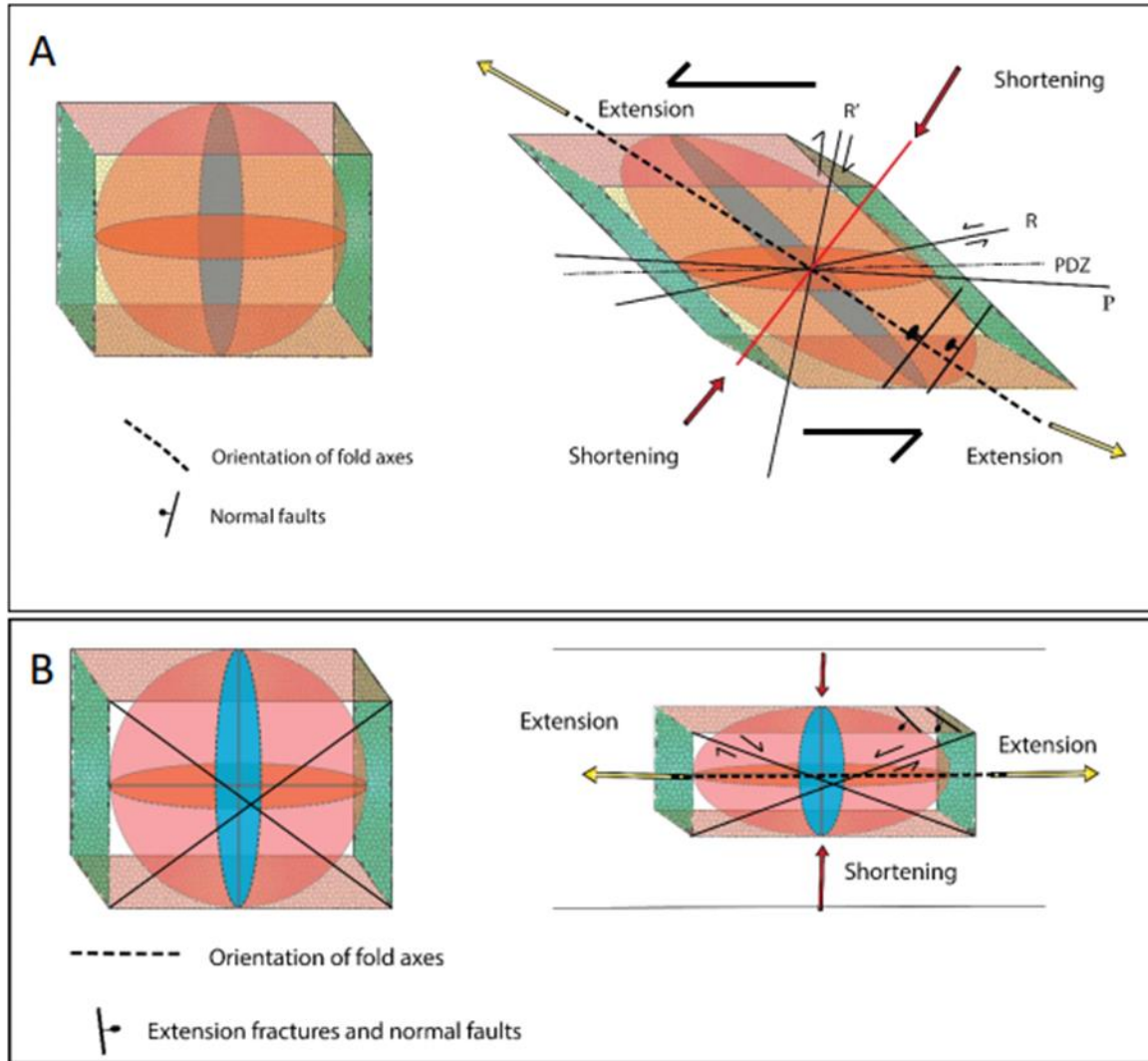


Figure 7. Strain ellipsoid of strike-slip deformation (Muhammad, 2016). A. Simple shear deformation and its associated structures. R and R' are synthetic and antithetic shears, respectively; P is a secondary fracture that may have synthetic shear; PDZ = principal displacement zone. B. Pure shear deformation and its associated structures.

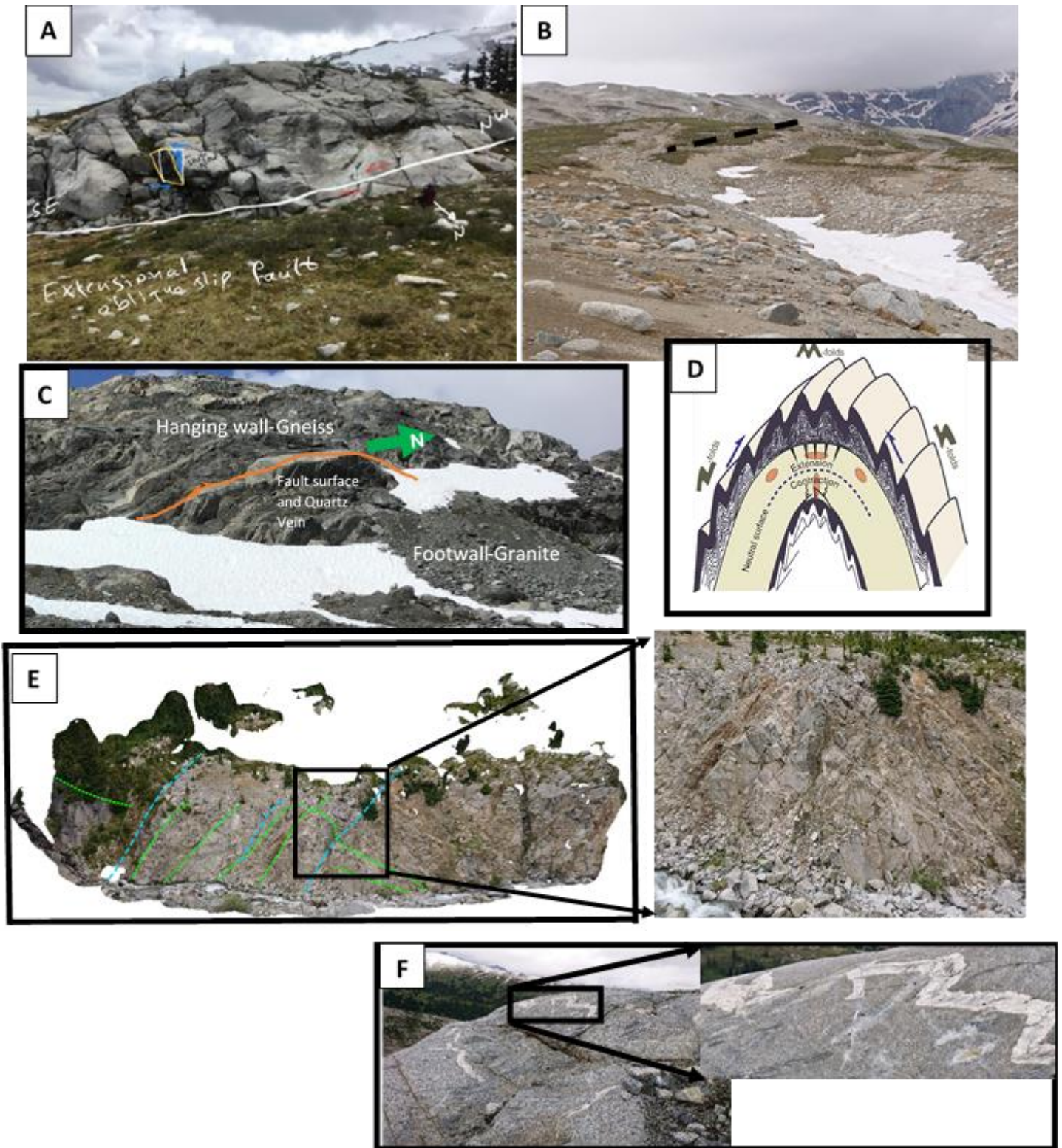


Figure 8. A) NW-SE striking strike-slip fault (approximately 1 m offset). B) NE-SW striking fault scarp (potentially normal fault). C) N-S striking compressional fault and S-shape minor fold. D) A cartoon model explains geometry of buckling fold on limbs of major folds. E) N-S striking compressional fault and Z-shape minor fold. F) NE-SW striking quartz vein folded (M-shape minor fold) within the hinge area of a major fold structure. Notice that the folded quartz vein is cut by a NW-SE striking xenolith vein.

Table 1. Principle Component Analysis (PCA) for the selected paleomagnetism sites and interpretation of paleomagnetic direction of samples at each site. Notes: NC=number of samples collected; NU=number of samples used in calculation; D=declination; I=inclination; α_{95} = radius of 95% circle of confidence; k=precision parameter; P=geomagnetic polarity (N is Normal and R is Reverse) directions.

Site	NC	NU	D (°)	I (°)	α_{95} (°)	k	P	Possible Tilting	Possible Rotation	Rock Type	Approx. Age
1	8	8	134.9	-66.5	4.3	164.7	R	NA	10-20°	Andesitic Lava	0.78-0.9 Ma or 1.06-1.78 Ma
2	8	6	134.9	-68.3	2.7	610.1	R	NA	10-20°	Andesitic Lava	0.78-0.9 Ma or 1.06-1.78 Ma
3	8	8	136.7	-65.6	3.9	179.3	R	NA	10-20°	Salal Pluton?	~8 Ma
4	8	6	352.5	29.8	4	274.6	N	>25°	NA	Dacitic Lava	0.3-0 Ma or 2-1.2 Ma
5	8	5	134	19	14	30.5	N	>40°	10-20°	Granodiorite	55-47 Ma

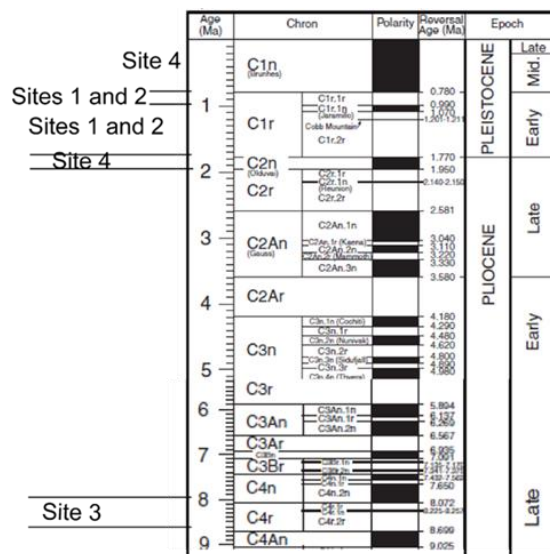


Figure 9. Reversals of Earth's magnetic field for the last 11 Ma (Pliocene-Pleistocene and late Miocene). Dark bands indicate times when the Earth's magnetic field matches that of today, i.e., a normal magnetic field. White bands signify times when the Earth's magnetic field was reversed - reversed polarity. Paleomagnetic ages assigned to samples collected at sites 1 to 4 based on Read (1990) and Woodsworth (1977) age classification of young volcanic rocks on the Mt. Meager massif.

Table 2. Show detailed Principle Component Analysis (PCA) for sites 1, 2, 3, 4 and 5.

Site No.	LAT	LONG	Sample No.	Name	State	Dec	Inc	MAD	Limit1	Limit2
Site1	50.727489	-123.512440	1	SFU001A	CPCA	138.4	-65.7	1.3	20	60
			2	SFU002A	CPCA	123.4	-64.8	0.6	20	60
			3	SFU003A	CPCA	161.6	-66.8	0.8	20	70
			4	SFU004A	CPCA	123.1	-63.8	0.6	20	60
			5	SFU005A	CPCA	150.5	-68.1	1.2	20	60
			6	SFU006A	CPCA	118.7	-65.6	1.9	20	80
			7	SFU007A	CPCA	142.7	-65.4	1.5	10	80
			8	SFU008A	CPCA	125	-66.3	1.3	20	60
						Sample No.	Name	State	Dec	Inc
Site 2	50.727533	-123.512642	1	SFU009A	CPCA	129.8	-69.7	2.2	40	70
			2	SFU011A	CPCA	139.5	-67	1.6	40	80
			3	SFU012A	CPCA	145.3	-68	2.9	40	80
			4	SFU013A	CPCA	139.8	-66.4	2.3	20	60
			5	SFU014A	CPCA	126.1	-67.7	0.9	20	80
			6	SFU015A	CPCA	127.2	-70	3.2	20	80
Site 3	50.727873	-123.512350	Sample No.	Name	State	Dec	Inc	MAD	Limit1	Limit2
			1	SFU017A	CPCA	130.1	-67.8	0.8	20	80
			2	SFU018A	CPCA	142.5	-69.9	1	20	80
			3	SFU019A	CPCA	140.0	-60.4	1.6	20	80
			4	SFU020A	CPCA	149.0	-63.5	6.7	50	70
			5	SFU021A	CPCA	134.2	-63.2	2.1	50	70
			6	SFU022A	CPCA	157.8	-64.9	1.7	40	80
			7	SFU023A	CPCA	122.3	-61.1	2.2	20	80
			8	SFU024A	CPCA	126.7	-65.8	4	60	90
			9	SFU025A	CPCA	127.2	-70.2	1.6	20	60
Site 4	50.730778	-123.581708	Sample No.	Name	State	Dec	Inc	MAD	Limit1	Limit2
			1	SFU026A	CPCA	352.1	26	0.7	10	70
			2	SFU027A	CPCA	351.7	33.3	0.5	20	60
			3	SFU028A	CPCA	355.1	26.8	1.0	20	60
			4	SFU029A	CPCA	349.2	32.9	0.5	20	60
			5	SFU032A	CPCA	353.5	35.4	1.5	40	60
6	SFU033A	CPCA	353.2	24.5	1.5	30	70			
Site 5	50.735662	-123.577983	Sample No.	Name	State	Dec	Inc	MAD	Limit1	Limit2
			1	SFU034B	CPCA	135.2	21.8	6.4	100° C	300° C
			2	SFU035A	CPCA	138.1	30.2	2.9	NRM	20
			3	SFU035B	CPCA	136.6	1.3	4.7	100° C	400° C
			4	SFU037A	CPCA	133.1	2.4	8.5	NRM	40
5	SFU038A	CPCA	126.5	28.8	6.7	10	30			

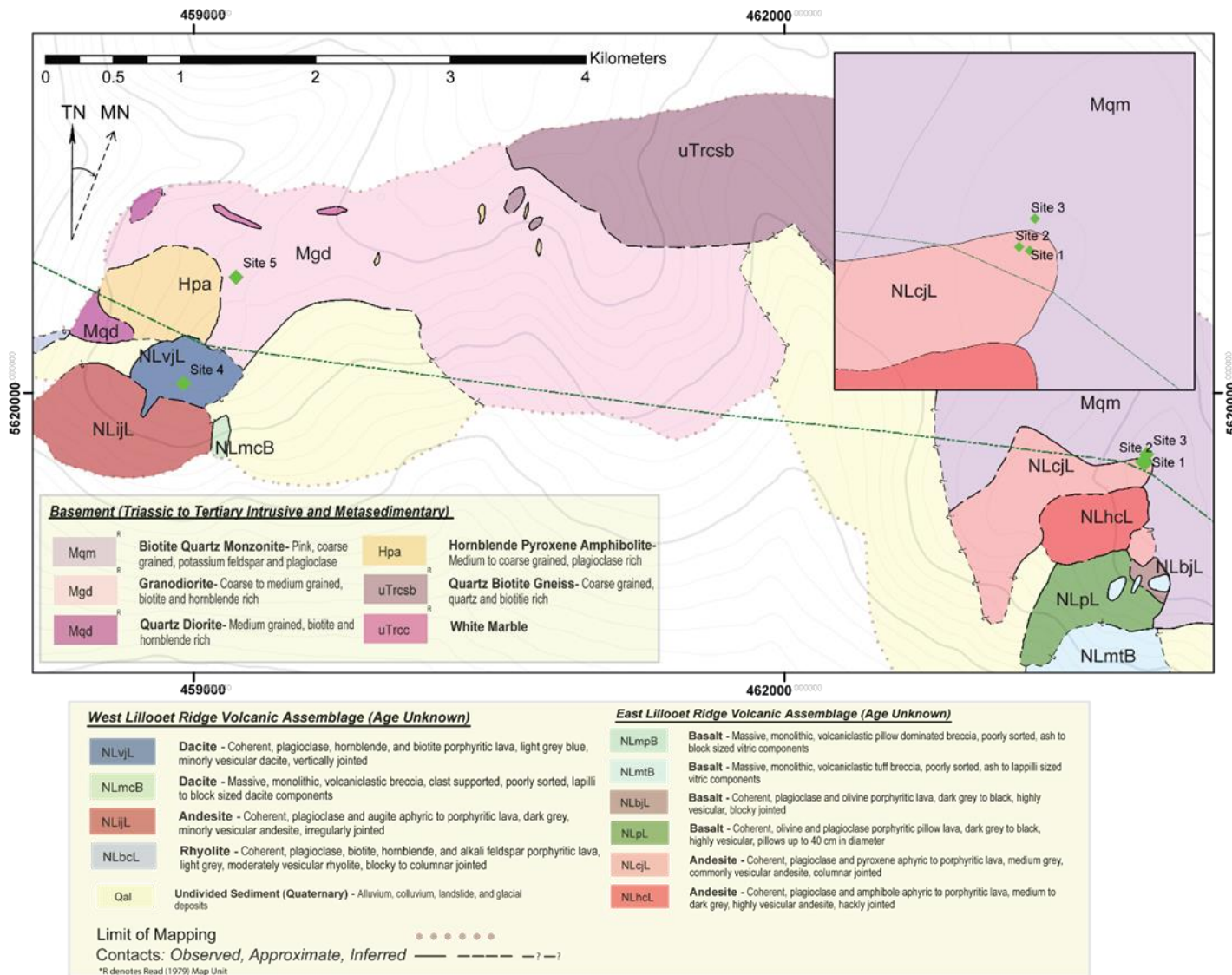


Figure 10. Bedrock geology map for the North Lillooet ridge, north of the Mt. Meager; green dots show sites of paleomagnetism samples. At each site, a minimum of 8 samples were collected. Modified from Harris et al. (2020).

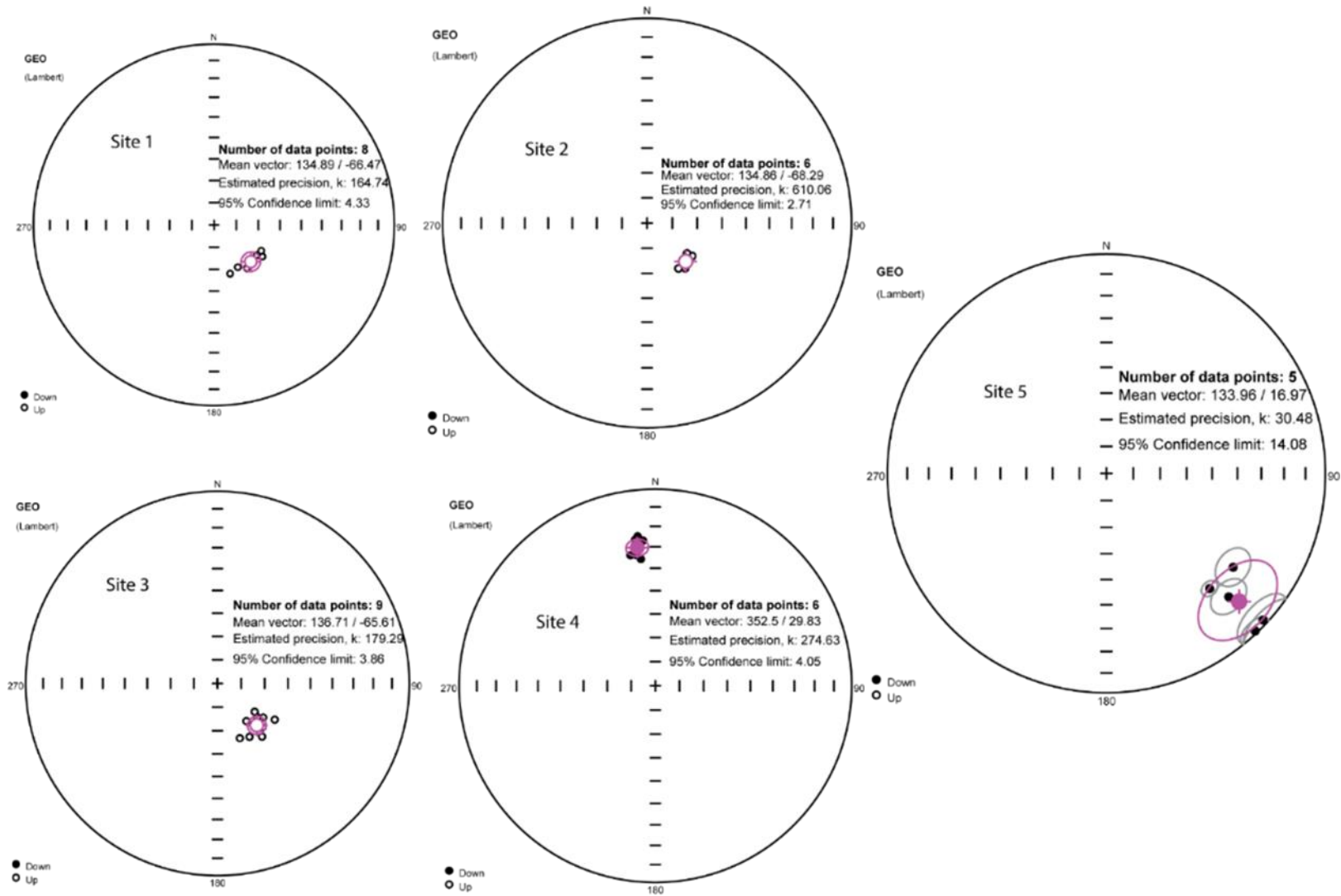


Figure 11. Stereographic projections of data points (black) and mean, including error circle (in red).

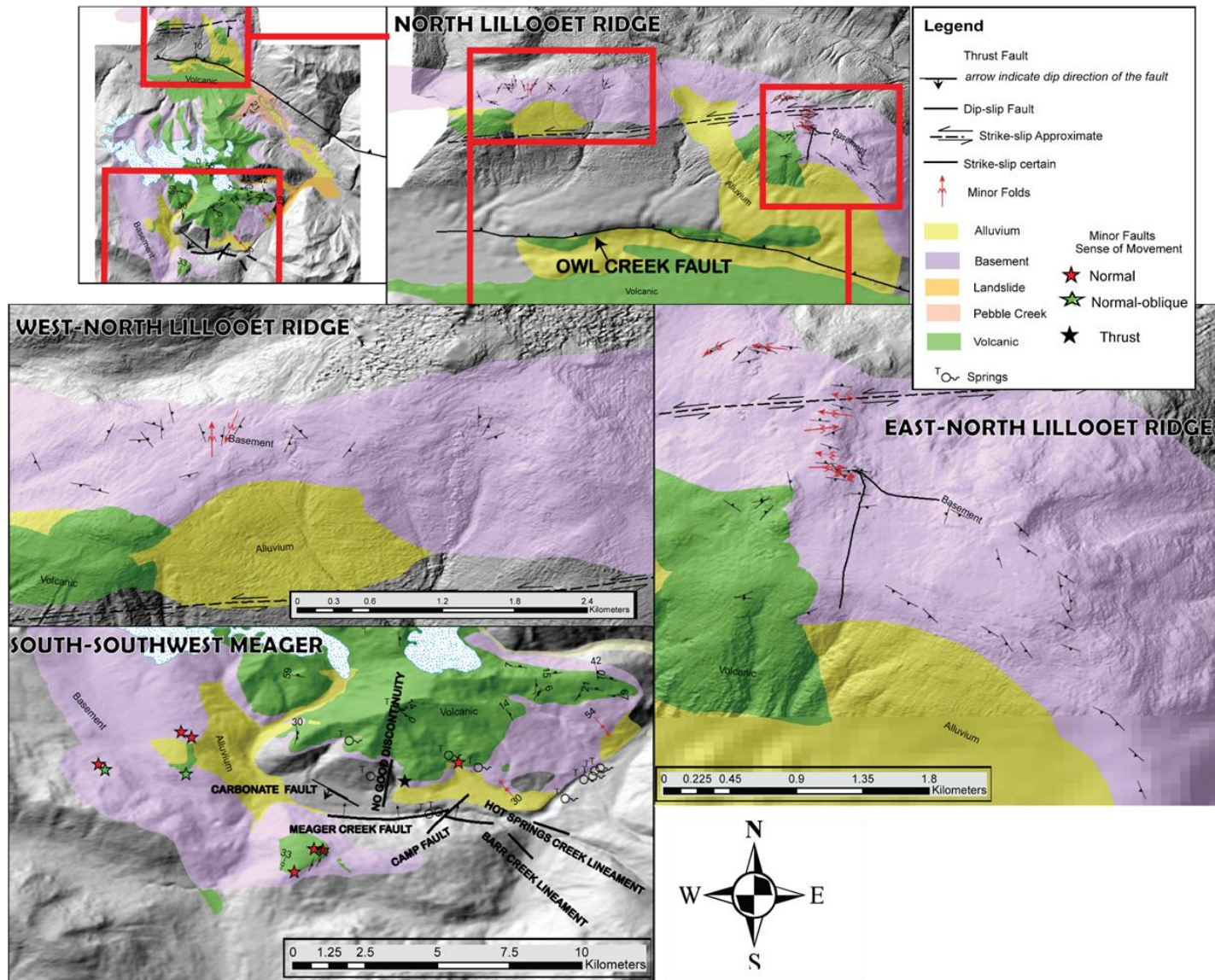


Figure 12. Shows pattern of faults within and around Mount Meager. Areas indicated with red box mapped during summers 2019 and 2020.

Remarks for Figure 12

The above map show distributions and patterns of regional faults within mount Meager Volcanic Complex (MMVC). Previously, two potential geothermal reservoirs identified within MMVC. The northern Reservoir located at the footwalls of Owl Creek fault system and the southern reservoir located at the vicinity of a fault system within and nearby Meager Creek area.

In this study, we documented major structural geology structures (Near the Northern Reservoir) in terms of the timing (kinematic history) and geometry of the structural geology features (Kinematic compatibility). We used both outcrop mapping of geologic structures and paleomagnetic study of structures of interest to define timing of latest tectonic activity that formed the fault system.

This knowledge can be used to perform proper steps to increase the permeability of the basement rocks through a process called induced fracture method. In order to successfully generate useful fracture system that increase fluid circulation within the reservoir; it is essential to have accurate understanding of the fault system in the region. This study is meant to serve as foundation to understand the patterns of faults and fault system distribution in MMVC.

Although, in this study we partially mapped faults within the southern reservoir, but the mapped area is complemented by the previous works in the region. At this stage, we were unable to perform detail analysis for faults within the southern reservoir because we need to have reasonable age constraints of structures. The age constraints of the structures can be performed through paleomagnetic sampling and radiometric dating for structures of interest.



Figure 13. Field photo of one of the fault surfaces of the 300-meter-long N-S striking fault Located on Eastern ridge of North Lillooet Ridge

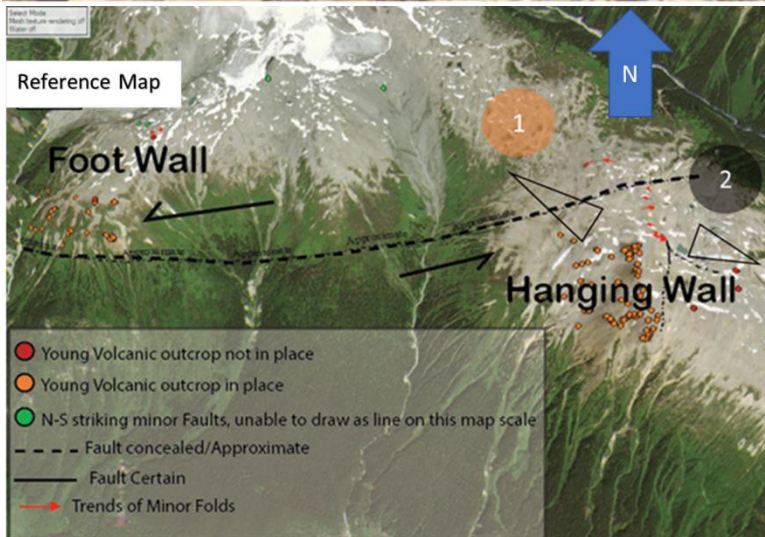
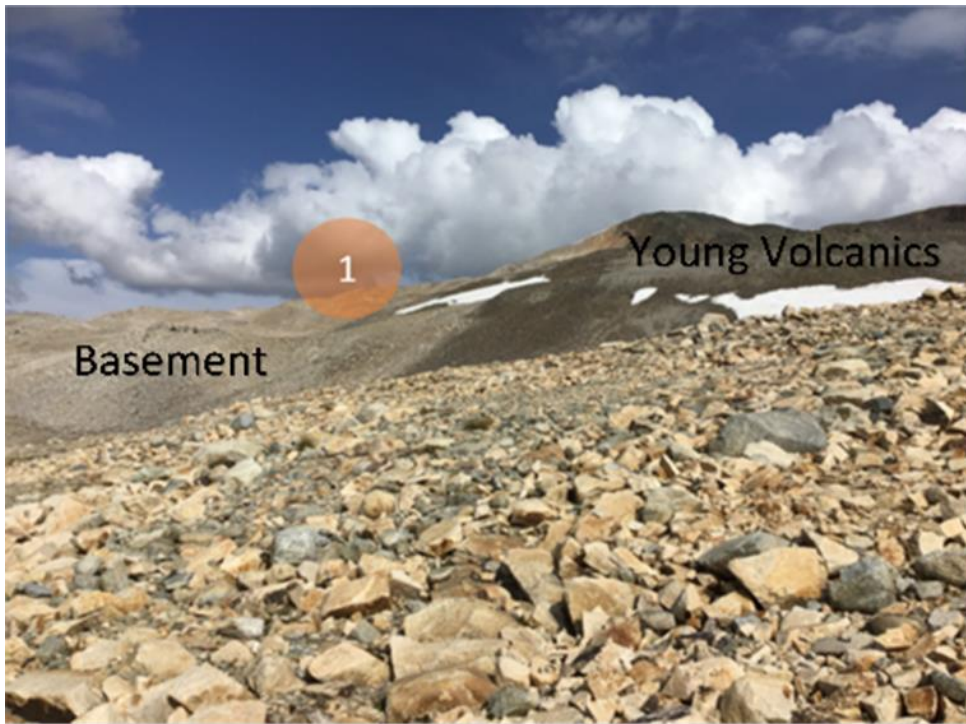


Figure 14. Field photo shows the sharp contact between Young Volcanics rocks (less than 2 Ma in age) and older Granitoid basement rock. See the reference map to locate the position of the field photograph.

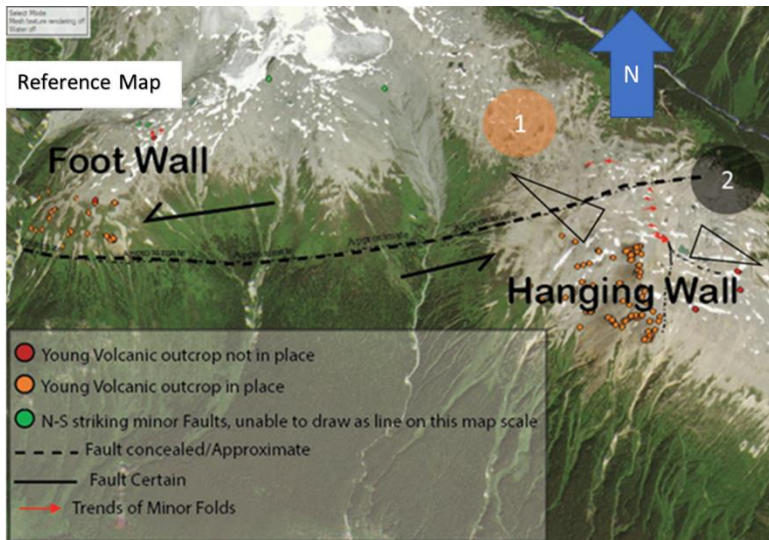
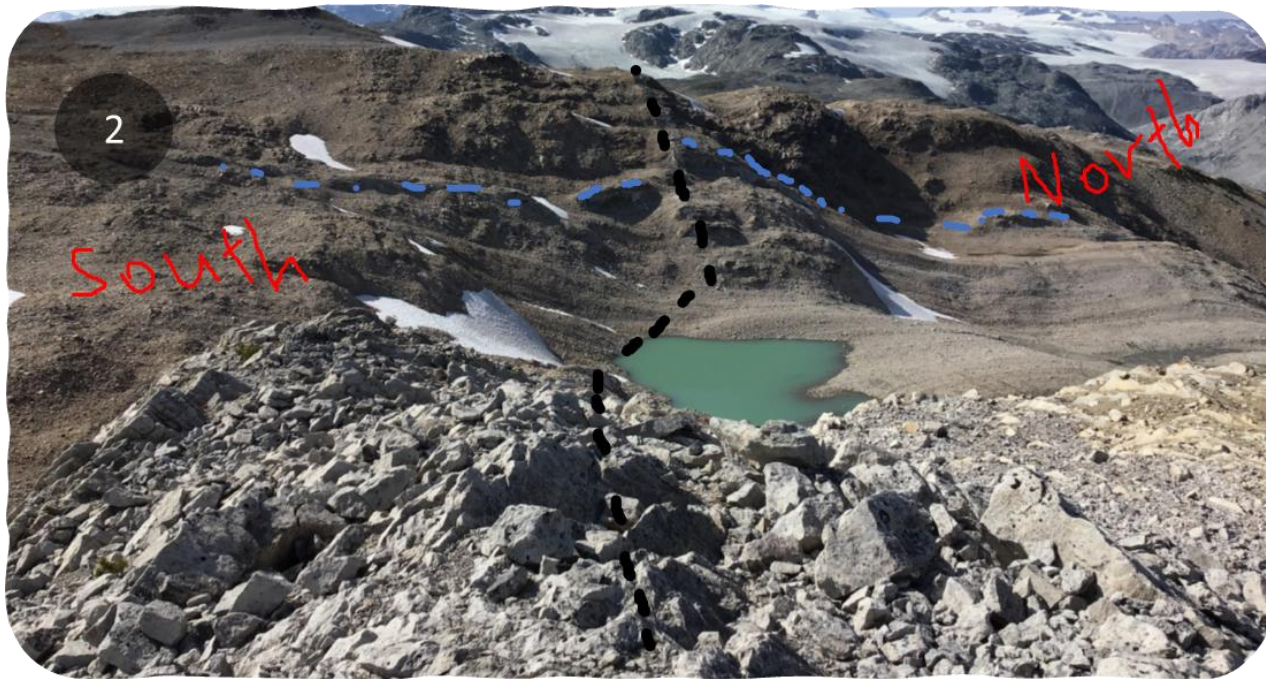


Figure 15. Field photo shows the cross-cutting relationship between two faults on the eastern side of North Lillooet ridge. See the reference map and Figure 12 to locate the position of the field photograph.

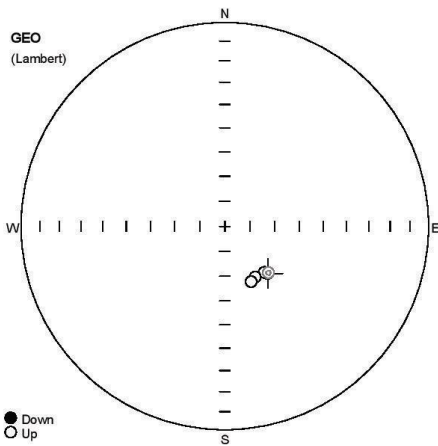
References

- Arianpoo, N., 2009, The Geothermal Potential Of Clarke Lake And Milo Gas Fields In Northeast British Columbia: The University of British Columbia, 107 p.
- Balfour, N.J., Cassidy, J.F., Dosso, S.E., and Mazzotti, S., 2011, Mapping crustal stress and strain in southwest British Columbia: *Journal of Geophysical Research: Solid Earth*, v. 116, p. 1–11, doi:10.1029/2010JB008003.
- Beck, M.E., Drake, R.E., and Butler, R.F., 1986, Paleomagnetism of Cretaceous volcanic rocks from central Chile and implications for the tectonics of the Andes: *Geology*, v. 14, p. 132, doi:10.1130/0091-7613(1986)14<132:POCVRF>2.0.CO;2.
- Bustin, A.M.M., Clowes, R.M., Monger, J.W.H., and Journeay, J.M., 2013, The southern Coast Mountains, British Columbia: New interpretations from geological, seismic reflection, and gravity data (G. Spence, Ed.): *Canadian Journal of Earth Sciences*, v. 50, p. 1033–1050, doi:10.1139/cjes-2012-0122.
- Butler, R., 2004, Paleomagnetism : Magnetic Domains to Geologic PALEOMAGNETISM : Magnetic Domains to Geologic Terranes: Electronic Edition , September 2004 University of Portland, 249 p.
- Chadima, M., and Hroudá, F., 2006, Remasoft 3.0 – A user-friendly paleomagnetic data browser and analyzer.: *Travaux Géophysiques*, v. XXVII, p. 20–21.
- Enkin, R.J., 2003, The direction - correction tilt test: An all-purpose tilt/fold test for paleomagnetic studies: *Earth and Planetary Science Letters*, v. 212, p. 151–166, doi:10.1016/S0012-821X(03)00238-3.
- Fairbank, B., Reader, J., and Nevin Sadlier-Brown, T., 1980, NSBG Ltd 1980 Mar - 1979 Drilling & Exploration Program, Meager Creek Geoth Area, Upper Lillooet River, BC.GT23.pdf.:
- Fairbank, B., Reader, J., Openshaw, R.E., and Nevin Sadlier-Brown, T., 1981, 1981 Jun. 1980 Drilling and Exploration Program - Meager Creek Geothermal Area, Upper Lillooet River, BC.GT33.:
- Filipovich, R. et al., 2020, Geological Map of the Tocomar Basin (Puna Plateau, NW Argentina). Implication for the Geothermal System Investigation: *Energies*, v. 13, p. 5492, doi:10.3390/en13205492.
- Ghomshei, M.M., Brown, T.L.S., and MacRae, J.M., 1992, Geothermal prospects in British Columbia: resource, market and regulatory aspects, *in* *Transactions - Geothermal Resources Council*, v. 16, p. 57–63.
- Ghomshei, M.M., Croft, S.A.S., and Stauder, J.J., 1986, Geochemical evidence of chemical equilibria in the South Meager Creek geothermal system, British Columbia, Canada: *Geothermics*, v. 15, p. 49–61, doi:10.1016/0375-6505(86)90028-3.
- Ghomshei, M.M., Meech, T.L.S.J. a, Dakin, R. a, Geopower, W., West, C., Street, H., Granville, S., Canada, B.C., Associates, P., and Vancouver, N., 2005, Canadian Geothermal Energy Poised for Takeoff: Proceedings World Geothermal Congress 2005, p. 1–4, <http://www.carnotechenergy.com/wp-content/uploads/2013/07/Canadian-Geothermal-Energy-Poised-for-Takeoff.pdf>.
- Ghomshei, M., Sanyal, S., MacLeod, K., Henneberger, R., Ryder, A., Meech, J., and Fainbank, B., 2004, Status of the South Meager geothermal project British Columbia, Canada: Resource evaluation and

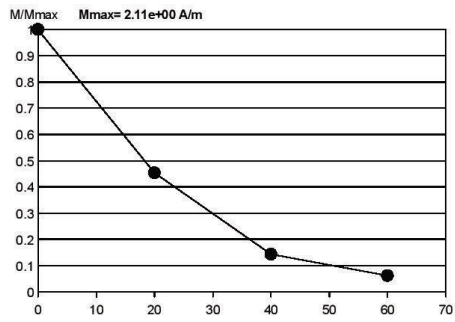
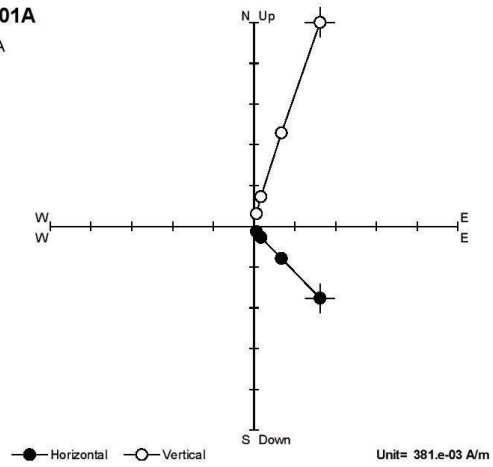
- plans for development, *in* Transactions - Geothermal Resources Council, v. 28, p. 339–344.
- Harris, M., Muhammad, M., Williams-Jones, G., and Russell, J., 2020, Bedrock mapping for Mount Meager Geothermal Research Initiative: In The Garibaldi Volcanic Belt Geothermal Energy Project – Mount Meager 2019 Field Program; doi:10.13140/RG.2.2.15103.64169.
- Kirschvink, J.L., 1980, The least-squares line and plane and the analysis of palaeomagnetic data: *Geophysical Journal International*, v. 62, p. 699–718, doi:10.1111/j.1365-246X.1980.tb02601.x.
- Leonard, L.J., Currie, C.A., Mazzotti, S., and Hyndman, R.D., 2010, Rupture area and displacement of past Cascadia great earthquakes from coastal coseismic subsidence: *Bulletin of the Geological Society of America*, v. 122, p. 2079–2096, doi:10.1130/B30108.1.
- Liotta, D., Brogi, A., Ruggieri, G., and Zucchi, M., 2021, Fossil vs. Active Geothermal Systems: A Field and Laboratory Method to Disclose the Relationships between Geothermal Fluid Flow and Geological Structures at Depth: *Energies*, v. 14, p. 933, doi:10.3390/en14040933.
- Moeck, I.S., 2014, Catalog of geothermal play types based on geologic controls: *Renewable and Sustainable Energy Reviews*, v. 37, p. 867–882, doi:10.1016/j.rser.2014.05.032.
- Muhammad, M., 2016, Structural evolution of the Maynard Lake Fault (Mlf) within the left-lateral Pahranaagat Shear Zone (PSZ), Nevada, USA: University of Nevada, Las Vegas, <https://digitalscholarship.unlv.edu/thesesdissertations/2798> (accessed May 2021).
- Parrish, R.R., 1982, Cenozoic Thermal and Tectonic History of the Coast Mountains of British Columbia as Revealed by Fission Track and geological Data and Quantitative Thermal Models: 1–10 p.
- Philipp, S.L., Gudmundsson, A., and Oelrich, A.R.I., 2007, How structural geology can contribute to make geothermal projects successful: *Proceedings European Geothermal Congress 2007*, p. 1–10.
- Read, P.B., 1979, Geology, Meager Creek geothermal area, British Columbia; doi:10.4095/129507.
- Read, P., 1990, Mt Meager Complex, Garibaldi Belt, Southwestern BC.: *Geoscience Canada*, v. 17, p. 167–170.
- Richards, D.R., Butler, R.F., and Sempere, T., 2004a, Vertical-axis rotations determined from paleomagnetism of Mesozoic and Cenozoic strata of the Bolivian Andes: *Journal of Geophysical Research: Solid Earth*, v. 109, p. 1–21, doi:10.1029/2004JB002977.
- Richards, D.R., Butler, R.F., Sempere, T., and Enkin, R.J., 2004b, The direction - correction tilt test: An all-purpose tilt/fold test for paleomagnetic studies: *Earth and Planetary Science Letters*, v. 212, p. 151–166, doi:10.1029/2004JB002977.
- Riddihough, R.P., and Hyndman, R.D., 1976, Canada ' s Active Western Margin - The Case for Subduction: v. 3, <https://journals.lib.unb.ca/index.php/GC/article/view/1211>.
- Roberti, G., 2018, Mount Meager , a glaciated volcano in a changing cryosphere: hazards and risk challenges: *Université Clermont Auvergne*, 207 p.
- Ryder, J.M., Fulton, R.J., and Clague, J.J., 1991, The Cordilleran Ice Sheet and the glacial geomorphology of southern and central British Columbia: *Geographie Physique et Quaternaire*, v. 45, p. 365–377, doi:10.7202/032882ar.
- Woodsworth, G., 1977, Geology of Pemberton (92J) Map Area: Geological Survey of Canada, p. 1 sheet.

Appendix

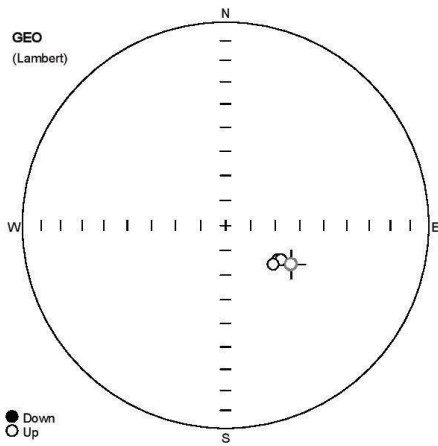
Examples of demagnetization data obtained from more than 38 samples of sites 1 to 5 at North Lillooet ridge (Tables 2). For each sample, the stereographic plots (left figures) show magnetization directions after stepwise demagnetization, where the filled circles lie on the lower hemisphere. The orthogonal plots (right figures) show horizontal projections as filled circles and vertical projections as open circles. Both alternating field and thermal demagnetization plots are given. Units are in amperes per metre.



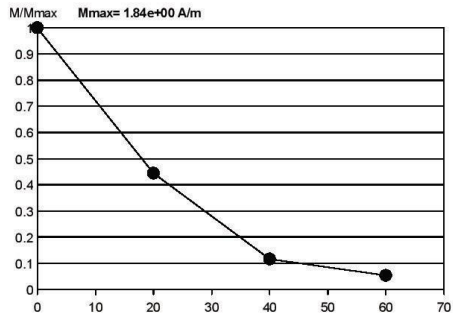
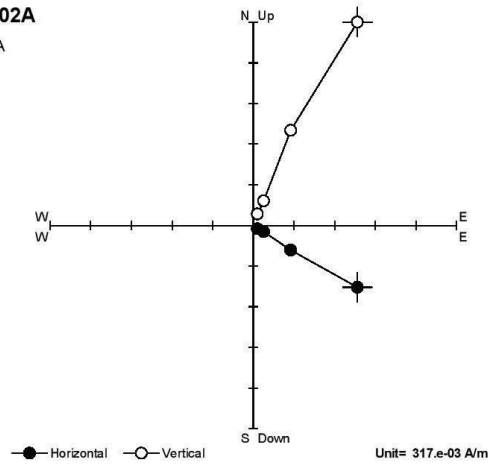
SFU001A
N/A



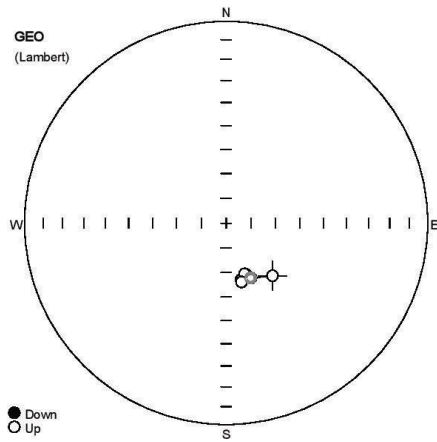
Name	Site	Latitude	Longitude	Height	Rock	Age	Fm	SDec	Sinc	BDec	Binc	FDec	Finc	P1	P2	P3	P4	Note
SFU001A								315	28					6	0	6	90	
#	State	M[A/m]	Dsp	Isp	Dge	Ige	Dtc	Itc	Dfc	Ifc	Prec	Limit1	Limit2	Note				K[e-06 SI]
1	NRM	2.11e+00	181.3	-36.5	137.5	-64.4					1.0							
2	20	958.e-03	182.3	-37.8	139.4	-65.7					1.0							
3	40	301.e-03	187.1	-38.7	148.9	-66.3					1.0							
4	60	129.e-03	190.3	-38.2	154.6	-65.4					1.0							
5	CPCA	1.41e+00	180.9	-36.5	136.8	-64.5					0.9	NRM	60	O				



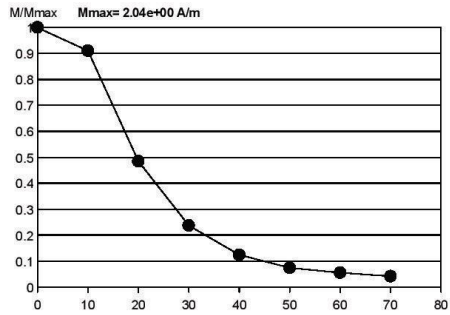
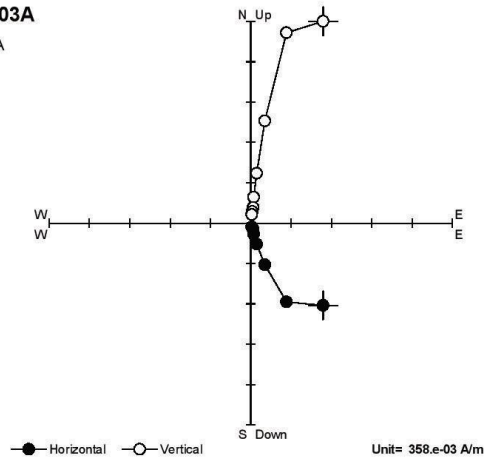
SFU002A
N/A



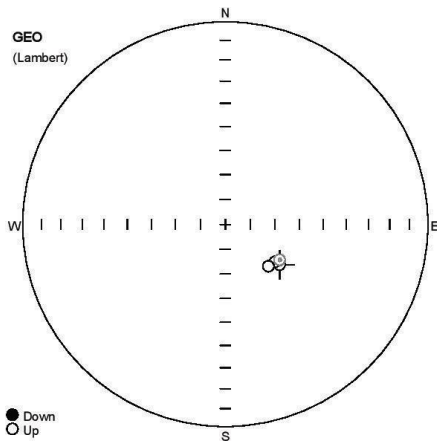
Name	Site	Latitude	Longitude	Height	Rock	Age	Fm	SDec	Sinc	BDec	Blnc	FDec	Finc	P1	P2	P3	P4	Note
SFU002A								320	31					6	0	6	90	
#	State	M[A/m]	Dsp	Isp	Dge	Ige	Dtc	Itc	Dfc	Ifc	Prec	Limit1	Limit2	Note				K[e-06 SI]
1	NRM	1.84e+00	168.8	-29.2	120.7	-59.2					1.0							
2	20	819.e-03	171.6	-34.4	123.5	-64.8					1.0							
3	40	213.e-03	170.5	-33.5	121.8	-63.7					1.0							
4	60	97.4e-03	174.6	-34.6	129.2	-65.3					2.0							
5	CPCA	1.25e+00	168.8	-29.3	120.7	-59.4					2.5	NRM	60 O					



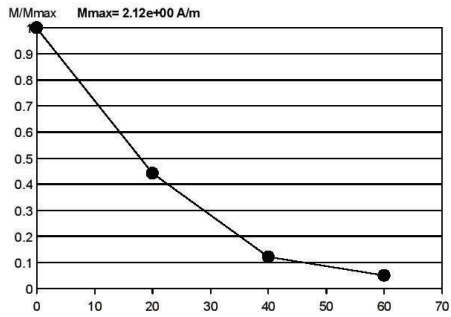
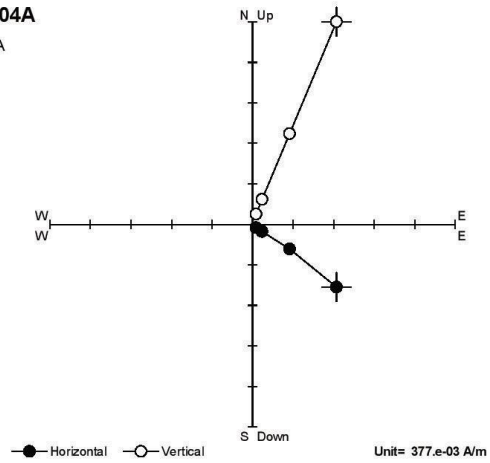
SFU003A
N/A



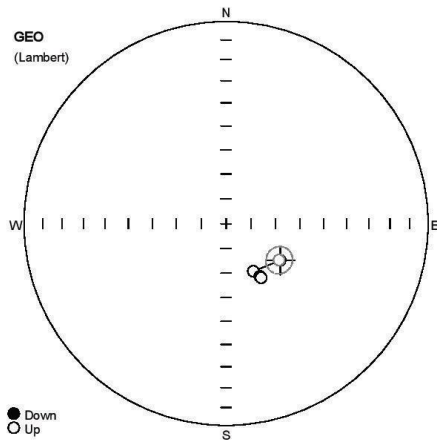
Name	Site	Latitude	Longitude	Height	Rock	Age	Fm	SDec	Sinc	BDec	Binc	FDec	Finc	P1	P2	P3	P4	Note
SFU003A								337	27					6	0	6	90	
#	State	M[A/m]	Dsp	Isp	Dge	Ige	Dtc	Itc	Dfc	Ifc	Prec	Limit1	Limit2	Note	K[e-06 S]			
1	NRM	2.04e+00	169.4	-35.2	138.6	-61.5						0.0						
2	10	1.85e+00	179.2	-38.6	155.6	-65.6						1.0						
3	20	986.e-03	182.2	-39.9	161.3	-66.8						1.0						
4	30	482.e-03	183.7	-39.5	164.2	-66.4						1.0						
5	40	252.e-03	184.2	-39.4	165.1	-66.3						1.0						
6	50	150.e-03	180.9	-40.6	158.8	-67.6						1.0						
7	60	111.e-03	181.4	-41.1	159.9	-68.1						1.0						
8	70	83.1e-03	184.4	-38.4	165.3	-65.3						1.0						
9	CPCA	1.36e+00	179.5	-38.7	156.0	-65.7					1.5	10	70	O				



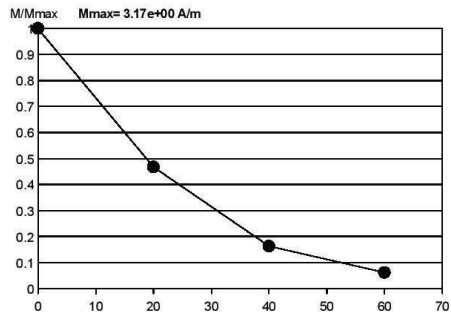
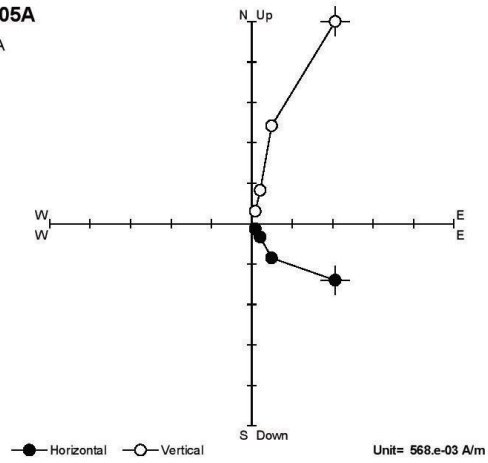
SFU004A
N/A



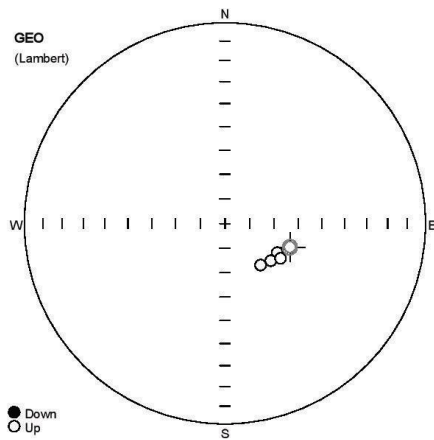
Name	Site	Latitude	Longitude	Height	Rock	Age	Fm	SDec	Sinc	BDec	Binc	FDec	Finc	P1	P2	P3	P4	Note
SFU004A								338	26					6	0	6	90	
#	State	M[A/m]	Dsp	Isp	Dge	Ige	Dtc	Itc	Dfc	Ifc	Prec	Limit1	Limit2	Note	K[e-06 SI]			
1	NRM	2.12e+00	162.3	-38.8	126.8	-62.7					0.0							
2	20	939.e-03	161.0	-40.4	123.6	-63.9					1.0							
3	40	257.e-03	163.0	-40.8	126.8	-64.8					1.0							
4	60	106.e-03	167.4	-40.8	134.3	-65.7					2.0							
5	CPCA	614.e-03	160.7	-40.4	123.1	-63.8					0.6	20	60	O				



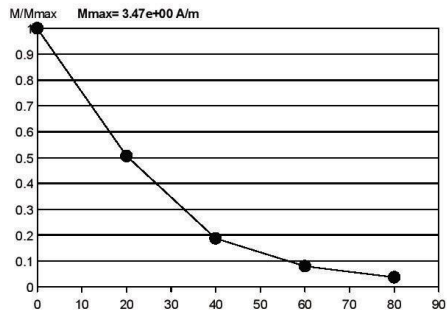
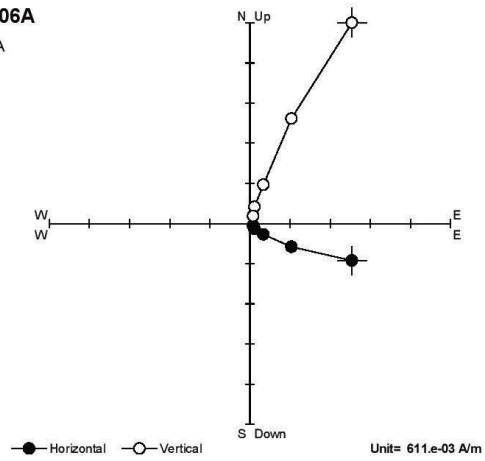
SFU005A
N/A



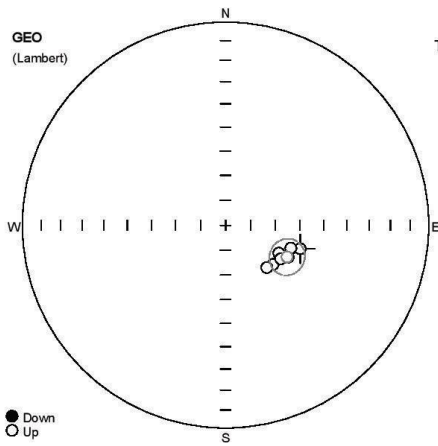
Name	Site	Latitude	Longitude	Height	Rock	Age	Fm	SDec	Sinc	BDec	Binc	FDec	Finc	P1	P2	P3	P4	Note
SFU005A								339	28					6	0	6	90	
#	State	M[A/m]	Dsp	Isp	Dge	Ige	Dtc	Itc	Dfc	Ifc	Prec	Limit1	Limit2	Note				K[e-06 SI]
1	NRM	3.17e+00	161.1	-38.2	124.2	-63.5					1.0							
2	20	1.48e+00	175.7	-40.0	150.2	-67.9					0.0							
3	40	516.e-03	173.9	-37.0	147.5	-64.7					1.0							
4	60	195.e-03	173.4	-36.2	146.9	-63.9					1.0							
5	CPCA	2.11e+00	161.4	-38.5	124.5	-63.9					5.4	NRM	60 O					



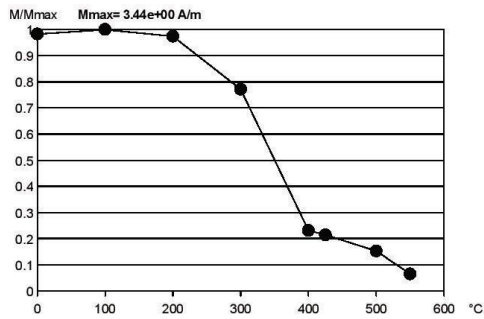
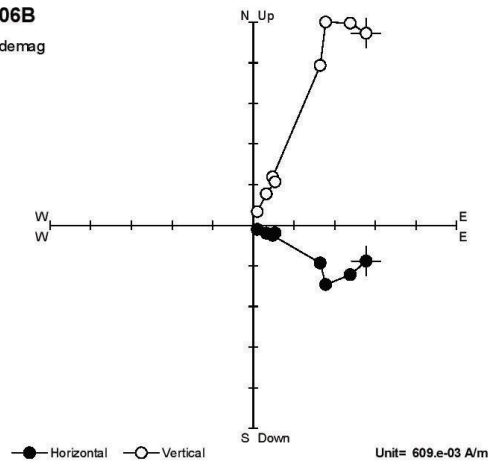
SFU006A
N/A



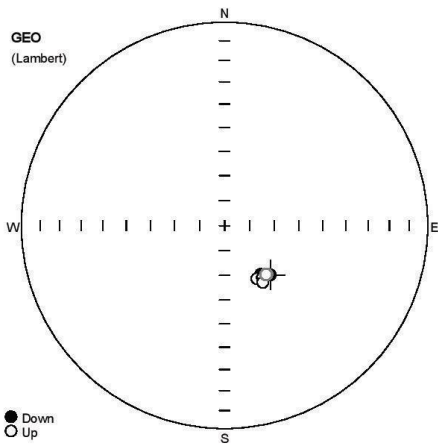
Name	Site	Latitude	Longitude	Height	Rock	Age	Fm	SDec	Sinc	BDec	Binc	FDec	Finc	P1	P2	P3	P4	Note
SFU006A								350	25					6	0	6	90	
#	State	M[A/m]	Dsp	Isp	Dge	Ige	Dtc	Itc	Dfc	Ifc	Prec	Limit1	Limit2	Note				K[e-06 SI]
1	NRM	3.47e+00	145.0	-44.2	110.0	-61.6					1.0							
2	20	1.76e+00	152.8	-45.7	119.2	-65.6					1.0							
3	40	647.e-03	158.1	-44.2	129.1	-65.9					1.0							
4	60	274.e-03	164.3	-44.5	139.4	-67.8					1.0							
5	80	127.e-03	152.8	-43.0	122.1	-63.2					2.0							
6	CPCA	2.43e+00	145.1	-44.4	110.0	-61.8					3.0	NRM	80 O					



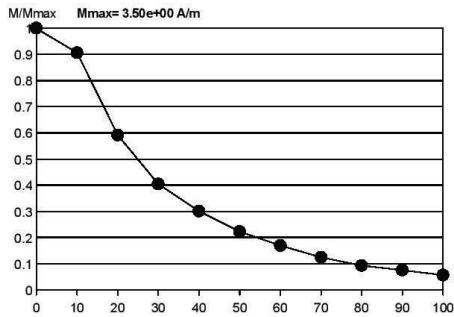
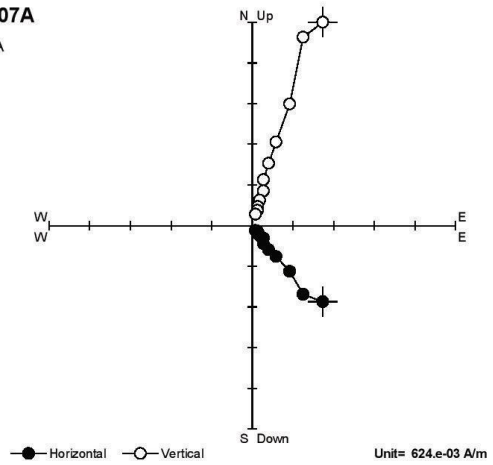
SFU006B
Thermal demag



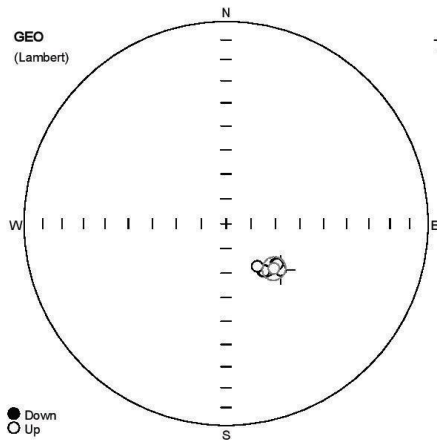
Name	Site	Latitude	Longitude	Height	Rock	Age	Fm	SDec	Sinc	BDec	Blnc	FDec	Finc	P1	P2	P3	P4	Note
SFU006B								350	25					6	0	6	90	
#	State	M[A/m]	Dsp	Isip	Dge	Ige	Dtc	Itc	Dfc	Ifc	Prec	Limit1	Limit2	Note				K[e-06 SI]
1	NRM	3.38e+00	141.3	-42.0	107.6	-58.4					1.0							
2	100°C	3.44e+00	149.1	-42.6	117.1	-61.7					1.0							
3	200°C	3.35e+00	158.0	-43.6	129.4	-65.3					1.0							
4	300°C	2.65e+00	152.0	-44.5	119.4	-64.3					1.0							
5	400°C	794.e-03	152.0	-46.1	117.6	-65.8					1.0							
6	425°C	736.e-03	145.0	-44.7	109.5	-62.1					1.0							
7	500°C	525.e-03	152.8	-43.8	121.3	-64.0					1.0							
8	550°C	221.e-03	161.7	-43.5	135.7	-66.2					1.0							
9	CPCA	1.73e+00	149.4	-42.9	117.3	-62.1					7.2	NRM	550°C O					



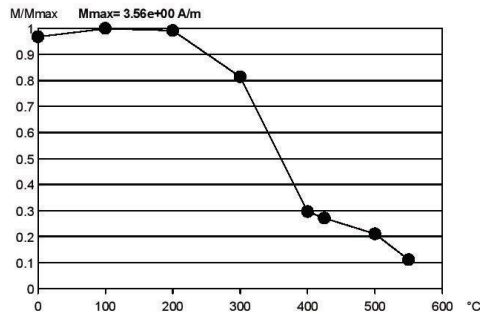
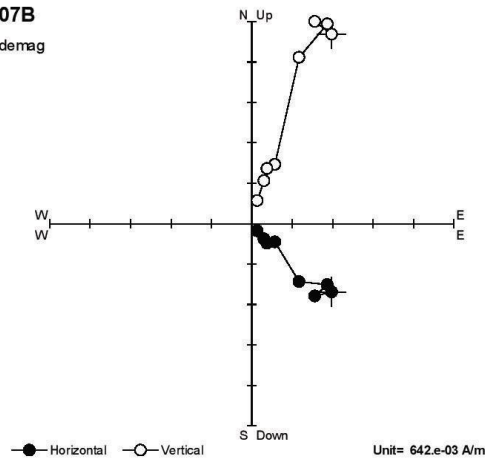
SFU007A
N/A



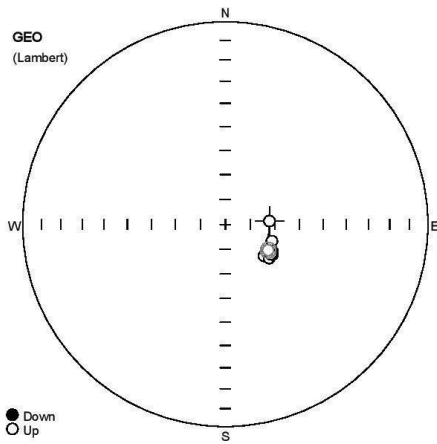
Name	Site	Latitude	Longitude	Height	Rock	Age	Fm	SDec	Sinc	BDec	Binc	FDec	Finc	P1	P2	P3	P4	Note
SFU007A								359	27					6	0	6	90	
#	State	M[A/m]	Dsp	Isp	Dge	Ige	Dtc	Itc	Dfc	lfc	Prec	Limit1	Limit2	Note	K[e-06 SI]			
1	NRM	3.50e+00	156.8	-39.8	137.2	-63.0					0.0							
2	10	3.17e+00	161.4	-41.2	143.5	-65.6					1.0							
3	20	2.07e+00	159.3	-40.2	140.8	-64.1					1.0							
4	30	1.42e+00	160.7	-40.9	142.6	-65.1					1.0							
5	40	1.05e+00	162.2	-40.3	145.6	-64.9					1.0							
6	50	776.e-03	163.9	-40.0	148.7	-65.1					1.0							
7	60	592.e-03	157.9	-40.5	138.4	-64.0					1.0							
8	70	432.e-03	161.0	-39.8	144.0	-64.2					1.0							
9	80	324.e-03	160.7	-40.0	143.3	-64.3					1.0							
10	90	261.e-03	157.7	-40.1	138.3	-63.6					0.0							
11	100	195.e-03	161.3	-37.8	145.9	-62.4					1.0							
12	CPCA	2.35e+00	158.7	-40.5	139.6	-64.2					2.5	NRM	100	○				



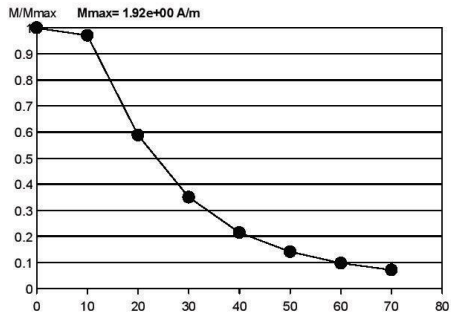
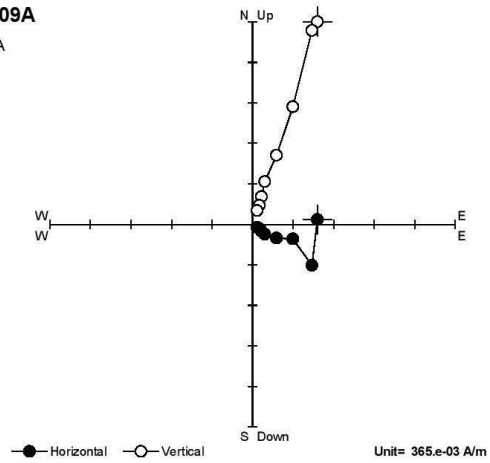
SFU007B
Thermal demag



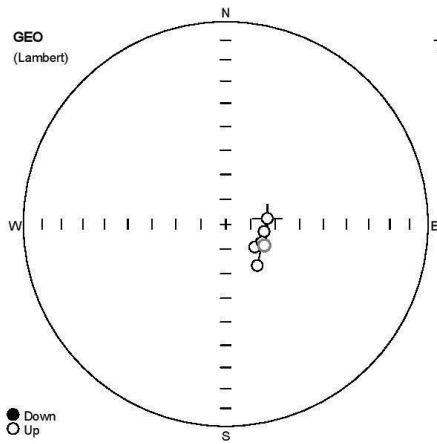
Name	Site	Latitude	Longitude	Height	Rock	Age	Fm	SDec	Sinc	BDec	Binc	FDec	Finc	P1	P2	P3	P4	Note
SFU007B								359	27					6	0	6	90	
#	State	M[A/m]	Dsp	Isp	Dge	Ige	Dtc	Itc	Dfc	Ifc	Prec	Limit1	Limit2	Note	K[e-06 SI]			
1	NRM	3.44e+00	152.0	-39.3	130.5	-61.0					1.0							
2	100°C	3.56e+00	158.6	-40.9	139.0	-64.6					1.0							
3	200°C	3.53e+00	153.0	-42.4	128.9	-64.1					1.0							
4	300°C	2.89e+00	160.2	-41.8	140.9	-65.8					1.0							
5	400°C	1.05e+00	152.5	-42.0	128.4	-63.6					1.0							
6	425°C	960.e-03	160.8	-41.6	142.1	-65.8					1.0							
7	500°C	747.e-03	160.2	-41.4	141.2	-65.5					1.0							
8	550°C	391.e-03	163.0	-44.0	143.8	-68.7					1.0							
9	CPCA	1.61e+00	154.9	-40.9	133.2	-63.4					4.7	NRM	550°C O					



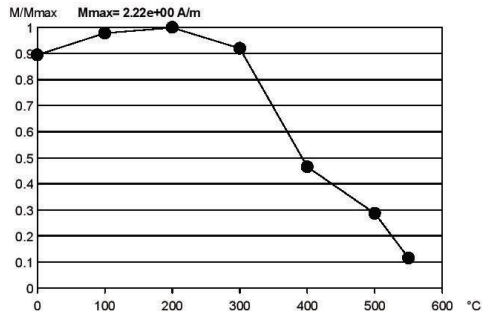
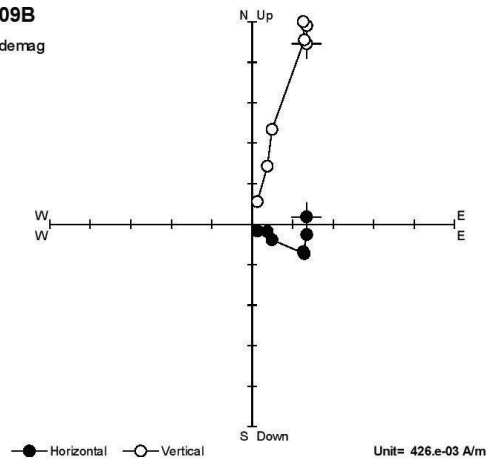
SFU009A
N/A



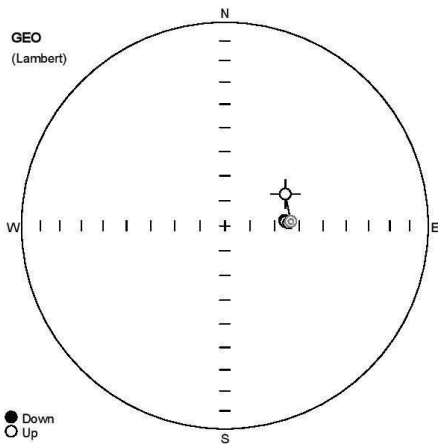
Name	Site	Latitude	Longitude	Height	Rock	Age	Fm	SDec	Sinc	BDec	BInc	FDec	Finc	P1	P2	P3	P4	Note	
SFU009A								307	20					6	0	6	90		
#	State	M[A/m]	Dsp	Isp	Dge	Ige	Dtc	Itc	Dfc	lfc	Prec	Limit1	Limit2	Note				K[e-06 SI]	
1	NRM	1.92e+00	159.6	-54.7	85.8	-72.2						1.0							
2	10	1.86e+00	178.7	-49.6	124.6	-69.6						1.0							
3	20	1.13e+00	170.9	-50.5	109.9	-70.0						1.0							
4	30	671.e-03	176.0	-48.4	119.8	-68.3						1.0							
5	40	410.e-03	181.3	-49.9	129.4	-69.9						1.0							
6	50	269.e-03	180.3	-47.7	127.5	-67.7						1.0							
7	60	185.e-03	177.6	-47.4	122.8	-67.4						1.0							
8	70	135.e-03	178.0	-48.0	123.4	-68.0						1.0							
9	CPCA	1.28e+00	176.9	-50.0	121.1	-69.9						3.1	10					70	○



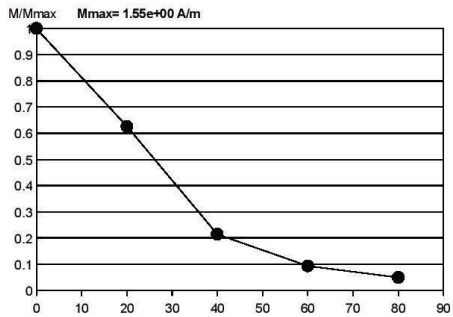
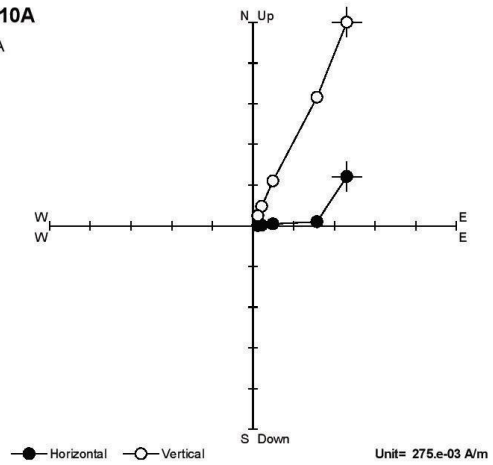
SFU009B
Thermal demag



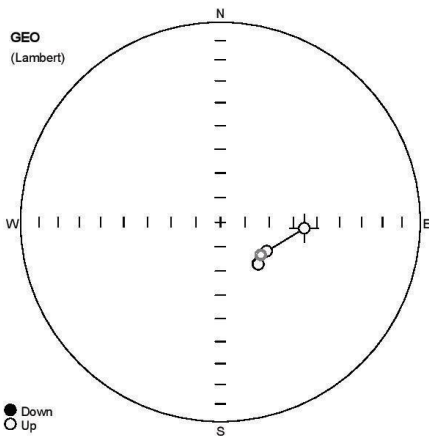
Name	Site	Latitude	Longitude	Height	Rock	Age	Fm	SDec	Sinc	BDec	Binc	FDec	Finc	P1	P2	P3	P4	Note
SFU009B								307	20					6	0	6	90	
#	State	M[A/m]	Dsp	Isp	Dge	Ige	Dtc	Itc	Dfc	Ifc	Prec	Limit1	Limit2	Note				K[e-06 SI]
1	NRM	1.98e+00	158.6	-55.9	82.4	-73.1						1.0						
2	100°C	2.17e+00	167.9	-55.2	100.8	-74.3						1.0						
3	200°C	2.22e+00	175.9	-54.1	118.3	-74.0						1.0						
4	300°C	2.04e+00	176.2	-52.1	119.4	-72.0						1.0						
5	400°C	1.03e+00	180.5	-55.1	128.1	-75.1						1.0						
6	500°C	634.e-03	174.9	-53.9	116.2	-73.7						1.0						
7	550°C	253.e-03	188.5	-49.4	142.6	-69.0						1.0						
8	CPCA	1.25e+00	175.9	-52.4	118.8	-72.3					2.5	300°C	550°C O					



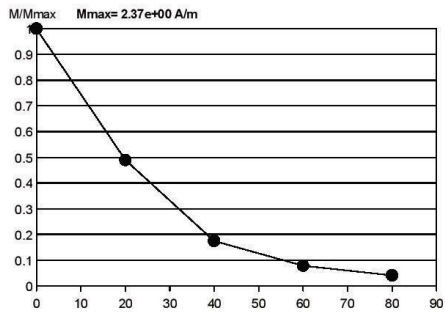
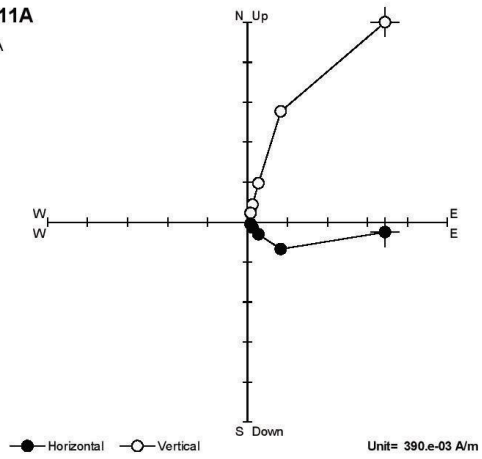
SFU010A
N/A



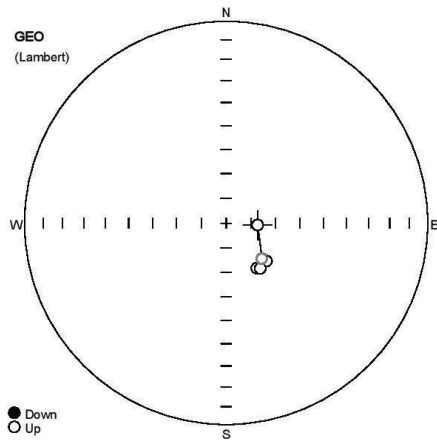
Name	Site	Latitude	Longitude	Height	Rock	Age	Fm	SDec	Sinc	BDec	Binc	FDec	Finc	P1	P2	P3	P4	Note
SFU010A								323	18					6	0	6	90	
#	State	M[A/m]	Dsp	IsP	Dge	Ige	Dtc	Itc	Dfc	Ifc	Prec	Limit1	Limit2	Note				K[e-06 SI]
1	NRM	1.55e+00	127.1	-55.1	62.3	-62.5					1.0							
2	20	970.e-03	143.8	-50.8	86.3	-63.5					1.0							
3	40	332.e-03	144.5	-53.4	84.7	-66.0					1.0							
4	60	144.e-03	145.1	-52.8	86.1	-65.6					1.0							
5	80	75.3e-03	145.1	-51.4	87.5	-64.3					2.0							
6	CPCA	666.e-03	143.7	-50.7	86.3	-63.4					1.0	20	80	O				



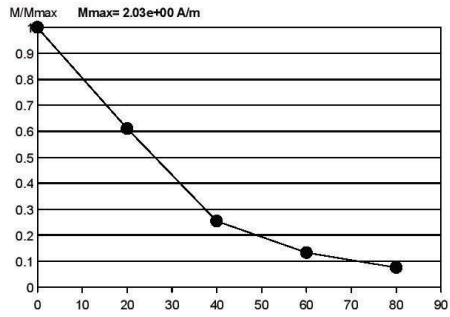
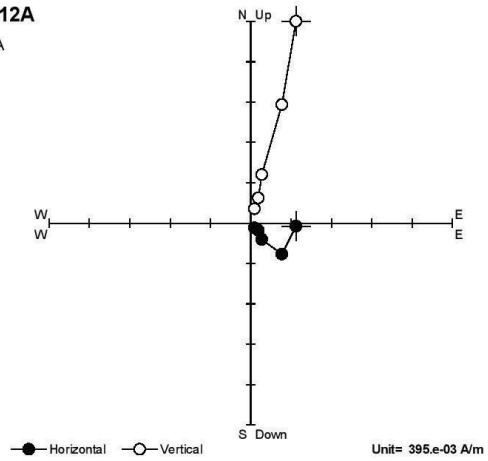
SFU011A
N/A



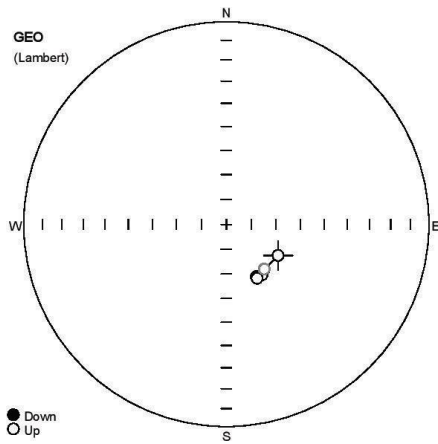
Name	Site	Latitude	Longitude	Height	Rock	Age	Fm	SDec	Sinc	BDec	Binc	FDec	Finc	P1	P2	P3	P4	Note	
SFU011A								305	22					6	0	6	90		
#	State	M[A/m]	Dsp	Isp	Dge	Ige	Dtc	Itc	Dfc	Ifc	Prec	Limit1	Limit2	Note				K[e-06 SI]	
1	NRM	2.37e+00	159.1	-35.5	94.2	-55.4						1.0							
2	20	1.16e+00	182.1	-46.8	129.0	-68.8						1.0							
3	40	412.e-03	187.3	-45.4	138.2	-67.1						1.0							
4	60	184.e-03	187.3	-45.1	138.2	-66.8						1.0							
5	80	95.0e-03	178.4	-45.7	122.1	-67.7						1.0							
6	CPCA	789.e-03	182.1	-46.9	129.0	-68.8						1.6	20					80 O	



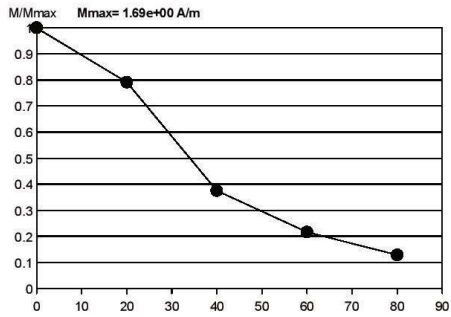
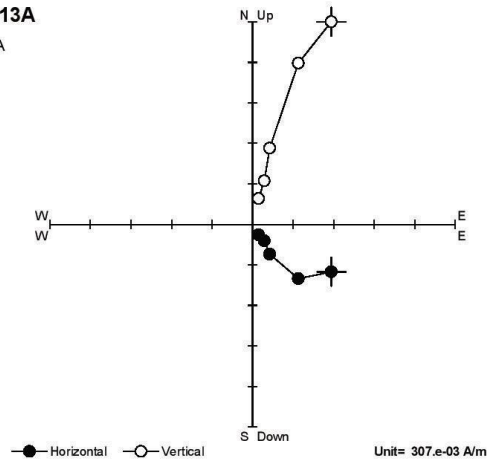
SFU012A
N/A



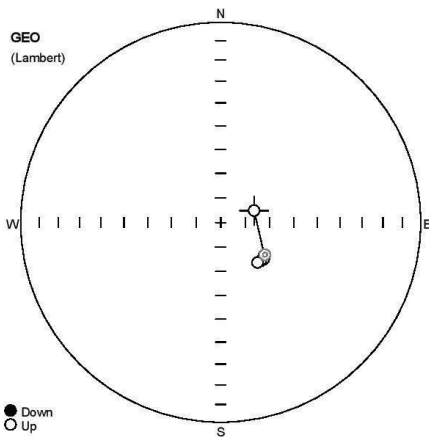
Name	Site	Latitude	Longitude	Height	Rock	Age	Fm	SDec	Sinc	BDec	Binc	FDec	Finc	P1	P2	P3	P4	Note
SFU012A								313	24					6	0	6	90	
#	State	M[A/m]	Dsp	Isp	Dge	Ige	Dtc	Itc	Dfc	Ifc	Prec	Limit1	Limit2	Note	K[e-06 SI]			
1	NRM	2.03e+00	165.9	-55.3	93.8	-77.3					1.0							
2	20	1.24e+00	180.9	-45.6	134.8	-69.6					1.0							
3	40	513.e-03	186.7	-44.2	145.8	-67.9					1.0							
4	60	267.e-03	180.1	-43.5	133.2	-67.5					1.0							
5	80	151.e-03	185.4	-43.2	143.1	-67.0					1.0							
6	CPCA	804.e-03	181.0	-45.7	135.0	-69.7					2.0	20	80 O					



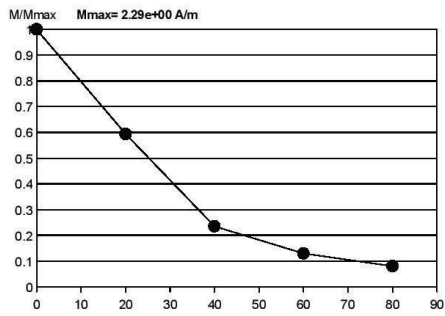
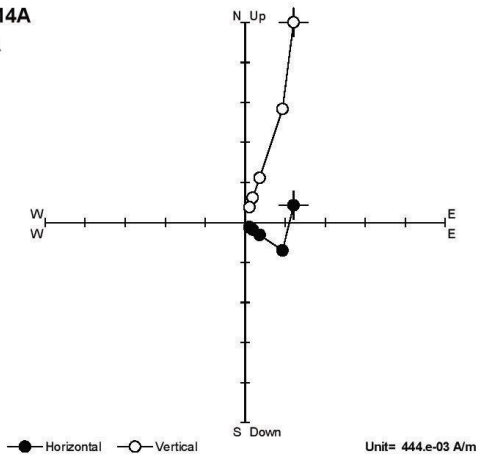
SFU013A
N/A



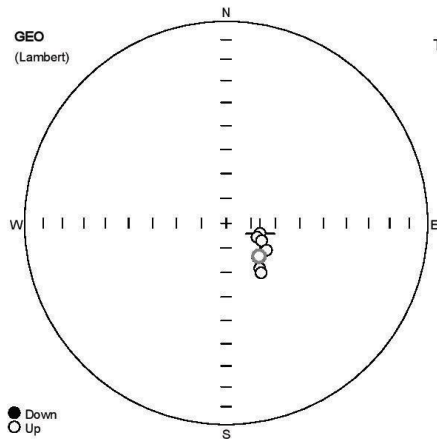
Name	Site	Latitude	Longitude	Height	Rock	Age	Fm	SDec	Sinc	BDec	Binc	FDec	Finc	P1	P2	P3	P4	Note
SFU013A								299	23					6	0	6	90	
#	State	M[A/m]	Dsp	Isp	Dge	Ige	Dtc	Itc	Dfc	Ifc	Prec	Limit1	Limit2	Note	K[e-06 SI]			
1	NRM	1.69e+00	181.1	-42.6	121.0	-65.6						1.0						
2	20	1.34e+00	191.5	-44.1	139.9	-66.3						0.0						
3	40	633.e-03	197.4	-44.5	150.2	-65.7						1.0						
4	60	364.e-03	194.5	-43.4	144.6	-65.1						1.0						
5	80	216.e-03	197.7	-43.8	150.2	-64.9						1.0						
6	CPCA	827.e-03	191.4	-44.2	139.7	-66.4					2.1	20		80	O			



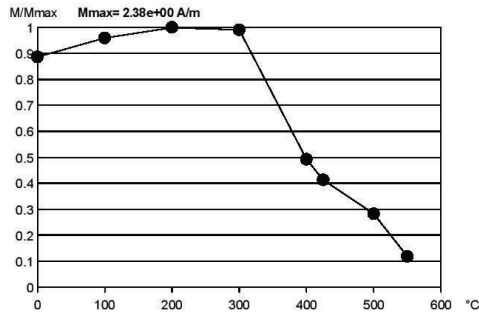
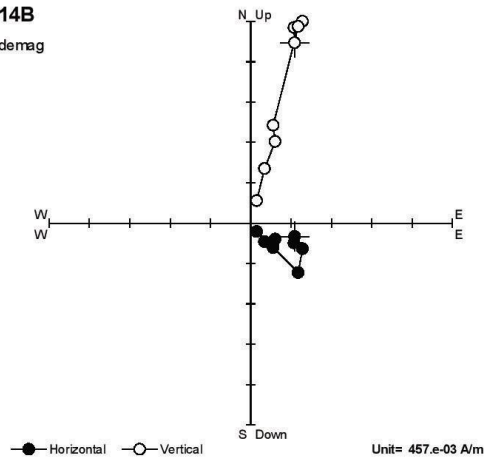
SFU014A
N/A



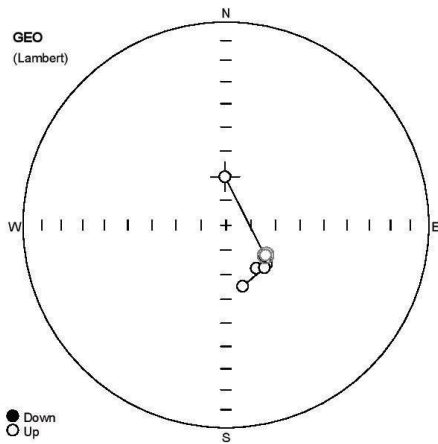
Name	Site	Latitude	Longitude	Height	Rock	Age	Fm	SDec	Sinc	BDec	Binc	FDec	Finc	P1	P2	P3	P4	Note
SFU014A								300	21					6	0	6	90	
#	State	M[A/m]	Dsp	Isp	Dge	Ige	Dtc	Itc	Dfc	lfc	Prec	Limit1	Limit2	Note	K[e-06 SI]			
1	NRM	2.29e+00	159.1	-57.8	70.4	-75.6					1.0							
2	20	1.36e+00	183.8	-46.8	126.9	-67.7					0.0							
3	40	540.e-03	186.0	-46.0	130.6	-66.8					1.0							
4	60	296.e-03	187.9	-46.7	134.2	-67.4					1.0							
5	80	184.e-03	189.6	-47.3	137.4	-67.8					1.0							
6	CPCA	885.e-03	183.4	-46.7	126.1	-67.7					0.9	20						80 O



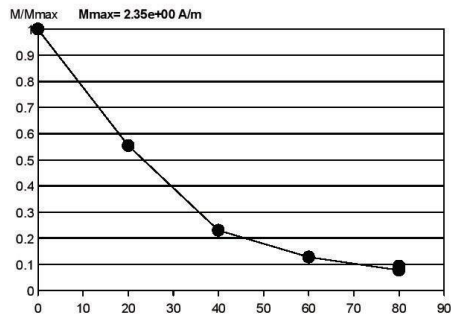
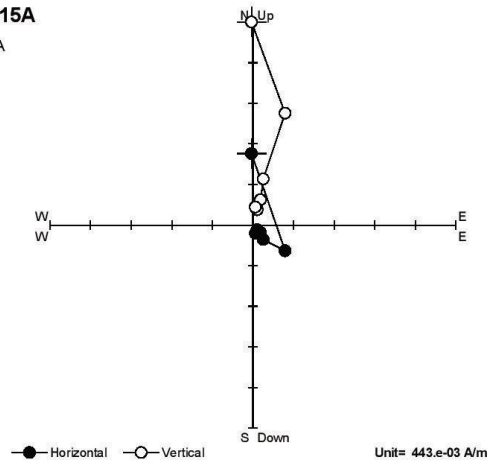
SFU014B
Thermal demag



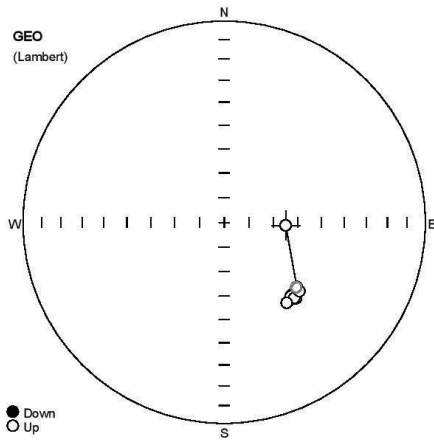
Name	Site	Latitude	Longitude	Height	Rock	Age	Fm	SDec	Sinc	BDec	BInc	FDec	FInc	P1	P2	P3	P4	Note
SFU014B								300	21					6	0	6	90	
#	State	M[A/m]	Dsp	Isp	Dge	Ige	Dtc	Itc	Dfc	Ifc	Prec	Limit1	Limit2	Note				K[e-06 SI]
1	NRM	2.11e+00	174.4	-54.9	106.9	-75.7					1.0							
2	100°C	2.28e+00	177.7	-55.3	114.5	-76.3					1.0							
3	200°C	2.38e+00	178.3	-53.0	116.3	-74.0					1.0							
4	300°C	2.36e+00	188.3	-50.2	136.3	-70.8					1.0							
5	400°C	1.17e+00	188.7	-50.7	137.3	-71.2					1.0							
6	425°C	982.e-03	181.9	-49.3	123.7	-70.3					1.0							
7	500°C	669.e-03	193.1	-47.1	143.4	-67.1					1.0							
8	550°C	280.e-03	194.5	-45.5	144.9	-65.4					1.0							
9	CPCA	1.45e+00	187.6	-50.6	135.2	-71.2					2.8	300°C	550°C O					



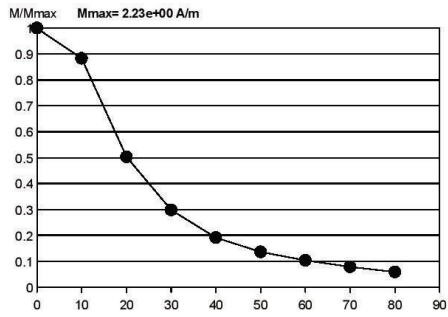
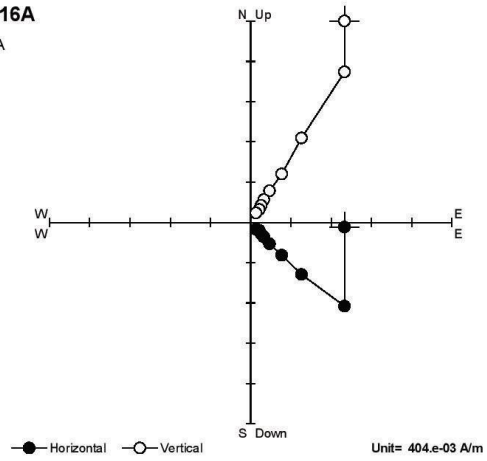
SFU015A
N/A



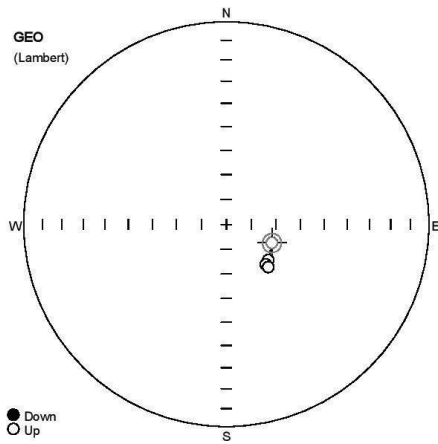
Name	Site	Latitude	Longitude	Height	Rock	Age	Fm	SDec	Slnc	BDec	Blnc	FDec	Finc	P1	P2	P3	P4	Note
SFU015A								316	23					6	0	6	90	
#	State	M[A/m]	Dsp	lsp	Dge	lge	Dtc	ltc	Dfc	lfc	Prec	Limit1	Limit2	Note	K[e-06 SI]			
1	NRM	2.35e+00	122.7	-74.4	358.9	-70.6					1.0							
2	20	1.30e+00	176.3	-46.9	128.7	-69.8					1.0							
3	40	540.e-03	184.6	-46.0	144.9	-68.8					1.0							
4	60	298.e-03	178.9	-44.5	134.0	-67.4					1.0							
5	80	180.e-03	181.1	-43.9	138.0	-66.9					1.0							
6	80	218.e-03	196.5	-43.1	164.7	-64.5					1.0							
7	CPCA	879.e-03	175.6	-47.1	127.2	-70.0					3.2	20		80	O			



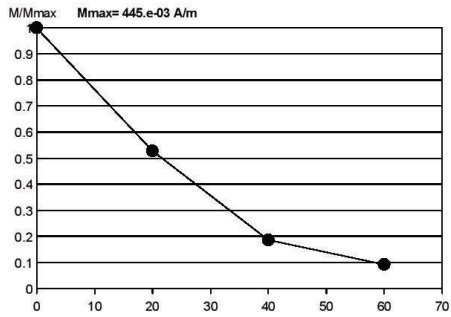
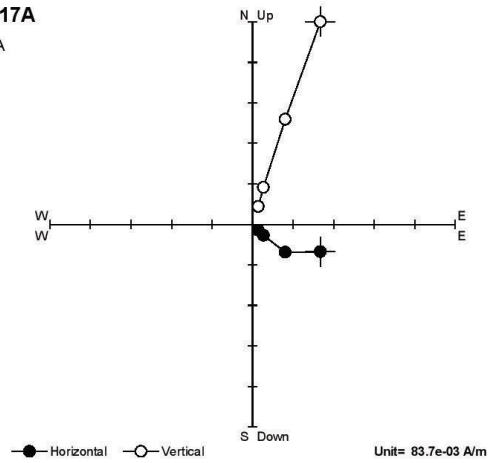
SFU016A
N/A



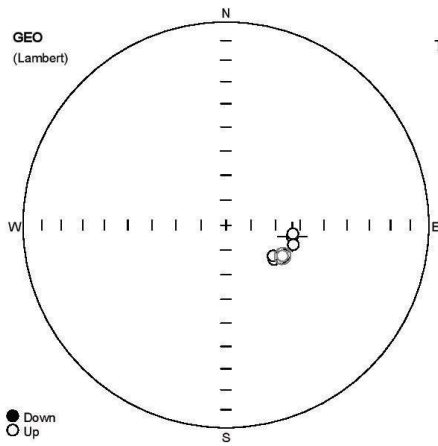
Name	Site	Latitude	Longitude	Height	Rock	Age	Fm	SDec	Sinc	BDec	Binc	FDec	Finc	P1	P2	P3	P4	Note
SFU016A								330	2					6	0	6	90	
#	State	M[A/m]	Dsp	Isp	Dge	Ige	Dtc	Itc	Dfc	Ifc	Prec	Limit1	Limit2	Note	K[e-06 S]			
1	NRM	2.23e+00	126.3	-63.9	92.8	-65.0					1.0							
2	10	1.97e+00	162.4	-48.2	131.7	-50.1					1.0							
3	20	1.12e+00	166.3	-47.3	135.7	-49.2					1.0							
4	30	663.e-03	166.9	-45.0	136.5	-46.9					1.0							
5	40	426.e-03	168.9	-45.9	138.5	-47.9					1.0							
6	50	301.e-03	168.5	-47.0	138.0	-49.0					1.0							
7	60	230.e-03	167.7	-45.5	137.2	-47.5					1.0							
8	70	173.e-03	163.1	-46.1	132.4	-48.0					1.0							
9	80	128.e-03	172.4	-46.1	142.1	-48.1					1.0							
10	CPCA	1.41e+00	162.7	-48.2	132.0	-50.1					1.9	10	80	O				



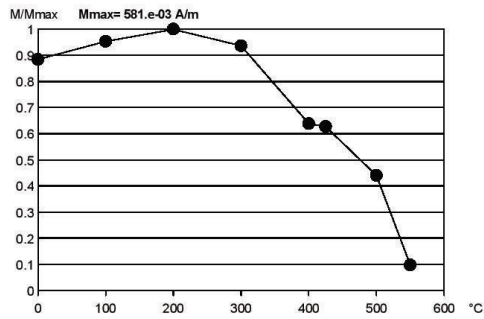
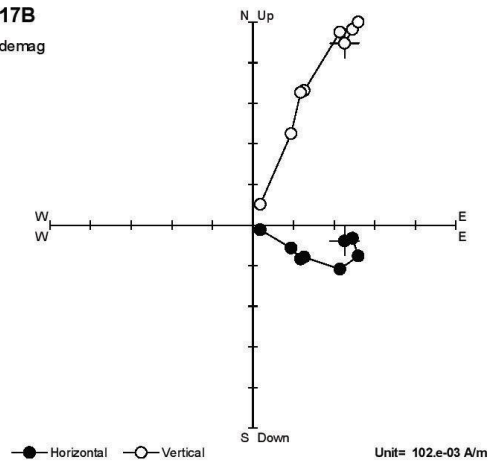
SFU017A
N/A



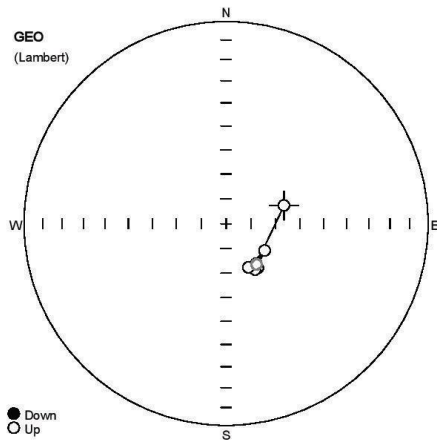
Name	Site	Latitude	Longitude	Height	Rock	Age	Fm	SDec	Sinc	BDec	Binc	FDec	Finc	P1	P2	P3	P4	Note
SFU017A								33	20					6	0	6	90	
#	State	M[A/m]	Dsp	Isp	Dge	Ige	Dtc	Itc	Dfc	lfc	Prec	Limit1	Limit2	Note	K[e-06 SI]			
1	NRM	445.e-03	128.1	-65.0	112.0	-70.2						0.0						
2	20	234.e-03	134.0	-58.5	130.4	-67.8						1.0						
3	40	82.7e-03	136.2	-57.0	135.4	-67.3						1.0						
4	60	40.5e-03	134.6	-55.8	135.5	-65.8						1.0						
5	CPCA	285.e-03	128.2	-64.9	112.3	-70.2						3.8	NRM					60 O



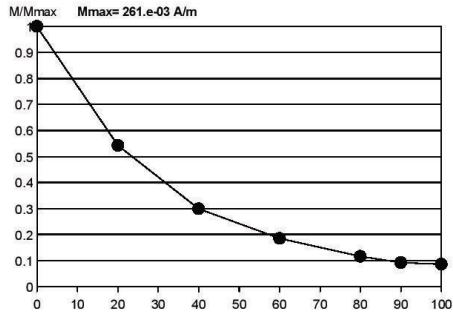
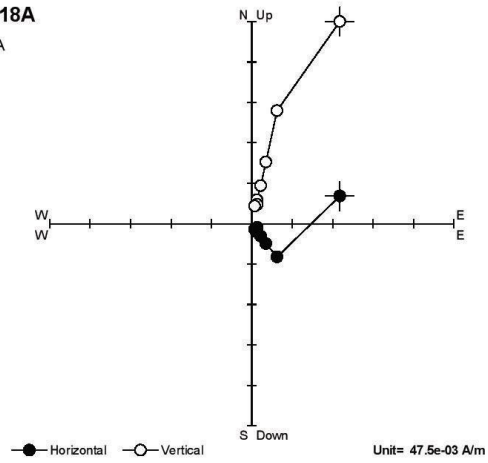
SFU017B
Thermal demag



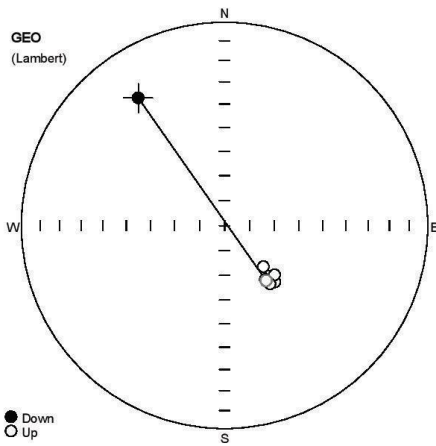
Name	Site	Latitude	Longitude	Height	Rock	Age	Fm	SDec	Sinc	BDec	Binc	FDec	Finc	P1	P2	P3	P4	Note
SFU017B								33	20					6	0	6	90	
#	State	M[A/m]	Dsp	isp	Dge	Ige	Dtc	Itc	Dfc	lfc	Prec	Limit1	Limit2	Note				K[e-06 SI]
1	NRM	513.e-03	108.0	-63.9	99.9	-62.9						1.0						
2	100°C	553.e-03	106.1	-64.6	97.5	-62.8						1.0						
3	200°C	581.e-03	110.7	-60.8	106.3	-61.6						1.0						
4	300°C	544.e-03	120.0	-58.8	116.8	-63.2						1.0						
5	400°C	371.e-03	126.6	-59.3	121.9	-65.8						1.0						
6	425°C	364.e-03	129.2	-58.6	125.5	-66.2						1.0						
7	500°C	255.e-03	123.8	-58.2	121.1	-64.0						1.0						
8	550°C	56.1e-03	129.5	-60.1	123.3	-67.3						1.0						
9	CPCA	279.e-03	122.2	-58.8	118.6	-64.0					3.3	300°C	550°C O					



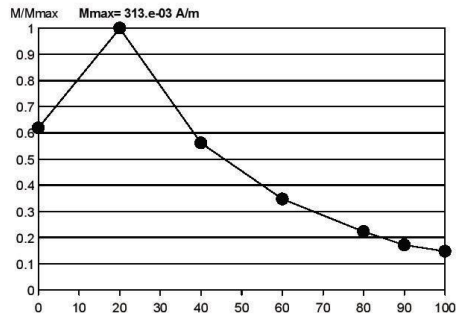
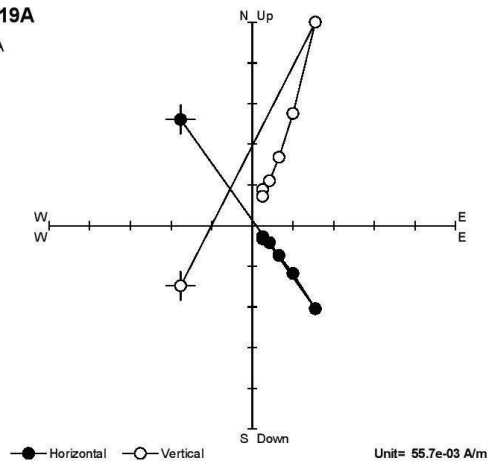
SFU018A
N/A



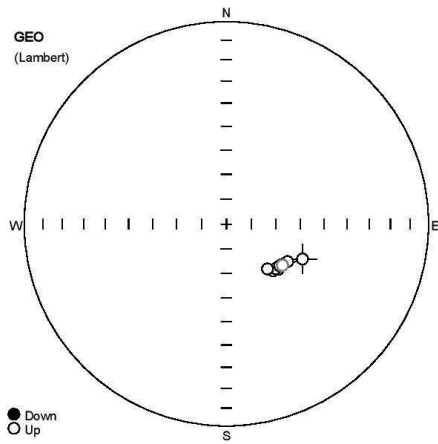
Name	Site	Latitude	Longitude	Height	Rock	Age	Fm	SDec	Sinc	BDec	Binc	FDec	Finc	P1	P2	P3	P4	Note
SFU018A								25	25					6	0	6	90	
#	State	M[A/m]	Dsp	Isp	Dge	Ige	Dtc	Itc	Dfc	Ifc	Prec	Limit1	Limit2	Note				K[e-06 SI]
1	NRM	261.e-03	113.0	-70.5	72.6	-65.5					1.0							
2	20	142.e-03	150.6	-51.5	142.8	-69.8					1.0							
3	40	77.9e-03	150.3	-50.1	144.6	-68.5					2.0							
4	60	48.2e-03	149.6	-49.6	144.3	-67.9					1.0							
5	80	30.1e-03	151.2	-49.0	147.6	-68.0					1.0							
6	90	23.8e-03	144.6	-56.5	124.9	-71.0					1.0							
7	100	22.1e-03	155.5	-49.9	152.8	-70.2					1.0							
8	CPCA	92.5e-03	150.5	-51.2	143.2	-69.5					1.9	20	100	O				



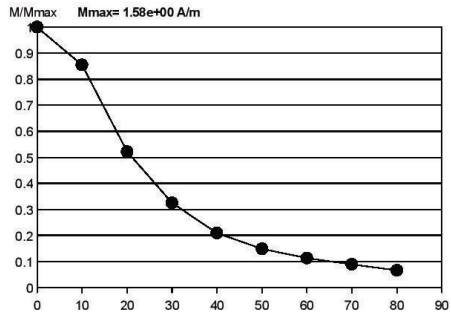
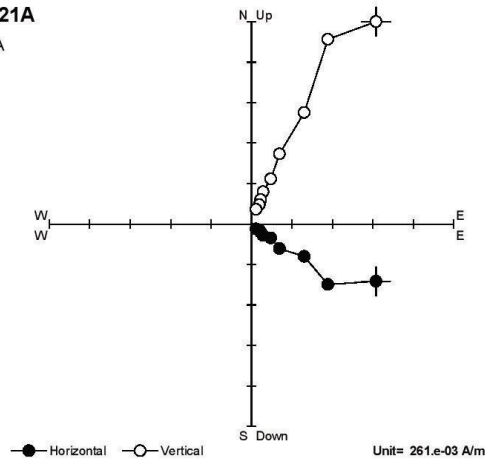
SFU019A
N/A



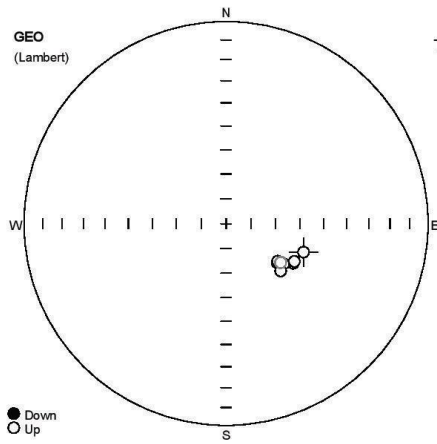
Name	Site	Latitude	Longitude	Height	Rock	Age	Fm	SDec	Sinc	BDec	Blnc	FDec	Finc	P1	P2	P3	P4	Note	
SFU019A								65	36					6	0	6	90		
#	State	M[A/m]	Dsp	Isp	Dge	Ige	Dtc	Itc	Dfc	lfc	Prec	Limit1	Limit2	Note				K[e-06 SI]	
1	NRM	194.e-03	278.5	25.4	325.9	25.2						1.0							
2	20	313.e-03	134.8	-50.9	142.8	-62.8						1.0							
3	40	176.e-03	130.8	-51.3	139.8	-60.7						1.0							
4	60	109.e-03	128.6	-51.6	138.2	-59.5						1.0							
5	80	69.7e-03	130.7	-54.0	134.6	-61.7						1.0							
6	90	53.6e-03	140.5	-54.9	136.5	-67.3						1.0							
7	100	45.9e-03	131.0	-50.1	142.1	-60.2						2.0							
8	CPCA	204.e-03	134.2	-50.7	142.9	-62.3						2.3	20					100	O



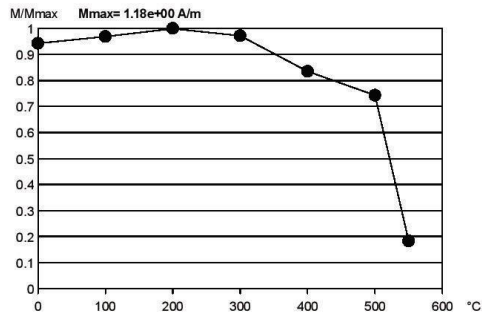
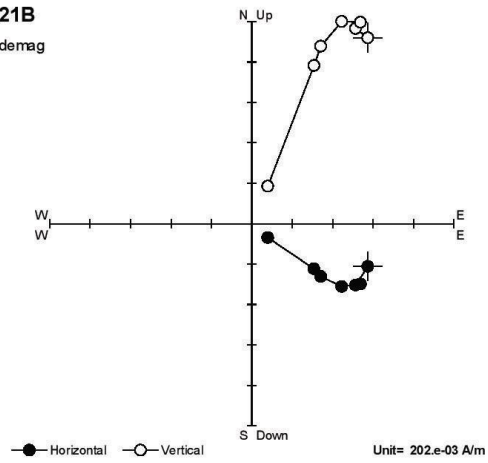
SFU021A
N/A



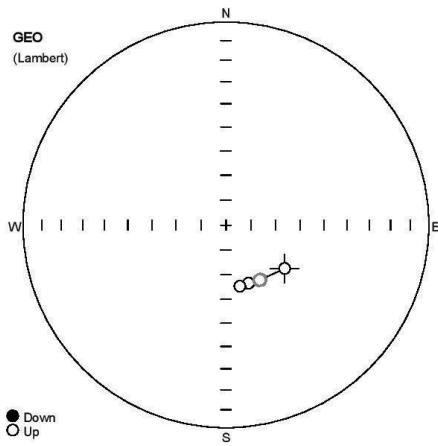
Name	Site	Latitude	Longitude	Height	Rock	Age	Fm	SDec	Sinc	BDec	Binc	FDec	Finc	P1	P2	P3	P4	Note
SFU021A								355	27					6	0	6	90	
#	State	M[A/m]	Dsp	Isp	Dge	Ige	Dtc	Itc	Dfc	lfc	Prec	Limit1	Limit2	Note	K[e-06 SI]			
1	NRM	1.58e+00	142.0	-37.7	114.7	-55.9					1.0							
2	10	1.35e+00	153.7	-40.0	128.3	-62.2					1.0							
3	20	823.e-03	149.2	-40.4	121.6	-60.9					1.0							
4	30	513.e-03	155.2	-39.3	131.2	-62.1					1.0							
5	40	330.e-03	152.5	-40.4	126.2	-62.2					1.0							
6	50	234.e-03	157.8	-39.7	134.9	-63.2					1.0							
7	60	177.e-03	156.3	-40.0	132.2	-63.1					1.0							
8	70	140.e-03	153.8	-40.3	128.1	-62.5					1.0							
9	80	104.e-03	160.4	-41.3	137.6	-65.4					1.0							
10	CPCA	942.e-03	152.4	-40.0	126.4	-61.8					2.3	10	80	O				



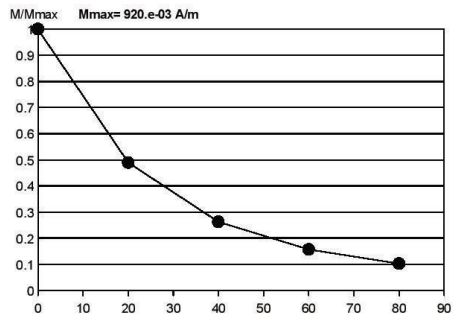
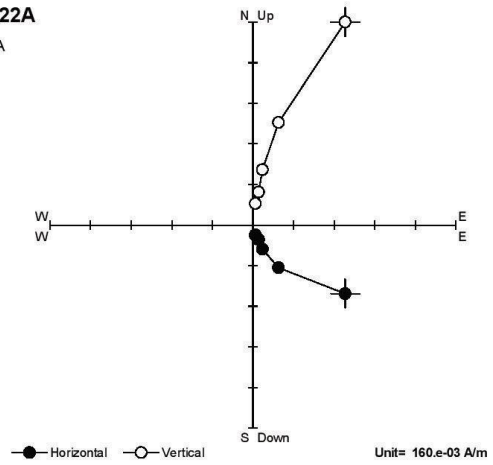
SFU021B
Thermal damag



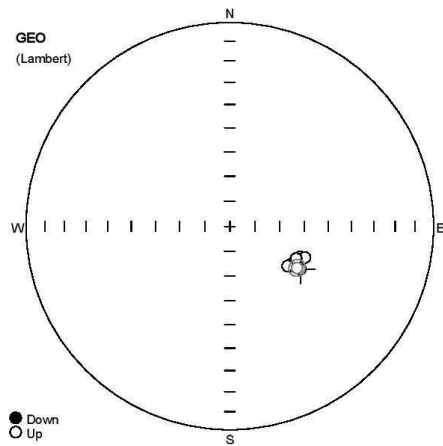
Name	Site	Latitude	Longitude	Height	Rock	Age	Fm	SDec	Sinc	BDec	Binc	FDec	Finc	P1	P2	P3	P4	Note
SFU021B								355	27					6	0	6	90	
#	State	M[A/m]	Dsp	IsP	Dge	Ige	Dtc	Itc	Dfc	Ifc	Prec	Limit1	Limit2	Note				K[e-06 SI]
1	NRM	1.11e+00	139.6	-39.4	110.2	-56.4						1.0						
2	100°C	1.14e+00	147.0	-38.2	120.6	-58.3						1.0						
3	200°C	1.18e+00	146.1	-38.6	119.0	-58.3						1.0						
4	300°C	1.15e+00	151.5	-40.1	125.0	-61.5						1.0						
5	400°C	985.e-03	154.2	-41.7	127.5	-63.9						1.0						
6	500°C	877.e-03	153.6	-42.2	126.0	-64.1						1.0						
7	550°C	215.e-03	154.4	-38.1	131.0	-60.7						1.0						
8	CPCA	503.e-03	152.5	-41.2	125.4	-62.9					2.3	300°C	550°C O					



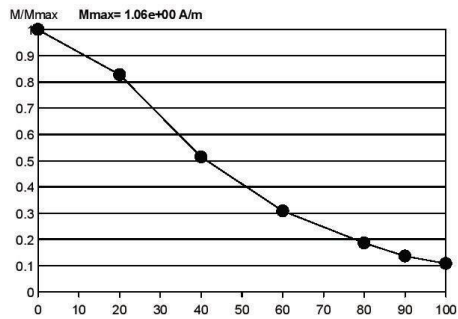
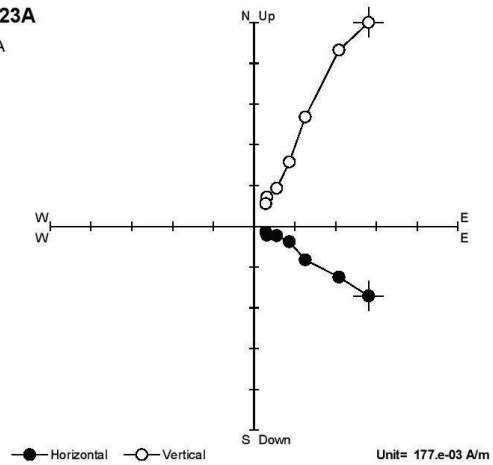
SFU022A
N/A



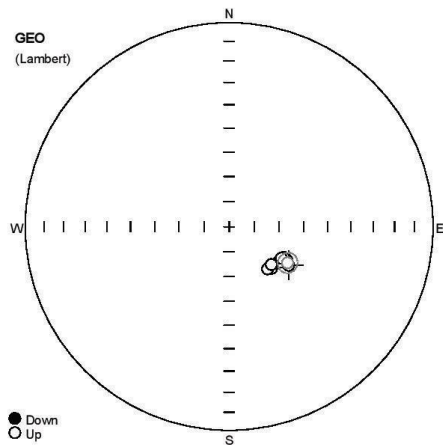
Name	Site	Latitude	Longitude	Height	Rock	Age	Fm	SDec	Sinc	BDec	Binc	FDec	Finc	P1	P2	P3	P4	Note
SFU022A								353	25					6	0	6	90	
#	State	M[A/m]	Dsp	IsP	Dge	Ige	Dtc	Itc	Dfc	Ifc	Prec	Limit1	Limit2	Note	K[e-06 SI]			
1	NRM	920.e-03	152.2	-40.2	126.6	-60.5					1.0							
2	20	450.e-03	166.5	-40.3	149.0	-64.1					1.0							
3	40	242.e-03	172.0	-40.3	158.4	-64.9					1.0							
4	60	144.e-03	172.0	-40.2	158.6	-64.8					1.0							
5	80	94.0e-03	176.7	-39.8	167.1	-64.7					1.0							
6	CPCA	265.e-03	166.1	-40.3	148.2	-64.0					2.6	20						80 O



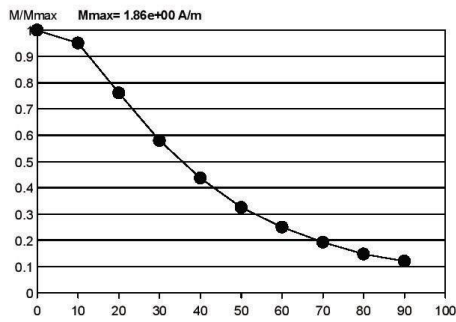
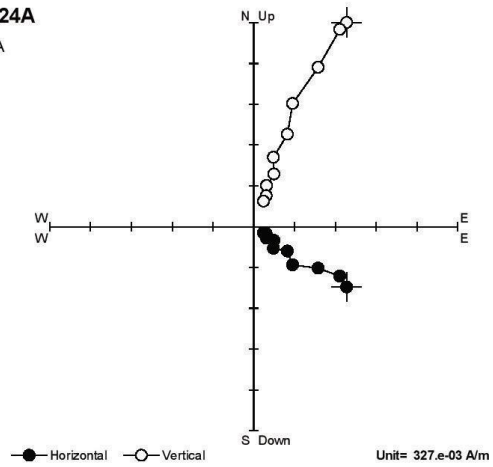
SFU023A
N/A



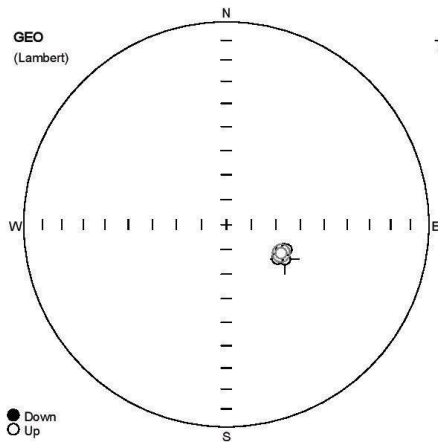
Name	Site	Latitude	Longitude	Height	Rock	Age	Fm	SDec	Sinc	BDec	Binc	FDec	Finc	P1	P2	P3	P4	Note
SFU023A								359	28					6	0	6	90	
#	State	M[A/m]	Dsp	lsp	Dge	Ige	Dtc	ltc	Dfc	lfc	Prec	Limit1	Limit2	Note				K[e-06 SI]
1	NRM	1.06e+00	144.5	-36.9	121.3	-56.7					1.0							
2	20	878.e-03	146.9	-40.5	120.9	-60.7					1.0							
3	40	545.e-03	148.2	-40.0	123.1	-60.8					1.0							
4	60	326.e-03	141.8	-41.2	113.6	-59.2					1.0							
5	80	197.e-03	139.8	-39.8	112.7	-57.2					1.0							
6	90	144.e-03	149.7	-40.5	124.6	-61.8					1.0							
7	100	114.e-03	143.9	-41.4	116.0	-60.3					2.0							
8	CPCA	654.e-03	145.8	-38.0	121.8	-58.2					3.3	NRM	100	O				



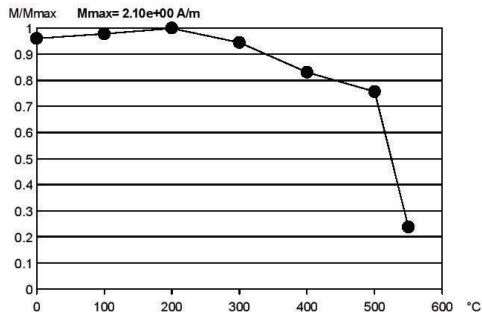
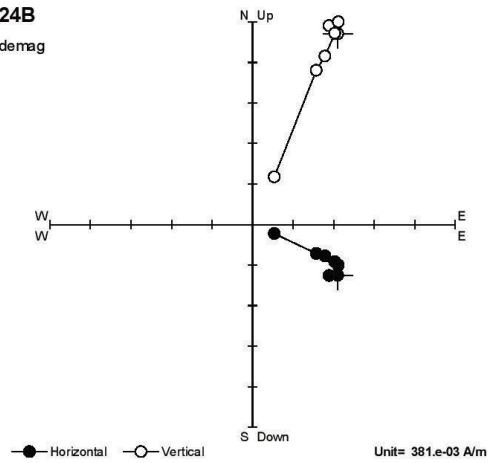
SFU024A
N/A



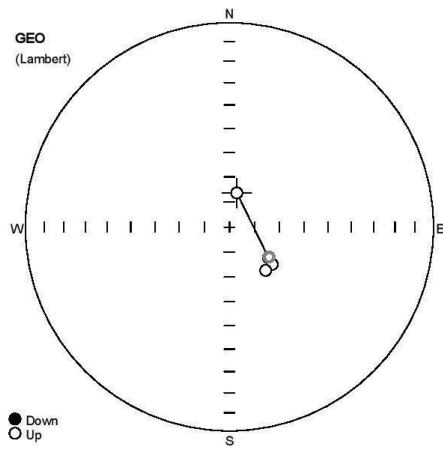
Name	Site	Latitude	Longitude	Height	Rock	Age	Fm	SDec	Sinc	BDec	Binc	FDec	Finc	P1	P2	P3	P4	Note
SFU024A								330	27					6	0	6	90	
#	State	M[A/m]	Dsp	Isp	Dge	Ige	Dtc	Itc	Dfc	Ifc	Prec	Limit1	Limit2	Note	K[e-06 SI]			
1	NRM	1.86e+00	164.4	-36.2	123.0	-61.5					1.0							
2	10	1.77e+00	163.3	-38.2	119.9	-63.3					1.0							
3	20	1.42e+00	165.2	-38.9	122.8	-64.3					1.0							
4	30	1.08e+00	171.9	-39.6	134.5	-66.1					1.0							
5	40	813.e-03	167.5	-40.0	126.1	-65.8					1.0							
6	50	604.e-03	173.8	-40.5	137.7	-67.1					1.0							
7	60	465.e-03	166.5	-39.5	124.6	-65.1					1.0							
8	70	358.e-03	170.9	-41.0	131.9	-67.3					1.0							
9	80	273.e-03	163.6	-39.9	119.4	-64.9					1.0							
10	90	224.e-03	164.9	-40.3	121.3	-65.6					1.0							
11	CPCA	1.06e+00	164.1	-37.1	121.8	-62.4					4.0	NRM	90 O					



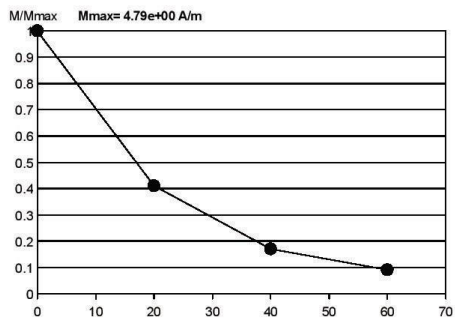
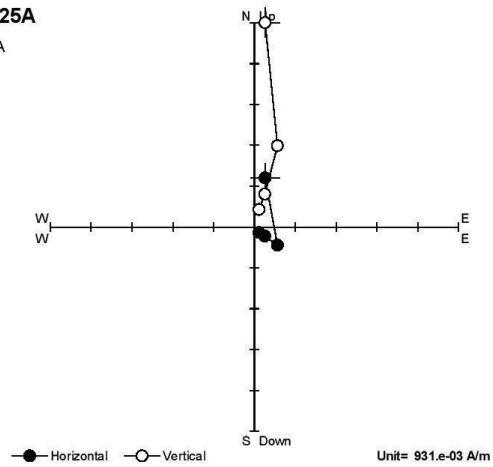
SFU024B
Thermal demag



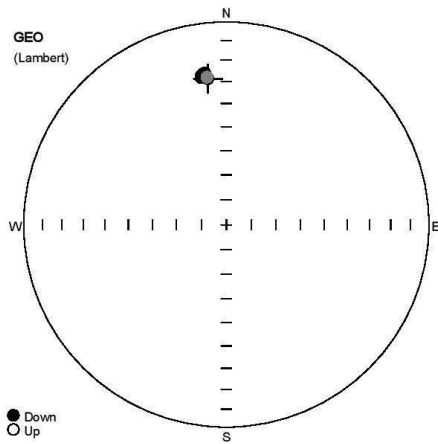
Name	Site	Latitude	Longitude	Height	Rock	Age	Fm	SDec	Sinc	BDec	Binc	FDec	Finc	P1	P2	P3	P4	Note
SFU024B								330	27					6	0	6	90	
#	State	M[A/m]	Dsp	isp	Dge	Ige	Dtc	Itc	Dfc	lfc	Prec	Limit1	Limit2	Note				K[e-06 SI]
1	NRM	2.02e+00	163.5	-37.4	120.7	-62.5						1.0						
2	100°C	2.06e+00	166.0	-39.6	123.7	-65.2						1.0						
3	200°C	2.10e+00	161.5	-40.4	115.3	-64.9						1.0						
4	300°C	1.98e+00	160.9	-40.4	114.3	-64.7						1.0						
5	400°C	1.75e+00	160.5	-40.7	113.4	-64.9						1.0						
6	500°C	1.59e+00	161.4	-41.2	114.4	-65.6						1.0						
7	550°C	498.e-03	159.7	-39.7	112.8	-63.7						1.0						
8	CPCA	639.e-03	162.8	-40.3	117.6	-65.1					3.5	100°C	550°C O					



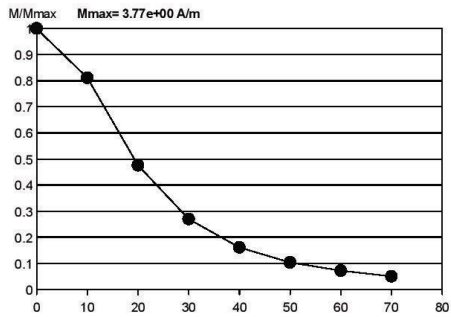
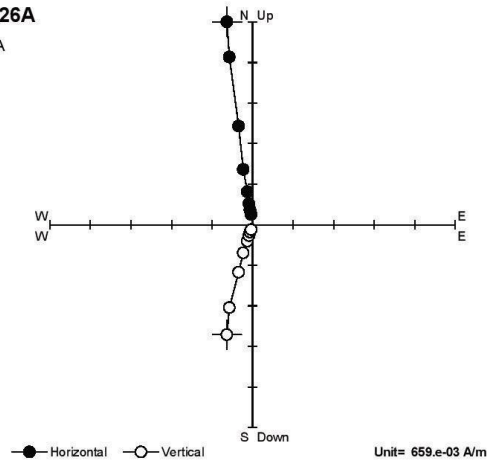
SFU025A
N/A



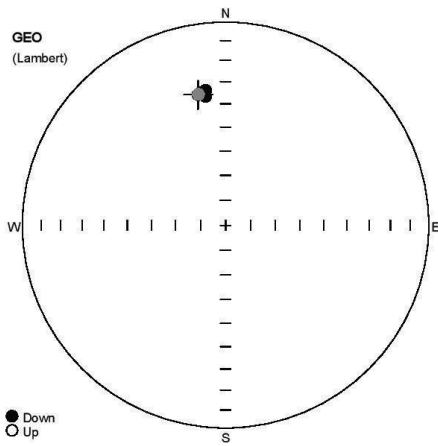
Name	Site	Latitude	Longitude	Height	Rock	Age	Fm	SDec	Sinc	BDec	Binc	FDec	Finc	P1	P2	P3	P4	Note
SFU025A								323	33					6	0	6	90	
#	State	M[A/m]	Dsp	Isp	Dge	Ige	Dtc	Itc	Dfc	Ifc	Prec	Limit1	Limit2	Note				K[e-06 SI]
1	NRM	4.79e+00	155.5	-64.0	12.4	-76.2					1.0							
2	20	1.97e+00	173.7	-37.5	128.3	-70.1					1.0							
3	40	813.e-03	174.5	-34.6	131.2	-67.3					1.0							
4	60	432.e-03	178.7	-34.4	140.2	-67.4					1.0							
5	CPCA	1.17e+00	173.3	-37.7	127.2	-70.2					1.6	20	60	O				



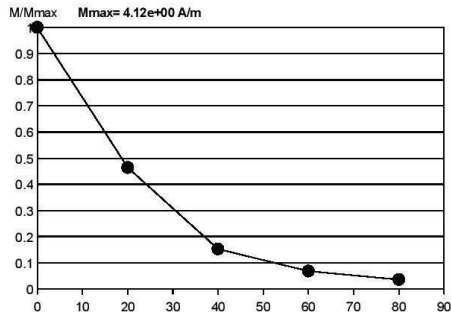
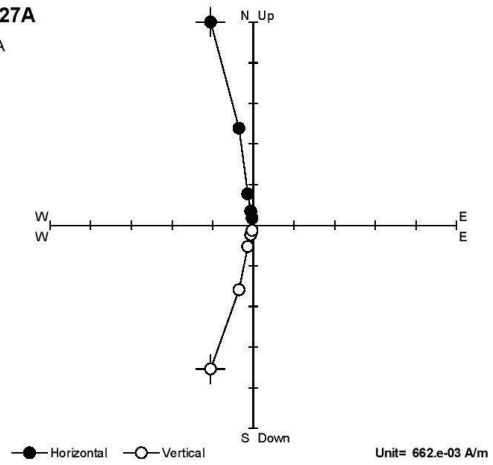
SFU026A
N/A



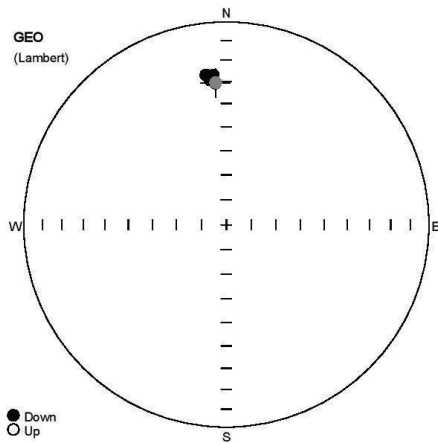
Name	Site	Latitude	Longitude	Height	Rock	Age	Fm	SDec	Sinc	BDec	Binc	FDec	Finc	P1	P2	P3	P4	Note
SFU026A								170	55					6	0	6	90	
#	State	M[A/m]	Dsp	Isp	Dge	Ige	Dtc	Itc	Dfc	lfc	Prec	Limit1	Limit2	Note				K[e-06 SI]
1	NRM	3.77e+00	200.0	82.9	352.8	28.3					1.0							
2	10	3.06e+00	192.0	81.0	352.1	26.1					1.0							
3	20	1.79e+00	190.5	80.3	351.9	25.5					1.0							
4	30	1.02e+00	182.7	81.6	350.4	26.6					1.0							
5	40	604.e-03	185.6	81.3	351.0	26.3					1.0							
6	50	389.e-03	181.1	82.3	350.2	27.3					1.0							
7	60	269.e-03	184.2	81.2	350.7	26.2					1.0							
8	70	188.e-03	188.7	80.5	351.6	25.6					1.0							
9	CPCA	2.54e+00	197.3	82.1	352.6	27.5					1.6	NRM	70 O					



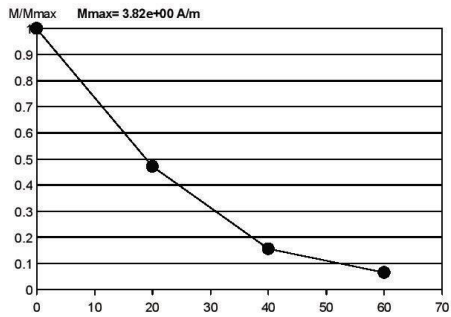
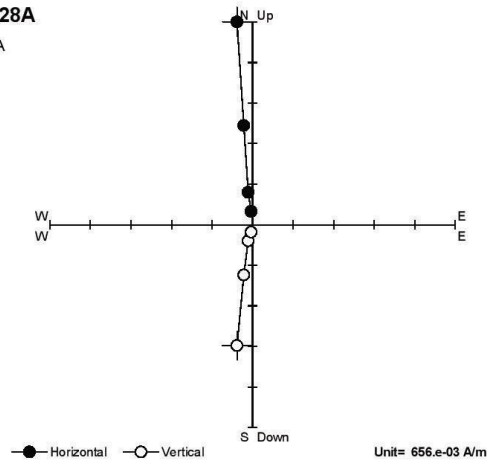
SFU027A
N/A



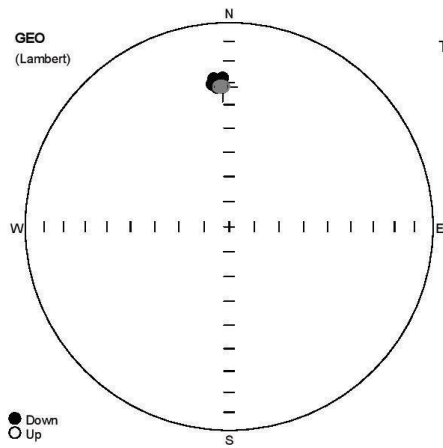
Name	Site	Latitude	Longitude	Height	Rock	Age	Fm	SDec	Sinc	BDec	Binc	FDec	Finc	P1	P2	P3	P4	Note	
SFU027A								174	47					6	0	6	90		
#	State	M[A/m]	Dsp	Isp	Dge	Ige	Dtc	Itc	Dfc	lfc	Prec	Limit1	Limit2	Note					K[e-06 SI]
1	NRM	4.12e+00	148.9	80.5	348.1	34.7					0.0								
2	20	1.91e+00	168.1	80.2	351.6	33.4					1.0								
3	40	626.e-03	160.7	80.5	350.2	34.0					1.0								
4	60	278.e-03	155.7	80.5	349.3	34.2					1.0								
5	80	142.e-03	161.7	82.8	351.2	36.1					1.0								
6	CPCA	2.94e+00	150.5	80.5	348.3	34.6					1.5	NRM	80	O					



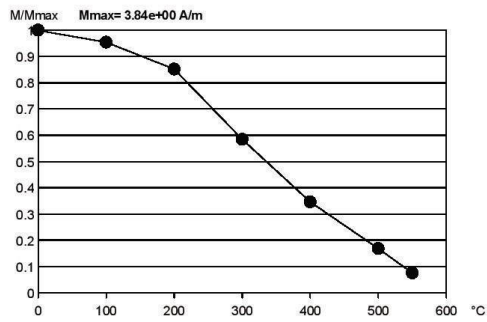
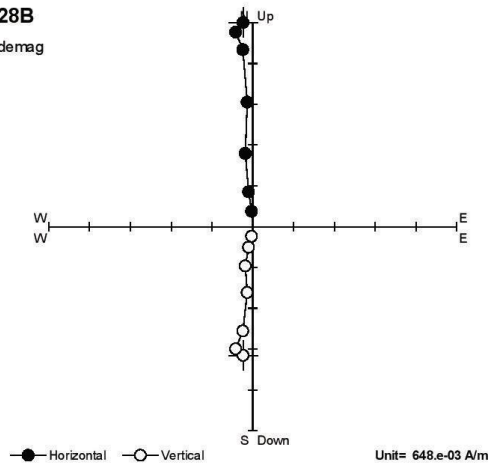
SFU028A
N/A



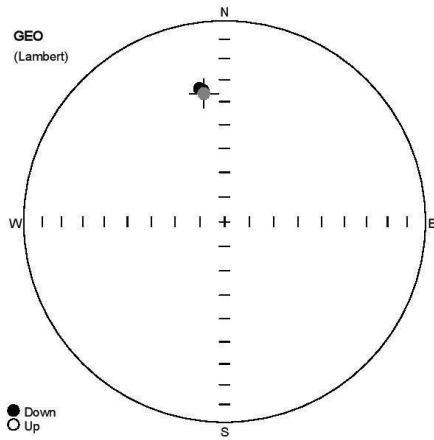
Name	Site	Latitude	Longitude	Height	Rock	Age	Fm	SDec	Sinc	BDec	Binc	FDec	Finc	P1	P2	P3	P4	Note
SFU028A								167	47					6	0	6	90	
#	State	M[A/m]	Dsp	Isp	Dge	Ige	Dtc	Itc	Dfc	lfc	Prec	Limit1	Limit2	Note	K[e-06 SI]			
1	NRM	3.82e+00	211.8	75.9	355.6	30.7						1.0						
2	20	1.80e+00	204.5	72.6	355.0	26.8						1.0						
3	40	592.e-03	195.9	72.8	352.2	26.4						1.0						
4	60	247.e-03	203.0	75.0	353.6	29.0						1.0						
5	CPCA	2.53e+00	212.0	75.7	355.7	30.5					1.9	NRM	60	O				



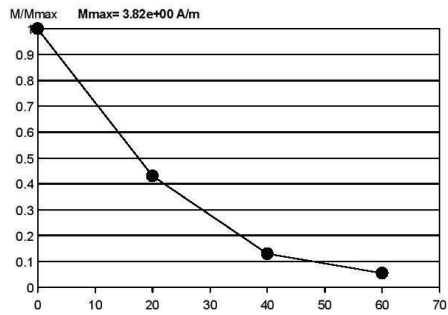
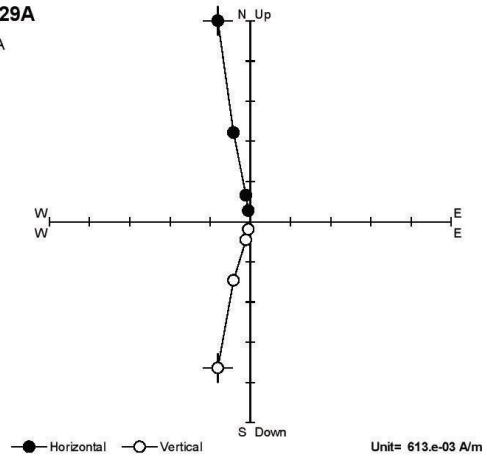
SFU028B
Thermal demag



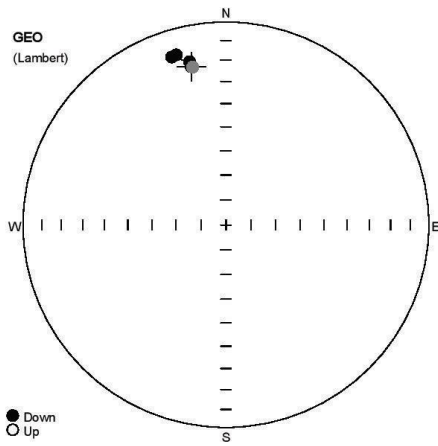
Name	Site	Latitude	Longitude	Height	Rock	Age	Fm	SDec	Sinc	BDec	Binc	FDec	Finc	P1	P2	P3	P4	Note
SFU028B								167	47					6	0	6	90	
#	State	M[A/m]	Dsp	Isp	Dge	Ige	Dtc	Itc	Dfc	Ifc	Prec	Limit1	Limit2	Note				K[e-06 SI]
1	NRM	3.84e+00	220.5	76.5	357.3	32.2						1.0						
2	100°C	3.66e+00	212.3	77.3	355.0	32.0						1.0						
3	200°C	3.27e+00	215.2	75.2	356.8	30.5						1.0						
4	300°C	2.24e+00	212.7	72.7	357.5	27.9						1.0						
5	400°C	1.33e+00	203.3	74.0	354.1	28.0						1.0						
6	500°C	644.e-03	203.7	76.6	353.2	30.5						1.0						
7	550°C	289.e-03	214.4	76.9	355.7	31.8						1.0						
8	CPCA	1.93e+00	217.5	76.4	356.7	31.8					2.8	NRM	550°C	O				



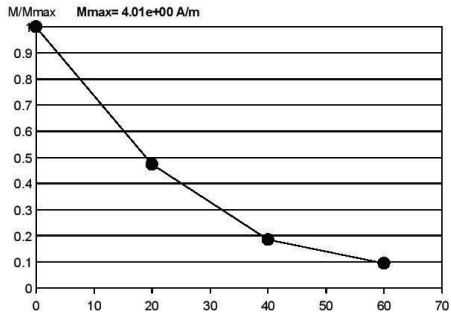
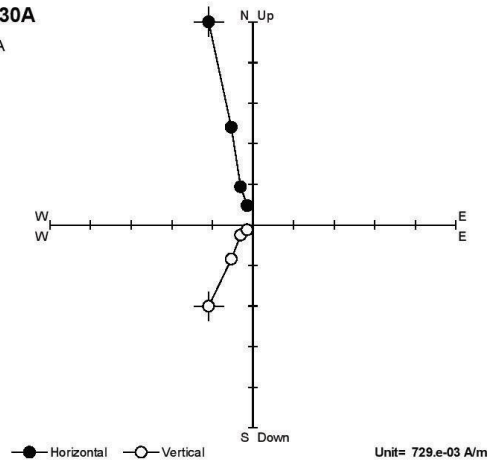
SFU029A
N/A



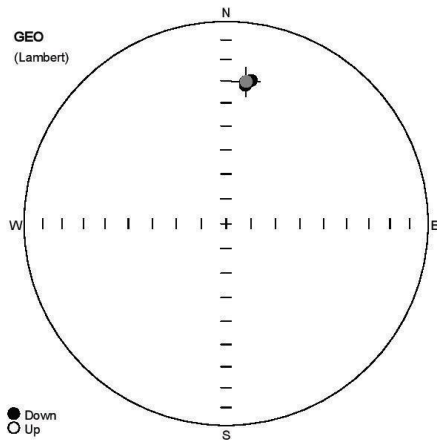
Name	Site	Latitude	Longitude	Height	Rock	Age	Fm	SDec	Sinc	BDec	Binc	FDec	Finc	P1	P2	P3	P4	Note
SFU029A								176	43					6	0	6	90	
#	State	M[A/m]	Dsp	Isp	Dge	Ige	Dtc	Itc	Dfc	Ifc	Prec	Limit1	Limit2	Note	K[e-06 SI]			
1	NRM	3.82e+00	159.3	78.1	350.8	35.7					0.0							
2	20	1.65e+00	157.7	75.1	349.3	33.0					1.0							
3	40	495.e-03	160.8	76.5	350.7	34.1					1.0							
4	60	205.e-03	160.0	76.5	350.4	34.1					1.0							
5	CPCA	2.59e+00	159.1	78.0	350.8	35.6					1.3	NRM	60	O				



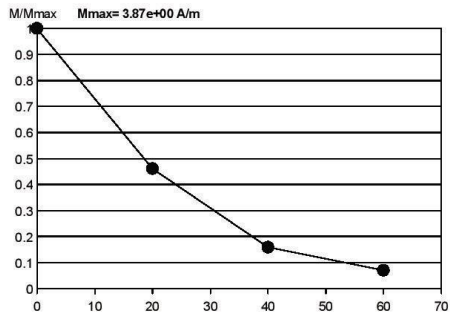
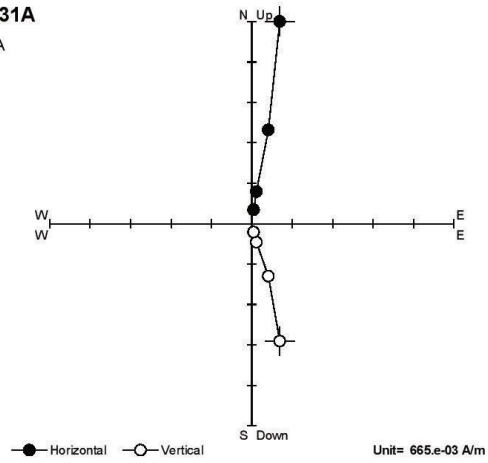
SFU030A
N/A



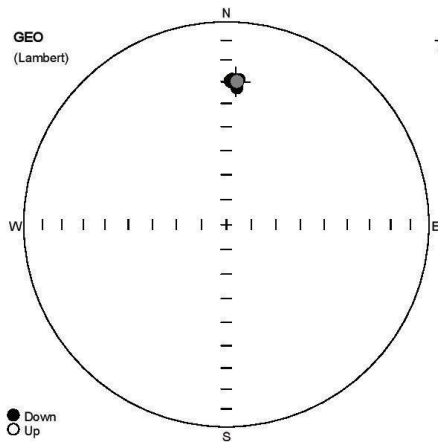
Name	Site	Latitude	Longitude	Height	Rock	Age	Fm	SDec	Sinc	BDec	Binc	FDec	Finc	P1	P2	P3	P4	Note
SFU030A								117	32					6	0	6	90	
#	State	M[A/m]	Dsp	Isp	Dge	Ige	Dtc	Itc	Dfc	lfc	Prec	Limit1	Limit2	Note	K[e-06 SI]			
1	NRM	4.01e+00	246.9	38.4	347.7	21.4						1.0						
2	20	1.90e+00	245.0	36.4	347.5	18.8						1.0						
3	40	741.e-03	236.7	34.8	342.1	14.2						1.0						
4	60	375.e-03	238.2	33.7	343.7	13.8						1.0						
5	CPCA	2.61e+00	247.6	38.5	348.1	21.7					1.8	NRM	60	O				



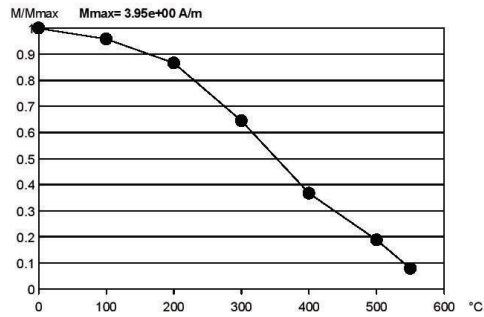
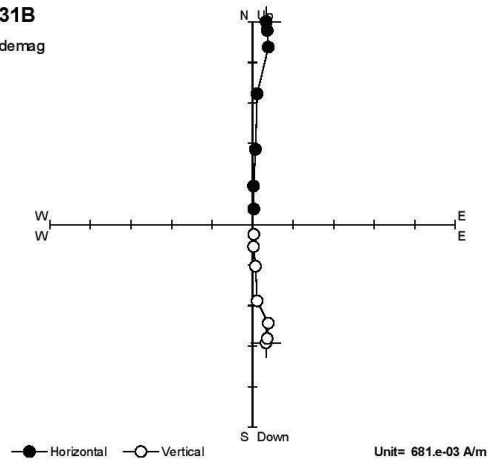
SFU031A
N/A



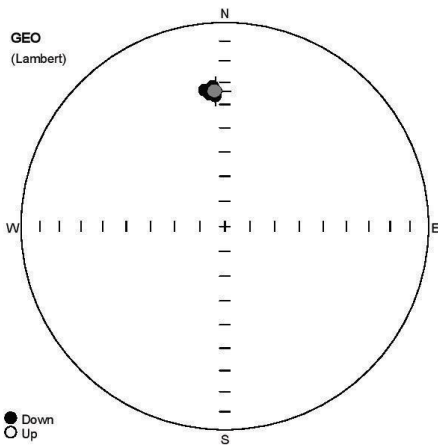
Name	Site	Latitude	Longitude	Height	Rock	Age	Fm	SDec	Sinc	BDec	Binc	FDec	Finc	P1	P2	P3	P4	Note
SFU031A								192	46					6	0	6	90	
#	State	M[A/m]	Dsp	Isp	Dge	Ige	Dtc	Itc	Dfc	Ifc	Prec	Limit1	Limit2	Note				K[e-06 SI]
1	NRM	3.87e+00	165.7	75.5	7.9	29.9					0.0							
2	20	1.79e+00	173.4	74.8	10.0	28.9					1.0							
3	40	612.e-03	166.4	75.5	8.1	29.8					1.0							
4	60	270.e-03	164.6	77.1	8.0	31.5					1.0							
5	CPCA	2.57e+00	166.4	75.4	8.1	29.7					1.0	NRM	60 O					



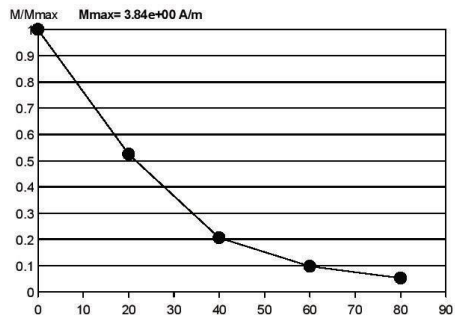
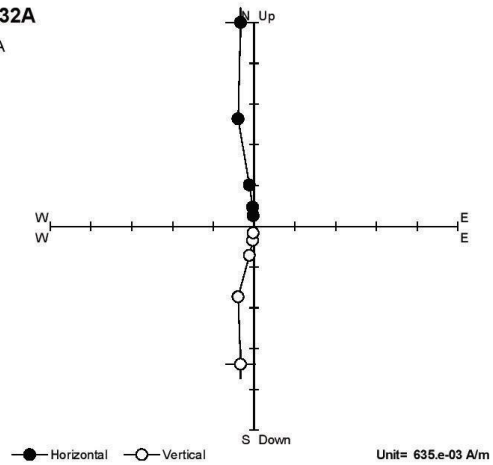
SFU031B
Thermal demag



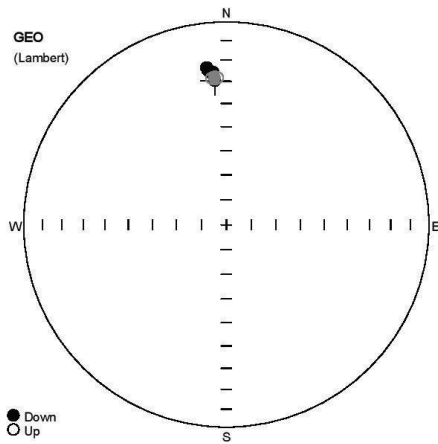
Name	Site	Latitude	Longitude	Height	Rock	Age	Fm	SDec	Sinc	BDec	Binc	FDec	Finc	P1	P2	P3	P4	Note
SFU031B								192	46					6	0	6	90	
#	State	M[A/m]	Dsp	Isp	Dge	Ige	Dtc	Itc	Dfc	Ifc	Prec	Limit1	Limit2	Note	K[e-06 SI]			
1	NRM	3.95e+00	152.0	74.7	3.8	30.2						1.0						
2	100°C	3.79e+00	153.2	75.1	4.3	30.4						1.0						
3	200°C	3.42e+00	157.5	74.0	5.1	29.0						1.0						
4	300°C	2.55e+00	146.8	74.2	2.0	30.3						1.0						
5	400°C	1.45e+00	149.4	73.2	2.3	29.1						1.0						
6	500°C	743.e-03	145.9	73.7	1.5	29.9						1.0						
7	550°C	309.e-03	149.6	77.4	4.5	32.9						1.0						
8	CPCA	1.92e+00	154.1	74.7	4.3	29.9					1.7	NRM	550°C O					



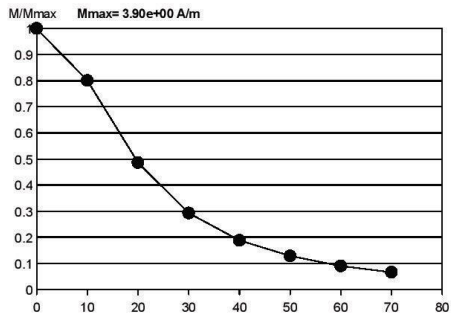
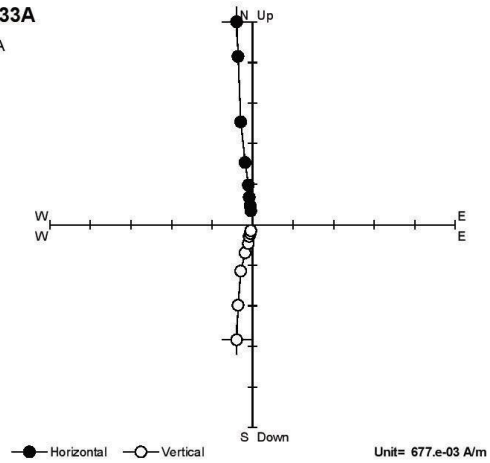
SFU032A
N/A



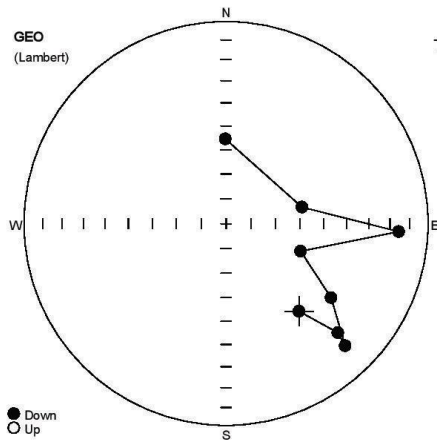
Name	Site	Latitude	Longitude	Height	Rock	Age	Fm	SDec	Sinc	BDec	Binc	FDec	Finc	P1	P2	P3	P4	Note
SFU032A								185	50					6	0	6	90	
#	State	M[A/m]	Dsp	Isp	Dge	Ige	Dtc	Itc	Dfc	Ifc	Prec	Limit1	Limit2	Note				K[e-06 SI]
1	NRM	3.84e+00	127.8	80.7	356.2	34.0					0.0							
2	20	2.02e+00	118.8	77.2	351.6	33.0					0.0							
3	40	790.e-03	114.6	79.7	353.5	35.1					1.0							
4	60	370.e-03	115.6	81.7	355.8	36.0					1.0							
5	80	197.e-03	132.6	78.5	355.1	31.8					1.0							
6	CPCA	2.64e+00	126.7	80.2	355.6	33.8					2.1	NRM	80	O				



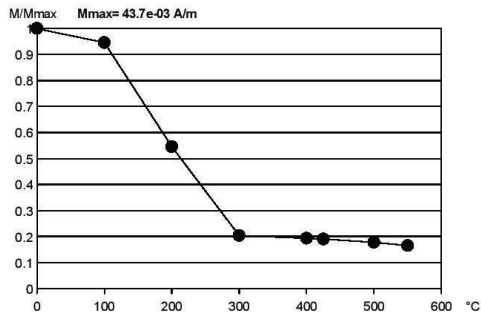
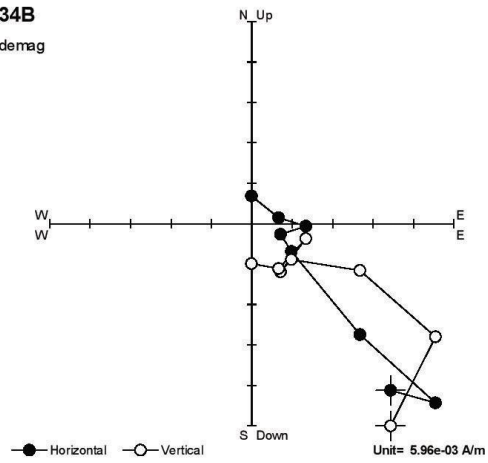
SFU033A
N/A



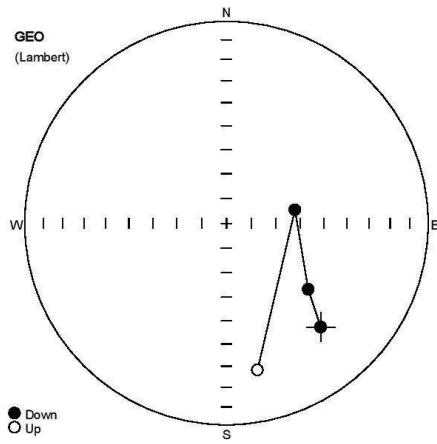
Name	Site	Latitude	Longitude	Height	Rock	Age	Fm	SDec	Sinc	BDec	Binc	FDec	Finc	P1	P2	P3	P4	Note	
SFU033A								146	49					6	0	6	90		
#	State	M[A/m]	Dsp	Isp	Dge	Ige	Dtc	Itc	Dfc	lfc	Prec	Limit1	Limit2	Note					K[e-06 SI]
1	NRM	3.90e+00	253.6	63.5	355.5	29.5						1.0							
2	10	3.12e+00	246.3	61.4	355.1	25.5						1.0							
3	20	1.89e+00	242.2	61.6	353.4	24.2						1.0							
4	30	1.14e+00	241.6	61.9	353.1	24.2						1.0							
5	40	733.e-03	245.2	62.1	354.1	25.6						1.0							
6	50	500.e-03	239.7	61.1	353.0	23.0						1.0							
7	60	347.e-03	243.0	62.1	353.4	24.8						0.0							
8	70	253.e-03	239.4	61.2	352.8	23.0						1.0							
9	CPCA	2.58e+00	251.2	62.8	355.4	28.2						3.0	NRM					70	O



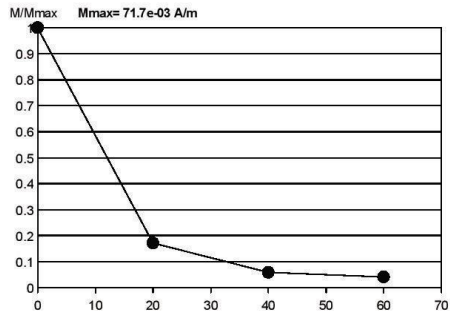
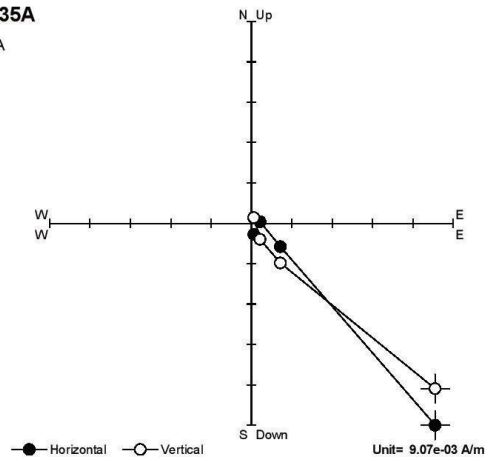
SFU034B
Thermal demag



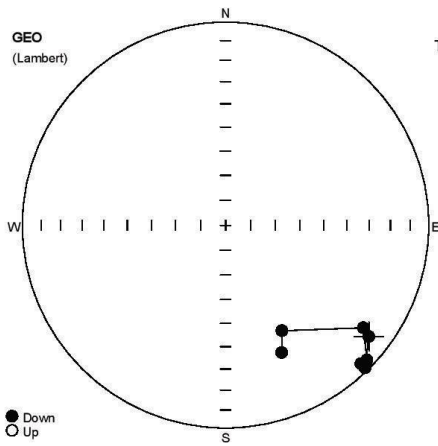
Name	Site	Latitude	Longitude	Height	Rock	Age	Fm	SDec	Sinc	BDec	Binc	FDec	Finc	P1	P2	P3	P4	Note
SFU034B								113	36					6	0	6	90	
#	State	M[A/m]	Dsp	Isp	Dge	Ige	Dtc	Itc	Dfc	Ifc	Prec	Limit1	Limit2	Note				K[e-06 SI]
1	NRM	43.7e-03	19.8	9.8	140.2	43.0					2.0							
2	100°C	41.3e-03	19.7	-10.0	134.3	23.8					0.0							
3	200°C	23.9e-03	22.6	-16.6	135.7	16.8					1.0							
4	300°C	8.87e-03	9.7	1.2	125.2	36.6					1.0							
5	400°C	8.42e-03	358.5	21.7	110.3	57.7					2.0							
6	425°C	8.29e-03	339.3	-18.3	92.6	15.6					2.0							
7	500°C	7.74e-03	340.3	26.1	77.7	58.5					2.0							
8	550°C	7.18e-03	300.2	53.1	359.5	55.5					4.0							



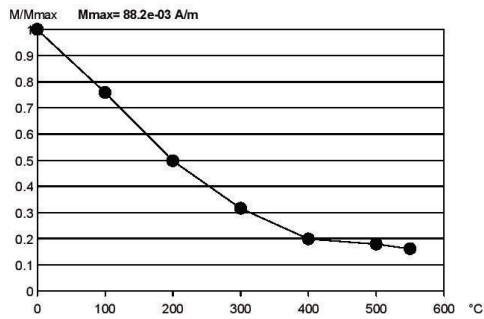
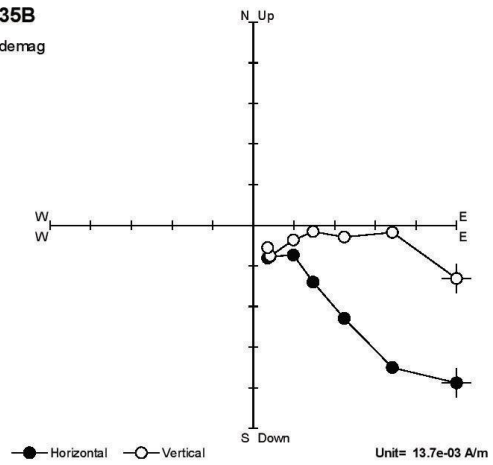
SFU035A
N/A



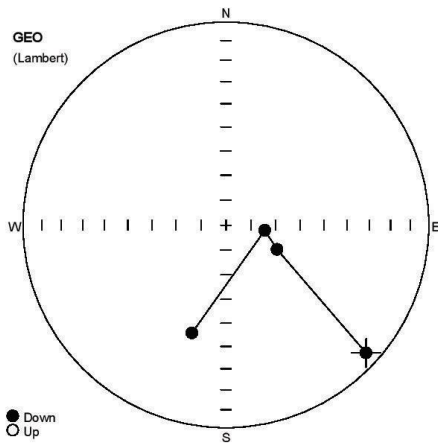
Name	Site	Latitude	Longitude	Height	Rock	Age	Fm	SDec	Sinc	BDec	Binc	FDec	Finc	P1	P2	P3	P4	Note
SFU035A								211	31					6	0	6	90	
#	State	M[A/m]	Dsp	Isp	Dge	Ige	Dtc	Itc	Dfc	Ifc	Prec	Limit1	Limit2	Note				K[e-06 SI]
1	NRM	71.7e-03	300.2	18.6	137.7	31.2					1.0							
2	20	12.3e-03	304.0	35.2	129.0	46.8					1.0							
3	40	4.13e-03	297.3	66.7	78.9	61.7					2.0							
4	60	2.88e-03	298.5	-46.2	168.1	-26.7					3.0							



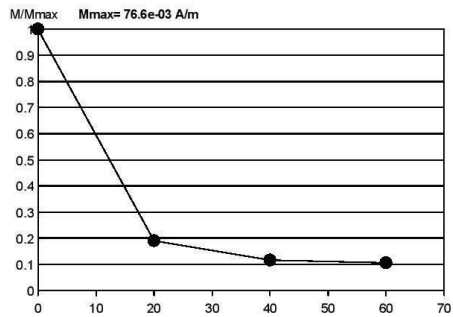
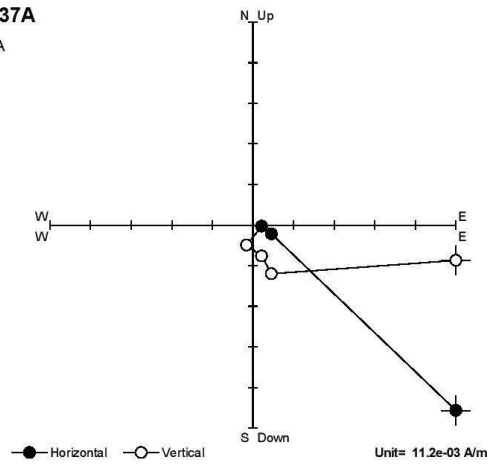
SFU035B
Thermal demag



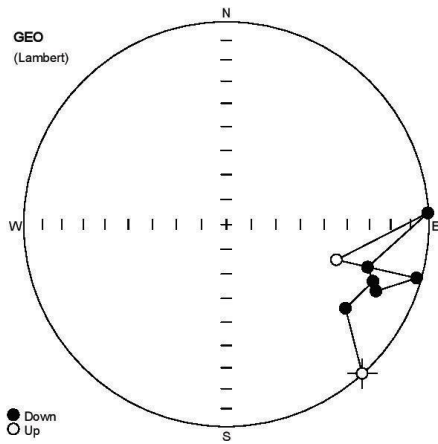
Name	Site	Latitude	Longitude	Height	Rock	Age	Fm	SDec	Sinc	BDec	Binc	FDec	Finc	P1	P2	P3	P4	Note
SFU035B								211	31					6	0	6	90	
#	State	M[A/m]	Dsp	Isp	Dge	Ige	Dtc	Itc	Dfc	Ifc	Prec	Limit1	Limit2	Note				K[e-06 SI]
1	NRM	88.2e-03	281.8	6.6	127.8	11.7					1.0							
2	100°C	66.9e-03	283.7	-5.7	135.7	2.1					1.0							
3	200°C	43.9e-03	285.3	-3.0	135.7	5.2					1.0							
4	300°C	27.9e-03	283.1	-2.7	133.6	4.4					1.0							
5	400°C	17.5e-03	283.5	11.3	126.7	16.6					1.0							
6	500°C	15.8e-03	315.9	21.1	151.9	40.8					1.0							
7	550°C	14.2e-03	315.1	11.8	156.2	32.1					1.0							



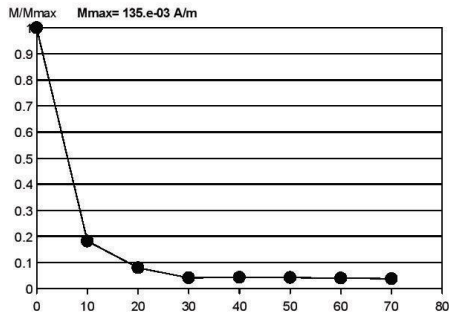
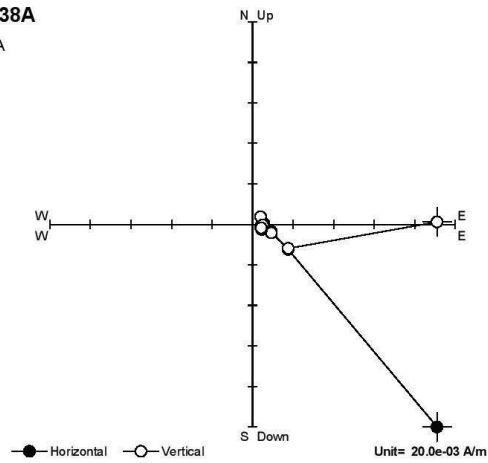
SFU037A
N/A



Name	Site	Latitude	Longitude	Height	Rock	Age	Fm	SDec	Sinc	BDec	Binc	FDec	Finc	P1	P2	P3	P4	Note
SFU037A								197	42					6	0	6	90	
#	State	M[A/m]	Dsp	Isp	Dge	Ige	Dtc	Itc	Dfc	lfc	Prec	Limit1	Limit2	Note				K[e-06 SI]
1	NRM	76.6e-03	294.1	-11.0	132.4	7.3					0.0							
2	20	14.5e-03	329.8	40.3	115.5	67.2					1.0							
3	40	8.86e-03	336.5	48.1	97.7	74.3					1.0							
4	60	8.02e-03	0.4	1.6	197.5	43.6					1.0							



SFU038A
N/A



Name	Site	Latitude	Longitude	Height	Rock	Age	Fm	SDec	Sinc	BDec	Binc	FDec	Finc	P1	P2	P3	P4	Note
SFU038A								219	44					6	0	6	90	
#	State	M[A/m]	Dsp	Isp	Dge	Ige	Dtc	Itc	Dfc	Ifc	Prec	Limit1	Limit2	Note				K[e-06 SI]
1	NRM	135.e-03	275.9	-6.4	137.7	-0.5					1.0							
2	10	24.5e-03	288.6	22.8	125.2	28.9					1.0							
3	20	10.7e-03	274.8	28.7	111.2	23.4					1.0							
4	30	5.40e-03	276.1	34.6	106.9	28.0					1.0							
5	40	5.65e-03	237.2	28.2	86.8	0.5					2.0							
6	50	5.62e-03	226.4	-17.4	107.9	-42.3					2.0							
7	60	5.28e-03	254.9	18.0	105.8	2.8					2.0							
8	70	5.00e-03	274.2	24.6	114.1	20.2					1.0							

Chapter 9 - Physical and chemical characteristics of hydrothermally altered volcanic deposits Cracked Mountain, Mt Meager Volcanic Complex, British Columbia

Leiter, Sophia and Russell, James K.

Earth, Ocean and Atmospheric Sciences, the University of British Columbia

Introduction

Cracked Mountain is a small monogenetic volcano situated in the southwest Mount Meager Volcanic Complex (MMVC). The volcano comprises poorly sorted volcanoclastic deposits, primary pyroclastic deposits, coherent intrusive (e.g., dykes, sills), and extrusive (e.g., lavas) units (Harris et al., 2020). The primary volcanic products have been subjected to hydrothermal alteration processes producing variably palagonitized deposits.

Palagonite is a mineraloid resulting most commonly from alteration of basaltic glasses found in subaqueous or subglacial volcanic settings (Stroncik and Schmincke, 2002). Volcanic glasses are metastable phases and are especially unstable at temperatures exceeding 200° C and in the presence of hot fluids and over time will breakdown to palagonite: an alteration assemblage of clays and zeolites (Stroncik and Schmincke, 2002). The composition of palagonite is neither mineralogically nor chemically fixed, and it is typically identified in the field by a pronounced orange-yellow coloured alteration of the primary deposits (Stroncik and Schmincke, 2002). The timescale of the palagonitization process is highly variable operating on timescales of kilo-years to weeks to days and controlled by environmental conditions (e.g., temperature, fluid compositions, etc.) (Prause et al., 2020). Progressive palagonitization is typically thought of as linear, with higher degrees of alteration leading to darker oranges and more clays and zeolites (Stroncik and Schmincke, 2002). The minerals that form as a result of palagonitization can be useful indicators of temperature, as many clays and zeolites have specific temperature windows of formation (Antibus et al., 2014). The palagonitization process can also transform unconsolidated deposits into fully lithified rocks making them more resistant to erosion.

Reservoir rocks within geothermal fields are subject to sustained elevated temperatures and fluid flow causing physical and mineralogical alteration. Hydrothermal alteration processes, such as palagonitization, are of particular interest within the Mt. Meager volcanic complex (MMVC) where some reservoir rocks are expected to have a (sub-)volcanic origin. The stabilities and compositions of clays and zeolites are highly sensitive to ~100°C fluctuations in temperature and, thus, can provide understanding of the physical and chemical processes operating in geothermal fields (Heap et al., 2012). These mineralogical transformations can strongly affect rock properties, including porosity, permeability, and rock strength (Weaver et al., 2020).

The palagonitized volcanoclastic deposits exposed at Cracked Mountain provide a means of studying the physical and chemical consequences of hydrothermal alteration characteristic of ore deposits and geothermal systems. We present, here, preliminary data providing physical, mineralogical, and chemical characterization of these hydrothermally altered volcanic products.

We focused the mapping and sampling of the Cracked Mountain edifice on a range of volcanoclastic lithofacies showing variable degrees of palagonitization (i.e., based on colour and lithification). Our intent is to use variations in laboratory-measurements of physical properties (e.g., density, porosity, permeability) and mineralogy (modal clay and zeolite contents) to gain an understanding into the dynamics of and controls on palagonitization processes. Here we present the results of the investigations into the relationship between porosity and mineralogy in hydrothermally altered volcanoclastic rocks.

Methods

Study Area

Mapping and sampling of the Cracked Mountain volcanoclastic deposits utilized the maps and stratigraphic sections of Harris et al. (2020). Harris et al. (2020) produced a volcanological map for the edifice, established a stratigraphic framework including coherent and volcanoclastic volcanic lithofacies, and postulated a glaciovolcanic origin for the edifice. Harris et al. (2020) also subdivided the volcanoclastic lithofacies into pyroclastic flow and surge deposits and mass flows. They also described a variety of deposits as being palagonitized. The geology of the edifice is relatively simple (Fig. 1), with the eruption having occurred mostly or entirely under ice and then eroded by subsequent glacial movement. The top of the edifice covers an area of 1.5 km² and poorly vegetated offering offers access to many outcrops. In addition, the edifice features large (up to 5 m wide and 50 m long) deep (up to 10 m) cracks which provides access to lower stratigraphic units. The lateral margins of the edifice are very steep and inaccessible. Harris et al 2019 provided a preliminary stratigraphic model for the edifice. Nearly all volcanoclastic deposits appear palagonitized in hand sample, ranging from buff grey to bright orange in colour.

Sampling

Sampling was undertaken using a core drill powered by a modified chainsaw, of the type used for paleomagnetic sampling (Butler, 1991). The field drill provided a means of securing cores for lab experimentation and obviated the need for drilling samples for cores in the lab which would have required collection of very large blocks of rock. The field-collected cores are one inch in diameter and up to six inches long. In order to capture the full spectrum of palagonitization an effort was made to sample every rock type (mass flow, surge deposit, pyroclastic density current, proximal and distal to the presumed vent location, and presumed heat source (intruded by dike, intruded by pillows, latent heat of eruption). Cores were also sampled up section in outcrops and proximal and distal to presumed heat sources. At one location material was collected from veins that presumably carried alteration fluids. Sampling yielded 140 cores to measure for physical and chemical properties and an additional forty cores for measurement of magnetic properties, including paleomagnetic direction (Figure 1).

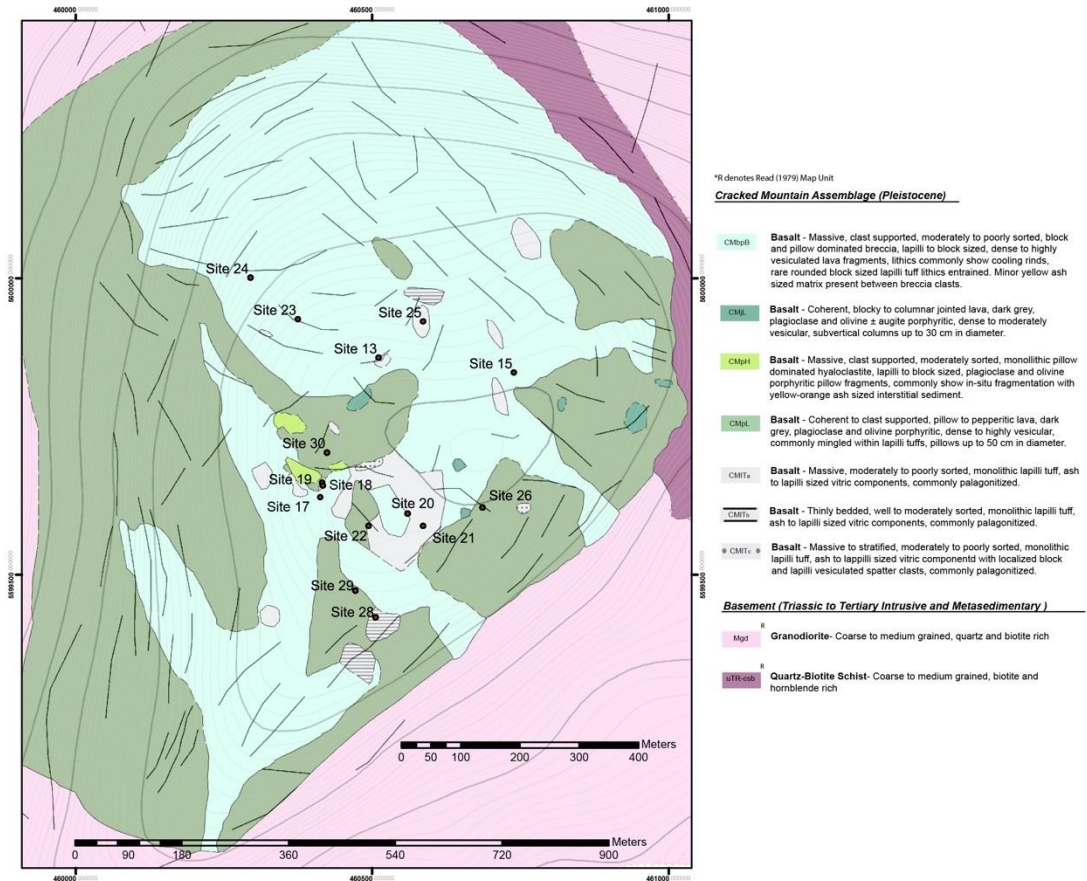


Figure 1: Field map modified from Harris et al. (2020) showing labelled sites where cores were drilled.

The volcanoclastic samples ranged in colour from grey to dark orange across the edifice and within outcrops. In the field, samples were assigned a rank of 1-3 reflecting the apparent degree of palagonitization (VDP) based on depth of colour (Figure 2). A VDP of one indicates minimal visible alteration and grey to buff in colour. VDP two is moderately altered and typically light orange. VDP three is dark orange to reddish brown. There is significant surficial alteration and weathering that we believe is unrelated to the initial process of palagonitization such that cores may show a small orange rind at the surface, but underneath be grey.

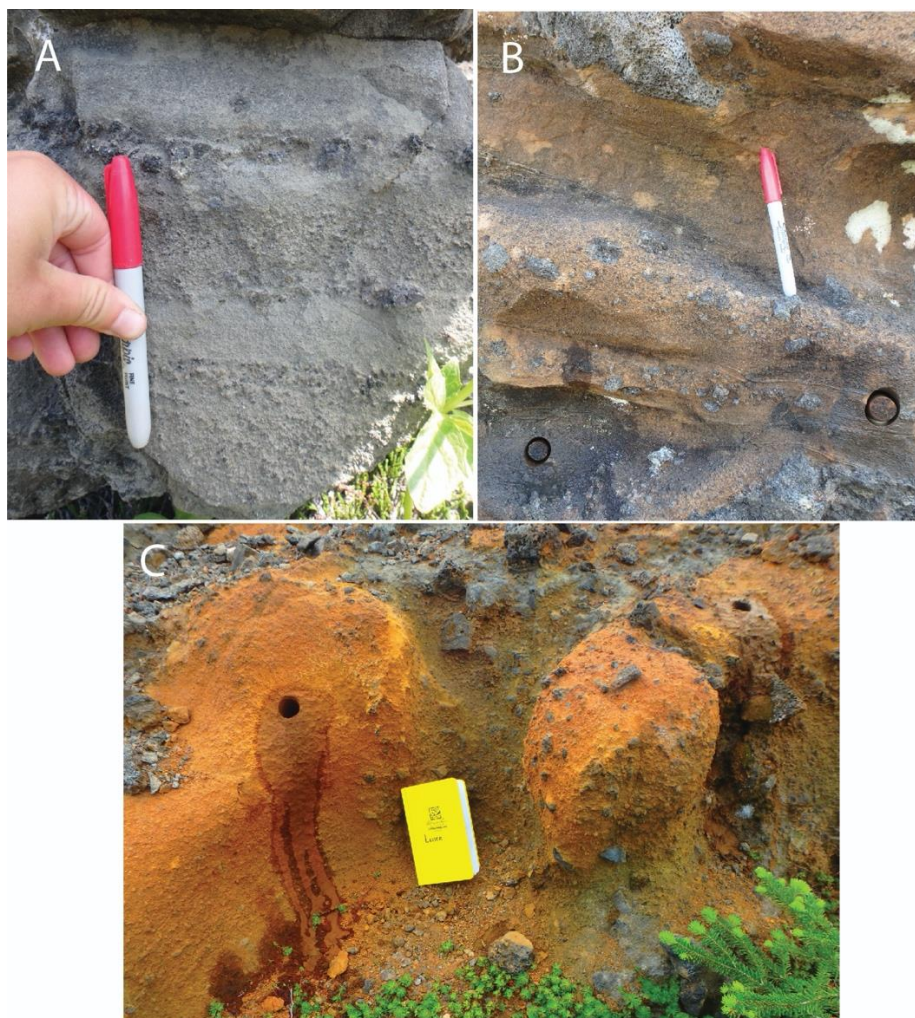


Figure 2: Representative field photos of each degree of VDP. A) VDP 1. Photo taken from a small surge deposit at Site 28. B) VDP 2. Faintly orange mass flow with unaltered basaltic clasts ranging ~3 cm (Site 28). C) VDP 3. Deep orange mass flow from Site 25. Samples of this colour tend to be very friable and don't hold up well under the drill.

Cracked Mountain erupted under ice and it was expected that many of the volcaniclastic deposits would show variable degrees of palagonitization. As such we sampled every type of volcaniclastic and pyroclastic deposit, regardless of appearance of palagonitization, though there was a focus on sampling deep orange, characteristic palagonite. The presence of clays could be roughly identified by the ease of drilling. Clays tended to mix with the cooling water from the drill, making drilling slow and difficult. Several outcrops also appeared very orange at the surface, but the deeper sections of the core revealed more subdued colours.

Field Short Wave Infrared Spectrometry

We also used short wave infrared spectrometer (SWIR) as another means of mapping variation in mineralogy within these variable palagonitized volcanic deposits. We used a NIRQUEST 512 SWIR spectrometer (manufactured by OceanOptics). The spectrometer measures reflectance spectra in the short-wave infrared (SWIR) portion of the electromagnetic spectrum (1000 to 2500 nm) with an average interpolated spectral resolution of 2 nm. In the field we had access to a small

library of mineral spectra, but the instrument proved most useful for comparison of relative alteration between samples rather than individual mineral identification. These data were used in real time to plan what rock types to sample in the following days.

Sample Preparation

All cores were trimmed 1" diameter right cylinders having lengths between 1-3" and dried overnight at 90° C in preparation for measurements of physical properties. The diameter and length of all trimmed cores were measured three times with digital calipers to provide a calculated bulk volume. Cores were also weighed three times and those weights were averaged to determine mass. Off cuts from trimming cores were saved and powdered for chemical analyses.

Pycnometry

The skeletal volumes of cores were measured using a Micromeritics AccuPyc II 1340 helium pycnometer (note this volume is solid material plus isolated porosity) . The AccuPyc II 1340 makes 10 measurements of each core, which are then averaged. We discard any analyses that show a systematic trend, either increasing or decreasing, over the course of the run and re-run that sample to mitigate temperature shifts or other environmental pollution. We also run multiple samples several times and the same material at different volumes to check machine accuracy. Skeletal density, connected porosity, and total gas volume were calculated based on these measurements.

X-ray Diffraction

We performed X-ray powder diffraction analysis on 25 samples; smear-glass-mounts were run on a Bruker AXS D8 Focus at UBC for qualitative mineral identification. Mineral identifications were made using the Bruker Topas software. Of these samples, five were selected for re-analysis after heating and glycolation. The original smear mount was placed in a glycol chamber overnight and another mount was prepared and heated in a 500°C oven for one hour. X-ray diffractograms for these samples were focused on clay identification and used reduced scans of 0-30 Å.

Results

Pycnometry

Pycnometry is a gas infiltration technique designed to measure the volume of samples placed within a reservoir by displacement. The sample volume is the difference in gas volumes between the empty calibrated cell and the cell holding the core. The volume measured is the skeletal volume of the core (including isolated porosity) and skeletal density is calculated by dividing the mass of the core by this volume. The volume of the connected pore space is calculated by subtracting the skeletal volume from the geometric volume of the core and provides an estimate of the connected porosity after (Ryan et al., 2018).

Bulk density decreases with increasing connected porosity and the slope and intercept of corresponding trendlines define the skeletal density (Figure 3). The bulk density of most samples ranges from 1.118 to 2.064 g/cm³ and measured values of connected porosity (ϕ_c) of 0.141 to 0.647.

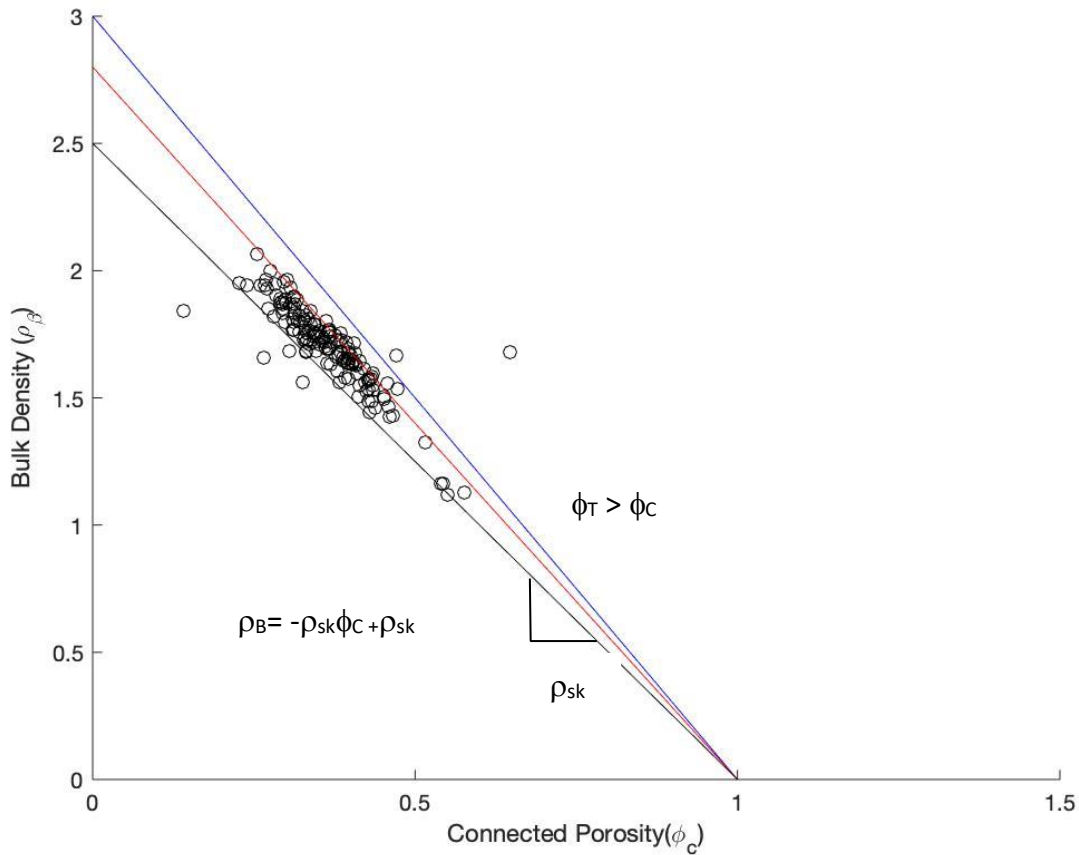


Figure 3: Connected porosity (ϕ_c) versus bulk density (ρ_B). Theoretical trend lines are shown for assumed skeletal densities (ρ_{sk}) of 3.0, 2.86, and 2.5 g cm⁻³. For a fixed ρ_{sk} , samples having significant isolated porosity (ϕ_i) will plot above the theoretical trend line.

Samples appear to become less dense and more porous with increased visual degree of alteration (Figure 4). Interestingly field SWIR and XRD results show that many samples assumed to be relatively unaltered (i.e., VDP ranked as 1) actually contain abundant alteration minerals such as clays. In fact, many of the buff and grey samples contain clays while deep orange samples appear not to. It may be that as these alteration minerals form, they fill the existing pore space resulting in denser and less porous rocks. However, many samples that appear unaltered in hand sample, similarly are not shown to contain clays or zeolites using either SWIR or XRD, indicating that the deep orange samples differ in more than just porosity and density.

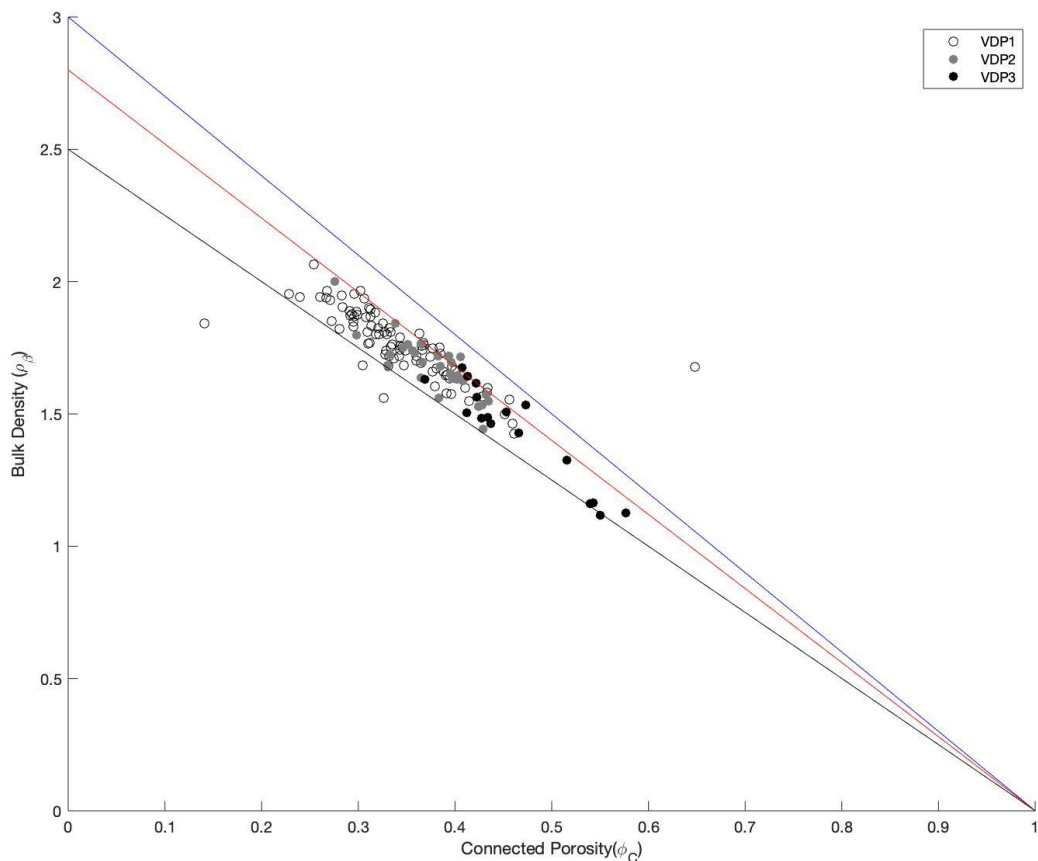


Figure 4: Same plot as above, connected porosity versus bulk density, with each sample coded from 1-3 by visual degree of palagonitization (VDP) where 1 is not altered and grey to buff in colour, 2 is moderately altered and faintly orange, and three is heavily altered and dark orange to reddish brown.

XRD

We use X-ray diffraction analysis to identify clays and zeolites in our sample suite and, here, we report representative spectra with preliminary mineral identifications. All samples contain primary igneous minerals typical of a basalt including olivine and plagioclase; pyroxene (i.e., augite) is present in some but not all samples (Figure 5). This is consistent with mineral identifications previously made by Martin Harris (Harris et al., 2020).

Figure 5 shows the XRD pattern obtained for a sample assigned a VDP of 3 in the field. It is from a small (~ 5 m wide) section of bright orange tuff underlying a rubbly mass flow. The matrix is bright orange glassy material with 20-30% angular, glassy, and vesicular clasts under .5 cm. The matrix has a dusty appearance and seems to coat the clasts. Cores from this site clogged the drill, which seems to happen when the cooling water mixes with clay or ash in the rock. Despite the bright orange colour, the XRD spectrum shows only peaks associated with olivine and plagioclase; there is no discernible signal between 0-14 Å indicative of clay minerals (i.e., a hump or raised

background). There is a broad hump between 20-40 Å indicative of an amorphous glass component.

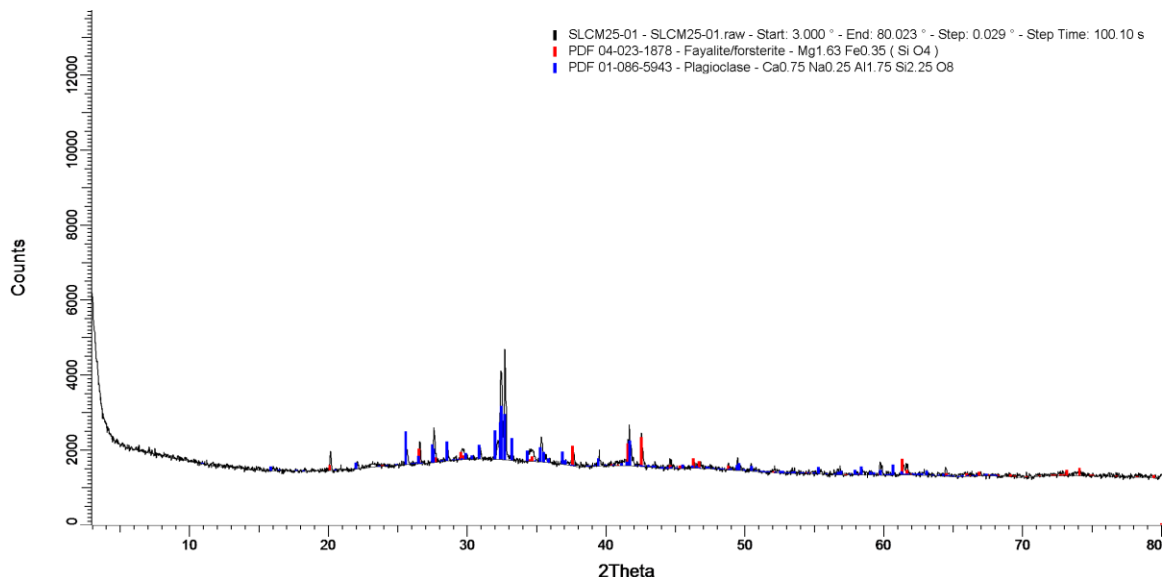


Figure 5: XRD spectra from sample 25-01. Despite its bright orange colour the only identifiable spectra were from plagioclase and olivine. The raised hump between 20-40 2θ is the signature of the amorphous glass component.

Other samples of similarly deep orange colour demonstrate relatively simple XRD spectra, showing neither clay peaks nor spectra indicative of zeolites, such as sample 21-01, collected from a variably palagonitized pyroclastic flow crosscut by veins (Fig. 6). However, samples with a VDP of 1 (23-02) demonstrate nearly identical spectra, save for the addition of pyroxene, and minor clays (Figure 6). Sample 23-02 was collected from a mass flow that was squeezed up by an intruding pillow pile. The squeeze up was crudely bedded and clasts fined upward. The matrix material was glassy and gold in colour. Material from the same site (23-09), which was drilled from a part of the mass flow that was not squeezed up by but was intruded by pillows, demonstrated a small peak indicative of clays as well as several peaks associated with analcime or wairakite, hydrothermal zeolite minerals that tend to form above 140-150° C (Steiner, 1955; Mimura et al., 1995) (Figure 6). The broad peak between 5-10 Å is typical of mixed smectite and vermiculite. The broad shape is due to differing degrees of hydration. In a humid climate like Vancouver, where these samples were run, atmospheric humidity infiltrates the layers, making them appear as a broad rather than a sharp peak. The same phenomenon is occurring to a lesser degree in 23-02, though the abundance is lower, so no clear peak is visible, just a slight raised area relative to no clays (21-01).

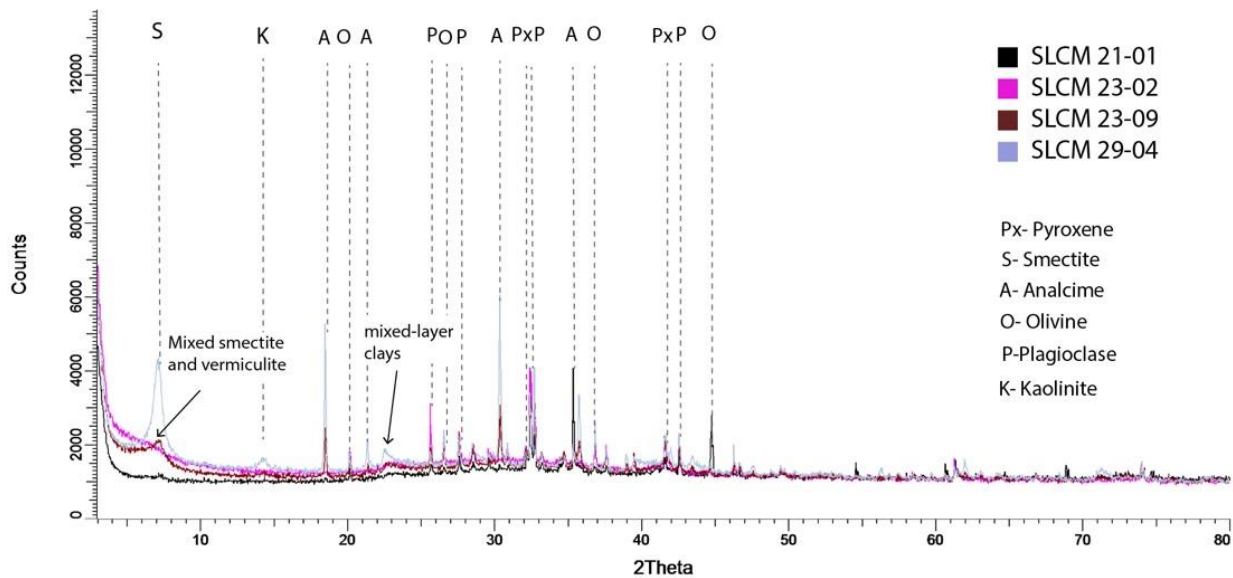


Figure 6: Spectra from several samples stacked on top of each other. Discrepancies in peak height may be due to differences in smear thickness. Peaks are identified and labelled at the top.

The samples that tend to show the most zeolite and clay minerals in XRD spectra were drilled from near dikes (29-04). This sample was drilled directly next to a dike, where heat from the dike had indurated the surrounding pyroclastic flow about 1 m out on either side. This sample shows a sharp peak with a basal spacing of 15, typical of smectite. It also shows peaks indicative of analcime or wairakite, similar to 23-09 (Figure 6), as well as kaolinite and mixed layer clays.

More altered samples show sharper peaks at low 2θ's (i.e., clay zone) while also showing either analcime or wairakite (Figure 7). The two minerals have nearly identical structures, with wairakite swapping a Ca for Na in analcime's structure. Both minerals are highly temperature dependent so exact identification will reveal important information about the alteration environment. Both tend to form at temperatures about 140-150° C, so their presence in samples does provide a useful temperature benchmark (Steiner, 1955; Mimura et al., 1995).

Sample 17-04 (Fig. 7) was collected from a small exposure of light brown, locally indurated, finely bedded pyroclastic flow. The mostly grey/brown section was moderately sorted, and matrix supported. The flow contained 10% vitric, angular clasts up to 5 cm but most ~1 mm. In addition to typical basaltic minerals this sample contained analcime or wairakite, smectite, and kaolinite.

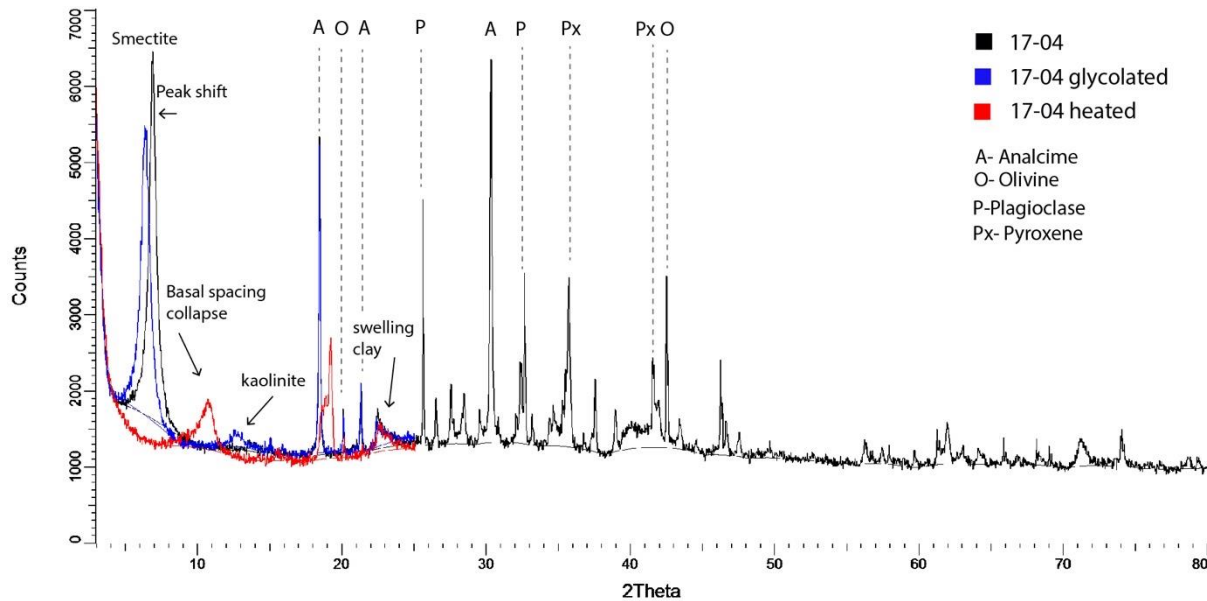


Figure 7: Spectra for sample 17-04 including: original untreated sample (black line), glycolated sample (blue line), and heated (~500° C for 1 h) sample (red line).

An identical sample from the same outcrop was also heated and glycolated in order to identify the clay peak (Figure 7). The initial peak shifts slightly from a basal spacing of 15 to 17 when glycolated, indicating the presence of swelling clays. Glycolation is not always complete, and so this small shift is not unexpected. The initial sharp peak collapses to a basal spacing of 9.5, which further indicates the presence of smectite. This is due to all of the water in between the clay sheets being forced out.

Discussion

Palagonitization is a form of hydrothermal alteration characteristic of many subaqueous or glaciovolcanic deposits. Qualitatively it can be identified by changes in colour, as sideromelane breaks down to the alteration assemblage the deposits attain a deep, characteristic orange colour. Here we have used XRD, porosity, and density to provide a quantitative analysis of the intensity and consequences of the palagonitization process.

Our preliminary results show higher porosity values corresponding to darker alteration colours. However, it seems that alteration colours in hand sample are not always an accurate indicator of degree of palagonitization. Samples containing significant clays and zeolites, products of high degrees of alteration, do not display the colors characteristic of palagonite alteration. They do, however, display reductions in porosity indicative of infill from alteration clays and zeolites. Future ongoing work is testing and refining our ideas concerning covariations between physical, chemical and mineralogical properties and intensity of palagonitization. Mineralization may also reveal whether the physical and chemical changes attending palagonitization move forward linearly or feature discontinuities or branching paths dependent on time and environmental factors (e.g., temperature, fluid composition).

Conclusion

Geothermal power generation depends on the presence of fluid, a sustained heat source, and the transmissivity of that fluid. The latter is dictated by permeability. The permeability of volcanic rocks depends on primary properties and the effects of post-depositional alteration. Here we present physical and mineralogical properties of palagonitized deposits from Cracked Mountain in an attempt to better understand the temperature of alteration fluids and their effect on permeability of volcanic products. The mineralogy of these altered deposits will hopefully lead us to temperature determinations, as several clays and zeolites form in specific temperature windows.

References

- Antibus, J.V., Panter, K.S., Wilch, T.I., Dunbar, N., McIntosh, W., Tripathi, A., Bindeman, I., and Blusztajn, J., 2014, Alteration of volcanoclastic deposits at Minna Bluff: Geochemical insights on mineralizing environment and climate during the Late Miocene in Antarctica: *Geochemistry, Geophysics, Geosystems*, v. 15, p. 3258–3280, doi:10.1002/2014GC005422.
- Butler, R.F., 1991, *Paleomagnetism: Magnetic Domains to Geologic Terranes*: Boston, Blackwell Science Inc, 336 p.
- Harris, M., Muhammad, M., Williams-Jones, G., and Russell, J.K., 2020, Bedrock mapping for Mount Meager: Geothermal Research Initiative: *Geoscience BC*, p. 6–29, doi:doi:10.13140/RG.2.2.15103.64169.
- Heap, M.J., Lavallée, Y., Laumann, A., Hess, K.-U., Meredith, P.G., and Dingwell, D.B., 2012, How tough is tuff in the event of fire? *Geology*, v. 40, p. 311–314, doi:10.1130/G32940.1.
- Mimura, H., Tezuka, T., and Akiba, K., 1995, Formation of Analcime Film under Hydrothermal Conditions: *Journal of Nuclear Science and Technology*, v. 32, p. 1250–1258, doi:10.1080/18811248.1995.9731848.
- Prause, S., Weisenberger, T.B., Cappelletti, P., Grimaldi, C., Rispoli, C., Jónasson, K., Jackson, M.D., and Gudmundsson, M.T., 2020, Alteration progress within the Surtsey hydrothermal system, SW Iceland – A time-lapse petrographic study of cores drilled in 1979 and 2017: *Journal of Volcanology and Geothermal Research*, v. 392, p. 106754, doi:10.1016/j.jvolgeores.2019.106754.
- Ryan, A., Russell, J., and Heap, M.J., 2018, Rapid solid-state sintering in volcanic systems: *American Mineralogist*, v. 103, p. 2028–2031, doi:10.2138/am-2018-6714.
- Steiner, A., 1955, Wairakite, the calcium analogue of analcime, a new zeolite mineral: *Mineralogical Magazine and Journal of the Mineralogical Society*, v. 30, p. 691–698, doi:10.1180/minmag.1955.030.230.02.

Stroncik, N.A., and Schmincke, H.-U., 2002, Palagonite – a review: *International Journal of Earth Sciences*, v. 91, p. 680–697, doi:10.1007/s00531-001-0238-7.

Weaver, J., Eggertsson, G.H., Utley, J.E.P., Wallace, P.A., Lamur, A., Kendrick, J.E., Tuffen, H., Markússon, S.H., and Lavallée, Y., 2020, Thermal Liability of Hyaloclastite in the Krafla Geothermal Reservoir, Iceland: The Impact of Phyllosilicates on Permeability and Rock Strength: *Geofluids*, v. 2020, p. e9057193, doi:<https://doi.org/10.1155/2020/9057193>.

Chapter 10 - Distribution and Age of the Cheakamus Basalts, Garibaldi Volcanic Belt, British Columbia

Borch, A.¹, Russell, J.K.¹, Barendregt, R.², Quane, S.L.³, Wilson, A.⁴

¹Earth, Ocean and Atmospheric Sciences, The University of British Columbia

²Department of Geography, The University of Lethbridge

³Sea to Sky Fire & Ice Geopark

⁴Minerva Intelligence

Introduction

The Garibaldi Volcanic Belt (GVB) represents the northern extension of the subduction-driven, calc-alkaline Cascade volcanic arc into southwestern British Columbia. The GVB is host to more than 100 eruptive centers (Wilson & Russell, 2018) ranging in composition from basalt to rhyolite and represents a potential source of geothermal energy (Jessop, 2008; Grasby et al., 2011; Witter, 2019).

The GVB was evaluated at several sites for its geothermal energy potential during the mid-1970s (Lewis, Judge & Souther, 1979; Clark et al., 1982). One target of the 1970s was the Mount Meager volcanic complex (MMVC) situated 60 km northwest of Pemberton, British Columbia; it is currently being re-evaluated by Natural Resources Canada (NRCAN) scientists (Grasby et al., 2020). As part of this research program, volcanic edifices proximal to the MMVC are also being investigated for their potential as geothermal energy sources.

The Cheakamus River basalt flows (herein called the Cheakamus basalts) comprise a group of Quaternary basaltic lavas in the Garibaldi volcanic belt (GVB) of British Columbia distributed within the Cheakamus River and Callaghan valleys, 30 km north of Squamish and 12 km southwest of Whistler (Mathews, 1948). Our current understanding of the origins, distribution, stratigraphic relationships, and age of the Cheakamus basalts derives from the field mapping of Mathews (1958) and air photo mapping, petrological, geochemical, and geochronological studies of Green (1977; 1981; 1988; 1990).

The Cheakamus basalts are some of the youngest volcanic rocks within the GVB and, based on their distribution, volume and age, may indicate a region with geothermal energy potential. The Cheakamus basalts span a length of 26 km from Daisy Lake in the south to Callaghan Lake in the north, reach lateral extents (i.e. widths) of 1-2 km and cover an area of $\sim 35 \text{ km}^2$ (Fig. 1). Where exposed in sections through paleo-valleys, the stacked lavas reach thicknesses of 80 m. Previous estimates place the minimum volume of the Cheakamus basalts at 1.25 km^3 (Mathews, 1958) and this erupted volume is likely to be matched by 3-10 times greater volumes of stored magma (Huppert & Woods, 2002; Townsend & Huber, 2020). Geochronological data, although sparse, combined with field mapping suggest the volcanism could be as young as $< 50 \text{ ka}$. Lastly, the Cheakamus basalts are significantly closer to critical infrastructure and population centres than the MMVC or other larger GVB volcanoes (i.e. Mt Cayley).

Balancing these promising attributes is a general lack of knowledge regarding the Cheakamus basalts, especially concerning the location of their source(s), where we might expect the greatest geothermal

potential. Here we report on preliminary observations and data from the 2020 field mapping program on the Cheakamus basalts. The overarching goals of this program that are most relevant to geothermal prospectivity include:

- A) establishing a precise distribution of the basalts including: vent/source locations, thickness estimates, number of flow units, and volumes;
- B) determining the age(s) of these Quaternary lavas and especially the youngest age of this volcanism;
- C) using geochemistry and petrography to divide the lavas into discrete packages or groups, or to show that they derive from a single magma batch, and;
- D) testing for genetic and volcanological connections (or lack of) with the Ring Mountain volcano (Kelman, Russell & Hickson, 2001), the Elaho basalts, and other proximal volcanic complexes.

This research will also reconstruct the pre-eruptive, paleo-surface of the Cheakamus valley, which can inform on the origins of the present-day landforms and the present-day distribution of basalt lava outcrops.

Background Geology

Work on the Cheakamus basalts was first carried out by Mathews (1948), who named them, described their basaltic lithology, and mapped their distribution within the context of Quaternary volcanism in the GVB (Fig. 1). He included the basalt lavas filling the Callaghan River valley and postulated a source at Callaghan Lake. He used outcrop morphology and the presence of interbedded glacial sands and gravels to suggest an eruptive history that spanned the waxing and waning of the Wisconsin ice sheet (Mathews, 1948). In later work, he proposed a minimum volume estimate of 1.25 km³ and suggested that the youngest Cheakamus basalt lavas were late Pleistocene to Recent based on the extent of fluvial dissection (Mathews, 1958). Mathews postulated a glaciovolcanic origin of the stratigraphically youngest lavas, noting their striking, esker-like shapes, and hypothesized a subglacial formation at the close of the Fraser glaciation (~10-11 Ka) (Mathews, 1958; Clague & Ward, 2011).

Green (1977; 1981) and Green et al. (1988) used new chemical and petrological datasets to subdivide Mathews' single map unit (i.e. the Cheakamus basalts) into multiple stages of emplacement. Green (1977) used differences in mineralogy and major and trace element abundances, combined with detailed stratigraphic work, to postulate three separate phases of emplacement for the Cheakamus basalt lavas: the Alpine Lodge phase (oldest), Cheakamus Dam phase, and Brandywine Falls phase (youngest) (Fig. 2). Green et al. (1988) suggested that each GVB eruptive group evolved from a separate, chemically distinct parent magma (Green, 1990) which contradicted Mathew's (1957) hypothesis that the Cheakamus basalts represented the parent magmas of the GVB intermediate and felsic volcanic rocks.

There are few radiometric estimates for the eruption age of the Cheakamus lavas. An organic sample collected from sediment underlying Brandywine Falls phase lavas has a ¹⁴C age of 34,000 ± 800 (Green, 1981; McNeely, 1989) and was linked to the Salmon Springs Glaciation. Green et al. (1988) also obtained a K-Ar age date of 50 ka ± 50 ka for a lava sample representing the Alpine Lodge phase, providing corroboration of Mathews' assertion of a pre- and syn-glacial eruptive history.

These studies delineated the distribution, lithology, geochemistry and mineralogy of the Cheakamus basalts, provided some geochronological information, and explored their paleo-environmental implications. However, gaps in our understanding persist which were the focus of our 2020 field mapping of the Cheakamus basalts. Specifically, our goals included: i) refining the mapped distribution and volume

of the lavas; ii) locating the eruption source(s); iii) revising some stratigraphic relationships; and iv) better constraining the age and duration of volcanism. Whether the eruption and emplacement of these lavas was rapid or protracted has implications for the existence of a long-standing heat source in the area. We investigate these questions using detailed lithostratigraphic mapping, along with geochemical, radiometric, and paleomagnetic sampling.

The 2020 Field Season

Field Mapping

The main contributions of the 2020 field season include: i) a detailed volcanological map (Fig. 3) of the Cheakamus basalts that extends their distribution farther northwest up the Callaghan valley; ii) detailed stratigraphic logs for the lava sequences across the map area; and iii) a revised stratigraphic framework (Fig. 2). Detailed graphic logs were created for multiple sites in the Cheakamus valley to inform and support the construction of map units. Distinct groups of lava were recognized on the basis of lava morphology, (micro-)phenocryst mineralogy, and key stratigraphic features including the presence of interbedded sediments and glaciated surfaces. Our revised stratigraphic succession retains Greens' Brandywine Falls phase and associated glaciofluvial sedimentary deposits as the youngest mappable units. Underlying the Brandywine Falls phase, we recognize two distinct units we refer to informally as the Glaciated Brandywine phase (younger) and the Early Brandywine phase (older). These two phases of volcanism appear to be separated by a pervasive sediment horizon. The Glaciated Brandywine phase comprises the laterally-extensive, youngest lava of Green's Cheakamus Dam phase. The older Early Brandywine phase includes both the Alpine phase and most of the Cheakamus Dam phase as defined by Green (1977). Our decision to include the lower lavas of the Cheakamus Dam phase and the entire Alpine phase into the Early Brandywine phase is based on comparisons of mineralogy, glaciated surfaces, and the presence of sediment horizons in exposed lava sequences at Brandywine Falls, exposures on Daisy Lake Island, and outcrops on the southwestern shore of Daisy Lake. The top lava exposed in these outcrops of olivine plagioclase pyritic basalt features upper glaciated surfaces and is separated from lower lavas by a silt-, sand- and gravel-bearing sediment horizon of variable thickness.

Cheakamus basalt lavas are poorly exposed in the Callaghan valley due to glacial cover which has hindered stratigraphic correlations. We have sampled these lava exposures extensively with the goal of using geochemical and paleomagnetic information to constrain stratigraphic relationships with the lavas exposed down-valley and in the Cheakamus valley. Local exposures have shown that the Callaghan valley hosts multiple lavas that reach total minimum thicknesses of 45 m.

Callaghan Lake Bathymetric Mapping

At the beginning of the field season, we hypothesized that the source of the Cheakamus Basalts was near or at Callaghan Lake, based on the termination of previous mapped extents of the basalt lavas (Mathews, 1948; Green, 1981, 1990). Paddleboard-mounted sonar bathymetric mapping of Callaghan Lake in August 2020 revealed the underwater edge of a lava flow on the southern shore protruding into the lake (Fig. 4). The lake floor otherwise resembles a glaciated alpine valley, with steep bedrock walls on the northern, western, and eastern shores. We suggest that Callaghan Lake is not the source of the Cheakamus Basalts, and was instead formed when a lobe of basalt blocked the mouth of the valley, restricting drainage. The bathymetric results at Callaghan Lake and the presence of basalt at Conflict Lake suggests a source farther up-valley, potentially proximal to, or at, Ring Mountain. Major field work goals for 2021 include continuing the search for a volcanic source in the northwest Callaghan Valley through additional bathymetric work on Conflict and Ring lakes, and continued geological mapping.

Sampling for Age and Duration of Volcanism

We collected 47 samples of lavas and 5 samples of sediment from units found between basalt lavas for subsequent laboratory study including: geochemical analysis, geochronometry, and petrographic work. The current published estimates of age for this volcanism include a single K/Ar age of $50 \text{ ka} \pm 50$ for a sample of basalt lava located 1 km north of the Chance Creek FSR turnoff (previously referred to as Garibaldi Station; Green, 1971), a more recent $^{40}\text{Ar}/^{39}\text{Ar}$ age of $141 \text{ ka} \pm 12.9$ sampled from the junction of Callaghan Creek and the Cheakamus River valley (Wilson & Russell, 2018), and a single ^{14}C date from organic material recovered from the sedimentary horizon underlying the Brandywine Falls phase lavas, situated 0.5 km north of the Callaghan Valley FSR turnoff and exposed along Highway 99 (Green, 1981; McNeely, 1989). The K/Ar age estimate is undermined by its large uncertainty: $50 \text{ ka} \pm 50$. This age determination allows for lava contemporaneous with post-Fraser glaciation or Recent (i.e. $< 10 \text{ ka}$) or as old as 100 ka coinciding with the Olympia non-glacial interval (Clague, Armstrong & Mathews, 1980; Clague, 1981; Clague & Ward, 2011). The more recently published $^{40}\text{Ar}/^{39}\text{Ar}$ age of $141 \text{ Ka} \pm 12.9$ is not in agreement with pre-existing radiometric results or preliminary paleomagnetic results. The published ^{14}C age of $34,200 \pm 800$ (Green, 1981) is based on a sample comprised of material of uncertain origin with low amounts of ^{14}C (McNeely, 1989).

To better constrain the maximum age of the Cheakamus volcanism, we sampled the base of an 80 m thick sequence of Early Brandywine Phase lavas exposed at Brandywine Falls where it unconformably overlies granitic bedrock (Figs. 2, 3). The resulting $^{40}\text{Ar}/^{39}\text{Ar}$ age is $23.9 \pm 15.7 \text{ Ka}$ (Fig. 5) and overlaps the ^{14}C age estimate reported by Green (1981). We have collected material from key stratigraphic localities for further radiometric dating of the Cheakamus basalt lavas with the goal of establishing the age and duration of volcanism.

Paleomagnetic Estimates of Duration

Geochronological dating is key for obtaining absolute ages but ultimately geological and analytical precision limits its capacity to separate individual phases of eruption or to estimate durations of volcanism over small time windows. Measurements of paleomagnetic directions recorded by volcanic rocks represent an important complement to dating volcanic sequences (Hagstrum & Champion, 2002) and especially for informing on durations of volcanism (Hagstrum & Champion, 1994; Sherrod et al., 2006; Speranza et al., 2006, 2008, 2010; Di Chiara et al., 2012). Variations in paleomagnetic direction that exceed measurement uncertainties indicate significant time differences between eruptions. Conversely, where paleomagnetic directions between volcanic rocks are equal to or less than measurement uncertainties, volcanic eruptions can be considered as coincident in time or to have occurred within a paleomagnetic moment (Greve et al., 2016; Williams-Jones et al., 2020).

During the 2020 field season we collected a sample suite consisting of 128 cores from 17 sites spanning the stratigraphic diversity of the Cheakamus basalts. Preliminary data collected on sites covering a wide geographic and stratigraphic range (Table 1) suggest that the Cheakamus lavas were emplaced over a short amount of time ($< 5 \text{ Ka}$; Hagstrum & Champion, 2002). Fieldwork in 2021 will extend this program by collecting data on lavas exposed in the Callaghan Valley, Conflict Lake area, and volcanic centers farther afield for comparison. Future work will involve comparing radiocarbon dates and paleomagnetic moment results with constructed paleosecular variation curves (Hagstrum & Champion, 2002) to better constrain the timing and duration of the Cheakamus basalts' emplacement.

Summary

Detailed mapping and stratigraphic work undertaken in the 2020 field season expanded on the work of Mathews (1948) and Green (1977, 1981, 1988) by updating and extending the stratigraphy, confirming the presence of the Cheakamus Basalts in the Callaghan Valley, ruling out Callaghan Lake as their eruptive

source, and pushing their extent toward Conflict Lake. The extensive geochronology program carried out in 2020 encompasses the entire exposed stratigraphy and will interrogate and add to the existing suite of $^{40}\text{Ar}/^{39}\text{Ar}$ and ^{14}C dates. Coupled with paleomagnetic results, $^{40}\text{Ar}/^{39}\text{Ar}$ and ^{14}C results will help constrain emplacement duration. Continued mapping, location of the source vent, and more detailed volume calculations based on paleo-topographic valley reconstructions will aid in calculating eruption rates and constructing the overall eruptive history of the Cheakamus basalts. A more complete understanding of the distribution, volume, eruptive duration, and age of the Cheakamus basalts will help clarify their feasibility as a potential for a geothermal energy source.

Acknowledgments

Many thanks to Dr. Randy Enkin for his training and the loan of sampling equipment; and to N. McKenzie, E. Martin, M. Borch, B. McKenzie, A. Balint, K. Perrin, J. McCollum, and S. Leiter for their assistance in the field.

References

- Clague, J.J., Armstrong, J.E., Mathews, W.H., 1980, Advance of the late Wisconsinan Cordilleran ice sheet in southern British Columbia since 22,000 yr BP. *Quaternary Research*, v. 13, p. 322–326.
- Clague, J.J., 1981, Late Quaternary geology and geochronology of British Columbia, Part 2: summary and discussion of radiocarbon-dated Quaternary history. Geological Survey of Canada, Paper 80-35.
- Clague, J.J., and Ward, B.C., 2011, Pliocene Glaciation of British Columbia. *Developments in Quaternary Science*, v. 15, p. 563–573.
- Cui, Y., Miller, D., Schiarizza, P., and Diakow, L.J., 2017, British Columbia digital geology. British Columbia Ministry of Energy, Mines and Petroleum Resources, British Columbia Geological Survey Open File 2017-8, 9p.
- Di Chiara, A., Speranza, F., and Porreca, M., 2012, Paleomagnetic secular variation at the Azores during the last 3 ka: *Journal of Geophysics*, Res.117 B07101, doi:10.1029/2012JB009285
- Huppert, H.E., and Woods, A.W., 2002, The role of volatiles in magma chamber dynamics: *Nature*, v. 420, p. 493–495, <https://doi.org/10.1038/nature01211>.
- Jessop, A., 2008, Review of National Geothermal Energy Program, Phase 2 – geothermal potential of the Cordillera: Geological Survey of Canada, Open File 5906, p. 86, <https://doi.org/10.4095/225917>
- Kelman, M.C., Russell, J.K., and Hickson, C.J., 2001, Preliminary petrography and chemistry of the Mount Cayley volcanic field, British Columbia: Geological Survey of Canada, Current Research 2001-A11, p. 9
- Grasby, S.E., Allen, D.M., Bell, S., Chen, Z., Ferguson, G., Jessop, A., Kelman, M., Ko, M., Majorowicz, J., Moore, M., Raymond, J. and Therrien, R., 2011, Geothermal energy resource potential of Canada: Geological Survey of Canada, Open File 6914, p. 322, <https://doi.org/10.4095/288745>.
- Grasby, S.E., Ansari, S.M., Calahorrano-Di Patre, A., Chen, Z., Craven, J.A., Dettmer, J., Gilbert, H., Hanneson, C., Harris, M., Liu, J., Muhammad, M., Russell, K., Salvage, R.O. Savard, G. Tschirhart, V., Unsworth, M.J., Vigouroux-Caillibot, N. and Williams-Jones, G., 2020, Geothermal resource potential of the Garibaldi volcanic belt, southwestern British Columbia (part of NTS 092J): GeoscienceBC Summary of Activities 2019: Energy and Water, Geoscience BC, Report 2020-02, p. 103–108.
- Green, N.L., 1977, Multistage andesite genesis in the Garibaldi Lake area, southwestern British Columbia: University of British Columbia, p. 1–256.
- Green, N.L., 1977, Multistage andesite genesis in the Garibaldi Lake area, southwestern British Columbia [Ph.D. thesis]: Vancouver, British Columbia, Canada, University of British Columbia.
- Green, N.L., 1981, Geology and petrology of the Quaternary volcanic rocks, Garibaldi Lake area, southwestern British Columbia: *Geological Society of America Bulletin*, v. 92, p. 1359–1470.

- Green, N.L., Harakal, J.E., Souther, I.J.G., and Read, P.B., 1988, Eruptive history and K-Ar geochronology of the late Cenozoic Garibaldi volcanic belt, southwestern British Columbia: Geological Society of America Bulletin, v. 100, p. 563–579.
- Green, N.L., 1990, Late Cenozoic volcanism in the Mount Garibaldi and Garibaldi Lake areas, Garibaldi volcanic belt, southwestern British Columbia: Journal of the Geological Association of Canada, v. 17, p. 171-175.
- Greve, A., Turner, G.M., Conway, C.E., Townsend, D.B., Gamble, J.A., Leonard, G.S., 2016, Palaeomagnetic refinement of the eruption ages of Holocene lava flows, and implications for the eruptive history of the Tongariro Volcanic Centre, New Zealand: Geophysical Journal International, v. 207, p. 702–718, <https://doi.org/10.1093/gji/ggw296>.
- Hagstrum, J.T., and Champion, D.E., 2002, A Holocene paleosecular variation record from ¹⁴C-dated volcanic rocks in western North America. Journal of Geophysical Research: Solid Earth, **107**(B1): 2025. doi:10.1029/2001JB000524.
- Hagstrum, J.T. and Champion, D.E., 1994, Paleomagnetic correlation of Late Quaternary lava flows in the lower east rift zone of Kilauea Volcano, Hawaii Journal of Geophysics, Res. 99 B11 21 47921 690.
- Mathews, W.H., 1948, Geology of the Mount Garibaldi Map-Area, Southwestern British Columbia [Ph.D. thesis]: Berkeley, University of California, Berkeley.
- Mathews, W.H., 1958, Geology of the Mount Garibaldi map area, southwestern British Columbia, Canada. Part II: Geomorphology and Quaternary Volcanic Rocks: Geological Society of America Bulletin, v. 69, p. 179–196.
- McNeely, R., 1989. Geological Survey of Canada radiocarbon dates XXVIII: Geological Survey of Canada Paper 88-7, p. 44, <https://emrlibrary.gov.yk.ca/gsc/papers/88-7.pdf>.
- Souther, J.G., 1980, Geothermal reconnaissance in the central Garibaldi Belt, British Columbia:; in Current Research, Part A: Geological Survey of Canada, Paper 80-1A, p. 1–11.
- Sherrod, D.R., Hagstrum, J.T., McGeehin, J.P., Champion, D.E., and Trusdell, F.A., 2006, Distribution, ¹⁴C chronology, and paleomagnetism of latest Pleistocene and Holocene lava flows at Haleakalā volcano, Island of Maui, Hawai‘i: a revision of lava flow hazard zones: Journal of Geophysics, Res. 111 B5 B05205 doi:10.1029/2005JB003876.
- Speranza, F., Branca, S., Coltelli, M., Caracciolo, F.D.A, and Vigliotti, L., 2006, How accurate is ‘paleomagnetic dating’? New evidence from historical lavas from Mount Etna: Journal of Geophysics, Res 111 B12S33 doi:10.1029/2006JB004496.
- Speranza, F., Pompilio, M., D’Ajello Caracciolo, F., and Sagnotti, L., 2008, Holocene eruptive history of the Stromboli volcano: constraints from paleomagnetic dating: Journal of Geophysics, Res 113 B9 doi:10.1029/2007JB005139.
- Speranza, F., Landi, P., D’Ajello Caracciolo, F., and Pignatelli, A., 2010, Paleomagnetic dating of the most recent silicic eruptive activity at Pantelleria (Strait of Sicily): Bulletin of Volcanology, v. 72 p. 874-858.
- Townsend, M., and Huber, C., 2020, A critical magma chamber size for volcanic eruptions: Geology, v. 48, p. 431–435, <https://doi.org/10.1130/G47045.1>.
- Williams-Jones, G., Barendregt, R.W., Russell, J.K., Le Moigne, Y., Enkin, R.J., and Gallo, R., 2020, The age of the Tseax volcanic eruption, British Columbia, Canada: Canadian Journal of Earth Sciences, v. 57, <https://cdnsiencepub.com/doi/10.1139/cjes-2019-0240>.
- Wilson, A.M., and Russell, J.K., 2018, Quaternary glaciovolcanism in the Canadian Cascade volcanic arc—Paleoenvironmental implications, in Poland, M., Garcia, M., Camp, V., and Grunder, A., eds., Field Volcanology: A Tribute to the Distinguished Career of Don Swanson: Geological Society of America Special Paper 538, p. 1–XXX, [https://doi.org/10.1130/2018.2538\(06\)](https://doi.org/10.1130/2018.2538(06)).
- Witter, J., 2019, South Meager geothermal project – new perspectives from recently unearthed data: Geoscience BC, Report 2019-07, p. 5, <http://www.geosciencebc.com/i/pdf/Report-2019-07-Innovate-Geothermal.pdf>.

Table 1. Paleomagnetic sites mapped and sampled during the 2020 field season. Each site produced N cores and each core label has a prefix CBB.

Site	Cores	N	Longitude	Latitude	Elev.	Location
AB10	101A-108A	8	49.973601	-123.149141	346.9	North of Chance Creek FSR
AB11	111A-118A	7	50.000234	-123.132984	398.9	McGuire FSR
AB12	121A-128A	6	50.000234	-123.132984	398.9	McGuire FSR
AB13	131A-138A	8	49.98629	-123.144838	386.9	Daisy Lake Channel
AB14	141A-148A	8	49.986693	-123.144584	365.4	Daisy Lake Channel
AB15	151A-158A	8	50.128865	-123.126047	747.2	Alexander Falls Turnoff
AB16	161A-168A	8	50.127408	-123.131499	713.3	Madeley Creek
AB17	171A-178A	8	49.975628	-123.152969	389.3	Lucille Lake North
AB18	181A-188A	8	49.984868	-123.146591	395.6	Shadow Lake
AB2	201A-208A	8	50.047178	-123.099842	496.8	Daisy Lake FSR
AB3	301A-308A	7	50.069344	-123.09364	506.8	BC Rail Quarry
AB4	401A-408A	8	50.061335	-123.112999	524.4	McGuire Transfer Station
AB5	501A-508A	8	50.069716	-123.094314	515.6	BC Rail Quarry
AB6	601A-608A	7	50.069344	-123.09364	506.8	BC Rail Quarry
AB7	701A-708A	7	50.069344	-123.09364	506.8	BC Rail Quarry
AB8	801A-808A	6	50.071166	-123.109156	575.3	Callaghan Valley Road
AB9	901A-908A	8	49.973601	-123.149141	346.9	North of Chance Creek FSR

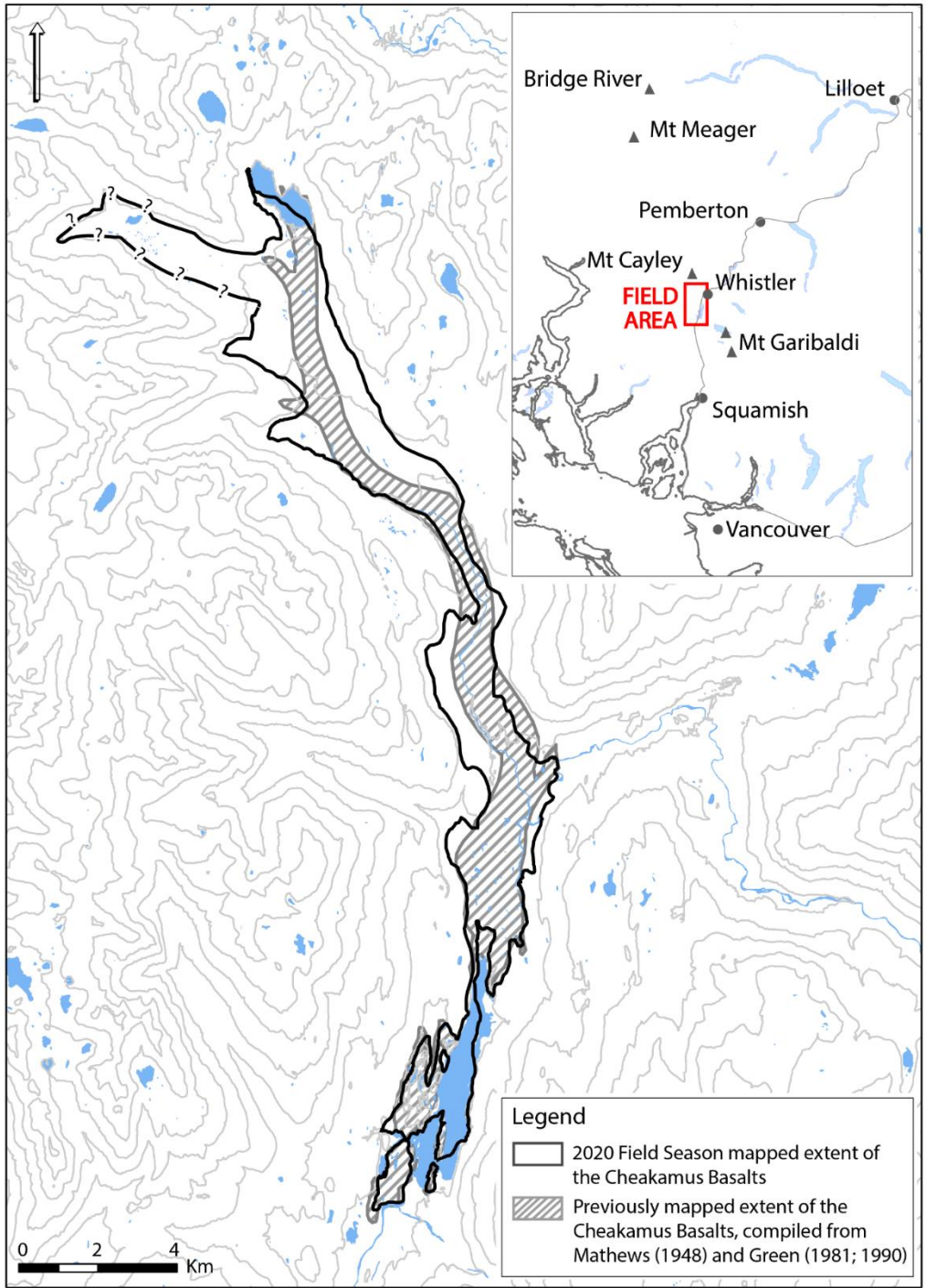


Figure 1. Field area location and extent of the Cheakamus basalts

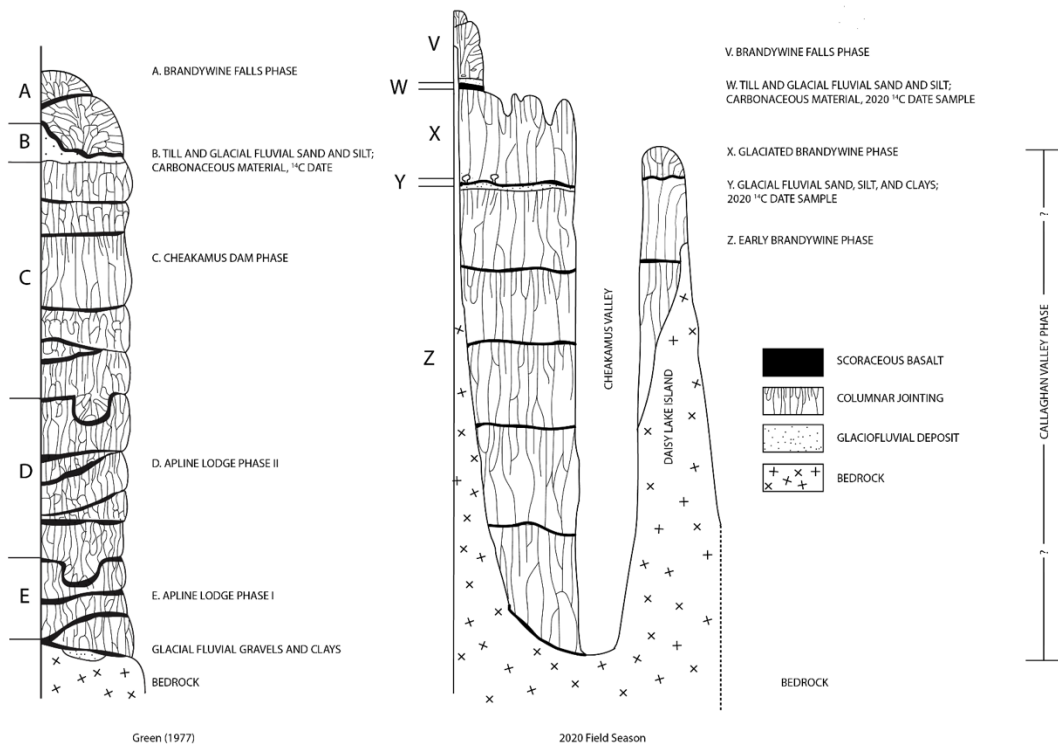


Figure 2. Comparison of Cheakamus basalt stratigraphy developed in the 2020 field season and Green's 1977 stratigraphic section.

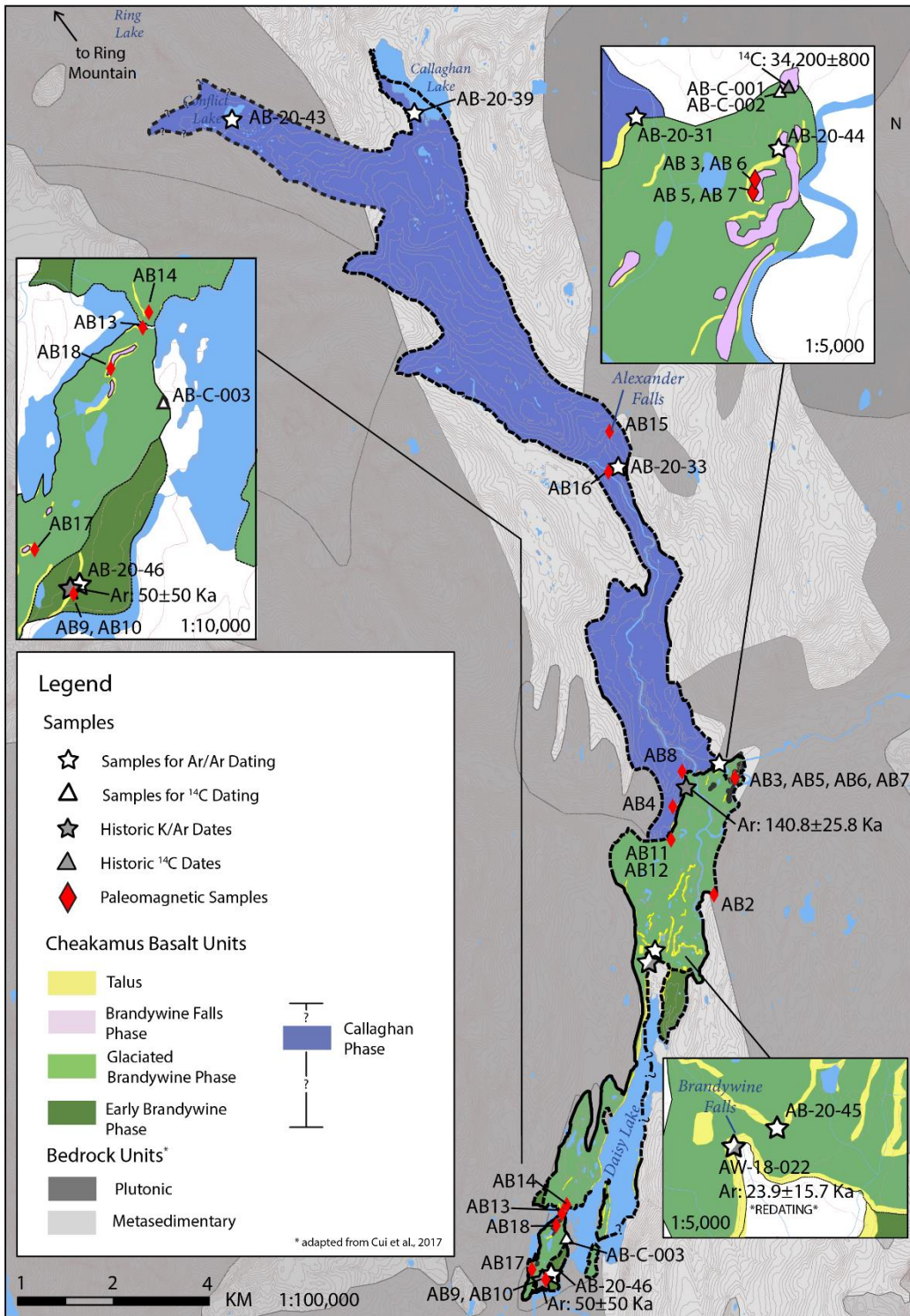


Figure 3. Volcanological map of the Cheakamus basalts with locations of samples used for radiometric dating and sites sampled for paleomagnetic study (see text).

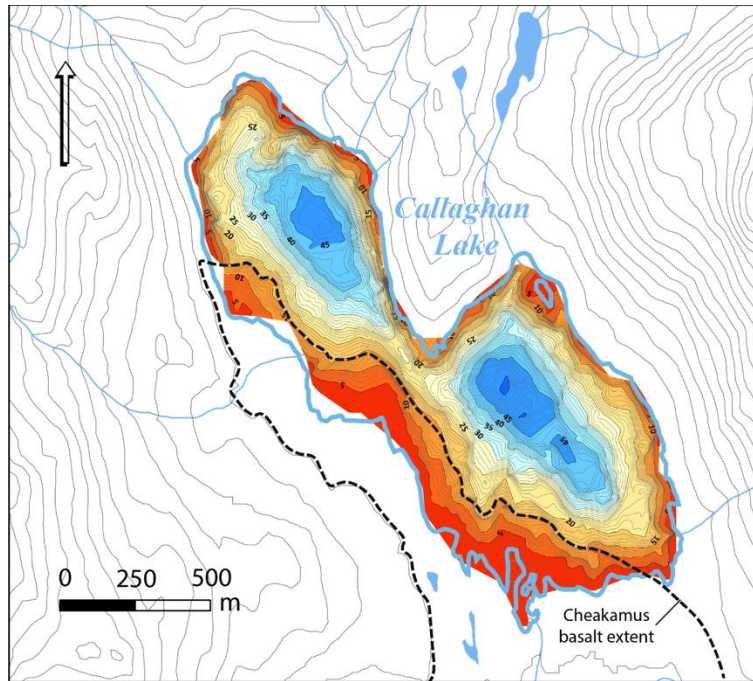


Figure 4. Bathymetric contour map (in m) developed from sonar data collected during the 2020 field season. A lobe of Cheakamus basalt extends into the lake from the southwest shore.

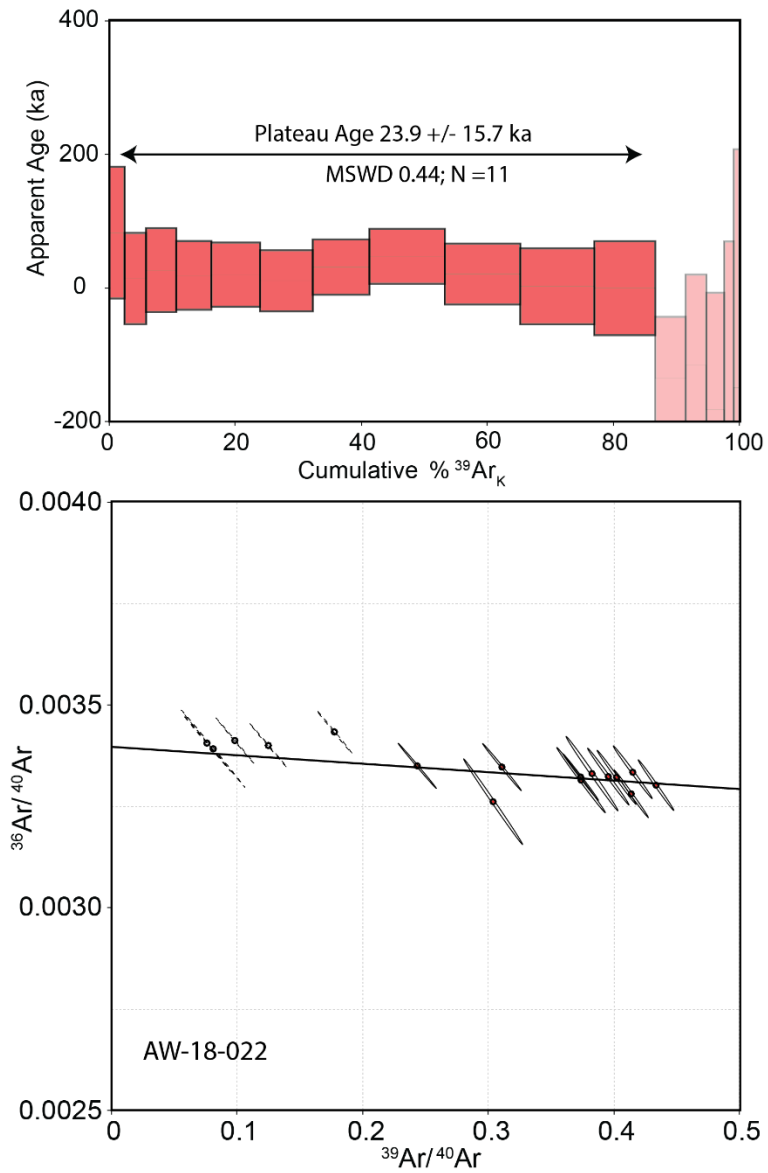


Figure 5. $^{40}\text{Ar}/^{39}\text{Ar}$ geochronometry for sample from the base of Brandywine Falls (AW-18-022). (A) Plateau diagram based on analysis of groundmass material; height of individual boxes equals 2σ errors. (B) Inverse isochron plot for showing all heating steps. Ellipses denote 2σ uncertainties.